

https://dspace.org/

Hydrothermal (CO) treatment of coal discards and sewage sludge for production of advanced materials

Kahilu, Gentil Mwengula

2024

https://hdl.handle.net/10539/37377

Downloaded from a DSpace repository. https://dspace.org/

HYDROTHERMAL (Co) TREATMENT OF COAL DISCARDS AND SEWAGE SLUDGE FOR PRODUCTION OF ADVANCED MATERIALS

Thesis submitted in partial fulfillment of the degree of Doctor of philosophy

Prepared by

Gentil Mwengula Kahilu (1902723)

Date: 28th of March 2023

School of Chemical and Metallurgical Engineering, Faculty of Engineering and the Built Environment, University of the Witwatersrand, Johannesburg, South Africa

Supervisor: Prof Jean Mulopo

Co-Supervisor: Prof Samson Bada

Keywords

Coal discards, sewage sludge, hydrothermal carbonization, hydrochars, carbon adsorbent, nevirapine, lamivudine, activated carbon, hydrogen storage.

Abstract

The disposal of coal discards (CD) and sewage sludge (SS) is a substantial problem to waste management in coal beneficiation and wastewater treatment plants (WWT). This work investigates essential aspects for contributing to the reduction of environmental effects, with a particular emphasis on the hydrothermal carbonization (HTC) technology for the synergetic treatment of CD and SS to produce value-added carbonaceous materials (CM). When compared to the individual treatment of CD and SS, the Co-hydrothermal carbonization (Co-HTC) method improved the physicochemical attributes of the produced hydrochars (HCs). The produced HCs could be suitable for a wide range of potential applications i.e., soil amendment, WWT, production of activated carbon (AC). The findings of this thesis indicate that profitable commodities may be made from the aforementioned waste materials, lowering the cost of waste disposal and ecological damage while also providing new green jobs. South Africa, as one of the world's top coal producers, creates approximately 60 million tons of coal waste each year, which is typically stockpiled in the form of a discard dump and slurry ponds. The environmental risk and public health risk posed by the presence of these wastes represent a significant impediment to the socioeconomic growth of the coal mining sector. As a result, waste coal management is advised to devise innovative approaches for the reuse and recovery of coal waste. In this thesis, the HTC and co-HTC of CD and CD-SS blend respectively has been experimentally performed for the upgrading of the fuel properties and adsorbent characteristics of the raw material utilized proving the ability of HTC to produce high-quality HCs from CD alone or in conjunction with SS as precursors for decontamination of polluted waters and energy storage.

The absorbent properties of the obtained HCs were evaluated in this study on the removal of nonbiodegradable pharmaceutical products dissolved in recycled water. The Co-HTC-derived hydrochar (HCB) had a high SBET of 20.35 m^2/g and pore volume of 0.38 cm^3/g, leading to significant adsorptive reductions of nevirapine (NEV) and lamivudine (LAM) (97.19% and 93.32%, respectively). The HC from coal tailing (HCT) and HC from coal slurry (HCS) displayed high NEV and LAM adsorption

capacities (50 mg g^{-1}, 42 mg g^{-1} and 52 mg g^{-1}, 41 mg g^{-1}) respectively despite being less effective than HCB (53.8 mg g^{-1}, 42.8 mg g^{-1}). In addition, the use of spent adsorption residues for energy storage applications was investigated further. The results revealed that the textural structure of the produced ACs electrode from the spent residues has a significant impact on the electric conductivity qualities. The produced ACs exhibited roughly rectangular cyclic voltammetry shape, good reversibility and stability as observed from the ideal electrical double-layer capacitors (EDLCs). These findings showed that spent adsorption residues are an effective CM precursor for the production of excellent EDLCs for current densities ranging from 1 A/g to 5 A/g in energy storage applications.

Furthermore, the synthesis of AC from the obtained HCs for adsorptive hydrogen storage was conducted. The hydrogen adsorption characteristics of the produced ACs were evaluated at 77 K and 293 K and 40 bars. The results indicate that the values of hydrogen adsorbed onto the ACs were approximatively 6.12wt%, 6.8wt% and 6.57 wt% for AC-HCT, AC-HCS and AC-HCB respectively at 35 bars implying that they could be used for hydrogen storage, sustainable carbon emissions management and provide viable pathways for cost-effective energy and material circular economies for both WWTPSs and the mining industry.

Table of Contents

Keywords i
Abstract ii
Table of Contents iv
List of Figures vii
List of Tables xi
List of Abbreviations xiii
Declaration xvii
List of publications xviii
Acknowledgements xix
Chapter 1: Introduction 1
1.1. Background 1
1.2. Context 6
1.3. Objectives and research questions 6
1.4. Significance, scope, and Definitions 7
1.5. Thesis outline 9
1.6. Summary 12
Chapter 2: Literature Review 15
2.1. Municipal and industrial wastes management 15
2.2. Wastewater treatment plant sludges 16
2.3. Coal beneficiation plant wastes 17
2.4. General treatment of sewage sludge and coal discards wastes 25
2.5. Hydrothermal carbonization treatment 32
2.6. Hydrothermal treatment of sewage sludge and coal discards 41
2.7. Production and characterization of activated carbon 60
2.8. Overview of adsorbed gas storage system 70
2.9. Hydrogen energy and economy 74
2.10. Summary and implications 87
References 88
Chapter 3: Research Methodology 101
3.1. Methodology and research design 101
3.2. Materials 107
3.3. Instruments 108
3.4. Analysis 110

3.5. Summary 127

Chapter 4. Physicochemical, structural analysis of coal discards (and sewage sludge) (co)-HTC derived biochar for a sustainable carbon economy and evaluation of the liquid by-product 131

4.1. Abstract 131

4.2. Introduction 132

4.3. Experimental method 135

4.4. Results and discussion 143

4.5. Conclusion 192

Chapter 5: Coal discards and sewage sludge derived-hydrochar for HIV antiretroviral pollutant removal from wastewater and spent adsorption residue evaluation for sustainable carbon management 199

5.1. Abstract 199

5.2. Introduction 200

5.3. Experimental method 203

5.4. Physicochemical and textural Analyses 206

5.5. Results and Discussion 207

5.6. Conclusion 238

Chapter 6: Systematic physicochemical characterization, carbon balance and cost of production analyses of activated carbons derived from (Co)-HTC of coal discards and sewage sludge for hydrogen storage applications 246

6.1. Overview 246

6.2. Introduction 247

6.3. Experimental method 249

6.4. Results and discussions 254

6.5. Conclusion 306

Chapter 7: Conclusions 315

7.1. Background of the study 315

7.2. Major findings and contribution to the body of knowledge 315

7.3. Recommendations for Future Research 318

Appendices 319

Appendix A . ANOVA results for Quadratic model of fixed carbon for coal tailing's hydrochar (HCT) 319

Appendix B . ANOVA for linear model of fixed carbon for coal slurry's hydrochar (HCS) 320

Appendix C ANOVA for Quadratic x Linear model of fixed carbon for the produced carbonaceous material (CM) from the mixture of coals (CT+CS) and sewage sludge (SS) 321

Appendix D . Process parameters constraints used for the optimization of the HTC 322

Appendix E . HCT desirability Solutions 323
Appendix F . HCS desirability Solutions 325
Appendix G . HCB desirability Solutions 327
Appendix H . Organic compounds in filtrate from NEV absorption by HCT 330
Appendix I . Organic compounds in filtrate from NEV absorption by HCS 332
Appendix J . Organic compounds in filtrate from LAM absorption by HCT 334
Appendix K . Organic compounds in filtrate from LAM absorption by HCS 337
Appendix L . ANOVA for quadratic model of S_{BET} for the AC-HCT 340
Appendix M . ANOVA for quadratic model of S_{BET} for the AC-HCS 341
Appendix N . ANOVA for quadratic model of S_{BET} for the AC-HCB 342
Appendix O . AC-HCT desirability Solutions 343
Appendix P . AC-HCS desirability Solutions 344
Appendix Q . AC-HCB desirability Solutions 346
Appendix R . Chemical activation models' confirmation results 347

List of Figures

Figure 2-1: Processing in a wastewater treatment plant.....17

Figure 2-2: Mechanized mining in action.....17

Figure 2-3:Typical Coal beneficiation process (Olga Krelin Design Associates).....19

Figure 2-4: (1) Self-heating of run -of-mine fines, (2) Aerial view of Mpumalanga Highveld coal discard stockpile in South Africa (Rights, 2015).....20

Figure 2-5: Spontaneous combustion of coal waste heap.....25

Figure 2-6:General structure of biomass.....35

Figure 2-7: Simplified reaction pathways for hydrothermal carbonization of sewage sludge.....43

Figure 3-1: Flow sheet of the experimental procedures.....102

Figure 3-2: Images of raw materials.....108

Figure 3-3:Image of hydrothermal experiment set up.....109

Figure 3-4: Activated Carbon Preparation equipment.....110

Figure 3-5: Micrometrics Accupyc II 1340 Pycnometer.....115

Figure 3-6: Quatachrome instruments, Autosorb IQ.....116

Figure 3-7:Carl Sigma Field Emission Scanning Electron Microscope equipped with an Oxford X-act EDS detector.....120

Figure 3-8:Image of Particulate Systems High Pressure Volumetric Analyzer (HPVA-200).....121

Figure 3-9:Sample Analysis Compartment.....123

Figure 3-10:HPVA II System Experiment Definition Window.....123

Figure 3-11: ICP-OES to analyse the samples.....125

Figure 3-12 :Thermo Scientific Flash EA 1112 Elemental Analyser.....126

Figure. 4-1. collected waste coal slurry (A), waste coal tailing (B) and sewage sludge sample (C).....136

Figure 4-2: HTC and Co-HTC experimental methodology.....138

Figure 4-3: Raw samples XRD pattern.....145

Figure 4-4:FTIR spectrum of raw samples.....147

Figure 4-5:Surface plot showing the influence of temperature and pressure on fixed carbon (left) and Ash content (right) of Coal tailing's HC.....155

Figure 4-6:Surface plot showing the influence of temperature and pressure on fixed carbon (left) and Ash content (right) of Coal slurry's HC.....155

Figure 4-7:Surface plot showing the influence of temperature and pressure on fixed carbon (left) and Ash content (right) of the mixture of Sewage sludge and Coals....156

Figure 4-8:Predicted vs Actual plots of the Fixed Carbon of produced HCs from Coal tailing's HCT (left) and Coal slurry's HCS (right)……158

Figure 4-9:Predicted vs Actual plots of the Fixed Carbon of produced HCs from the mixture of coals (CT+CS) and sewage sludge (SS)……159

Figure 4-10:Van-Krevelen diagram for untreated, HTC, and Co-HTC hydrochar……166

Figure 4-11:HTC, and Co-HTC process mass balance……168

Figure 4-12:XRD patterns of coal, sewage sludge and produced hydrochar (A) and FTIR spectra of coals, sewage sludge and produced hydrochar (B)……174

Figure 4-13:SEM images (a, c) and EDX elemental spectrums (b, d) of coal tailing (up), and coal tailing's hydrochar (down)……175

Figure 4-14:SEM images (a, c) and EDX elemental spectrums (b, d) of coal slurry (up), and coal slurry's hydrochar (down)……176

Figure 4-15:SEM images (a, c) and EDX elemental spectrums (b, d) of the mixture of coals and sewage sludge blended in optimized ratio (1CT+1CS:0.4SS) (up), and the Co-HTC produced hydrochar (HCB) (down)……177

Figure 4-16 :Isothermal adsorption plots of and Co-HTC hydrochar……178

Figure 4-17:ICP-OES analysis results of LCT: HTC liquid phase from Coal tailing; LCS: HTC liquid phase from coal slurry and LCB: HTC liquid phase from the blending of coal and sewage sludge……188

Figure 5-1:collected waste CS (A), waste CT (B) and sewage sludge sample (C)……204

Figure 5-2: Surface plot showing the influence of temperature and pressure on the Fixed Carbon of Coal tailing's HC (A) and Coal slurry's HC (B)…… 209

Figure 5-3:Surface plot showing the influence of temperature, pressure, time and the (CT+CS): SS ratio on the Fixed Carbon of produced hydrochar……209

Figure 5-4 :Percentage variation of LAM and NEV into the produced hydrochars versus the concentration of adsorbent (a) and residence time (b)……213

Figure 5-5: Isothermal adsorption plots of raw materials produced hydrochar and spent adsorption residues……220

Figure 5-6:SEM images and EDS elemental spectrums of coal tailing's hydrochar (HCT) and spent residues from nevirapine (HCT-NEV) and lamivudine (HCT-LAM) absorption ……222

Figure 5-7:SEM images and EDS elemental spectrums of coal slurry's hydrochar (HCS) and spent residues from nevirapine (HCS-NEV) and lamivudine (HCS-LAM) absorption ……223

Figure 5-8:SEM images and EDS elemental spectrums of coals and sewage sludge blend's hydrochar (HCB) and spent residues from nevirapine (HCB-NEV) and lamivudine (HCB-LAM) absorption……223

Figure 5-9:Absorbance spectra of nevirapine (A) and lamivudine (B). Source: Forensic Spectral Research John Wiley &Sons, Inc……225

Figure 5-10:Absorbance spectra of nevirapine and lamivudine on the coal tailing's hydrochar (HCT)……226

Figure 5-11:Absorbance spectra of nevirapine and lamivudine on the coal slurry's hydrochar (HCS)……226

Figure 5-12:. Absorbance spectra of nevirapine and lamivudine on the hydrochar from the blend (HCB) of CD and sewage sludge (SS)……227

Figure 5-13:FTIR profile of chemically activated spent hydrochar residues from nevirapine and lamivudine adsorption tests using HCT (a) and HCS (b)……231

Figure 5-14:FTIR profile of chemically activated spent hydrochar residues from nevirapine and lamivudine adsorption tests using HCB……232

Figure 5-15:SEM images of ACs obtained using spent hydrochar residues from nevirapine and lamivudine adsorption tests……234

Figure 5-16:(a) Cyclic voltammetry curves @ 100 mV/s (b) and Specific capacitance results from greatest common divisor (GCD) of ACs from spent adsorptions residues (HCT-NEV: A1, HCT-LAM: A2, HCS-NEV: B1, HCS-LAM: B2, HCB-NEV:C1 and HCT-LAM:C2)……236

Figure 5-17:Electrochemical impedance spectroscopy (EIS) of the ACs from spent adsorptions residues (HCT-NEV: A1, HCT-LAM: A2, HCS-NEV: B1, HCS-LAM: B2, HCB-NEV:C1 and HCT-LAM:C2) ……238

Figure 6-1:Activated Carbon Preparation equipment……250

Figure 6-2:Flowsheet of the experimental procedures……252

Figure 6-4:SEM images and EDX elemental spectrums respectively of coal tailing (a & c), and coal tailing's hydrochar (b & d)……261

Figure 6-5:SEM images and EDX elemental spectrums respectively of coal slurry (a & c), and coal slurry's hydrochar (b & d)……261

Figure 6-6 :SEM images and EDX elemental spectrums respectively of the mixture of coals and sewage sludge blended in optimized ratio (1CT+1CS:0.4SS) (a & c), and the Co-HTC produced hydrochar (HCB) (b & d)……262

Figure 6-7 :Surface plot showing the influence of temperature and Activation time on surface area of the produced Activated carbon from HCT (left) and HCS (right)…… 267

Figure 6-8 :Surface plot showing the influence of activation temperature and residence time on surface area of the produced Activated carbon form HCB……267

Figure 6-9:Predicted vs Actual plots of the Specific surface area of produced Activated carbons from Coal tailing's HC (left) and Coal slurry's HCs (right)……268

Figure 6-10 :Predicted vs Actual plots of the Specific surface area of produced Activated carbons from Coal discards and sewage sludge blend 's HC (AC-HCB)…..268

Figure 6-11:Nitrogen adsorption isotherms (A) and surface area plots (B)of produced activated carbons…… 277

Figure 6-12:Pore size distribution of produced activated carbons obtained from the NLDFT (A) and BJH (B) methods……281

Figure 6-13: SEM images &EDS spectrums and result of AC-HCS (a-c), AC-HCT (d-f) and AC-HCB (g-i)……282

Figure 6-14: FTIR spectra (A) and XRD pattens(B) of produced activated carbons…284

Figure 6-15: Diffractogram profile changes from CT (a), CS (b) and SS (c) through HCT(d), HCS (e) and HCB (f) to AC-HTC(g); AC-HCS (h) and AC-HCB (i)…….. 285

Figure 6-16:Hydrogen isotherms at (A) 77 K and (B) 273 K for the produced ACs. Filled and empty symbols correspond to adsorption and desorption data, respectively…. 292

Figure 6-17:Hydrogen isotherms at (A) 77 K versus relative pressure (P/P0) for the produced ACs……. 292

Figure 6-18:Hydrogen isotherms at (A) 77 K and (B) 273 K in wt% versus relative pressure (P/P0) for the produced ACs. Filled and empty symbols correspond to adsorption and desorption data, respectively.……293

Figure 6-19:Process mass balance……296

Figure 6-20:Proposed process configuration for the manufacture of AC……297

List of Tables

Table 2-1. Energy application of different sewage sludge……28
Table 2-2. Yield of solid, liquid and gas for different HTC experiments……37
Table 2-3. Effect of HTC on some of the mechanical properties of biomass……39
Table 2-4. HPLC analysis of liquid products for different feeds……40
Table 2-5. Effect of HTC on several feed stock……50
Table 2-6. Comparison of operational parameters and product distribution for thermal carbonization…… 59
Table 2-7. Comparison of some selected energy contents of fuels……76
Table 2-8. The six main hydrogen storage methods and procedures……79
Table 3-1. Hydrothermal carbonization (HTC) Design matrix……104
Table 3-2. Co-Hydrothermal carbonization (Co-HTC) Design matrix……105
Table 3-3. Chemical activation design matrix……107
Table 4-1. Physicochemical analysis results……143
Table 4-2. XRF results of raw materials……148
Table 4-3. Physicochemical analysis results of produced HC from Coal tailing (CT)……149
Table 4-4. Physicochemical analysis results of produced HC from Coal slurry (CS)..150
Table 4-5. Physicochemical results of HC from mixture of CD and SS……152
Table 4-6. Hydrothermal carbonization models' confirmation results……160
Table 4-7. Hydrothermal carbonization and Co-Hydrothermal carbonization optimum operating conditions……161
Table 4-8.Physicochemical properties of produced hydrochar……165
Table 4-9.BET analysis results of the coals, produced HCs and AC……179
Table 4-10:XRF results of HC products……182
Table 4-11:Comparison of hydrochar synthesised in this work with literature values183
Table 4-12.Identification and concentration of organic compounds in PW……190
Table 4-13.Total Carbon and Total organic carbon……191
Table 5-1. Hydrothermal carbonization and Co- Hydrothermal carbonization optimum operating solutions…… 210
Table 5-2. Experimental results of NEV and LAM adsorption on the produced hydrochars …… 212
Table 5-3.Organic compounds in filtrate from NEV adsorption by HCB……215
Table 5-4.Organic compounds in filtrate from LAM adsorption by HCB……217

Table 5-5.Physicochemical properties of wastes precursors produced hydrochar and spent residues from NEV and LAM adsorption……221

Table 5-6. Absorbents reported for the removal of ARVDs and other pharmaceutical products in different water matrices……228

Table 5-7.BET analysis results of the synthesized ACs using spent hydrochar residues from nevirapine and lamivudine adsorption tests……234

Table 6-1. Proximate and ultimate analysis results of HTC process versus temperature variation……..255

Table 6-2. Proximate and ultimate analysis results of HTC process versus pressure variation……256

Table 6-3. BET analysis results of the produced activated carbons from HCT and HCS……264

Table 6-4. BET analysis results of the produced activated carbon from HCB……265

Table 6-5. Parameters constraints used for the optimization of the activation process…… 269

Table 6-6. Chemical activation optimum solutions……270

Table 6-7. BET analysis results of the coals, produced HCs and AC……273

Table 6-8. Textural properties of the produced AC from other coals sources……274

Table 6-9.Physicochemical properties of coal, produced hydrochars and activated carbons……276

Table 6-10.Physical and structural properties of the produced activated carbons… 278

Table 6-11. Hydrogen Uptake Capacities of selected ACs……295

Table 6-12. Production costs estimation of synthesized ACs……298

Table 6-13. Preliminary estimation of capitals of investment……299

Table 6-14. Components of investment cost……300

Table 6-15. Evaluation of the production costs of coal discard and sewage-based activated carbon (ACs) compared to the production cost of some coal and sewage wastes based ACs together with details on the production methods, surface area and AC production yield……302

Table 6-16. Calculation of Carbon Emission for synthesized ACs from HCT, HCS and HCB……306

List of Abbreviations

A	: Ash content
AC	: Activated carbons
AD:	: Anaerobic digestion
ANOVA	: Analysis of variance
ART	: Antiretroviral therapy
ARV	: Antiretroviral
ATR	: Attenuated total reflectance
BET	: Brunauer Emmet Teller
BOD	: Biological Oxygen Demand
BSE	: Backscattered electrons
CAGR	: Compound annual growth rate
CB	: Blend of coal discards and sewage sludge
CCD	: Central Composite Design
CCd	: Charge Coupled device
Cd	: Custom Design
CD	: Coal Discard
CFR	: Code of federal regulations
CM	: Carbonaceous material
COD	: Chemical Oxygen Demand
CS	: Coal Slurry
CT	: Coal Tailing
CV	: Calorific Value (MJ/kg)
CY	: Carbonization yield
DA	: Diode Array
DNA	: Deoxyribonucleic acid
DO	: Dissolved Oxygen
DOE	: Design of experiments
EDLC	: Electrical double-layer capacitors
EDS	: Electron Detector Spectrometer

ECL : Environmental critical level

EIS : Electrochemical impedance spectroscopy

EPA : Environmental protection agency

ERWAT : Ekurhuleni Water Care Company

FC : Fixed carbon

FCI : Fixed capital of investment

FCS : Filtrate from HCS

FCT : Filtrate from HCT

FTC : Emtricitabine

FTIR : Fourier Transform Infra-Red

GC : Gas chromatograph

GCB : Gas from HCB

GCD : Greatest common divisor

GCS : Gas from HCS

GCT : Gas from HCT

GHG : Greenhouse gases

GIS : Geographic information system

GSM : Global System for Mobile Communications GPRS

GPRS : General Packet Radio Services

H/C : Atomic ratio of hydrogen to carbon

HBV : Hepatitis B virus

HC : Hydrochar

HCB : Hydrochar from the Blend of coal discards and sewage sludge

HCS : Hydrochar from Coal Slurry

HCT : Hydrochar from Coal Tailing

HHV : Higher heating value (MJ/kg)

HPLC : High performance liquid chromatography

HTC : Hydrothermal carbonization

HTG: : Hydrothermal gasification

HTL: : Hydrothermal liquefaction

I : Investment cost (USD)

IC : Ion Chromatography

ICP : Inductively coupled plasma

KOH : Potassium hydroxide

LAM : Lamivudine

LCA : Life cycle assessment

LCB : Liquid phase from HTC of the blend coal discard and sewage sludge

LCS : Liquid phase from HTC of Coal Slurry

LCT : Liquid phase from HTC of Coal Tailing

M : Inherent Moisture

MS : Mass spectrometry

MY : Mass yield

NEV : Nevirapine

NNRTI : Non-nucleoside reverse transcriptase inhibitor

NRTI : Nucleotide reverse transcriptase inhibitors

O/C: : Atomic ratio of oxygen to carbon

O/C: : Atomic ratio of oxygen to carbon

OCM : Optimal Combined Design

POA : Percentage of Absolute Error

PW : Process water

Q: : Rate of heat transfer (W)

R. F : Radio frequency

RFI : Radio frequency identification

r: : Radius (m)

R: : Universal gas constant (8.314 J/mol.K)

RI : Refractive Index

RNA : Ribonucleic acid

RSM : Response Surface Methodology

SEM : Scanning electron microscope

SS : Sewage sludge

SW : Solid waste

T: : Temperature (K)

t: : Time

TC : Total Carbon
TCD : Thermal Conductivity Detector
TCI : Total capital of investment
TGA : Thermo-gravimetric analysis
TIC : Total Inorganic Carbon
TOC : Total Organic Carbon
USD : United state dollars
UV: : Ultraviolet
VM : Volatile matter
WC : Working capital
WC : Water content
WD : Working distance
WHO : World Health Organization
WW : Wastewater
WWTP : Wastewater treatment plant
XRD : X-Ray Diffraction
XRF : X-RAY Fluorescence
ZAR : South African rand

Declaration

The work contained in this thesis has not been previously submitted to meet requirements for an award at this or any other higher education institution. To the best of my knowledge and belief, the thesis contains no material previously published or written by another person except where due reference is made.

Signature: 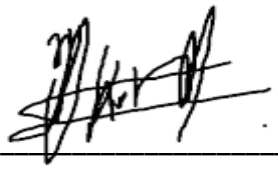

Date: 28/03/2023

List of publications

1. Kahilu, G. M., Bada, S., & Mulopo, J. (2022). Physicochemical, structural analysis of coal discards (and sewage sludge) (co)-HTC derived biochar for a sustainable carbon economy and evaluation of the liquid by-product. *Sci Rep*, *12*(1). https://doi.org/10.1038/s41598-022-22528-y

2. Kahilu, G. M., Bada, S., & Mulopo, J. (2022a). Coal Discards and Sewage Sludge Derived-Hydrochar for HIV Antiretroviral Pollutant Removal from Wastewater and Spent Adsorption Residue Evaluation for Sustainable Carbon Management. *Sustainability*, *14*(22), 15113. https://doi.org/10.3390/su142215113

Acknowledgements

My gratitude will firstly be addressed to the Almighty God, for His mercy, His protection and his tremendous grace upon my life which supported me all along and made me able to complete this research.

I would like to commend the enormous contribution of my principal supervisor, Professor Jean Mulopo, whose insightful comments, suggestions, encouragement, and constructive directions have sharpened this study.

I am also grateful to my Co-Supervisor, Prof. Samson Bada for his invaluable contribution to the success of this study.

I would like to express my gratitude the Coaltech Research Association of South Africa for funding this research and the Clean Coal Research Group for the technical participation.

I wish to extend my appreciation to Mr. Motlatsi Phali, Mr. Bruce Mothibedi, Miss Ntokozo Dube, Mrs. Reghana Burns and Miss Sibongile Maswanganye for their contribution to the successful completion of this study.

I would like to thank the National Research Foundation of South Africa's SARChI Clean Coal Technology Grant (Grant Number: 86421) for their financial support for this project.

Last but not least, my deepest gratitude to my parents Fidel Kahilu and Besa Musonda, my wife Dinah Mbuyu Kahilu, my daughter Geliana Besa Kahilu and all family for their understanding, kindness, and encouragement during my study.

Chapter 1: Introduction

This chapter highlights on key aspects related to environmental changes caused by waste coals and waste sewage sludge, as well as current waste management systems and potential improved treatment approaches. The first part (1.1) establishes the conceptual milestones of the study, while the second (1.2) directs the framework of the research in the area of interest and leads to the anticipated objectives set up (1.3) for experimental tasks carried out in this work. Section 1.4 outlines the research's background and importance, as well as the methodologies employed. Finally, section 1.5 examines and summarizes the remaining chapters of the thesis.

1.1. Background

This study is part of an effort to generate novel inexpensive carbonaceous materials that are both environmentally benign and nontoxic. A revived interest in the synthesis of activated carbon from biomass wastes has resulted from the rising need for improved adsorbent materials for different environmental remediation procedures. The economic potential of the simple and direct synthesis of activated carbon (AC) from sewage sludge (SS), a plentiful and renewable resource, is substantial. SS comprises a variety of organic and inorganic components, and the carbon content of sewage sludge makes it an ideal precursor for producing carbonaceous materials (Aliakbari *et al*., 2018). Carbon technologies have seen rapid growth in recent two decades due to 1) the introduction of new synthetic techniques such as pyrolysis, high-voltage-arc discharge, chemical vapor deposition, hydrothermal carbonization, and laser ablation approach to prepare amorphous or crystalline nanostructured carbon materials with different sizes, shapes, and chemical compositions; 2) the requirement for carbon-neutral alternatives because of environmental concerns (Bi *et al*., 2019). In this regard biomass materials represent an opportunity because of their high availability and environmentally friendly renewable nature (Maqhuzu *et al*., 2019). In parallel, during the past few decades hydrothermal carbonization (HTC) has shown high potential among other techniques in producing tailored carbon structures for a wide range of applications

(Hu *et al*., 2010). The advantage of hydrothermal processing over conventional thermal treatments is that it can directly process liquid and slurry waste materials thus avoiding the need for an energy-intensive dewatering step (Munir *et al*., 2018).

Hydrothermal processing has been seen as a viable method for dealing with biomass wastes, though essential information on mass transport throughout the process have not yet been well defined for modelling and practical applications (Heidari *et al*., 2018). Although there have been a number of lab-scale advancements in HTC, the inadequacy of kinetics and heat transfer reaction models necessitates more research for HTC's commercialization (Wilk *et al*., 2019).

In particular, the use of the HTC method in changing CD-SS blends into advanced carbon materials offers a unique possibility for a variety of applications due to its low energy cost and environmentally favorable characteristics.

The most significant disadvantage of the HTC application is the absence of kinetics data and heat transfer for the many reactions involved in this process for the several raw materials evaluated (Krylova *et al*., 2018). Previously, modelling of the HTC process assumed that the temperature and residence time remain constant throughout the process (Heidari *et al*., 2018). This approach hinders the ability to evaluate the energy involved in a process and the process's overall energy balance. Consequently, the masse balance equation and the description of the stochiometric transformation of the raw material used in the HTC process might provide substantial insights into its kinetics and thermodynamic modelling for the industrial application.

South Africa (SA) is one of the world's greatest coal producers and exploits coal as its primary energy source (Bohlmann *et al*., 2018) and generate about 65 million tons of CD yearly which are disposed of in tailings piles and slurry dams (Van de Venter *et al*., 2021). Due to the potential solubilization of harmful contaminants (sulfur, mercury, phosphorus, etc.) and the possibility of spontaneous combustion, the disposal of CD is seen as a severe threat to the country's waste management system (Mills, 2018). Despite the fact that finding a solution might be expensive and challenging, the accountability and appropriation compensation seems to be difficult since the prior coal mining owners responsible for coal discards wastes cannot be often located and the responsible mining companies often no longer exist (Taha *et*

al., 2018). Even though some companies have been replaced by legal successors who continue to operate them, their prior waste repository histories are not always documented (Keefer *et al*., 2020).

Beneficiation technologies, such as physico-chemical processes and regeneration techniques, have evolved throughout time, however, they are regarded as inefficient, not ecologically friendly, difficult, and costly (Petlovanyi *et al*., 2018). As a consequence, additional waste is generated yearly and added to existing stockpiles, posing the aforementioned environmental dangers (Stolboushkin *et al*., 2016). Conversely, South African Wastewater Treatment Plants (SA WWTP) generate considerable quantities of sewage SS (Grobelak *et al*., 2019).

Over the last two decades, South Africa's population has expanded significantly, from 48.8 million in 2005 to 51.58 million in 2010 to 57.7 million in 2018, with more than half of the population now living and working in densely populated metropolitan districts (Asvat *et al*., 2018). This fast population development and increasing urbanization have placed extra stress on existing WWTP infrastructure, resulting in a rise in SS generation at these facilities (Khanam *et al*., 2022). The SS includes a number of organic and inorganic contaminants that are regarded to be the cause of diseases (asthma, pneumonia) in persons living in close proximity to discarded stockpiles (Aliakbari *et al*., 2018). Current SS management techniques, such as on-site landfilling and waste dumping, are deemed unsustainable (Shaddel *et al*., 2019). Multiple lines of data suggest that landfilling SS is not a viable method for managing SS (Meisel *et al*., 2019). Despite the risk for soil and subsoil contamination, over 80% of wastewater treatment facilities continue to dispose of SS in designated areas (Kacprzak, *et al*., 2017). The demand for innovative solutions to reduce SS waste has become a social and environmental priority.

Additionally, according to the World Health Organization (WHO) Global Health Observatory, 70% of the estimated 36.7 million people living with HIV/AIDS worldwide at the end of 2016 were from Africa (Del Rio, 2017). In 2016, an estimated 19.8 million persons used ARV treatment. South Africa's antiretroviral treatment (ART) program is the biggest in the world, with an estimated 3.9 million individuals getting ARVs, representing around 24% of the worldwide ART program. ARVs are used to treat and prevent several viral illnesses, such as HIV, influenza, hepatitis, and

herpes (Tompa et al., 2021). In South Africa, they are mostly used for HIV/AIDS treatment. South Africa is the country that utilizes the most antiretroviral medications per capita. According to the World Health Organization (WHO), around 2,150,800 people received ARVs in South Africa in 2012. Comparatively, around 199 000 people in Eastern Europe received ARV treatment (WHO, 2013). Even though several studies have shown that ARVs are transformed during wastewater treatment, little study or reporting has been conducted on the occurrence of ARVs, their transformation products, or their removal in wastewater (Reddy *et al*., 2021). In addition, antiviral drugs have the potential to cause the development of disease-resistant strains in people and animals, which is a source of concern (Looi *et al*., 2018). With the high prevalence of HIV/AIDS in South Africa, it is possible that a rising amount of antiretroviral drugs are eluding the WWTP systems and entering the water networks.

This research focuses on two antiretroviral drugs: I Nevirapine (NVP), an oral drug used to treat and prevent retroviral infections, especially those caused by human immunodeficiency virus type 1; and ii) efavirenz (EFV), an injectable antiretroviral drug. (HIV-1). HIV-1 is a virus that infects CD4-T cells, which are immune system cells, most often. HIV-1 antiretroviral treatment, on the other hand, neither cures nor eradicates the virus; instead, it inhibits or delays its reproduction (Deeks *et al*., 2018). It is often administered with other ARV medications. Nevirapine is a non-nucleoside reverse transcriptase inhibitor (NNRTI) antiretroviral drug (ARVD) that is often used to prevent HIV transmission to the foetus. The nucleoside/nucleotide reverse transcriptase inhibitors (NRTIs) prevent the HIV viral RNA's reverse transcription into its DNA, which is a prerequisite for the virus to integrate into the host cell. This is achieved by inhibiting the viral enzyme reverse transcriptase, which is responsible for carrying out this action. It is eliminated in urine at a rate of 2.7% after ingestion (Schoeman *et al*., 2017), Lamivudine (3TC) is a nucleoside reverse transcriptase inhibitor (NRTI) of the first generation that was approved in 1995 for the treatment of HIV-1 and hepatitis B virus (HBV) infections. EPIVIR (2013); EPIVIR-HBV (2016) The World Health Organization (WHO) has advised HIV treatment regimens since 2002, and 3TC or emtricitabine (FTC) are nearly usually the preferred components of fixed-dose combinations (WHO, 2016). Using HPLC/MS, just one study determined its concentration in water, which was less than ngL-1 (Prejean *et al*., 2011).

Consequently, this research highlights the potential development of sustainable and effective treatment technologies for the removal of ARVs or their transformed derivatives from recycled water in order to prevent their entry into the environment and, thus, reduce their impact on water quality and human/animal health. Several studies have shown the effectiveness of adsorption in removing pharmaceutical pollutants from water (Silva *et al*., 2018; Sousa *et al*., 2022). In contrast to adsorbents such as clays, metal oxides, polymeric resins, and chitosan, carbon-based compounds have shown a considerable adsorption yield (Xiang *et al*., 2019). Due to their great availability, cheap cost, suitability for carbonization and large surface area of carbon-based materials, CD and SS wastes might serve as possible precursors for the production of carbon-based adsorbents such as HCs (Maqhuzu *et al*., 2019).

Jordá-Beneyto *et al*. (2007) carried out a study using AC at 77 K and 4 MPa and found that 6.5 wt% of hydrogen may be stored per gram of specified AC. Further, Jordá-Beneyto *et al*. (2007) reported that AC with a minimum specific surface (S_{BET}) and pore diameter of 1000 m^2/g and 2 nm-3.5 nm (10^{-9} m) may be employed to store hydrogen.

In addition, studies conducted to produce a proper adsorbent with a high storage capacity and lower AG system costs indicated that AC from coal has a minimum storage volume capacity of 54 v/v (Alhasan *et al*., 2016) and that commercial AC could store the same volume of H_2 gas at a 6 times lower pressure than is necessary when using the CG system (Esteves *et al*., 2008).

This work first focuses on the synthesis of HCs from CD and SS, then examined their efficacy for adsorption of dissolved pharmaceutical contaminants (nevirapine and lamivudine) in wastewater and their implications for hydrogen storage. The findings may lead to the development of low-cost energy storage materials, increased energy security, clean water supply from wastewater and acid mine drainage (AMD), and sustainable coal beneficiation plant waste management, all of which are crucial to the mining industry.

1.2. Context

This research examines the potential of HTC for high-quality, low-cost AC synthesis. Studies on the application of HTC for the synthesis of ACs from coal discards and/or sewage sludge are still scarce (Munir *et al*., 2018; Wilk *et al*., 2019), and in particular the underlying intrinsic chemical mechanisms that occur throughout the HTC process are not yet thoroughly grasped (Heidari *et al*., 2018). This thesis focuses on the HTC development of AC from CD and/or SS for a) the removal of HIV drug pollutants from wastewaters, as previous studies have established that the removal of dissolved pharmaceutical product by adsorption onto a porous CM is an effective, versatile, and cost-effective method that does not produce by-products in treated waters (Sekulic *et al*., 2019); and b) for adsorptive H_2 storage.

1.3. Objectives and research questions

This work seeks to address the following questions:

- Are coal discards and sewage sludge suitable as raw material for hydrothermal or co-hydrothermal carbonization process and further production of activated carbon?
- Is hydrothermal or co-hydrothermal carbonization efficient for the improvement of coal discards and sewage sludge carbonaceous properties?
- What is the benefit of using hydrothermal carbonization (Co-) process than other thermal methods to produce carbonaceous materials?
- What is the impact of co-hydrothermal carbonization process on the properties of the produced carbonaceous materials?
- What is the potential of the produced hydrochars and activated carbons for hydrogen storage applications?

The objectives of this thesis are:

- Characterization of coal discards and sewage sludge used as raw materials in order to get the levels of the compounds that are presents in CD and SS,
- Assessment and optimization of hydrothermal carbonization (Co-) process of the coal discards and sewage sludge wastes for the production of hydrochars to get the depth of the substances that are formed after the processes,

- Characterization of the produced hydrochars for further activation procedure (moisture, ash, volatile matter, fixed carbon, crystallinity, elemental composition, morphology, porosity),
- Evaluation of hydrochars adsorption capacity for dissolved pharmaceutical product of wastewaters,
- Evaluation of electrochemical properties of activated carbons from pharmaceutical adsorption spent residues,
- Assessment of hydrogen storage onto the synthesized activated carbons from the produced hydrochars.

1.4. Significance, scope, and Definitions

HTC was used to enhance the physicochemical properties of coal tailing (CT), coal slurry (CS) and SS in order to produce AC, and other valuable CM. HTC is a thermochemical process that converts biomass to liquid organic compounds (furfural, phenol, etc.), trace amounts of gas, and a solid HC product. Through an additional heat treatment (chemical, physical, or combined activation) (Wüst *et al*., 2019), HC can be transformed into high-added-value materials such as AC. The HTC is an environmentally friendly method that reduces the need for an energy-intensive dewatering step compared to conventional thermal processes (Munir *et al*., 2018). HTC employs hot pressurized water as a reactant and catalyst to enhance the physicochemical properties of various raw materials. Studies have shown that HTC can successfully improve the fuel characteristics of the produced HC through HTC of low-carbon-content coal between 150°C and 270°C (Saveyn *et al*., 2009; Hoekman *et al*., 2011; Tasca *et al*., 2019; Zhang *et al*., 2022). In addition, Akbari *et al*. (2019) found that the high reactivity and non-polar solvent behavior of subcritical water decreased the values of undesirable impurities such as fraction of total ash, oxygen, and sulphur while increasing the carbon content. Akbari *et al*. (2019) found that the carbonization and mass yields of Co-HTC treatment of different coal-biomass mixtures were significantly more efficient than HTC treatment of coal and biomass separately. These findings indicate that the decomposition of biomass under the Co-HTC process produced an acidic environment that promotes the dissolution of the feedstock's mineral content.

The increasing global demand for energy has increased interest in the use of H_2 as energy carrier. Among various energy sources, H_2 deserves special consideration (Hamedi *et al*., 2014). It is not simple to supply H_2 to independent secondary consumers, such as cities, power plants, and housing clusters, due to the complexity and high capital cost of delivering hydrogen using current technology (Mulopo *et al*., 2019). The construction of large-scale compressor equipment, pipelines, and their maintenance requires a substantial amount of capital. Using H_2 as a vehicle fuel for clean combustion would alleviate the need for a substantial quantity of polluting petroleum. The current lower utilization of H_2 as an energy source is attributable to the costly storage system available, which requires high-pressure for its achievement (Alhasan *et al*., 2016). Moreover, the risk of transporting high-pressure gas cylinders hinders users. Despite the fact that some studies have been conducted on the improvement of H_2 storage technology, further work is still required (Züttel, 2007; Niaz *et al*., 2015; Wang *et al*., 2018). Multiple storage strategies have been investigated, with porous carbon materials, such as ACs, having a higher hydrogen absorption capacity than metal hybrids and complex hydrides. However, extensive research on the economics of producing ACs from waste for hydrogen energy and the carbon footprint of such systems is still lacking. The production of AC with a high H_2 adsorption capacity from low-cost precursors such as waste biomasses may facilitate the development of H_2 storage applications.

Additionally, the suitability of HCs as alternative adsorbents to conventional adsorbents for the removal of pollutants from wastewaters is also investigated, as is the production of ACs for electrochemical applications and hydrogen storage. Although AC adsorption has been implemented in drinking water treatment for a long time, it has only recently gained popularity for reducing micropollutant concentrations in WWTP discharges. Little research has been conducted on the removal of micropollutants from WWTP discharges, particularly ARV micropollutants. This is an additional motivation for this study, which aims to synthesize low-cost AC from sewage sludge and coal discards for the removal of ARVs micropollutants from WWTPs, thus contributing to the closure of the waste loop in WWTPs.

1.5. Thesis outline

This thesis is composed by 7 chapters including a general conclusion and recommendations for future research described as follow:

Chapter 1: Introduction

In this part of the thesis, the research title is elucidated and 5 main sections which are the overview (background) of the study, the problem statement (context), the objectives and the research questions (purposes), the significance of the research, and the structure of the thesis are brought in to introduce the project.

Chapter 2: Literature Review

There are 10 sections in this chapter which give an explained full literature review of different types of wastes, industrial and domestic (municipal) wastes managements, WWTP and SS generation and its possible applications, coal beneficiation plant wastes, available treatments of industrial wastes, HTC process, different types of biomasses, HCs characteristics and applications, carbon activation processes, the gas storage applications of AC and finally H_2 storage system.

Section 1: the section provided a description of different type of wastes, followed by principal waste management methods. Different sources of wastes are briefly presented

Section 2: in this section, WWTP and different sludge generated by the process and their possible reuse or recycling for environment protection are described. The section highlights previous research on SS treatment process, the economic benefit, the necessity of SS treatment and some scientific gapes.

Section 3: the section presents the significance of CD beneficiation on economic and environmental point of view. This section provided a review of past studies on the importance and different procedure of CD valorisation.

Section 4: In this section, the available treatments of industrial wastes are described. The section highlighted the comparison between procedures of wastes treatment. The relevant methods are discussed with recommendations.

Section 5: Definition and description of HTC process are given in this part following by the comparison between different thermal carbonization processes. The section also shows different research gapes on HTC application to be filled for projected industrial scale applications

Section 6: this part evaluates the HTC of SS and CD, the physicochemical characteristics and possible end uses of HCs produced from different carbon precursors and the impact of HTC parameters on the produced HCs. This section ends with a comparison between HTC and some other thermal carbonization process
Section 7: activation process methods of carbonaceous materials are well described in this section. Different applications of AC as an adsorbent are given and the potential of AC as future source for clean energy are described compared to the conventional fossil fuels source. AC adsorption principles are described in this section and required properties of adsorbent for H_2 storage system are defined,
Section 8: An overview of gas adsorption (AG) techniques is described. Different methods of gas storage and associated advantages are depicted in this section. Furthermore, a review of current knowledge on the developments of AG system is done
Section 9: Hydrogen storage techniques are presented in this section. The advantage of physisorption of hydrogen for his storage is highlighted. The economic benefit of hydrogen storage as potential energy producer is discussed.
Section 10: the section summarizes the whole chapter and gives the directions for future research

Chapter 3: Research methodology

This chapter describes different experimental approches used for raw materials and products physicochemical characterization, HTC process, and activation process. Details of different test, equipment, and procedures for the understanding of experimental methods are provided in this chapter.

The experimental approch is described as follow: sample preparation, and characterization test (moisture, elemental composition and morphological constitution), HTC experiments and HC products characterization (optimization and kinetics study) and HTC process efficiency estimation. In the experimental procedure, HC activation process will be conducted using an activation agent for production of AC. The characteristics of the produced AC will be determined and discussed (ultimate, total sulphur, morphology, surface area and pore volume analysis). Adsorption characteristics of the produced AC will be included in experimental running through measurement of isotherms of hydrogen adsorption.

Chapter 4: Physicochemical, structural analysis of CD (and SS) (Co)-HTC derived HCs for a sustainable carbon economy and evaluation of the liquid by-product

Physicochemical HCs data from CD and CD-SS blend are presented and discussed in this chapter. The carbonization technique used (HTC) is assessed and optimized. The produced HCs are analysed to determine the carbon content and morphology structure compared to the raw material. To evaluate the nitrogen adsorption capacity, the crystallinity, and the chemical functional group of the produced HCs in this chapter, results from BET, XRD analysis have been presented and discussed. The HTC and Co-HTC process mass balance and carbonization yields are calculated and provided to assess the impact of different parameters on the chemical transformation of the raw materials. In chapter the HTC and Co-HTC liquid by-products were chemically characterized for a possible recycling and/or disposal in the waterbodies.

Chapter 5: CD and SS derived HCs for HIV antiretroviral pollutant removal from WW and spent adsorption residue evaluation for sustainable carbon management

In this chapter, the capacity of the produced HCs for two pharmaceutical products removal from water was assessed as environmental application of HTC process. The physicochemical description of adsorption process is described. The characterization of filtrate and spent residue was performed to evaluate the adsorption capacity of the HCs. The adsorption spent residues were chemically activated using KOH and evaluated for electrochemical applications.

Chapter 6: Adsorption properties of hydrogen onto ACs from CD and SS derived HCs

In this chapter, the physicochemical and textural properties of the produced AC from HCs were evaluated. The impact of different activation parameters and KOH: HCs ratios was highlighted. The adsorption isotherms analysis results, the impact of S_{BET}, pore size distribution, the pressure and the adsorption heat of H_2 onto the produced ACs are displayed and discussed.

Chapter 7: Conclusions and recommendations

This chapter presents major findings of the study and discussions based on experimental outcomes and simulation model. In this chapter the findings and further recommendations are provided. Furthermore, the contribution to knowledge in the crucial field of wastes treatment and circular economy is provided. This chapter

presents the economic benefits of wastes treatment for the production of value-added materials and recommendations for the industrial scale up feasibility.

1.6. Summary

The chapter one has presented the main objectives, motivation, focus and structure of the research thesis. The importance of South African CD and SS wastes treatment and beneficiation has been highlighted in this chapter for economic and environmental profit. In the next chapter, literature review of research matching the subject will be provided.

REFERENCES

1. Aliakbari, Z., Younesi, H., Ghoreyshi, A. A., Bahramifar, N., & Heidari, A. (2018). Production and characterization of sewage-sludge based activated carbons under different post-activation conditions. *Waste and biomass valorization*, *9*(3), 451-463.
2. Bi, P., Zhang, M., Li, S., Lu, H., Wang, H., Liang, X., Liang, H. and Zhang, Y., 2022. Ultra-sensitive and wide applicable strain sensor enabled by carbon nanofibers with dual alignment for human machine interfaces. *Nano Research*.
3. Maqhuzu, A.B., Yoshikawa, K. and Takahashi, F., 2020. Stochastic economic analysis of coal-alternative fuel production from municipal solid wastes employing hydrothermal carbonization in Zimbabwe. *Science of The Total Environment*, *716*, p.135337.
4. Hu, B., Wang, K., Wu, L., Yu, S.H., Antonietti, M. and Titirici, M.M., 2010. Engineering carbon materials from the hydrothermal carbonization process of biomass. *Advanced materials*, *22*(7), pp.813-828.
5. Munir, M.T., Mansouri, S.S., Udugama, I.A., Baroutian, S., Gernaey, K.V. and Young, B.R., 2018. Resource recovery from organic solid waste using hydrothermal processing: Opportunities and challenges. *Renewable and Sustainable Energy Reviews*, *96*, pp.64-75.
6. Heidari, M., Salaudeen, S., Dutta, A. and Acharya, B., 2018. Effects of process water recycling and particle sizes on hydrothermal carbonization of biomass. *Energy & fuels*, *32*(11), pp.11576-11586.
7. Wilk, M., Magdziarz, A., Jayaraman, K., Szymańska-Chargot, M. and Gökalp, I., 2019. Hydrothermal carbonization characteristics of sewage sludge and lignocellulosic biomass. A comparative study. *Biomass and Bioenergy*, *120*, pp.166-175.
8. Krylova, A.Y. and Zaitchenko, V.M., 2018. Hydrothermal carbonization of biomass: a review. *Solid Fuel Chemistry*, *52*(2), pp.91-103.
9. Bohlmann, J.A. and Inglesi-Lotz, R., 2018. Analyzing the South African residential sector's energy profile. *Renewable and Sustainable Energy Reviews*, *96*, pp.240-252.
10. Van de Venter, F.F., 2021. *Producing briquettes for domestic household fuel applications from coal tailings* (Doctoral dissertation).
11. Mills, S., 2018. Combining solar power with coal-fired power plants, or cofiring natural gas. *Clean Energy*, *2*(1), pp.1-9.
12. Onifade, M. and Genc, B., 2018. Spontaneous combustion of coals and coal-shales. *International Journal of Mining Science and Technology*, *28*(6), pp.933-940.
13. Taha, Y., Benzaazoua, M., Edahbi, M., Mansori, M. and Hakkou, R., 2018. Leaching and geochemical behavior of fired bricks containing coal wastes. *Journal of environmental management*, *209*, pp.227-235.
14. Keefer, R.F., 2020. Coal Ashes—Industrial Wastes or Beneficial By-Products? In *Trace elements in coal and coal combustion residues* (pp. 3-9). CRC Press.
15. Petlovanyi, M.V. and Medianyk, V.Y., 2018. Assessment of coal mine waste dumps development priority. *Науковий вісник Національного гірничого університету*, (4), pp.28-35.

16. Stolboushkin, E., Gilliat, J., Hillis, P. and Zuklic, S., 2016, September. Successful Deployment of Electro-Hydraulic TCP Firing Head Improves Safety and Reduces Rig-Time. In *SPE Deepwater Drilling and Completions Conference*. OnePetro.
17. Grobelak, A., Grosser, A., Kacprzak, M., & Kamizela, T. (2019). Sewage sludge processing and management in small and medium-sized municipal wastewater treatment plant-new technical solution. *Journal of environmental management*, *234*, 90-96.
18. Asvat, R., Bisschoff, C.A. and Botha, C.J., 2018. Factors to measure the performance of private business schools in South Africa. *Journal of Economics and Behavioral Studies*, *10*(6 (J)), pp.50-69.
19. Khanam, N., Singh, A.A., Singh, A.K. and Hamidi, M.K., 2022. Water Quality Characterization of Industrial and Municipal Wastewater, Issues, Challenges, Health Effects, and Control Techniques. In *Recent Trends in Wastewater Treatment* (pp. 1-30). Springer, Cham.
20. Shaddel, S., Bakhtiary-Davijany, H., Kabbe, C., Dadgar, F. and Østerhus, S.W., 2019. Sustainable sewage sludge management: From current practices to emerging nutrient recovery technologies. *Sustainability*, *11*(12), p.3435.
21. Meisel, K., Clemens, A., Fühner, C., Breulmann, M., Majer, S. and Thrän, D., 2019. Comparative life cycle assessment of HTC concepts valorizing sewage sludge for energetic and agricultural use. *Energies*, *12*(5), p.786.
22. Kacprzak, M., Neczaj, E., Fijałkowski, K., Grobelak, A., Grosser, A., Worwag, M., Rorat, A., Brattebo, H., Almås, Å. and Singh, B.R., 2017. Sewage sludge disposal strategies for sustainable development. *Environmental research*, *156*, pp.39-46.
23. Del Rio, C., 2017, July. The global HIV epidemic: What the pathologist needs to know. In *Seminars in diagnostic pathology* (Vol. 34, No. 4, pp. 314-317). WB Saunders.
24. Tompa, D.R., Immanuel, A., Srikanth, S. and Kadhirvel, S., 2021. Trends and strategies to combat viral infections: A review on FDA approved antiviral drugs. *International journal of biological macromolecules*, *172*, pp.524-541.
25. World Health Organization, 2013. *WHO traditional medicine strategy: 2014-2023*. World Health Organization.
26. Reddy, K., Renuka, N., Kumari, S. and Bux, F., 2021. Algae-mediated processes for the treatment of antiretroviral drugs in wastewater: Prospects and challenges. *Chemosphere*, *280*, p.130674.
27. Looi, F.Y., Baker, M.L., Townson, T., Richard, M., Novak, B., Doran, T.J. and Short, K.R., 2018. Creating disease resistant chickens: a viable solution to avian influenza? *Viruses*, *10*(10), p.561.
28. Goulder, P. and Deeks, S.G., 2018. HIV control: Is getting there the same as staying there? *PLoS pathogens*, *14*(11), p.e1007222.
29. Schoeman, C., Dlamini, M. and Okonkwo, O.J., 2017. The impact of a Wastewater Treatment Works in Southern Gauteng, South Africa on efavirenz and nevirapine discharges into the aquatic environment. *Emerging Contaminants*, *3*(2), pp.95-106.
30. Prejean, J., Song, R., Hernandez, A., Ziebell, R., Green, T., Walker, F., Lin, L.S., An, Q., Mermin, J., Lansky, A. and Hall, H.I., 2011. Estimated HIV incidence in the United States, 2006–2009. *PloS one*, *6*(8), p.e17502.
31. Silva, A., Delerue-Matos, C., Figueiredo, S.A. and Freitas, O.M., 2019. The use of algae and fungi for removal of pharmaceuticals by bioremediation and biosorption processes: a review. *Water*, *11*(8), p.1555.
32. Sousa, É.M.L.; Otero, M.; Rocha, L.S.; Gil, M.V.; Ferreira, P.; Esteves, V.I.; Calisto, V. Multivariable optimization of activated carbon production from microwave pyrolysis of brewery wastes - Application in the removal of antibiotics from water. *Journal of Hazardous Materials* **2022**, *431*, 128556.
33. Xiang, Y., Xu, Z., Wei, Y., Zhou, Y., Yang, X., Yang, Y., Yang, J., Zhang, J., Luo, L. and Zhou, Z., 2019. Carbon-based materials as adsorbent for antibiotics removal: mechanisms and influencing factors. *Journal of environmental management*, *237*, pp.128-138.
34. Jordá-Beneyto, M., Suárez-García, F., Lozano-Castello, D., Cazorla-Amorós, D. and Linares-Solano, A., 2007. Hydrogen storage on chemically activated carbons and carbon nanomaterials at high pressures. *Carbon*, *45*(2), pp.293-303.
35. Alhasan, S., Carriveau, R. and Ting, D.K., 2016. A review of adsorbed natural gas storage technologies. *International Journal of Environmental Studies*, *73*(3), pp.343-356.
36. Esteves, I.A., Lopes, M.S., Nunes, P.M. and Mota, J.P., 2008. Adsorption of natural gas and biogas components on activated carbon. *Separation and Purification Technology*, *62*(2), pp.281-296.

37. Sekulic, M.T., Boskovic, N., Slavkovic, A., Garunovic, J., Kolakovic, S. and Pap, S., 2019. Surface functionalised adsorbent for emerging pharmaceutical removal: adsorption performance and mechanisms. *Process Safety and Environmental Protection*, *125*, pp.50-63.
38. Saveyn, H., Curvers, D., Schoutteten, M., Krott, E. and Van der Meeren, P., 2009. Improved dewatering by hydrothermal conversion of sludge. *J Residuals Sci Technol*, *6*(1), pp.51-56.
39. Hoekman, S.K., Broch, A. and Robbins, C., 2011. Hydrothermal carbonization (HTC) of lignocellulosic biomass. *Energy & Fuels*, *25*(4), pp.1802-1810.
40. Tasca, A. L., Puccini, M., Gori, R., Corsi, I., Galletti, A. M. R., & Vitolo, S. (2019). Hydrothermal carbonization of sewage sludge: a critical analysis of process severity, hydrochar properties and environmental implications. *Waste Management*, *93*, 1-13.
41. Zhang N, Wang G, Yu C, Zhang J, Dang H, Zhang C, Ning X, Wang C. Physicochemical structure characteristics and combustion kinetics of low-rank coal by hydrothermal carbonization. Energy. 2022 Jan 1; 238:121682
42. Hamedi, M.R., Tsolakis, A. and Lau, C.S., 2014. Biogas upgrading for on-board hydrogen production: reforming process CFD modelling. *International journal of hydrogen energy*, *39*(24), pp.12532-12540.
43. Mulopo, J. and Abdulsalam, J., 2019. Energy storage properties of graphene nanofillers. In *Graphene-Based Nanotechnologies for Energy and Environmental Applications* (pp. 155-179). Elsevier.
44. Züttel, A., 2007. Hydrogen storage and distribution systems. *Mitigation and Adaptation Strategies for Global Change*, *12*(3), pp.343-365.
45. Niaz, S., Manzoor, T. and Pandith, A.H., 2015. Hydrogen storage: Materials, methods and perspectives. *Renewable and Sustainable Energy Reviews*, *50*, pp.457-469.

.

Chapter 2: Literature Review

This chapter reviews the substantial literature pertaining to newly published research on the HTC process of different materials, as well as the potential of wastewater and coal beneficiation plant wastes to yield carbonaceous materials and in particular this emphasizes the adsorption of contaminants utilizing carbon-based adsorbents from wastes and the gas adsorption (AG) system for hydrogen (H_2) as effective environmental management strategies. The processing of HTC biomass, biochar applications, and the use of cost-effective char-based adsorbents in wastewater treatment and AG storage systems have all been investigated. Various wastes and biomasses are described, together with the potential of CD from coal beneficiation plants and SS from WWTP for the production of high-quality carbon materials through HTC. This chapter examines the possible uses of carbon material for the adsorption of dissolved pharmaceutical chemicals in WWT and H2 storage. In addition, research data on CD beneficiation, energy usage, and H_2 storage systems are provided.

2.1. Municipal and industrial wastes management

By 2050, Kumar (2017) predicted that the worldwide production rate of industrial and municipal garbage would approach 4,2 billion tonnes per year. Large-scale technologies that are economically and ecologically feasible, such as HTC, Co-HTC, will thus play a vital part in the reuse, recycling, and/or considerable reduction of waste disposal.

Due to a lack of infrastructure and technology, both developed and developing nations face waste management issues. The major challenge in waste management is how waste is collected and processed (collection, transport, treatment, and disposal procedures). The waste management technique allocated to a particular type of waste is determined by its content. The appropriate waste management strategy is to identify less expensive, industrial-scale, continuous treatment solutions that conform to environmental requirements (Kumar *et al*., 2017). Various novel solutions introduced in recent decades for solid waste (SW)

treatment face constraints such as energy consumption, human skill, storage capacity, and footprint. According to Hamer (2003) and Tripathi (2018), the world's population's industrial need will continue to create solid wastes made up of numerous components. Because the vast majority of solid wastes is neither combustible nor biodegradable, it is inevitable that more complex technologies are developed in order to meet the objective of zero waste (Kumar *et al*., 2017). Among the many varieties of solid wastes are wastewater treatment plant sewage sludge and coal beneficiation wastes produced in massive amounts by countries such as South Africa, which constitute a significant environmental threat (Liu *et a*l., 2015).

2.2. Wastewater treatment plant sludges

Wastewater treatment facilities process municipal and domestic wastewaters, which generate sludge known as sewage sludge (SS) (Grobelak *et al*., 2019). The process and the amount of wastewater treated can have an influence on the quality of effluent and the amount of SS generated (Demirbas *et al*., 2017). There are many types of sewage sludge, including primary, waste activated, and digested sludge, all of which may be converted into valuable carbonaceous material. Figure 2-1 shows an example of WWTP with SS generation described extensively by Russel (2019). South Africa has about 824 WWT systems across 152 municipalities with a collective design capacity to receive 6.5 billion litres of WW a day which generate a considerable amount of SS (Donnenfeld *et al*., 2018). Therefore, large on-site land disposal and waste piling observed across the country have become the standard management option for many WWTP in SA (Shaddel *et al*., 2021).

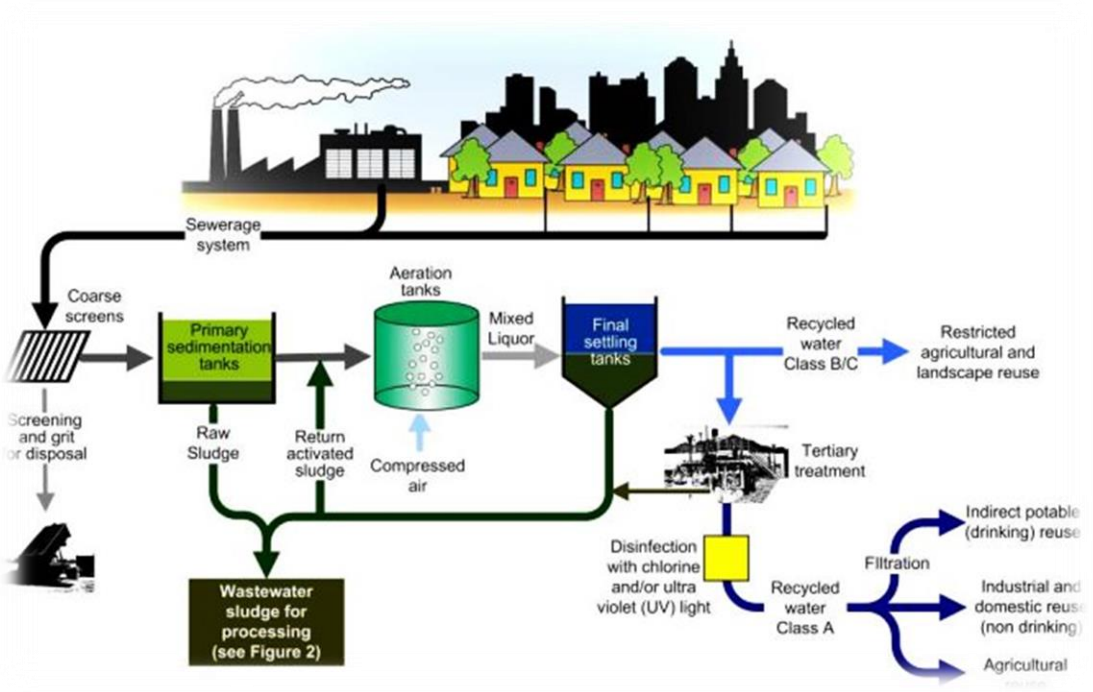

Figure 2-1:Schematic of a typical wastewater treatment plant (Russel, 2019)

2.3. Coal beneficiation plant wastes

In the last century the mechanisation of coal mining has increased the amount of generated coal fines particles (Mills 2016).

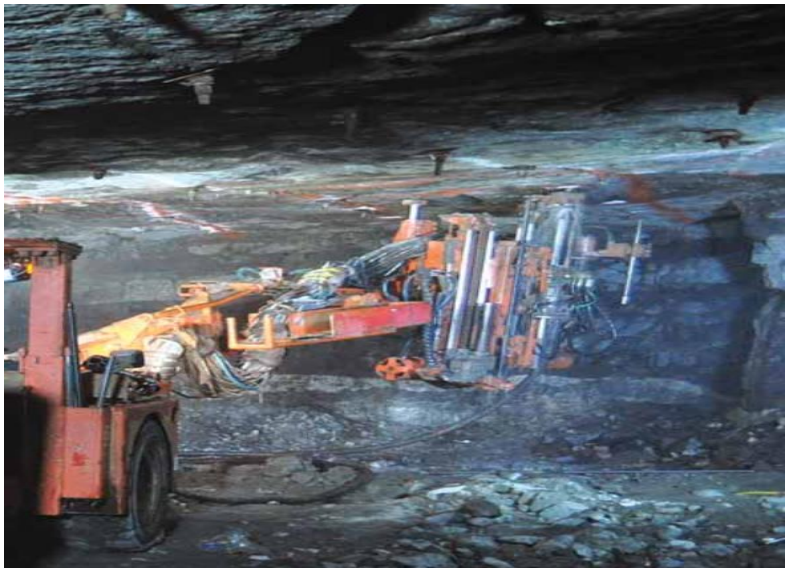

Figure 2-2: Mechanized mining in action (Mills 2016)

Hence, a large amount of coal waste is discarded from mining and coal beneficiation plant including coarse, fines run-of-mines (ROM), coal tailing (CT) and coal slurry (CS) (Mishra *et al*., 2015). The compositions of coal wastes depend on different factors such as coal type, mining method used, the geology of the coal site and the recovery technology (Mills, 2011). The primary SA coal users' requirements are based on particle size (+6mm) and carbon content; therefore, coal mines producers must screen the raw materials and classify coal particle size below 6mm as fines from run-of-mine (Piechura, 2014). In the coal beneficiation process, the float-sink from flotation characterized by high ash content is called coal tailing and the wet product which cannot be mechanically dewatered to an acceptable level, unusable in conventional combustion equipment is the coal slurry (Moyo *et al*., 2018). The first generated coal form mining called ROM is the unprocessed and fresh coal. Its ash content and sulphur are removed by washing as shown in Figure 2-3, other products generated from this process are coarse-grained and fines-grained materials. To reach the market required quality and specification of coal, SA coal mining need to proceed with a depth coal washing process because the quality of raw coal has declined considerably over years (Koplitz *et al*, 2017). Therefore, after mining the coal is washed through solid-liquid methods before it is been transported. The purpose of the process is to improve the quality of the ROM by removing a great quantity of ash, sulphur, and other undesirable compounds. The coal washing process is described as follow; crushing of the ROM followed by screening and classification of coarse, fines and ultrafine particles. The associated gangue is removed through dense medium process (DMS, sink/float) and the ultrafine particles are recovered by froth flotation process (Kasomo *et al*., 2018). Waters from coarse and fines coal are separated through centrifuges and belt, vacuum filter, sometimes thermal drying techniques respectively.

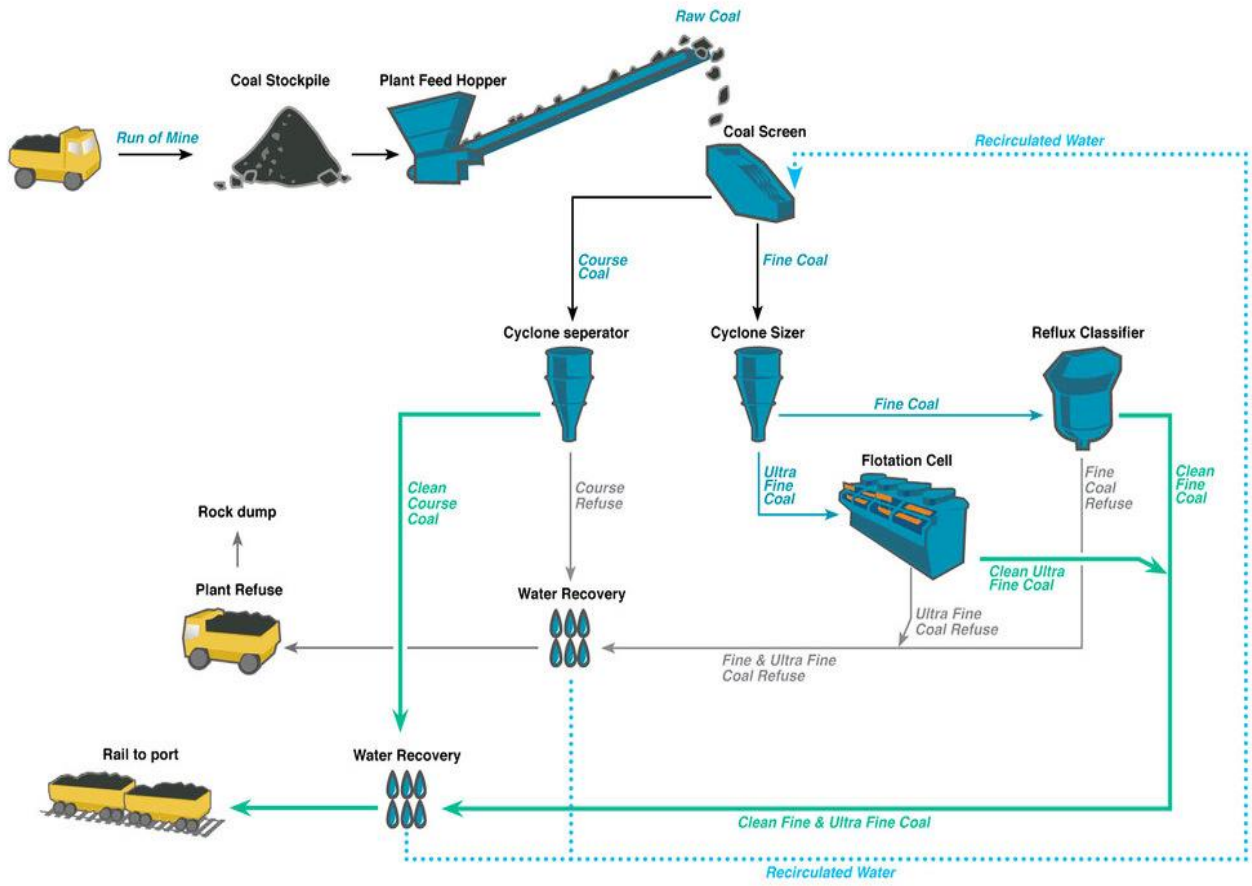

Figure 2-3:Typical Coal beneficiation process (Olga Krelin Design Associates)

Due to inattention and negligence in waste beneficiation focus, there is a massive accumulation of CD that is damaging the environment's integrity and consuming significant areas of useable land. Figure 2-4 shows image of self-heating ROM fines (1) and an aerial view of Mpumalanga Highveld CD stockpiles (2). Analysis of the dump showed that it contains usable carbon in significant quantities which can be extracted and used for production of value-added materials (Abdusalam Jibril *et al*., 2019). Furthermore, the methods used to remove water from fines coal are often challenging and costly, hence, there are often discarded as slurry settlement pond containing wet coal fines, silt, clay and other fines mineral particles. The recycling of these wastes will lessen the extent of environmental concerns caused by their prevalence while also enabling prospective new technological applications (adsorption, energy storage). Governmental legislation and policies pertaining to environmental protection have been established, resulting

in the imperative reduction of waste stockpiling via the development of alternate methods of usage (Listiyani *et al*., 2018). CD has a variety of potential applications, including combustible, fuel, adsorbent, and many other. However, some CDs need pre-treatment or upgrading before usage (Mills. 2018). Beneficiation of coal waste is essential for economic reasons and strict compliance with environmental requirements.



Figure 2-4: (1) Self-heating of run -of-mine fines, (2) Aerial view of Mpumalanga Highveld coal discard stockpile in South Africa (Rights, 2015)

2.3.1. South African coal discards and acid mine drainages

Ranked among the world largest coal producers, SA uses coal as the main source of energy. As reported by the SA gazetted integrated resource plan for electricity, the contribution of coal to SA total energy mix is projected to reduce from 77% to 60% by the end of 2030 (Wright *et al*., 2019). However, according to the Department of Energy (DME) (http://www.energy.gov.za/files/coal _frame.html), no suitable alternatives to coal as primary energy source is yet to be approved. Therefore, it could be anticipated that coal will still be SA major energy source for the next decades. The DME 2011 national CD and slurry inventory reported that over 65 million tons of coal wastes are produced annually. These coal wastes are either disposed of in tailings piles and slurry dams (Van de Venter *et al*., 2021). Coal waste disposal is considered a major threat to the country's environmental waste management due to possible solubilization of toxic pollutants from CD and the risk of spontaneous combustion (Onifade and Genc 2018). The disposal of these wastes across coal mining zones is an environmental and regional challenge

because of the toxic composition and the land occupation which even prevent other useful utilization of those areas for the development of the country (Mills, 2018). Therefore, the need arises to find economic and environmental solutions for the treatment or reuse of these wastes. Beneficiation techniques such as physico-chemical processes and regeneration techniques have developed over the year but are considered inefficient, not environmentally benign, challenging, and expensive (Petlovanyi *et al*., 2018). In SA, the fact that CD stockpiles still stand and increases in same cases shows that different management techniques still insufficient to address their resurgence, making the subject of research into other methods of management. The carbon content of CD gives them potential for energy generation but other component in big proportion such as ash, sulphur and moisture prevent their use, furthermore, their beneficiation equipment cost remains a great challenge for the large-scale application (Swanepoel, 2014). Lands and useful spaces taken by CD are subject to global environmental regulations (legislation, penalties, and incentives) because of their impact on the public health and the ecosystem. In the United States for example, a Federal Mine Reclamation Fund (FMRF) is provided for the rehabilitation of CD dump by the government for environmental protection (Mills, 2018). As a result, 2800 ha of land previously occupied by CD stockpiles have been restored for useful projects. Urbanization and the demographic growing in country like India have made the recovery and rehabilitation of CD occupying land a priority. The spaces needed for coal operation and coal wastes management are expected to increase from 1470 km^2 in 2007 to 2925 km^2 by 2025 (Maiti, 2012). South Africa has established a legislation in the restoration of CD dumps to its useful state following a guideline composed by three principal objectives: the satisfaction of the host community by the restoration of CD dump to its previous closer state (mainly those with agriculture values), rehabilitation of land for useful community occupations and restoration of CD dump land by recovery of its previous biodiversity state (Tanner 2009).

A considerable amount of metal present in CD such as Aluminium, iron, manganese, and chromium, could continually be leached and generated Acid mine drainage (AMD) which contaminate surface and underground natural water (Skousen *et al*., 2019). The AMD is the consequence of the exposure of sulfurous

minerals to water and oxygen in the presence of microorganisms (Skousen *et al*., 2019; Mulopo *et al*., 2022). The potential for the formation of AMD is therefore increased by the presence of sulphides in the waste from mining activities (Moodley *et al*., 2018). AMD is one of the majors' environmental risks associated with inactive mines and embankments of mine discharges which result in soil deterioration and water pollution (Skousen *et al*., 2019). Treatment of mineral waste containing sulphides would require selective separation followed by a costly desulphurization and use of toxic products (Ait-Khounia *et al*., 2021). Therefore, it is important to develop a treatment approach to deal with the mining wastes with less risks and damaging of the environment. Moreover, toxic elements like mercury have been reported in CD dumps on different compositions ranges (Chen *et al*., 2014). The grade of these element depends on the origin of the coal (Mills, 2018). The major inorganic components of most South African CD have been identified as; iron, sulphur, antimony, arsenic, manganese, mercury, and metal trace elements, which have a huge harmful potential effect on the surrounding environment (Moyo *et al*., 2018). The AMD is produced when sulphate bearing minerals, are exposed to oxygen (Biddau *et al*., 2018). The process, termed pyrite oxidation, is enhanced when water moves through and over the surfaces of acid bearing rock having been exposed because of mining activities that disturbed the underlying geology (Biddau *et al*., 2018). The AMD is generally characterised by one or more of the following: low pH, high Total Dissolved Solids (TDS), high sulphates (SO_4), and/ or high levels of heavy metals - particularly Iron (Fe), Manganese (Mn), Nickel (Ni) and/ or Cobalt (Co) (Nyström *et al*., 2018). Heavy metals (and in some instances radioactivity) being mobilised at low pH, and elevated salt levels can pose a risk to human health and to the safety of the aquatic ecosystem while also having a significant negative economic impact (Biddau *et al*., 2018). As a result of the inter-linking of many underground mine workings, the cumulative effect on both the quantities of underground mine water that has to be pumped during mining basin dewatering, as well as the quality impacts resulting from AMD formation (Mulopo, 2022), are substantial. It is important to note that the underground mine water being pumped in the three mining basins, notably the Eastern, Central and West Rand Mining Basins, collectively contribute approximately 5% of the total Vaal River system yield,

while being responsible for an estimated 20% of the total salinity load, that may also include heavy metals (Tempelhoff *et al*., 2019).Numerous abandoned or ownerless mines are situated within the larger Vaal River water supply area (Mduduma *et al*., 2018). This implies that the State is likely to have to assume the responsibility for many of these mines, if ownership cannot be traced, or if the mines had become government responsibility in terms of the Fanie Botha Accord (agreement by DWA with the Chamber of Mines) (Simate *et al*., 2021). Although the Department should scrupulously enforce all applicable water legislation, this fact underlines the necessity that government and the mining industry will have to work in close partnership (Simate *et al*., 2021). In addition, it must be noted that the issue of ownership potentially holds huge implications for the State in respect of contributing towards the costs associated with a regional underground mine water and AMD solution (Simate *et al*., 2021, Mulopo *et al*., 2022). The closure of gold mines on the Witwatersrand has been identified as a threat to the environment due to AMD seepage from flooded underground mine workings, especially the potential impact on the ground water environment (Tempelhoff *et al*., 2019). Seepage of contaminated leachate from tailings piles or dams can be a significant cause of surface and ground water pollution in many mining areas (Sibanda *et al*., 2019). Arguably the most valuable resource that can be recovered from AMD remediation is high quality water for safe environmental discharge or reuse (Mulopo, 2022). The removal of organic and inorganic pollutants from acid mine drainage, is a very important application of CM adsorbent (Rodríguez *et al*., 2019). It has been reported that around 80% of the world production of ACs is used in liquid-phase applications (Danish *et al*., 2018). The adsorption in aqueous phase using CM results from interactions between the carbon surface and the adsorbates. These detailed physical and chemical natures of these interactions vary with the nature of the adsorbate as well as the surface chemistry of the CM (Rodríguez *et al*., 2019). Abundant surface functional groups and a highly developed porosity of CM make them versatile adsorbents for applications to aqueous systems (Gao *et al*., 2018). Variable amounts of heteroatoms in the surface groups of the CM, oxygen, hydrogens, nitrogen, and sulphur, allow various functionalities. These atoms and molecular structures, which might have origin in the raw material or could be

introduced during preparation or post treatments (activation), largely influence the charge, hydrophobicity, and electronic density of the surface of CM (Mulopo, 2012).

The self-heating of CD stockpiles in an adequate oxygen medium leads to spontaneous combustion and hurt the environment. The combustion of the CD stockpiles could be longer and release toxic components into the atmosphere. The spontaneous combustion often generates fire occurrence which is a recurring issue in many coal producer countries. To illustrate the context, example of forty CD stockpiles is expected to burn at any time in Pennsylvania in the United State (Mills, 2018). About one-third of the 3000 Chinese CD stockpiles experience spontaneous combustion which occasion air pollution (Chen *et al*., 2014). It has been also reported that; spontaneous combustion of CD stockpiles in Ukraine release about 500,000 tons of NO_x, SO_2 and CO_2 every year (Mills, 2018). Frequent spontaneous combustion occurs from South African CD stockpiles as reported by Onifade and Genc (2018). The Figure 2-5 illustrates the burn out of a CD heap initiated by spontaneous combustion. The study of Onifade and Genc (2018) also reported that the government of SA has interpleaded coal industries concerning the emission of greenhouse gases (GHG) like CO_2 and CH_4 from self-heating of CD dumps. Environmental issues caused by the spontaneous combustion of CD dumps are deeply preoccupying the government, therefore, it is imperative to find long term solutions to the problems and contribute to the available techniques of reducing the spontaneous combustion influences.



Figure 2-5: Spontaneous combustion of coal waste heap (Onifade and Genc, 2018)

2.4. General treatment of sewage sludge and coal discards wastes

The WWT sludges generally undergoes progressive treatments which are stabilization with lime, thickening, draining, drying and anaerobic digestion before being disposed. Some of these treatments depend directly on the method of decontamination and on its concentration strength, positively or negatively (Demirbas *et al*., 2017). In general, digestion is the commonly used method of stabilization of WWT sludge followed by regional disposal, incineration, or agropastoral use (de Sousa *et al*., 2020). The agropastoral use of WWT sludges should be the most indicated method of reuse preceding incineration and landfill. Nevertheless, the most used method of SS management is landfill because of its lower cost of execution (Ross *et al*., 2018). Therefore, studies conducted by Harrison and Mc Bride (1999) of Cornell waste management institute for the purpose of assessing the environmental impact of SS and action on health have shown different infections and even death caused by the proximity of SS stockpiles. Furthermore, farmers using SS as fertilizer displayed health weakness and microbiological infections. It was therefore concluded after these studies that measures to monitor and protect human and animal populations against the risks of contamination caused by exposure to this sludge must be carefully developed and taken into consideration. The limits of pollutants from the SS were defined

according to the rule established by the environmental protection agency (EPA 503). The agency defines a pollutant as compound (organic, inorganic or their combinations), or a pathogenic organism that after discharge, exposure, inhalation and direct or indirect assimilation to an organism via the food chain can cause death, disease, cancer, anomalies, physical deformities, reproductive problems etc (Venkatesan *et al*., 2015). The study conducted by Raklami (2021) on the addition of SS to neutralize soil acidity reported that the SS fertilize practice was not recommended if large amounts must be used. This because the SS has a potential to produce acids compound when it oxidizes. Several other studies have demonstrated that the use of SS as fertilizer for agricultural soils is only very little recommended. Especially when it comes to large quantities because it would have a direct or indirect impact on the environment and the health of the surrounding population or products consumers due to the chemical contamination of growing plants by the affected the soils (Venkatesan *et al*., 2015, Dos Santos *et al*., 2020). The incineration of SS is a practice which produces exhaustive air pollution by gases as well as a problem with the environmental disposal of its ashes which could contain heavy metals (Venkatesan *et al*., 2015). This is therefore a major challenge of WWT sludge management. However, it is possible to produce carbon derivatives such as compound called biochar from the SS by pyrolysis or HTC with formation of gas syngas as in practice of biofuel combustion for electricity and steam production (Racek *et al*., 2020). Despite the fact that measures are frequently taken to manage these wastes, they have proven to be insufficient as the quantity of waste stockpiles continues to grow and thus poses a risk to human health due to their constituents (Teoh *et al*., 2020). As a result, heat-based treatments appear to have the potential to alleviate the problem of managing this type of waste for health and environmental reasons. SS management then becomes a procedure for reducing the quantity, volume, and cost of disposal, thereby reducing the potential health risk associated with their current disposal techniques. In South Africa, where water is scarce, the generation and disposal of wastewater SS remains a major challenge (Petterson, 2019). Depending on the treatment stage at which they are generated, the SS typically contains between 34 and 37% carbon materials. One of the issues with SS is their high metal content, which makes disposal difficult due to the

dangers of contamination of the soil, subsoil, and aquatic life. However, using SS as a fertilizer or energy source is generally expensive due to the need for prior appropriate pre-treatment (De la Rubia et al., 2018; Wilk et al., 2019). As a result, the goal of this project is to evaluate the use of SS in the production of high-value carbon-based products such as activated carbon (AC). Table 2-1 summarizes the findings of studies on energy generation from various SS biochars. The table results show that energy generation is a promising environmental SS management strategy. More research is needed, however, to describe a generic reaction pathway and the economic feasibility of the effective thermal process. Furthermore, the potential synergetic treatment of SS with other wastes such as CD should be investigated in order to generate value-added materials at a low cost.

Table 2-1. Energy application of different sewage sludge

Source	Thermal treatment	Product	Energy generated	Remark	Reference
Viborg located in Bruunshåb, Denmark	Hydrothermal liquefaction 325°C	Biocrude	33.6 MJ/kg	Pharmaceutical products remaining in PW	Thomsen *et al* (2020).
Croatia	Pyrolysis	Bio-oil and Biogas	30-37 MJ/kg	Effectiveness and feasibility of large-scale techniques to be study	Đurđević *et al* (2019).
Bionor Sludge from pilot-testing scale	Pyrolysis700°C –800 C	Biochar	18.4 MJ/kg	More research is required for adaptation of the installation apparatus to large-scale wastewater treatment plants. The evaluation of the environmental aspects of presented sewage sludge management option needs to be done	Grobelak *et al* (2019).
Different sources	Pyrolysis	Biochar	29-40 MJ/kg	More detailed studies are required on the barriers (high moisture, ash and heavy metal content) to enhance the products quality and to make them readily available for commercial purposes.	Gao *et al* (2020).
Topinoja (Turku, Finland)	HTC 250°C	Hydrochar	11.3–12.2 MJ/kg	HTC conditions applied in this study generated hydrochars of little variations in properties, it could be recommended to use the lowest temperature (210°C) and shortest residence time (30 min) for hydrochar production from digestate.	Hämäläinen *et al* (2021).
UK sewage sludge	HTC 160°C - 250°C	Hydrochar	312.9kW h of energy produced per tonne of treated sludge	Many aspects have to be considered regarding the process and capital costs for retrofitting existing WWTWs and the addition of complementary equipment for the use of hydrochar as an energy source.	Aragón-Briceño *et al* (2021).

Rostock, Germany	HTC 200°C - 240°C	Hydrochar	14.99–15.75 MJ/kg	The use of H_2SO_4 and NaOH as additives has decreased the FC content of produced hydrochar, which negatively influences the heating value of the consequently produced hydrochar. In addition, because of the lack in reaction pathway, compromises must be made in the fuel characteristic of the hydrochar for a large-scale perspective	Shettigondahalli Ekanthalu *et al* (2021).
Ekaterinburg in Russia	Anaerobic digestion	Biogas	1065.23 - 7099.29 MWh/year	The limitations of the methodology presented, it that the study mainly focused on the aspects related to biogas/biomethane production and use, without entering the details of the nutrient recovery from digestate. In addition, it is expected that other factors not analyzed in this study (first and foremost economic factors) will contribute to the final selection of the conversion technology.	Kiselev *et al* (2019).
West of Tehran Iran	Pyrolysis 600 °C - 700°C	Biochar	13.5– 19.4 MJ/kg	Simulation of results to be extrapolated to industrial scale. Economic and environmental aspects of the process still undescribed	Shahbeig *et al* (2020).
Poland	Anaerobic digestion combustion, pyrolysis, and gasification	Chars and biogas	11.10–22.10 MJ/Kg	the lack of data to accurately back the high efficiency of most pyrolysis and gasification systems as they fail to account for the energy intensive pre-processing stage which offsets a considerable fraction of the recovered energy and could lead to negative energy balance. As a result, innovative pathways and research using these technologies commercially are required such as coupling of biochemical and thermochemical systems to optimise energy recovery.	Oladejo *et al* (2018).
Katowickie Wodociągi S. A	Pyrolysis	biogas	23 -35.7MJ/m^3	The implementation of the global rules of a circular economy concept and environmentally	Kacprzak *et al* (2021).

				friendly process should be done to up scale the transformation of sewage sludge into biogas.	
Neuse River Resource Recovery Facility (NRRRF), Raleigh, North Carolina	Supercritical carbon dioxide drying 15 min at 75°C	Char	14 MJ/kg	Environmental and safety concerns have to be addressed while looking at acceptable pathways to sludge drying and more energy to the system into the CO_2 extraction process need to be evaluated for potential creation of effective solution in surface water as well as bound water removal.	Aggarwal *et al* (2021).

HTC: Hydrothermal carbonization

The beneficiation of CD holds a significant economic potential. Numerous applicable uses of rehabilitated CD dumps are projected through beneficiation. The process guides to a coal recovery or transformation of waste in value-added products. The use of coal from CD beneficiation in power generation plants could reduce the consumption of fuel (Nyoni *et al*., 2020). That gives an alternative energy feedstock, reduce the cost of normal living, and help power plant to generate low-cost energy. As an illustration, the biggest steel company in Russia named Severstral uses coal wastes (CW) for energy generation and has saved about 25 million rubbles (Martus *et al*., 2022) in its power plant. The coal waste beneficiation holds many advantages and in SA it is even more considerable because of issues that coal industries and power generation plant are going through. The electricity could be supply by the coal recovered from CD stockpiles (slurry pond and coal dumps) and the diversity of national energy mix and security could be improved across the country. Studies on the use of CD in nonexclusively energy generation have led to the production of bricks in some countries such as Russia (Boltakova *et al.,* 2016). These bricks have appeared to be very competitive according to their physical properties such as the compression resistance between 9 and 11MPa, water adsorption capacity around 17% as well as the freezing resistance. Other researcher used CD in the bioremediation technique for the rehabilitation of coal dump transformed into enriched soil like humus; the production of the hydrocarbons micro-thin for liquid fuel feed stock and the production of charcoal briquettes (Papin *et al*., 2015; Sekhohola *et al*., 2017;Tudor *et al*., 2021). The commercial using of South African CD for briquettes production faces challenges due to the high cost of binders' process (Borowski *et al*., 2021). Therefore, potential energy production from CD beneficiation holds a particular environmental and economic. Several research have been conducted on the CD beneficiation mostly using coal fly ash. However, CD fines and slurry have only few studies on their utilization to improve the quality for power generation uses (Borowski *et al*., 2021; Martus *et al*., 2022). Potential on the beneficiation of some south African coal fines has been studied and the results showed different values of weathering degree, oxidation rank, composition and techniques used (Ramudzagi *et al*., 2020).

Three different South African CD from Witbank/Highveld coalfields have been characterized for their potential coal upgrading using two different methods which are gravity separation and froth flotation. It was discovered that froth flotation delivered high beneficiation potential of coal fines more influenced by the micro-lithotype form of the coal than the mineral constituents or the individual maceral. The study conducted by Lloyd (2018) provided a database of estimated composition of different South African CD. There were in that database 97 mines working listed, their location, their geological formation, the mining procedures used, their generated quantity of CD as well as their total capacity of production. The results of the study showed that South African CD are mostly characterized by; <35% fixed carbon, >40% ash, 15-25% volatile matter and 2 % of sulphur content. The sulphur contained is lower than the north American and European DC (Lloyd *et al*.,2018). Therefore, South African CD have great potential for energy production if the material is treated with an appropriated method developed in well-designed equipment. Nevertheless, the cost and environmental challenges of pre-treatment methods of CD limit the large-scale expansion.

Hence, hydrothermal treatment of CD and SS could be an effective synergetic and environmentally friendly option of utilizing these wastes. In this research the suitability of HTC and Co-HTC technique to produce value added hydrochars (HC) for adsorption application and further activated carbons (AC) was investigated. It is noteworthy to show that to the best of the author knowledge, this study examined for the first time the potentiality of ACs produced from the spent adsorption residues in electrochemical technology. Moreover, there is no literature available on the Co-HTC of SS and CD as carbonization pre-treatment to produce ACs used for hydrogen storage.

2.5. Hydrothermal carbonization treatment

The HTC is a thermochemical process mainly employed in the treatment of biomass containing significant moisture to produce advanced material used in extended applications. The Hydrothermal process occurs when reaction's temperature varies between 150 and 350℃ while the main feed undergoes into heated and pressured (2 and 6 Mpa) water for about 10 min to days (Arellanoa *et*

al., 2016). The HTC products are solid named hydrochar (HC), liquid named process water (PW) and little quantity of gas. The HC is the main product of the process, and it is accompanied by aqueous soluble present in the PW and mainly CO_2 by-products (Ischia *et al*., 2021). Potentiality of biomass is revealed by his used-on HTC process for production of cleaner materials. Chemistry of HTC process has been involved in numerous scientific research, but some challenges remained unsolved properly like reaction kinetics, heat transfer, catalysts, operational parameters, energy, and heat recovery. Hence a technical procedure for expended applications is needed (Heidari *et al*., 2018). Even though the batch reactor was the most type used in many HTC process studies, researchers deduced that the principal factor of HTC process application is the type of reactor. (Arellanoa *et al*., 2016; Heidari *et al*., 2019). However, for industrial scale, high pressure and temperature continuous reactors must be well apprehended (Kumar *et al*., 2017; Raklami *et al*., 2021). Therefore, in this project better clarifications, experimental modelling proposition and improvement orientations of HTC process application constituted the main objective. HTC occurs under water critical point, liquid phase is formed while polar reactions are achieved at lower temperatures, however, gas phase appear when free radical reactions take place at higher temperature (Kruse *et al*., 2015). When aqueous medium reaches a critical point or closer, molecular reactions are mainly settling (Wang *et al*., 2018). HTC takes place when the temperature is usually between 150°C and 350°C, and the composition of the product depends on the raw biomass, the temperature, and the reaction time (Peng *et al*., 2016; Lucian *et al*., 2018). The degree of carbonization increases with increasing temperature (Lucian *et al*., 2018). Advantages of HTC are the mild reaction conditions and unnecessary pre-treatment stages. HTC technique allows production of carbon materials with well-developed porosity and surface functional features from wide range of starting materials (Heidari *et al*., 2018)

Generally, many reactions take place during HTC process, nevertheless they still accuse a lack of understanding in term of nature and pathways. The fact that energy activation of hydrolysis is lower than most of other reactions guide to the evidence that HTC is firstly covered by hydrolysis (Heidari *et al*., 2018). Ester and ether bond of hemicellulose, cellulose and lignin are broken into fragments at 180℃,

200 and 220℃ respectively during HTC process (Titirici *et al*., 2010), after hydrolysis, two main reactions occur namely dehydration and decarboxylation which facilitate decreasing of H/C and O/C ratios (Wang *et al*., 2018). It has been found that solid product from HTC process varies between 35% and 65% of the dry feedstock and has a higher heating value (Liu *et al*., 2018). To illustrate the fact, the reaction in equation (2-1) shows an example of dehydration of glucose.

$$C_6H_{12}O_6 \longrightarrow C_6H_4O_2 + 4H_2O \qquad (2\text{-}1)$$

Dehydration result on release of water (2-1) and during decarboxylation CO_2 and CO are released by degradation of carboxyl and carbonyl groups. Condensation polymerization comes after those previews reactions and are initiated from their fragments (Wang *et al*., 2018). Hence, the overall of the HTC become a combination of a complex polymer with water producing a large, rearranged polymer commonly accompanied by liquid containing dissolved materials and CO_2 (Kruse *et al*., 2015). A stable aromatic polymer is formed from reactions rearrangement during HTC process and built the main frame block of the HC (Knappe *et al*., 2019). The large amount of carbon contained in the initial feed is retained in a solid product during HTC process, liquid and gas by-product from the raw biomass could be released between the temperature range of 250-350°C, and process is then called hydrothermal liquefaction (Zhang *et al*., 2014). The HTC reaction's order and chemistry still not well discovered yet which make difficult their definition (Heidari *et al*., 2018). A van Krevelen diagram is useful to understand how the atomic composition changes during HTC, and how the resulting hydrothermally carbonized biomass relates to naturally occurring materials such as coal or lignite (Trinh *et al*., 2019).

Biomass could be defined as the organic product from sun lighted stockpiles of animals and plants materials and are potential source of chemical energy (Achinas *et al*., 2017). There are different types of biomasses classed onto two main categories known as: non-lignocellulosic and cellulosic biomass. The main difference between types of biomasses is their structure (Titirici *et al*., 2010). The animal manure, organic wastes, municipal solid wastes, organic wastes (dead plants, decomposed woods, etc..) and SS are classified into biomass types (Kambo

et al., 2014). However, animal manure and SS are habitually categorized as non-lignocellulosic biomass because they contain protein, fatty acid, hemicellulose in small quantity, cellulose, and lignin. The second category of biomass called lignocellulosic is composed by material with a large amount of hemicellulose, cellulose, and lignin. However, it is to be known that all these two types of biomasses contain ash and extractives water (Achinas *et al*., 2017). The main sources of lignocellulosic biomass are municipal biological, forest and farms solid wastes (Acharya *et al*., 2015). Composition of biomass depends on the climate conditions, maturity, and type of precursor. The Figure 2-6 shows the cell wall and structure of main biomasses. Differences of biomass are important for their characterisations, behaviour, during the HTC process and expected properties of the produced HC (Reza *et al*., 2014).

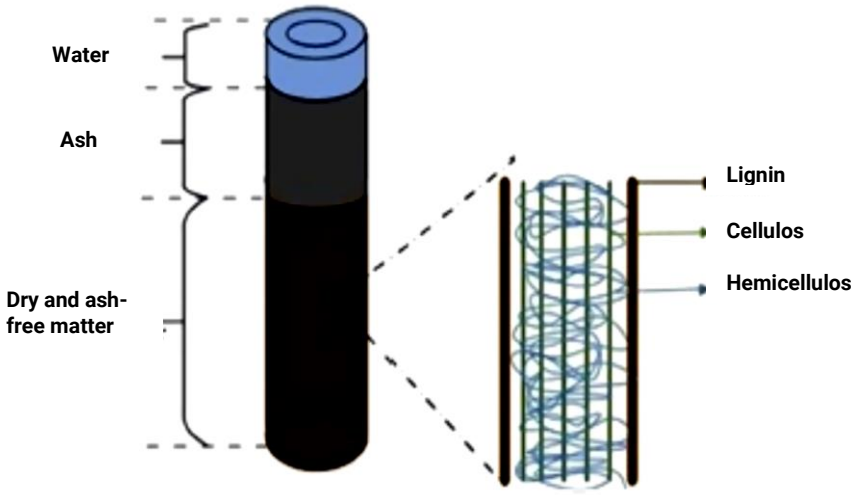

Figure 2-6:General structure of biomass (Reza *et al*., 2014)

HTC process has the big advantage of using many kinds of feedstock including lignocellulosic and non-lignocellulosic biomass. Thermal treatment of biomass results in the decomposition of hemicellulose, cellulose, and lignin (Heidari *et al*., 2018). During HTC, different components undergo decomposition at specific process parameters; hemicellulos decomposes at 160°C and 200-300℃ in subcritical water and ambient conditions respectively, when cellulose and lignin begin decomposition between 180 -200°C and above 220℃ respectively in

subcritical water and between 300-400℃ and above 400℃ respectively in ambient conditions (Kambo *et al*., 2014). The natural coalification which normally takes million-years to be performed could be accelerated by HTC while processing in high pressure and temperature a composite of biomass and water. In HTC process, million years of reactions are reduced in a lapse time (Heidari *et al*., 2018). Therefore, in recent passed, for environment problem caused by GHG emissions resulting on climate changes, HTC appeared to be potentially relevant technique of regulation (Dos Santos *et al*., 2020). The greatest advantage of HTC it's the fact that it occurs in watering medium which allowed the treatment of high moisture content biomass without the need of primary dry like others thermal processes (torrefaction, gasification, ect.) (Arellanoa *et al*., 2016). Moreover, HTC is also reliable to be combined with different processes for production of specials characterized materials (Heidari *et al*., 2018) which have different property like porosity, morphology etc… for appropriated applications such as water purification, nanoparticles, power generation, carbon capture and soil amendment. This work focused on HTC and Co-HTC of CD and SS b as they are part of the main environmental challenges faced these recent years.

In the HTC process, liquefaction and gasification are limited and a carbon-rich solid product dominates. The large amount of carbon from biomass is generally retained in the solid product called hydrochar (HC) after HTC process. Liquid and gas by-product of HTC process are proportional to process condition and feedstock used (Biller *et al*., 2016). Previous studies on HTC process of different feedstocks presented in Table 2-2 revealed that solid, liquid and gas yields are mainly related to the process parameters and the properties of the raw material.

Table 2-2. Yield of solid, liquid and gas for different HTC experiments

Feedstock	Temp (℃)	Time	Solid yield (%)	Liquid yield (%)	Gas yield (%)	Refernces
Different wastes	180-250	1h-12h	50-80	5-20	2-5	Libra *et al* (2011)
Different wastes	180-250	3h-18h	75-80	15-20	5	Ugbebor *et al* (2019)
Jeffery Pine and white Fir	215-295	30 min	50-69	12-14	5-12	Hoekman *et al* (2011)
Loblolly pine	220	5 min	63-83	8-17	9-20	Reza *et al* (2013)
Sugar cane bagasse	215	30 min	64	20	4	Hoekman *et al* (2013)
Tahoe mix	235	30 min	63.68	17.66	7.86	
Pinyon/juniper	235	30 min	62.73	30.37	6.13	
Corn stove	235	30 min	54.41	32.41	7.79	
Rice hulls	235	30 min	64.33	25.37	5.23	

The HC characterization is provided by different analysis i.e., proximate, and ultimate analysis, HHV, mass, durability, hydrophobicity, energy density, compression strength, water resistance (Heidari *et al*., 2018). The HC is usually transported in the form of densified pellet obtained via a mechanical press controlled (Reza *et al*., 2013). There is compression control machine called Instron which can record the maximum force before first crack of the pellet. Pneumatic or mechanical agitation of pellet could provide the quantity of fines particles which determine the durability of the compressed pellet (Kambo *et al*., 2014). By placing HC sample in a controlled environment (i.e., RH ¼ 48 – 52 % at 22°C), its EMC could be determined. Hydrophobicity of HC is calculated after weighting original sample and dried (100°C) sample. Immersion of sample in water, dry and scaling is to process of water resistance, swelling and standard durability determination (Yan *et al*., 2014). Pellets from HC produced at low HTC process temperature (200-275℃) are seems to have good durability as studied by Yan (2014), however better durability is obtained while higher temperatures. Referred to that, the durability of the pellet depends to the HTC process temperature used for HC production (Reza *et al*., 2014). Main's properties of pellets from hydrochars are provided in Table 2-3 as described in some studies from literature (Reza *et al*., 2014). O/C and H/C ratios evolutions are more clearly displayed on the Van Krevelen diagram reported to its X and Y axis respectively. Percentage of carbon increases during HTC process by

dehydration and decarboxylation reactions which result on the decrease of H/C and O/C ratios. Hydrophobicity of solid product increases during the process and its properties become more related to coal (He *et al*., 2013). The HCs characteristics from different biomass HTC process are provided in the Table 3. It is noted from previews studies that HHV of certain CDs varies between 17 and 19 MJ/kg and they content 35 to 45% of carbon which led to 1.7 to 1.9 and 0.7 to 0.9 the H/C and O/C ratio respectively. Thermochemical analysis of HC product is generally performed on TGA by heating its sample for lost weigh percentage determination versus temperature in an inert place. Provided data from TGA could determine reaction zones and activation energies of HC decomposition (Singh *et al*., 2020). The specific surface area determination is conducted by BET analysis and the amount of standard gas (Nitrogen) molecule adsorbed in the pores allows its calculation (Bardestani *et al*., 2019). Morphologies and microstructure of both untreated feedstock and produced HC are provided by SEM analysis to set the structure difference before and after the HTC process. Mainly increasing of temperature changes the surface morphology of the biomass until it becomes microsphere showing carbonisation achievement (Kannan *et al*., 2018).

Liquid phase product from HTC process is generally characterised by HPLC technique based on its absorbance difference with the mobile phase by a stationary phase (Kannan *et al*., 2018). Liquid phase from HTC process is also called Process water (PW). Standard samples lead to identification of different compound in PW on HPLC analysis. HPLC analysis of liquid phase from different biomass HTC process are showed in Table 2-4. Several organic matter and sugars appear from HPLC analysis of PW, but others still not discovered yet. GC and IC analysis could well be used for organic, lactic, formic, acetic methane sulfonic, glutaric, succinic, malonic, maleic, and oxalic acids analysis and HPLC for quantification of defined sugars, furfural and 5-HMF in PW of HTC process as it has been studied by Hoekman (2013). In addition to all those analysis, TOC and pH tests remain most commonly as they are the fast way of PW chemical characterisation.

Therefore, detection of all organic and carbon element content substances could be done by TOC analysis without giving their chemical classification. TOC analysis gives a total organic carbon content. During HTC process, organic

substance as formic and acetic acid are dissolved in PW adding to them volatile fatty acids (VOCs), furfural, phenol and other different compound depending on the main biomass feed and HTC process condition (Reza *et al*., 2014).

Table 2-3. Effect of HTC on some of the mechanical properties of biomass

Feed	HTC condition	Hydrophobicity Percentage moisture content at RH 74-78%	Durability (%)	Mass density(kg/m3)	References
Tahoe Mix	No treatment		98.69	1220	Hoekman *et al* (2014)
	225℃, 30 min		99.22	1300	
Loblolly pine	No treatment	-	97.5	1080	Reza *et al* (2014)
	260℃, 5 min	-	99.8	1478	
Miscanthus	No treatment	11	92.2	834	Kambo *et al* (2015)
	190℃, 5 min	75	93	887	
	225℃, 5min	62	94	959	
	260℃, 5 min	36	88.8	1035	

More gas is produced when HTC process temperature is increased, large amount of gas is produced from decarboxylation reactions, CO_2 gas concentration is ranged between 70 and 90% and gas like CH_4, CO and H_2 cover 10 to 30% (Achinas *et al*., 2017). In subcritical aqueous medium condition, hydrolysis of biomass leads to intermediate liquid products formation like acetic acid and formic acid (Heidari *et al*., 2018) which will then be submitted to decarboxylation process. Decarboxylation reactions are described in reactions (2-2) and (2-3) as follow.

$$CH_2O_2 \longrightarrow CO_2 + H_2 \quad (2\text{-}2)$$

$$CH_3COOH \longrightarrow CO_2 + CH_4 \quad (2\text{-}3)$$

Using standard –state enthalpy of formation and absolute entropy data and considering the temperature as 200 ℃, the Gibbs free energy of the reaction (ΔG^0) can be found from equation. (2-4):

$$\Delta G^0 = \Delta H^0 - T\Delta S^0 \quad (2\text{-}4)$$

Where T (K) is the temperature at which the reaction occurs and ΔH^0 (kj/mol K) and ΔS^0 (J/mol K) are enthalpy and entropy change of the reaction and can be found by equstions. (2-5) and (2-6):

$$\Delta H^0 = \sum H_f(products) - \sum H_f(reactants) \quad (2\text{-}5)$$

$$\Delta S^0 = \sum S^0(products) - \sum S^0(reactants) \quad (2\text{-}6)$$

Where H_f (kJ/mol. K) and S^0 (J/mol. K) are the enthalpy of formation and standard entropy.

Gibbs free energies of those above reactions could be founded from available standard entropy and enthalpy of product formation and are respectively 70.43 kJ/mol and 26.22 kJ/mol. With those value for ΔGo it can be conclude that decarboxylation reactions can be spontaneous, and CO_2 yield could increase during HTC process.

Table 2-4. HPLC analysis of liquid products for different feeds

Feeds	Detector	Mobile phase	Identified compounds	References
Forest biomass	UV/RI	Sulphuric acid	Formic acid, Acetic acid, glycol aldehyde, Laevoglucose, Acetol Glyoxal	Titirici *et al* (2010)
Wheat straw, popular wood, pine wood	DA	Water/acetonitrile	Acetic acid, Propionic acid, Furfural, Hydroxy-methyl-furfural,2-Methoxyphenol, 2-Methylbenzofuran	Becker *et al* (2014)
Sugarcane Bagasse, Loblolly pine	RI	Water	5-HMF, Furfural, Eluted sugars (sucrose/trehalose, galactose/mannose/fructose)	Broch *et al* (2013)
Wheat straw	RI	Sulphuric Acid	Formic acid, Lactic acid, Furfural, Phenol, Guaiacol, Catechol, Cresol, Fructose, Sucrose, Glucose	Reza *et al*. (2014)
Loblolly pine	RI	Water/sulphuric acid	Acetic acid, formic acid, lactic acid	Lynam *et al* (2013)

Uv: Ultraviolet. RI: Refractive Index. DA: Diode array

2.6. Hydrothermal treatment of sewage sludge and coal discards

The HTC of SS is defined as an exothermal chemical process into which feed stock under autogenously saturated pressures at a temperature between 180 and 250℃ for a certain time is transformed into carbonaceous product associated with by-products (liquid phase and gas) (Lucian *et al*., 2018). Different studies on HTC demonstrated that the process medium (mainly water) had an important impact on the procedure and chemicals reaction's chains respectively hydrolyse, decarboxylation, polymerization and coalification occurred under determined degree of reaction severity (Heidari *et al*., 2018). HTC of SS for production of valuable products has been considered in some studies these past years not only for waste disposal management but also for economic profitability and the possibility of greenhouse gas capture for environmental challenges (Kumar *et al*., 2017). Up to date relevant studies which are specific to HTC of SS are very scarce. Few published studies have only focused on general aspects related to evaluation of process parameters, reaction mechanisms, process product's physicochemical characteristics and economic advantages (Wang *et al*., 2019). Therefore, further research is still needed to provide better understanding, reaction mechanisms, design of continuous process reactor and practical application of HTC of SS process. Hence settlement of a bulk reaction model linked to SS initial composition and final product characteristics as well as process parameters and yield could be well described (Tasca *et al*., 2019). Wang (2019) concluded after a review of different studies on HTC of SS that the energy efficiency and environmentally friendly capacity of HTC give a considerable potential to the process for energy and resource recovery. However, they mentioned the requirement of further studies to provide a general kinetics model associated with process parameters, sewage sludge composition, life cycle assessment and techno-economic feasibility of the process. In HTC of SS, heavy metals and phosphorus are immobilized in stable forms into the HC product which is formed from condensation, polymerization, and aromatization of furans compounds from dehydration of monosaccharide and N-containing ring from Maillard reaction (Wang *et al*., 2019). However, reaction pathways still unwell determined up to date despite some mechanism deduction form analysis of process products (Tasca *et al*., 2019).

Current results of research on HTC of SS do not provide proper identification and quantification of the product's composition for well understanding of continuously feasibility of the process as well as the efficiency of reuse and recycling of sewage sludge (Wang *et al*., 2020). Therefore, this project focused on providing a clear picture of HTC of SS and further characterisation and used of HCs product as well as a co-treatment HTC process of SS and CD for production of value-added CM. Considering previous research on HTC of SS, it must be mentioned that more often they have given more attention on reaction conditions processing. The parameters affecting the yields, product constitution and properties were deducted to be relied on temperature and residence time (Tasca *et al*., 2019). The HTC process of SS has been described by following reactions; depolymerization of SS, decomposition of biopolymers and recombination of reactive intermediates (Afolabi *et al*., 2017). Wang (2019) defined the HTC process as the solubilization of solid matters into evaporative and non-evaporative matters followed by their interconversion. An understandable HTC reaction mechanism was described by Imbierowicz and Chacuk (2012) as a firstly direct dissolution of SS followed by the dissolution of particles from destruction of insoluble high molecular for the formation of liquid and gas phases. Based on these precedents' studies, latest research has given a simplified framework containing detailed description of biochemical intermediates of HTC of SS consisting of two major steps which are; dissolution of SS into macromolecular products (polysaccharides and proteins mainly) and consequently conversion by hydrolysis and oxidation of soluble organic products into liquid phase conducting to formation of final product like acetic acid, ammonia, water, CO_2 etc… (Yin *et al*., 2015). Theses descriptions showed that the solubilisation and decomposition of SS are the most important reactions rather than the polymerization which appeared to be an outsider reaction. The Figure 2-7 shows the simplified HTC process of SS reaction pathways, it is mentioned that reactions steps followed the order below;

1. Hydrolysis since his activation energy is lower than other HTC reactions,
2. Decarboxylation,
3. Aromatization and

4. Condensation where biopolymers react with water which breaks their chemical bonds using a low activation energy and produces soluble oligomers, monomers, and other intermediates.

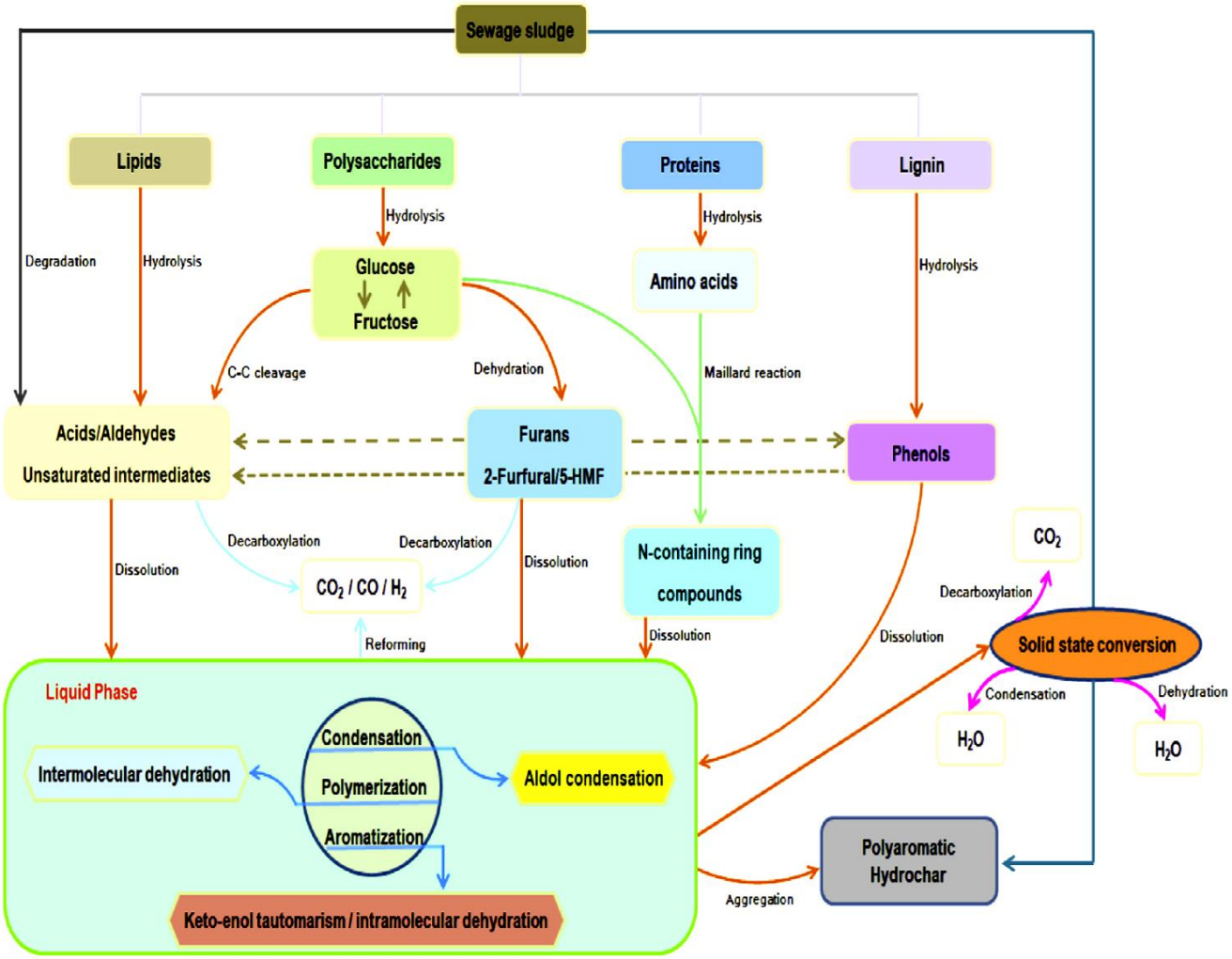

Figure 2-7:Simplified reaction pathways for hydrothermal carbonization of sewage sludge (Source: Yin *et al*., 2015)

During HTC process, hydrolysis is followed directly by dehydration and decarboxylation of hydrolysed matters. The furans compounds (2 Furfural and 5 HMF) form monosaccharides dehydration pass through condensation, polymerization and aromatization associated with the N-containing ring matters from Mailllars reaction. However, phenolic products from hydrolysis of lignin and highly reactive intermediates (aldols, aldehydes, and others organic acids) are transformed into solid matters (Reza *et al*., 2014). Aggregation and carbonization of produced solids generate the HTC HC via intermolecular dehydration associated with devolatilization, condensation and decarboxylation (Kruse *et al*., 2015). Therefore, formation of HC is mainly leaded by condensation-polymerization which can be increased by reaction's severity factor (Kruse *et al*., 2015). It is important to mention that, up to date, there is not enough strong experimental evidence for HTC of SS. This could be due to the lack of data in current developed technology. Latest studies on HTC of SS showed effort on determination of kinetics of sewage transformation based on previous described reaction's mechanism, the Arrhenius approach was firstly applied to develop the HTC kinetics model and experimental data aligned to describe first-order reactions. According to Yin (2015), proteins and saccharides as macromolecular products are the primary intermediates on initial period of HTC of SS accompanied with an activation energy of 51 kJ mol^{-1} at a temperature situated between 108℃ and 300℃. Afterward dissolved biochemical matters degraded into gaseous product which was inconsiderable between 150 and 250℃. Hence the production limit of gaseous phase appeared to be caused by the direct thermal decomposition of organic matters on the surface of solid product leading to an activation energy of 63 kJ mol^{-1}, added to the fact that gas formation is a principal consequence of aqueous phase decomposition (Imbierowicz *et al*., 2012). Activation energy of 70 $kJmol^{-1}$ has been concluded as the energy needed for HTC of SS in a temperature range of 140-200°C and have been described to fit the first–order reaction (Danso-Boateng *et al*., 2013). The model with carbonization progress prediction based on oxygen content and HTC conditions proposed by Hwang (2021) seems to be the unique available in literature because detailed kinetic models which considers all HTC process parameters, feedstock composition and intermediates still not provided. Molecularly explained models generated by HTC

process of SS related an approach of HTC process chemistry modelling based on the molecular composition of feedstock and products (formation of oligomers and glucose monomers). The SS contains polysaccharides which are polymers of monosaccharide like glucose, mannose and fructose, they are in the form of cellulose, hemicellulose, and starch (Wang *et al*., 2019). Cellulose is a long linear chain constituted by glucose monomers which are bonded by β-1, 4 glycosidic connections. However, due to the formation of strong intra and inter-molecular hydrogen bonds, the presence of high degree of crystallinity appeared, then solubilization and hydrolysis of cellulose are accelerated in HTC conditions (Cui *et al*., 2020) However, some individual mechanism still unwell described and HTC molecular-level definition remains a challenge because variety of carbonized products could be obtained even tough glucose is the primary hydrolysis product of cellulose during HTC process (Sasaki *et al*., 2022). Further decomposition leads to the formation of fructose, furan derivatives and aldehydes as intermediates by dehydration, isomerization, and C-C bond cleavage (Kruse *et al*., 2015). The main reactive element from dehydration of glucose in HTC process should then be the 5-HMF in heterogeneous medium and favours the production of HC by condensation and polymerization (Titirici *et al*., 2010). The mechanism of solid HC spheres production from carbohydrates during HTC process have been displayed by Zhang (2014). These HC microspheres formed show the core-shell chemical structure characterized by highly hydrophobic aromatic nucleus. Hence, as hemicellulose is an heteropolysaccharide constituted by pentose, hexose, uronic acid units and xylan, the all-model substance decomposition could be described as the transformation of xylan (Wang *et al*., 2019). Moreover, the hydrolysis rate of hemicellulose appeared to be higher than celluloses because hemicellulose has a wick random and amorphous structure (Reza *et al*., 2013). Whereas, at 180℃ hemicellulose starts its decomposition, cellulose hydrothermal degradation needs higher temperature and starts around 200°C (Wang *et al*., 2019). Therefore, hydrolysis and cleavage of glycosidic bonds leaded by depolymerisation of hemicellulose are followed by dehydration and retro-aldol condensation of xylose which allowed the production of furfural (2-furaldehyde) and small parts of glycolaldehyde, glyceraldehyde and dihydroxyacetone as intermediates

(Carvalheiro *et al*., 2022). Increasing of residence time led to a significant gasification (Pińkowska *et al*., 2020). Hydrolysis of starch, which is constituted by many glucose monomers connected by α-1, 4 and α-1, 6 glycosidic bonds seem to be quicker than decomposition of cellulose during HTC (Yousefifar *et al*., 2020). The complete solubilisation of starch has been observed at 180℃ during 10 min while glucose formation yield was higher at 200℃ during 30 min and during 10 min at 220℃ (Kato *et al*., 2019). Glucose degraded proportionally with raising of temperature and was firstly converted into 5-HMF. Starch hydrolysis below the temperature of 220℃, produced small amount of dextrose and maltose while liquid phase is produced by its caramelization (Kato *et al*., 2019). Based on these descriptions, it is therefore evident that HTC of polysaccharide is characterized by three principal reaction pathways described as follow;

1. Conversion of polysaccharide into pentose and hexose elements according to HTC severity,
2. Transformation of monosaccharides into furfural intermediates through intramolecular dehydration (2-furaldehyde or 5-HMF),
3. HC formation from furans through intermolecular dehydration

The polyaromatic networks and polyfuranic structure basic building block of the produced HC is formed by a condensation and cyclization of degraded polysaccharides products which increased the aromatics formation with high stability during HTC process (Kumar *et al*., 2017). Triglycerides in SS are represented by three fatty acids bounded to a glycerol backbone, they form lipids content of the feedstock (Xu *et al*., 2020). The fatty acids content in SS, are originating from phospholipids from cell membranes, direct adsorption from wastewater and by-products of microbial metabolites and cell lysis (Kumar *et al*., 2017). Therefore, form of principal fatty acids is presented as; stearic acid, oleic acid, palmitoleic acid, palmitic acid, and linoleic acid (Wang *et al*., 2019). Volatile fatty acid formation depends on reaction temperature and saturation degree of fatty acid chain during HTC process, they result from decomposition of lipids (Wang *et al*., 2019). The solubilisation of lipids is accelerated by reaction severity. The increase in production of volatile fatty was observed from 170℃ and above rather due to the breakdown of unsaturated lipids than saturated lipids (Hovland *et al*.,

2018). At the liquid-water interface, hydrolysis of lipids firstly takes place and step on progressively toward homogenisation and liberate fatty acids through lipids decomposition favoured by auto-catalytic effect (Baig *et al*., 2020). Degradation of lipids has been then described as a first order kinetics reaction (Baig *et al*., 2020). The production of volatile fatty acids results from hydrolysis of lipids during HTC of SS using a temperature below 220℃ (Hovland *et al*., 2018). Microbial degradation of organic products resulted in formation of humic substances consisting in a heterogenous mixture of aromatic, nucleic and carboxylic groups (Baig *et al*., 2020). Humic substances are classified in three main groups as; humic acids, fulvic acids and humins (Baig *et al*., 2020). Under all pH conditions, it has been noted that fulvic acids are soluble in water whilst humins are non-soluble and humic acids are not soluble in water under acidic conditions (Xu *et al* 2020). Therefore, humics substances appeared resistant to biodegradation during wastewater treatment process and settled in SS composed by 80% of humic acids (Gong *et al*., 2021). Hence, humics substances behaviours should be followed during HTC process of SS for a well description of the process. Hydrolysis of humic and fulvic acids under subcritical conditions of HTC process has been studied by Fekete (2012). The study concluded that the formation of alkylbenzenes, polycyclic aromatic hydrocarbons and heteroatomic was most leaded by reaction's temperature and the degradation of humic and fulvic acids was observed at temperatures higher than 220℃. Humic substances decomposition occurred with a longer residence time and was led by reaction temperature as aromatization, polycondensation. C-C and C-heteroatom bonds were depending on reaction temperature (Feteke *et al*., 2012). After increasing temperature and reaching out 600℃, conducted studies on supercritical conditions water gasification of humic carried out by Azadi (2013) and Gong (2017) concluded that it is tough to form gaseous phase from humic substances due to lower carbon conversion relied to the recalcitrant condensed structures and supposed that humic substances settled with insoluble products into HC through polymerization of reactive intermediates during hydrothermal degradation of SS.

The HTC technique is generally used to improve physicochemical properties of different raw materials as extensively described in literature (Tasca *et al*., 2019). For example, the HTC of low carbon content coal between 150°C and 270°C performed

by Liao (2016) successfully upgraded the fuel characteristics of the produced HC. In addition, the HTC of different type of coal performed by Zhang (2015), Liao (2016) and recently by Saba (2019) revealed that the high reactivity and non-polar solvent behaviour of subcritical water decreased the values of undesirable impurities such as fraction of total ash, oxygen, and sulphur, and increased the carbon content. It is worthy to mention that, up to date, there is not enough experimental evidence for the HTC of SS (Wang *et al*., 2019). However, the studies conducted by Mumme (2015) and Saba (2017) revealed that the carbonization and mass yields of Co-HTC treatment of different coal-biomass mixtures were highly efficient compared to the HTC treatment of individual coal and biomass used. These studies revealed that the decomposition of biomass under Co-HTC process produced acidic condition which favours the dissolution of mineral content of the feedstock. Hence, the Co-HTC treatment of coals-sewage sludge mixture holds a significant potential to increase carbon content of the feedstock compared to the HTC of coal and sewage sludge individually. For the first time, by means of a design of experiment, this study presents important experimental and statistical information on the use of HTC technique to address coal discard and sewage sludge wastes environmental management challenges.

2.6.1. Effect of HTC process parameters

A. Temperature

The main parameter of HTC process reactions is temperature. Biomass conversion yield is efficient when many intermolecular bonds are broken by energy strength (Nakason *et al*., 2018). The liquid and gas yields increase with temperature while solid yield decreases. Researchers found that increasing of 30℃ on HTC process decreased 10% of HC yield because a large amount of biomass (cellulose and lignin) reacts at higher temperature (Yan *et al*., 2014). The cellulose and hemicellulose are release at high HTC process temperature. Above 350℃ HTC process becomes HTL (hydrothermal liquefaction) where liquid yield is higher than solid and gas yields. At supercritical state, process temperature is very high and gas yield over dominate from the occurrence of radical reactions. In these conditions, the process is called HTG (hydrothermal gasification) (Heidari *et al*., 2018).

B. Pressure

HTC process pressure varies with temperature, polar compounds could be moved by water due to its liquid state which act as a solvent of catalyst and organic matter. Therefore, remaining of water in liquid state conduct to most acceptable hydrothermal conversion efficiency (Fiori *et al*., 2014). Three different pressures above 4692 kPa which is the saturation point of water at 260℃ have been involved into the study conducted by Minaret (2016) to evaluate their effects on HTC process. The study concluded that, physical structure of produced HC is not mainly influenced by pressure increasing according to SEM and BET analysis. However, high HTC process pressure produces smaller particles which require more specifications. High pressure process increases HC pore volume while low pressure increases HC radius. Hydrogen content increase proportionally with pressure while oxygen decreases. It has been reported that above 100 MPa, graphitization of HC is facilitated and HHV is increased considerably. Prior pressurized reactor is often used in lab to perform HTC process experiments, that will prevent vapour formation and will maintain water in its liquid state, but for large scale operation, it's economically efficient to use an autogenous reactor.

Table 2-5. Effect of HTC on several feed stock

Feed	Temp.°C	Time (min)	Solid yield (%)	Carbon content (%)	Ash content (%)	HHV (MJ/Kg)	H/C ratio	O/C ratio	Reference
Lawn grass	200	180	48	45	-	19	1.5	0.45	Guo *et al* (2015)
	240	180	32	55	-	20.8	1.2	0.4	
Corn husk	260	15	33.2	63.41	3.74	27.66	1.1	0.3	Minaret *et al* (2016)
Bambu	190	20	48	56.5	-	21	1.27	0.6	Li, Xan *et al* (2015)
Cellulose	220	30	58.4	63.5	1.4	26.5	0.9	0.36	Kim *et a*l (2015)
Wheat straw	260	360	35.7	64.2	10.8	26.2	1.02	0.22	Reza *et al* (2015)
Grape pomace	275	30	48	68.32	2.7	28.31	1.01	0.25	Pala *et al* (2014)
Miscanthus	180	240	80	53.5	1.75	21.2	1.33	0.55	Wilk *et al* (2017)
	200	240	65	56.6	0.88	21.4	1.25	0.48	
	220	240	58	63	1.05	23.9	1.1	0.36	
	200	120	65	54.9	1.75	21.1	1.29	0.51	
	200	720	65	58.7	0.83	23.4	1.24	0.25	
Rice husk	200	360	65	40.81	24.54	15.7	1.3	0.39	Kalderis *et al* (2014)
Saw dust	240	30	49.45	-	0.84	24.5	-	-	Oktaviananda *et al* (2017)
Loblolly pine	230	120	63.65	-	0.5	22.7	-	-	Reza *et al* (2013)
Sugar cane bagasse	175	30	69.6	48.3	-	18	1.41	0.72	Broch *et al* (2014)
	215	30	67.7	48.4	-	19.7	1.19	0.56	
Loblolly pine	175	30	77.7	52.2	-	21	1.38	0.58	
	215	30	72.4	54.8	-	22.1	1.55	0.54	

C. **Time**

HTC process products composition and energy consumption are clearly influenced by reaction time (Guangzhi *et al*., 2017). Literature provides different times range used for several HTC process studies, in most case high conversion yield has been achieved on longer reaction's times (Nakason *et al*., 2018). However, a longer residence time result in production of more PW or gaseous phase (Nizamuddin *et al*., 2017). For an increasing time, range of 0.5 to 6 h in HTC process of corn cob using at temperature of 250℃, Zhang (2015) mentioned an HHV variation of HC from 24.3 MJ/ Kg to 24.9 MJ /Kg. HTC process time and temperature influences as well as reaction severity could be found based on Arrhenius equations (2-7) and (2-8) below;

$$R_0 = t.e^{(T-100)/14.75} \quad (2\text{-}7)$$

$$SF = logR_0 \quad (2\text{-}8)$$

In these equations, R_0 is the reaction ordinate (min), t is reaction time (min) and T is the reaction temperature (℃). The logarithm of the reaction (log R_o) gives its severity factor; therefore, the first order of the equation is assumed by an Arrhenius temperature dependence. Abatzoglou (1992) displayed an equation used a temperature of 100°C to spread the severity concept to determine the impact of temperature and time on oil cracking. The study concluded that the increasing of 17℃ on HTC process reaction will conduct to use half of the time recommended for same result getting out. And on the other side, 14.75℃ increasing temperature in HTC process has with the reaction order an exponential relation on the changes of HC product.

$$Sl = 2^{t(T-480)/17} \quad (2\text{-}9)$$

Sl is the time-temperature index, T is the temperature and t is the time

Therefore, according to equation. (2-9) it has been demonstrated that the reaction severity is more influenced by the temperature increasing. Certain examples are given in literature which showed that the increasing of SF reduce the hydrochar mass yield while the HHV and the carbon content increase (Hoekman *et al*., 2017).

D. **Water**

Real dispersion of biomass in aqueous HTC reaction medium could only occur in presence of enough amount of water and will lead to a highly efficient process (Heidari *et al*., 2019). Whereas the high water to biomass ratio increases the water consumption and heating energy needed. High amount of water impact in HTC process has been studied by Reza (2015). The study fell on the conclusion that the use of a great amount of water in HTC process would result in the intensification of hydrolysis reactions and increasing of carbonization rate. Some other research found that physical characteristics such as pore volume and surface area are pronounced when using a great amount of water in HTC process (Minerat *et al*., 2015). However, polymerisation and hydrochar yield are favoured by a lower using of water in the process (Robbiani *et al*., 2013). Therefore, the amount of water in

HTC process must be sufficient to ensure total dispersion of biomass for hydrothermal reactions and heat and mass transfer, which are also depending on the hydrophobicity, structure and density of the biomass. The design of the HTC reactor should allow efficient and uniform heat transfer into his whole volume for less use of water facilitation.

E. **Catalyst**

Hydrothermal carbonization could happen with or without the presence of a catalyst. Under the hydrothermal treatment, the atomic ratios of O/C and H/C of the biomass material decrease (Kumar *et al.,* 2018). The need of catalyst in HTC process depends on expected products as its use transforms the mechanism of the reaction. The final use of the HTC product determines the type of catalyst needed (Kumar *et al.,* 2018). Therefore, it has been found that acid and basic catalyst used respectively increases and decreases the formation of HC in HTC process by changing the proportionality of formed phases (Nizamuddin *et al*., 2017). Hence, gases emissions produced by combustion of biomass and HC could be controlled by the presence of catalyst in the process (Zhao *et al.*, 2014). According to the study leaded by Mumme (2015), carbon content of HC and energy from HTC process of agricultural digestate and cellulose increase when Zeolite is used as catalyst which also enhance physical characteristics of the HC. To join this fact, it has been found that complete carbonation is performed by the using of Lewis acid catalyst like $FeCl_2$ and $FeCl_3$ at lower temperature (200℃), while acetic acid and basic catalyst (KOH, KCl, Na_2CO_3 and NH_4Cl) decrease the formation of HC product (Rather *et al*., 2017).

F. **Process water**

The use of water has been described above as it is proportional to energy demand, therefore for economic procedure of HTC process it's necessary to reduce it as possible. Recycling of PW gives a way to handle the problem, however it must be conducted to solid – liquid-gas separation before that use as PW from HTC process contains organic compounds and volatile matter (Becker *et al*., 2013). Treatment of PW has been studied and it has been found that oxidation produced short-chain organic acid which is environmentally friendly (Reza *et al*., 2016). Recycling of PW

leaded in few research available shows some changes on HC physical characteristics and mass yield (Weiner *et al*., 2014). However, compare to water, temperature increasing favours acidity of PW which contains organic acid therefore increases HC mass and energy yield (Kambo *et al*., 2018). Acidity of HTC reaction medium strengthens polymerization of biomass content, benzyl alcohol structure in lignin for example is produced via the carbonium ion which is the intermediate of the reaction and favours the polymerization (Picone *et al*., 2021).

G. **Particle size**

Biomass particle sizes effect on thermochemical process has been studied in different research, it has been concluded that the conversion is highly performed with smallest particles which gives higher calorific values but lower mass yield (Heidari *et al*., 2018). Heat and mass transfer are increased when biomass particle sizes are small. This is due to the great surface area of the feedstock presented which favours easy circulation of water. Therefore, reaction kinetics could be enhanced by biomass particle sizes reduction resulting in feedstock matrix disintegration (Heidari *et al*., 2018). However, in HTC process of smaller biomass particles, carbon content of hydrochar and HHV increased due to an increase of decarboxylation and dehydration reactions (Heidari *et al*., 2018). Degradation of lignin forms is initiated by the reduction of biomass particle sizes (Meehnian *et al*., 2016), which also lead to cellulose crystallinity characteristics reduction, therefore HTC process's mass and heat transfer could be improved and favour hydrolysis reaction (Heidari *et al*., 2018). Due to economic challenges, particles sizes reduction must be treated with particular insight even though it facilitates the effectiveness conversion of lignocellulosic biomass, then an optimum size should be determined to avoid over expenses (Oktaviananda et al., 2017). The energetic recovery could be efficient while reducing biomass particle sizes despite the decreasing of mass yield and HHV (Heidari *et al*., 2018). Equation. (2-10) below determines the formula of energetic recovery efficiency:

$$Energetic\ recovery\ efficiency = Hydrochar\ yield\ x\ Energy\ densification \quad (2\text{-}10)$$

$$Energy\ densification = \frac{HHV\ of\ the\ hydrochar}{HHV\ of\ the\ feedstock} \quad (2\text{-}11)$$

2.6.2. Hydrochar products applications

Applicability of HC has been tested in several fields such as power generation, soil improvement in agriculture, adsorption in liquid and gas phase (e.g., metal ion removal, CO_2 capture and methane storage), heterogeneous catalysis, photocatalysis, energy storage (e.g., Li/Na ion batteries, supercapacitors, fuel cells and bioimaging (Yihunu *et al*., 2019). Furthermore, the hydrothermally carbonized material could also be refined into high value products, for instance, into activated carbons and modified functional materials of various kinds (Song *et al*., 2019). Activated carbons belong to a set of carbon materials with a highly developed internal pore structure, a large surface area (as high as 3000 m^2/g), variable surface chemistry characteristics, and a high degree of surface reactivity. Activated carbons are not truly amorphous, but they have microcrystalline structures (Gao *et al*., 2018). The elemental composition of a typical activated carbon has been found to be 88% C, 0.5% H, 0.5% N. 1.0 % S, and 6-7% O, with balancing constituents of ash compounds (Sethia *et al.,* 2016). The surface chemical characteristics are much dependent on non-carbon elements and their corresponding moieties.

A. Power generation

Formation of ash in combustion due to the presence of alkali materials could be deflected by prior HTC process of combustible product (Libra *et al*., 2011). In different mass proportion of biomass and coal, combustion has been leaded in some research, equation. (2-12) below shows the combustion characteristics factor (CCF) parameter of 50% mass ratio used for ease of firing, velocity, burnout temperature and ignition (Parshetti *et al*., 2014);

$$CCF = \frac{\left(\frac{dw}{dt}\right)_{max}\left(\frac{dw}{dt}\right)_{min}}{T_i^2 T_h} \qquad (2\text{-}12)$$

Where $\left(\frac{\mathrm{dw}}{\mathrm{dt}}\right)_{\mathrm{max}}$ is the rate of weight loss (% min^{-1}), $\left(\frac{\mathrm{dw}}{\mathrm{dt}}\right)_{\mathrm{min}}$ is the average burning velocity (% min^{-1}), T_i is the ignition temperature and T_h is the burnout temperature (K).

That research has shown that HC addition to combustibles improved the combustion characteristics because prior HTC process increased carbon content of raw biomass and removed a large proportion of volatile materials. Moreover, it has been deduced that gases emissions from combustion (CO_2, CH_4, SO_2, NO and CO) are significantly decreased by HC and coal combination (Parshetti *et al*., 2014). However, the study on biomass HTC process temperature has shown that energetic recovery efficiency reached a higher value at 210℃ and the process temperature increasing increased the ignition combustion and burnout temperature of HC product due to elimination of volatile matter (Reza *et al*., 2016). Combustion's kinetics of HC has been described by Yang; Gao and co-workers (2016), they concluded that fixed carbon, lower ash and energy content are the most influencing characteristics of power generation materials, efficiency of combustion is also impacted by inorganic component. However, characteristics of HTC products are more accorded to the type of feedstock and process conditions (Smith *et al*., 2018).

B. Soil amendment

Mineralization, carbon sequestration, germination, growth, nutrients release of different crops are in the more case the raison of HC using for soil amendment (Afroze *et al*., 2018). Nutrient prevention could be performed by HC surface absorption which result in soil fertilization and ensured leaching (Spokas *et al*., 2018). GHG released N_2O from plants is a result of nitrogen absorption as ammonia for their growing mechanism, underground water could also be polluted by nitrate, control of nitrogen is then necessary for environment keeping. Therefore, studies conducted on HC effects for control of nitrogen presence in the soil for plant growth have shown that nitrogen could be decrease by a high carbon HC content, H/C and O/C efficient HC ratios should be less than 0.6 and 0.4 respectively (Schemmelpfennig *et al*., 2019). Porosity must be retained as one of the important characteristics of HC for soil amendment because nutrient and water retention capacity are relied onto it, they could be capped by the porous structure with decreases the water demand (Puccini *et al*., 2018). Therefore, carbon sequestration is well performed while using a high carbon content HC, produced from an optimized HTC process.

C. Separation

Hydrogen sulphide, nitrogen, and carbon dioxide gaseous from mixed stream could be separated by HC (Creamer *et al*., 2016). Moreover, heavy metals and water's contaminants can be adsorbed by porous HCs (Hagos *et al*., 2022). Each metal could be removed by a specific HC produced by controlled HTC process. For example, it has been found that 52% of Cu^{2+}absorption capacity was reached from water streams while using grapefruit HC produced at higher temperature (270°C) (Semercioz *et al*., 2017). The HCs can be use as ACs precursors for a wide range of further applications Pore diameter of AC lead to their classification as microporous (2 nm), mesoporous (2 to 50 nm) and macroporous (more than 50 nm). The activation process of HCs increases their generic surface area S_{BET}. The highest S_{BET} of mesoporous and microporous HCs developed by Fang (2015) are respectively 10 m^2/g and 150m^2/g. The HC from lignocellulosic biomass has in general high porosity due to breaking of functional groups (Jain *et al*., 2016). Therefore, CO_2 could be absorbed for molecular dimension up to 0.23nm. The HC adsorption capacity depend on the process conditions, S_{BET}, pore volume, surface functionality and charge. These characteristics could be improved during or after HTC process by using chemical reagents or by activation (Liu *et al*., 2018). Moreover, temperature increasing reduce the pH of the HTC medium which favours the release of elements in the water phase while the pore volume and S_{BET} increase with the severity of the reaction (Liu *et al*., 2018). Particularly important are the carbon-oxygen surface groups, because they influence the wettability, polarity, acidity, and other physico-chemical properties (Liu *et al*., 2018). The ACs can be produced from synthesized HCs by physical or chemical activation. The physical activation process is a two-step process (Bergna *et al*., 2018). The first step involves carbonization of the precursor at high temperature under an inert atmosphere (usually N_2 for economic consideration) and the second step is activation in oxidizing atmosphere, such as steam or CO_2, without any other reactants added in the precursor (Bergna *et al*., 2018). However, the chemical activation process can be done in one step with the use of activation reagent such as KOH, NaOH, $ZnSO_4$ etc, at high temperature in an inert atmosphere (N_2 generally).

2.6.3. Advantages of hydrothermal carbonization

Pyrolysis is a traditional carbonization method which is a thermal treatment of a carbonaceous raw material at temperatures of 400-800 °C in an inert atmosphere. During this treatment, the precursor decomposes into three fractions: chars, tars and gases (Li *et al*., 2020). The temperature, heating rate, nitrogen flow rate and residence time affect the result of pyrolysis. In general, an increasing temperature reduces the yields of chars, but increases the yield of tars and gases (Sulaiman *et al*., 2018). The carbonization process using pyrolysis can be replaced by a more sustainable process such as hydrothermal carbonization. Compared with the high temperature used in pyrolysis, a relatively low temperature (150-250 °C) is used in HTC (Heidari *et al*., 2018). The carbon content of the raw material increases while oxygen and hydrogen decrease after the HTC. It is obvious that water is needed in the HTC system. Moreover, ACs prepared from hydrothermally carbonized precursors have equally high surface area as those from pyrolyzed precursors (Bedin *et al*., 2018). The use of HTC in preparing ACs has the advantage in carbon emission efficiency, because it releases much less gases than pyrolysis, and all the decomposed by-products are in the water phase (Bedin *et al*., 2018).

Different thermal carbonization processes such as pyrolysis, incineration, gasification, and HTC are used to increase the carbon content of different carbonaceous material precursors. Among those carbonization techniques, HTC has the greatest potential to provide an energy efficient and environmentally friendly process. Furthermore, HTC offers several advantages over conventional dry thermal pre-treatments, as no prior drying is requested, and the high quality of the char produced promotes its further applications. However, the HTC further requires more research as there is still lack of data in literature in term of reaction mechanism, overall kinetics model associated with process parameters and raw materials composition. Table 2-6 below gives comparative results between the different thermal carbonization processes to produce carbonaceous materials. The results show that the HTC process produced 50 to 58 % of a solid HC with a 58 to 83% of carbon content, from different biomass precursors which implies that using the HTC process on the SA the CD and SS could increase their carbon content and lead to a

superior HC, mainly due to the fact that during HTC process all soluble salt present in the raw material dissolve in the liquid phase (Lu, *et al*., 2012).

Table 2-6.Comparison of operational parameters and product distribution for thermal carbonization

Process	Reaction temp (°C)	Reaction time	Reaction atmosphere	Feedstock moisture content	Production distribution						
					Char			Liquid		Gas	
					Dist (%wt)	Carbon (% wt)	Energy (MJ/kg)	Dist (%wt)	Energy (MJ/ kg)	Dist (%wt)	Energy (MJ/ m^3)
Pyrolysis	300-500	S-W	Inert	Dry	12-35	24-95	11-35	30-75	10-35	13-35	5-30
Gasification	500-800	S	Air/O_2	Dry	10	4-46	N/A	5	N/A	85	2-20
Incineration	850-1200	S – M	Air/O_2	Dry	15-20	2-10	N/A	N/A	N/A	80-90	12-16 MJ/kg
HTC	180-250	H-D	Inert/limited O_2: sat press	Wet	50-58	58-83	18-36	5-20	N/A	2-5	N/A

S : Seconde .M : Minutes. H : Hour. D : Day. W : Week. N/A : Not Available. Source: (Lu *et al*., 2012)

2.7. Production and characterization of activated carbon

Activated carbon is defined as a carbonaceous material with high adsorption capacity. The high adsorption capacity is conferred by the material's inherent properties such as high surface area, large pore volume and specific pore size distribution. The presence of micropores, mesopores and macropores structure in activated carbon favours the access of the adsorbed entity into the interior of the carbon particle (Hagemann *et al*., 2018). These properties give to the activated carbon the great capacity for the ANG storage system (Ayinla *et al*., 2019). The production of activated carbon has been the basis of several studies. A large number of raw materials such as petroleum coke, empty fruit bunch, bean husk, wood, palm solid waste, coconut shell, bituminous coals and coal char has been used to produce activated carbon (Yorgun *et al*., 2015). Among these available materials, coal has been often used to produce activated carbon because characterized by high microporous structure and surface chemical properties. From various outcomes of many studies completed on the production of activated carbon, it is reported that coal raw materials produce high carbon content of activated carbon (Heidarinejad *et al*., 2020). Activated carbon (AC) have been efficiently used in many applications of separation like; cleaning of pharmaceutical content from wastewater treatment effluent and retaining of heavy metals as chromium and arsenic from aqueous solution (Niazi *et al*., 2018). Moreover, in electrical energy application (Arena *et al*., 2016), greenhouse gas adsorption (Sawant *et al*., 2017), H_2 storage and air pollution control (Mohan *et al*., 2019) and CO_2 capture and adsorption (Rashidi et al., 2021), AC takes a major procedure role. it has been used also as ultra-capacitor for his wide contact surface (Kim *et al*., 2016). From carbon materials, AC could be produced by using two different procedures which are physical and chemical activations (Dos Reis *et al*., 2016). Therefore, physical AC is obtained through carbonization followed by activation in CO_2 or steam whilst chemical AC is produced through a combined carbonization and activation process using an activating agent such as potassium hydroxide (KOH) and Zinc chloride ($ZnCl_2$) (Ahmed *et al*., 2019). However, it was concluded that chemical AC was more efficient than physical AC in a wide range of applications due to his higher surface areas and smaller pore sizes (Ahmed *et al*.,

2019). There are different chemical activating agents used for AC preparation available in literature like; $ZnCl_2$, KOH, K_2CO_3, NaOH, HNO_3, H_3PO_4 (Luo *et al*., 2018). However, recovery of activating agents still tough for economic efficiency (Dobele *et al*., 2012). Nevertheless, it has been reported that for reduction of CO_2 emission from energy plants (fossil fuel combustion) into the atmosphere and the global warning control, AC could have a great impact on CO_2 capture and separation (Zhang *et al*., 2016) rather than other materials which could be used for CO_2 gas capture under different conditions, AC presented a higher contact surface and porosity (Zhou *et al*., 2019). Previous studies deduced that KOH activation for production of activated carbon, etching the carbon surface and justify the AC's excellent carbon dioxide adsorption performance (Thommes *et al*., 2015; Idrees *et al*., 2018) Characteristics of carbonaceous materials like porosity, surface area, etc… could be measured using the CO_2 gas capture capacity (Ahmed *et al*., 2019). HTC conditions support the development of defined micropores, and excellent textural properties of AC as HTC highly decreased the oxygen containing functional groups which are available to react with the activating chemicals (Dobele *et al*., 2012). This project processed HTC of mixed SWS and DC as a precursor process that facilitated the chemicals required to produce AC to face environmental challenges and produce a carbonaceous advanced useful material for different process applications. Characteristics of produced AC and optimum process of production parameter have been provided and compared with ACs produced in previous studies to fill up existent gapes. The synthesis, characterization and adsorption properties improvement have been assembled to reach an optimum adsorption storage capacity for the different use of activated carbon.

The study conducted by Ahmadpour (1996) focus on the characteristics of produced AC from bituminous coal using physical and chemical activation process. They used a 212- 250 um particle size coal and optimized the process by evaluating the influence of different parameters such as reaction temperature, particles size, activation time, chemical reagent, mixing procedure and impregnation ratio. The study showed that; chemical activation procedure was malleable and produced activated carbon with great surface properties and

porosity than physical activation method. It was also showed using KOH and $ZnCl_2$ that the impregnation ratio played a key role in chemical activation procedure of coal. The impact of reaction temperature in the development of pores has been found very significant in the study. 1 hour and 500°C were the optimum conditions parameters of activation process using $ZnCl_2$ reagent, whereas using KOH reagent the optimum was reach after 2 hours at 700°C. The AC produced from an Illinois basin bituminous coal in the United States of America by Sun (1997) using air oxidation procedure at temperature between 150 and 250°C followed by volatile removal between 500 and 730°C in a nitrogen medium and gasified at temperature between 730-880°C presented a 1000 m^2/g surface area and high porosity properties. The toluene adsorption capacity of the produced activated carbon was higher compared to Darco coconut charcoal commercial the activated carbon. The economical results showed that the cost of activated carbon depend not only on its surface area width but mostly on the production cost per square meter. Hsu and Teng (2000) assessed chemical reagents influence during the production of activated carbon from bituminous coal. They used $ZnCl_2$, H_3PO_4 and KOH as chemical reagents and checked the role of impregnate ratio of the coal sample and the chemical reagent. The chemical activation procedure was done in two steps which was the mixing of coal sample and the chemical reagent at different ratio followed by the activation at different temperatures under a nitrogen flow-in. Produced activated carbon using KOH reagent had a lower carbon yield compared to the activated carbon obtained using $ZnCl_2$ and H_3PO_4 reagent. The porosity of the activated carbon was increasing proportionally with the temperature for all chemical reagent used and reached an optimum point from whom it started decreasing as the temperature was further increased. The highest surface area ($3300m^2/g$) was obtained with KOH reagent then followed by $ZnCl_2$ and H_3PO_4(960 and $770m^2/g$). The research concluded that base reagent was producing activated carbon with high porosity than acid reagents. Moreover, larger particle size of coal sample reduced the carbonization and porosity yield of activated carbon due to their small external surface area providing a small contact between the reagent and the coal, which result in higher resistance of intraparticle diffusion of the reagent. Analysis of the activated carbon produced by Lozano-Castello (2002a)

conducted on the BET analyser showed a surface area comprised between 700 and 3290 m^2/g. Anthracite coal produced an activated carbon with higher surface area compared to bituminous coal using a KOH/coal impregnate ratio of 4/1 and a reaction time of 1 hour at 700°C. It was found from the results that higher methane adsorption capacity was observed on activated carbon with higher micropore volume. The chemical activation process showed more advantages compare to physical activation process as outcome from that research. Azargohar and Dalai (2005) used the central composite design for the study of activation temperature, time, and ratio of steam to char by weight effect in physical activation process of Luscar char. The optimum condition for yield and surface area were determined by the development of the model. The study concluded that the higher surface area obtained was 502 m^2/g with a yield of 54.1% for the better produced activated carbon using following conditions, temperature of 708°C, steam to char ratio of 0.93 and for 1 hour of reaction time. The results demonstrate the consistence of the models developed for the surface area and the yield compared to those produced under optimum condition test. Using bituminous coal KOH and NaOH to produce activated carbon, Cuhadaroglu and Uygun (2008) evaluated the characteristics of the product obtained. They focused on the influence of chemical reagent ratio and nature to the produced activated carbon. The BET analysis of the produced activated carbons showed that the increasing of weight ratio of chemical reagent and coal from 1 to 4 enhanced the surface area of the product from 785 to 1295 m^2/g using KOH and from 657 to 1566m^2/g when the chemical reagent used was NaOH.

A method to modify the pore size distribution of produced activated carbon from coal has been proposed by Gong (2009). The researchers studied possibility of the enhancement of mesopores formation in the synthesized activated carbon. The modification process was laid on previous knowledge about the increasing of the mesopore volume of activated carbon. The study indicated that catalysing of steam activation process using metals was the better procedure to enhance the mesopores formation. The project used pulverized bituminous coal which was mixed to KOH reagent in different ratio. The mixture has been placed in a furnace and heated at 600°C during 45min under nitrogen flow. The produced

char was then washed with HCl 5% mass fraction and distilled water to raise the pH at 6. The product washed was submitted to a steam activation procedure at 900°C. The characterization of the activated carbon obtained after this process showed that the number of K-containing compounds present in the char could be regulated by modifying the impregnate ratio of KOH and coal mixture. The adsorption capacity of the produced activated carbon was increasing proportionally with the increasing of KOH/coal ratio. The analysis of pore size showed an increasing from 2.379 to 2.636 mm and the mesoporosity increased from 30.9 to 46.1%. The study concluded that the modification of pore size distribution of activation carbons from coal was possible and influenced by the amount of chemical reagent used. The textural and surface properties of ACs produced from palm oil shell were studied by Arami-Niya (2011) comparing different methane adsorption capacity. The study used H_3PO_4 and $ZnCl_2$ reagent for chemical activation process which was followed by physical activation using CO_2. It was found that the combination of chemical and physical activation process for production of activated carbons from palm oil shell improved and strengthened the pore size distribution. The results of the study ended up to the conclusion that high surface area and pore development are the most important parameters of methane adsorption properties of activated carbon but at the same level, the homogeneity of pore sizes had a great influence. From Indonesian low-grade coal, activated carbon was produced and evaluated for methane adsorption capacity in the study conducted by Martin (2011). The results of physicochemical analysis showed that the coal sample had 13.56 % of moisture, 4.80 % of ash, 56.47% of carbon and 2.41% of total sulphur. Prior to physical activation process, the coal sample was pulverized to a particle size of 0.10mm. the physical activation was conducted with CO_2 at 950°C for 6 hours. The produced activated carbon analysed through BET revealed a surface area of 668 m^2/g, a pore volume of 4.7 cm^3/g and a density of 2200 kg/m^3. The evaluation of methane adsorption capacity of the produced activated carbon compares to the commercial activated carbon (Carbotech) with a surface area of 885 m^2/g and pore volume of 5.14 cm^3/g under 3.5 MPa of pressure at temperatures varying from 300 to 318 K was conducted. The study showed that the produced activated carbon from low-grade

coal had lower methane adsorption capacity than the Carbotech due to its smaller surface area and pore volume.

The influence of chemical reagent nature and weight ratio on activated carbon's pore structure from bituminous coal has been study by Okhovat (2012). The study experiment used 10 g of coal sample characterized by a particle size of 212 – 250 µm. The coal sample was mixed with KOH or $ZnCl_2$ reagents in varied weight ratio from 50% to 200% to produce activated carbon. The obtained mixture was dried and then heated up to 500°C for ZnCl2 and 700°C for KOH under nitrogen flow and kept at the final temperature for 1 hour. The obtained materials were washed with acid and distilled water then dried. The authors used four models (Dubinin-Stoeckli, Stoeckli, Horvath-Kawazoe and enhanced Horvath-Kowazoe) to analyse the adsorption isotherms of the produced AC. The study observed a similarity of results obtained from different model used. The increasing of impregnate weight ratio increased the pore volume of activated carbon produced using both chemical reagents. The difference of microporous structure of produced activated carbon was seen. The results showed that the $ZnCl_2$ reagent used for activation process produced high mesoporous structure when the impregnate ratio was increased. However, KOH reagent produced an activated carbon with high microporous structure when the impregnate ratio was increased which had an impact on the pore sizes. The production of AC has been studied by Srenscek-Nazzal (2013). The research used sugarcane molasses as raw material and chemical activation process with KOH reagent to produce activated carbon. The process parameters used were activation temperature range from 400 to 800°C for 1 hour and with different KOH weight ratio. The BET analysis results showed that, the highest surface area and pore volume of 2202 m^2/g and 1.30 cm^3/g respectively were obtained for the activated carbon produced at 780°C with a KOH/molasses weight ratio of 2.8/1. The AC from kenaf core fiber, agricultural biomass using phosphoric acid reagent (H_3PO_4) has been produced by Shamsuddin (2016). Shamsuddin (2016) evaluated the porous structure and surface properties of the synthesized activated carbon. The proximate analysis conducted on the kenaf core fiber showed a low ash and high fixed carbon content which implicated a potential use of these materials for production of activated

carbon. The kenaf core fiber was firstly washed in hot distilled water and then dried in an oven at 105°C. The obtained product was cut and sieved to a particle size between 500 and 600µm. The dried sample was then heated for carbonization at 400°C during 1 hour in a nitrogen medium. The carbonized product (char) was mixed with H_3PO_4 at a 4/1 impregnate ratio. The impregnated mixture was heated up to a temperature of 500°C and kept on that condition for 1 hour. The produced activated carbon was washed with acid solution and distilled water then dried in an oven. The BET analysis of the synthesized product showed that the process improved the surface area and pore development compared to the obtained char sample. The H_3PO_4 showed then its potential as an activation process reagent. The surface area and micropore volume of the produced activated carbon were 299.02 m^2/g and 0.12 cm^3/g respectively. The increase was observed compared to the surface area and micropore volume of the produced char which was 13.68 cm^2/g and 0.004 cm^3/g respectively. The pore development of the produced activated carbon was increased by the H_3PO_4 activation process as revealed by the comparison of char and produced activated carbon morphology. However, it has been remarqued that even tough, kenaf core fiber could be used to produce activated carbon through chemical activation process, the surface area and pore volume of the activated product are not enough for gas storage application. Therefore, the process needs to be changed or improved to produce a suitable activated carbon for gas adsorption and storage system.

Hydrothermal carbonization (HTC) process has been used for production of activated carbon from camphor and camellia leaves through chemical activation using KOH reagent by Yang (2019). The study focused on the impact of HTC temperature on pore structure and adsorption capacity of produced activated carbons from the two different leaves. The process was described as followed; a certain amount of treated leaved was immersed into 60 ml of deionized water and placed in a hydrothermal reactor then heated at temperature range from 180 to 300°C. The produced hydrochar was then mixed with KOH reagent at a weight ratio of 1/3. The obtained mixture was held for 1 hour at 800°C under nitrogen flow for production of activated carbon. The produced activated carbon was washed with acid solution, rinsed with distilled water, and dried in an oven. The characterization

of the produced activated carbon showed that HTC temperature impacted the structure of the product and its adsorption capacity. Analysis of results revealed that the activated carbon from camellia leaves through HTC process at 240°C had more micropores compared to the one from camphor leaves. The highest surface area obtained using this process was 1823.77 m^2/g. The study analysed the adsorption isotherms of produced activated carbons. The Langmuir isotherm model used to describe the adsorption process provided better results than Freundlich isotherm model. Activated carbon produced from camphor leaves presented experimental data well-fitted with a pseudo –first-order kinetic model. Whereas the activated carbon produced from camellia leaves displayed experimental data fitting with pseudo-first and second-order kinetic model factors. The authors conclude that HTC process favours the cost–effective production of activated carbon with high potential for gas storage. Recently a study has been conducted by Abdulsalam Jibril (2019) on the production of activated carbons from South African coal waste for natural gas storage application. The author evaluated the influence of carbon content, chemical reagent to coal material weight ratio and activation and activation temperature on the surface area and pore volume of the produced activated carbon. The author further investigated the ANG storage technology using the synthesized activated carbon. The results of the study showed that the fixed carbon content of south African coal wastes make them suitable for production of activated carbon. Moreover, the increasing of the activation temperature and KOH to coal material weight ratio was found proportional to the increasing of surface area and pore volume of the produced activated carbon. The study revealed that the highest surface area of 1925 m^2/g and pore volume of 1.290 cm^3/g were obtained at 800C using a KOH to coal ratio of 4/1 from coal containing the highest carbon content.

2.7.1. Types and characteristics of activated carbon for gas storage

Based on the precursor, physical characteristics and procedures used for their production, activated carbons have been classified by Suzuki (1990) as; powered activated carbon (PAC), granular activated carbon (GAC), activated carbon fiber (ACF) and carbon molecular sieve (CMS). Furthermore, studies on the storage

capacity of the four classes of activated carbon have been conducted by different researchers (Dos Reis, 2020). The methane storage capacity of two different activated carbons which are PAC and ACF has been evaluated by Lozano-Castello (2002b). It was found that the PAC had the highest packing density than the ACF, however, the highest methane adsorption capacity was attributed to the ACF due to its great micropore size distribution. GAC produced from coconut shell through combination of chemical activation using $ZnCl_2$ and physical activation under CO_2 at high temperature provided a natural gas storage capacity of 95v/v under 35 bar and ambient temperature (Prauchner and Rodriguez-Reinoso, 2020). The textural characteristics of the activated carbon have a big impact on its natural storage capacity as showed by Lozano-Castello (2018). Hence, characteristics of activated carbon for efficient gas storage are.

- Large micropore resulting in high adsorption capacity
- High available surface area, more than 1000m^2/g
- Small mesoporosity to favour the adsorption and desorption process's kinetics
- Narrow pore size distribution

The study conducted by Luo (2011) investigated the correlation between methane adsorption capacity and microporosity of the activated carbon produced from anthracite coal. The chemical activation process using KOH reagent was conducted to produce the activated carbon under the following conditions: varied KOH/coal weight ratio (1/1, 2/2, 3/1, 4/1 and 5/1), temperature of 750°C and 1hour of activation time. The adsorption pressure use for methane adsorption capacity of the produced activated carbon was raised up to 35 bar and the temperature was 25°C. The Dubinin-Astakhov (D-A) model was used to manage the obtained data. The largest methane adsorption capacity was obtained on the activated carbon produced using a KOH/coal ratio of 4/1 which had a surface area of 2071 m^2/g, a micropore volume of 0.833 cm^3/g and a pore diameter of 1.40mm. It was observed that the methane adsorption capacity of the produced activated carbon was increasing proportionally with the surface area and the micropore volume. The second order kinetic model described the methane adsorption kinetics. The methane adsorption rate was influenced directly by the adsorption capacity of the

produced activated carbon. The study showed from the measured data of the D-A that the most heterogeneous activated carbon had the highest methane adsorption capacity. The study concluded that the heterogeneity of the produced activated carbon influenced its methane adsorption capacity. The AC produced from microcrystal cellulose powder using physical activation process under CO_2 has been evaluated for methane adsorption by Policicchio (2017). The adsorption temperature used for methane adsorption process was 25°C and the pressure was raised up to 35 bar in a high-pressure volumetric vessel. The obtained results showed that the methane adsorption capacity of produced activated carbon depends on the surface area. The methane adsorption capacity was observed increasing from 77.1 to 146.4 v/v when the surface area increased from 346.86 to 1784.36 m^2/ g respectively. The adsorbed methane amount was found closed to the specification for methane storage in porous material for vehicle application (150 v/v at 35 bar and 25°C) established by the United State of America Department of Energy (DOE). The study concluded that the surface area of the porous materials played a key role in adsorption and storage process capacity. However, the ability of some porous materials depends not only on the surface area but also on the pore sizes and interaction between the pore's walls and the gas. Gao (2017) prepared activated carbon from petroleum pitch mixed with coal powder via chemical activation process using KOH. The project studied the impact of coal particle sizes on the pore structure and adsorption capacity of produced activated carbon. Coal sample was mixed with pulverized pre-treated pitch and KOH reagent in 1/1/1 weight ratio. The mixture was heated up to a temperature of 800°C in a horizontal furnace tube under argon atmosphere and kept in that conditions for 1 hour. The obtained product was washed with 0.2M HCl, rinsed with distilled water and then dried in an oven. The adsorption capacity of the produced activated carbon for gas such as CO_2, N_2 and CH_4 was studied through gravimetric sorption method under pressure of 3.5 MPa and at a temperature 298 K. The characterization and gas adsorption analysis revealed that coal with particle sizes of 0-53μm produced an activated carbon with the highest surface area of 1401 m^2/g and gas adsorption capacities of 8.87 mol/kg for CO_2, 5.43 mol/kg for CH_4 and 3.09 mol/kg for N_2 under a pressure of 3.5 MPa at 298K. the

stability of the produced activated carbon was also evaluated as a function of coal particles sizes. The evaluation was made by prior activation of the pre-treated pitch only using KOH reagent. The result revealed that pre-treated pitch overflowed from the furnace vessel (crucible) where it was placed and produced a non-stable activated carbon. The study revealed that, the produced activated carbon had high potential for pressure swing adsorption as it has high adsorption selectivity for CO_2 over other gas such as N_2 and CH_4. Abdulsalam Jibril (2019) studied the influence of adsorption process parameters and microporous structure of activated carbon on gas storage capacity. The results revealed that the gas storage capacity was influenced by the texture of the produced activated carbon which depended on the temperature and KOH/Coal weight ratio used. The author showed that the methane adsorption capacity of the produced activated carbon was impacted by the adsorption process temperature and pressure. The study concluded that; South African coal wastes are good raw material to produce activated carbon with large surface area and pore volume used as adsorbent in ANG technology. It is, therefore, important to note that the use of the coal's wastes and sewage sludge will reduce the environmental impact and public health risk associated with the exposure to their stockpiles disposed across the country. The reduced cost of adsorbent materials produced from coal wastes and sewage sludge will make commercially viable the ANG storage system.

2.8. **Overview of adsorbed gas storage system**

Through natural gas adsorption (ANG) system, the gas is stored in porous materials placed into a vessel under low pressure in an ANG system. The use of low pressure has two main advantages; it reduces storage cost compared to the high pressure needed to compress gas and provides design flexibility of storage tanks (Vasiliev *et al*., 2021). The ANG system include also low capital and cost-effective process of compression and refuelling equipment (Vasiliev *et al*., 2021). The ANG system comply with safety regards as it uses low pressure which enhance the security of the process (Rani *et al*., 2019). The main parameters that influence the gas adsorption capacity in an ANG system are the porous volume, temperature, pressure, and the porous material used (Rani *et al*., 2019). The

efficiency of the adsorption process increases proportionally with the pressure increasing, whereas the temperature reduction enhances the gas adsorption process efficiency. The gas adsorption capacity in ANG can also be impacted by adsorbent properties and the heat effect's management on the system (Alhasan *et al*., 2016).

The production of a super activated carbon for ANG application has been investigated by Singh (2016). The author combined chemical and physical activation process to develop an activated carbon with greater performance. The target was to enhance the micropore volume and size of the produced activated carbon which will confer it a high storage capacity. The adsorption analysis results revealed a higher adsorption capacity of produced activated carbon compared to the one produced via single chemical or physical activation process. Bulk density, high surface area and pore volume are adsorbent properties that determine the quality of the adsorbent for gas storage (Alhasan *et al*., 2016). The evaluation of an AG system is done by determining the volumetric capacity which results from the development of porous structure of the adsorbent material. The development of adsorbent's porous structure is one of the main determinant characteristics of the adsorbent material for potential ANG storage use. another factor influencing the performance of the ANG storage system is the thermal effect management. To ensure the storage of high volume of natural gas, it is important to remove the heat released during the charging process from the system. The gas is not efficiently adsorbed when the system is heated up by charging system remained heat, that reduces the adsorption and storage capacity of the natural gas. In the same way, reducing of temperature during the discharge process results in small natural gas released (Jiang *et al*., 2019). The heat effect needs to be managed for the enhancement of natural gas storage capacity.

2.8.1. Global Research position on ANG storage system

Improvement of the ANG storage system performance has been at the centre of numerous studies. The fact that ANG storage system is gaining more interest as a viable and alternative gas storage system over CNG, and LNG gives it a particular potential. Nowadays, the main parameters which have been studied for the

improvement of storage capacity; are the development of an adsorbent with high-adsorption capacity and the management of the adsorption system's heat effect. A review concerning the available gas storage techniques has been done by Sahoo (2016). Moreover, the study compared different storage systems (ANG, CNG and LNG) technically and corresponding refuelling cost. The results showed that there is a need of research to determine the technic of the driving range extension in vehicular application of ANG. The study assumed that the design of specific tank containing carbon adsorbent plays a key role in the improvement of natural gas storage and driving range extension of vehicles. The research suggested the following solutions against some AG technical challenges.

- The control of gas impurities onto the adsorbent bed can improve the adsorbent life cycle
- The enhancement of the adsorbent packing density can increase the volumetric storage efficiency from 150 to 200v/v
- The management of thermal effect during refuelling can favour a complete fill up to be reach out.

To study the thermal effect on an ANG system, a model has been firstly developed by Mahdi (2019). The model revealed a temperature drop during the discharging process which could minimized or completely removed by environmental heat transfer. The use of ANG system in bulk storage and gas vehicles (GVs) has been developed earlier by Golea (2020). The studied confirmed that the most important factors GVs technique is gas storage density and mileage range. Moreover, the study assumed that the conformity of storage tank and adsorbent properties determine the viability of ANG system in bulk storage. The study revealed also that the choice of the adsorbent determines the economic viability of the ANG system. The balance between the cost and the performance of the adsorbent is applied to find a low cost and highly efficient materials for the ANG technology applicability. Ribeiro (2015) studied the effects of the composition of natural gas on the ANG system efficiency. In this study, the author used a mathematical model, containing experimental results which displayed a significant reduction of gas adsorption system capacity due to the presence of heavy hydrocarbons in the natural gas. The

study advised to use of specific carbon-based filter during the charging and unloading process of gas to improve the performance of the storage system.

Two different carbon adsorbents; monolithic carbon and carbon fiber have been evaluated for storage performance in ANG system by Vasiliev (2021). The author developed a theoretically a cylinder containing an internal heat exchange system for thermal effect assessment, and he also evaluated the temperature and gas concentration changes during the discharge process. The results showed that carbon fiber material called “Busofit” produced from cellulose through pyrolysis delivered 150 v/v of methane under 35 bars. The study concluded by advising that for efficient natural gas storage and transportation, the use of a multi-cell tank designed with thermal control heat pipe is strongly recommended in ANG system.

The heat effect occurring during discharge process of ANG storage system has been studied by Sheikholeslami (2020). The maximum temperature fluctuation was seen in the middle of the adsorbent bed during the discharge process. A novel heating/cooling system with U-shaped heat exchange pipe designed at the center of the storage tank has been proposed to manage the fluctuation of temperature by circulating hot or cold water through the system. The study revealed that the use of the mentioned system could reduce the discharge time by 60%. The charging capacity of the activated carbon adsorption bed has been evaluated by Sahoo (2016) using experimental and simulation data. The COSMOL Multiphysics software was used for simulation. The simulated values were compared to those obtained from the experiments carried out at varied flow rate under different pressure and temperature. The predicted filling times and raising of temperature in the center of the bed were accurately determined by the model used. It was found that the effective application of AG system in vehicles using a known adsorbent depend on the amount of gas stored result from the storage capacity and also influenced by the discharge amount necessary to reach the targeted driving range. Moreover, it has been showed that the heat removing rate from the system controls the charge rate and that the storage volume efficiency was improved using an external convective cooling system. The influence of gas composition on activated carbon adsorption capacity in ANG system was investigated by Feroli (2018). The study used a prototype storage tank containing

activated carbon. The results showed that the adsorption of heavier component and CO_2 was partially deactivating the activated carbon bed hence reducing the storage capacity of the system.

The influence of temperature on the charging and discharging process of the ANG system was also studied by Park (2018). For methane storage, the study used a commercial activated carbon placed in a 0.5-liter vessel using 3.5Mpa of pressure. The results showed that the storage and delivery capacity of the system depend on the rate of charging and discharging of the adsorbed gas. Furthermore, the study revealed that a rapid charging rate will cause a temperature rise, whereas a rapid discharge rate will favour a temperature drop which could reduce the storage capacity and delivery efficiency of the system. An overview of the AG storage method showing five most important parameters of the system success has been provided by Alhasan (2016). Those main parameters are; thermal effects, adsorbent properties, adsorption and desorption rate. The author revealed that AG system challenges such as adsorption/desorption rate and global cost depend on the nature of the adsorbent materials. The study concluded as followed.

- For an efficient and viable ANG storage system, an activated carbon with large surface area, micropore volume, narrow micropore size distribution is needed
- It is also required to manage the thermal control system by using a cooling/heating arrangement to reduce the impact of thermal effects on the charging and discharging process.

2.9. **Hydrogen energy and economy**

The hydrogen is produced and used widely as a primary energy carrier in the system called hydrogen economy (Abe *et al*., 2019). The advantages linked to the use of hydrogen in term of environment, energy security, and economy are numerous (Sun *et al*., 2018). The development of hydrogen economy depends principally on the security, the effectiveness, and the cost of hydrogen storage system (Rusman *et al*., 2016). As the world population continues to grow, the global energy demand increases as well compared to past years. The high cost of fossil fuel energy use has become a big challenge for the global economy of the

world (Ren *et al*., 2015). Investigations made on fossil fuel reserve revealed that petroleum, natural gas, and coal can support the global energy production for 40, 60 and 156 years respectively (Boullouz *et al*.,2022). The present consumption of energy increases the prices of fuels and diminishes the global reserve that present a real economical danger (Sun *et al*., 2018). Furthermore, utilization of fossil fuels has an environmental concern as it releases greenhouse gases and other pollutants contributing to the planet warming (Rusman *et al*., 2016). Much research has proven that to solve global energy issues it is important to find an environmentally friendly, cost effective and more sustainable energy source to replace the actual fossil fuels system (Rand *et al*., 2021). Therefore, sustainable energy for the future must match the following conditions.

- Ensure security of energy supply.
- Use sustainable local energy resources.
- Reduce carbon dioxide emission on a global scale.
- Ensure improvement of urban air quality; and
- Produce new industrial and technological energy base necessary for the growing of the future economy (Rand *et al*., 2021).

Several studies showed that hydrogen could be the ideal sustainable future energy carrier (Zhang *et al*., 2017). Hydrogen has been evaluated as an energy carrier very long time before and its use was increased by the 1970 global energy crisis (Salman *et al*., 2021). The technology of hydrogen system was improved in 1980 (Niaz *et al*., 2015). The big challenge of energy production from hydrogen is its difficult storage due to its extremely low density (Ren *et al*., 2015). Therefore, development of hydrogen storage system needs to be conducted for the future energy production breakthrough (Abe *et al*., 2019). Hydrogen is the most abundant element of the universe, the calorific value of hydrogen is the highest compared to fuels, natural gas, and coal (Abe *et al*., 2019). Moreover, energy production from hydrogen is environmentally friendly and hydrogen can be produced from renewable (Hydrocarbon, wind, wave, solar, biomass and geothermal) and non-renewable (coal, natural gas and nuclear) energy sources (Rusman *et al*., 2016). The energy content of 1 kg of hydrogen has been estimated to 120MJ (33kWh) which is more than the double of conventional fuels energy (Teichmann *et al*.,

2016). The comparison of energy content between hydrogen and other fuels is presented in Table 2 7;

Table 2-7. Comparison of some selected energy contents of fuels

Fuel	Energy Contents (MJ/kg)	
	Lower Heating value	Higher Heating Value
Gaseous hydrogen	119.96	141.88
Liquid hydrogen	120.04	141.77
Natural gas	47.13	52.21
Liquified Natural Gas (LNG)	48.62	55.19
Still gas (in refineries)	46.89	50.94
Crude oil	42.68	45.53
Liquefied Petroleum Gas (LPG)	46.60	50.14
Conventional gasoline	43.44	46.52
Reformulated or Low-Sulfur	42.35	45.42
Conventional Diesel	42.78	45.76
Low-sulfur Diesel	4260	45.56
Coal (wet basis)	22.73	23.96
Bituminous coal (wet basis)	26.12	27.26
Coking coal (wet basis)	28.60	29.86
Methanol	20.09	22.88
Ethanol	26.95	29.84

Sources: Teichmann *et al*., 2016; Zhang *et al*., 2017; Abe *et al*., 2019

Hydrogen economy or hydrogen energy system is defined as a system where hydrogen is the main energy carrier. The term “hydrogen economy” was used for the first time by John Bockris in 1970 (Bockris, 2013) at General Motors Technical Center. The engineer conducted a study on the production of hydrogen from energy sources to replace the conventional fossil fuels used in transport, industrial, residential, and commercial sectors. The study showed that hydrogen economy has a potential to resolve world confronting issues concerning, natural resources depletion, global environmental problems, and energy demand due to the growing of global population. However, due to its low density which makes its storage difficult, hydrogen technology still need to be deeply studied for is industrial expansion world widely. Nowadays, hydrogen is mainly used by

refineries and only in some others chemical industries because of the high cost of its production, storage, and delivery non economical viable (Sadhasivama *et al*., 2017). However, governments are investing in research for the hydrogen energy application due to the incomparable advantages linked to the system (Niaz *et al*., 2015). Therefore, suggestion has been made by the European Commission High Level Group for Hydrogen and Fuel Cells Technologies which estimated that European Union in 2050 should attain a hydrogen-based economy and 35% of futures vehicles will be filled up with zero carbon hydrogen fuel by 2040 (Abe *et al*., 2019). Moreover, the U.S Department of Energy's Energy Efficiency and Renewable Energy, Fossil Energy, Nuclear Energy, and Science Offices was expected the conversion to hydrogen-powered fuel cell vehicles to be effective in 2020 (Durbin *et al*., 2013). Therefore, hydrogen has been found to be an indicated element for cost-efficient, clean, and sustainable energy production for the global economy and security of the future. The challenge of hydrogen economy application remains the storage system. It, therefore, worthy to study the possibility of hydrogen storage improvement for energy economy. On the other hand, a hydrogen economy is needed, to resolve current environmental and energy-related problems. For the introduction of hydrogen as an important energy vector, advanced materials are required for hydrogen storage technologies for mobile applications. Transitioning to a hydrogen-powered economy could bring great benefits for South Africa, both economically and socially, as the world explores new forms of energy. South Africa via the DST has bold plans to move from being a resource-based economy to a knowledge-based economy, facilitated by breakthrough innovations in the areas of science and technology. As the world's top producer of platinum group metals (PGMs), SA has a unique opportunity to capitalise on the global demand for energy and rising prominence of clean fuel technologies.

The DST has identified seizing opportunities in areas such as the hydrogen economy as part of its 'Ten-year plan for SA ', to establish capabilities "that will provide long-term, sustainable solutions in national priority areas such as health and energy, while boosting economic growth". The department recognises, however, that there are obstacles ahead: "Hydrogen and fuel cell technologies are

widely seen as possible energy solutions for the 21st century, yet it is far from clear how we will achieve what has been called the 'hydrogen economy', in which energy is stored and transported as hydrogen. We believe that designing successful hydrogen storage system by adsorption will provide the missing link for the SA hydrogen economy. However, designing an optimized adsorbent for hydrogen storage is a challenging task. In general, there are two basic requirements which need to be considered: On the one hand, many adsorption sites per weight and volume of adsorbate should be provided. This must be done by developing a highly porous material with large surface areas and pore volumes. On the other hand, the heat of adsorption of the adsorbent should be increased. A suitable activated carbon to store hydrogen gas should, therefore, possess the following characteristics: (1) A surface area greater than 1000 m^2 /g. (2) Large microporosity to increase adsorption capacity. (3) The narrow pore size distribution of about 8 A˚. (4) Low mesoporosity to ease the kinetics of adsorption and desorption processes (Shannon *et al*., 2018). Challenges of hydrogen storage are due to the following: 1) H_2 is lightest element; 2) H_2 has lowest density; 3) H_2 has Strong covalent bond; 4) H_2 has Low polarisation ability; 4) there is a weak interaction between H_2 molecules. Hydrogen is an energy vector; in that it must be produced from a primary energy source before it can be used.

2.9.1. Hydrogen storage techniques

There are generally six hydrogen storage methods matching with the reversibility of stored hydrogen volumetric and gravimetric density (Mohan *et al*., 2019). The Table 2-8 presents the different hydrogen storage methods and their principles.

Table 2-8. The six main hydrogen storage methods and procedures

Storage method	ρ_m (mass %)	ρ_v (kgH_2m^{-3})	T (°C)	P(bar)	Procedures
High pressure gas cylinders	13	<40	RT	800	Compressed gas (molecular H_2) in light weight composite cylinders (tensile strength of the material is 2000 MPa
Liquid Hydrogen in cryogenic tanks	Size dependent	70.8	-252	1	Liquid hydrogen (molecular H_2), continuous loss of a few % per day of hydrogen at RT
Adsorbed hydrogen	~2	20	-80	100	Physisorption (molecular H_2) on materials e.g., carbon with a very large specific surface area, fully reversible
Adsorbed on interstitial sites in a host metal	~2	150	RT	1	Hydrogen (atomic H) intercalation in host metals, metallic hydrides working at RT are fully reversible
Complex compounds	<18	150	>100	1	Complex compounds ($[AlH_4]^-$ or $[BH_4]^-$), desorption at elevated temperature, adsorption at high pressure
Metals and complexes together with water	<40	>150	RT	1	Chemical oxidation of metals with water and liberation of hydrogen, not directly reversible

The gravimetric density ρ_m the volumetric density ρ_v, the working temperature T and pressure are listed. RT stands for room temperature (25°C).

2.9.2 High-pressure gas cylinders for hydrogen storage

Hydrogen is commonly stored in high-pressurized cylinder under 20 MPa (Milanese *et al*., 2019). Nowadays, a lightweight composite cylinder has been developed to support pressure over 80 MPa. In that cylinder the density of stored hydrogen could reach 36 kg/m^{3}mostly constituted by liquid phase. The volumetric density of hydrogen inside the cylinder is proportional to the increasing of the pressure. However, the pressure increasing reduces the gravimetric density of hydrogen. Hence, the volumetric storage density is increased in pressurized gas technic by the reduction of gravimetric density. The challenge of high-pressure gas cylinders' technics is the safety of surrounding population. A standard piston-type mechanical compressor can be used to pressurize the hydrogen gas. However, the cost if this technic is increased by the non- isothermal compression procedure used (Zhang *et al*., 2019). Therefore, research on development of vessels with three layers; inner polymer liner, over-wrapped with carbon-fibre composite and outer layer of aramid material capable to resist to high pressure (100MPa) and corrosion should be deeply investigated. Furthermore, the high-pressure storage system needs to be study for a well-understanding of hydrogen density reduction under high pressure technics and economic viability.

2.9.3 Liquid hydrogen storage

Cryogenic tanks are used for liquid hydrogen storage under atmospheric pressure at 21.2K. Above 33K there is no more liquid phases of hydrogen. Therefore, the liquid hydrogen should only be stored in open systems as in a closed system the pressure could increase (10^4 bar) and arise the volumetric density of hydrogen up to 70.8 kg/m^3(Abdin *et al*., 2019). the energy needed in liquid hydrogen storage system for liquefaction and thermal isolation of cryogenic storage to prevent the boiling of hydrogen constitute the big challenges of the process. The Joule-Thomson cycle is the simplest liquefaction cycle use for hydrogen liquid production (Linde cycle) (Geng *et al*., 2019). The liquefaction cycle is described as follow; the gas is firstly compressed then cooled in a heat exchanger and after that passed through a throttle valve where it submitted under an isenthalpic Joule-Thompson expansion to produce the liquid. Into a closed circuit, the liquid is

separated with the cooled gas which returns to the compressor through the heat exchanger (Abdin *et al*., 2019). In Joule-Thompson cycle, hydrogen temperature increases under atmospheric pressure. Therefore, the hydrogen is usually pre-cooled at 78nK to maintain its inversion temperature below 202K upon expansion. The free enthalpy of exchange between gas at 300k and liquid at 20K state of hydrogen is 11.640 kJ/kg. The overall energy needed for hydrogen liquefaction is 15.2 kWh/kg (Al Ghafri *et al*., 2022). The sphere form of vessel is preferred because of its least surface to volume ratio and the uniform distribution of stress and strain onto it. Therefore, the heating rate of hydrogen liquid depend on the size, shape, and thermal insulation of the containing vessel. However, the spherical form's containers are difficult to manufacture on industrial scale which makes them very expensive. Whereas the increasing of the vessel size significantly reduces the evaporation rate because the surface to volume ratio of the container is inversely proportional to the boil-off evolution behaviour (Abdin *et al*., 2019). The liquid hydrogen storage system application is limited by the amount of energy needed for liquefaction process and the continuous boil-off of hydrogen gas.

2.9.4 Hydrogen adsorption

Hydrogen adsorption on a solid surface is a result of the impact of field force of the solid which attract the molecules of the gas. The solid responsible of the adsorption is called adsorbent and the gas is the adsorbate (Milanese *et al*., 2019). The physisorption of the gas molecules onto the surface of the solid generates the resonant fluctuations of the charge distribution. The phenomena are called the Van der Waals interactions or dispersive interactions. During the physisorption process, the molecules of the gas interact with several atoms of the solid surface (Vyawahare *et al*., 2022). The minimum distance of the potential energy for one molecular radius of the adsorbate has been determined by the study conducted by Brunauer. The author revealed that the minimum energy necessary on hydrogen adsorption is comprised in the range of 1 to 10 kJ. Therefore, the significant physisorption is found only at low temperature (<273 K) due to the weak interaction between the gas and the solid surface. The gaseous molecules interact with the surface of the solid when its monolayer is formed. Hence, the second layer

of the adsorbate is formed using a binding energy equal to the latent heat of sublimation or vaporization of the adsorbate. Therefore, at a temperature equal or greater than the boiling point of the adsorbate under determined pressure only one single monolayer is adsorbed (Vyawahare *et al*., 2022). The quantity of adsorbate in the monolayer could then be determined from the density and the volume of the gas. Hence, the minimum surface area S_m for one mole of adsorbate in the monolayer on the adsorbent can be calculated using the density of the gas ρ_g and the molecular mass of the adsorbate M_{ads} by the following equation (2-12).

$$s_m = \frac{\sqrt{3}}{2}\left(\sqrt{2N_A}\,.\frac{M_{ads}}{\rho_g}\right)^{\frac{2}{3}} \qquad (2\text{-}12)$$

Where NA is the Avogadro constant (NA=6.022x10^{23} mol^{-1}). The surface of hydrogen monolayer is Sm (H_2) = 85.917 $m^2.mol^{-1}$. The quantity of adsorbate Mads on a adsorbent material with a specific surface area S_{spec} can be calculated using the equation. (2-13) ;

$$M_{ads} = \frac{M_{ads}.S_{spec}}{S_m} \qquad (2\text{-}13)$$

Therefore, when carbon is used as adsorbent material, the highest specific area is 1.315 m^2/g and the biggest amount of hydrogen adsorbed is 3.0 mass% (Vyawahare *et al*., 2022). Hence, it has been found that the amount of adsorbed hydrogen is proportional to the specific area of the adsorbent the temperature used. Manirethan *et al* (2018) described the hydrogen desorption process in their research. The results showed that the hydrogen storage capacity of carbon nanotubes was 5-10 mass %. The study evaluated a carbon sample characterized by a 0.1-0.2 mass% single –wall carbon nanotubes (SWNT). It has been found that the amount of hydrogen desorbed at high-temperature peaks which was 5 -10 times smaller than the low physisorption temperature peak was 0.01mass%. The study showed that the gravimetric storage density per SWNT ranges from 5 to 10 mass%. Later, another study reported improved results by using higher temperatures (300-600K). The problem was clarified by the study conducted by

Hirscher (2021). The authors revealed that the desorption of hydrogen was favoured by the Ti alloy particles in the samples formed from during ultrasonic treatment than by the carbon nanotubes themselves. The curvature of the graphene sheets and the cavity inside the tube make the difference between high surface graphite and carbon nanotubes (Picheau *et al*., 2021). The adsorption potential and the amount of hydrogen adsorbed on a zigzag nanotube with a diameter of 1.018nm have been evaluated in the study conducted by Stan and Cole (1998). The authors used the Feynman (semi classical) effective potential approximation method. The results showed that the adsorption potential was 9 kJ mol^{-1} for hydrogen molecules inside the nanotubes at 50 K which was 25% higher than the flat surface of graphite due to the curvature of the surface. It has been found that the increasing of carbon atoms increased the number of carbons which interacts with the hydrogen molecules. The grand canonical ensemble Monte Carlo program has been used by Rzepka (2005) to determine the amount of hydrogen adsorbed on a slit pore and a tubular geometry. The results showed that the amount of adsorbed hydrogen depends on the surface area of the adsorbent and the maximum found was 0.6 mass% at 300 K under 6 MPa. 2 years later, Williams and Eklund realised the grand canonical Monte Carlo simulation of hydrogen physisorption using a finite-diameter carbon SWNT ropes. They revealed that the amount of hydrogen adsorbed decreased with the increasing of temperature. However, the increasing of pressure increased the amount of hydrogen adsorbed. The density-functional and density-functional-based tight binding calculations have been used by Lee (2018) to determine the chemisorption of hydrogen on a single-wall nanotubes. The assessment on the absorption of hydrogen inside the tubes revealed that it is energetically efficient for hydrogen atoms to recombine and form molecules which are then physisorbed inside the nanotube. Ma (2017) produced a molecular dynamics simulation for H_2 implantation. The atoms of hydrogen were implanted into the side walls of a single-wall carbon nanotube containing 150 atoms and characterized by a diameter of 0.683 nm. the results of the study showed that the hydrogen atoms recombined into the molecules through the tube and replaced themselves into concentric tube. The simulation didn't display the condensation of hydrogen inside

the nanotube. The similarity between nitrogen and hydrogen behavior revealed that at a temperature above the boiling point, hydrogen formed only one monolayer of liquid on the surface of carbon (Rostamoghli *et al*., 2018). The study of Zuettel (2012) reported the results of hydrogen adsorption on carbon nanotubes. The author showed that the maximum amount of adsorbed hydrogen was 2 masses% for single carbon nanotubes (SWNT) characterized by a specific area of 1.315 m^2 and at 77K. Ye (2019) investigated on the isotherms(80K) of hydrogen adsorption on a purified SWNT sample. The total surface area of the sample based on the multipoint Brunauer, Emmett and Teller method (BET) was 285 m^2/g and didn't change during adsorption process. At 80K and under 0.32 MPa, the amount of hydrogen adsorbed was 0.04 mass% on the SWNT sample and 0.28 mass% on the high-surface-area saran carbon (1600m^2/g). Furthermore, the increasing of hydrogen pressures up to 7MPa at the temperature of 80K, increased the initial amount of hydrogen adsorbed to 7.7 mass% on the SWNT sample. The study revealed that the adsorption isotherms was impacted by the variation of the pressure. Ouyang (2020) used high hydrogen pressure (12 MPa) at ambient temperature on the SWNT sample and investigated the change of the pressure as a function of time. The equilibrium was reached after 300 min and the maximum amount of adsorbed hydrogen was 4.2 mass%. The hydrogen adsorption of vapour-grown carbon nanofibers with a diameter of 5nm to 300nm was investigated by Fan (2021). The results showed that the under-hydrogen pressure of 12 MPa, the fibres adsorbed about 12.38 mass% of hydrogen. High amounts of adsorbed hydrogen (14-20 mass%) were found in the study of Chen (2020). The authors used the K^- and Li-doped MWNT under 0.1MPa. However, it was revealed that the K^- doped MWNT adsorbed hydrogen at ambient temperature was chemically stable but needed the heat up for maximum adsorption and desorption (473-673K). The high pressure was used on a large amount of carbon samples for the hydrogen adsorption in the study conducted by Heinemann. (2021). They used carbon sample characterized by a BET (N_2) surface area ranged from 100m^2/g to 3300m^2/g. It was found that, except for the nanofiber's samples, the amount of hydrogen adsorbed at 296K under 12.5MPa was function of the surface area following the equation (2-14):

$$X\ (mass\%) = 0.0005\ S\ (m^2/g) \quad (2\text{-}14)$$

The characterization of many carbonaceous adsorbents has been provided using N_2 physisorption at 77K under a pressure of 1 bar by Widjaya (2022). The study classified adsorbent by their surface area and micropore volume characteristics. The hydrogen adsorption analysis was conducted at 77K under pressures range of 0 to 1 bar. The results showed that the amount of adsorbed hydrogen depends on the surface area of the adsorbent. The study concluded that, the reversible hydrogen sorption process is based on the physisorption.

2.9.5 Metalhydrides

Generally, metals, intermetallic compound and alloys react with hydrogen to form mainly solid metal-hydrogen compounds (Zuettel. 2012). The three different hydrides forms are ionic, polymeric covalent, volatile covalent and metallic hydrides. Therefore, metals and inter metallic compound with hydrogen metallic hydrides. The electropositive elements such as scandium, yttrium, lanthanides, actinides and the member of the titanium and vanadium are the most reactive compounds. The metallic hybrids (MH_n) are used as conductors of electricity and liquid metal components. However, only a small number of transition metals are without known stable hydrides. Absorption is the reaction of hydrogen gas with a metal and is described as a simplified on-dimensional potential energy curve (Zuettel.2012). Studies conducted on hydrogen storage in metalhybride forms showed that metal hybrids have designated properties for hydrogen absorption due to the phase transition steps. Absorption and desorption of hydrogen on some metal hybrids are done at ambient temperature and under atmospheric pressure (Mohan *et al*., 2019). The authors concluded that the challenge of hydrogen metal hybrids is the gravimetric hydrogen density as all the reversible hybrids work at ambient temperature and atmospheric pressure.

2.9.6 Complex hybrids

Light elements from group one, two and three form a large variety of metal-hydrogen complexes. The number of hydrogen atoms per metal attracts the interest of their using for hydrogen storage. The difference between the metallic

hydrides and complex hydrides compounds is the transition to a covalent or ionic substances during hydrogen adsorption process (Usman *et al*., 2022). It must be noted that in the complex hydrides, hydrogen is situated in the corner of a tetrahedron with often aluminium or boron in the centre.

The Tetrahydro aluminate $M(AlH_4)$ and the tetra hydroborates $M(BH_4)$ are the mains hydrides complexes used for hydrogen storage. The stability of these elements constitutes a big challenge of storage application as they can only be decomposed at high temperature and in main case above the melting point of the compound. The adsorption and desorption properties of catalysed $NaAlH_4$ was investigated by Pluengphon, (2022). The study showed that at temperatures of 180°C and 210°C, the isotherms presented an absence of hysteresis and an approximately horizontal pressure plateau. Moreover, the catalysed system showed a reversibility in adsorption and desorption of hydrogen characterized by a two-step mechanism of reaction. Bogdanovic (2020) studied the details of $NaAlH_4$ in an improved catalysed system. The study revealed that the equilibrium hydrogen pressure at ambient temperature was 1 bar, and the reaction was reversible. However, Simanullang (2022) showed that the complete conversion of $NaAlH_4$ in a catalysed system was achieved at 270°C under 175 bar during 2 to 3 hours. On the other hand, Knosala (2018) produced the Mg $(AlH_4)_2$ which contained 9.6 mass% of hydrogen and was decomposed below 200°C.The research showed a limit on the determination of pure Mg $(AlH_4)_2$ structure as no single crystals could be produced from the compound. Studies revealed that the complex hydrides have great potential for hydrogen storage system (Khajuria *et al*., 2022). However, their stability, sorption kinetics and reversibility still not well understood as intermetallic compound do not exist after the removal of hydrogen.

2.9.7 Chemical reaction with water

Metals and chemicals compounds can produce hydrogen when reacting with water. The reaction is not directly reversible, but the metal hydroxide could be reduced in a furnace into a metallic compound (Mohan *et al*., 2019). Hydrogen could also be produced from a water molecule generated in combustion. The main challenge of hydrogen storage system using chemical reaction with water is the reversibility and the thermal reduction control in the furnace (Usman *et al*., 2022).

2.10. Summary and implications

Hydrogen has enormous energy production potential and could be the fuel of the future. The heating value of hydrogen, as well as the possibility of producing it using renewable energy, increase its appeal for use in energy production. Depending on the future applications, hydrogen could be stored in various ways. Potential hydrogen storage materials must be developed and thoroughly described. They can travel 500 kilometers per kilogram of hydrogen used as car fuel, whereas a standard car can only travel 100 kilometers per kilogram of gasoline. However, due to the low density of hydrogen, 4 kg of hydrogen requires a tank with a volume of approximately 60 litters. As a result, research into the development of energy conversion equipment and hydrogen storage systems for hydrogen is considered necessary.

HTC process could produce AC from industrial wastes such as CD and SS. HTC has the greatest potential to provide an environmentally friendly and energy efficient process. The HTC process has the advantage of treating wet feedstock without prior drying and producing porous materials. Because of its porous nature, the HC produced can also be used as an adsorbent in the removal of pharmaceutical contaminants from wastewater. With the South African government's vision of a hydrogen economy, a suitable porous carbon material for hydrogen storage application synthesised from waste materials will reduce waste disposal costs and environmental pollution.

REFERENCES

1. Kumar, A. and Samadder, S.R., 2017. A review on technological options of waste to energy for effective management of municipal solid waste. *Waste Management*, *69*, pp.407-422.
2. Hamer, G., 2003. Solid waste treatment and disposal: effects on public health and environmental safety. *Biotechnology advances*, *22*(1-2), pp.71-79.
3. Tripathi, A., Tyagi, V.K., Vivekanand, V., Bose, P. and Suthar, S., 2020. Challenges, opportunities and progress in solid waste management during COVID-19 pandemic. *Case Studies in Chemical and Environmental Engineering*, *2*, p.100060.
4. Liu, S., Wei, M., Qiao, Y., Yang, Z., Gui, B., Yu, Y. and Xu, M., 2015. Release of organic sulfur as sulfur-containing gases during low temperature pyrolysis of sewage sludge. *Proceedings of the Combustion Institute*, *35*(3), pp.2767-2775.
5. Grobelak, A., Grosser, A., Kacprzak, M. and Kamizela, T., 2019. Sewage sludge processing and management in small and medium-sized municipal wastewater treatment plant-new technical solution. *Journal of Environmental Management*, *234*, pp.90-96.
6. Demirbas, A., Edris, G. and Alalayah, W.M., 2017. Sludge production from municipal wastewater treatment in sewage treatment plant. *Energy Sources, Part A: Recovery, Utilization, and Environmental Effects*, *39*(10), pp.999-1006.
7. Russell, D.L., 2019. *Practical wastewater treatment*. John Wiley & Sons.
8. Donnenfeld, Z., Hedden, S. and Crookes, C., 2018. A delicate balance: Water scarcity in South Africa.
9. Shaddel, S., Shaddel, R. and Østerhus, S.W., 2021. Phosphorus recovery from nutrient-rich streams at wastewater treatment plants. In *Integrated and Hybrid Process Technology for Water and Wastewater Treatment* (pp. 463-486). Elsevier.
10. Mills, C., 2016. *Regulating health and safety in the British mining industries, 1800–1914*. Routledge.
11. Mishra, B.K., Das, B., Biswal, S.K. and Reddy, P.S.R., 2015, September. Overview of beneficiation, utilization and environmental issues in relation to coal processing. In *Proc Indian Natn Sci Acad* (Vol. 81, No. 4, pp. 725-37).
12. Mills, S.J., 2011. Global perspective on the use of low-quality coals. *IEA Clean Coal Centre*, *180*, pp.1-2.
13. Piechura, H., 2014. Application of Doosan Lentjes' CFB technology to discard coals. *S Afr J Chem Eng*, *19*, pp.99-111.
14. Moyo, A., Filho, J.A., Harrison, S. and Broadhurst, J., 2018. Characterising the environmental risks of coal preparation wastes: A study of fine coal slurry waste and discards from South African collieries. In *IMWA 2018 Annual Conference; Pretoria, South Africa*.
15. Koplitz, S.N., Jacob, D.J., Sulprizio, M.P., Myllyvirta, L. and Reid, C., 2017. Burden of disease from rising coal-fired power plant emissions in Southeast Asia. *Environmental science & technology*, *51*(3), pp.1467-1476.
16. Kasomo, R.M., Ombiro, S., Rop, B. and Mutua, N.M., 2018. Investigation and comparison of emulsified diesel oil and flomin C 9202 as a collector in the beneficiation of ultra-fine coal by agglo-flotation. *methods*, *1*(2), p.11.
17. Abdulsalam, J., Mulopo, J., Oboirien, B., Bada, S. and Falcon, R., 2019. Experimental evaluation of activated carbon derived from South Africa discard coal for natural gas storage. *International Journal of Coal Science & Technology*, *6*(3), pp.459-477.
18. Listiyani, N. and Said, M.Y., 2018. Political law on the environment: the authority of the government and local government to file litigation in Law Number 32 Year 2009 on environmental protection and management. *Resources*, *7*(4), p.77.
19. Mills, S., 2018. Combining solar power with coal-fired power plants, or cofiring natural gas. *Clean Energy*, *2*(1), pp.1-9.
20. Wright, J.G., Bischof-Niemz, T., Calitz, J.R., Mushwana, C. and Van Heerden, R., 2019. Long-term electricity sector expansion planning: A unique opportunity for a least cost energy transition in South Africa. *Renewable Energy Focus*, *30*, pp.21-45.
21. http://www.energy.gov.za/files/coal _frame.html
22. Van de Venter, F.F., 2021. *Producing briquettes for domestic household fuel applications from coal tailings* (Doctoral dissertation).

23. Onifade, M. and Genc, B., 2018. Spontaneous combustion of coals and coal-shales. *International Journal of Mining Science and Technology*, *28*(6), pp.933-940.
24. Petlovanyi, M.V. and Medianyk, V.Y., 2018. Assessment of coal mine waste dumps development priority. *Науковий вісник Національного гірничого університету*, (4), pp.28-35.
25. Swanepoel, J.W., 2014. *Waste management at Free State abattoirs* (Doctoral dissertation, University of the Free State).
26. Maiti, S.K., 2012. *Ecorestoration of the coalmine degraded lands*. Springer Science & Business Media.
27. Tanner, T., Mitchell, T., Polack, E. and Guenther, B., 2009. Urban governance for adaptation: assessing climate change resilience in ten Asian cities. *IDS Working Papers*, *2009*(315), pp.01-47.
28. Skousen, J.G., Ziemkiewicz, P.F. and McDonald, L.M., 2019. Acid mine drainage formation, control and treatment: Approaches and strategies. *The Extractive Industries and Society*, *6*(1), pp.241-249.
29. Mulopo, J., 2022. Active Physical Remediation of Acid Mine Drainage: Technologies Review and Perspectives. *Journal of Ecological Engineering*, *23*(6).
30. Moodley, I., Sheridan, C.M., Kappelmeyer, U. and Akcil, A., 2018. Environmentally sustainable acid mine drainage remediation: Research developments with a focus on waste/by-products. *Minerals Engineering*, *126*, pp.207-220.
31. Ait-Khouia, Y., Benzaazoua, M. and Demers, I., 2021. Environmental desulfurization of mine wastes using various mineral processing techniques: Recent advances and opportunities. *Minerals Engineering*, *174*, p.107225.
32. Chen, J., Liu, G., Kang, Y., Wu, B., Sun, R., Zhou, C. and Wu, D., 2014. Coal utilization in China: environmental impacts and human health. *Environmental Geochemistry and Health*, *36*(4), pp.735-753.
33. Biddau, R., Cidu, R. and Da Pelo, S., 2018. From acid-rock drainage to acid-mine drainage: extreme contamination in waters at the Furtei Au-mine (Sardinia, Italy). In *'Geosciences for the environment, natural hazards and cultural heritage'* (pp. 682-682). Società geologica Italiana.
34. Nyström, E., 2018. *Suitability of industrial residues for preventing acid rock drainage generation from waste rock* (Doctoral dissertation, Luleå University of Technology).
35. Tempelhoff, J.W. and Winde, F., 2019. Acid mine water drainage in South Africa: policy, economic issues and public concerns. *Water Services Management and Governance*, p.77.
36. Mduduma, H., 2018. *Hydrochemical characterisation of Northern KwaZulu-Natal historic coal mining districts, Northeastern South Africa* (Doctoral dissertation).
37. Simate, G.S., 2021. Legislation and Policies Governing the Management of Acid Mine Drainage. In *Acid Mine Drainage* (pp. 73-96). CRC Press.
38. Sibanda, M., 2019. *The impact of capital structure on the profitability of the industrial metals and mining sector on the JSE*. University of Johannesburg (South Africa).
39. Rodríguez, C. and Leiva, E., 2019. Enhanced heavy metal removal from acid mine drainage wastewater using double-oxidized multiwalled carbon nanotubes. *Molecules*, *25*(1), p.111.
40. Danish, M., Ahmad, T., Majeed, S., Ahmad, M., Ziyang, L., Pin, Z. and Iqubal, S.S., 2018. Use of banana trunk waste as activated carbon in scavenging methylene blue dye: kinetic, thermodynamic, and isotherm studies. *Bioresource technology reports*, *3*, pp.127-137.
41. Zou, W., Gao, B., Ok, Y.S. and Dong, L., 2019. Integrated adsorption and photocatalytic degradation of volatile organic compounds (VOCs) using carbon-based nanocomposites: A critical review. *Chemosphere*, *218*, pp.845-859.
42. de Sousa Rollemberg, S.L., De Oliveira, L.Q., De Barros, A.N., Firmino, P.I.M. and Dos Santos, A.B., 2020. Pilot-scale aerobic granular sludge in the treatment of municipal wastewater: Optimizations in the start-up, methodology of sludge discharge, and evaluation of resource recovery. *Bioresource Technology*, *311*, p.123467.
43. Ross, I., McDonough, J., Miles, J., Storch, P., Thelakkat Kochunarayanan, P., Kalve, E., Hurst, J., S. Dasgupta, S. and Burdick, J., 2018. A review of emerging technologies for remediation of PFASs. *Remediation Journal*, *28*(2), pp.101-126.
44. Harrison, E.Z., McBride, M.B. and Bouldin, D.R., 1999. Land application of sewage sludges: an appraisal of the US regulations. *International Journal of Environment and Pollution*, *11*(1), pp.1-36.
45. Venkatesan, A.K., Done, H.Y. and Halden, R.U., 2015. United States National Sewage Sludge Repository at Arizona State University—a new resource and research tool for environmental

scientists, engineers, and epidemiologists. *Environmental Science and Pollution Research*, *22*(3), pp.1577-1586.
46. Raklami, A., Tahiri, A.I., Bechtaoui, N., Pajuelo, E., Baslam, M., Meddich, A. and Oufdou, K., 2021. Restoring the plant productivity of heavy metal-contaminated soil using phosphate sludge, marble waste, and beneficial microorganisms. *Journal of Environmental Sciences*, *99*, pp.210-221.
47. dos Santos Pereira, I., Bamberg, A.L., de Sousa, R.O., Monteiro, A.B., Martinazzo, R., Silveira, C.A.P. and de Oliveira Silveira, A., 2020. Agricultural use and pH correction of anaerobic sewage sludge with acid pH. *Journal of Environmental Management*, *275*, p.111203.
48. Racek, J., Sevcik, J., Chorazy, T., Kucerik, J. and Hlavinek, P., 2020. Biochar–recovery material from pyrolysis of sewage sludge: a review. *Waste and biomass valorization*, *11*(7), pp.3677-3709.
49. Teoh, S.K. and Li, L.Y., 2020. Feasibility of alternative sewage sludge treatment methods from a lifecycle assessment (LCA) perspective. *Journal of Cleaner Production*, *247*, p.119495.
50. Petterson, D., 2019. The future of sustainable sludge management. *Water&Sanitation Africa*, *14*(2), pp.34-36.
51. Villamil, J.A., Mohedano, A.F., Rodriguez, J.J. and de la Rubia, M.A., 2018. Valorisation of the liquid fraction from hydrothermal carbonisation of sewage sludge by anaerobic digestion. *Journal of Chemical Technology & Biotechnology*, *93*(2), pp.450-456.
52. Wilk, M., Magdziarz, A., Jayaraman, K., Szymańska-Chargot, M. and Gökalp, I., 2019. Hydrothermal carbonization characteristics of sewage sludge and lignocellulosic biomass. A comparative study. *Biomass and Bioenergy*, *120*, pp.166-175.
53. Thomsen, L.B.S., Carvalho, P.N., Dos Passos, J.S., Anastasakis, K., Bester, K. and Biller, P., 2020. Hydrothermal liquefaction of sewage sludge; energy considerations and fate of micropollutants during pilot scale processing. *Water Research*, *183*, p.116101.
54. Đurđević, D., Blecich, P. and Jurić, Ž., 2019. Energy recovery from sewage sludge: the case study of Croatia. *Energies*, *12*(10), p.1927.
55. Grobelak, A., Grosser, A., Kacprzak, M. and Kamizela, T., 2019. Sewage sludge processing and management in small and medium-sized municipal wastewater treatment plant-new technical solution. *Journal of Environmental Management*, *234*, pp.90-96.
56. Gao, N., Kamran, K., Quan, C. and Williams, P.T., 2020. Thermochemical conversion of sewage sludge: A critical review. *Progress in Energy and Combustion Science*, *79*, p.100843.
57. Hämäläinen, A., Kokko, M., Kinnunen, V., Hilli, T. and Rintala, J., 2021. Hydrothermal carbonisation of mechanically dewatered digested sewage sludge—Energy and nutrient recovery in centralised biogas plant. *Water Research*, *201*, p.117284
58. Aragón-Briceño, C.I., Ross, A.B. and Camargo-Valero, M.A., 2021. Mass and energy integration study of hydrothermal carbonization with anaerobic digestion of sewage sludge. *Renewable energy*, *167*, pp.473-483
59. Shettigondahalli Ekanthalu, V., Narra, S., Sprafke, J. and Nelles, M., 2021. Influence of acids and alkali as additives on hydrothermally treating sewage sludge: effect on phosphorus recovery, yield, and energy value of hydrochar. *Processes*, *9*(4), p.618.
60. Kiselev, A., Magaril, E., Magaril, R., Panepinto, D., Ravina, M. and Zanetti, M.C., 2019. Towards circular economy: Evaluation of sewage sludge biogas solutions. *Resources*, *8*(2), p.91.
61. Shahbeig, H. and Nosrati, M., 2020. Pyrolysis of municipal sewage sludge for bioenergy production: thermo-kinetic studies, evolved gas analysis, and techno-socio-economic assessment. *Renewable and Sustainable Energy Reviews*, *119*, p.109567
62. Oladejo, J., Shi, K., Luo, X., Yang, G. and Wu, T., 2018. A review of sludge-to-energy recovery methods. *Energies*, *12*(1), p.60.
63. Kacprzak, M.J. and Kupich, I., 2021. The specificities of the circular economy (CE) in the municipal wastewater and sewage sludge sector—local circumstances in Poland. *Clean Technologies and Environmental Policy*, pp.1-17.
64. Aggarwal, S. and Hakovirta, M., 2021. Supercritical carbon dioxide drying of municipal sewage sludge–novel waste-to-energy valorization pathway. *Journal of Environmental Management*, *285*, p.112148.

65. Nyoni, S., Bwalya, M. and Chimwani, N., 2020. Beneficiation potential of a low-grade coal from the Emalahleni (Witbank) coalfield. *Physicochemical Problems of Mineral Processing*, *56*.
66. Martus, E. and Fortescue, S., 2022. Russian coal in a changing climate: risks and opportunities for industry and government. *Climatic Change*, *173*(3), pp.1-21.
67. Boltakova, N.V., Faseeva, G.R., Kabirov, R.R., Nafikov, R.M. and Zakharov, Y.A., 2017. Utilization of inorganic industrial wastes in producing construction ceramics. Review of Russian experience for the years 2000–2015. *Waste management*, *60*, pp.230-246.
68. Papin, A.V., Ignatova, A.Y., Nevedrov, A.V. and Cherkasova, T.G., 2015. Fuel briquetting using finely disperse waste of coal mining and processing. *Journal of Mining Science*, *51*(5), pp.895-900.
69. Tudor, T. and JC, C. eds., 2021. *The Routledge Handbook of Waste, Resources, and the Circular Economy*. Routledge.
70. Borowski, G., Alsaqoor, S. and Alahmer, A., 2021. Using agglomeration techniques for coal and ash waste management in the circular economy. *Advances in Science and Technology. Research Journal*, *15*(3).
71. Ramudzwagi, M., Tshiongo-Makgwe, N. and Nheta, W., 2020. Recent developments in beneficiation of fine and ultra-fine coal-review paper. *Journal of Cleaner Production*, *276*, p.122693.
72. Lloyd, P.J., 2018, April. Introducing low-smoke coal in South Africa. In *2018 International Conference on the Domestic Use of Energy (DUE)* (pp. 1-4). IEEE.
73. Arellanoa, O., Flores, M., Guerra, J., Hidalgo, A., Rojas, D. and Strubinger, A., 2016. Hydrothermal carbonization (HTC) of corncob and characterization of the obtained hydrochar. *CHEMICAL ENGINEERING*, *50*.
74. Ischia, G. and Fiori, L., 2021. Hydrothermal carbonization of organic waste and biomass: a review on process, reactor, and plant modeling. *Waste and Biomass Valorization*, *12*(6), pp.2797-2824.
75. Heidari, M., Salaudeen, S., Dutta, A. and Acharya, B., 2018. Effects of process water recycling and particle sizes on hydrothermal carbonization of biomass. *Energy & fuels*, *32*(11), pp.11576-11586.
76. Kruse, A. and Grandl, R., 2015. Hydrothermal carbonization: 3. Kinetic model. *Chemie Ingenieur Technik*, *87*(4), pp.449-456.
77. Wang, T., Zhai, Y., Zhu, Y., Li, C. and Zeng, G., 2018. A review of the hydrothermal carbonization of biomass waste for hydrochar formation: Process conditions, fundamentals, and physicochemical properties. *Renewable and Sustainable Energy Reviews*, *90*, pp.223-247.
78. Peng, C., Zhai, Y., Zhu, Y., Xu, B., Wang, T., Li, C. and Zeng, G., 2016. Production of char from sewage sludge employing hydrothermal carbonization: char properties, combustion behavior and thermal characteristics. *Fuel*, *176*, pp.110-118.
79. Lucian, M., Volpe, M., Gao, L., Piro, G., Goldfarb, J.L. and Fiori, L., 2018. Impact of hydrothermal carbonization conditions on the formation of hydrochars and secondary chars from the organic fraction of municipal solid waste. *Fuel*, *233*, pp.257-268.
80. Titirici, M.M. and Antonietti, M., 2010. Chemistry and materials options of sustainable carbon materials made by hydrothermal carbonization. *Chemical Society Reviews*, *39*(1), pp.103-116.
81. Liu, F., Yu, R., Ji, X. and Guo, M., 2018. Hydrothermal carbonization of holocellulose into hydrochar: Structural, chemical characteristics, and combustion behavior. *Bioresource technology*, *263*, pp.508-516.
82. Knappe, V., Paczkowski, S., Robles, L.A.D., Gonzales, A. and Pelz, S., 2019. Reducing willow wood fuel emission by low temperature microwave assisted hydrothermal carbonization. *JoVE (Journal of Visualized Experiments)*, (147), p.e58970.
83. Zhang, Z.B., Zhou, Z.W., Cao, X.H., Liu, Y.H., Xiong, G.X. and Liang, P., 2014. Removal of uranium (VI) from aqueous solutions by new phosphorus-containing carbon spheres synthesized via one-step hydrothermal carbonization of glucose in the presence of phosphoric acid. *Journal of Radioanalytical and Nuclear Chemistry*, *299*(3), pp.1479-1487.
84. Trinh, T.H. and Uemura, Y., 2019. A theoretical equation presenting slope in van Krevelen diagram for biomass pyrolysis. *Platform: A Journal of Engineering*, *3*(1), pp.56-64.
85. Achinas, S., Achinas, V. and Euverink, G.J.W., 2017. A technological overview of biogas production from biowaste. *Engineering*, *3*(3), pp.299-307.

86. Kambo, H.S. and Dutta, A., 2014. Strength, storage, and combustion characteristics of densified lignocellulosic biomass produced via torrefaction and hydrothermal carbonization. *Applied Energy*, *135*, pp.182-191.
87. Acharya, B., Dutta, A. and Minaret, J., 2015. Review on comparative study of dry and wet torrefaction. *Sustainable Energy Technologies and Assessments*, *12*, pp.26-37.
88. Reza, M.T., Yan, W., Uddin, M.H., Lynam, J.G., Hoekman, S.K., Coronella, C.J. and Vásquez, V.R., 2013. Reaction kinetics of hydrothermal carbonization of loblolly pine. *Bioresource technology*, *139*, pp.161-169.
89. Biller, P. and Ross, A.B., 2016. Production of biofuels via hydrothermal conversion. In *Handbook of biofuels production* (pp. 509-547). Woodhead Publishing.
90. Libra, J.A., Ro, K.S., Kammann, C., Funke, A., Berge, N.D., Neubauer, Y., Titirici, M.M., Fühner, C., Bens, O., Kern, J. and Emmerich, K.H., 2011. Hydrothermal carbonization of biomass residuals: a comparative review of the chemistry, processes, and applications of wet and dry pyrolysis. *Biofuels*, *2*(1), pp.71-106.
91. Ugbebor, Bobby. "Feasibility of Activated Carbon via Hydrothermally Carbonized Sewage Sludge." (2019).
92. Hoekman, S.K., Broch, A. and Robbins, C., 2011. Hydrothermal carbonization (HTC) of lignocellulosic biomass. *Energy & Fuels*, *25*(4), pp.1802-1810.
93. Hoekman, S.K., Broch, A., Robbins, C., Zielinska, B. and Felix, L., 2013. Hydrothermal carbonization (HTC) of selected woody and herbaceous biomass feedstocks. *Biomass Conversion and Biorefinery*, *3*(2), pp.113-126.
94. Yan, W., Hoekman, S.K., Broch, A. and Coronella, C.J., 2014. Effect of hydrothermal carbonization reaction parameters on the properties of hydrochar and pellets. *Environmental Progress & Sustainable Energy*, *33*(3), pp.676-680.
95. He, C., Giannis, A. and Wang, J.Y., 2013. Conversion of sewage sludge to clean solid fuel using hydrothermal carbonization: hydrochar fuel characteristics and combustion behavior. *Applied Energy*, *111*, pp.257-266.
96. Singh, P., Singh, R.K., Gokul, P.V., Hasan, S.U. and Sawarkar, A.N., 2020. Thermal degradation and pyrolysis kinetics of two Indian rice husk varieties using thermogravimetric analysis. *Energy Sources, Part A: Recovery, Utilization, and Environmental Effects*, pp.1-12.
97. Bardestani, R., Patience, G.S. and Kaliaguine, S., 2019. Experimental methods in chemical engineering: specific surface area and pore size distribution measurements—BET, BJH, and DFT. *The Canadian Journal of Chemical Engineering*, *97*(11), pp.2781-2791.
98. Kannan, S., Gariepy, Y. and Vijaya Raghavan, G.S., 2018. Optimization of the conventional hydrothermal carbonization to produce hydrochar from fish waste. *Biomass Conversion and Biorefinery*, *8*(3), pp.563-576.
99. Becker, R.,Kumar Dorgerloh, U., Paulke, E., Mumme, J. and Nehls, I., 2014. Hydrothermal carbonization of biomass: major organic components of the aqueous phase. *Chemical engineering & technology*, *37*(3), pp.511-518.
100. Wang, L., Chang, Y. and Li, A., 2019. Hydrothermal carbonization for energy-efficient processing of sewage sludge: A review. *Renewable and Sustainable Energy Reviews*, *108*, pp.423-440.
101. Tasca, A.L., Puccini, M., Gori, R., Corsi, I., Galletti, A.M.R. and Vitolo, S., 2019. Hydrothermal carbonization of sewage sludge: A critical analysis of process severity, hydrochar properties and environmental implications. *Waste Management*, *93*, pp.1-13.
102. Afolabi, O.O., Sohail, M. and Cheng, Y.L., 2020. Optimization and characterization of hydrochar production from spent coffee grounds by hydrothermal carbonization. *Renewable Energy*, *147*, pp.1380-1391.
103. Imbierowicz, M. and Chacuk, A., 2012. Kinetic model of excess activated sludge thermohydrolysis. *Water research*, *46*(17), pp.5747-5755.
104. Yin, L., Farimani, A.B., Min, K., Vishal, N., Lam, J., Lee, Y.K., Aluru, N.R. and Rogers, J.A., 2015. Mechanisms for hydrolysis of silicon nanomembranes as used in bioresorbable electronics. *Advanced Materials*, *27*(11), pp.1857-1864.
105. Danso-Boateng, E., Holdich, R.G., Shama, G., Wheatley, A.D., Sohail, M. and Martin, S.J., 2013. Kinetics of faecal biomass hydrothermal carbonisation for hydrochar production. *Applied energy*, *111*, pp.351-357.

106. Hwang, U.T., Bae, J., Lee, T., Hwang, S.Y., Kim, J.C., Park, J., Choi, I.G., Kwak, H.W., Hwang, S.W. and Yeo, H., 2021. Analysis of Carbonization Behavior of Hydrochar Produced by Hydrothermal Carbonization of Lignin and Development of a Prediction Model for Carbonization Degree Using Near-Infrared Spectroscopy. *Journal of the Korean Wood Science and Technology*, *49*(3), pp.213-225.
107. Cui, X., Lu, M., Khan, M.B., Lai, C., Yang, X., He, Z., Chen, G. and Yan, B., 2020. Hydrothermal carbonization of different wetland biomass wastes: Phosphorus reclamation and hydrochar production. *Waste Management*, *102*, pp.106-113.
108. Sasaki, M., Manalu, H.T., Kamogawa, R., Issasi, C.S.C., Quitain, A.T. and Kida, T., 2022. Fast and Selective Production of Quercetin and Saccharides from Rutin using Microwave-Assisted Hydrothermal Treatment in the Presence of Graphene Oxide. *Food Chemistry*, p.134808.
109. Codato-Zumpano, C.B., Gírio, F., Carvalheiro, F., Marques, S., Ceccato-Antonini, S.R. and Bastos, R.G., 2022. Kinetics of the Release of Sugars from the Enzymatic and Physico-Chemical Pre-treated Sugarcane Bagasse and Residual Forest Biomass. *Waste and Biomass Valorization*, pp.1-9.
110. Pińkowska, H., Krzywonos, M., Wolak, P., Seruga, P., Górniak, A., Złocińska, A. and Ptak, M., 2020. Sustainable Production of 5-Hydroxymethylfurfural from Pectin-Free Sugar Beet Pulp in a Simple Aqueous Phase System-Optimization with Doehlert Design. *Energies*, *13*(21), p.5649.
111. Yousefifar, A., Farid, M.M., Gapes, D.J. and Young, B.R., 2020. An improved model for the kinetics of non-oxidative hydrothermal process. *Journal of environmental management*, *253*, p.109704.
112. Kato, S., Itoh, T., Yuki, M., Nagamori, M., Ohnishi, M., Uematsu, K., Suzuki, K., Takashina, T. and Ohkuma, M., 2019. Isolation and characterization of a thermophilic sulfur-and iron-reducing thaumarchaeote from a terrestrial acidic hot spring. *The ISME journal*, *13*(10), pp.2465-2474.
113. Xu, Z.X., Song, H., Li, P.J., He, Z.X., Wang, Q., Wang, K. and Duan, P.G., 2020. Hydrothermal carbonization of sewage sludge: Effect of aqueous phase recycling. *Chemical Engineering Journal*, *387*, p.123410.
114. Hovland, M., Rueslåtten, H. and Johnsen, H.K., 2018. Large salt accumulations as a consequence of hydrothermal processes associated with 'Wilson cycles': A review, Part 2: Application of a new salt-forming model on selected cases. *Marine and Petroleum Geology*, *92*, pp.128-148.
115. Baig, K.S., 2020. Interaction of enzymes with lignocellulosic materials: causes, mechanism and influencing factors. *Bioresources and bioprocessing*, *7*(1), pp.1-19.
116. Gong, M., Li, Z., Wang, M., Feng, A., Wang, L. and Yuan, S., 2021. Effects of Lewis acid on catalyzing gasification of sewage sludge and model compounds in supercritical water. *International Journal of Hydrogen Energy*, *46*(13), pp.9008-9018.
117. Fekete, S., Veuthey, J.L. and Guillarme, D., 2012. New trends in reversed-phase liquid chromatographic separations of therapeutic peptides and proteins: theory and applications. *Journal of pharmaceutical and biomedical analysis*, *69*, pp.9-27.
118. Azadi, P., Afif, E., Foroughi, H., Dai, T., Azadi, F. and Farnood, R., 2013. Catalytic reforming of activated sludge model compounds in supercritical water using nickel and ruthenium catalysts. *Applied Catalysis B: Environmental*, *134*, pp.265-273.
119. Gong, M., Nanda, S., Romero, M.J., Zhu, W. and Kozinski, J.A., 2017. Subcritical and supercritical water gasification of humic acid as a model compound of humic substances in sewage sludge. *The Journal of Supercritical Fluids*, *119*, pp.130-138.
120. Liao, J., Cheng, Z. and Zhou, L., 2016. Nitrogen-doping enhanced fluorescent carbon dots: green synthesis and their applications for bioimaging and label-free detection of Au3+ ions. *ACS Sustainable Chemistry & Engineering*, *4*(6), pp.3053-3061.
121. Saha, N., Saba, A. and Reza, M.T., 2019. Effect of hydrothermal carbonization temperature on pH, dissociation constants, and acidic functional groups on hydrochar from cellulose and wood. *Journal of Analytical and Applied Pyrolysis*, *137*, pp.138-145.
122. Mumme, J., Titirici, M.M., Pfeiffer, A., Lüder, U., Reza, M.T. and Mašek, O., 2015. Hydrothermal carbonization of digestate in the presence of zeolite: process efficiency and composite properties. *ACS Sustainable Chemistry & Engineering*, *3*(11), pp.2967-2974.
123. Saba, A., Saha, P. and Reza, M.T., 2017. Co-Hydrothermal Carbonization of coal-biomass blend: Influence of temperature on solid fuel properties. *Fuel processing technology*, *167*, pp.711-720.

124. Nakason, K., Panyapinyopol, B., Kanokkantapong, V., Viriya-empikul, N., Kraithong, W. and Pavasant, P., 2018. Hydrothermal carbonization of unwanted biomass materials: Effect of process temperature and retention time on hydrochar and liquid fraction. *Journal of the Energy Institute*, *91*(5), pp.786-796.
125. Fiori, L., Bassoa, D., Castelloa, D. and Baratierib, M., 2014. Hydrothermal carbonization of biomass: Design of a batch reactor and preliminary experimental results. *Chem. Eng. Trans*, *37*(5).
126. Minaret, J. and Dutta, A., 2016. Comparison of liquid and vapor hydrothermal carbonization of corn husk for the use as a solid fuel. *Bioresource technology*, *200*, pp.804-811.
127. Li, X., Li, M.F., Bian, J., Wang, B., Xu, J.K. and Sun, R.C., 2015. Hydrothermal carbonization of bamboo in an oxalic acid solution: effects of acid concentration and retention time on the characteristics of products. *RSC advances*, *5*(94), pp.77147-77153.
128. Kim, D., Yoshikawa, K. and Park, K.Y., 2015. Characteristics of biochar obtained by hydrothermal carbonization of cellulose for renewable energy. *Energies*, *8*(12), pp.14040-14048.
129. Pala, M., Kantarli, I.C., Buyukisik, H.B. and Yanik, J., 2014. Hydrothermal carbonization and torrefaction of grape pomace: A comparative evaluation. *Bioresource technology*, *161*, pp.255-262.
130. Kalderis, D., Kotti, M.S., Méndez, A. and Gascó, G., 2014. Characterization of hydrochars produced by hydrothermal carbonization of rice husk. *Solid Earth*, *5*(1), pp.477-483.
131. Oktaviananda, C., Rahmawati, R.F., Prasetya, A., Purnomo, C.W., Yuliansyah, A.T. and Cahyono, R.B., 2017, March. Effect of temperature and biomass-water ratio to yield and product characteristics of hydrothermal treatment of biomass. In *AIP Conference Proceedings* (Vol. 1823, No. 1, p. 020029). AIP Publishing LLC.
132. Hoekman, S.K., Broch, A., Felix, L. and Farthing, W., 2017. Hydrothermal carbonization (HTC) of loblolly pine using a continuous, reactive twin-screw extruder. *Energy conversion and management*, *134*, pp.247-259.
133. Guangzhi, Y., Jinyu, Y., Yuhua, Y., Zhihong, T., DengGuang, Y. and Junhe, Y., 2017. Preparation and CO 2 adsorption properties of porous carbon from camphor leaves by hydrothermal carbonization and sequential potassium hydroxide activation. *RSC advances*, *7*(7), pp.4152-4160.
134. Nizamuddin, S., Baloch, H.A., Griffin, G.J., Mubarak, N.M., Bhutto, A.W., Abro, R., Mazari, S.A. and Ali, B.S., 2017. An overview of effect of process parameters on hydrothermal carbonization of biomass. *Renewable and Sustainable Energy Reviews*, *73*, pp.1289-1299.
135. Abatzoglou, N., Chornet, E., Belkacemi, K. and Overend, R.P., 1992. Phenomenological kinetics of complex systems: the development of a generalized severity parameter and its application to lignocellulosics fractionation. *Chemical Engineering Science*, *47*(5), pp.1109-1122.
136. Robbiani, Z., 2013. Hydrothermal carbonization of biowaste/fecal sludge. *Conception and construction of a HTC prototype research unit for developing countries. Department of Mechanical Engineering ETHZ in collaboration with Eawag/Sandec*.
137. Zhao, P., Shen, Y., Ge, S., Chen, Z. and Yoshikawa, K., 2014. Clean solid biofuel production from high moisture content waste biomass employing hydrothermal treatment. *Applied energy*, *131*, pp.345-367.
138. Rather, M.A., Khan, N.S. and Gupta, R., 2017. Catalytic hydrothermal carbonization of invasive macrophyte Hornwort (Ceratophyllum demersum) for production of hydrochar: a potential biofuel. *International Journal of Environmental Science and Technology*, *14*(6), pp.1243-1252.
139. Weiner, B., Poerschmann, J., Wedwitschka, H., Koehler, R. and Kopinke, F.D., 2014. Influence of process water reuse on the hydrothermal carbonization of paper. *ACS Sustainable Chemistry & Engineering*, *2*(9), pp.2165-2171.
140. Picone, A., Volpe, M. and Messineo, A., 2021. Process water recirculation during hydrothermal carbonization of waste biomass: Current knowledge and challenges. *Energies*, *14*(10), p.2962.
141. Meehnian, H. and Jana, A.K., 2017. Cotton stalk pretreatment using Daedalea flavida, Phlebia radiata, and Flavodon flavus: lignin degradation, cellulose recovery, and enzymatic saccharification. *Applied biochemistry and biotechnology*, *181*(4), pp.1465-1484.
142. Yihunu, E.W., Minale, M., Abebe, S. and Limin, M., 2019. Preparation, characterization and cost analysis of activated biochar and hydrochar derived from agricultural waste: a comparative study. *SN Applied Sciences*, *1*(8), pp.1-8.

143. Song, E., Park, S. and Kim, H., 2019. Upgrading hydrothermal carbonization (HTC) hydrochar from sewage sludge. *Energies*, *12*(12), p.2383.
144. Gao, M., Liu, X., Irfan, M., Shi, J., Wang, X. and Zhang, P., 2018. Nickle-cobalt composite catalyst-modified activated carbon anode for direct glucose alkaline fuel cell. *International Journal of Hydrogen Energy*, *43*(3), pp.1805-1815.
145. Sethia, G. and Sayari, A., 2016. Activated carbon with optimum pore size distribution for hydrogen storage. *Carbon*, *99*, pp.289-294.
146. Parshetti, G.K., Quek, A., Betha, R. and Balasubramanian, R., 2014. TGA–FTIR investigation of co-combustion characteristics of blends of hydrothermally carbonized oil palm biomass (EFB) and coal. *Fuel processing technology*, *118*, pp.228-234.
147. Reza, M.T., Yang, X., Coronella, C.J., Lin, H., Hathwaik, U., Shintani, D., Neupane, B.P. and Miller, G.C., 2016. Hydrothermal carbonization (HTC) and pelletization of two arid land plants bagasse for energy densification. *ACS Sustainable Chemistry & Engineering*, *4*(3), pp.1106-1114.
148. Borges, M., Symington, A., Coltin, B., Smith, T. and Ventura, R., 2018, October. HTC vive: Analysis and accuracy improvement. In *2018 IEEE/RSJ International Conference on Intelligent Robots and Systems (IROS)* (pp. 2610-2615). IEEE.
149. Afroze, S.N., Ramulu, S., Rao, G.V., Taneeru, S., Bashamalla, R. and Vadla, P., 2018. Demystifying the nature of hard tissues in odontogenic tumors using Modified Gallego's stain: A preliminary study. *Journal of oral and maxillofacial pathology: JOMFP*, *22*(3), p.448.
150. Novak JM, Johnson MG, Spokas KA. Concentration and release of phosphorus and potassium from lignocellulosic-and manure-based biochars for fertilizer reuse. Frontiers in Sustainable Food Systems. 2018 Sep 11;2:54.
151. Schimmelpfennig, D., 2019. Improvements in on-farm resource stewardship with profitable information technologies in rice production. *Journal of Environmental Economics and Policy*, *8*(3), pp.250-267.
152. Puccini, M., Ceccarini, L., Antichi, D., Seggiani, M., Tavarini, S., Hernandez Latorre, M. and Vitolo, S., 2018. Hydrothermal carbonization of municipal woody and herbaceous prunings: hydrochar valorisation as soil amendment and growth medium for horticulture. *Sustainability*, *10*(3), p.846.
153. Creamer, A.E. and Gao, B., 2016. Carbon-based adsorbents for postcombustion CO2 capture: a critical review. *Environmental science & technology*, *50*(14), pp.7276-7289.
154. Hagos, F.M., Qian, H., Di, J., Shan, S., Yang, R., Li, Y. and Gai, X., 2022. Rice Husk Hydrochars Prepared with Different Posttreatment Methods for the Adsorption of Dyes and Antibiotics. *BioResources*, *17*(1).
155. Semerciöz, A.S., Göğüş, F., Celekli, A. and Bozkurt, H., 2017. Development of carbonaceous material from grapefruit peel with microwave implemented-low temperature hydrothermal carbonization technique for the adsorption of Cu (II). *Journal of Cleaner Production*, *165*, pp.599-610.
156. Fang, J., Gao, B., Chen, J. and Zimmerman, A.R., 2015. Hydrochars derived from plant biomass under various conditions: Characterization and potential applications and impacts. *Chemical Engineering Journal*, *267*, pp.253-259.
157. Jain, A., Balasubramanian, R. and Srinivasan, M.P., 2016. Hydrothermal conversion of biomass waste to activated carbon with high porosity: A review. *Chemical Engineering Journal*, *283*, pp.789-805.
158. Liu, F., Yu, R., Ji, X. and Guo, M., 2018. Hydrothermal carbonization of holocellulose into hydrochar: Structural, chemical characteristics, and combustion behavior. *Bioresource technology*, *263*, pp.508-516.
159. Bergna, D., Varila, T., Romar, H. and Lassi, U., 2018. Comparison of the properties of activated carbons produced in one-stage and two-stage processes. *C*, *4*(3), p.41.
160. Li, Y., Xing, B., Ding, Y., Han, X. and Wang, S., 2020. A critical review of the production and advanced utilization of biochar via selective pyrolysis of lignocellulosic biomass.*Bioresource Technology*, *312*, p.123614.
161. Sulaiman, F. and Abdullah, N., 2011. Optimum conditions for maximising pyrolysis liquids of oil palm empty fruit bunches. *Energy*,*36*(5), pp.2352-2359.
162. Bedin, K.C., Cazetta, A.L., Souza, I.P., Pezoti, O., Souza, L.S., Souza, P.S., Yokoyama, J.T. and Almeida, V.C., 2018. Porosity enhancement of spherical activated carbon: Influence and

optimization of hydrothermal synthesis conditions using response surface methodology.*Journal of environmental chemical engineering*, *6*(1), pp.991-999.
163. Lu, X., Jordan, B. and Berge, N.D., 2012. Thermal conversion of municipal solid waste via hydrothermal carbonization: Comparison of carbonization products to products from current waste management techniques. *Waste management 32*(7), pp.1353-1365.
164. Hagemann, N., Spokas, K., Schmidt, H.P., Kägi, R., Böhler, M.A. and Bucheli, T.D., 2018. Activated Carbon, Biochar and Charcoal: Linkages and Synergies across Pyrogenic Carbon's ABC s. *Water*, *10*(2), p.182.
165. Ayinla, R.T., Dennis, J.O., Zaid, H.M., Sanusi, Y.K., Usman, F. and Adebayo, L.L., 2019. A review of technical advances of recent palm bio-waste conversion to activated carbon for energy storage. *Journal of cleaner production*, *229*, pp.1427-1442.
166. Yorgun, S., Yıldız, D. and Şimşek, Y.E., 2016. Activated carbon from paulownia wood: Yields of chemical activation stages. *Energy Sources, Part A: Recovery, Utilization, and Environmental Effects*, *38*(14), pp.2035-2042.
167. Heidarinejad, Z., Dehghani, M.H., Heidari, M., Javedan, G., Ali, I. and Sillanpää, M., 2020. Methods for preparation and activation of activated carbon: a review. *Environmental Chemistry Letters*, *18*(2), pp.393-415.
168. Niazi, L., Lashanizadegan, A. and Sharififard, H., 2018. Chestnut oak shells activated carbon: Preparation, characterization and application for Cr (VI) removal from dilute aqueous solutions. *Journal of cleaner production*, *185*, pp.554-561.
169. Arena, N., Lee, J. and Clift, R., 2016. Life Cycle Assessment of activated carbon production from coconut shells. *Journal of Cleaner Production*, *125*, pp.68-77.
170. Sawant, S.Y., Munusamy, K., Somani, R.S., John, M., Newalkar, B.L. and Bajaj, H.C., 2017. Precursor suitability and pilot scale production of super activated carbon for greenhouse gas adsorption and fuel gas storage. *Chemical Engineering Journal*, *315*, pp.415-425.
171. Mohan, Man, Vinod Kumar Sharma, E. Anil Kumar, and V. Gayathri. "Hydrogen storage in carbon materials—A review. *"Energy Storage"* 1, no. 2 (2019): e35.
172. Rashidi, N.A., Bokhari, A. and Yusup, S., 2021. Evaluation of kinetics and mechanism properties of CO2 adsorption onto the palm kernel shell activated carbon. *Environmental Science and Pollution Research*, *28*(26), pp.33967-33979.
173. Kim, M.H., Kim, K.B., Park, S.M. and Roh, K.C., 2016. Hierarchically structured activated carbon for ultracapacitors. *Scientific reports*, *6*(1), pp.1-6.
174. dos Reis, G.S., Bin Mahbub, M.K., Wilhelm, M., Lima, E.C., Sampaio, C.H., Saucier, C. and Pereira Dias, S.L., 2016. Activated carbon from sewage sludge for removal of sodium diclofenac and nimesulide from aqueous solutions. *Korean Journal of Chemical Engineering*, *33*(11), pp.3149-3161.
175. Ahmed, M.B., Johir, M.A.H., Zhou, J.L., Ngo, H.H., Nghiem, L.D., Richardson, C., Moni, M.A. and Bryant, M.R., 2019. Activated carbon preparation from biomass feedstock: clean production and carbon dioxide adsorption. *Journal of Cleaner Production*, *225*, pp.405-413.
176. Zhou, J., Luo, A. and Zhao, Y., 2018. Preparation and characterisation of activated carbon from waste tea by physical activation using steam. *Journal of the Air & Waste Management Association*, *68*(12), pp.1269-1277.
177. Zhang, J., Li, Z., Wu, Y., Guo, X., Ye, J., Yuan, B., Wang, S. and Jiang, L., 2019. Recent advances on the thermal destabilization of Mg-based hydrogen storage materials. *RSC advances*, *9*(1), pp.408-428.
178. Ahmadpour, A. and Do, D.D., 1996. The preparation of active carbons from coal by chemical and physical activation. *Carbon*, *34*(4), pp.471-479.
179. Sun, J., Hippo, E.J., Marsh, H., O'Brien, W.S. and Crelling, J.C., 1997. Activated carbon produced from an Illinois basin coal. *Carbon*, *35*(3), pp.341-352.
180. Hsu, L.Y. and Teng, H., 2000. Influence of different chemical reagents on the preparation of activated carbons from bituminous coal. *Fuel Processing Technology*, *64*(1-3), pp.155-166.
181. Lozano-Castelló, D., Cazorla-Amorós, D., Linares-Solano, A. and Quinn, D.F., 2002. Activated carbon monoliths for methane storage: influence of binder. *Carbon*, *40*(15), pp.2817-2825.
182. Azargohar, R. and Dalai, A.K., 2005. Production of activated carbon from Luscar char: experimental and modeling studies. *Microporous and mesoporous materials*, *85*(3), pp.219-225.
183. Cuhadaroglu, D. and Uygun, O.A., 2008. Production and characterization of activated carbon from a bituminous coal by chemical activation. *African journal of Biotechnology*, *7*(20).

184. Gong, G.Z., Qiang, X., Zheng, Y.F., Ye, S.F. and Chen, Y.F., 2009. Regulation of pore size distribution in coal-based activated carbon. *New Carbon Materials*, *24*(2), pp.141-146.
185. Arami-Niya, A., Daud, W.M.A.W. and Mjalli, F.S., 2011. Comparative study of the textural characteristics of oil palm shell activated carbon produced by chemical and physical activation for methane adsorption. *Chemical Engineering Research and Design*, *89*(6), pp.657-664.
186. Martin, A., Loh, W.S., Rahman, K.A., Thu, K., Surayawan, B., Alhamid, M.I. and Ng, K.C., 2011. Adsorption isotherms of CH4 on activated carbon from Indonesian low grade coal. *Journal of Chemical & Engineering Data*, *56*(3), pp.361-367.
187. Okhovat, A., Ahmadpour, A., Ahmadpour, F. and Khaki Yadegar, Z., 2012. Pore size distribution analysis of coal-based activated carbons: Investigating the effects of activating agent and chemical ratio. *International Scholarly Research Notices*, *2012*.
188. Sreńscek-Nazzal, J., Kamińska, W., Michalkiewicz, B. and Koren, Z.C., 2013. Production, characterization and methane storage potential of KOH-activated carbon from sugarcane molasses. *Industrial Crops and Products*, *47*, pp.153-159.
189. Shamsuddin, M.S., Yusoff, N.R.N. and Sulaiman, M.A., 2016. Synthesis and characterization of activated carbon produced from kenaf core fiber using H3PO4 activation. *Procedia Chemistry*, *19*, pp.558-565.
190. Yang, B., Liu, Y., Liang, Q., Chen, M., Ma, L., Li, L., Liu, Q., Tu, W., Lan, D. and Chen, Y., 2019. Evaluation of activated carbon synthesized by one-stage and two-stage co-pyrolysis from sludge and coconut shell. *Ecotoxicology and environmental safety*, *170*, pp.722-731.
191. Suzuki, M., 1994. Activated carbon fiber: fundamentals and applications. *Carbon*, *32*(4), pp.577-586.
192. Dos Reis, G.S., Larsson, S.H., de Oliveira, H.P., Thyrel, M. and Claudio Lima, E., 2020. Sustainable biomass activated carbons as electrodes for battery and supercapacitors—A mini-review. *Nanomaterials*, *10*(7), p.1398.
193. Prauchner, M.J., Oliveira, S.D.C. and Rodríguez-Reinoso, F., 2020. Tailoring low-cost granular activated carbons intended for CO2 adsorption. *Frontiers in chemistry*, *8*, p.581133.
194. Lozano-Castelló, D., Suárez-García, F., Alcañiz-Monge, J., Cazorla-Amorós, D. and Linares-Solano, A., 2018. Gas-Adsorbing Nanoporous Carbons. In *Carbon Nanomaterials Sourcebook* (pp. 465-486). CRC Press.
195. Luo, J., Liu, Y., Sun, W., Jiang, C., Xie, H. and Chu, W., 2014. Influence of structural parameters on methane adsorption over activated carbon: evaluation by using D–A model. *Fuel*, *123*, pp.241-247.
196. Policicchio, A., Filosa, R., Abate, S., Desiderio, G. and Colavita, E., 2017. Activated carbon and metal organic framework as adsorbent for low-pressure methane storage applications: an overview. *Journal of Porous Materials*, *24*(4), pp.905-922.
197. Gao, S., Ge, L., Rufford, T.E. and Zhu, Z., 2017. The preparation of activated carbon discs from tar pitch and coal powder for adsorption of CO2, CH4 and N2. *Microporous and Mesoporous Materials*, *238*, pp.19-26.
198. Vasiliev, L., Kanonchik, L., Kuzmich, M. and Kulikouski, V., 2021. Development of thermosyphon controlled adsorptive natural gas storage system. *Applied Thermal Engineering*,*185*, p.116184.
199. Rani, S., Padmanabhan, E. and Prusty, B.K., 2019. Review of gas adsorption in shales for enhanced methane recovery and CO2 storage. *Journal of Petroleum Science and Engineering*, *175*, pp.634-643.
200. Alhasan, S., Carriveau, R. and Ting, D.K., 2016. A review of adsorbed natural gas storage technologies. *International Journal of Environmental Studies*, *73*(3), pp.343-356.
201. Singh, V.K. and Kumar, E.A., 2016. Measurement and analysis of adsorption isotherms of CO2 on activated carbon. *Applied Thermal Engineering*, *97*, pp.77-86.
202. Jiang, L., Gonzalez-Diaz, A., Ling-Chin, J., Roskilly, A.P. and Smallbone, A.J., 2019. Post-combustion CO2 capture from a natural gas combined cycle power plant using activated carbon adsorption. *Applied Energy*, *245*, pp.1-15.
203. Sahoo, S. and Ramgopal, M., 2016. Theoretical performance of an adsorbed natural gas storage system subjected to variable charge–discharge conditions. *International Journal of Ambient Energy*, *37*(4), pp.372-383.

204. Mahdi, J.M., Lohrasbi, S. and Nsofor, E.C., 2019. Hybrid heat transfer enhancement for latent-heat thermal energy storage systems: A review. *International Journal of Heat and Mass Transfer*, *137*, pp.630-649.
205. Golea, D.M., Jarvis, P., Jefferson, B., Moore, G., Sutherland, S., Parsons, S.A. and Judd, S.J., 2020. Influence of granular activated carbon media properties on natural organic matter and disinfection by-product precursor removal from drinking water. *Water research*, *174*, p.115613.
206. Ribeiro RP, Silva RJ, Esteves IA, Mota JP. Development, construction, and operation of a multisample volumetric apparatus for the study of gas adsorption equilibrium. Journal of Chemical Education. 2015 Apr 14;92(4):757-61.
207. Sheikholeslami, M., Jafaryar, M., Shafee, A. and Babazadeh, H., 2020. Acceleration of discharge process of clean energy storage unit with insertion of porous foam considering nanoparticle enhanced paraffin. *Journal of Cleaner Production*, *261*, p.121206.
208. Feroldi, M., Neves, A.C., Borba, C.E. and Alves, H.J., 2018. Methane storage in activated carbon at low pressure under different temperatures and flow rates of charge. *Journal of cleaner production*, *172*, pp.921-926.
209. Park, J.E., Lee, G.B., Hwang, S.Y., Kim, J.H., Hong, B.U., Kim, H. and Kim, S., 2018. The effects of methane storage capacity using upgraded activated carbon by KOH. *Applied Sciences*, *8*(9), p.1596.
210. Abe, J.O., Popoola, A.P.I., Ajenifuja, E. and Popoola, O.M., 2019. Hydrogen energy, economy, and storage: review and recommendation. *International journal of hydrogen energy*, *44*(29), pp.15072-15086.
211. Liu, W., Sun, L., Li, Z., Fujii, M., Geng, Y., Dong, L. and Fujita, T., 2020. Trends and future challenges in hydrogen production and storage research. *Environmental Science and Pollution Research*, *27*(25), pp.31092-31104.
212. Rusman, N.A.A. and Dahari, M., 2016. A review on the current progress of metal hydrides material for solid-state hydrogen storage applications. *International Journal of Hydrogen Energy*, *41*(28), pp.12108-12126.
213. Ren, J., Gao, S., Tan, S., Dong, L., Scipioni, A. and Mazzi, A., 2015. Role prioritization of hydrogen production technologies for promoting hydrogen economy in the current state of China. *Renewable and Sustainable Energy Reviews*, *41*, pp.1217-1229.
214. Boullouz S, Faquir S, Yahyaouy A. A New Approach to Manage the Energy Flow in a Hybrid Renewable Energy System Based on Green Hydrogen. InInternational Conference on Digital Technologies and Applications 2022 (pp. 562-570). Springer, Cham.
215. Wiser, R., Rand, J., Seel, J., Beiter, P., Baker, E., Lantz, E. and Gilman, P., 2021. Expert elicitation survey predicts 37% to 49% declines in wind energy costs by 2050. *Nature Energy*, *6*(5), pp.555-565.
216. Zhang, C., Wu, J., Long, C. and Cheng, M., 2017. Review of existing peer-to-peer energy trading projects. *Energy Procedia*, *105*, pp.2563-2568.
217. Salman, M.S., Rambhujun, N., Pratthana, C., Lai, Q., Sapkota, P. and Aguey-Zinsou, K.F., 2021. Solid-state hydrogen storage as a future renewable energy technology. In *Nano Tools and Devices for Enhanced Renewable Energy* (pp. 263-287). Elsevier.
218. Niaz, S., Manzoor, T. and Pandith, A.H., 2015. Hydrogen storage: Materials, methods and perspectives. *Renewable and Sustainable Energy Reviews*, *50*, pp.457-469.
219. Teichmann, D., Arlt, W., Schlücker, E. and Wasserscheid, P., 2016. Transport and storage of hydrogen via liquid organic hydrogen carrier (LOHC) systems. *Hydrogen science and engineering: materials, processes, systems and technology*, pp.811-830.
220. Bockris, J.O.M., 2013. The hydrogen economy: Its history. *International Journal of Hydrogen Energy*, *38*(6), pp.2579-2588.
221. Sadhasivam, T., Dhanabalan, K., Roh, S.H., Kim, T.H., Park, K.W., Jung, S., Kurkuri, M.D. and Jung, H.Y., 2017. A comprehensive review on unitized regenerative fuel cells: Crucial challenges and developments. *international journal of hydrogen energy*, *42*(7), pp.4415-4433.
222. Durbin, D.J. and Malardier-Jugroot, C., 2013. Review of hydrogen storage techniques for on board vehicle applications. *International journal of hydrogen energy*, *38*(34), pp.14595-14617.
223. Shannon, J.M., Clark, J.H., Ingrid de Heer, M., Ekblad, T. and Matharu, A.S., 2018. Kinetic and Desorption Study of Selected Bioactive Compounds on Mesoporous Starbons: A Comparison with Microporous-Activated Carbon. *ACS Omega*, *3*(12), pp.18361-18369.

224. Milanese, C., Jensen, T.R., Hauback, B.C., Pistidda, C., Dornheim, M., Yang, H., Lombardo, L., Zuettel, A., Filinchuk, Y., Ngene, P. and de Jongh, P.E., 2019. Complex hydrides for energy storage. *international journal of hydrogen energy*, *44*(15), pp.7860-7874.
225. Zhang, M., Lv, H., Kang, H., Zhou, W. and Zhang, C., 2019. A literature review of failure prediction and analysis methods for composite high-pressure hydrogen storage tanks. *International Journal of Hydrogen Energy*, *44*(47), pp.25777-25799.
226. Abdin, Z., Tang, C., Liu, Y. and Catchpole, K., 2021. Large-scale stationary hydrogen storage via liquid organic hydrogen carriers. *Iscience*, *24*(9), p.102966.
227. Geng, H., Cui, X., Weng, J., She, H. and Wang, W., 2019. Review of experimental research on Joule–Thomson cryogenic refrigeration system. *Applied Thermal Engineering*, *157*, p.113640
228. Al Ghafri, S., Munro, S., Cardella, U., Funke, T., Notardonato, W., Trusler, J.M., Leachman, J., Span, R., Kamiya, S., Pearce, G. and Swanger, A., 2022. Hydrogen liquefaction: a review of the fundamental physics, engineering practice and future opportunities. *Energy & Environmental Science*.
229. Vyawahare, P., Tun, H., Vaughn, M.W. and Chen, C.C., 2022. From Langmuir isotherm to Brunauer–Emmett–teller isotherm. *AIChE Journal*, *68*(3), p.e17523.
230. Manirethan, V., Raval, K., Rajan, R., Thaira, H. and Balakrishnan, R.M., 2018. Kinetic and thermodynamic studies on the adsorption of heavy metals from aqueous solution by melanin nanopigment obtained from marine source: Pseudomonas stutzeri. *Journal of environmental management*, *214*, pp.315-324.
231. Broom, D.P. and Hirscher, M., 2021. Improving reproducibility in hydrogen storage material research. *ChemPhysChem*, *22*(21), pp.2141-2157.
232. Picheau, E., Impellizzeri, A., Rybkovskiy, D., Bayle, M., Mevellec, J.Y., Hof, F., Saadaoui, H., Noé, L., Torres Dias, A.C., Duvail, J.L. and Monthioux, M., 2021. Intense Raman D band without disorder in flattened carbon nanotubes. *ACS nano*, *15*(1), pp.596-603.
233. Stan, G. and Cole, M.W., 1998. Hydrogen adsorption in nanotubes. *Journal of Low Temperature Physics*, *110*(1), pp.539-544.
234. Rzepka, M., Bauer, E., Reichenauer, G., Schliermann, T., Bernhardt, B., Bohmhammel, K., Henneberg, E., Knoll, U., Maneck, H.E. and Braue, W., 2005. Hydrogen storage capacity of catalytically grown carbon nanofibers. *The Journal of Physical Chemistry B*, *109*(31), pp.14979-14989.
235. Lee, S., Filatov, M., Lee, S. and Choi, C.H., 2018. Eliminating spin-contamination of spin-flip time dependent density functional theory within linear response formalism by the use of zeroth-order mixed-reference (MR) reduced density matrix. *The Journal of chemical physics*, *149*(10), p.104101.
236. Ma, M., Duan, R., Ouyang, L., Zhu, X., Chen, Z., Peng, C. and Zhu, M., 2017. Hydrogen storage and hydrogen generation properties of CaMg2-based alloys. *Journal of Alloys and Compounds*, *691*, pp.929-935.
237. Rostamoghli, R., Vakili, M., Banaei, A., Pourbasheer, E. and Jalalierad, K., 2018. Applying the B12N12 nanoparticle as the CO, CO2, H2O and NH3 sensor. *Chemical Review and Letters*, *1*(1), pp.31-36.
238. Milanese, C., Jensen, T.R., Hauback, B.C., Pistidda, C., Dornheim, M., Yang, H., Lombardo, L., Zuettel, A., Filinchuk, Y., Ngene, P. and de Jongh, P.E., 2019. Complex hydrides for energy storage. *international journal of hydrogen energy*, *44*(15), pp.7860-7874.
239. Ouyang, L., Liu, F., Wang, H., Liu, J., Yang, X.S., Sun, L. and Zhu, M., 2020. Magnesium-based hydrogen storage compounds: A review. *Journal of Alloys and Compounds*, *832*, p.154865.
240. Fan, L., Tu, Z. and Chan, S.H., 2021. Recent development of hydrogen and fuel cell technologies: A review. *Energy Reports*, *7*, pp.8421-8446.
241. Chen, M., Xiao, X., Zhang, M., Mao, J., Zheng, J., Liu, M., Wang, X. and Chen, L., 2020. Insights into 2D graphene-like TiO2 (B) nanosheets as highly efficient catalyst for improved low-temperature hydrogen storage properties of MgH2. *Materials Today Energy*, *16*, p.100411.
242. Heinemann, N., Alcalde, J., Miocic, J.M., Hangx, S.J., Kallmeyer, J., Ostertag-Henning, C., Hassanpouryouzband, A., Thaysen, E.M., Strobel, G.J., Schmidt-Hattenberger, C. and Edlmann, K., 2021. Enabling large-scale hydrogen storage in porous media–the scientific challenges. *Energy & Environmental Science*, *14*(2), pp.853-864.
243. Widjaya, D., Sinatrya, A.N., Kusumandaru, W., Jupriyanto, A. and Nijkamp, R.T., 2022. Utilization of Several Agricultural Wastes into Briquette as Renewable Energy Source. *PLANTA TROPIKA: Jurnal Agrosains (Journal of Agro Science)*, *10*(2), pp.169-176.

244. Usman, M.R., 2022. Hydrogen storage methods: Review and current status. *Renewable and Sustainable Energy Reviews*, *167*, p.112743.
245. Pluengphon, P., Tsuppayakorn-aek, P., Sukmas, W., Inceesungvorn, B., Ahuja, R. and Bovornratanaraks, T., 2022. TM dopant-induced H-vacancy diffusion kinetics of sodium-lithium alanates: Ab initio study for hydrogen storage improvement. *International Journal of Hydrogen Energy*, *47*(43), pp.18763-18771.
246. Janićijević, D., Uskoković-Marković, S., Ranković, D., Milenković, M., Jevremović, A., Vasiljević, B.N., Milojević-Rakić, M. and Bajuk-Bogdanović, D., 2020. Double active BEA zeolite/silver tungstophosphates–Antimicrobial effects and pesticide removal. *Science of the Total Environment*, *735*, p.139530.
247. Simanullang, M. and Prost, L., 2022. Nanomaterials for on-board solid-state hydrogen storage applications. *International Journal of Hydrogen Energy*.
248. Knosala, K., Kotzur, L., Röben, F.T., Stenzel, P., Blum, L., Robinius, M. and Stolten, D., 2021. Hybrid hydrogen home storage for decentralized energy autonomy. *international journal of hydrogen energy*, *46*(42), pp.21748-21763.
249. Khajuria, A., Sudan, S. and Kapoor, M., 2022. Brief Overview on Synthesis and Application of Ni–Doped Carbon Dots. *ECS Transactions*, *107*(1), p.6129.
250.
251. Khuder, S., Milz, S.A., Bisesi, M., Vincent, R., McNulty, W. and Czajkowski, K., 2007. Health survey of residents living near farm fields permitted to receive biosolids. *Archives of Environmental & Occupational Health*, *62*(1), pp.5-11.
252. Racek, J., Sevcik, J., Chorazy, T., Kucerik, J. and Hlavinek, P., 2020. Biochar–recovery material from pyrolysis of sewage sludge: a review. *Waste and biomass valorization*, *11*(7), pp.3677-3709.
253. Li, C., Dos Reis, A.A., Ansari, A., Bertelli, L., Carr, Z., Dainiak, N., Degteva, M., Efimov, A., Kalinich, J., Kryuchkov, V. and Kukhta, B., 2022. Public health response and medical management of internal contamination in past radiological or nuclear incidents: A narrative review. *Environment International*, p.107222.
254. AR, D., Ranjan, N. and Ramaprabhu, S., Hydrogen storage studies of Co, Fe, Fe3C nanoparticles encapsulated nitrogen doped Carbon Nanotubes. *Energy Storage*, p.e421.

Chapter 3: Research Methodology

3.1. Methodology and research design

3.1.1. Methodology

Figure 3-1 summarizes the methodology used in this project, which describes procedures ranging from CD and SS sample preparation and characterization to HTC process optimization and activation. AC synthesis is carried out from the produced HC via chemical activation process using potassium hydroxide (KOH). The objective of HTC process was the production of micropore structure's HC with increased carbon content to further produce an activated carbon with higher surface area and gas storage capacity properties.

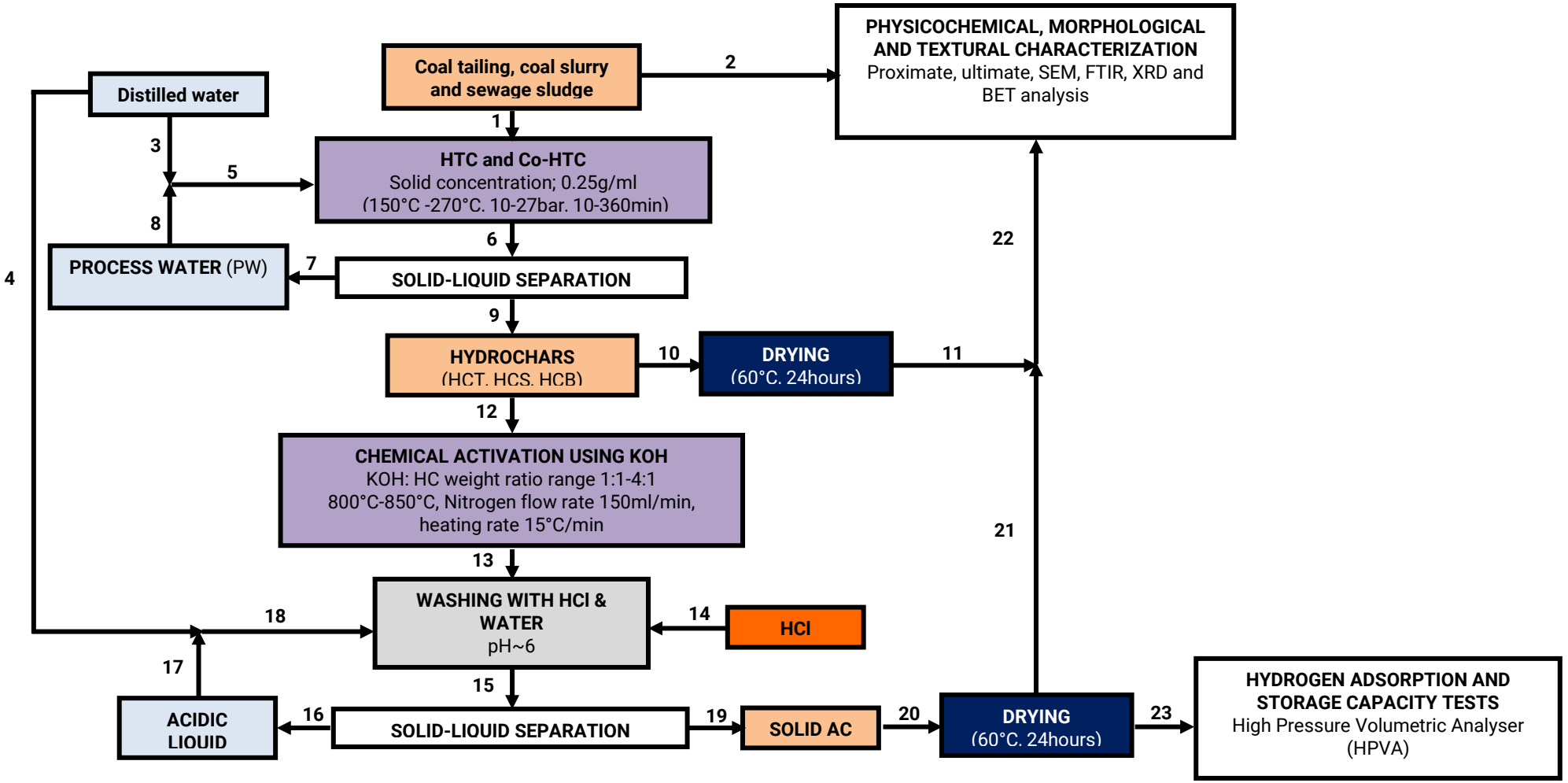

Figure 3-1 :Flow sheet of the experimental procedures

3.1.2. Research Design

HTC experiments, adsorption experiments, and activation studies using synthesized hydrochars all required the development of experimental protocols and methodologies. The experiments were carried out in accordance with the flow chart shown in Figure 3-1. The Hydrothermal carbonization (HTC) and Co-hydrothermal (Co-HTC) experimental test runs were designed using Design-Expert software (Version 13, State–Ease, Inc, Minneapolis, USA). The design of experiment response surface methodology (DoE-RSM) approach for investigating the combined interactive effects between independent (input) variables on a process has been widely used (Afolabi *et al*., 2020; Barghi *et al*., 2021). In this work, four parameters for the HTC process, namely temperature, pressure, residence time and the coals: sewage sludge (CT+CS: SS) blend ratio, were considered. For experimental designs, the central composite design (CCD) and the custom design (CD) were used to determine the number of runs that will be required to optimize the HTC and Co-HTC process respectively. HTC experiments were conducted using changes in temperature, pressure and time ranging from 150 to 270°C, 10 and 27 bar, 10 and 180 minutes respectively. However, the Co-HTC experiments were performed using variations in residence time ranging from 10 to 360 minutes for the same range of temperature and pressure utilized in HTC experiments i.e., 150 to 270°C, 10 and 27 bar respectively. It is important to note that the Co-HTC experiments used a coal feedstock blend (CT+CS) consisted of a 50 wt% coal tailing to 50 wt% coal slurry blends. The 1:1 coal tailing to coal slurry blend was chosen for experimental simplicity. The coal-sewage sludge blending ratio (CT+CS: SS) used for Co-HTC experiments varied from 0:25 to 25:0 (wt:wt). The design matrix obtained for HTC and Co-HTC experimental runs are presented in Tables 3-1 and 3-2. Based on the CCD, 20 experimental runs were performed for the HTC of CT and CS (Table 3-1), six center points, height factorial points and six axial points and was repeated five times to ensure reproducibility of the responses and to determine accurate experimental error. However, 40 experimental runs were performed according to the CD matrix of the Co-HTC process (Table 3-2). The CD matrix predicted 20 edge* interior points and 20 vertex* interior points to accurately determine the process optimum conditions. High fixed carbon (FC) content HCs by means of the DoE was selected using the Response surface methodology (RSM) and the optimal combined methodology (OCM)

methods for HTC and Co-HTC respectively. RSM and OCM were adopted to understand the interactions of the HTC and Co-HTC factors on the fixed carbon of the HC produced from the individual CT, CS, and from the mixture of coals with sewage sludge respectively. Furthermore, RSM and OCM were used to develop suitable models that could predict the optimal operating parameters required to produce high carbon content HC. To assess the significance of the developed models, the analysis of variance (ANOVA) was used. The numerical optimal response approach option was then employed to choose the best HTC and Co-HTC process parameters, with the greatest FC content of the produced HC acting as the optimization criterion. The adsorption performance of the synthesized HCs for the removal of NEV and LAM from prepared aqueous solutions was evaluated in batch studies.

Table 3-1. Hydrothermal carbonization (HTC) Design matrix

Run	Actual factors			Coded factors		
	A: Temperature	B: Pressure	C: Time	A: Temperature	B: Pressure	C: Time
	Degree Celsius	bar	Minutes	Degree Celsius	bar	Minutes
1	150	10	180	-1	-1	1
2	150	27	10	-1	1	-1
3	150	18.5	95	-1	0	0
4	150	10	10	-1	-1	-1
5	150	27	180	-1	1	1
6	210	18.5	95	0	0	0
7	210	18.5	95	0	0	0
8	210	18.5	10	0	0	-1
9	210	18.5	95	0	0	0
10	210	18.5	95	0	0	0
11	210	18.5	95	0	0	0
12	210	18.5	180	0	0	1
13	210	18.5	95	0	0	0
14	210	27	95	0	1	0
15	210	10	95	0	-1	0
16	270	10	180	1	-1	1
17	270	27	180	1	1	1
18	270	18.5	95	1	0	0
19	270	10	10	1	-1	-1
20	270	27	10	1	1	-1

Table 3-2. Co-Hydrothermal carbonization (Co-HTC) Design matrix.

Run	Mixture components		Actual factors			Coded factors		
	Component 1 (A): 0.5(CT+CS)	Component 2 (B): SS	C: Temperature	D: Pressure	E: Time	C: Temperature	D: Pressure	E: Time
	gram	gram	Degree Celsius	Bar	Minutes	Celsius	Bar	Minutes
1	12.24	12.76	150	10	135.78	-1	-1	-0.82
2	12.32	12.68	150	20.54	360	-1	0.24	-0.50
3	24.37	0.63	150	10	10	-1	-1	-0.99
4	24.37	0.63	150	27	360	-1	1	-0.50
5	0	25	150	16.29	10	-1	-0.26	-0.99
6	12.47	12.53	150	27	10	-1	1	-0.99
7	12.24	12.76	150	10	135.78	-1	-1	-0.82
8	0.63	24.37	150	10	360	-1	-1	-0.50
9	25	0	150	27	10	-1	1	-0.99
10	0	25	150	27	229.05	-1	1	-0.69
11	0	25	150	18.22	220.08	-1	-0.03	-0.70
12	25	0	152.4	17.65	198.56	-0.96	-0.1	-0.73
13	12.28	12.72	183.6	14.505	264.93	-0.44	-0.47	-0.64
14	25	0	194.4	10	360	-0.26	-1	-0.50
15	12.36	12.64	203.4	26.745	200.35	-0.11	0.97	-0.72
16	12.35	12.65	203.4	26.745	200.35	-0.11	0.97	-0.72
17	12.54	12.46	204	17.65	20	-0.1	-0.1	-0.97
18	0	25	204	19.35	354.61	-0.1	0.1	-0.51
19	12.54	12.46	204	17.65	20	-0.1	-0.1	-0.98
20	0	25	204	10.34	162.68	-0.1	-0.96	-0.78
21	2.50	22.50	206.4	19.69	159.1	-0.06	0.14	-0.78
22	20.22	4.78	208.10	22.28	360	-0.032	0.44	-0.50
23	25	0	216	17.65	30	0.1	-0.1	-0.96
24	25	0	216.6	26.745	198.56	0.11	0.97	-0.73
25	25	0	222.6	15.95	198.56	0.21	-0.3	-0.73
26	0	25	224.4	27	10	0.24	1	-0.99
27	12.92	12.08	225.6	10	360	0.26	-1	-0.50
28	0	25	267	19.435	162.68	0.95	0.11	-0.78
29	12.25	12.75	267	17.65	198.56	0.95	-0.1	-0.73
30	12.25	12.75	267	17.65	198.56	0.95	-0.1	-0.73
31	12.25	12.75	267	17.65	198.56	0.95	-0.1	-0.73
32	1.12	23.88	270	10	360	1	-1	-0.50
33	12.68	12.32	270	27	360	1	1	-0.50
34	12.69	12.31	270	10	10	1	-1	-0.99
35	0	25	270	10	10	1	-1	-0.99
36	12.37	12.63	270	27	10	1	1	-0.99
37	25	0	270	10	135.78	1	-1	-0.81
38	25	0	270	27	10	1	1	-0.99
39	25	0	270	20.625	360	1	0.25	-0.50
40	0	25	270	27	360	1	1	-0.50

The hydrothermally treated carbonaceous material and adsorption wasted residues were chemically activated at varying ratios using analytic grade potassium hydroxide (KOH). The porous material generated from the activation process was neutralized using hydrochloric acid (HCl, 0.5N). Throughout the washing procedure of the neutralized items, deionized water was used. The chemical activation studies were carried out in a tube furnace at various temperatures and with a flowrate of 150ml/min of nitrogen gas. Design-Expert software (DoE) was used to create the activation experimental test runs (Version 13, State–Ease, Inc, Minneapolis, USA). Temperature and residence time, two parameters of the chemical activation process, were taken into account in the design. The central composite design (CCD) was used for the experimental design to determine the number of runs necessary to optimize the process. Chemical activation tests were carried out at temperatures ranging from 800°C to 850°C, with retention durations ranging from 90 to 180 minutes. Table 3-3 displays the design matrix for the chemical activation experiment. 13 experimental runs were carried out based on the CCD to optimize the chemical activation of HCT, HCS, and HCB. Five center points, four factorial points, and four axial points were used, and the experiment was performed five times to guarantee repeatability of the results. To study the interactions of chemical activation variables on the SBET of activated carbon (AC) generated from both HCs samples, the response surface methodology (RSM) was used. The AC with the highest SBET as determined by the DoE was chosen as the optimized product using the RSM. Furthermore, RSM was used to develop adequate models that allowed for the prediction of the optimal operating parameters necessary to yield high SBET. To assess the significance of the developed models, the analysis of variance (ANOVA) was used. The numerical optimal response technique option was then utilized to choose the best chemical activation process parameters, using the highest SBET of the generated ACs as the optimization criterion.

Table 3-3. Chemical activation design matrix

Run	Actual factor		Coded factors	
	A: Temperature	B: Activation Time	A: Temperature	B: Activation Time
	Degree Celsius	Minutes	Degree Celsius	Minutes
1	800	135	-1	0
2	800	90	-1	-1
3	800	180	-1	1
4	825	135	0	0
5	825	135	0	0
6	825	180	0	1
7	825	135	0	0
8	825	135	0	0
9	825	90	0	-1
10	825	135	0	0
11	850	135	1	0
12	850	180	1	1
13	850	90	1	-1

3.2. Materials

Coal samples were collected (using ply sampling method) from coal beneficiation plant situated at 15 km south-west of Witbank in Mpumalanga, South Africa. The samples were stored as followed: 5 kg Slurry from coal beneficiation process (labelled) stored in an airtight bag, 5 kg of tailing press discard coal (labelled) stored in an airtight bag. The coal samples were transported and kept in laboratory conditions (ambient temperature). 40 kg of final wastewater treatment sewage sludge from Ekurhuleni Water Care Company (ERWAT) plant situated in Hartebeestfontein office park South Africawere collected in two 20-litre containers at separate dump stock sites and homogenized using a probe sampler for a balanced distribution that is typical of the composition and general features of the overall generated sewage sludge from the water treatment plant on a regular basis. The main sewage samples were also divided in 1000 g portions samples and placed in covered pot labelled SS for future experiments. After weighing collected portions of SS samples were maintained in a laboratory for 48 hours before being dried in a laboratory drier. at 125°C for 24 hours. One portion of the dried sample has been milled using a pulveriser to reduce the particle size (0.15-0.212 mm) for proximate, ultimate, total sulphur, Fourier transform infrared (FTIR), X-ray diffraction (XRD) and X-ray florescence (XRF) analysis.

The coal samples were prepared for further experiment as follow:

- Coal samples were dried under laboratory conditions for 24 hours

- Each coal sample was mixed and then splitted (Rotary splitter Eriez) 1000 g portions and then placed in different tight bags.

- Every bag containing coal sample was labelled for identification and stored under laboratory conditions (ambient temperature), CS for slurry and CT for tailing.

- Two portions of coal samples (CT and CS) were then milled using a pulveriser to reduce the particle size (0.150-0.250 mm) for further physicochemical tests; proximate, ultimate, total sulphur, FTIR and XRD.



Figure 3-2: Illustrative images of raw materials

3.3. Instruments

The HTC reactors set up used in this study to produce high carbon content HC is displayed on Figure 3-3. Other instruments used for experimental works and physicochemical characterization in this study are listed below:

- Pulveriser (milling)
- Laboratory dryer Prolab (PL010)
- Thermo gravimetric analyser (TGA 710) for proximate analysis
- Bomb calorimeter (LECO AC500) for calorific value analysis
- LECO TruSpec CHN analyser for ultimate analysis
- LECO C & S analyser for total sulphur determination
- X-ray diffraction (Bruker D2 PXRD phaser) for mineral phase identification
- X-ray Fluorescence Analyzer PANalytical AXIOS for elemental analysis
- Perkin Elmer FTIR Spectrometer for chemical functionality determination

- Hydrothermal carbonization reactors for experimental runs (number of runs determined by Expert design V12; 40).
- Chemical activation set up (tube furnace with nitrogen flow connected)
- Scanning Electron Microscopy equipped with an EDS for particle morphology structure
- Quantachrome Autosorb IQ (automated gas sorption analyser)
- The Micrometrics Accupyc II 1340 equipment for density measurement
- Micrometric Flow Prep 060-unit, Micrometrics TriStrar 3000 intrument for nitrogen adsorption
- The Inductively Coupled Plasma-Optical Emission Spectrometer ICP-OES for liquid phase elemental composition analysis
- Thermo Scientific FlashEA 1112 Elemental Analyser for total organic carbon content analysis

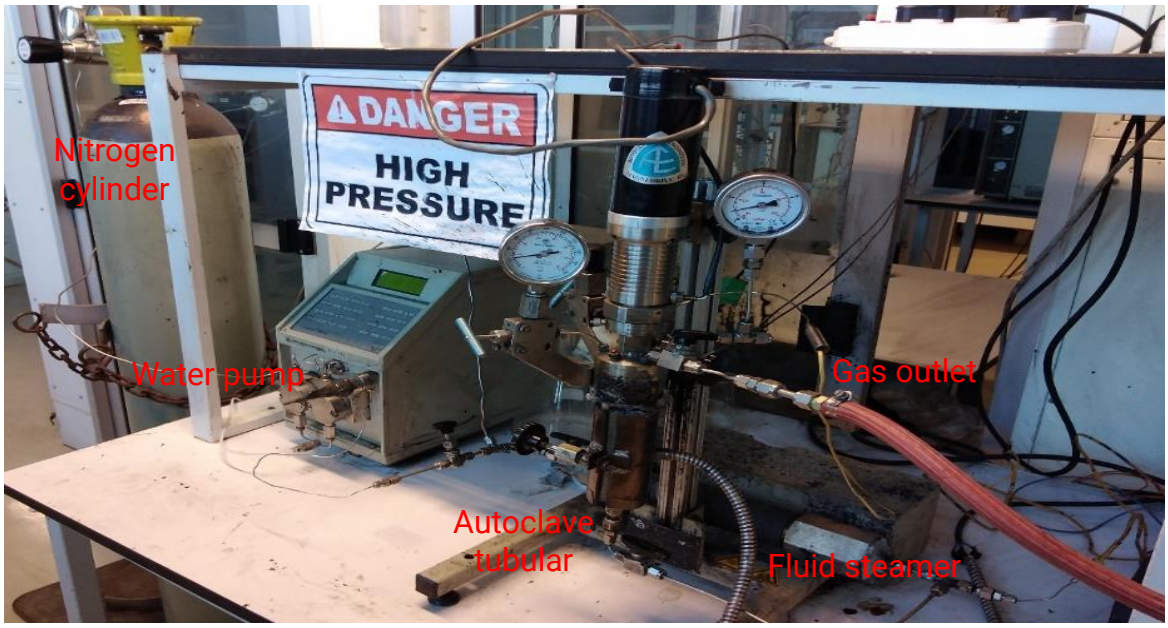

Figure 3-3:Image of hydrothermal experiment set up

The study used potassium hydroxide (KOH) as a chemical activation reagent. The activation process was conducted at temperature range of 800 to 850°C with a KOH/HC ratio range of 1 to 4. The dried optimized HCs from HTC and Co-HTC were mixed with KOH at fixed weight ratio and the mixture was heated up into the furnace. The heat rate was 15°C/min and the furnace was connected to a nitrogen gas flow rate

of 100 ml/min. The experimental procedure was based on the method provided by Abdulsalam Jibril (2019) for preparation of activated carbon. When the final temperature was reached, the produced activated carbon was held for 2 hours and then cooled under nitrogen flow. After cooling, the product was washed with 0.5 N HCl for residual alkali removal then with distilled water using a centrifuge until the mixture (product/distilled water) reached the approximated pH of 6.5 (Liu *et al*., 2020). The washed product was dried at 60°C in an oven for 24 hours. The obtained dried product was kept in airtight bag for further analysis. The studies conducted by Qu (2018), Omri (2019) and Abdulsalam Jibril (2022) supported the efficacy of the mounted activation equipment showed in Figure 3-4.

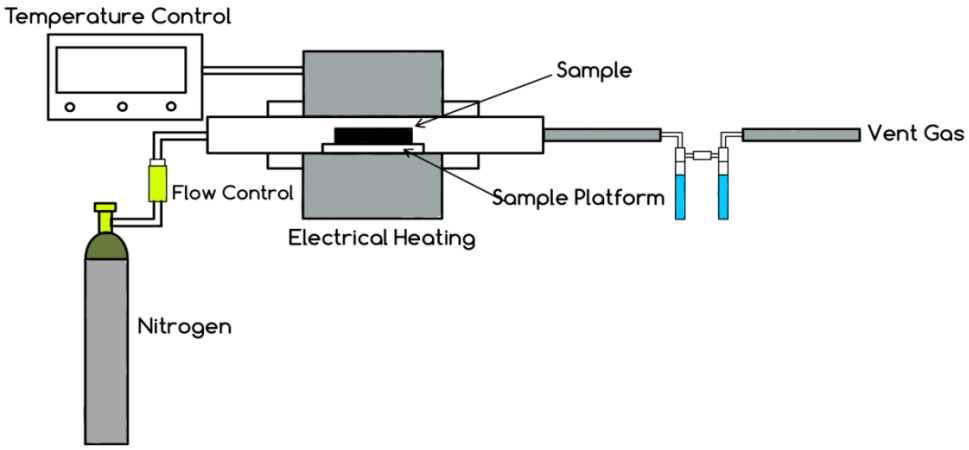

Figure 3-4: Activated Carbon Preparation equipment.

3.4. Analysis

3.4.1 Proximate analysis

Proximate analysis of coal samples and produced hydrochars have been carried out using the Thermo Gravimetric analyser equipment (TGA 701) in accordance with ASTM D5142 standard to determine moisture, volatile matter, fixed carbon, and *ash* content of samples (Abdulsalam Jibril *et al*., 2019). In this analysis, 1 g of each sample was placed in a determined crucible of the instrument's carousel and the fixed carbon content was determined as100%-(ash content + Volatile matter + moisture content). Typical sample size was -212 µm.

3 4.2 Ultimate analysis and total sulphur determination

The determination of the elemental composition of the raw materials samples (total carbon, hydrogen, nitrogen) has been done by ultimate analysis in accordance with ISO 12902, instrumental method (Abdulsalam Jibril *et al*., 2019). The total sulphur in raw material has been determined according to ISO 19579. The percentage of oxygen content was calculated by difference. The instruments used for ultimate analysis was the LECO Truspec CHN whereas total sulphur was determined using the LECO & S analyser.

3 4.3 Determination of Carbon, Hydrogen, and Nitrogen (ISO 12902)

One gram (1g) of the coal sample was placed in a carousel and placed into the furnace to heat to 950 °C in the presence of oxygen for combustion. An infrared detector has been used to quantify the emitted gases of carbon and hydrogen, while a thermal conductivity detector was detecting the nitrogen within the coal.

3.4.4 Determination of oxygen content

The difference of the total percentage of moisture, ash, carbon, hydrogen, nitrogen, and the total sulphur content defined the Oxygen content (%) of the samples on air-dried basis as per the following equation. (3-1);

$$\mathrm{O}\% = 100 - (\mathrm{M} + \mathrm{A} + \mathrm{C} + \mathrm{H} + \mathrm{N} + \mathrm{S})\% \qquad (3\text{-}1)$$

Where, M is the percentage of moisture; A is the percentage ash content; C is the percentage total carbon; H is the percentage of hydrogen; N is the percentage of nitrogen and S is percentage of total sulphur.

3.4.5 The Total sulphur determination (ISO 19579)

A determined amount of the samples was completely burned in oxygen. Sulphur inherent in the samples reacted during the combustion to form sulphur dioxide (SO_2). The combustion gases were purified after passing through a dust filter and moisture absorber. Infrared scanning of the evolved gas was used to measure the sulphur content.

3.4.6. X-ray Diffraction (XRD) analysis

Qualitative determination of the common, predominant phases present in the coals samples was conducted using D2 PHASER Bruker Meas Srv D2-208365 with SSD 160 operating at 30 kV and 10 ma. The principle of XRD analysis test is based on the

interference of monochromatic X-rays and crystalline material. The diffractometer (XRD instrument) is composed by an X-ray tube, a sample holder, and an X-ray detector. The X-rays are produced by the cathode ray and separated in monochromatic radiation then oriented to the sample for analysis. A diffracted ray is generated from the interaction between the incident rays and the material when conditions obey to Bragg's Law given by the following equation (3-2).

$$n\lambda = 2d\sin\theta \quad (3\text{-}2)$$

Where, n is an integer depicting the order of the diffraction peak, λ is the wavelength, d is the lattice spacing and θ is the scattering angle (Birkholz, 2006).

The wavelength of electromagnetic radiation is linked to the scattering angle and the lattice spacing in crystalline material through Bragg's law described above. Typical patterns of crystals present in the material are obtained according to the XRD analysis factors used. The exact interpretation of the produced pattern is done by its comparison with available reference patterns, therefore conduce to the accurate classification. The HighScore X'pert software was used to compare diffraction peaks with reference patterns and create peak data for the identification of different phases.

3.4.7. X-ray Fluorescence (analysis)

A. Procedure used to Prepare Fusion Disks for Major Analysis

- Place all clean Pt crucibles and porcelain LOI (loss on ignition) dishes in the furnace at 1020°C for half an hour to remove any organic residues.
- Once clean and cool place approximately 1g of each sample into each LOI dish. Recording both the LOI dish ID number and the weight of the LOI dish before and after addition on the weight chart on the laptop. Ignite at 1020°C for 40 minutes. Once complete remove from furnace and allow to cool in a desiccator.
- Weigh approximately 1.75g of flux (Spectroflux 105) into each Pt crucible. Recording both the Pt crucibles ID number and the weight of the Pt crucible before and after addition on the weight chart on the laptop. Ignite at 1020°C for 40 minutes. Once complete remove from furnace and allow to cool in a desiccator.
- Switch on the hot plate in the furnace room (must be on for a minimum of 1 hour prior to pouring).

- Once both the LOI and the Pt crucibles are cool measure and record the after-ignition weights of the LOI dishes to determine the samples LOI. Similarly measure and record the after-ignition weights of the Pt crucibles to obtain the flux weights.
- Using the Pt crucible ID and LOI dishes ID number to match the samples (see weighing sheet). Measure approximately 0.34g of pre-ignited sample into each corresponding Pt crucible. Ignite at 1020°C for 50 minutes. Once complete remove from furnace and allow to cool in a desiccator. Once cool if you notice that there are solid particles still present in the fused mixture reignite for an additional half an hour.
- Weigh and record the Pt crucibles and return to the furnace at 1020°C.
- Individually pour and press the fusion beads on the hot plate. Making sure to lay the Pt crucibles in the same order as the beads are poured. Should any beads contain bubbles or solid material break and re-pour.
- Once all samples are poured and the Pt crucibles are cool. Map the crucible IDs so that you will be able to label the beads the following day.
- Allow the beads to set for 90 minutes on the hot plate. Then switch off the hot plate and allow to anneal overnight.
- Clean the Pt crucibles in dilute HCl for 90 minutes on the hotplate. Rinse thoroughly.
- Transfer the remaining ignited material from the LOI dishes to vials and store for future use. Clean the LOI dishes.

B. XRF analysis of major elements

Major elements were determined using the Norrish Fusion (Fitzpatrick *et al*., 2018) technique using in-house correction procedures. The X-ray Fluorescence Analyzer PANALYTICAL AXIOS advanced equipped with End-window Rh Xray tube SST-MAX with 4kW output, LiF (220), PX1, PX8, PX10, Ge111 curved analyser crystal, was the equipment used for this analysis. 150-, 300- and 700-microns primary collimators, 6, 10, 20, 27, 30, 37 millimeters collimator masks,150-micron (Be), 100-micron (brass), 400-micron (brass), 750-micron (Al) tube filter and Argon flow proportional and scintillation detectors, sealed Xe detector was used to analyse the samples. Major elements were fused using Johnson Matthey Spectrolflux 105 at 1000°C and raw data corrected using in-house software. Standard calibrations were made up using synthetic oxide mixtures

and international standard rocks as well as in-house controls. Sample weight used was 0.35 gm and flux weight 2.0 gm. Calibration standards were primary International Reference Materials USGS series (USA) and NIM series (South Africa). Precision is taken as 1% for elements in abundance of greater than 5% by weight, and 5% for elements in abundance less than 5%.

3.4.8. Fourier Transform infrared analysis

The Infrared spectroscopy analysis is the interpretation of the interaction between the infrared light and material to be analysed. The principal measurement provided in infrared spectroscopy is an infrared spectrum, which is a graph of measured infrared intensity versus wavelength (or wavenumber) of light (Smith Brian, 2018). The instrument used for spectroscopy analysis in this study was the Fourier transform infrared spectrometer Perkin Elmer Spectrometer–Spectrum Two. Infrared spectroscopy reacts to show the presence of chemical functional groups in analysed sample. A chemical functional group is defined as a structural fragment into a molecule. Functional groups have chemical properties that are often the same from molecule to molecule. In FTIR analysis the wavenumber positions of the bands of a functional group are firstly measured, afterward the determined measurement will be used to identify that functional group in the analysed samples. Moreover, the FTIR can also be used to confirm chemical identities. That is done by comparing the spectra of the samples to available reference spectra which have known composition. The intensities of the absorption peaks in an infrared spectrum are proportional to the chemical functional group concentration. In this study, the FTIR analysis was conducted in the wavenumber range situated between 4000 and 450 cm^{-1} in transmittance mode. In a FTIR spectrum the peaks point down and represent wavenumbers at which the sample transmitted small infrared radiation. The units of transmittance are percent. The region of the infrared spectrum situated between 1600 and 1000 cm^{-1} is named the fingerprint region. This region is the one which contains the large number of infrared bands displayed. However, the region from 1000 to 400 cm^{-1} is often called the aromatic region due to the intense bands of benzene rings presented. Portion (0.25 g) of dried and pulverized samples were placed on the instrument diamond attenuated total reflectance (ATR) accessory. The sample was positioned on the instrument holder. The knob was used to exert pressure on the sample for it to produce the spectrum.

3.4.9. Density Measurement

The density of the produced activated carbon was measured using the Helium Pycnometer with Micrometrics Accupyc II 1340 equipment (Figure 3-5). The equipment measures the volume accurately via the displacement of the gas used. The gas used for the measurement is Helium due to it extend penetration capacity into surfaces. The produced activated carbon is placed onto a calibrated chamber with predetermined volume and the helium gas is then flowed. The void volume of the chamber and the pores of the product are instantly filled by the flowing gas. The pressure from the filled chamber is transferred into another empty chamber to facilitate the measurement of the product solid phase volume. The analysis is repeated automatically with the aid of the Accupyc which purges water and volatiles from the analysed product. The repetition of analysis continues until the measurement converges accurate results. The density is determined by the ratio of the measure volume to the weight of the analysed product.



Figure 3-5:Micrometrics Accupyc II 1340 Pycnometer

3.4.10. Determination of surface area, pore volume and size

The characterization of activated carbon was done by using the gas adsorption method which has been proved as consistent (Abdulsalam Jibril *et al*., 2019). The nitrogen adsorption test allows the determination of surface area, total pore volume and pore size of the porous material.

A. Nitrogen Gas adsorption method

In the nitrogen Gas adsorption method at 77K, 0.2 g of the porous material was firstly degassed at 150°C during 6 hours under nitrogen flow using Quatachrome instruments, Autosorb IQ to the degassing section side situated on the right of the instrument (Figure 3-6). Then after, the degassed product was moved to the BET analysis side situated on the left side of the equipment (Figure 3-6). The nitrogen adsorption measures permitted the determination of; (i) Surface area (S_{BET}) by using the BET method (Jayakantha *et al*., 2021), (ii) the total pore volume (V_T) calculated at relative pressure of P/Po =0.99 (Ouf *et al*., 2019), (iii) the pore size which was measured from nitrogen desorption isotherms data according to Barrett-Joyner-Halenda (BJH) technic (Bardestani *et al*., 2019).

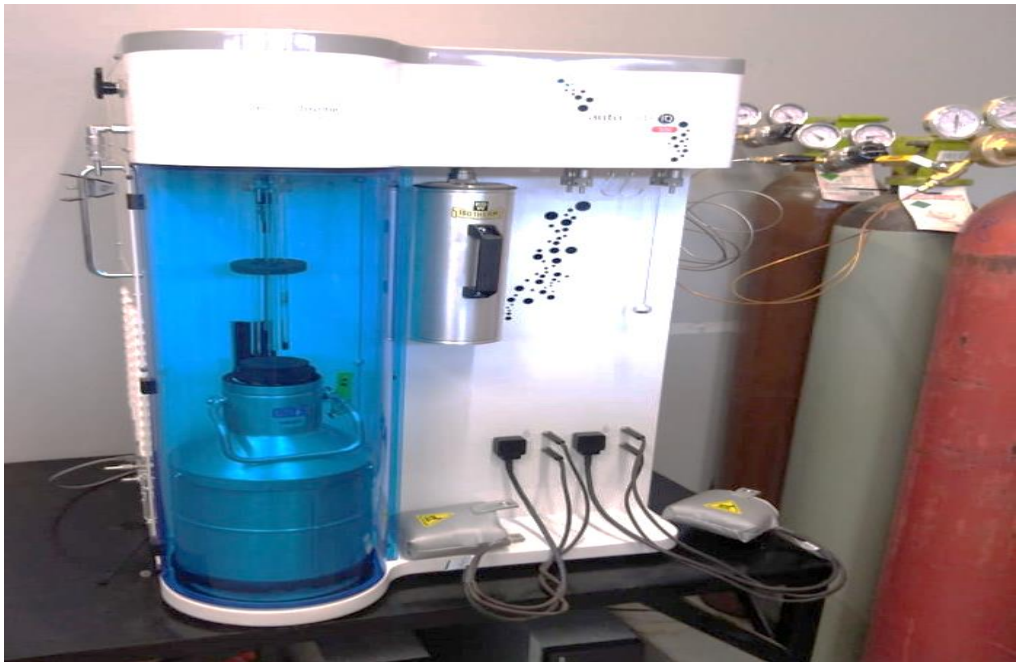

Figure 3-6:Quatachrome instruments, Autosorb IQ

B. Brunnet Emmet Teller (BET) Method

By convention, the surface area and pore volume of porous material are obtained via the BET model which analyzed the nitrogen adsorption isotherms. The surface area and porosity of the porous materials are the main physical properties influencing its storage capacity. The BET method has been utilised several times and

extendedly to determine the surface area, total pore volume and pore diameter of porous materials (Rouquerol *et al*., 2013). The BET method is divided in two steps; the transformation of the physical adsorption (physisorption) isotherm into BET plot from which the BET monolayer capacity (n_m) is determined and the calculation of the BET surface area (S_{BET}) using the determined n_m with an appropriate value of the molecular cross-sectional area σ (Thommes *et al*., 2015). The BET linearized equation is displayed in equation (3-3) (Rouquerol *et al*., 2013);

$$\frac{\frac{P}{P_0}}{n\left(1-\frac{P}{P_0}\right)} = \frac{1}{n_m C} + \frac{C-1}{n_m}\left(\frac{P}{P_0}\right) \quad (3\text{-}3)$$

Where, n is the amount of gas adsorbed at relative pressure and n_m is the specific monolayer capacity. The BET monolayer capacity nm is determined from BET equation by using the BET plot which elucidate the relationship between $\frac{\frac{P}{P_0}}{n\left(1-\frac{P}{P_0}\right)}$ and P/Po. The monolayer capacity n_m allows the determination of the BET area. However, it is necessary to determine the average area σ_m (molecular cross-sectional area) occupied by the adsorbate molecule into the entire monolayer (Rouquerol *et al*., 2013). The equation (3-4) gives the relationship between the specific area and the amount of adsorbate molecule as follow;

$$a_s(\mathrm{BET}) = n_m . \frac{L\sigma_m}{m} \quad (3\text{-}4)$$

Where, a_s (BET) is the BET specific area of the porous material (of mass m)

$$\frac{1}{v[(po/p)-1)]} = \frac{c-1}{v_m c}\left(\frac{p}{po}\right) + \frac{1}{v_m c} \quad (3\text{-}5)$$

v = adsorbed gas quantity

$p0$ = saturation pressure of adsorbate

p = equilibrium pressure of adsorbate

c = BET constant = $\exp\left(\frac{E_1 - E_l}{RT}\right)$

E_1 = heat of adsorption for the first layer

E_L = heat of vaporization

$$\frac{\mathbf{1}}{\boldsymbol{v}[(\boldsymbol{po}/\boldsymbol{p})-\mathbf{1}]} = \frac{c-1}{v_m c}\left(\frac{p}{po}\right) + \frac{1}{v_m c} \quad (3\text{-}6)$$

$$\boldsymbol{y} = mx + b \quad (3\text{-}7)$$

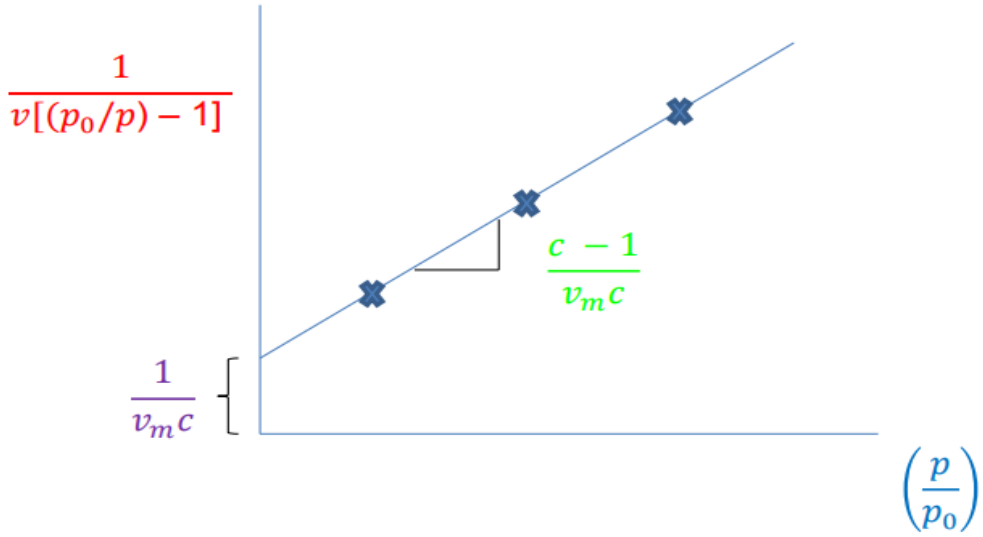

$$Slope = \frac{c-1}{v_m c} \quad (3\text{-}8)$$

$$intercept = \frac{1}{v_m c} \quad (3\text{-}9)$$

$$v_m = \frac{1}{slope+intercept} \quad (3\text{-}10)$$

$$c = 1 + \frac{slope}{intercept} \quad (3\text{-}11)$$

$$S_{BET} = \frac{v_m N_S}{V} \quad (3\text{-}12)$$

S_t = total surface area of sample material

v_m= monolayer absorbed gas volume

N = Avogadro's number = 6.02 x 1023 molecules/mol

s= cross-sectional area of adsorbed gas molecule

V = molar volume of adsorbed gas

3.4.11. Pore Size Distribution (PSD)

The characterization and description of porous materials internal structure are done by the determination of pore size distribution analysis (Okhovat *et al*., 2012). The internal structure of the porous material is shown by PSD analysis using a simplified model determined as follow;

$$\mathrm{f(W)} = \frac{\mathrm{dV}}{\mathrm{dW}} \quad (3\text{-}13)$$

Where W is pore width and V is the pore volume.

The Adsorption integral equation (AIE) (20) below is used to calculate the PSD of a porous. material. This equation defines the correlation between the PSD function (3-14) and the adsorption isotherm of the porous material (Wang *et al*., 2018).

$$N(P_i) = \int_0^{\infty} f(w)\rho(w,P)dwi = 1 \ldots . n \qquad (3\text{-}14)$$

Where N(P) is the experimental measure of adsorption isotherm of the porous material, ρ (w, P) is the adsorption density in a model pore of width w and f(W) is the PSD and n is the number of adsorption measurement used for the analysis.

Nitrogen adsorption isotherm at 77K is severally used for the PSD determination of activated carbons (Li *et al*., 2022). The nonlocal density functional theory (NLDFT) method is mainly used to analyse the nitrogen adsorption isotherm together with a mathematical model for PSD determination. However, even though there are other methods of PSD determination apart from the NLDFT such as Barret, Joyner and Halenda (BJH), Horvath and Kawazoe (HK) the NLDFT method has given the more accurate of pore structure characterization of porous material (Li *et al*., 2022). In this research, Quantachrome® ASiQwinTM software which interfaces the autosorb iQ to a computer was used for data acquisition and data reduction. Information on the distribution of micropores, mesopores, and macropores was obtained from adsorption data of the N_2 isotherm using the nonlocal density functional theory (NLDFT) method.

3.4.12. SEM/EDS analysis

The Scanning Electron Microscopy (SEM) analysis of the sewage sludge, coals samples and produced activated carbon was done using Carl Zeiss Sigma Field Scanning Electron Microscope connected to the Oxford X-act EDS detector. The analysis was carried out this procedure according to the operational mode of the equipment. The samples were mounted on a stub where a carbon tape was tacked. Then the samples were coated in carbon (graphite) and gold/palladium alloy for electrical conductivity which minimized the charging and related imaging artefacts during analysis. The coated samples on the stubs were labelled and loaded into the specimen chamber of the SEM equipment. The analysis was done while the electron beam was striking the surface of the sample in an angle, generating a secondary electrons discharge trajectory from the surface atoms. The electron beam hits the inner shell of an atom, knocking off an electron from the shell, while leaving a positively

charged electron hole. When the electron is displaced, it attracts another electron from an outer shell to fill the vacancy and release the results. The generated electrons bited a detector which is placed at a determined angle to the surface. The photomultiplier enhanced the signal and generated and image. The SEM/EDS analysis settings was on 10 kV and a working distance (WD) of 7.2 mm using backscattered electrons (BSE) signal. The SEM analysis provided surface structure of the samples (Liu *et al*., 2020).

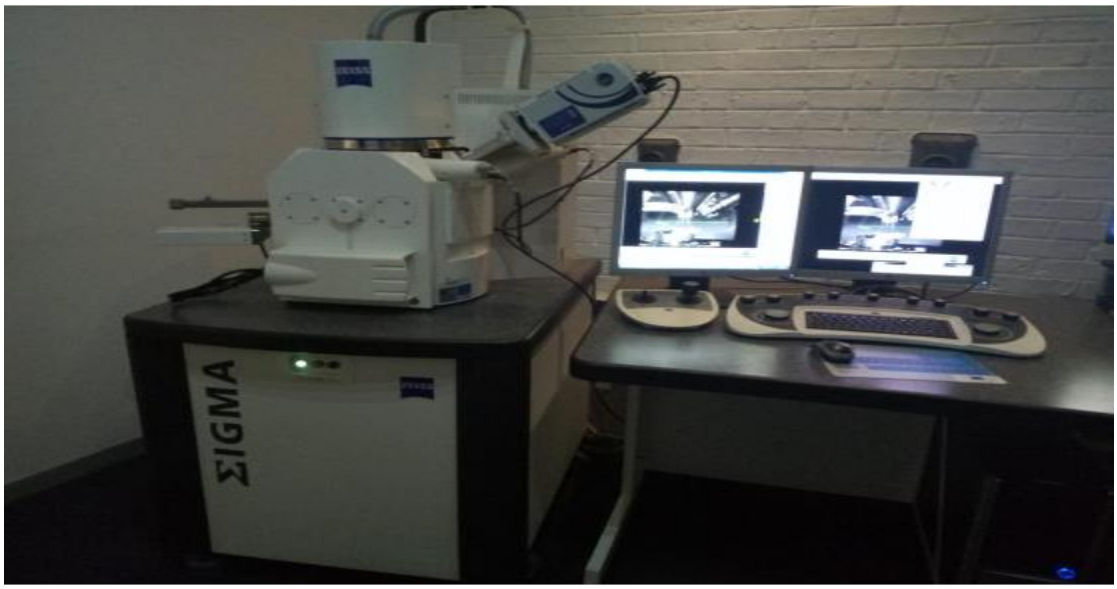

Figure 3-7:Carl Sigma Field Emission Scanning Electron Microscope equipped with an Oxford X-act EDS detector

3.4.13. Measurements of hydrogen Adsorption

The hydrogen adsorption capacity of the produced activated carbon from coal discard/slurry and sewage sludge hydrochar has been assessed at different temperatures and pressures using Particulate Systems High Pressure Volumetric Analyser (HPVA II) (Figure 3-8). The volumetric method is carried out through the HPVA II equipment which produced high pressure gas adsorption and desorption isotherms (Ekundayo *et al*, 2019). A determined volume of gas is injected into the sample chamber for analysis under volumetric method. The pressure is noted when the equilibrium is reached between the gas and the sample. Specified pressure intervals are used to reach the maximum set pressure during repeated adsorption analysis. The equilibrium pressure data allowed the determination of the amount of gas adsorbed by the sample. The adsorption isotherm data are determined from the quantity of gas adsorbed plotted

against the equilibrium pressure. Hence, during the desorption analysis the pressure diminished steadily, and the desorption isotherms is determined.

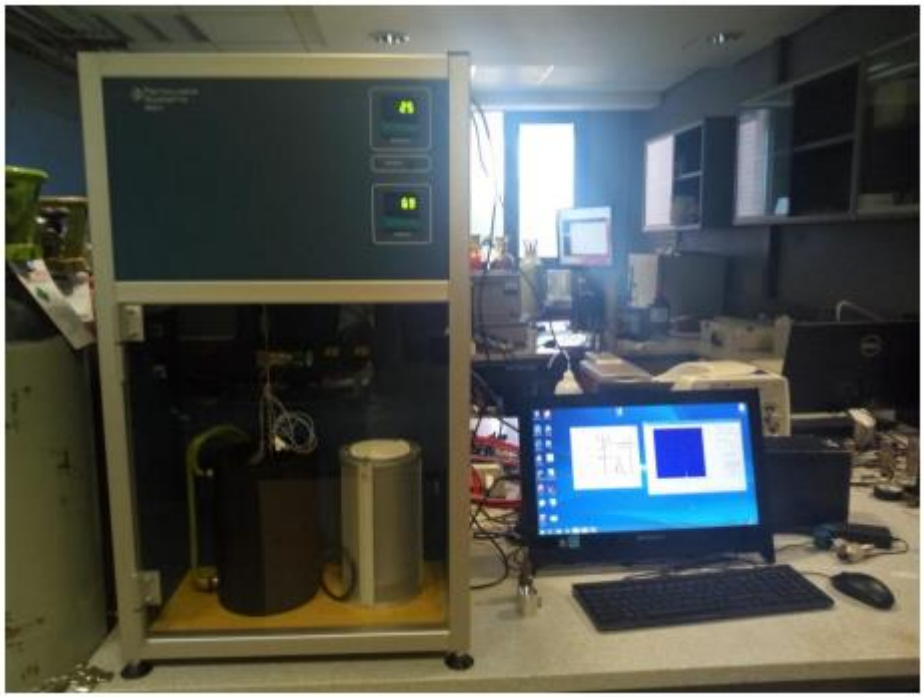

Figure 3-8:Image of Particulate Systems High Pressure Volumetric Analyzer (HPVA-200)

A. Samples Preparation

During sample preparation, the sample cylinder was cleaned with alcohol and rinsed using warm water. After that, the sample cylinder was preheated in an oven and held at 110°C for two hours. the sample cylinder was then removed from the oven and placed in ambient atmosphere to cool down. Thereafter, the empty sample cylinder was scaled, and the weight was noted as W1. After that, the sample was loaded into the cylinder using a funnel placed on top of it. The loaded cylinder was weighted, and the weight was noted as W2. The weight of the sample Ws was the determined as the difference between the weight of the loaded cylinder and the empty cylinder as shown in equation (3-15)

$$Ws = W2 - W1 \quad (3\text{-}15)$$

After recording the weight of the sample, a 20M VCR metal gasket seal from Swagelok was tightly fixed on the top of the cylinder to avoid leaks.

B. Samples Degassing

In degassing, the sample holder was installed in the sample compartment of the HPVA equipment connected to the thermocouple cables placed into the thermocouple connectors of the sample compartment. The sample holder was then manually connected to the degassing port using the connector. Afterward, the evacuation was proceeded to ensure that the vacuum is in place. Thereafter, the temperature of the furnace was set first at 90°C and was increased sequentially until it reached 200°C. The procedure allowed the sample to degas as recommended for accurate analysis of activated carbon sample. After degassing process, the furnace temperature was set at 0°C and the sample cooled to ambient temperature and has been removed from the degassing port.

C. Hydrogen adsorption

The hydrogen adsorption /desorption analysis was done as follow; water was filled into the sample analysis compartment than the sample holder removed from the degassing port was installed inside the sample analysis compartment and connected to the analysis port of the HPVA equipment (Figure 3-9). Therefore, the temperature probe was inserted in the water filled sample compartment to indicate the variation of temperature during the analysis. The adsorption/desorption experiment was conducted by firstly defining the pressure, temperature, and gas port (hydrogen) parameters onto the system experiment definition window (Figure 3-10). After the parameters were defined, the experiment was allowed to run by clicking the “Run Experiment” icon on the window.



Figure 3-9:Sample Analysis Compartment

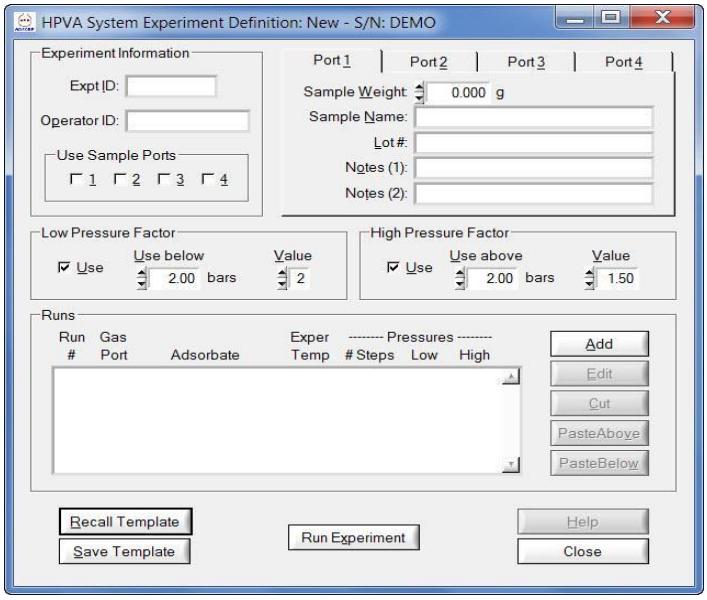

Figure 3-10:HPVA II System Experiment Definition Window

3.4.14. Calorific value

The quantity of heat released on combustion of 1 kg of coal-based material at the reference state of products of combustion (POC) represents its calorific value (CV). The products obtained after complete combustion of a hydrocarbon material containing C, H and S are CO_2, H_2O and SO_2. The reference state of POC is:

25°C CO_2 (g), SO_2(g) and H_2O (l) = Gross Calorific Value (GCV)

100°C CO_2 (g), SO_2 (g) and H_2O (l) = Net Calorific Value (NCV)

So GCV > NCV by an amount equal to latent heat of condensation. CV can be expressed as cal/g, kcal/kg, kJ/kg, Btu/lb or cal/gmol, kcal/kgmol, kJ/kgmol, Btu/lbmol. The conversion factors are:

1 kcal = 3.968 Btu = 4186 Joules= 0.00116 kWh

1 kWh = 1.34hP-h = 3.6 x 10^8J = 860 kcal = 3412.14 Btu

1 hP-h = 0.746 kWh.

Therefore, CV can be determined experimentally using the bomb calorimeter by the combustion of 1g coal at constant volume and the recording of temperature risen. The calorific value can also be determined theoretically by using the heat of formation of product after complete combustion according to the Dulong's formula in terms of % of elements (Gupta *et al*., 2016).

GCV = 81%C +341 (%H - %O/8) + 22%S kcal/kg or (3-16)

GCV = 339%C + 1427 (%H - %O/8) + 92%S kJ/kg (3-17)

NCV = GCV – Heat of vaporization of water (3-18)

NCV = GCV – 5.84 (9%H + %M) kcal/kg (3-19)

NCV = GCV – 24.44 (9%H + %M) kJ/Kg (3-20)

In this formula it's has been assumed that.

- The heat of formation of coal is zero.
- The coal contains H and O. therefore, available H for combustion with gaseous oxygen = (%H - %O/8)
- The CV of coal is sum of CV of heat of formation of complete combustion products.
- The heat of vaporization of water at 100°C = 542 kcal/kg (975 Btu/lb); whereas at 25°C it is 584 kcal/kg (1050Btu/lb).

3.4.15. HTC liquid Product characterization

A. Analysis of dissolved element by ICP-OES

To determine the elemental composition of HTC's liquid phase the ICP-OES technique (Inductively Coupled Plasma-Optical Emission Spectrometry) was used. ICP-OES analysis was based on the ionization of a sample by hot plasma originated from an argon gas. High purity (99.99%) argon was used as plasma, auxiliary and nebulizer gas. The gas flows were kept at 15.0 l/min for plasma, 1.50 l/min for auxiliary and 0.56 l/min for nebulizer. Radiofrequency (R.F) power of the plasma generator was 1.35 kW. Vertical

height of the plasma was fixed at 7 mm. CCD detector and 21 CFR 11 version 4.1.0 software (for data acquisition) was used to analyse the samples as displayed in Figure 3-11. Prior to sample analysis, interference corrections, instrument performance, instrument detection limit, method limit and linear dynamic range was established. Samples were analyzed following US EPA Method 6010 (Method for analyzing element using-OES). To provide a quality result, data have been verified and validated.

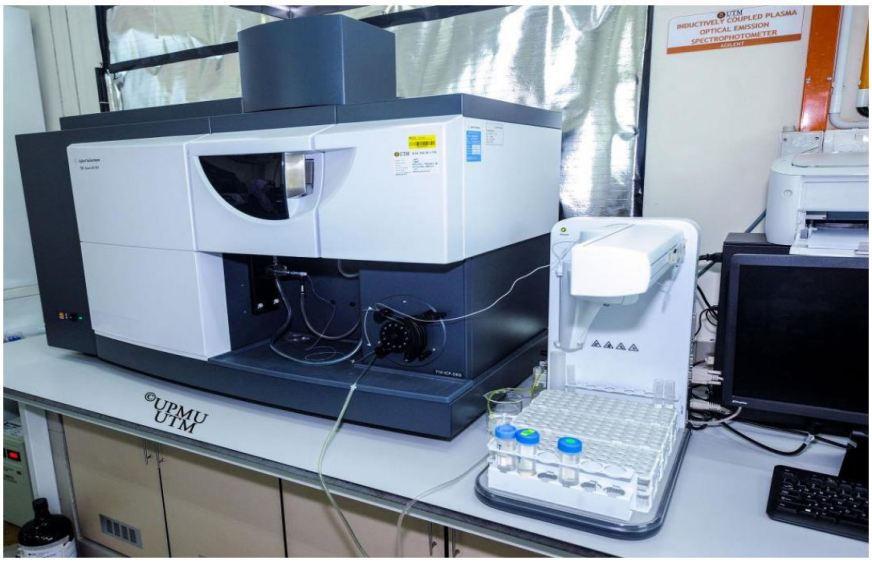

Figure 3-11: ICP-OES to analyse the samples.

B. Total carbon and total organic carbon and ions dissolve analysis

1 Determination of anions

The EPA Method 1685, Nitrate/Nitrite-N in Water and Bio solids by Automated Photometry, Draft January 2001 was used to determine anions in the solution samples. The solution samples were shaken on a shaker table for 60 minutes at 70 RPM. The mixture was then centrifuged for 10 minutes at 2000 RPM. The samples were then filtered by gravity through a Whatman filter. The aqueous leachate samples were preserved by adding H_2SO_4.

2 Determination of Total Organic Carbon (TOC)

The Total organic carbon content in liquid phases from HTC process was determined by a chromatographic method using the Thermo Scientific Flash EA 1112 Elemental Analyser according to SR EN 15936: 2013standard (Figure 3-12). The Flash EA 1112 is based on the well-known Flash Dynamic Combustion method, which

produces complete combustion of the sample within a high temperature reactor, followed by an accurate and precise determination of the elemental gases produced using a TCD thermal conductivity detector. The sample combustion temperature was 950°C.



Figure 3-12 :Thermo Scientific Flash EA 1112 Elemental Analyser

For the Total Organic Carbon content determination in liquid phase from HTC and Co-HTC process, the analytical process started with the elimination of all inorganic carbons in the form of carbon dioxide by the effect of acidification with a small volume of phosphoric acid in special container. The liquid phase produced was dried at a temperature lower than 40 °C, and the special container was then closed and loaded into the auto sampler carousel and analyzed. The sample quantity was chosen in such a way that the carbon dioxide released during combustion was in the analyzer working range. For Thermo Scientific Flash EA 1112 elemental analyzer calibration, calcium carbonate reference material was used. The value obtained after analysis is the sum of both inorganic and organic carbon in the sample or Total Carbon (TC). If the sample is free of carbonates the TC value is equivalent to the TOC value.

TOC was measured by oxidizing the organic compounds in consideration of analytical requirements such as speed and sensitivity. The following equation was used to calculate TOC of liquid phase.

Total organic carbon (from coulometer) = Total carbon – total inorganic carbon (from coulometer) (3-21)

3.5. Summary

This chapter outlined the experimental methodology used for raw material (CT, CS, and SS) and product (HCs and ACs) analysis. The various samples used in this study were characterized by proximal, ultimate, total sulphur, x-ray fluorescence, x-ray diffraction, and scanning electron analyses. The process for evaluating the H_2 adsorption capacity of the activated carbons synthesized has been also provided. The next chapter presents the results of experimental characterisation of coal discards, sewage sludge, and activated carbons synthesized. The approach employed for each application of this investigation will be detailed and elucidated separately in each chapter.

REFERENCES

1. Afolabi, O.O., Sohail, M. and Cheng, Y.L., 2020. Optimization and characterization of hydrochar production from spent coffee grounds by hydrothermal carbonization. *Renewable Energy*, *147*, pp.1380-1391.
2. Barghi, B., Jurisoo, M., Volokhova, M., Seinberg, L., Reile, I., Mikli, V. and Niidu, A., 2022. Process Optimization for Catalytic Oxidation of Dibenzothiophene over UiO-66-NH2 by Using a Response Surface Methodology. *ACS omega*.
3. Abdulsalam, J., Mulopo, J., Oboirien, B., Bada, S. and Falcon, R., 2019. Experimental evaluation of activated carbon derived from South Africa discard coal for natural gas storage. *International Journal of Coal Science Technology,* 6(3), pp. 459 - 477.
4. Liu, D., Li, C., Wu, J. and Liu, Y., 2020. Novel carbon-based sorbents for elemental mercury removal from gas streams: A review. *Chemical Engineering Journal*, *391*, p.123514.
5. Qu, S., Wan, J., Dai, C., Jin, T. and Ma, F., 2018. Promising as high-performance supercapacitor electrode materials porous carbons derived from biological lotus leaf. *Journal of Alloys and Compounds*, *751*, pp.107-116.
6. Omri, A. and Benzina, M., 2019. Influence of the origin of carbon support on the structure and properties of TiO2 nanoparticles prepared by dip coating method. *Arabian Journal of Chemistry*, *12*(8), pp.2926-2936.
7. Abdulsalam, J., Onifade, M., Bada, S., Mulopo, J. and Genc, B., 2022. The spontaneous combustion of chemically activated carbons from south African coal waste. *Combustion Science and Technology*, *194*(10), pp.2025-2041.
8. Fitzpatrick, R.W., 2018. Dr Keith Norrish (1924–2017): Distinguished soil scientist and pioneer of X-ray Fluorescence spectroscopy. *Canberra, ACT, Australia, 18-23 November 2018*, p.188.
9. Smith, B., 2018. *Infrared spectral interpretation: a systematic approach*. CRC press.
10. Jayakantha, D.R., Gunawardhana, N., Bandara, H.M.N., Comini, E., Gunawardana, N.M. and Karunarathne, S.M.M.L., 2021. Low-cost automated instrumentation for the measurement of the specific surface area of powders by the Brunauer–Emmett–Teller (BET) method. *Instrumentation Science & Technology*, *50*(1), pp.47-56.
11. Ouf, F.X., Bourrous, S., Vallières, C., Yon, J. and Lintis, L., 2019. Specific surface area of combustion emitted particles: Impact of primary particle diameter and organic content. *Journal of Aerosol Science*, *137*, p.105436.
12. Bardestani, R., Patience, G.S. and Kaliaguine, S., 2019. Experimental methods in chemical engineering: specific surface area and pore size distribution measurements—BET, BJH, and DFT. *The Canadian Journal of Chemical Engineering*, *97*(11), pp.2781-2791.
13. Rouquerol, J., Rouquerol, F., Llewellyn, P., Maurin, G. and Sing, K.S., 2013. *Adsorption by powders and porous solids: principles, methodology and applications*. Academic press.
14. Thommes, M., Kaneko, K., Neimark, A.V., Olivier, J.P., Rodriguez-Reinoso, F., Rouquerol, J. and Sing, K.S., 2015. Physisorption of gases, with special reference to the evaluation of surface area and pore size distribution (IUPAC Technical Report).*Pure and applied chemistry*, *87*(9-10), pp.1051-1069.
15. Okhovat, A., Ahmadpour, A., Ahmadpour, F. and Khaki Yadegar, Z., 2012. Pore size distribution analysis of coal-based activated carbons: Investigating the effects of activating agent and chemical ratio. *International Scholarly Research Notices*, *2012*.
16. Li, C., Liu, X., You, F., Wang, P., Feng, X. and Hu, Z., 2022. Pore Size Distribution Characterization by Joint Interpretation of MICP and NMR: A Case Study of Chang 7 Tight Sandstone in the Ordos Basin. *Processes*, *10*(10), p.1941.

17. Liu W, Li Y, Lin S, Tang L, Dong Z, Xing F, Dong B, Hong S. Changes in chemical phases and microscopic characteristics of fly ash blended cement pastes in different CO2 concentrations. Construction And Building Materials. 2020 Oct 10; 257:119598.
18. Ekundayo JM, Rezaee R. Effect of Equation of States on High-Pressure Volumetric Measurements of Methane–Coal Sorption Isotherms—Part 1: Volumes of Free Space and Methane Adsorption Isotherms. Energy & fuels. 2019 Jan 24;33(2):1029-36.
19. Gupta, N.K., Prakash, P., Kalaichelvi, P. and Sheeba, K.N., 2016. The effect of temperature and hemicellulose-lignin, cellulose-lignin, and cellulose-hemicellulose on char yield from the slow pyrolysis of rice husk. *Energy Sources, Part A: Recovery, Utilization, and Environmental Effects*, *38*(10), pp.1428-1434.

Chapter 4. Physicochemical, structural analysis of coal discards (and sewage sludge) (co)-HTC derived biochar for a sustainable carbon economy and evaluation of the liquid by-product

This chapter has been published in the Scientific Reports, 2022 - nature.com Journal *cited as Kahilu, G. M., Bada, S., & Mulopo, J. (2022). Physicochemical, structural analysis of coal discards (and sewage sludge) (co)-HTC derived biochar for a sustainable carbon economy and evaluation of the liquid by-product. Sci Rep, 12(1). https://doi.org/10.1038/s41598-022-22528-*y

4.1. Abstract

This chapter focused on the hydrothermal treatment (HTC) of coal tailings (CT) and coal slurry (CS) and the co-hydrothermal treatment (Co-HTC) of CT, CS, and sewage sludge (SS) to assess the potential for increasing the carbon content of the hydrochar (HC) produced as an enabler for a sustainable carbon economy. The optimal combination methodology (OCM) and response surface methodology (RSM) were used to study the relationship between the important process parameters, namely temperature, pressure, residence time, the coal-to-sewage-sludge ratio, and the carbon yield of the produced HC. The optimized conditions for HC from coal tailing (HCT) and HC from coal slurry (HCS) (150°C, 27bar, 95 min) increased fixed carbon (FC) from 37.31% and 53.02% to 40.31% and 57.69%, respectively, the total carbon content improved from 42.82 to 49.80% and from 61.85 to 66.90% respectively whereas the ash content of coal discards decreased from 40.32 and 24.17% to 38.3 and 20.0% when

compared CT and CS respectively. Optimized Co-HTC conditions (208°C, 22.5bars, and 360 minutes) for HC from the blend of coal discards and sewage sludge (HCB) increased the fixed carbon on a dry basis and the total carbon content from 38.67% and 45.64 % to 58.82% and 67.0%, when compared CT and CS respectively. Carbonization yields (Cy) for HCT, HCS, and HCB were, respectively, 113.58%, 102.42%, and 129.88%. HTC and Co-HTC increase the calorific value of CT and CS, to 19,33MJ/kg, 25,79MJ/kg, respectively. The results further show that under Co-HTC conditions, the raw biomass undergoes dehydration and decarboxylation, resulting in a decrease in hydrogen from 3.01%, 3.56%, and 3.05% to 2.87%, 2.98%, and 2.75%, and oxygen from 8.79%, 4.78, and 8.2% to 5.83%, 2.75%, and 6.00% in the resulting HCT, HCS, and HCB, respectively. HTC and Co-HTC optimal conditions increased the specific surface area (SBET) of the feedstock from 6.066 m^2/g and 6.37 m^2/g to 11.88 m2/g and 14.35 m^2/g, for CT and CS, respectively. total pore volume rose to 0.071 cm3/g from 0.034 cm3/g, 0.048 cm3/g, and 0.09 cm^3/g proving the ability of HTC to produce high-quality HC from coal discards alone or in conjunction with sewage sludge as precursors for decontamination of polluted waters, soil decontamination applications, solid combustibles, energy storage, and environmental protection.

4.2. Introduction

South Africa (SA), one of the world's leading coal producers, is largely reliant on coal to supply its energy needs (Bohlmann *et al*., 2018). According to the Department of Energy's 2001 National Coal Discard and Slurry Inventory, about 65 million tons of coal-wastes are produced each year, with the bulk of these wastes being disposed of in tailings piles and slurry dams (Van d Venter *et al*., 2021). Coal waste disposal is viewed as a serious threat to the country's environmental waste management due to the solubilization of toxic chemicals from coal waste and the possibility of spontaneous

combustion (Onifade *et al*., 2020). Beneficiation methods such as physicochemical processes and regeneration techniques have emerged over time, however they are viewed as inefficient, unfriendly to the environment, laborious, and expensive (Petlovanyi *et al*., 2020). However, sewage sludge (SS) is produced in substantial quantities by SA wastewater treatment plants (Fijalkowski *et al*., 2017). The SS contains a variety of organic and inorganic pollutants that are suspected to causing illnesses (asthma, pneumonia) in people who live near disposal stockpiles (Venkatesan *et al*., 2015). Current SS management methods, such as on-site land disposal and rubbish piling, are considered unsustainable and remains a major issue (Shaddel *et al*., 2019). As a result, innovative strategies to coal waste and SS management are deemed necessary. This study focuses on the hydrothermal carbonization (HTC) to enhance the physicochemical properties of coal tailing (CT), coal slurry (CS), and a blend of the two coal and SS to produce potential carbon precursors for activated carbon, and other valuable carbonaceous materials (value added products). Because it minimizes the need for an energy-intensive dewatering phase, the HTC approach is more environmentally friendly than other typical thermal processes (Munir *et al*., 2018). HTC is a thermochemical process that uses hot pressurized water as a reactant and catalyst to improve the physicochemical properties of diverse raw materials (Tasca *et al*., 2019). The HTC products consist of a solid termed as hydrochar (HC), a liquid and a small amount of gas by-products (Tasca *et al*., 2019). Previous work on the HTC process assumed that CO_2 is the predominant gas (>95%) emitted during decarboxylation, accompanied by other gases such as CH_4, CO, and H_2. Under HTC conditions, the majority of the carbon and inorganic components (Ash) from the feedstocks are concentrated in the produced HC, hence reducing the quantity of CO_2 released (Zhang et al., 2015; Tasca *et al*., 2019). The HC synthesized is generally a stable aromatic compound with a porous structure and a high hydrophobicity level (Liao *et al*, 2016).

These features inhibit the further solubilization of inorganic materials (including hazardous components) in the HC when used as adsorbent for water decontamination for instance (Saba *et al*., 2017). The fuel characteristics of hydrochar produced were successfully enhanced by HTC of low carbon content coal between 150°C and 270°C (HC). Furthermore, HTC of various types of coal has indicated that the high reactivity and non-polar solvent behavior of subcritical water reduced the values of undesirable impurities such as fraction of total ash, oxygen, and sulfur while increasing the carbon content (Saba *et al*., 2017). However, there remain a need for further experimental data to corroborate previous works on the HTC of SS or SS combined with other biomasses (Wang *et al*., 2019). Additionally, previous works indicated that the carbonization and mass yields of different coal-biomass blends were extremely efficient when compared to HTC treatment of individual coal and biomass materials. The Co-HTC process provided acidic conditions that promoted the solubility of the feedstock's mineral content. As a result, when compared to HTC treatment of coal and SS individually, Co-HTC treatment of coals-sewage sludge mixture has a high likelihood of increasing feedstock carbon content (Zhang et al., 2015; Mumme et al., 2015; Liao *et al*, 2016).

In coal beneficiation plants and wastewater treatment plants, the disposal of waste coal and sewage sludge, respectively, presents a significant waste management burden. Hydrothermal carbonization (HTC) is an attractive thermochemical conversion method because it can directly convert moist biomass into energy and chemical products without the need for pretreatment and provides a long-term method for reducing human-caused CO_2 emissions by enhancing CO_2 immobilization on a durable carbon support. Hydrochar's capacity to generate active carbon precursors for decontamination of polluted waters, soil decontamination applications, solid combustibles, energy storage, and environmental protection has led to its increasing popularity.

Even though hydrothermal conversion, hydrochar formation mechanisms, and hydrochar properties have been relatively well studied (Zhang et al., 2015; Mumme et al., 2015; Wang *et al*., 2019), a deeper understanding of the interactions between process parameters related to the hydrothermal conversion of biomass and synthesized hydrochar structural and physicochemical proprieties for various available biomass materials is still necessary to expand hydrochar production and applications. Moreover, these correlations between the hydrothermal process conditions (temperature, heating rate, particle size, substrate concentration, catalyst addition, residence, etc.) and the physicochemical and structural properties of the hydrochar are essential in order to improve conversion. efficiency and provide reference data for industrial design and manufacturing. In addition, the liquid byproduct of hydrothermal conversion (HTC) has received little consideration, despite the necessity for a more in-depth investigation to clarify the relationship between HTC and the synthesis of hydrochar. The aforementioned provides the motivation behind paper.

4.3. Experimental method

4.3.1. Materials

Coal tailing (CT) and coal slurry (CS) were collected from a coal beneficiation plant in Mpumalanga, South Africa, for use in this study (Figure 4-1). Before use, the samples were kept in an airtight bag in the laboratory and dried at room temperature. The dried samples were screened into various particle sizes in accordance with ASTM D5142 standards for proximal, ultimate, and total sulphur analysis. Sewage Sludge (SS) collected from a wastewater treatment plant (Ekurhuleni Water Care Company (ERWAT)) was split into two portions. The first portion was dried in a laboratory dryer at 105 °C for 24 hours and crushed according to ASTM D5142 standards for

physiochemical characterization, while the second portion was used for HTC tests in its collected condition.

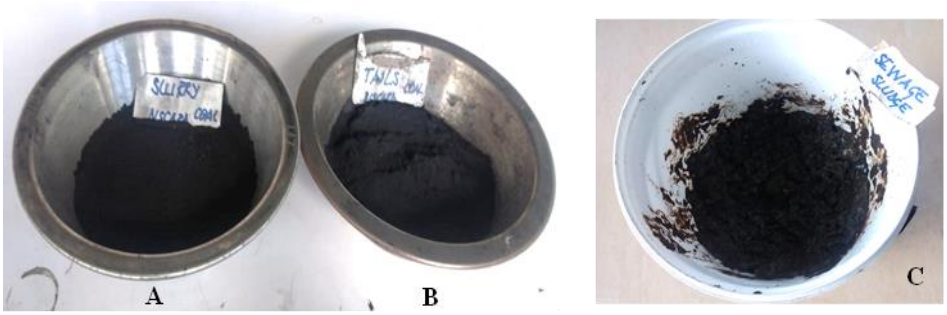

Figure. 4-1. collected waste coal slurry (A), waste coal tailing (B) and sewage sludge sample (C).

4.3.2. Methods

Hydrothermal (HTC) and Co-hydrothermal (Co-HTC) studies were carried out in a high-pressure tube reactor connected to temperature module regulator and water steamer for the heat input. HTC were done on coal tailing (CT) and coal slurry (CS) separately using -1mm coal samples, whereas Co-HTC were performed on CD-SS mixes. 25 g of feedstock (coal or mixtures of coal and sewage sludge) was mixed with water as an input solvent in a solid to liquid ratio of 1:4. Design-Expert software (Version 13, State–Ease, Inc, Minneapolis, USA) was used to design the hydrothermal carbonization (HTC) and co-hydrothermal (HTC) experimental test runs (Hlangwani *et al*., 2021). According to the design expert matrix, the HTC and Co-HTC process parameters (temperature, pressure, residence time, and CT+CS:SS ratio) were varied. Nitrogen flow was used to keep the reactor in an inert state. After the reaction, the temperature module regulator and steamer were turned off, and the reactor was allowed to cool naturally (cooling time 180 minutes). To separate the liquid and solid phases, the reactor

mixtures were filtered on a GF22µm filter paper disc. Hydrochar coal tailing (HCT), hydrochar coal slurry (HCS), and hydrochar blended coal and SS (HCB) are the solid products collected from HTC and Co-HTC experiments. Both solid samples were dried in an oven at 60°C for 24 hours before being prepared for characterization in accordance with ASTM D5142 standards. The design of experiment response surface methodology (DoE-RSM) technique has widely proved its accuracy in evaluating the combined interaction effects of independent (input) factors on a process (Afolabi *et al*., 2020; Barghi *et al*., 2022). Four hydrothermal process factors were considered in the designs: temperature, pressure, residence time, and the CD:SS (CT+CS: SS) mix ratio. The central composite design (CCD) and the custom design (CD) were used for experimental designs to determine the number of runs necessary to optimize the HTC and Co-HTC processes, respectively. HTC studies were carried out with temperature, pressure, and time changes ranging from 150 to 270°C, 10 and 27 bar, and 10 and 180 minutes, respectively. The Co-HTC tests, on the other hand, were carried out with changes in residence time ranging from 10 to 360 minutes for the same temperature and pressure range used in HTC studies, namely 150 to 270°C, 10 and 27 bar, respectively. Co-HTC experiments used a coal feedstock combination (CT+CS) of 50% CT and 50% CS. Response surface methodology (RSM), and the optimum combination methodology (OCM) were used to investigate the effects of the HTC and Co-HTC factors on the fixed carbon of the HC generated from individual CT, CS, and CD-SS mixtures, respectively. Furthermore, RSM and OCM were utilized to construct adequate models for predicting the optimum operating conditions necessary to produce high carbon content hydrochar. To assess the significance of the developed models, the analysis of variance (ANOVA) was used. The numerical optimal response approach option was then used to choose the best HTC and Co-HTC process settings, with the greatest fixed carbon (FC) content of the resultant hydrochar serving as the optimization criteria. Finally, the optimal

hydrochar (HC) synthesis parameters were established and used to synthesize HCs from hydrothermal and Co-hydrothermal experiments for further physicochemical characterization. Figure 4-2 summarizes the methodology implemented for the experimental HTC and Co-HTC treatments.

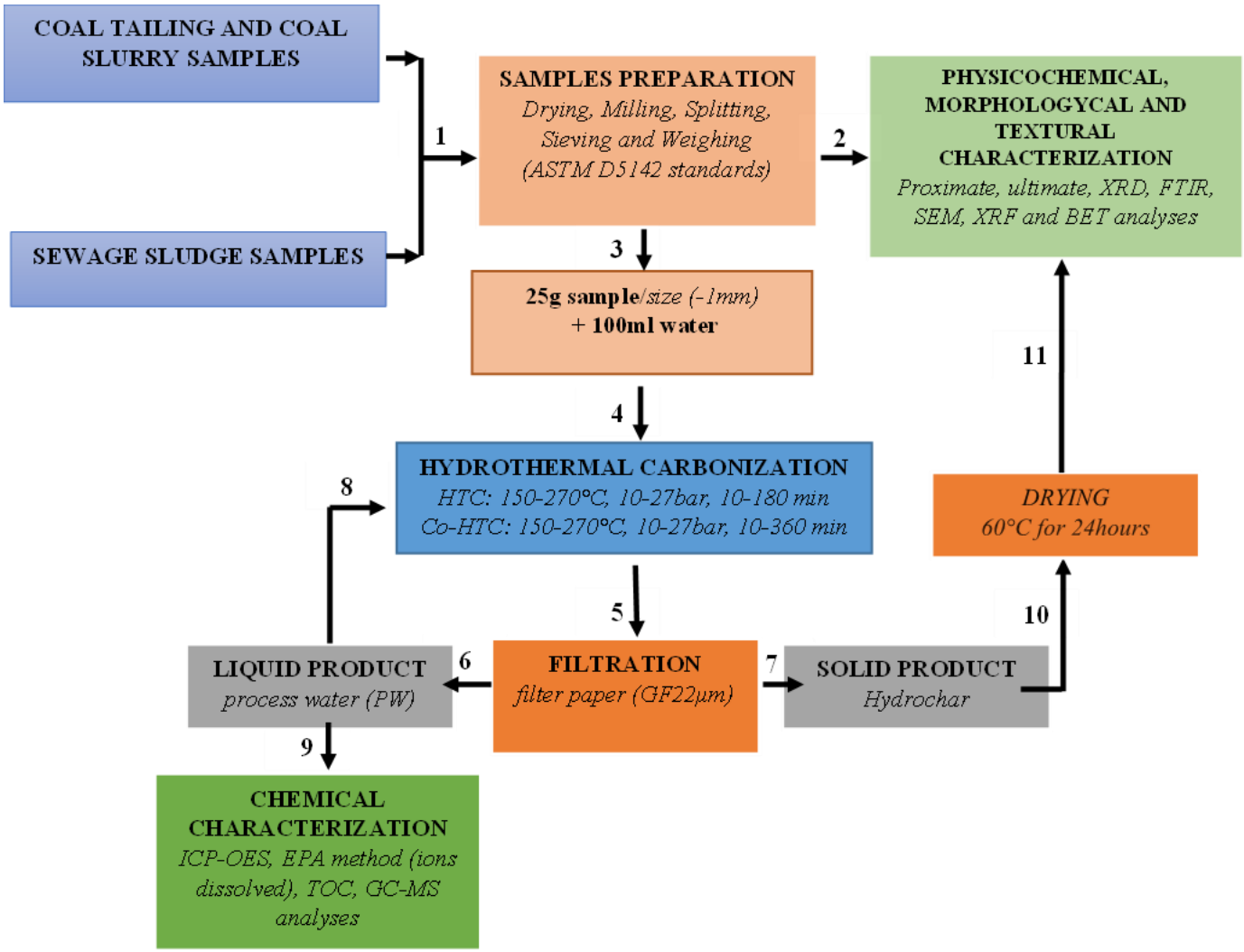

Figure 4-2: HTC and Co-HTC experimental methodology

4.3.3. Chemical Analyses

Proximate analysis of 1 g of -212 µm of raw sample and produced hydrochar were carried out using the Thermogravimetric analyser equipment (Leco TGA 701) in accordance with ASTM D5142. The determination of the elemental composition (CHN) of the raw samples and produced hydrochar was done in accordance with ISO 12902 standard method using a Flash 2000 Organic Elemental Analyzer (Thermo Scientific); oxygen was calculated separately as the difference from 100% using equation (4-1).

$$O\% = 100 - (M + A + C + H + N + S)\% \quad (4\text{-}1)$$

The mass produced hydrochar mass yield was calculated using equation (4-2).

$$Mass\ Yield\ (\%) = \frac{Wt(dried)\ of\ HC}{Wt\ (dried) of\ raw\ material} \quad (4\text{-}2)$$

The carbon densification factors of the produced hydrochar were obtained using the equation (4-3)

$$Carbon\ desification\ factor\ C_{DF} = \frac{\%\ C\ in\ HC}{\%\ C\ in\ feed} \quad (4\text{-}3)$$

The equation (4-4) was used to determine the HTC and Co-HTC carbonization yields (Cy) to assess the degree of carbonization.

$$Carbonization\ yield\ (\%), Cy = My\frac{\%\ C\ in\ HC}{\%\ C\ in\ feed} \quad (4\text{-}4)$$

Qualitative determination of the mineral phases in the raw material and the produced hydrochar was conducted using D2 PHASER Bruker. The XRD instrument employed Cu-Kα radiation as the excitation source over a 2θ range, and a generator setting of 30 kV and 20 mA. The resulting diffractograms from the XRD analysis were matched on the Bruker D2 mineral phase database to identify the major mineral phases in the samples. The minerals phases were identified using X'PERT High-Score Plus analysis software. The FTIR analysis of raw material and produced hydrochar was

conducted on a spectrometer Perkin Elmer instrument coupled with a diamond attenuated total reflectance (ATR) accessory in the wavenumber range between 4000 and 450 cm^{-1} (Smith. 2011). The Scanning Electron Microscopy (SEM) of the raw material and produced hydrochar, was done using Carl Zeiss Sigma Field Scanning Electron Microscope connected to the Oxford X-act EDS detector. The analysis was carried out in this procedure according to the operational mode of the equipment. The SEM/EDS analysis settings was on 10kV and a working distance (WD) of 7.2-8.2mm using backscattered electrons (BSE) signal. The SEM/EDS analysis provided the surface structure and the homogeneity of the samples (Lin *et al*., 2003).

The specific surface area and average pore diameter of the raw material and produced hydrochar were determined using nitrogen adsorption test at 77K. The autosorb iQ gas sorption instrument (Quantachrome Instruments, USA) was used while the Quantachrome® ASiQwinTM software was used for data acquisition and data reduction. Information on the distribution of micropores, mesopores, and macropores was obtained from adsorption data of the N_2 isotherm using the nonlocal density functional theory (NLDFT) method. The XRF analysis results of raw materials and produced hydrochar were obtained using the Panalytical AXIOS advanced Analyzer equipped with End-window Rh Xray tube in accordance with the Norrish Fusion technique (Norrish *et al*., 1969). Major elements were fused using Johnson Matthey Spectrolflux 105 at 1000°C and raw data corrected using in-house software. Standard calibrations were made up using synthetic oxide mixtures and international standard rocks as well as in-house controls.

The produced process water (PW) from the HTC of CT, CS and Co-HTC of CB identified as LCT, LCS and LCB respectively were analyzed for potential environmental disposal assessment. The elemental inorganic and total organic matter concentration

of the produced PW were determined by (ICP-OES) using an ICP-OES Agilent technologies spectrophotometer (UPMU-UTM). Prior to sample analysis, interference corrections, instrument performance, instrument detection limit, method limit and linear dynamic range were established. Samples were analyzed according to US EPA 6010 standard. The analysis was based on the ionization of a sample by hot plasma originated from an argon gas. High purity (99.99%) argon was used as plasma, auxiliary and nebulizer gas. The gas flows were kept at 15.0l/min for plasma, 1.50 l/min for auxiliary and 0.56 l/min for nebulizer. Radio frequency (R.F) power of the plasma generator was 1.35 kW. Vertical height of the plasma was fixed at 7 mm. The charge coupled device (CCD) detector and 21 code of federal regulations (CFR) 11 version 4.1.0 software (for data acquisition) was used to analyze the samples. The chemical oxygen demand (COD) was determined using the 410.4 method of analysis (Liu *et al*., 2022). The method involves using a strong oxidizing chemical, potassium dichromate $Cr_2O_7^{2-}$, to oxidize the organic matter in solution to produce carbon dioxide and water under acidic conditions.

The dissolved organic compounds of the produced PW were determined using the gas chromatograph linked to the mass spectrometer Shimadzu (GCMS-2010) The instrument was set at initial temperature of 140ºC. The initial temperature was held for five minutes then increased at 250ºC using a heating rate of 4 ºC/min and maintained for 12.5 minutes. The samples were injected at 220 ºC using the spitless mode. The analysis was performed using the following procedure: sampling time: 1.00 minute; flow control mode: pressure: 100.00 kPa, total flow: 50.00 ml/min; column flow: 1.13 ml/min; linear velocity: 3.00 ml/min. The identification of the organic compounds in the PW was conducted using the NIST 14 database and compared with published mass spectra.

The total organic carbon content (TOC) of the produced PW were estimated using a chromatographic method on the Thermo-Scientific Flash elemental analyzer (TSF EA 1112) according to NF EN 15936:2013 standard. The Flash EA 1112 is based on the well-known Flash Dynamic Combustion method, which produces complete combustion of the sample within a high temperature reactor, followed by an accurate and precise determination of the elemental gases produced using a TCD thermal conductivity detector. The sample combustion temperature was 950°C. The TOC content determination starts with the elimination of all inorganic carbons in the form of carbon dioxide by the effect of acidification of the sample with a small volume of phosphoric acid in special container. The liquid phase produced was dried at a temperature lower than 40 °C, and the special container was then closed and loaded into the auto sampler carousel for analysis. The sample quantity (100ml) was chosen in such a way that the carbon dioxide released during combustion was in the analyzer working range. For Thermo Scientific Flash EA 1112 elemental analyzer calibration, calcium carbonate reference material was used. The value obtained after analysis is the sum of both inorganic and organic carbon in the PW or Total Carbon (TC). The following equations were used to calculate TOC of the produced PW

$$\mathrm{TC} = \mathrm{TOC} + \mathrm{TIC} \quad (4\text{-}5)$$

Where TIC represents the total inorganic carbon of the PW obtained from the coulometer reading.

4.4. Results and discussion

4.4.1. Samples Characterization

The physicochemical analysis of coals and sewage sludge samples was performed using proximate, ultimate, and total sulphur analysis to determine the quality and elemental composition of the samples. The results showed in Table 4-1 are reported on air dry basis.

Table 4-1. Physicochemical analysis results

Analysis	Standards used	CT	CS	SS
Proximate Analysis (wt%, adb)				
Moisture content	ASTDM 5142	4.17	3.94	8.12
Ash	ASTDM 5142	38.64	23.22	36.07
Volatile Matter	ASTDM 5142	21.44	21.28	47.07
Fixed Carbon	ASTDM 5142	35.75	50.98	8.75
Ultimate Analysis (wt. %, adb)				
Carbon	ISO 12, 902	42.82	61.85	29.7
Hydrogen	ISO 12, 902	3.01	3.56	4.88
Nitrogen	ISO 12, 902	1.14	1.39	4.15
Oxygen	By difference	8.79	4.78	15.22
Total Sulfur (wt. %, adb)	ISO.19579 : 2006	1.43	1.26	1.86

CT: Coal tailing. CS: Coal slurry. SS: Sewage sludge. adb: air dried basis. wt%: weight percentage

The inherent moisture content of SS was found to be higher than that of CT and CS due to the nature of the sample, the process by which it was generated, and particle size distribution attributes. The CS sample has higher FC (50.98%) than the CT sample (35.75%), and SS (8.75%). Thermal treatment was required to improve the total carbon content of SS for future uses. As a result, the HTC method could improve the FC grade of the raw materials, resulting in improved porous structure properties of the produced HCs. The raw samples' ash concentration varied from 38.64% to 36.07% to 23.22% for CT, SS, and CS, respectively. The quantity of ash in the coal samples designates them

as high and moderately high ash content coal (Standard South Africa ISO11760, 2005 E). This is consistent with the fact that all the coal samples used in this study are byproducts of the coal beneficiation process. The results from XRD analysis of raw materials are showed in Figure 4-3. The observation and analysis of X-ray diffraction patterns of the coal samples revealed a predominance of crystalline mineral phases represented by intense peaks (Samson *et al*., 2010). The findings indicate that mineral phases such as quartz, kaolinite, muscovite, orthoclase anorthite, hematite, chlinochlore, moganite, calcite, siderite, and pyrite dominated the composition of raw samples. A significant hump was noticed on the X-ray diffraction pattern of the CS sample compared to the CT pattern, indicating the presence of more organic components in the CS sample. The intensity of the peaks decreased from quartz, kaolinite, muscovite, orthoclase, and pyrite, reflecting the falling quantity of each phase. The CT sample shows more mineral phase peaks than the CS and SS samples. The cause might be related to the findings of proximate examination, which revealed excessive ash and mineral matter levels in the CT, CS, and SS samples, respectively. The intensity of quartz peak in SS revealed its predominance. The results of analysis showed the pyrite sulphur mineral phase present in the two coal samples and corresponded to same position 2θ peaks. The organic hump showed a relatively less intensity in the CS sample and much less in the CS sample which corresponded to quantity of amorphous material in the samples (Hutton *et al*., 1996).

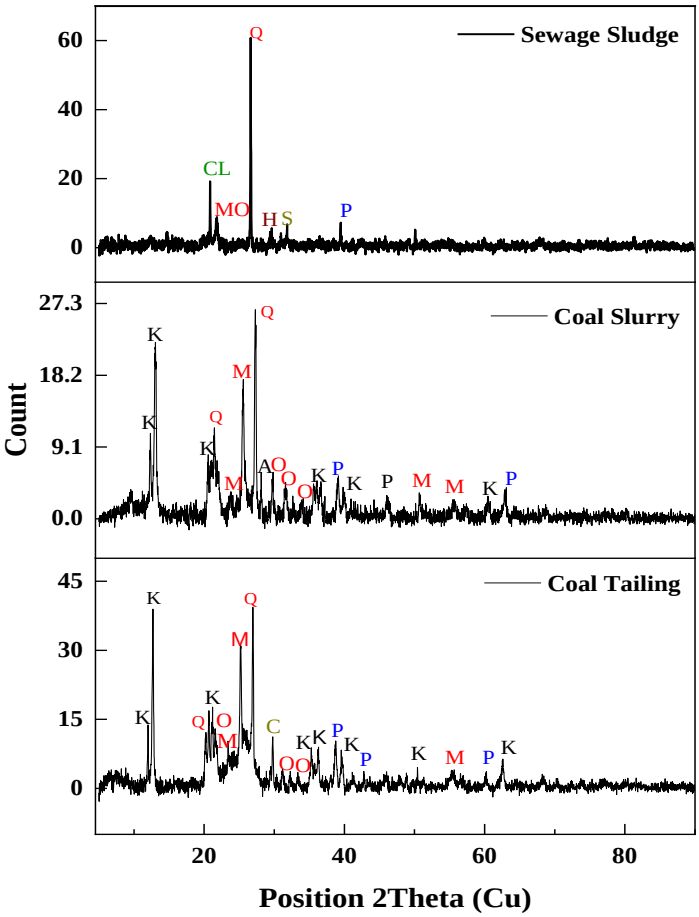

Figure 4-3:Raw samples XRD pattern.

Clay Mineral phases; K (Kaolinite); Silicate mineral; M (Muscovite), AN (Anorthite), Q (Quartz), MO (Moganite), O(Orthoclase) Oxide mineral; H (Hematite), Sulphur mineral; P (Pyrite), Carbonate mineral; S (Siderite), C (Calcite); Chlorite mineral; CL (Clinochlore).

The results of Fourier transform infrared analysis are presented in Figure 4-4. The spectrums of raw samples present functional groups absorption peaks at corresponding wavelength. The analysis of the spectrums in absorption band between 3650 and 3250 cm^{-1} revealed the peaks at 3620 cm^{-1} for both waste coal samples showing the presence of hydrogen bond. The peaks confirm the existence of hydroxyl compound because the two spectrums contain also peaks at wavelength of 1595.25,

1029.70, 1006.19, 750.58, 691.44 cm^{-1} and 1031.34, 1008.62,749.39 cm^{-1} for CT and CS sample respectively. The sharp intensity absorption in the absorption band range between 3670 and 3550 cm^{-1} show the presence of oxygen related group (alcohol or phenol). The absorption peaks observed at 1595.25 cm^{-1} wavelength revealed the presence of double bound carbonyl group combined with another double bound (aromatic stretch). The aromatic stretches groups reduce the intensity of carbonyl groups absorption band. The region comprised between the 1450 and 450cm^{-1} wavelength has been found to be specific for each coal sample and is the fingerprint region of the two coal samples. Multiple band absorption groups were observed at wavelength of 1029.7, 1006.19 and 911.92 cm^{-1} on the CT spectrum and 1031.34, 1008.62 and 913.12 cm^{-1} on the CS spectrum. Vinyl-related compound corresponded to the absorption peaks at 911.92 and 913.12 cm^{-1} coal spectrums. Orto-aromatic groups was reported at wavelength of 750.58 and 749.39 cm^{-1} on the CT and CS spectrums respectively. The intense absorption peaks at wavelength of 1006.19, 465.61 cm^{-1} on the CT and 1008.69, 467.25 cm^{-1} on the CS spectrums revealed the presence of silica asymmetric stretch (Si-O-Si). The intensity of the peaks showed that the concentration of silica compound is higher in the CT sample compared to CS and SS samples. This is consistent with the results from XRD and proximate analysis. The absorption peaks at wavelength of 691.44 cm^{-1} on the CT spectrum showed the presence of monosubstituted alkynes, alkenes groups (C-H), primary and secondary amine groups (NH_2, N-H). The absorption bands identified at 465.72 cm^{-1} wavelength in the SS sample revealed the presence mineral matter in the fingerprint region of the spectrum which was followed by an adsorption band at 1032.44 cm^{-1} showing the presence of amine, phosphate, sulfoxide, and halogenated groups. The carbonyl group with unsaturated bond has been identified at a wavelength of 1634.41 cm^{-1} on the sewage sludge

spectrum. The aliphatic group identified at wavenumber 2922.63 cm^{-1} on the sewage sludge spectrum revealed the presence of long linear chains.

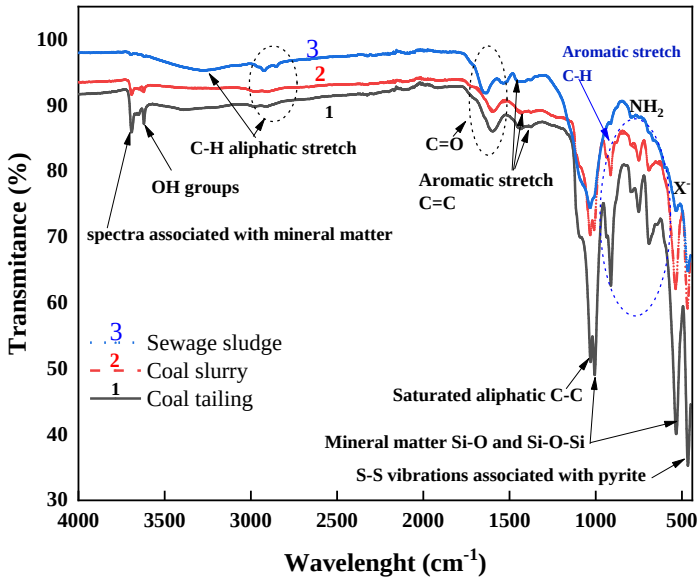

Figure 4-4:FTIR spectrum of raw samples

The results of XRF analysis are presented in Table 4-2 below. These results revealed the predominance of silicon (Si) and aluminum in the raw samples used. The highest percentages of silicon and aluminum have been found into the CT (17.021%Si and 7.14%Al) followed by the SS (11.43%Si and 5.94%Al) and CS (6.89% Si and 4.48%Al) respectively. The ferrous compounds were more indicated in the SS (5.97% Fe) compared to CT (3.31%Fe) and CS which contains a lowest percentage (1.21% Fe). Moreover, it has been observed that the CT contains high calcium (5.1% Ca) followed by SS (2.7 % Ca) and CS (1.72% Ca). Those are predominant mineral's elements present in the raw materials used. However, the analysis revealed that the samples of materials

used contained also traces of some other elements such as magnesium, sodium, titanium, phosphorus, chromium manganese and nickel as shown in Table 4-2.

Table 4-2. XRF results of raw materials

Element Composition	CT	CS	SS
SiO_2	36.42	14.76	24.46
Al_2O_3	13.50	8.48	11.23
CaO	7.14	2.41	3.79
Fe_2O_3	4.74	1.81	8.53
MgO	0.77	0.39	1.92
TiO_2	0.67	0.56	0.76
K_2O	0.52	0.23	1.03
P_2O_5	0.33	0.35	9.86
Na_2O	0.10	0.08	0.78
MnO	0.03	0.02	0.21
Cr_2O_3	0.00	0.00	0.13
NiO	0.00	0.00	0.04
LOI	35.22	70.21	39.78
Total	99.44	99.30	99.52

CT: Coal tailing. CS: Coal slurry. SS: Sewage sludge.

The XRF results confirmed the results of precedents analysis which revealed the high content of mineral (ash) in the CT followed by SS and CS respectively. Therefore, to reduce the percentage of mineral content in the raw material, the HTC process was used to dissolve a fraction of elements via hydrolysis for the increase of carbon content.

4.4.2. HTC process results

Table 4-3. Physicochemical analysis results of produced HC from Coal tailing (CT)

Run	Factors			Responses				
	A	B	C	R1	R2	R3	R4	R5
	Temperature (°C)	Pressure (bar)	Time (min)	A* (%)	FC* (%)	VM* (%)	Mass Yield (%)	Carbon Yield (%)
Raw sample	-	-	-	**40.32**	**37.31**	**22.37**	**100**	**100**
1	150	10	180	38.92	39.27	21.81	83.56	87.95
2	150	27	10	39.11	39.83	21.06	83.51	89.15
3	150	18.5	95	**38.36**	**40.37**	**21.27**	**82.67**	**89.44**
4	150	10	10	39	39.38	21.62	82.55	87.13
5	150	27	180	38.16	40	21.84	78.66	84.33
6	210	18.5	95	40.74	37.55	21.71	83.63	84.17
7	210	18.5	95	40.32	37.53	22.15	83.22	83.71
8	210	18.5	10	41.39	37.45	21.16	81.73	82.04
9	210	18.5	95	40.28	37.57	22.15	81.76	82.33
10	210	18.5	95	40.31	37.54	22.15	82.03	82.53
11	210	18.5	95	40.37	37.48	22.15	81.99	82.36
12	210	18.5	180	40.89	37.68	21.43	81.36	82.16
13	210	18.5	95	40.25	37.6	22.15	81.78	82.41
14	210	27	95	40.20	37.65	22.15	81.26	82.00
15	210	10	95	40.16	38.25	21.59	81.50	83.55
16	270	10	180	41.28	37.19	21.53	80.67	80.41
17	270	27	180	40.22	37.44	22.34	77.31	77.58
18	270	18.5	95	41.26	37.38	21.36	77.21	77.35
19	270	10	10	38.13	37.31	24.56	78.39	78.39
20	270	27	10	40.41	37.57	22.02	78.24	78.79

A: Ash content. FC: Fixed carbon. VM: Volatile matter. *: dried basis (moisture free). Solid/liquid ratio: ¼

Table 4-4. Physicochemical analysis results of produced HC from Coal slurry (CS)

Run	Factors			Responses				
	A	B	C	R1	R2	R3	R4	R5
	Temperature (°C)	Pressure (bar)	Time (min)	A* (%)	FC* (%)	VM* (%)	Mass Yield (%)	Carbon yield (%)
Raw sample	-	-	-	**24.17**	**53.02**	**22.69**	**100**	**100**
1	150	10	180	23.12	55.72	22.16	82.45	86.64
2	150	27	10	21.53	57.08	21.39	89.91	96.79
3	150	18.5	95	**20.12**	**57.69**	**22.19**	**86.74**	**94.38**
4	150	10	10	22.17	55.87	21.96	85.65	90.25
5	150	27	180	22.65	55.75	21.6	85.80	90.21
6	210	18.5	95	25.67	52.27	22.06	84.66	83.46
7	210	18.5	95	25.2	52.34	22.46	84.91	83.82
8	210	18.5	10	25.57	52.96	21.47	84.86	84.77
9	210	18.5	95	25.33	52.21	22.46	86.08	84.77
10	210	18.5	95	25.27	52.27	22.46	84.44	83.25
11	210	18.5	95	25.96	52.29	21.75	84.93	83.76
12	210	18.5	180	25.24	52.3	22.46	87.28	86.09
13	210	18.5	95	26.19	51.35	22.46	86.87	84.13
14	210	27	95	21.27	56.27	22.46	84.96	90.17
15	210	10	95	23.4	54.68	21.92	83.55	86.17
16	270	10	180	28.29	48.85	22.86	82.26	75.79
17	270	27	180	27.26	50.06	22.68	84.90	80.16
18	270	18.5	95	28.19	50.12	21.69	85.10	80.45
19	270	10	10	27.61	49.44	22.95	82.45	76.88
20	270	27	10	26.81	50.83	22.36	83.57	80.12

A: Ash content. FC: Fixed carbon. VM: Volatile matter. *: dried basis (moisture free). Solid/liquid ratio: ¼

Tables 4-3 and 4-4 show the FC, A, and VM of the HC synthesized from HTC of CT and CS with a solid/liquid ratio of 1/4. The results suggest that the reaction temperature, and pressure had the greatest impact on the HTC experimental procedure, which is consistent with other works (Hutton *et al*., 1996; Akhtar *et al*., 2012). However, raising the temperature from 150 to 270°C lowered the FC content of the synthesized HC i.e. after 10 minutes of reaction, the greatest FC grades (40.37% and 57.69%) were

achieved at 150°C with a matching pressure of 10 bar. Additionally, the SS and CD samples were mixed to produce an HC with high carbon content and porous structure. The goal was to assess the combination of these three forms of waste materials in a predetermined proportion to enhance the hydrochar synthesised. Though, some researchers have undertaken studies on the HTC of SS (Nakason *et al*., 2018; Heidari *et al*., 2019), none of them have documented systematically the physicochemical properties of the products resulting from the blending of SS and CD in the HTC process. Preliminary results in Table 4-5 indicate that using SS in combination with CD enhance the hydrochar synthesised as the FC content of the HCs synthesised increases. This may be due to the presence of acid functional groups in the SS sample as indicated in Figure 4-2. These acid functional groups i.e., phosphate, amine, and sulfoxide play an important role in the dissolving of mineral materials in coal samples during the HTC process. This is congruent with other findings that indicated that the presence of acid promotes HC synthesis during the HTC process by altering the proportionality of produced phases (Nizamuddin *et al*., 2017). As a result, the carbon content of the generated HC rises, which improves its physical properties while decreasing the atomic ratios of O/C and H/C (Mumme *et al*., 2015). Tables 4-5 show the influence of temperature, pressure, and residence time on the ash content, fixed carbon, and volatile matter of the hydrochar (HCs) synthesised in this study using coal discards (CD) and sewage sludge (SS).

Table 4-5. Physicochemical results of HC from mixture of CD and SS

Run	Mixture components		Factors			Responses				
	A: 0.5(CT+CS) (g)	B: SS (g)	C	D	E	R 1	R 2	R3	R4	R5
			Temperature (°C)	Pressure (bar)	Time (min)	A* (%)	FC* (%)	VM* (%)	Mass yield (%)	Carbon yield (%)
CT	-	-	-	-	-	**40.32**	**37.31**	**22.37**	-	
CS	-	-	-	-	-	**24.29**	**53.02**	**22.69**	-	
SS	-	-	-	-	-	**39.25**	**9.52**	**51.23**	-	
CB	-	-	-	-	-	**38.8**	**38.67**	**22.53**	100	100
1	12.24	12.76	150	10	135.78	33.31	39.21	27.48	66.39	67.31
2	12.32	12.68	150	20.54	360	31.13	44.93	23.94	66.66	77.45
3	24.37	0.63	150	10	10	27.73	48.99	23.28	67.77	85.85
4	24.37	0.63	150	27	360	33.32	45.63	21.05	71.83	84.75
5	0	25	150	16.29	10	41.59	13.12	45.28	54.40	18.46
6	12.47	12.53	150	27	10	29.68	43.54	26.78	68.85	77.52
7	12.24	12.76	150	10	135.78	31.46	43.43	25.11	67.56	75.87
8	0.63	24.37	150	10	360	40.91	17.43	41.66	51.56	23.24
9	25	0	150	27	10	28.11	50.09	21.80	73.06	94.63
10	0	25	150	27	229.05	46.97	12.18	40.84	53.31	16.79
11	0	25	150	18.22	220.08	42.54	17.48	39.98	54.43	24.60

12	25	0	152.4	17.65	198.56	27.28	50.86	21.86	71.59	94.15
13	12.28	12.72	183.6	14.505	264.93	28.53	48.32	23.15	59.56	74.43
14	25	0	194.4	10	360	29.29	46.96	23.75	70.38	85.47
15	12.36	12.64	203.4	26.74	200.35	30.76	47.03	22.21	59.26	72.08
16	12.35	12.65	203.4	26.74	200.35	27.81	48.38	23.81	57.47	71.90
17	12.54	12.46	204	17.65	20	30.52	44.12	25.36	56.41	64.36
18	0	25	204	19.35	354.61	59.47	8.98	31.55	71.10	16.51
19	12.54	12.46	204	17.65	20	31.03	43.22	25.74	59.35	66.34
20	0	25	204	10.34	162.68	58.72	8.59	32.69	52.08	11.57
21	2.50	22.50	206.4	19.69	159.1	44.21	30.29	25.50	48.96	38.35
22	20.22	4.78	208.10	22.28	360	**19.71**	**58.82**	**21.46**	**65.38**	**99.45**
23	25	0	216	17.65	30	29.06	47.73	23.22	72.76	89.80
24	25	0	216.6	26.745	198.56	26.72	51.59	21.69	71.34	95.18
25	25	0	222.6	15.95	198.56	26.51	51.77	21.71	67.80	90.77
26	0	25	224.4	27	10	52.14	14.02	33.85	48.26	17.50
27	12.92	12.08	225.6	10	360	31.65	46.84	21.51	53.40	64.69
28	0	25	267	19.435	162.68	30.39	48.17	21.45	38.26	47.66
29	12.25	12.75	267	17.65	198.56	32.20	46.94	20.86	50.01	60.70
30	12.25	12.75	267	17.65	198.56	31.13	46.49	22.38	48.72	58.57
31	12.25	12.75	267	17.65	198.56	33.75	45.12	21.13	49.41	57.65
32	1.12	23.88	270	10	360	62.17	20.02	17.81	33.90	17.55
33	12.68	12.32	270	27	360	32.44	44.51	23.05	47.90	55.14
34	12.69	12.31	270	10	10	29.27	45.27	25.47	46.73	54.71

35	0	25	270	10	10	51.13	14.23	34.64	36.57	13.46
36	12.37	12.63	270	27	10	34.17	41.19	24.64	49.38	52.59
37	25	0	270	10	135.78	29.03	49.24	21.73	69.35	88.30
38	25	0	270	27	10	29.72	47.82	22.46	72.16	89.23
39	25	0	270	20.625	360	35.87	42.37	21.75	71.16	77.97
40	0	25	270	27	360	30.29	48.06	21.65	33.75	41.94

*: dry basis (moisture free). HC: Hydrochar. SS: Sewage sludge. CT: coal tailing. CS: Coal Slurry Min: minutes. °C: degrees Celsius. A: Ash content. FC: Fixed carbon. VM: Volatile matter. Solid/liquid ratio: ¼

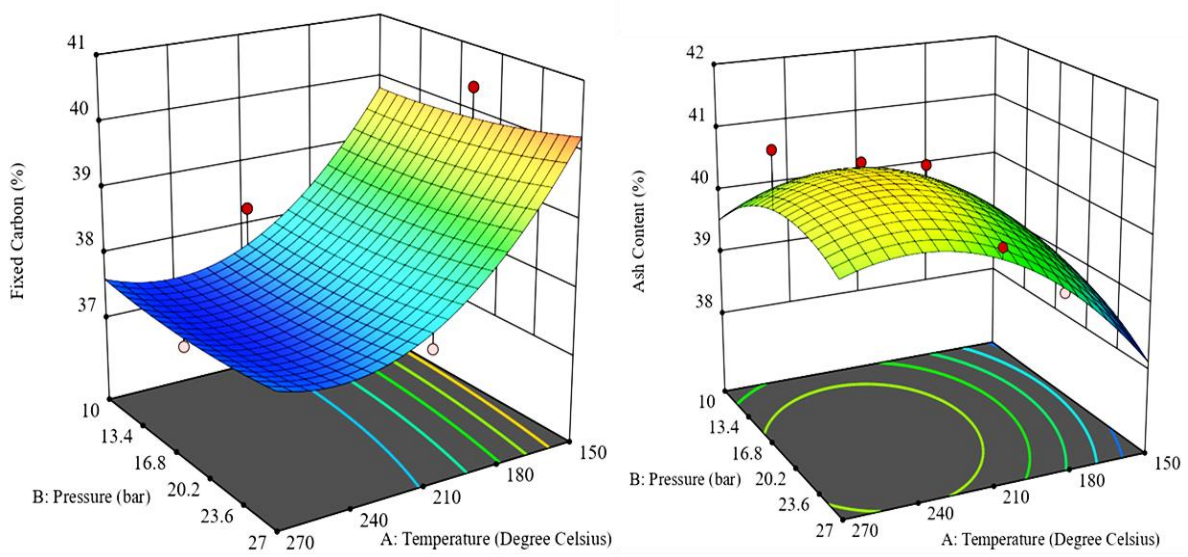

Figure 4-5:Surface plot showing the influence of temperature and pressure on fixed carbon (left) and Ash content (right) of Coal tailing's HC

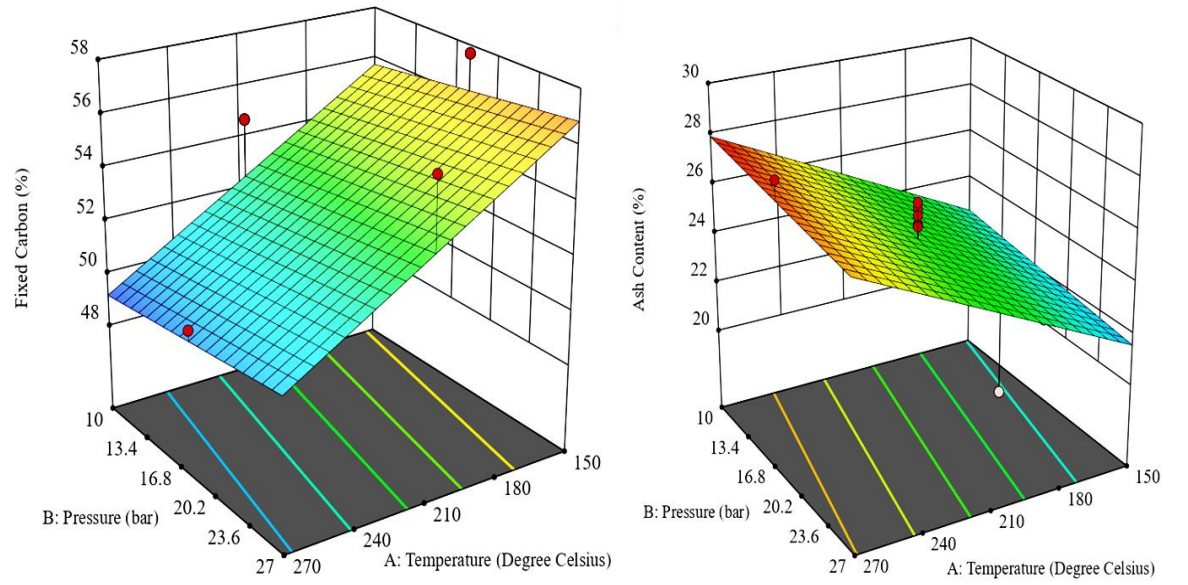

Figure 4-6:Surface plot showing the influence of temperature and pressure on fixed carbon (left) and Ash content (right) of Coal slurry's HC.

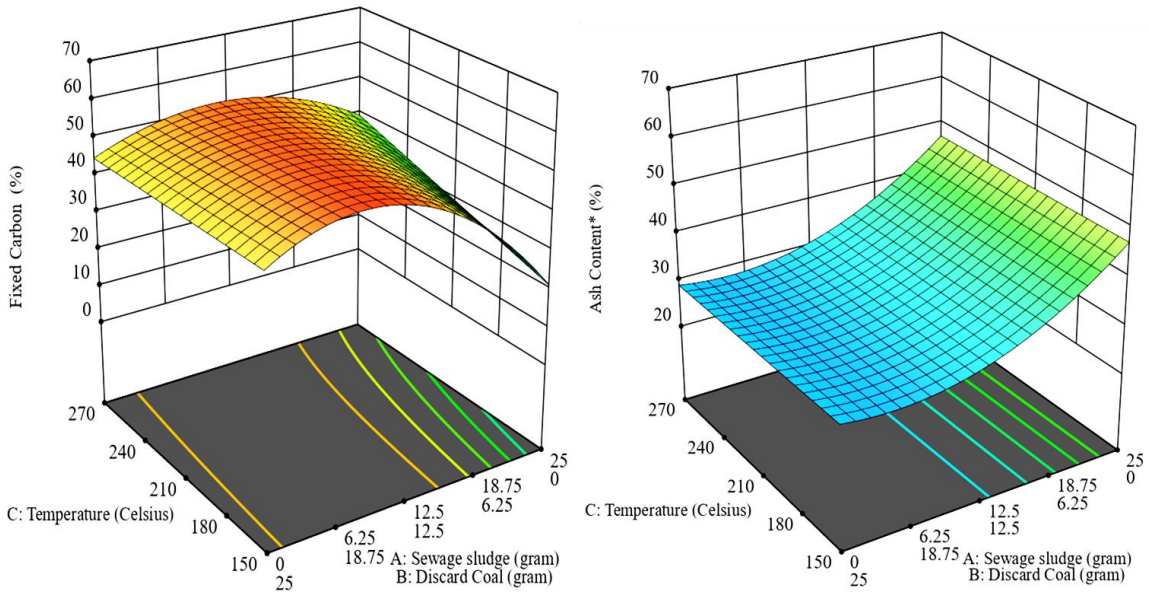

Figure 4-7:Surface plot showing the influence of temperature and pressure on fixed carbon (left) and Ash content (right) of the mixture of Sewage sludge and Coals

Optimal HTC parameters were found considering the physicochemical data of the HC produced i.e., the optimized HC should have the maximum fixed carbon content and the lowest ash content and volatile substances. Surface response approach was used to develop linear and quadratic models. The statistical parameters were evaluated using the analysis of variance (ANOVA) (Appendix A, B and C) on the HTC and Co-HTC experimental results obtained from proximate analysis presented in Tables 4-3, 4-4 and 4-5. The regression models (Equations 5-7) obtained for HTC and Co-HTC using RSM and CD were used to evaluate the influence of HTC and Co-HTC factors on the FC of the produced hydrochar (HCs). In addition, these regression models were tested using the probability (p-value) and Fischer test values (F-value) for the obtained responses. All models were found

statistically significant due to high F-value and lower p-value (Afolabi *et al*., 2020). The FC models for HCT and HCS were observed as a good fit, (R^2 =0.9517, R^2 =0.8430 respectively at p-value<0.0001) and are represented by equations (4-6) and (4-7) respectively. In addition, FC model of produced HCB was established as a good fit, (R^2 0.8434 at p-value < 0.0001) and is represented by equation (4-8).

$$HCT\ Fixed\ Carbon = 37.66 - 1.20A + 0.1090B + 0.0040C - 0.0837AB - 0.0388AC + 0.0337BC + 1.04A^2 + 0.113B^2 - 0.2714C^2 \quad (4\text{-}1)$$

$$HCS\ Fixed\ Carbon = 53.01 - 3.29A + 0.5520B - 0.3410C \quad (4\text{-}2)$$

$$HCB\ Fixed\ Carbon = 30.46A + 45.36B + 55.13AB + 9.11AC + 6.58AD + 13.69AE - 0.6847BC - 0.1279BD - 4.28BE - 15.83ABC - 10.52ABD + 14.57AB \quad (4\text{-}3)$$

The negative coefficient of the input variables indicates its antagonistic effect of on the FC value of the produced HC. The synergetic effect of the output responses was revealed by the positive coefficients within the equations (Behera *et al*., 2018). The effect of operating conditions on the FC of the produced hydrochar (HC) was illustrated by the 3D plot of the response surface (Figures 4-5, 4-6 and 4-7). The accuracy of the models was evaluated by the plot of experimental versus predicted values (Figures 4-8, 4-9). The normal distributions of the residuals are confirmed by the straight lines in the graphs in consistence with the study of Afolabi (2020) on the statistical analysis of the HTC process. The figures revealed a good fit confirmed by the clustered data points observed on the regression line showing the correlation between the actual and predicted values for the points of the design matrix. In addition, the figures reveal the accuracy of the designed models and demonstrated the reliability of the models for the determination of FC of the

produced hydrochars (HC) based on the variation of parameters used within the investigated ranges.

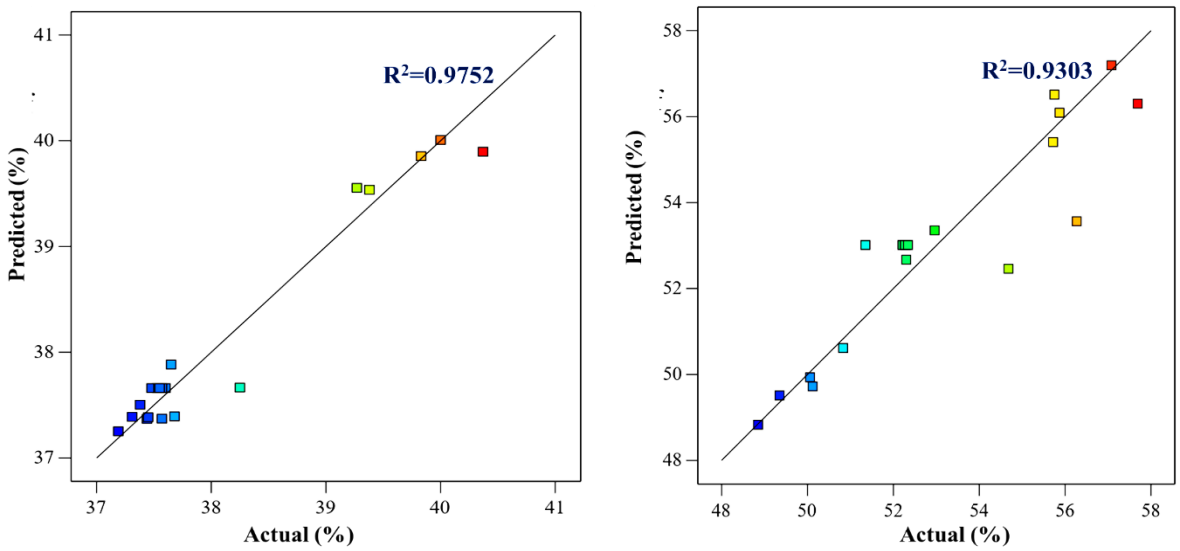

Figure 4-8:Predicted vs Actual plots of the Fixed Carbon of produced HCs from Coal tailing's HCT (left) and Coal slurry's HCS (right).

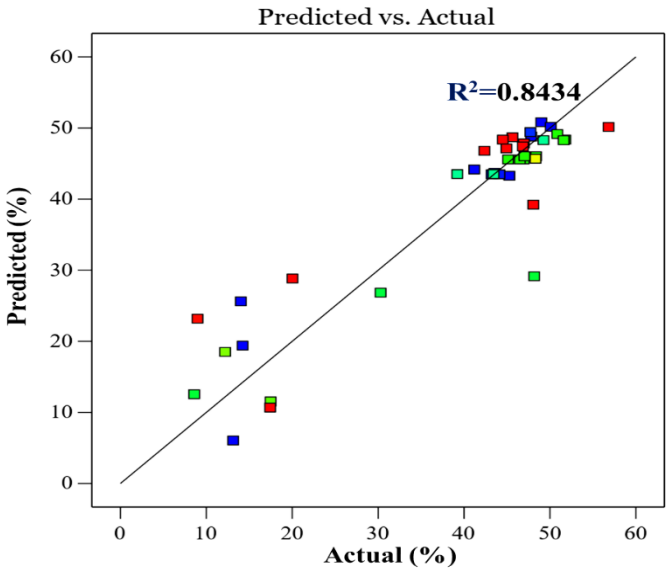

Figure 4-9:Predicted vs Actual plots of the Fixed Carbon of produced HCs from the mixture of coals (CT+CS) and sewage sludge (SS).

4.4.3. HTC and Co-HTC optimum operating conditions

The analysis and evaluation of obtained data were completed by the optimization of the input and responses factors (Table 4-6). The objective was to evaluate the input factors for the maximization of FC for the produced HCs. The input factors ranged from 150°C, 10bar and 10 minutes as lower limits to 270 °C and 27 bar, 180 minutes as upper limits of yielded optimization solutions for HTC process. On the other hand, the Co-HTC yielded optimization solutions were determined using input factors ranged from 150°C, 10 bar, 10 minutes and 0:25g (CT+CS: SS) as lower limits and 270°C, 27bar, 360 minutes and 25:0g (CT+CS: SS) as upper limits. Using the desirability function, the conditions that provided the maximum desirability factor was chosen as the optimum process parameters (Appendix E, F and G). The results presented in Tables 4-3, 4-4 and 4-5 show that 150°C, 27bar and 92.13 minutes were optimum HTC conditions, while 208°C, 22.5

bar, 331 minutes and 20.02:4.98(CT+CS: SS) were optimum conditions for the Co-HTC process. The error percentages found are presented in Table 4-7. and show that the optimized results were consistent compared to the experimental measurement.

Table 4-6. Hydrothermal carbonization models' confirmation results

Material	Responses	Predicted Mean	Predicted Median	Std Dev	SE Pred	95% PI low	95% PI high
HCT	Ash Content	38.13	38.13	0.53	0.70	36.56	39.69
	Fixed Carbon	40.19	40.19	0.31	0.40	39.29	41.10
	Volatile matter	21.44	21.44	0.56	0.65	20.02	22.86
	Mass Yield	96.18	96.18	1.13	1.48	92.87	99.49
HCS	Ash Content	21.12	21.12	1.27	1.47	17.99	24.25
	Fixed Carbon	57.19	57.19	1.14	1.32	54.37	60.01
	Volatile matter	21.47	21.47	0.35	0.46	20.46	22.48
	Mass Yield	96.05	96.05	1.50	1.74	92.35	99.76
HCB	Ash Content	17.42	17.42	0.64	0.58	32.61	15.45
	Fixed Carbon	58.88	58.88	1.69	1.67	20.38	59.88
	Volatile matter	23.69	23.69	1.82	2.06	11.64	25.68
	Mass Yield	84.67	84.67	1.21	1.37	73.83	88.97

Two-sided Confidence = 95%. Std.Dev: Standard deviation. SE: Standard error. HCT: Hydrochar coal tailing. HCS: Hydrochar coal slurry. PI: Probability interval

The comparison of the conditions used in this work with the HTC and Co-HTC operating conditions of different feedstock utilized in previous show that the Co-HTC process has a significant carbonization potential to produce HCB comparable to HCB obtained from other feedstocks reported in literature (Mumme *et al*., 2015; Saba *et al*., 2017; Tasca *et al*., 2019). Furthermore, the conditions

selected in this study could reduce the energy need and the cost of the process from the development and economic feasibility perspectives compared to reported operations conditions used for other thermal process such as pyrolysis and gasification (Afolabi *et al*., 2020).

Table 4-7. Hydrothermal carbonization and Co-Hydrothermal carbonization optimum operating conditions.

Name	HCT	HCS	HCB	POAE
Parameters				
Temperature (°C)	150	150	208.70	0-0.33
Pressure (bar)	27	27	22.55	0-0.22-
Time (Min)	92.13	10	331.02	0.35-7.4
CT+CS: SS	-	-	20.02:4.98	1.96
Results (%)				
Ash content	38.13	21.12	17.43	0.07–1.09
Fixed Carbon	40.20	57.19	58.88	0.5–1.21
Volatile Matter	21.67	21.69	23.69	1.08–0.37
Mass yield	96.18	96.05	84.67	1.35-2.00

HCT: Coal tailing's hydrochar. HCS: Coal slurry's hydrochar. HCB: hydrochar from the Co-HTC of coal and sewage sludge. SS: Sewage sludge. POE: Percentage of absolute error

Post analyses were performed to assess the accuracy of the model using optimum parameters as confirmation points (Appendix D). Post experiment results with fixed carbon (FC) of 40.19%, 57.19% and 58.88% content for HCT, HCS and HCB respectively were used to validate the regression models. The predicted means were compared to the medians using the regression models and the standard deviations and standard errors obtained were in acceptable range (<2%). This further confirms that the models developed were valid and could be used to predict the FC of the produced hydrochar (Teimouri *et al*., 2020).

4.4.4. Characterization of the synthesised hydrochar

The proximate analysis results of raw materials and produced hydrochar (HC) from hydrothermal carbonization (HTC) and Co-hydrothermal carbonization (Co-HTC) at optimum conditions are presented in Tables 4-8. The results show that the FC content of the raw samples increased through HTC and Co-HTC process as presented in Table 4-8. The HTC and Co-HTC process present an opportunity to upgrade the FC content of raw materials through the release of mineral matter, oxygen, and sulphur content from their molecular structures (Aliakbari *et al*., 2018). The HTC and Co-HTC optimum conditions maintained the water at a liquid state and favoured the hydrolysis of aliphatic components, dissolution of minerals matter and prevent the escaping of the carboxylate's gas. The change in FC of coals-sewage sludge blend (CB) after Co-HTC process was greater compared to the hydrothermal carbonization (HTC) of coal tailing (CT) and coal slurry (CS) individually as shown in Table 4-8. This may be due to the increase of acidic conditions produced from the decomposition of cellulose, chlorine, and hemicellulose constituents of the sewage sludge into organic acid monomers during decarboxylation and dehydration reactions of Co-HTC process (Jin *et al*., 2014). Consequently, the lower pH of Co-HTC process liquid increases the sulphur removal (formation of sulphite and sulphate) and allows the inorganic elements to be released into the liquid phase (Hoekman *et al*., 2011; Saba *et al*., 2017). This eventually led to a reduction of the ash content present in the feedstock and increases the FC of the produced hydrochar. However, the increase of temperature above the 150°C and 208°C for HTC and Co-HTC respectively (Tables 4-3, 4-4 and 4-5) proportionally increases the ash content of the produced HC due to the condensation of components dissolved in the solid hydrochar and liquefaction of carbon from the feedstock (Mursito *et al*.,

2010). The results presented in Table 4-5 show that Co-HTC products had significantly lower ash content than the feedstock used, produced HCT and HCS respectively. The higher decrease in mass yield observed from the HCB compared to the HCT and HCS can be attributed to the increased decomposition of the blend feedstock occurring under Co-HTC conditions (Pińkowska *et al*., 2011). The further increase in temperature severity of the HTC and Co-HTC (respectively above 150°C and 208°C) operating conditions leads to a higher degree of thermolytic decomposition, fragmentation, and solubilisation of macromolecules (coals, biomass, etc.) resulting in decreasing mass yield (Sahu *et al*., 2010). The high CD: SS mass ratio maintained higher mass yield of the produced hydrochar from Co-HTC process possibly due to the hydrothermal stability of the coal compared to the SS (Saba *et al*., 2017). However, excess of coal leads to agglomeration and stability of mineral matter content in the reaction medium and reduces the formation of acidic mild condition which negatively affects the carbonization yield by decreasing the FC content of the produced HCB (Table 4-5).

The HTC and Co-HTC operating conditions considerably modified the elemental compositions of the HCT, HCS and HCB produced from CT, CS and CB respectively (Table 4-8). At optimum conditions, much of the atomic carbon content from the feedstock appear to remain retained in the solid HC produced showing the potential of sequestration and repolymerization of HTC and Co-HTC process (Lu *et al*., 2013). The increase in total carbon content in the produced HC corresponds to the decrease in the hydrogen, oxygen, and total sulphur content (Table 4-8). The decrease of sulphur content in the produced hydrochar, possibly also contributes to the liberalization of pores and improve the textural structure as demonstrated in previous studies (Channiwala *et al*., 2022; Afolabi *et al*., 2020). The carbon

densification factors for the HCT, HCS and HCB, were higher than 1 in all cases and were consistent with the values reported in previous studies on HTC and Co-HTC process and showed the evidence of carbonization (Saba *et al*., 2017). HTC and Co-HTC carbonization yields (Cy) were determined to evaluate the degree of carbonization. The results obtained show that carbonization yields (Cy) of 96.13%, 93.82% and 96.03% for HCT, HCS and HCB respectively which were consistent with previous results on HTC of sub-bituminous coal and Co-HTC of coal and biomass (Saba *et al*., 2017). The results also show that nitrogen increased slightly possibly due to the stagnation of nitrogen under HTC and Co-HTC operating conditions, and the utilization of nitrogen gas inlet to maintain the inert medium. The sulphur content of the HCB (0.39%) was lower compared to the sulphur content of the feedstocks, HTC and HCS respectively, demonstrating the efficiency of Co-HTC process for synergetic sulphur content reduction in coals and biomass. The elemental composition changes implied the structural changes of the produced HCT, HCS and HCB (Kang *et al*., 2012).

Table 4-8.Physicochemical properties of produced hydrochar

Analysis	Standards used	CT	HCT	CS	HCS	SS	CB	HCB
Proximate Analysis (wt%, adb)								
Moisture	ASTDM 5142	4.17	1.07	3.94	1.73	8.12	2.71	1.72
Ash	ASTDM 5142	38.64	37.96	23.22	22.78	36.07	37.75	19.56
Volatile Matter	ASTDM 5142	21.44	21.04	21.28	18.38	47.07	21.92	20.31
Fixed Carbon	ASTDM 5142	35.75	39.94	50.98	57.11	8.75	37.62	58.41
Ultimate Analysis (wt. %, adb)								
Carbon	ISO 12, 902	42.82	49.8	61.85	66.9	29.7	45.64	67.04
Hydrogen	ISO 12, 902	3.01	2.87	3.56	2.98	4.88	3.05	2.78
Nitrogen	ISO 12, 902	1.14	1.72	1.39	1.99	4.15	1.82	2.43
Oxygen	By difference	8.79	5.83	4.78	2.75	15.22	8.2	6.08
Total Sulfur (wt. %, adb)	ISO 19579 : 2006	1.43	0.75	1.26	0.87	1.86	0.83	0.39
Mass yield (%)			82.66		86.74			65.38
Calorific values (MJ/kg)		16.59	19.33	24.4	25.79	13.2	17.68	24.31

CT: Coal Tailing. CS: Coal Slurry HCT: Hydrochar coal tailing. HCS: Hydrochar coal slurry. SS: Sewage Sludge. CB: Blend CT+CS+SS. HCB: Hydrochar from the Blend CT+CS+SS. Solid/liquid ratio: ¼. adb: air dried basis. Oxygen%=100-(Moiture+Ash+Total Carbon+Hydrogen+Nitrogen+Sulphur)
Carbon+Hydrogen+Nitrogen+Sulphur)

The atomic ratios of H/C and O/C were determined from elemental compositions (Table 4-8) and evaluated using the plot of Van Krevelen diagram, as shown in Figure 4-10. The atomic ratios plots show that the raw materials shifted from up to down and from the right to the left, demonstrating the progression of carbonisation process and the effects of HTC and Co-HTC operating conditions on the carbonisation degree. The observation of the Figure 8 implies that the HTC and Co-HTC processes may be driven by a succession of dehydration, and decarboxylation reactions causing the decrease of H/C and O/C atomic ratios

respectively. The material representative point closer to the origin indicates a higher carbon content. The CT and CS were found close to the origin compared to the SS, as coal discards have higher carbon content. The produced hydrochar points are lower and further toward the left showing the decrease of hydrogen and oxygen content. Figure 4-10 further shows that the feedstock possibly undergoes dehydration as primary reaction followed by decarboxylation during HTC and Co-HTC process. The carbon content of the CB increases by 30.65%, while hydrogen and oxygen decrease by 8.85% and 25.85% respectively. This may be attributed to the loss of hydroxyl groups as shown in Figure 4-4 possibly supporting the evidence that the dehydration reaction trend for HTC and Co-HTC ending with condensation of carboxylates created during decarboxylation reaction to produce a hydrophobic restructured carbonaceous material as shown in Figure 4-10 (Saba *et al*., 2017).

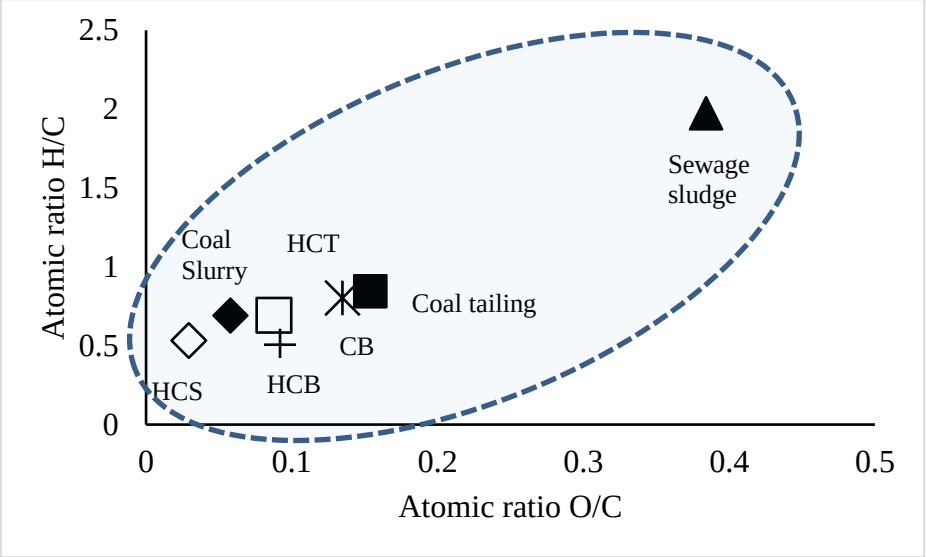

Figure 4-10:Van-Krevelen diagram for untreated, HTC, and Co-HTC hydrochar

Figure 4-11 presents the overall experimental mass balance of HTC and Co-HTC for this work. These results show that after thermochemical decomposition of CT, CS and CB, the major carbon content of the feedstock ends in the restructured and condensed HCs (aromatic polymer). This is consistent with previous studies that described the overall HTC products as primarily consisting of acetic acid, methanol, carbon dioxide, and a solid hydrochar (Saba *et al*., 2017), and that the overall thermal decomposition during HTC could be represented by the reaction (4-9), where the chemical composition of the HTC solid products is estimated in terms of C, H, and O deduced from elemental compositions, as shown in Table 4-8.

$$C_xH_yO_z + H_2O \rightarrow C_mH_nO + CH_3COOH + CH_3OH + CO_2 \quad (4\text{-}9)$$

In this reaction, the solid HC is noted C_mH_nO, the liquid phase was assumed to be composed by CH_3COOH and CH_3OH produced after the hydrolysis, decarboxylation and demethanation when methane and carboxylates ions reacted in aqueous phase (Pińkowska *et al*., 2011; Lu *et al*., 2013; Saba *et al*., 2017).

The overall theoretical HTC mass balance represented by the combined reactions 4-10 to 4-12:

$$2.16C_7H_6O + 2.16H_2O \rightarrow C_{12}H_8O + 0.66C_2H_4O_2 + 1.66CH_3OH + 0.16CO_2 \quad (4\text{-}10)$$

$$2.1C_{18}H_{12}O + 3.8H_2O \rightarrow C_{33}H_{18}O + C_2H_4O_2 + 2.7CH_3OH + 0.1CO_2 \quad (4\text{-}11)$$

$$2.6C_8H_6O + 4.8H_2O \rightarrow C_{15}H_{14}O + 2.4C_2H_4O_2 + 0.4CH_3OH + 0.6CO_2 \quad (4\text{-}12)$$

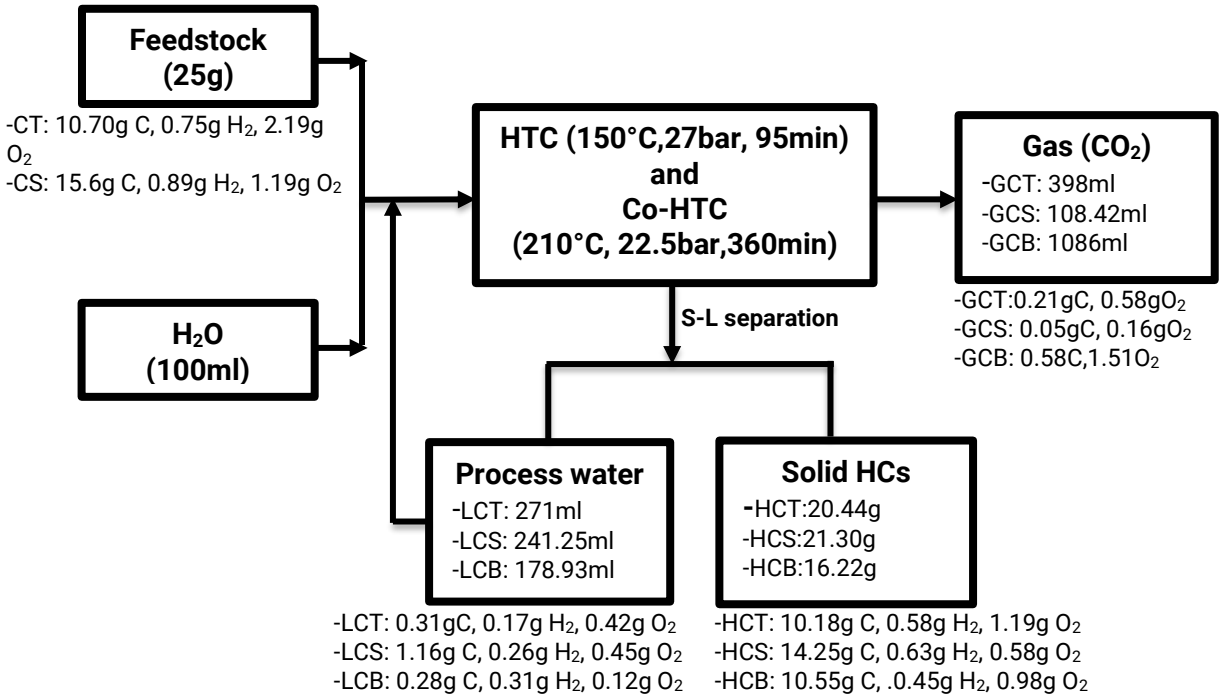

Figure 4-11:HTC, and Co-HTC process mass balance

The diffractogram presented in Figure 4-12 (A) shows XRD results of the CT, CS, SS and produced HCs samples which show that CT and CS have broad peaks corresponding to coal patterns rich in amorphous phases while the SS presented a predominant crystal lattice (Yin *et al*., 2018). The amorphous hump observed on the XRD pattern of CS reveals its high content in organic matter compared to CT (Yin *et al*., 2018). The mineral phases identified and labelled accordingly on the diffraction patterns presented on Figure 4-12 (A) are; Clays: K(Kaolinite); Silicates: M(Muscovite), A(Anorthite), Q(Quartz), MO (Moganite), O(Orthoclase)); Carbonates: S(Siderite), C(Calcite); Oxide: H(Hematite); Sulphurs: P(Pyrite), and Chlorite: CL(Clinochlore). The mineral phase identification indicate that silicates ($[SiO_{(4-x)}]n$)

and aluminosilicates ($KAl_2(AlSi_3O_{10})(OH)_2$) (clay) minerals are present in significant proportion in the CT and CS while the predominant mineral phases in the SS are quartz (SiO_2) and clinochlore (($(Mg, Fe^{(2+)})5Al_2Si_3O_{10}(OH)_8$), showing the trigonal, hexagonal, triclinic and monoclinique, crystal systems of the three materials respectively (Jeffery *et al*., 1952). The diffraction patterns of the mixtures of the three materials CB revealed an interaction between minerals phases resulting in change of structure (orthorhombic) and peaks intensity (Neto et al., 2022). The decrease of peaks intensities of mineral phases observed in the diffraction patterns of the produced hydrochar followed the HTC and Co-HTC operating conditions effect on the possible the dissolution of mineral content of the feedstock. Figure 4-12 (A) also indicate a significant decrease of mineral phases peak's intensities for Co-HTC process which may be due to the decomposition of SS into organic acid monomers during decarboxylation and dehydration reactions as also shown in Figure 8. The organic humps become intense and broader around 20◦ 2θ in the HCB diffractogram (Figure 4-12 (A)). Previous works attributed these formations of hump on XRD diffractogram to the progressive transformation of crystalline structure into amorphous structure. That has been corroborated in previous studies which showed that the condensation and polymerisation of carboxyl and carbonyl groups produced from decarboxylation during HTC and Co-HTC forms an amorphous hydrophobic aromatic polymer (Kruse *et al*., 2013; Knappe *et al*., 2019). These may explain the observed residual intense peaks on the HCT and HCS from the CT and CS respectively, showing higher degree of crystallinity compared to HCB.

The FTIR spectra (Figure 4-12 (B)) were used to describe the chemical structural properties of the raw materials and produced hydrochar. The peaks at 3620 cm^{-1} band were attributed to O-H stretching vibration linked with kaolinite mineral phase

presented on the XRD patterns in the form of silanol (Si-OH). The Si-OH groups are instable due to the polarization in aqueous medium (anionic charge) during HTC and Co-HTC process. Hence, water is eliminated and weakens the Si-O back bonds to generate -Si-H and new Si-OH bonds as seen on Figure 4-12 (B) (Jal *et al*., 2004). The lower intensity of the O-H observed on the spectrum band of the produced hydrochar compared to untreated coals demonstrated the evidence of dehydration reactions during HTC and Co-HTC process resulting in the release of hydroxyl groups in liquid phase which form water (Equation 1 and 2) and as also suggested by the van krevelen plot (Figure 4-10). The intense peak at 2922.63 cm^{-1} band was due to higher presence of aliphatic group in the SS characterized by long linear chains $-CH_2$ and $-CH_3$ asymmetric and symmetric vibrations(alkanes) respectively (Mishra *et al*., 2018). The shoulder peaks at 2960 cm^{-1} band observed on the HCT and HCB spectra were assigned to asymmetric aliphatic $-CH_3$ stretching vibration (Hattingh *et al*., 2013). The increase of peaks intensity of the C-H aliphatic stretch observed at 2850 cm^{-1} and 2920 cm^{-1} from CT and CS spectrums may be due to the interaction between C-H alkyl groups (Mumme *et al*., 2015; Mishra *et al*., 2018). The peak observed at 1700cm^{-1} band was attributed to the aliphatic C=O and -COOH stretching vibrations of carboxyl and carbonyls, mainly ketones, aldehydes, and esters in the SS (Mishra *et al*., 2018). At 1600cm^{-1} bands, corresponding to the aromatic C = C structure, HCS possesses the strongest peak intensity followed by HCB, CS, CB, HCT, CT and SS. It has been argued that a strong transmittance peak at 1600cm^{-1} wavelength indicates a high carbon content present in the material analysed validating the presence of lignin (Balachandran *et al*., 2014). This explanation is consistent with the distribution of total carbon content obtained from ultimate analysis of materials presented in Table 4-8. The peaks observed at

1595.25 cm^{-1} wavelength indicated the presence of double bound carbonyl groups (C=O) combined with aromatic stretch confirming the presence of cellulose (Achinas *et al*., 2017). The intensity of C=O peaks of the produced hydrochar was clearly weak compared to the feedstock. This is possibly an indication of the decarboxylation reaction occurring during HTC and Co-HTC process as described by reaction 3. The peaks at 1391 and 1240cm^{-1} band were identified in the CT, CS and CB but not in the SS. These peaks were attributed to the symmetric deformation associated with the $-CH_3$ groups and phenol (Painter *et al*., 2012). The peaks observed at 1250 cm^{-1} revealed the saturated aliphatic skeletal C-C vibrations (Painter *et al*., 2012; Okolo *et al*., 2015). The transmittance peak within the fingerprint region of the spectrum at 1030 and 570 cm-1 band in all spectra with decreasing intensity from CT, SS, CS, CB, HCS, HCT to HCB were assigned to the vibrations associated with Si-O-Si in quartz and kaolinite (Hatting *et al*., 2013). Multiple peaks observed between 900 and 800 cm^{-1} not appearing in the SS were assigned to aromatic species in aromatic rings; trans- and cis-CH_2 in long saturated aromatic -CH-CH chains, C-O stretching vibration of ether groups; O-H bending vibrations in phenolic, phenoxy and hydroxybenzene structures and were mostly observed with strong intensity in the feedstock compared to produced hydrochar. This may be due to the condensation and polymerization reactions occurring in HTC and Co-HTC processes resulting in elimination of the oxygen and hydrogen into water in liquid phases and restructuration of the carbon skeleton (Tan *et al*., 2019). This is also supported by elemental analyses (Table 4-8) which show the decrease of oxygen content from the feedstock to the produced hydrochar with HCB is the most oxidized product obtained due to the decomposition of cellulose (Balachandran *et al*., 2014; Achinas *et al*., 2017). The peaks at 866cm^{-1}, 805cm^{-1}, and

745cm^{-1} bands revealed the presence of aromatic nucleus -CH bending vibrations in the coals, the CB, and the HCB (Painter *et al*., 2012; Mishra *et al*., 2018). Hence, HTC and Co-HTC can be characterized as thermochemical process driven by dehydration (4-13 and 4-14), decarboxylation (4-15), and demethanation (4-16 and 4-17) (Wang *et al*., 2019).

$$2\ R{-}OH \rightarrow R{-}O{-}R + H_2O \quad (4\text{-}13)$$

$$2\ R\text{-}CH_2\text{-}O\text{-}CH_2\text{-}R \rightarrow R\text{-}CH{=}CH\text{-}R + H_2O \quad (4\text{-}14)$$

$$RCOOH \rightarrow RH + CO_2 \quad (4\text{-}15)$$

$$2\ R\text{-}CH_3 \rightarrow R\text{-}CH_2\text{-}R + CH_4 \quad (4\text{-}16)$$

$$R\text{-}CH_2\text{-}CH_2\text{-}CH_2\text{-}R \rightarrow R\text{-}CH{=}CH\text{-}R + CH_4 \quad (4\text{-}17)$$

Where R represents the remainder of a cellulose or lignin molecule to which the reacting groups are attached.

Additionally, the surface structural arrangement of feedstocks and produced HC were investigated by scanning electron microscopy (SEM). Figures 4-13 to 4-15 reveal that the physicochemical properties of the feedstock were vastly impacted by HTC and Co-HTC optimum conditions. The element spectrums of the produced HC displayed the predominance of carbon confirmed by higher peaks. The reduction (Si, O and Fe) and disappearance (Al, Mg and Na) of peaks on the spectrums from the feedstocks to the produced HC were proportional to the decrease of elemental mineral composing the ash content under HTC and Co-HTC conditions (Li *et al*., 2016). This correlates with the proximate and elemental analyses. The SEM image of CB (Figure 4-15 a) shows aggregating particles identified as SS on the coal surface, which is supported by the presence of carbon, oxygen, silica, and aluminium peaks on the element spectrum of the selected region.

Thus, coal served as a reaction site for sewage sludge particles, which interacted and favoured complete mixing of the feedstock during Co-HTC, resulting in surface homogenisation of the produced hydrochar (Figure 4-15c). Furthermore, the SEM images of the feedstock and produced hydrochar revealed a hydrothermal-induced rearrangement from rough and irregular morphology in the raw materials (Figures 4-13a, 4-4a,4-15a) to well distributed porous morphology in the produced hydrochar (Figures 4-13c, 4-14c, 4-15c). Images of the produced hydrochar indicated spotting features and the formation of microstructural pores. These properties provided potential absorbent properties for the hydrochar produced (Lu *et al*., 2014). The thermolytic effect of HTC and Co-HTC temperature increase on the feedstock generates pores in the material structure through the release of hydrogen, oxygen, sulphur, and the degree of mineral content dissolution. This is in accordance with other results that demonstrated that the process severity conditions affect the thermolytic decomposition, devolatilization reaction characteristics, and porous structure formation of HTC and Co-HTC (Shui *et al*., 2012; Sabe *et al*., 2017). Hydrochar has smoother and more homogeneous surface morphologies than feedstock. The pores size uniformity on the surface images of produced hydrochar show a difference in the degree of mineral dissolution for HTC (Figures 4-13a, 4-14a) and Co-HTC (Figure 4-15a) caused by an increase in acidic mild conditions (Shui *et al*., 2012; Sabe *et al*., 2017). The surface morphology of the produced hydrochar obtained from SEM favoured the evaluation of microstructural changes of the coals and the mixture coal-sewage sludge after HTC (Figures 4-13a,4-14a) and Co-HTC (Figure 4-15a) process respectively.

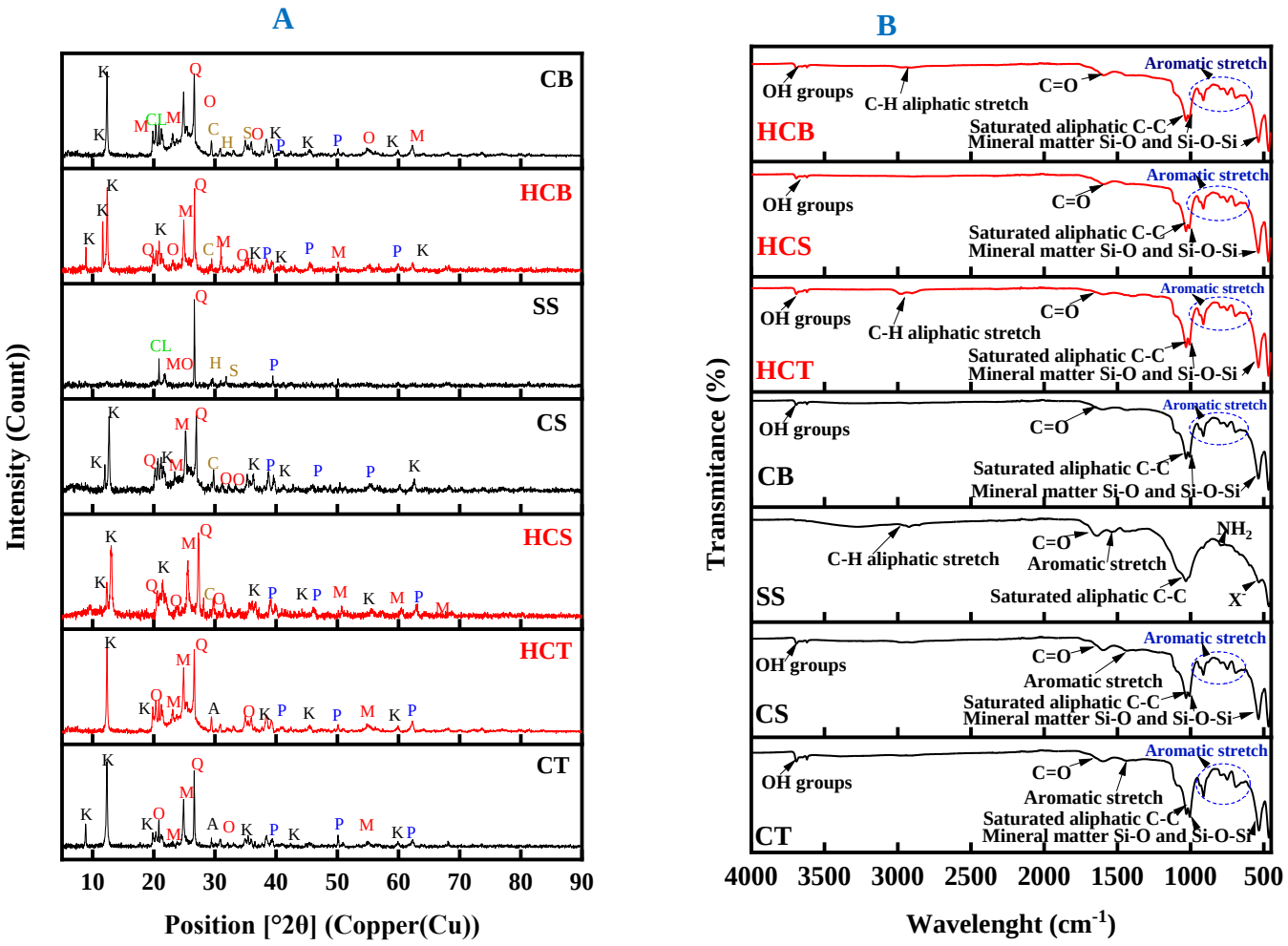

Figure 4-12:XRD patterns of coal, sewage sludge and produced hydrochar (A) and FTIR spectra of coals, sewage sludge and produced hydrochar (B)

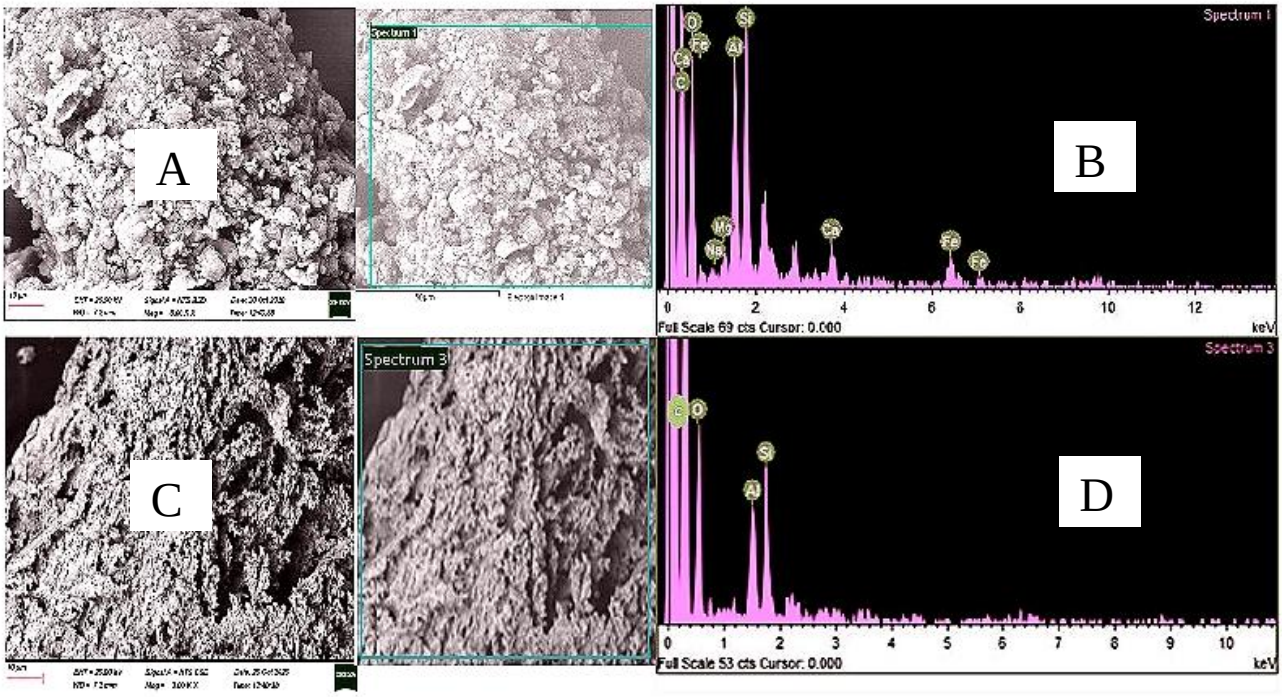

Figure 4-13:SEM images (a, c) and EDX elemental spectrums (b, d) of coal tailing (up), and coal tailing's hydrochar (down).

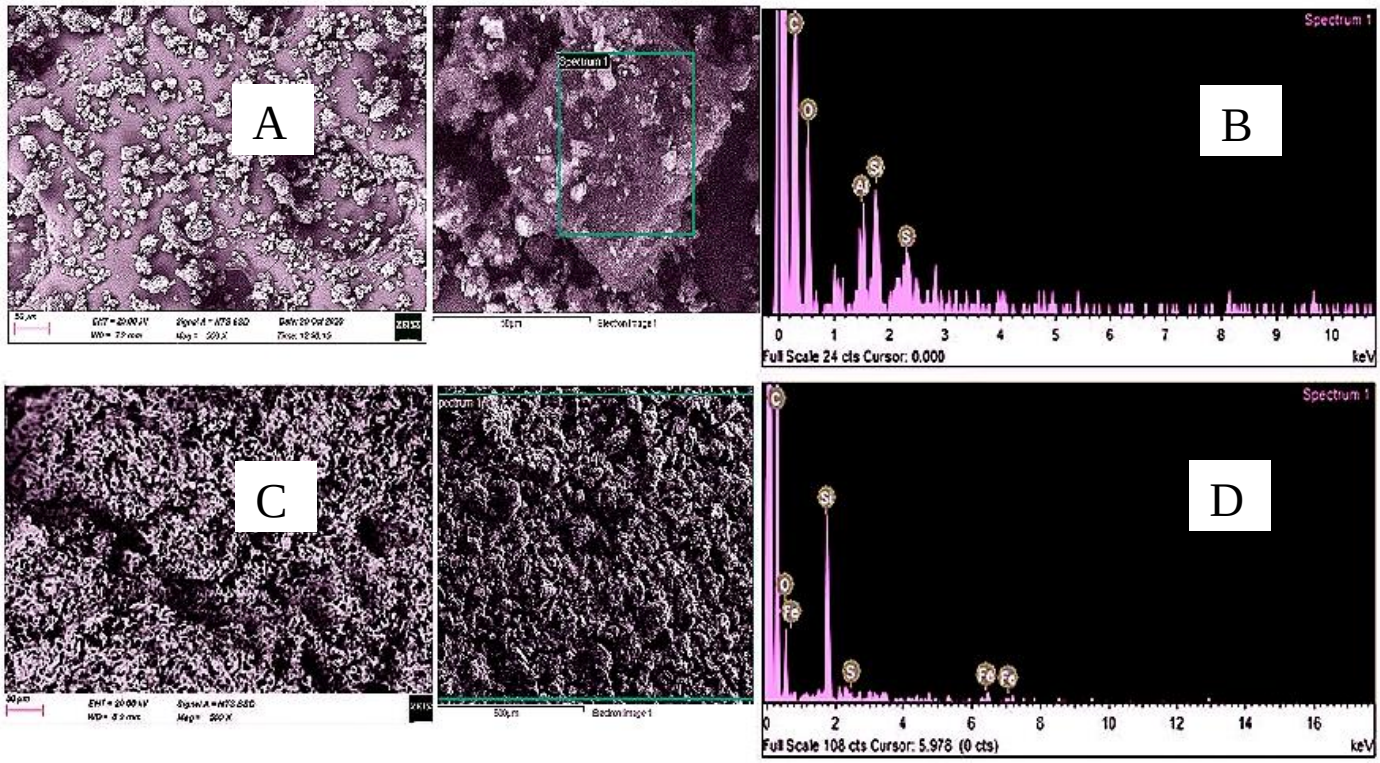

Figure 4-14:SEM images (a, c) and EDX elemental spectrums (b, d) of coal slurry (up), and coal slurry's hydrochar (down).

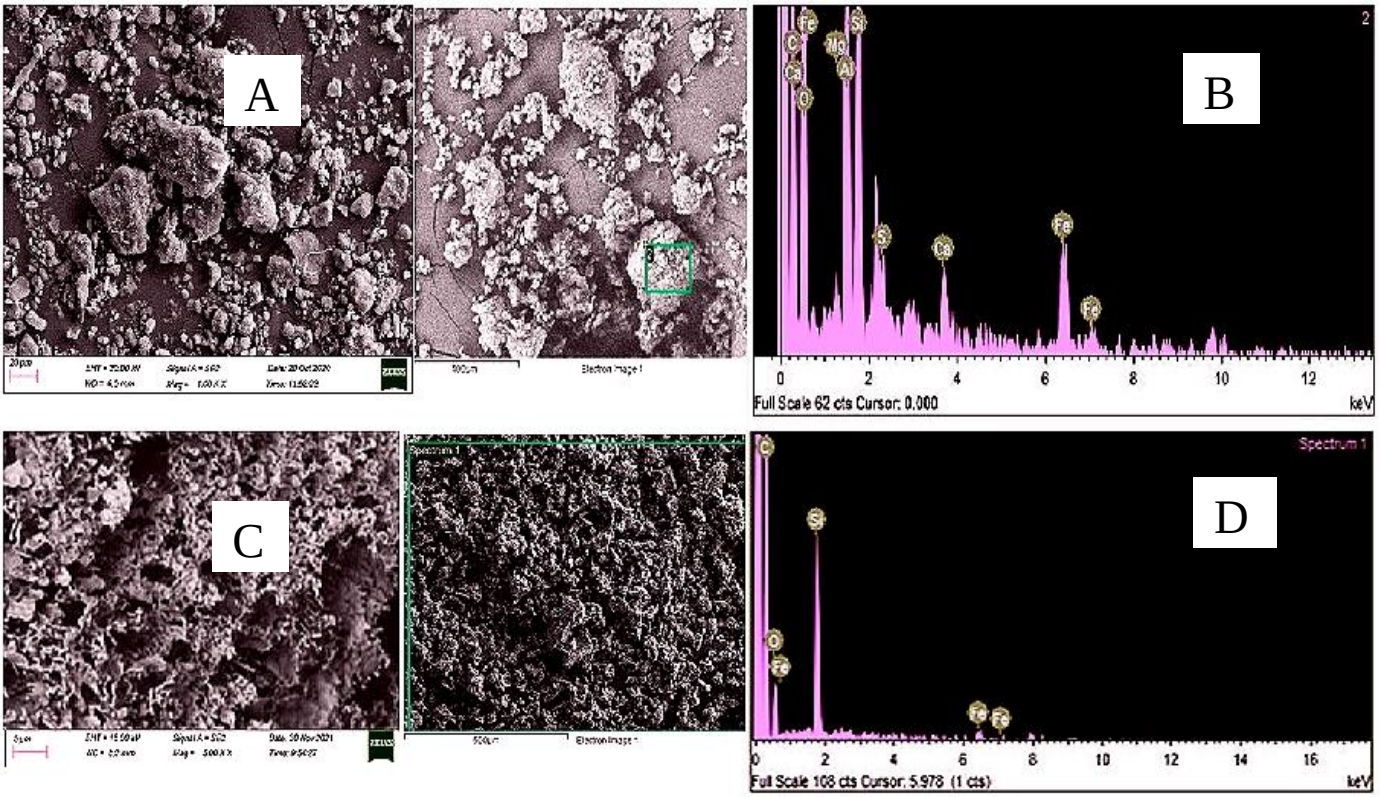

Figure 4-15:SEM images (a, c) and EDX elemental spectrums (b, d) of the mixture of coals and sewage sludge blended in optimized ratio (1CT+1CS:0.4SS) (up), and the Co-HTC produced hydrochar (HCB) (down).

The isotherms of nitrogen adsorption of the feedstocks and produced hydrochar are presented in Figure 4-16 and were categorized as type III isotherms according to IUPAC isotherm plots classification (lateral interactions between adsorbed molecules are strong in comparison to interactions between the adsorbent surface and adsorbate) (Thommes *et al*., 2015). These isotherms show the volume of nitrogen adsorbed at lower P/Po and displayed folds followed by loops revealing the development of mesopores created by the devolatilization and sulphur release under HTC and Co-HTC conditions (Han *et al*., 2019).

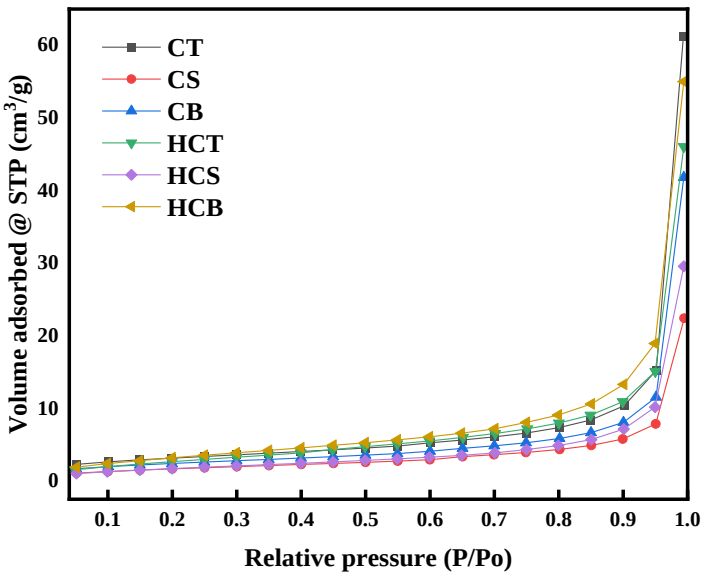

Figure 4-16 :Isothermal adsorption plots of and Co-HTC hydrochar

The coal slurry's hydrochar pore diameter was larger than the CT and produced HCT which decreases the nitrogen storage capacity as seen on the limit relative pressure of the associated isotherm loop (Jabłońska *et al*., 2017). The HCB isotherm show that the Co-HTC conditions allowed the SS (biomass) to settle on the coal surface, adsorb, and form a rudimentary layer resulting in a reduced pore diameter obtained (Figure 4-16). The aggregation of SS particles observed on SEM images of CB contributes to the formation of narrowed pores of the produced HCB which increases the nitrogen adsorption observed on the associated isotherm from the relative pressure of 0.8 and upward (Jabłońska *et al*., 2017). The description of porous materials internal structure is done by the determination of pore size

distribution analysis using a simplified model determined as follow (Okhovat *et al*., 2012).

$$f(W) = \frac{dV}{dW} \quad (4\text{-}18)$$

Where W is pore width and V is the pore volume.

The average pore diameters of CD, SS and produced HCs are presented in Table 4-9. The obtained results show a unimodal distribution referring to the presence of pores in the mesopores region (2nm >pore diameter<50nm) (Okhovat *et al*., 2012). The average pore diameters of the produced HC confirm (Table 4-9) the development of mesopores provoked by HTC and Co-HTC consistent with the pores size distribution of hydrochar and biochar materials produced in previous studies (Okhovat *et al*., 2012; Han *et al*., 2019).

Table 4-9.BET analysis results of the coals, produced HCs and AC

Material	Surface area (m^2/g)	Total pore volume (cm^3/g)	Average pore diameter (nm)
HCT	11.882	0.071	2.62
CS	6.37	0.048	3.34
HCS	14.35	0.094	2.65
CB	6.17	0.09	3.04
HCB	20.35	1.38	2.05

CT: Coal tailing. CS: coal slurry. CB: blend of coals and sewage sludge.
HCT: Coal tailing's hydrochar. HCS: Coal slurry's hydrochar.
HCB: hydrochar form CB BET: Brunauer Emmet Teller

The XRF results presented in Table 4-10 show the predominance of Silicon (Si), Aluminum (Al), Iron (Fe), Magnesium (Mg), Manganese (Mn) and Calcium (Ca)

in the raw materials (CT, CS, SS) analyzed. Thus, in agreement with the XRD analysis which identified the dominant presence of silicates (quartz, muscovite, orthose) and clay or aluminosilicates (kaolinite) minerals followed by pyrite, calcite, hematite, clinochlore and siderite. The decrease of mineral element in the ash of CT, CS and CB after HTC and Co-HTC respectively as shown in Table 4-10 is proportional to the reduction of mineral phases peaks intensity observed in Figure 4-12(A). This may be due to the release of mineral element into the HTC and Co-HTC liquid phases (Uddin *et al*., 2014; Reza *et al*., 2022). Previous studies have shown that in acidic medium silicates mineral dissolve via multi-step process initiates by rapid exchange of cations at the mineral surface, followed by hydrolysis and subsequent detachment of silica and alumina component from the remaining carbon skeleton (McKee *et al*., 2018). This agrees with the FTIR results in Figure 4-12B where the release of -OH groups was observed on the spectra of the produced hydrochar. As a result, under acidic conditions produced by HTC and Co-HTC, silicates and aluminosilicates minerals are decomposed by metal and silica dissolution, whereas the carbon skeleton accuses a smaller decomposition before condensation and repolymerization (Okhovat *et al*., 2012; Mumme *et al*., 2015). Therefore, the decarboxylation that occur during HTC and Co-HTC, lead to a breakdown of C=O and -COOH identified in the feedstock spectra, producing organic acids in the aqueous system. This decreases the pH and subsequently causes a partial dissolution of mineral elements. The lower pH medium produced by the decomposition of extended aliphatic groups combined to double bound carbonyl groups (C=O) present in SS under Co-HTC enhance the dissolution of minerals. Consequently, the mineral elemental composition in the produced hydrochar decrease significantly (HCB). The analysis of liquid phases from HTC (LCT, LCS)

and Co-HTC (LCB) indicate the amount of metal dissolved following each process. Consequently, the XRF results presented in Table 4-10 indicate a decrease in the major mineral elements present in CB, CT, and CS, respectively. As shown in Table 4-10, minor elements such as Potassium (K), Sodium (Na), Titanium (Ti), Manganese (Mn), Phosphorus (P), Chromium (Cr), and Nickel (Ni) decreased and in some cases disappeared from the produced hydrochar. The XRF results (Table 4-10) shows the comparative mineral dissolution evaluation of Co-HTC and HTC. Table 4-10 shows that most of the mineral components identified in the feedstocks were present in relatively stable form in the synthesized HCs, as determined by XRF. Therefore, the adsorption application of synthesized HCs for decontamination of polluted waters or environmental remediation is unlikely to be able to separate the stable element mineral complexes of the HCs back into the environment. The increase in LOI is consistent with previous findings that determined that the increase in LOI in carbonaceous material corresponds to the increase in its organic matter, which contains carbon (Nakhli *et al*., 2019). The results show that the blended treatment of CT, CS, and SS in Co-HTC results in a higher carbonization yield (%) than HTC of CT and CS alone.

Table 4-10:XRF results of HC products

Element Formula	Element Composition	Standard Deviation	CT	CS	SS	CB	HCT	HCS	HCB
Conc (%)	Conc (%)	(+/-) ppm							
Si	SiO_2	2	17.021	6.89	11.43	11.78	14.99	6.72	8.43
Al	Al_2O_3	3	7.14	4.48	5.94	5.85	6.29	4.37	4.19
Fe	Fe2O3	1	3.31	1.26	5.97	3.51	2.91	1.23	2.51
Ca	CaO	3	5.1	1.72	2.7	3.17	4.49	1.68	2.27
Mg	MgO	2	0.46	0.23	1.15	0.61	0.41	0.22	0.44
K	K_2O	2	0.43	0.19	0.85	0.49	0.38	0.19	0.35
Na	NaO_2	2	0.074	0.059	0.58	0.24	0.07	0.06	0.17
Ti	TiO_2	1	0.4	0.33	0.51	0.41	0.35	0.32	0.30
Mn	MnO	3	0.023	0.015	0.16	0.07	0.02	0.01	0.05
P	P_2O_5	2	0.14	0.15	4.3	1.53	0.12	0.15	1.09
Cr	Cr_2O_3	3	0	0	0.088	0.03	0	0	0.021
Ni	NiO	3	0	0	0.031	0.01	0	0	0.007
LOI	LOI	4	39.78	70.21	66.29	58.76	45.18	71.94	76.28

CT: Coal tailing. CS: Coal slurry. SS: Sewage sludge. CB: blend of coal and sewage sludge. HCT: Hydrochar from coal tailing. HCS: Hydrochar from Coal Slurry. HCB: Hydrochar from the Blend (SS+CS+CT). C:0.5(CT+CS)

Table 4-11:Comparison of hydrochar synthesised in this work with literature values

Material	HTC conditions		Proximate analysis (wt.%)			Ultimate analysis (wt.%)					References
	Temperature (°C)	Time (Min)	Ash*	Fixed carbon*	Volatile matter *	C	H	N	O*	S	
Clarion coal (Cc)	-	-	11.7	54.0	34.3	63.8	4.1	1.5	26	4.6	Saba *et al* (2017)
HC	200	30	7.1	54.7	38.2	71.4	4.8	1.8	19	3.0	
HC	230	30	10.4	53.2	36.4	69.2	4.6	1.7	20.8	3.8	
HC	260	30	7.3	57.3	35.4	69.1	4.3	1.7	21.3	3.5	
Miscanthus (Ms)	-	-	2.7	12.8	84.5	48.7	5.7	0.2	45.4	0	
HC	200	30	0.6	15.0	84.4	52.4	5.8	0.3	41.2	0	
HC	230	30	2.5	19.9	77.6	59.3	5.4	0.3	35.0	0	
HC	260	30	0.7	47.8	51.5	69.6	4.4	0.3	25.6	0	
Blend (Cc + Ms)	200	90	4.2	33.1	62.7	58.2	5.3	0.8	34.4	1.2	
HC	230	90	5.8	52.9	41.3	67.2	4.2	1.1	25.6	2.0	
HC	260	90	3.5	53.4	43.1	68.7	4.1	1.1	24.4	1.6	
Sewage sludge (SS)	-	-	56.11	5.32	38.57	48.46	8.2	7.59	34.61	1.14	Kang *et al*. (2018)
HC	120	30	62.14	4.87	32.99	49.28	8.24	6.63	34.58	1.27	
HC	300	30	79.41	3.42	17.17	57.41	8.74	4.42	28.07	1.36	
Lignite (Ln)			6.22	45.37	48.41	65.70	5.02	0.90	27.84	0.54	
	300	30	6.89	48.61	44.50	68.70	4.78	1.07	25.18	0.27	
Mixture (Ln + SS)	240	30	35.2	28.74	36.06	64.85	5.59	1.94	27.17	0.45	

Bituminous Coal (CW1)	-	-	64.4	15.5	20.1	20.5	1.9	0.5	4.2	9.6	Reza *et al* (2022)
HC	230	30	62.8	18.7	18.5	22.5	1.5	0.5	5.4	8.4	
Bituminous Coal (CW2)			67.4	14.2	18.4	18.6	1.8	0.6	4.1	8.5	
HC	230	30	65.4	17.6	17.0	20.2	1.6	0.7	5.2	7.9	
Food waste (FW)			9.6	18.8	71.6	39.3	6.0	1.5	44.0	0	
HC	280	30	5.1	39.4	55.5	71.7	5.9	4.6	12.8	0	
CW1+FW	230	30	31.3	29.1	39.6	46.7	2.3	1.0	17.2	2.1	
CW2+FW	230	30	28.6	31.2	40.2	49.5	4.5	1.9	14.8	1.4	
Sub-bituminous coal (SbC)	-	-	25.5	40.5	34	75.1	5.1	1.1	18.4	0.33	Saqib *et al* (2018)
Food waste	-	-	6.41	14.48	79.11	39	7.32	5.7	47.68	0.2	He *et al* (2013)
SbC +FW	300	60	2.21	47.43	50.36	73	7.01	5.17	17.09	0.2	
Sewage sludge	-	-	28.6	1.42	69.98	36.7	6.4	5.5	35.9	9.5	
HC	200	360	43.89	5.47	50.64	33.3	4.4	2.1	18.5	3.8	
Coal			11.74	55.48	32.78	64.07	4.24	1.23	18.07	0.65	Zhao *et al*. (2021)
HC	340	60	7.16	65.12	27.72	74.81	3.5	1.88	12.15	0.56	
Coal discard (CD)	-	-	41.95	35.83	20.17	48.90	2.67	1.15	1.93	1.34	Setsepu *et al* (2021)
Searsia lancea Trees Grown (Ssl)	-	-	3.89	18.41	69.40	45.12	6.35	0.44	35.78	<0.10	
HC (CD + Ssl)	280	30	1.49	50.33	46.12	-	-	-	-	-	
Coal tailing (CT)	-	-	40.32	37.31	22.37	42.82	3.01	1.14	12.96	1.43	This study
HC	150	95	38.36	40.37	21.27	49.80	2.87	1.72	6.9	0.75	

Coal slurry (CS)			24.17	53.02	22.69	61.85	3.56	1.39	8.72	1.26	
HC	150	95	20.12	57.69	22.19	66.90	2.98	1.99	4.48	0.87	
Sewage sludge (SS)	-	-	39.25	9.52	51.23	29.7	4.88	4.15	23.34	1.86	
CT+CS+SS blend	-	-	38.8	38.67	22.53	45.64	3.05	1.82	10.91	0.83	
HC	208.10	360	19.71	58.82	21.46	67.04	2.78	2.43	7.8	0.39	

Ash: Ash content. FC: Fixed carbon. VM: Volatile matter. *: dried basis (moisture free). HC: Hydrochar. Oxygen%=100-(Moiture+Ash+Total Carbon+Hydrogen+Nitrogen+Sulphur)

5

As shown in Table 4-11, the optimized operating conditions obtained in this study were relatively lower than HTC and Co-HTC operating conditions of various feedstock used in previous studies. The carbon content of the HCs generated in this study was comparable to that of the HCs listed in Table 4-11. In addition, the results of this study indicate that the Co-HTC process has a significant carbonization potential (high carbon content) to produce hydrochar from the combination of coal discard and sewage sludge (HCB), comparable to HCB produced from other feedstock as reported in previous studies. In addition, the conditions selected in this study have the potential to reduce the energy requirement and cost of the process from a development and economic feasibility standpoint, when compared to the reported operating conditions for other thermal processes, such as pyrolysis and gasification (Afolabi *et al*., 2022).

4.4.5. Characterization of the HTC process water

The concentration of inorganic elements in produced PW provides information about its treatment prior to discharge or use. The chemical oxygen demand (COD) is the amount of oxygen required to completely oxidize organic carbon to CO_2 and H_2O (Cai *et al*., 2018). The COD is an important water quality parameter because, like the BOD (Biological Oxygen Demand), it provides an index to assess the impact of discharged wastewater on the receiving environment (Cai *et al*., 2018; Liu *et al*., 2022). Higher COD levels indicate a greater amount of oxidizable organic material in the sample, which reduces dissolved oxygen (DO) levels. A decrease in DO can cause anaerobic conditions, which are harmful to higher aquatic life forms (Kang *et al*., 2018; Zhang *et al*., 2022). According to a recent study, the produced PW from HTC of different feedstock had a relatively low concentration of inorganic and organic elements when compared to the standard for environmental disposal (Setsepu *et al*., 2021).

The results presented in Figure 4-17 show different element dissolved in the liquid phases after HTC and Co-HTC process. The most abundant elements found in the produced PW were calcium (Ca) > silicon (Si) > nitrogen(N) > phosphorous (P) > Nickel (Ni) > Magnesium (Mg) > cadmium (Cd) > chromium (Cr) > Manganese (Mn). The other elements such as zinc (Zn), copper (Cu), and mercury (Hg) were at lower levels. The absence of the iron (Fe) and sodium (Na) in the analyzed PW indicates that all the Fe and Na content of the raw materials have been retained in the produced hydrochar

(Grindley *et al*., 2015). The high concentrations of inorganic contaminants and lower pH was observed from the produced LCB compared to LCT and LCS. Thus, confirmed the increased degree of mineral dissolution during Co-HTC due to the decomposition of sewage sludge which produced acidic medium (Jin *et al*., 2014). In addition, according to the standard for the discharge of the PW into the fresh waterbodies, the concentrations of Nitrogen (N), phosphorous (P), cadmium (Cd), chromium (Cr), mercury (Hg), Zinc (Zn), Nickel (Ni) and silicon (Si) approached or exceed the legal limits (DAM.1999).The concentration of organic matter in the produced PW revealed the decomposition of organic elements from feedstock under HTC and Co-HTC conditions(Painter *et al*., 2012; Balachandran *et al*., 2014). The concentration of organic matter in the LCB illustrated the complexity of thermal decomposition reactions, interactions between coals and SS which resulted in the fragmentation, and solubilization of carbon macromolecules (Achinas *et al*., 2017). The results presented in Figure 4-17 show that COD of the produced LCB estimated from organic matter obtained by ICP-OES analysis exceeds the special limit (special limit 30mg/l) for discharge to fresh waterbodies. The general and special standard limit of elements dissolved in water refer to the maximum concentrations of the elements stated in water used for irrigation and aquatic discharge respectively (Koechermann *et al*., 2018).

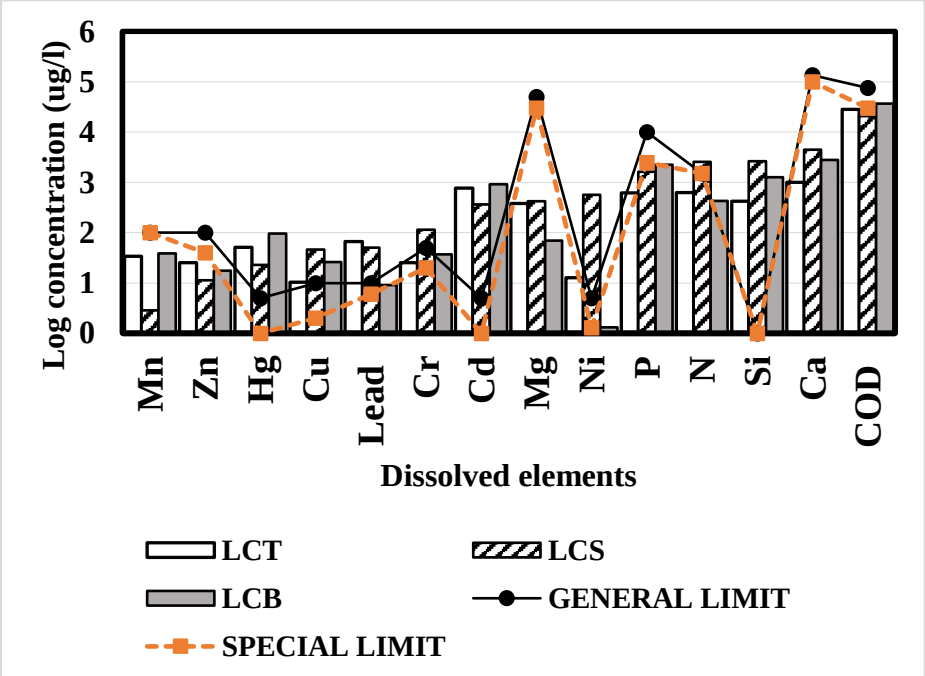

Figure 4-17:ICP-OES analysis results of LCT: HTC liquid phase from Coal tailing; LCS: HTC liquid phase from coal slurry and LCB: HTC liquid phase from the blending of coal and sewage sludge.

4.5.5.1. Identification of Organic compounds

The GC-MS results depicted in Table 4-12 show that the produced PW from HTC and Co-HTC process contain a variety of dissolved organic compounds, such as organic acids, sugars, phenols etc. The organic compounds are produced from dehydration, decarboxylation and demethylation reactions occurring under hydrothermal process conditions (Jin *et al*., 2014). These compounds are typical of decomposed biomass in the natural environment, but high concentrations in discharge water can pollute receiving waterbodies (Grindley *et al*., 2015; Koechermann *et al*., 2018). From the results in Table 4-12, the concentration of oxime methoxy-phenyl was found higher followed by ascorbic acid 2,6-dihexadecanoate-tricyclo (3.2.2.0) nonan-2-yl 4-nitrophenyl carbonate and silane- (4-bromophenyl) triphenyl. The higher concentration of these component was observed in the LCB compared to LCT and LCS respectively. The results agreed with the concentration of organic matter determined previously from ICP-OES analysis. Thus, confirmed the increased decomposition of coal and sewage under Co-HTC (Li *et al*., 2007). The concentrations of organic elements dissolved in the produced PW indicate the significancy of its dilution before discharge in waterbodies (Liu *et al*., 2016). However, the produced PW could be recycled to avoid generation of additional wastes. In addition, previous works demonstrated that the use of PW in HTC and Co-HTC increases the carbonization mass yield due to their acidic properties and the condensation of aliphatic fragments content dissolved during precedent hydrothermal process (Uddin *et al*., 2014). The acidity of hydrothermal reaction medium strengthens polymerization of benzyl alcohol structure of raw material via the carbonium ion which is the intermediate of the reaction (Li *et al*., 2007; Liu *et al*., 2016). The chemical identification of dissolved organic compound reveals the predominance of carboxylic acid, aromatic compound and low aliphatic hydrocarbons in the produced PW as described in Table 4-12.

Table 4-12.Identification and concentration of organic compounds in PW

PW	Retention time (minutes)	Organic Compound Name	Concentration (%)
LCB	4.055	Oxime-, methoxy-phenyl-	44.85
	4.447	3-pyridinecarboxamide, 6-amino-5-cyano-1,2-dihydro-2-oxo-	3.29
	5.564	Cyclotrisiloxane, hexamethyl- (CAS)	10.07
	11.696	l-(+)-Ascorbic acid 2,6-dihexadecanoate	15.19
	12.493	2-Oxepanone, 7-hexyl-	6.28
	13.46	Beta. Alanine, N-methyl-N-(1-methyl-4-nitro-1H-imidazol-5-yl) -, methyl ester	3.64
	14.657	Hexadecanoic acid, 2-hydroxy-1-(hydroxymethyl)ethyl ester	3.35
	18.412	1-(2-Chloroethyl) -4-dimethylamino-6-methoxy-1,3,5-triazin-2(1H) -one	6.34
	19.323	JWH 398 N-(4-hydroxypentyl) metabolite	3.74
	22.639	3-{[(2-CHLOROETHYL) (METHYL)AMINO] METHYL} -1,2-DIHYDROXYANTHRA-9,10-QUINONE	3.26
LCT	4.061	Oxime-, methoxy-phenyl-	25.44
	5.306	Tricyclo[3.2.2.0]nonan-2-yl 4-nitrophenyl carbonate	12.85
	6.247	Silane, methyltripropoxy-	4.86
	8.376	6-tert-Butylthiochroman-3-carboxylic acid	5.24
	11.699	Pentadecanoic acid (CAS)	9.94
	12.494	2-Oxepanone, 7-hexyl- (CAS)	6.44
	13.897	2,2,9,9-tetrachloro-3,8-dioxo-4,7-dithia-10,12,12-trimethylbicyclo [8.3.1] tetradec-1(14) -ene	5.56
	14.46	N-(3-Dimethylaminopropyl) indole	9.58
	14.66	Hexadecanoic acid, 2-hydroxy-1-(hydroxymethyl)ethyl ester	13.66
	22.62	METHYL 10D-HYDROXYOCTADECANOATE	6.43
LCS	4.006	Oxime-, methoxy-phenyl-	26.77
	4.224	Silane, (4-bromophenyl) triphenyl-	9.54
	6.45	3-(2-Oxooxolan-3-yl) propanoic acid	9.37
	10.2	1,3,4-Thiadiazole, 2,3-dihydro-2-(2-naphthyl)-5-phenyl-	6.84
	10.632	. Beta. -L-Idopyranoside, phenylmethyl 2,4-bis(acetylamino)-2,4,6-trideoxy-, 3-acetate	7.72
	12.407	9-Octadecenoic acid (Z)-, methyl ester	7.95
	12.496	2-Oxepanone, 7-hexyl-	8.1
	13.07	(4,6-DICHLORO- [1,3,5] TRIAZIN-2-YL) -(2,6-DIMETHYL-PHENYL)-AMINE	7.29
	14.659	Hexadecanoic acid, 2-hydroxy-1-(hydroxymethyl)ethyl ester	9.72
	15.554	3,5-Dichloro-2-hydroxybenzenesulfonyl chloride	6.7

PW: Process water from HTC and Co-HTC process. LCT: PW from coal tailing's HTC. LCS: PW from coal slurry's HTC .LB: PW from Co-HTC of coal and sewage sludge

4.5.5.2. Determination of total carbon TC and total organic carbon TOC of the produced PW

The results in Table 4-12 show the overall levels of organic compounds present without a direct correlation between TOC and the total concentration of organic compounds present in the produced PW. However, the TOC composition illustrates the general organic contamination of the PW (Hoekman *et al*., 2011). The results show that TOC weight percentages are lower than the total inorganic carbon (TIC) weight percentage due to the release of organic carbon in the liquid phase during the hydrothermal process (Achinas *et al*., 2017). The total organic carbon property of water gives an insight of the amount of oxygen necessary to oxidize all the organic carbon completely (Cai *et al*., 2018). The TOC of LCT and LCB exceeding the special limit for discharge in rivers (11,5mg/l) of the SA national water discharge regulations creates aerobic conditions which threats aquatic lives (Zhang *et al*., 2022). The results in Table 4-13 show that the produced TOC of PW exceed the special limit of discharge in rivers. This is consistent with the COD results obtained from organic matter determined by ICP-OES analysis. Hence, prior treatment of PW is necessary before its envisioned potential discharge in rivers. A combination of dilution, wet oxidation for the degradation of organic components into CO_2 and water, and adsorption for the removal of the residual mineral elements could be employed to treat produced PW prior to its discharge in water bodies (Zhang et al., 2022). Koechermann (2018) reported that recirculating PW in the HTC process increases the carbonization yield of the produced HCs. Therefore, from an economic and environmental aspect, the PW generated by the HTC and Co-HTC processes was recycled in this study, as indicated in the methodology (Figure 2).

Table 4-13.Total Carbon and Total organic carbon

PW	TC (W %)	TIC (W %)	TOC (W %)
			TOC=TC-TIC
LCT	25.69	13.34	12.71
LCS	23.62	12.83	10.79
LCB	26.05	12.51	13.18

PW: Process water from HTC and Co-HTC process.
LCT: PW from coal tailing's HTC. LCS: PW from coal slurry's HTC.
LCB: PW from Co-HTC of coal and sewage sludge. TOC: Total organic carbon. TC: Total carbon. TIC: Total inorganic carbon

4.5. Conclusion

This study optimized the hydrothermal carbonisation (HTC) of coal discards from coal beneficiation operations and/or sewage sludge by optimizing a number of process parameters, including biomass type, temperature, and residence time, in order to produce hydrochar with improved physicochemical properties.

The optimized HTC conditions (150°C, 27bar, 95min) for individual CT and CS increased the amount of fixed carbon from 37.31% and 53.02% to 40.31% and 57.69%, respectively, on a dry basis. As a result, the total carbon content of the coal discards increased from 42.82 and 61.85 % to 49.80 and 66.90% in the HCT and HCS produced, respectively. In addition, the ash content of coal discards reported on a dry basis decreased from 40.32 and 24.17 % to 38.3 and 20.17 % in the HCT and HCS produced under optimized HTC conditions. While the optimized Co-HTC conditions of 208°C, 22.5bars, and 360 minutes for a CT+CS: SS blend ratio of 5:1 increased the fixed carbon reported on a dry basis and total carbon content of CB (a blend of CT+CS+SS) from 38.67% and 45.64%, respectively, to 58.82% and 67.0%, respectively. The HCB ash concentration decreased from 38.8% to 19.71%. The carbonization yields (Cy) for HCT, HCS, and HCB were determined to be 113.58%, 102.42%, and 129.88%, respectively. Co-carbonization HTC's yield (Cy) was higher than that of HTC alone, possibly as a result of an increase in acidic conditions caused by the degradation of cellulose, chlorine, and hemicellulose into organic acid monomers during decarboxylation and dehydration reactions of the Co-HTC process. As a result, the lower pH of the Co-HTC process liquid increases the sulphur removal (production of sulphite and sulphate) from 0.83 to 0.39 % and possibly allows the release of inorganic elements into the liquid phase. This demonstrates the effectiveness of the Co-HTC process for reducing the sulphur content of waste coals and sewage sludge. HCB synthesized from Co-HTC had comparable physicochemical properties to HCS synthesized from HTC, with the highest carbon content and the lowest ash content (CS). This demonstrated the viability of combining coal waste and sewage sludge to produce high-quality carbonaceous material for a variety of applications.

REFERENCES

1. Bohlmann, J. A., & Inglesi-Lotz, R. Analysing the South African residential sector's energy profile. *Renewable and Sustainable Energy Reviews*,*96*, 240-252. (2018).
2. Van de Venter, F. F. *Producing briquettes for domestic household fuel applications from coal tailings* (Doctoral dissertation). (2021).
3. Onifade, M., Genc, B., & Bada, S. Spontaneous combustion liability between coal seams: A thermogravimetric study. *International Journal of Mining Science and Technology*, *30*(5), 691-698. (2020).
4. Petlovanyi, M. V., Lozynskyi, V. H., Saik, P. B., & Sai, K. S.. Modern experience of low-coal seams underground mining in Ukraine. *International Journal of Mining Science and Technology*, *28*(6), 917-923. (2018)
5. Fijalkowski, K., Rorat, A., Grobelak, A., & Kacprzak, M. J. The presence of contaminations in sewage sludge–The current situation. *Journal of Environmental Management*, *203*, 1126-1136. (2017).
6. Venkatesan, A. K., Done, H. Y., & Halden, R. U. United States National Sewage Sludge Repository at Arizona State University—a new resource and research tool for environmental scientists, engineers, and epidemiologists. *Environmental Science and Pollution Research*, *22*(3), 1577-1586. (2015).
7. Shaddel, S., Bakhtiary-Davijany, H., Kabbe, C., Dadgar, F., & Østerhus, S. W. Sustainable sewage sludge management: From current practices to emerging nutrient recovery technologies. *Sustainability*, *11*(12), 3435. (2019).
8. Munir, M., Siddiqui, S. A., Dengel, A., & Ahmed, S. DeepAnT: A deep learning approach for unsupervised anomaly detection in time series. *Ieee Access*, *7*, 1991-2005. (2018).
9. Tasca, A. L., Puccini, M., Gori, R., Corsi, I., Galletti, A. M. R., & Vitolo, S. Hydrothermal carbonization of sewage sludge: A critical analysis of process severity, hydrochar properties and environmental implications. *Waste Management*, *93*, 1-13. (2019).
10. Zhang, L., Liu, S., Wang, B., Wang, Q., Yang, G., & Chen, J. Effect of residence time on hydrothermal carbonization of corn cob residual. *BioResources*, *10*(3), 3979-3986. (2015).
11. Liao, J., Fei, Y., Marshall, M., Chaffee, A. L., & Chang, L. Hydrothermal dewatering of a Chinese lignite and properties of the solid products. *Fuel*, *180*, 473-480. (2016).
12. Saba, A., Saha, P., & Reza, M. T. Co-Hydrothermal Carbonization of coal-biomass blend: Influence of temperature on solid fuel properties. *Fuel processing technology*, *167*, 711-720. (2017).
13. Wang, L., Chang, Y., & Li, A. Hydrothermal carbonization for energy-efficient processing of sewage sludge: A review. *Renewable and Sustainable Energy Reviews*, *108*, 423-440. (2019).
14. Mumme, J., Titirici, M. M., Pfeiffer, A., Lüder, U., Reza, M. T., & Mašek, O. Hydrothermal carbonization of digestate in the presence of zeolite: process efficiency and composite properties. *ACS Sustainable Chemistry & Engineering*, *3*(11), 2967-2974. (2015).
15. Hlangwani, E., Doorsamy, W., Adebiyi, J. A., Fajimi, L. I., & Adebo, O. A. A modeling method for the development of a bioprocess to optimally produce umqombothi (a South African traditional beer). *Scientific Reports*, *11*(1), 1-15. (2021).
16. Afolabi, O. O., Sohail, M., & Cheng, Y. L. Optimisation and characterisation of hydrochar production from spent coffee grounds by hydrothermal carbonisation. *Renewable Energy*, *147*, 1380-1391. (2020).
17. Barghi, B., Jürisoo, M., Volokhova, M., Seinberg, L., Reile, I., Mikli, V., & Niidu, A. Process Optimization for Catalytic Oxidation of Dibenzothiophene over UiO-66-NH2 by Using a Response Surface Methodology. *ACS omega*. (2022).
18. Smith, B. C. *Fundamentals of Fourier transform infrared spectroscopy*. CRC press. (2011).
19. Lin, Y., Wu, G. S., Yuan, X. Y., Xie, T., & Zhang, L. D. Fabrication and optical properties of TiO2 nanowire arrays made by sol–gel electrophoresis deposition into anodic alumina membranes. *Journal of Physics: Condensed Matter*, *15*(17), 2917. (2003).
20. Norrish, K., & Hutton, J. T. An accurate X-ray spectrographic method for the analysis of a wide range of geological samples. *Geochimica et cosmochimica acta*, *33*(4), 431-453. (1969).
21. Liu, L., Liu, W., Yu, L., Dong, J., Han, F., Hu, D., ... & Zhang, Y. Optimizing anaerobic technology by using electrochemistry and membrane module for treating pesticide wastewater: Chemical oxygen demand

components and fractions distribution, membrane fouling, effluent toxicity and economic analysis. *Bioresource Technology*, *346*, 126608. (2022).
22. Samson, B. A. D. A., Daniel, T. A. O., Honaker, R., Falcon, L., & Falcon, R. Parametric study of electrostatic separation of South African fine coal. *Mining Science and Technology (China)*, *20*(4), 535-541. (2010).
23. Hutton, A., & Mandile, A. J. Quantitative XRD measurement of mineral matter in Gondwana coals using the Rietveld method. *Journal of African Earth Sciences*, *23*(1), 61-72. (1996).
24. Akhtar, J., & Amin, N. S. A review on operating parameters for optimum liquid oil yield in biomass pyrolysis. *Renewable and Sustainable Energy Reviews*, *16*(7), 5101-5109. (2012).
25. Nakason, K., Panyapinyopol, B., Kanokkantapong, V., Viriya-empikul, N., Kraithong, W., & Pavasant, P. Hydrothermal carbonization of unwanted biomass materials: Effect of process temperature and retention time on hydrochar and liquid fraction. *Journal of the Energy Institute*, *91*(5), 786-796. (2018).
26. Heidari, M., Dutta, A., Acharya, B., & Mahmud, S. A review of the current knowledge and challenges of hydrothermal carbonization for biomass conversion. *Journal of the Energy Institute*, *92*(6), 1779-1799. (2019).
27. Nizamuddin, S., Baloch, H. A., Griffin, G. J., Mubarak, N. M., Bhutto, A. W., Abro, R., ... & Ali, B. S. An overview of effect of process parameters on hydrothermal carbonization of biomass. *Renewable and Sustainable Energy Reviews*, *73*, 1289-1299. (2017).
28. Mumme, J., Titirici, M. M., Pfeiffer, A., Lu̇der, U., Reza, M. T., & Maš̆ek, O. Hydrothermal carbonization of digestate in the presence of zeolite: process efficiency and composite properties. *ACS Sustainable Chemistry & Engineering*, *3*(11), 2967-2974. (2015).
29. Abdulsalam, J., Mulopo, J., Oboirien, B., Bada, S., & Falcon, R. Experimental evaluation of activated carbon derived from South Africa discard coal for natural gas storage. *International Journal of Coal Science & Technology*, *6*(3), 459-477. (2019).
30. Behera, S. K., Meena, H., Chakraborty, S., & Meikap, B. C. Application of response surface methodology (RSM) for optimization of leaching parameters for ash reduction from low-grade coal. *International Journal of Mining Science and Technology*, *28*(4), 621-629. (2018).
31. Teimouri, M., Abdolahnezhad, K., & Ghalandarayeshi, S. Evaluation of estimation methods for parameters of the probability functions in tree diameter distribution modeling. *Environmental Resources Research*, *8*(1), 25-40. (2020).
32. Aliakbari, Z., Younesi, H., Ghoreyshi, A. A., Bahramifar, N., & Heidari, A. Production and characterization of sewage-sludge based activated carbons under different post-activation conditions. *Waste and Biomass Valorization*, *9*(3), 451-463. (2018).
33. Jin, F., Wang, Y., Zeng, X., Shen, Z., & Yao, G. Water under high temperature and pressure conditions and its applications to develop green technologies for biomass conversion. In *Application of hydrothermal reactions to biomass conversion* (pp. 3-28). Springer, Berlin, Heidelberg. (2014).
34. Hoekman, S. K., Broch, A., & Robbins, C. Hydrothermal carbonization (HTC) of lignocellulosic biomass. *Energy & Fuels*, *25*(4), 1802-1810. (2011).
35. Mursito, A. T., Hirajima, T., & Sasaki, K. Upgrading and dewatering of raw tropical peat by hydrothermal treatment. *Fuel*, *89*(3), 635-641. (2010).
36. Pińkowska, H., Wolak, P., & Złocińska, A. Hydrothermal decomposition of xylan as a model substance for plant biomass waste–hydrothermolysis in subcritical water. *Biomass and bioenergy*, *35*(9), 3902-3912. (2011).
37. Sahu, S. G., Sarkar, P., Chakraborty, N., & Adak, A. K. Thermogravimetric assessment of combustion characteristics of blends of a coal with different biomass chars. *Fuel processing technology*, *91*(3), 369-378. (2010).
38. Lu, X., Pellechia, P. J., Flora, J. R., & Berge, N. D. Influence of reaction time and temperature on product formation and characteristics associated with the hydrothermal carbonization of cellulose. *Bioresource technology*, *138*, 180-190. (2013).
39. Channiwala, S. A., & Parikh, P. P. A unified correlation for estimating HHV of solid, liquid and gaseous fuels. *Fuel*, *81*(8), 1051-1063. (2002).
40. Kang, S., Li, X., Fan, J., & Chang, J. Characterization of hydrochars produced by hydrothermal carbonization of lignin, cellulose, D-xylose, and wood meal. *Industrial & engineering chemistry research*, *51*(26), 9023-9031. (2012).

41. Yin, Y., Yin, J., Zhang, W., Tian, H., Hu, Z., Ruan, M., ... & Chen, D. FT-IR and micro-Raman spectroscopic characterization of minerals in high-calcium coal ashes. *Journal of the Energy Institute*, *91*(3), 389-396. (2018).
42. Harris, W. I. L. L. I. E., & Norman White, G. X-ray diffraction techniques for soil mineral identification. *Methods of soil analysis part 5—Mineralogical methods*, *5*, 81-115. (2008).
43. Eterigho-Ikelegbe, O., Trammell, R., & Bada, S. Preparation and characterization of ceramic composites from South Africa coal discard. *Construction and Building Materials*, *302*, 124164. (2021).
44. Jeffery, J. W. The crystal structure of tricalcium silicate. *Acta Crystallographica*, *5*(1), 26-35. (1952).
45. Neto, J. S. A., de Matos, P. R., Angeles, G., Campos, C. E., Torres, S. M., Monteiro, P. J., & Kirchheim, A. P. Hydration and interactions between pure and doped C3S and C3A in the presence of different calcium sulfates. *Cement and Concrete Research*, *159*, 106893. (2022).
46. Liu, Y., He, Y., Wang, Z., Xia, J., Wan, K., Whiddon, R., & Cen, K. Characteristics of alkali species release from a burning coal/biomass blend. *Applied Energy*, *215*, 523-531. (2018).
47. Köseoğlu, E., & Akmil-Başar, C. Preparation, structural evaluation and adsorptive properties of activated carbon from agricultural waste biomass. *Advanced Powder Technology*, *26*(3), 811-818. (2015).
48. Kruse, A., Funke, A., & Titirici, M. M. Hydrothermal conversion of biomass to fuels and energetic materials. *Current opinion in chemical biology*, *17*(3), 515-521. (2013).
49. Knappe, V., Paczkowski, S., Robles, L. A. D., Gonzales, A., & Pelz, S. Reducing willow wood fuel emission by low temperature microwave assisted hydrothermal carbonization. *JoVE (Journal of Visualized Experiments)*, (147), e58970. (2019).
50. Jal, P. K., Patel, S., & Mishra, B. K. Chemical modification of silica surface by immobilization of functional groups for extractive concentration of metal ions. *Talanta*, *62*(5), 1005-1028. (2004).
51. Mishra, R. K., & Mohanty, K. Characterization of non-edible lignocellulosic biomass in terms of their candidacy towards alternative renewable fuels. *Biomass Conversion and Biorefinery*, *8*(4), 799-812. (2018).
52. Doshi, P., Srivastava, G., Pathak, G., & Dikshit, M. Physicochemical and thermal characterization of nonedible oilseed residual waste as sustainable solid biofuel. *Waste management*, *34*(10), 1836-1846. (2014).
53. Balachandran, M. Role of infrared spectroscopy in coal analysis—an investigation. *American Journal of Analytical Chemistry*,*2014*. (2014).
54. Achinas, S., Achinas, V., & Euverink, G. J. W. A technological overview of biogas production from biowaste. *Engineering*, *3*(3), 299-307. (2017).
55. Painter, P., Starsinic, M., & Coleman, M. Determination of functional groups in coal by Fourier transform interferometry. *Fourier transform infrared spectroscopy*, *4*, 169-240. (2012).
56. Okolo, G. N., Neomagus, H. W., Everson, R. C., Roberts, M. J., Bunt, J. R., Sakurovs, R., & Mathews, J. P. Chemical–structural properties of South African bituminous coals: Insights from wide angle XRD–carbon fraction analysis, ATR–FTIR, solid state 13C NMR, and HRTEM techniques. *Fuel*, *158*, 779-792. (2015).
57. Hattingh, B. B., Everson, R. C., Neomagus, H. W., Bunt, J. R., Van Niekerk, D., Jordaan, J. H., & Mathews, J. P. Elucidation of the structural and molecular properties of typical South African coals. *Energy & Fuels*, *27*(6), 3161-3172. (2013).
58. Tan, J., Cheng, H., Wei, L., Wei, C., Xing, Y., & Gui, X. Using low-rank coal slime as an eco-friendly replacement for carbon black filler in styrene butadiene rubber. *Journal of Cleaner Production*, *234*, 949-960. (2019).
59. Li, J., Zhu, M., Zhang, Z., Zhang, K., Shen, G., & Zhang, D. The mineralogy, morphology and sintering characteristics of ash deposits on a probe at different temperatures during combustion of blends of Zhundong lignite and a bituminous coal in a drop tube furnace. *Fuel Processing Technology*, *149*, 176-186. (2016).
60. Lu, X., & Berge, N. D. Influence of feedstock chemical composition on product formation and characteristics derived from the hydrothermal carbonization of mixed feedstocks. *Bioresource technology*, *166*, 120-131. (2014).

61. Shui, H., Zhang, X., Wang, Z., Lin, C., Lei, Z., Ren, S., & Kang, S. Modification of a sub-bituminous coal by hydrothermal treatment with the addition of CaO: Extraction and caking properties. *Energy & fuels*, *26*(5), 2928-2933. (2012).
62. Thommes, M., Kaneko, K., Neimark, A. V., Olivier, J. P., Rodriguez-Reinoso, F., Rouquerol, J., & Sing, K. S. Physisorption of gases, with special reference to the evaluation of surface area and pore size distribution (IUPAC Technical Report). *Pure and applied chemistry*, *87*(9-10), 1051-1069. (2015).
63. Han, J., Zhang, L., Zhao, B., Qin, L., Wang, Y., & Xing, F. The N-doped activated carbon derived from sugarcane bagasse for CO2 adsorption. *Industrial Crops and Products*, *128*, 290-297. (2019).
64. Jabłońska, B., Kityk, A. V., Busch, M., & Huber, P. The structural and surface properties of natural and modified coal gangue. *Journal of environmental management*, *190*, 80-90. (2017).
65. Okhovat, A., Ahmadpour, A., Ahmadpour, F., & Khaki Yadegar, Z. Pore size distribution analysis of coal-based activated carbons: Investigating the effects of activating agent and chemical ratio. *International Scholarly Research Notices*, *2012*. (2012).
66. Uddin, M. H., Reza, M. T., Lynam, J. G., & Coronella, C. J. Effects of water recycling in hydrothermal carbonization of loblolly pine. *Environmental Progress & Sustainable Energy*, *33*(4), 1309-1315. (2014).
67. Reza, M. T. Investigation of hydrothermal carbonization and chemical activation process conditions on hydrogen storage in loblolly pine-derived superactivated hydrochars. *International Journal of Hydrogen Energy*. (2022).
68. McKee, A. D., Solano, M., Saydjari, A., Bennett, C. J., Hud, N. V., & Orlando, T. M. A Possible Path to Prebiotic Peptides Involving Silica and Hydroxy Acid-Mediated Amide Bond Formation. *ChemBioChem*, *19*(18), 1913-1917. (2018).
69. Nakhli, S. A. A., Panta, S., Brown, J. D., Tian, J., & Imhoff, P. T. Quantifying biochar content in a field soil with varying organic matter content using a two-temperature loss on ignition method. *Science of The Total Environment*, *658*, 1106-1116. (2019).
70. Cai, Y., Fu, X., Gao, X., & Li, L. Research progress of on-line automatic monitoring of chemical oxygen demand (COD) of water. In *IOP Conference Series: Earth and Environmental Science* (Vol. 121, No. 2, p. 022039). IOP Publishing. (2018, February).
71. Kang, M., Peng, S., Tian, Y., & Zhang, H. Effects of dissolved oxygen and nutrient loading on phosphorus fluxes at the sediment–water interface in the Hai River Estuary, China. *Marine pollution bulletin*, *130*, 132-139. (2018).
72. Song, D., Yang, C., Zhang, X., Su, X., & Zhang, X. Structure of the organic crystallite unit in coal as determined by X-ray diffraction. *Mining Science and Technology (China)*, *21*(5), 667-671. (2011).
73. Saqib, N. U., Baroutian, S., & Sarmah, A. K. Physicochemical, structural and combustion characterization of food waste hydrochar obtained by hydrothermal carbonization. *Bioresource technology*, *266*, 357-363. (2018).
74. He, C., Giannis, A., & Wang, J. Y. Conversion of sewage sludge to clean solid fuel using hydrothermal carbonization: hydrochar fuel characteristics and combustion behavior. *Applied Energy*, *111*, 257-266. (2013).
75. Zhao, P., Lin, C., Zhang, J., Huang, N., Cui, X., Tian, H., & Guo, Q. Moisture re-adsorption characteristics of hydrochar generated from the Co-hydrothermal carbonization of PVC and alkali coal. *Fuel Processing Technology*, *213*, 106636. (2021).
76. Setsepu, R. L., Abdulsalam, J., Weiersbye, I. M., & Bada, S. O. Hydrothermal carbonization of Searsia lancea trees grown on mine drainage: Processing variables and product composition. *ACS omega*, *6*(31), 20292-20302. (2021).
77. Grindley, S. F. *Modelling the effects of trees on a contaminated groundwater plume from a gold tailings storage facility in the Orkney district* (Doctoral dissertation, University of the Witwatersrand, Faculty of Science, School of Geography, Archaeology & Environmental Studies). (2015).
78. Zhang, W., Rong, N., Jin, X., Meng, X., Han, S., Zhang, D., & Shan, B. Dissolved oxygen variation in the North China Plain River network region over 2011–2020 and the influencing factors. *Chemosphere*, *287*, 132354. (2022).
79. Department of Water Affairs and Forestry. GOVERNMENT GAZETTE NO. 20526 8 October 1999; DWAF; GOVERNMENT NOTICE; 8 October 1999. South Afica (1999).
80. DAM, F. P., DAM, M., & SINDANE, J. Department of Water Affairs and Forestry. (2008)

81. Koechermann, J., Goersch, K., Wirth, B., Muehlenberg, J., & Klemm, M. Hydrothermal carbonization: Temperature influence on hydrochar and aqueous phase composition during process water recirculation. *Journal of Environmental Chemical Engineering*, *6*(4), 5481-5487. (2018).
82. Li, J. G., Ishigaki, T., & Sun, X. Anatase, brookite, and rutile nanocrystals via redox reactions under mild hydrothermal conditions: phase-selective synthesis and physicochemical properties. *The Journal of Physical Chemistry C*, *111*(13), 4969-4976. (2007).
83. Liu, J., Wu, J., Zhu, J., Wang, Z., Zhou, J., & Cen, K. Removal of oxygen functional groups in lignite by hydrothermal dewatering: An experimental and DFT study. *Fuel*, *178*, 85-92. (2016).

Chapter 5: Coal discards and sewage sludge derived-hydrochar for HIV antiretroviral pollutant removal from wastewater and spent adsorption residue evaluation for sustainable carbon management

This chapter has been published in the Journal of Sustainability .

cited as Kahilu, G. M., Bada, S., & Mulopo, J. (2022a). Coal Discards and Sewage Sludge Derived-Hydrochar for HIV Antiretroviral Pollutant Removal from Wastewater and Spent Adsorption Residue Evaluation for Sustainable Carbon Management. Sustainability, 14(22), 15113. https://doi.org/10.3390/su142215113

5.1. Abstract

The effects of various parameter interactions on the textural structure of hydrochars produced via hydrothermal (HTC) and co-hydrothermal (Co-HTC) treatments of coal discards and sewage sludge (wastes), as well as the subsequent use of the hydrochar (HCs) synthesized for HIV drug (nevirapine and lamivudine) removal from wastewater, were investigated in this study. The HTC and Co-HTC process improved the carbon content of the raw material by 13.47%, 7.08% and 30.65% for coal tailing hydrochar (HCT), coal slurry hydrochar (HCS) and coals-sewage blend hydrochars (HCB) respectively. The Co-HTC-derived HCB had a high SBET of 20.35 m2/g and pore volume of 0.38 cm3/g, leading to significant adsorptive reductions of nevirapine (NEV) and lamivudine (LAM) (97.19% and 93.32%, respectively). HCT and HCS displayed high NEV and LAM adsorption capacities (50 mg g-1, 42 mg g-1 and 52 mg g-1, 41 mg g-1) respectively despite being less effective than HCB (53.8 mg g-1, 42.8 mg g-1). In addition, the use of spent adsorption residues for energy storage applications was investigated further. The findings showed that spent adsorption residues are an effective carbonaceous material precursor to produce electrical double-layer capacitors (EDLCs).

5.2. Introduction

South African coal beneficiation plants produced more than sixty million tons of coal waste annually (Mills et al., 2018). The majority of these coal wastes are disposed of in tailings piles and slurry dams. As a result, concerns about the solubilization and/or volatilization of toxic substances in coal waste are seen as a major threat to the nation's environmental waste management (Mills *et al*., 2018; Onifade *et al*., 2020). South Africa's population has grown rapidly during the past two decades, from 48.8 million in 2005 to 51.58 million in 2010 and 57.7 million in 2018. More than half the population is currently living and working in densely populated urban areas (Water Resources. 1977). This rapid population growth, combined with growing urbanization, has put additional strain on existing wastewater treatment plant (WWTP) infrastructure, resulting in increased sewage sludge production at these facilities (Libhaber *et al*., 2012). Several lines of evidence suggest that landfilling sewage sludge is not a sustainable solution for sewage sludge management (Zhou *et al*., 2020). Despite the potential concerns regarding soil and subsoil pollution, roughly 80% of wastewater treatment plants continue to dispose of their sewage sludge on specified locations (Kacprzak *et al*., 2017). The need for innovative techniques to minimize sewage sludge waste quantities has become an environmental and societal imperative. On the other hand, data from the World Health Organization (WHO) Global Health Observatory report that 70% of the estimated 36.7 million persons globally living with HIV/AIDS at the end of 2016 were from Africa (del Rio *et al*., 2017). South Africa's antiretroviral therapy (ART) program is the world's largest, with an estimated 3.9 million people receiving antiretrovirals (ARVs), accounting for roughly 24% of the global ART program as an estimated 19.8 million people uses ART in the world. ARVs are used to treat and prevent a variety of viral infections, including HIV, influenza, hepatitis, and herpes (Tompa *et al*., 2021). In South Africa, they are mainly used for the treatment of HIV/AIDS. South Africa uses the most antiretroviral drugs per capita of any country (Evans *et al*., 2013; Reddy *et al*., 2021). Although several studies have shown that ARVs are sterilized during wastewater treatment, little work or literature has been done on the presence of dissolved ARVs, their metabolic products, and removal strategies in wastewater (Tompa *et al*., 2021). Recent research in this area by Kebede (2020), Ndilimeke Akawa (2021), and Zitha (2022) demonstrated the existence of antiviral and other pharmacological compounds in bodies of water. According to

these studies, nevirapine and lamivudine were found in South African ambient water at a maximum concentration of 1.640 ng. L^{-1}, posing a substantial environmental risk due to their potential influence on aquatic life and medication resistance in humans (Zitha *et al*., 2022). As a result, there is a need for enhanced pharmaceutical component removal methods from water bodies. So far, research into the removal of pharmaceutical components from water bodies has been limited, owing to the high expense of prospective researched strategies such as adsorption, degradation, and phytoremediation (Kebede *et al*., 2020; Zitha *et al*., 2022). Furthermore, recent research conducted by Späth (2021) employing biochar as adsorbents revealed a moderate ARV removal efficacy in wastewater, which may be attributed to the textural properties of the adsorbent materials as well as the adsorption process parameters employed (Abafe *et al*., 2018). Despite the fact that a significant amount of biochar (100g/L) was required for efficient removal of nevirapine and lamivudine from wastewater at ambient temperature (rather than the 45°C reported in most studies), Späth's research demonstrated that the results were comparable to those achieved using high-cost synthetic adsorbents and that there was still potential for improvement. South Africa has a high HIV/AIDS prevalence, and it is anticipated that an increasing load of antiretroviral drugs may circumvent the WWTP systems and infiltrate the country's water networks (Hauser *et al*., 2012; Obidike *et al.*, 2018; Whiteley *et al*., 2020). The premise of this work is that the physicochemical and textural characteristics of HTC-derived biochar may be enhanced for usage as low-cost potential adsorbents for pharmaceutical component removal from water bodies.

In this study we focus on two antiretroviral drugs namely i) Nevirapine (NVP) which is an oral drug used to treat and prevent retroviral infections, particularly those caused by human immunodeficiency virus type 1. (HIV-1). HIV-1 is a virus that primarily infects CD4-T cells, which are immune system cells. HIV-1 ART, on the other hand, neither cures nor destroys the virus; rather, it suppresses or delays its reproduction (Deeks.2018). It is typically used in conjunction with other ARV medicines. Nevirapine is a non-nucleoside reverse transcriptase inhibitor (NNRTI) antiretroviral medication (ARVD) commonly used to prevent HIV transmission to the fetus. The nucleoside/nucleotide reverse transcriptase inhibitors (NRTIs) impede the HIV viral RNA's reverse transcription into its DNA, which is essential before the virus can integrate into the host cell. This is accomplished by interfering with the viral enzyme

reverse transcriptase, which oversees the performance of this activity. After intake, it is excreted in urine at a rate of 2.7% (Swanepoel *et al*., 2018; Yaqoob *et al*., 2020), ii) Lamivudine (3TC) is a first-generation nucleoside reverse transcriptase inhibitor that was licensed in 1995 for the treatment of HIV-1 infection and hepatitis B virus (HBV) infection. EPIVIR (2013); EPIVIR-HBV (2016) Since 2002, the WHO has recommended HIV treatment regimens, and 3TC or emtricitabine (FTC) are almost always the preferred components of fixed-dose combos (WHO, 2016). Only one study used HPLC/MS to determine its content in water, which was less than 1 ng. L^{-1} (Adeola *et al*., 2022).

The release of micropollutants into the environment via wastewater treatment plant (WWTP) effluents is one of the most important concerns with micropollutants in sanitation. For a long time, these discharges were recognized as a major source of micropollutant introduction into the environment, and their centrality to environmental contamination has been established (Prasse *et al*., 2010; WHO.2015). Pharmaceutical residues and hormones, pesticides, phthalates, artificial sweeteners, and personal care products are all detected in these discharges at trace amounts (ng/L to µg/L) (Prasse *et al*., 2010; Adeola *et al*., 2022). One of the current challenges is the removal of micropollutants from WWTP discharges which is crucial for creating cutting-edge innovations, guiding management strategies, and optimizing treatment operations and routes to reduce micropollutants concentrations in discharges, and hence in the environment. It is well known that traditional WWTP significantly reduces hydrophobic, volatile, or biodegradable chemicals while having little or no effect on many micropollutants such as pharmaceutical compounds (WHO.2015; Adeola *et al*., 2022). As a result, there is a need for additional pollution reduction solutions, and the implementation of additional tertiary treatments aimed at the eradication of micropollutants is a viable option, and among these the use of activated carbon adsorption appears to be a highly adaptable, efficient, and fairly priced method. Though activated carbon adsorption has been widely used in drinking water treatment, it has only recently attracted more attention in wastewater for the elimination of micropollutant concentrations in WWTP discharges. There is relatively few research on the elimination of micropollutants and in particular of ARVs micropollutants from WWTP discharges (Silva *et al*., 2019; Sousa *et al*., 2022). This is the motivation behind this research, which aims to synthesize low-cost AC from sewage sludge and coal

discards for the removal of ARVs micropollutants from WWTPs, thereby contributing to the closure of the waste loop in WWTPs by optimizing the carbon yield of HCs synthesized from CD and SS, examining their efficiency for the adsorption of dissolved pharmaceutical micropollutants in water (nevirapine and lamivudine), and then investigating the use of the spent adsorption residues obtained for energy storage applications.

5.3. Experimental method

5.3.1. Materials

The standard non-nucleoside nevirapine (NEV) and nucleoside lamivudine (LAM) reverse transcriptase inhibitor tablets supplied by Dischem pharmacy of South Africa with 99.9% of purity were utilized for adsorption tests. The tablets were crushed and dissolved in ultra-pure water obtained from a Direct-Q®3 with pump (Millipore, Merck system). The dissolution was carried out in a laboratory glass beaker using a predetermined volume of ultra-pure water (pH 6.8) at 20°C for stirring speed of 50rpm and time of 30 min. Coal tailing (CT) and coal slurry (CS) were collected from a coal beneficiation plant in Mpumalanga, South Africa, for use in this study (Figure 5-1A & Figure 5-1B). Before use, the collected samples were dried on ambient atmosphere, loaded, and transported in airtight bags onto the laboratory and dried once more at room temperature. The dried samples were mixed for homogenization and split in 2 portions from which one was screened into various particle sizes and the other was pulverized for physicochemical characterization (proximal, ultimate, total sulphur, SEM and FTIR). The sewage sludge (SS) used in this study (Figure 1C) was collected from a wastewater treatment plant (Ekurhuleni Water Care Company (ERWAT)) and split into two portions. The first portion was dried in a laboratory dryer (Prolab) at 105 °C for 24 hours and crushed for physiochemical characterization, while the second portion was used for HTC tests as received.

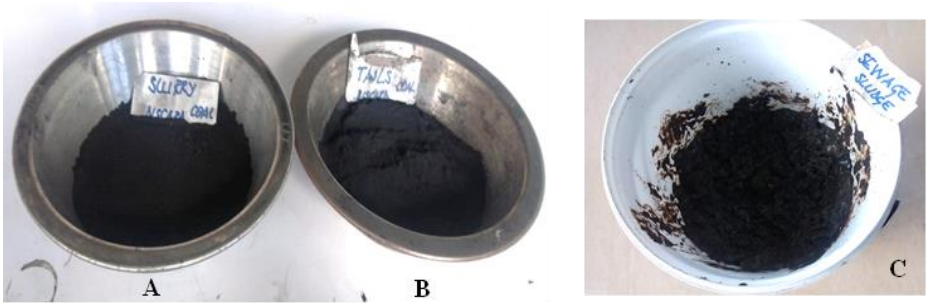

Figure 5-1:collected waste CS (A), waste CT (B) and sewage sludge sample (C).

5.3.2. Methods

Batch experimental experiments were conducted to evaluate the adsorption performance of the synthesized HCs for the removal of NEV and LAM from synthetic aqueous solutions made using ultra-pure water at an initial concentration of 20µmol L^{1}. The adsorption test was performed in volumetric polypropylene flasks of 200ml. The flasks were filled with a mixture of HCs and prepared aqueous solutions (containing the dissolved medicines) and shaken on a Platform shaker at 80 rpm and 25°C. (Labcon -Instrulab). Two adsorption parameters were considered: the concentration of adsorbent (r) and the residence time (t). For the experiments, 1g of each HC was combined with a similar amount of water solution. To assess the adsorption of NEV and LAM on the selected HCs concentration of 10 gL^{-1}, 20 gL^{-1}, 50 gL^{-1}, 100 gL^{-1} and 300 gL^{-1}, were used for a range of residence duration between 10 and 360 minutes. After allowing the mixtures to equilibrate for 24 hours to guarantee saturation, they were centrifuged for 15 minutes at 1500 rpm. The supernatant from each flask was then filtered through a 0.22 µm Whatman filter paper. The filtrates were then tested against corresponding produced aqueous solutions using a UV-1800 spectrophotometer and the gas chromatograph linked to the mass spectrometer Shimadzu (GCMS-2010) The experiments were repeated three times to guarantee the accuracy of the results. The dissolved drug concentrations (NEV and LAM) in the initial aqueous solutions were used as a reference for calculating adsorption percentages using equation (5-1):

Adsorption (%) =(Ci-Cf) /Ci x100 (5-1)

where Ci (µmol L^{-1}) is the concentration of the transcriptase inhibitor drugs in the corresponding initial solution and Cf (µmol L^{-1}) is the remaining drugs a concentration in the liquid phase at the end of the adsorption experiment with each HCs.

The Hydrothermal carbonization (HTC) and Co-hydrothermal (HTC) experimental test runs were designed using Design-Expert software (DoE) (Version 13, State–Ease, Inc, Minneapolis, USA). For experimental designs, the central composite design (CCD) and the custom design (CD) were utilized to know the number of runs that will be required to optimize the HTC and Co-HTC runs respectively. HTC experiments were conducted using variations in temperature, pressure and time ranging from 150 to 270°C, 10 and 27 bar, 10 and 180 minutes respectively. However, the Co-HTC experiments were performed using variations in residence time ranging from 10 to 360 minutes for the same range of temperature and pressure utilized in HTC experiments i.e., 150 to 270°C, 10 and 27 bar respectively. The Co-HTC experiments used a coal feedstock combination (CT+CS) of 50% coal tailing and 50% coal slurry. For the sake of simplicity, a 1:1 coal tailing to coal slurry blend was adopted. The coals-sewage sludge blend ratio (CT+CS: SS) used for Co-HTC experiments varied from 0:25 to 25:0 (wt:wt). High fixed carbon (FC) content hydrochars by means of the DoE was selected using the Response surface methodology (RSM) and the optimal combined methodology (OCM) techniques for HTC and Co-HTC respectively. RSM and OCM were adopted to understand the interactions of the HTC and Co-HTC factors on the fixed carbon contents of the HC produced from the individual CT, CS, and from the mixture of coals with sewage sludge respectively. In addition, RSM and OCM were used to develop appropriate models to enable the prediction of the optimum operating conditions required to produce high carbon content hydrochars. The analysis of variance (ANOVA) was used to evaluate the statistical significancy of the designed models.

The spent HC residues from nevirapine and lamivudine adsorption experiments were chemically activated using KOH reagent to produce activated carbon (ACs). Several research on the activation process of coal-based materials have shown that the impregnation ratio of KOH/carbonaceous material (CM) has an effect on the textural features of the generated ACs [27,69,70]. Furthermore, a recent study done by Abdulsalam Jibril (2019) found that increasing the activation temperature from 400°C to 800°C and the KOH/CM impregnation ratio from 1/1 to 4/1 increased the specific surface area (SBET) of the generated ACs. SBET values of 1925 m^2/g for run-of-mine coal, 1826.41 m^2/g for coal waste, and 1484.96 m^2/g for coal slurry ACs were obtained (Wazir *et al*., 2022). The optimum conditions established by Abdulsalam

Jibril (2019) were adopted in this investigation to synthesize ACs from nevirapine and lamivudine adsorption tests. To remove residual alkali, the ACs were rinsed with 0.5N HCl and then distilled water (Wazir *et al*., 2022). The washed samples were then dried in an oven at 60°C overnight before being kept in airtight bags for physicochemical analysis. ACs were labelled as follows: AC-HCT-NEV, AC-HCT-LAM, AC-HCS-NEV, AC-HCS-LAM, AC-HCB-NEV, and AC-HCB-LAM. Because of the abundant charge storage sites on the high porous surface of ACs, they may be used as electrode materials in supercapacitors (Adinaveen *et al*., 2013). As a consequence, ACs derived from nevirapine, and lamivudine adsorption tests were evaluated as electrode materials in ionic solutions ($Na^{(+)}$ $SO_4^{(2-)}$).

5.4. Physicochemical and textural Analyses

The concentrations and dissolved organic compounds of transcriptase inhibitor drugs (NEV and LAM) in the initial solution and produced filtrates from adsorption experiments were determined using the UV-1800 spectrophotometer and the gas chromatograph linked to the mass spectrometer Shimadzu (GC-MS-2010) The drug release concentration (CR%) was evaluated at the wavelength of 270 nm. The GC-MS instrument was set at initial temperature of 140ºC. The initial temperature was held for five minutes then increased to 50ºC at heating rate of 4 ºC/min and maintained for 12.5 minutes. The samples were injected at 220 ºC using the spitless mode. The analysis was performed using the following procedure: sampling time: 1.00minute; flow control mode: pressure: 100.00 kPa, total flow: 50.00 ml/min; column flow: 1.13 ml/min; linear velocity: 3.00ml/min. The identification of the organic compounds in the PW was conducted using the NIST 14 database and compared with published mass spectra. Spectra of nevirapine and lamivudine standard were built in the range from 200 to 350 nm using quartz cuvettes with 1cm of path length and water as blank. Solutions of NEV and LAM standard at $15gmL^{-1}$ prepared in water were used in this analysis. Ten tablets of each drug were weighed and powdered. The equivalent of 150 mg of nevirapine and lamivudine was weighed and transferred into a 200 ml volumetric flask with ultra-pure water. This solution was filtered, and 1.0ml was transferred into a 100ml volumetric flask using water to obtain a solution at $15gmL^{-1}$. A calibration curve with five points, in the range from 5 to 25 gmL^{-1}, was produced at the wavelength of 270 nm. (ICH Q2(R1) 2005)

A variety of analytical techniques were used to compare the physicochemical properties of the initial absorbent (HCs) and the residues obtained after adsorption experiments namely the proximate analysis of 1g of -212 µm of the sample was carried out using the Thermo Gravimetric analyser equipment (Leco TGA 701) in accordance with ASTM D5142. The FTIR analysis was conducted on a spectrometer Perkin Elmer Spectrometer coupled with a diamond attenuated total reflectance accessory in the wavenumber range between 4000 and 450 cm^{-1}. The interpretation of the spectra was performed based on reference tables provided by Smith Brian (2018). The Scanning Electron Microscopy (SEM) was done using Carl Zeiss Sigma Field Scanning Electron Microscope connected to the Oxford X-act EDS detector. The analysis was carried out in this procedure according to the operational mode of the equipment. The SEM/EDS analysis settings was on 10 kV and a working distance (WD) of 7.2-8.2 mm using backscattered electrons (BSE) signal. The SEM/EDS analysis provided the surface structure and the homogeneity of the samples (Kong *et al*., 2019). The porous properties were obtained from Brunauer Emmet Teller analysis (BET) using nitrogen adsorption test at 77 K. For BET analysis, the autosorb iQ gas sorption instrument (Quantachrome Instruments, USA) was used while the Quantachrome® ASiQwinTM software which interfaces the autosorb iQ to a computer was used for data acquisition and data reduction.

5.5. RESULTS AND DISCUSSION

5.5.1. HTC and Co-HTC statistical analysis

Table 1 shows the optimum parameters evaluated using design of experiment (DoE version 13) on the HTC (coal tailing and coal slurry) and Co-HTC (coal sewage sludge blend) experimental results obtained from proximate analysis. From the ANOVA, the regression models (equations 5-2, 5-3 and 5-4) developed using response surface methodology (RSM) for HTC and optimal combined methodology (OCM) for Co-HTC were then used to assess the impact of the process factors on the fixed carbon (FC)of the produced hydrochar (HCs). Due to the high F-value and low p-value, the results show that all models are of statistical significance (Abdulsalam Jibril *et al*., 2019). Temperature, pressure and residence time and the coal-sewage sludge blend ratio all influenced the FC of the HCT, HCS and HCB produced. The regression models obtained from RSM of the HTC and OCM of Co-HTC experimental data revealed that

temperature and the coal-sewage sludge blend ratio are the most significant model terms.

$$HCT\ Fixed\ Carbon = 37.66 - 1.20A + 0.1090B + 0.0040C - 0.0837AB - 0.0388AC + 0.0337BC + 1.04A^2 + 0.113B^2 - 0.2714C^2 \quad (5\text{-}2)$$

$$HCS\ Fixed\ Carbon = 53.01 - 3.29A + 0.5520B - 0.3410C \quad (5\text{-}3)$$

$$HCB\ Fixed\ Carbon = 30.46A + 45.36B + 55.13AB + 9.11AC + 6.58AD + 13.69AE - 0.6847BC - 0.1279BD - 4.28BE - 15.83ABC - 10.52ABD + 14.57AB \quad (5\text{-}4)$$

Where A is the temperature, B the pressure, C the time, D the mass of sewage sludge (SS), and E the mass of the mixture of coal tailing and coal slurry (CT+CS).

The effects of operating conditions on the FC of produced hydrochars (HCs) are depicted in Figures 5-2 & 5-3. The curvature seen in Figure 5-2A, and Figure 5-3 describes the significant impact of the interaction between the HTC and Co-HTC parameters. A linear slope observed in Figure 5-2B indicates insignificant interactions (high p-values > 0.2) between the HTC of CS process parameters. As a result, quadratic and linear models accurately fitted the HTC of CT, Co-HTC of CB, and HTC of CS, respectively. Temperatures above 150°C reduce the FC of the produced HCT and HCS. However, increasing the temperature to 208°C and the (CT+CS): SS ratio to 5:1 increases the FC of the produced HCB. The results shown in Figure 3 show that an interaction effect of reaction temperature and coal-sewage sludge mass ratio had a significant effect on the FC of produced HCB.

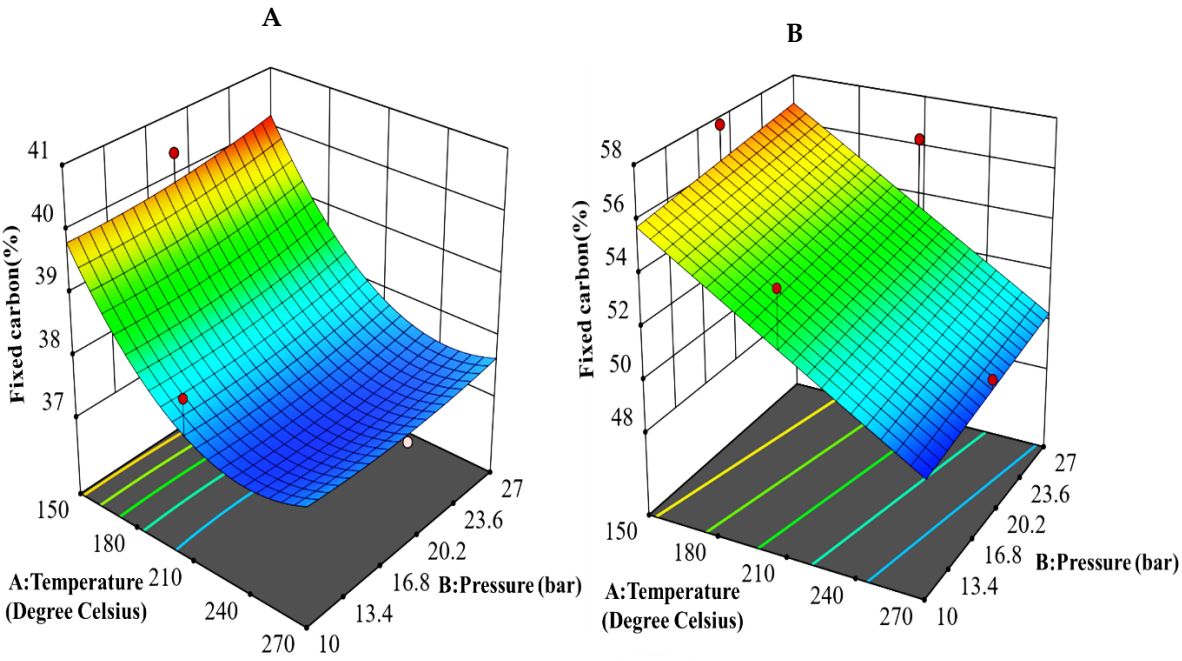

Figure 5-2: Surface plot showing the influence of temperature and pressure on the Fixed Carbon of Coal tailing's HC (A) and Coal slurry's HC (B).

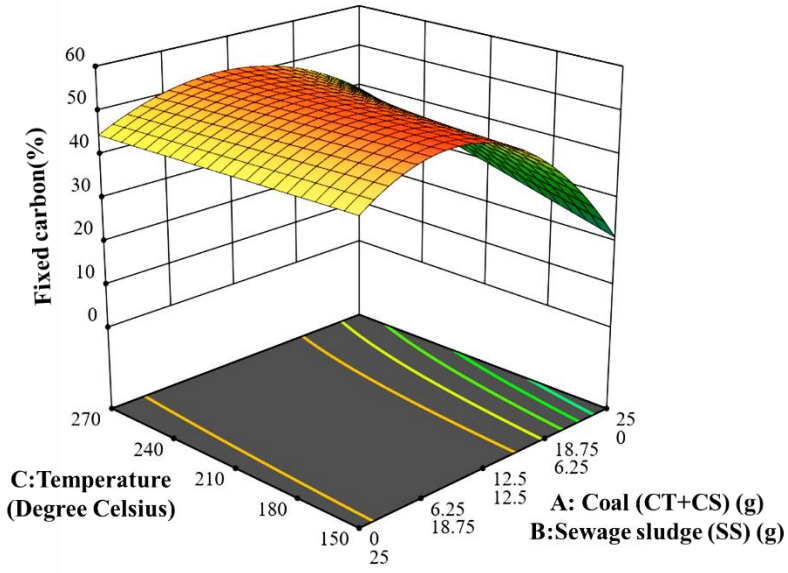

Figure 5-3:Surface plot showing the influence of temperature, pressure, time and the (CT+CS): SS ratio on the Fixed Carbon of produced hydrochar.

5.5.2. HTC and CO-HTC optimum operating conditions

Optimization of input factors and response surface constraints concluded the analysis and evaluation of the resulting data. The goal was to assess the input variables in order to maximize FC for the generated HCs. The input parameters for the HTC process ranged from 150°C, 10 bar, and 10 minutes as lower values and 270°C, 27 bar, and 180 minutes as upper limits. On the other hand, the Co-HTC produced optimization

solutions were established using input factors of 150°C, 10 bar, 10 minutes, and 0:25g (CT+CS: SS) as lower limits and 270°C, 27 bar, 360 minutes and 25:0 g (CT+CS: SS) as upper limit. The conditions that produced the highest desirability factor were selected as the optimum process parameters. The optimum HTC conditions obtained were 150°C, 27 bar, and 92.13 minutes, while the ideal Co-HTC conditions were 208°C, 22.5 bar, 331 minutes, and 20.02:4.98 (CT+CS: SS mass ratio). Results in Table 5-1 show that the optimized predicted results were in agreement with the experimental measurement.

absolte error (POAE) (fraction)= (Experimental-Predicted)/Experimental (5-5)

However, results from this study are more conservative than those obtained in previous research that used a different feedstock to optimize HTC and Co-HTC operating conditions (Afolabi *et al*., 2020). But still the implemnetation of the optimal conditions found in this study could have a significant positive effect on the economics of the HTC and Co-HTC process, and so this work lays the groundwork for the development and economic feasibility of the operating conditions used for other similar thermal processes, like pyrolysis and gasification (Tsai *et al*., 2012).

Table 5-1. Hydrothermal carbonization and Co- Hydrothermal carbonization optimum operating solutions.

Name	HCT	HCS	HCB	POAE
Parameters				
Temperature (°C)	150	150	208.70	0-0.33
Pressure (bar)	27	27	22.55	0-0.22-
Time (Min)	92.13	10	331.02	0.35-7.4
CT+CS: SS	-	-	20.02:4.98	1.96
Results (%) on a dried basis				
Ash content	38.13	21.12	17.43	0.07 – 1.09
Fixed Carbon	40.20	57.19	58.88	0.5 – 1.21
Volatile Matter	21.67	21.69	23.69	1.08 – 0.37
Mass yield	96.18	96.05	84.67	1.35 - 2.00

HCT: Coal tailing's hydrochar. HCS: Coal slurry's hydrochar. HCB: hydrochar from the Co-HTC of coals and sewage sludge. SS: Sewage sludge. POE: Percentage of absolute error.

5.5.3. Adsorption results

Table 5-2 presents the results of the NEV, and LAM adsorption experiments conducted with the synthesised HCs. The uptakes result for the different HCs (HCT, HCS, and HCB) are shown in Figures 5-4 (a) and (b), respectively. The highest uptake of NEV and LAM were achieved at 90 minutes and an adsorbent concentration of 100g/l. For all the tested HCs, increasing the process time (t) and lowering the adsorbent concentration improves NEV and LAM uptake. This is in line with Yang's (2007) finding that as process time and adsorbate concentration increase, the proportion of saturation in the adsorption process increases (Yang *et al.*, 2007). This happens because of the adsorbate remaining in contact with the adsorbent surface for a long time (Madan *et al*., 2017). The adsorbate had eventually saturated the porous media as there was a plateau after 90 minutes (Figure 5- 4(b)). Additionally, as the adsorbent concentration increase the uptakes of NEV and LAM on all HCs used decreased. The higher the adsorbent concentration, the less readily dissolved drugs move from the liquid (AS) to the solid pores (HC), and the stronger the driving force of liquid adsorption into the solid (HC) (Luan *et al*., 2020).

Table 5-2. Experimental results of NEV and LAM adsorption on the produced hydrochars.

Adsorbent (HC) concentration and residence time	HCT						HCS						HCB					
	NEV (μgL^{-1})	STD	pH	LAM (μgL^{-1})	STD	pH	NEV (μgL^{-1})	STD	pH	LAM (μgL^{-1})	STD	pH	NEV (μgL^{-1})	STD	pH	LAM (μgL^{-1})	STD	pH
Raw solution	5.53		5.58	4.58		5.34	5.53		5.58	4.58		5.34	5.53		5.58	4.58		5.34
HCs concentration (gL^{-1}) for a residence time of 90 minutes																		
10	3.87	1E-03	5.83	3.37	1.8E-03	5.44	4.42	2.3E-03	5.67	3.87	1.7E-03	5.48	3.81	2.7E-03	5.67	4.13	2.1E-03	5.46
25	2.41	1E-03	6.02	2.35	1.8E-03	5.76	3.98	2.3E-03	5.94	3.61	1.7E-03	5.61	1.94	2.7E-03	5.89	3.16	2.1E-03	5.59
50	0.81	1E-03	6.21	1.63	1.8E-03	5.98	1.18	2.3E-03	6.17	1.94	1.7E-03	6.01	0.65	2.7E-03	6.05	0.96	2.1E-03	5.77
100	0.53	1E-03	6.38	0.37	1.8E-03	6.08	0.33	2.3E-03	6.42	0.47	1.7E-03	6.17	0.15	2.7E-03	6.1	0.30	2.1E-03	5.84
300	0.68	8.1E-03	6.52	0.47	1.8E-03	6.14	0.44	2.3E-03	6.48	0.55	1.7E-03	6.25	0.26	2.7E-03	6.22	0.40	2.1E-03	5.91
Time (minutes) for a HC concentration of 100 gL^{-1}																		
10	1.57	8.1E-03	5.92	2.75	1.8E-03	5.59	2.60	2.3E-03	6.08	2.37	1.7E-03	5.79	1.27	2.7E-03	5.67	1.66	2.1E-03	5.48
30	0.77	1E-03	6.12	0.96	1.8E-03	5.87	1.35	2.3E-03	6.24	0.78	1.7E-03	6.05	0.62	2.7E-03	5.88	0.75	2.1E-03	5.61
90	0.53	1E-03	6.38	0.37	1.8E-03	6.08	0.33	2.3E-03	6.42	0.47	1.7E-03	6.17	0.15	2.7E-03	6.11	0.30	2.1E-03	5.84
180	0.53	1E-03	6.38	0.37	1.8E-03	6.08	0.33	2.3E-03	6.42	0.47	1.7E-03	6.17	0.15	2.7E-03	6.11	0.30	2.1E-03	5.84
360	0.53	1E-03	6.38	0.37	1.8E-03	6.08	0.33	2.3E-03	6.42	0.47	1.7E-03	6.17	0.16	2.7E-03	6.11	0.30	2.1E-03	5.84

HCT: Coal tailing's hydrochar. HCS: Coal slurry's hydrochar. HCB: hydrochar from the blend of coal tailing, coal slurry and sewage sludge. NEV: Nevirapine. LAM: Lamivudine. HC/AS: hydrochar-aqueous solution (charged with inhibitor drugs dissolved) solid/liquid ratio. STD: Standard deviation.

The results demonstrate that the HCB has a higher drugs uptakes performance (5.37 $\mu gL^{-1}$of NEV and 4.2737 μgL^{-1} of LAM) than the HCT and HCS. This may be due to HCB's higher porous textural structure (high S_{BET} and pore volume). In all cases, NEV uptake was higher than LAM uptake under the similar operating conditions. This could be attributable to NEV's higher capillary uptake degree in aqueous solution compared to LAM. Overall, the highest NEV and LAM uptakes were 90.32% and 91.78% for HCT, 93.97% and 89.67% for HCS, and 97.19% and 93.32% for HCB.

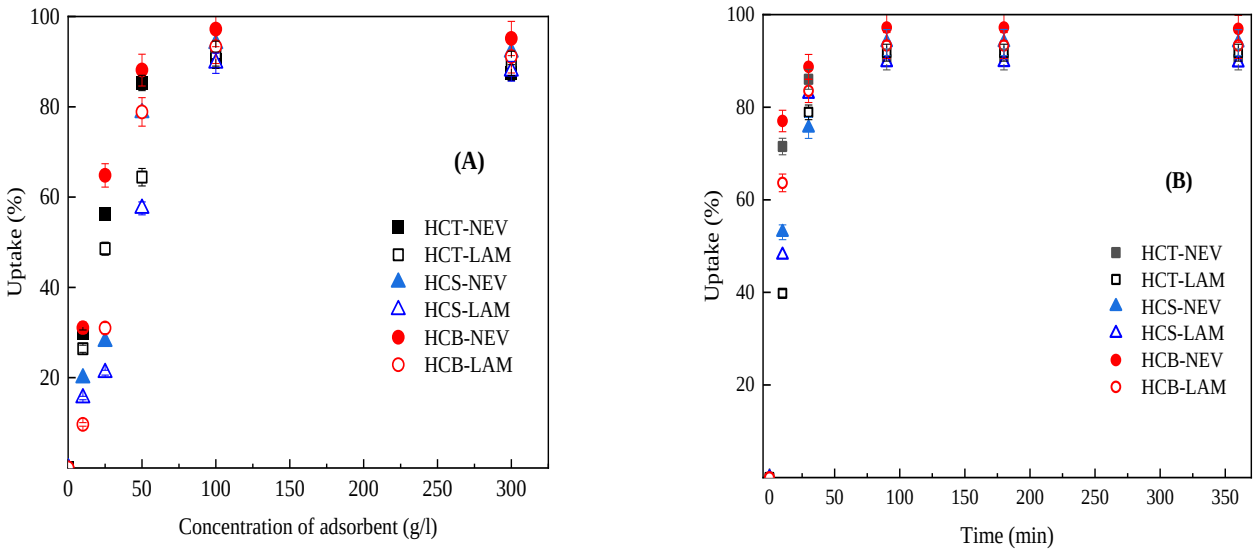

Figure 5-4 :Percentage variation of LAM and NEV into the produced hydrochars versus the concentration of adsorbent (a) and residence time (b).

The results obtained showed that the HCB owned the highest NEV and LAM uptake efficiency (Figure 5-4). Hence, the GC-MS analysis was performed on the final filtrates from HCB adsorbent to identify the remaining organic elements dissolved. Tables 5-3 and 5-4 demonstrate that the final adsorbates include fewer dissolved organic components than the antiretroviral-seeded solutions. Organic acids, sugars, and methyl compounds were among the organic molecules identified in traces in the final adsorbates. Further chemical analysis of the dissolved organic molecules in the final adsorbates revealed a preponderance of acid, aromatic, alcohol, and esters compounds,

as well as modest levels of aliphatic hydrocarbons (Tables 5-3 and 5-4). The organic chemicals are produced when NEV and LAM breakdown (dissolve) in water, and it is anticipated that their presence in discharge water will pose environmental risks to possible receiving waterbodies (Abafe *et al*., 2018). The most abundant organic acids were hexadecanoic acid, propanoic acid, 2-hydroxy, and 9,12-0ctadecadienoic acid, followed by l-l -Cyclopropyl-4-methyl-5,11-dihydro-6H, 6-0xa-bicyclo [3.1.0] hexan-3-one, and hexadecanoic acid. As depicted in Fig. 4, the GC-MS outcomes for LAM adsorption followed the same pattern as NEV adsorption (higher adsorption performance of HCB). In the adsorbate of LAM, hexenoic acid, methyl and heptadecyl ester, heptanol, 1,2,3-propanetriol, and alkanes were the most common organic molecules. The GC-MS analysis reveals a slightly more extensive dispersion of organic compounds for both NEV and LAM, and the presence of organic components in the final adsorbates likely indicates the necessity for an additional removal stage before contaminated water is released into bodies of water. The chemical identification of dissolved organic compound reveals the predominance of acid, aromatic, alcohol, esters compounds and low aliphatic hydrocarbons in all produced filtrates (Appendix H, I, J and K).

Table 5-3.Organic compounds in filtrate from NEV adsorption by HCB.

Initial solution from the Mixture (HCB+ Nevirapine)				Final solution after adsorption (HCB +Nevirapine)		
Peak	Retention Time (minutes)	Organic compound Name	Conc (%)	Retention Time (minutes)	Organic compound Name	Conc (%)
1	3.287	Cyclotrisiloxane, hexamethyl- (CAS)	4.19	11.536	Hexadecanoic acid (CAS)	26.19
2	3.412	Cyclotrisiloxane, hexamethyl- (CAS)	21.28	12.515	9,12-0ctadecadienoic acid (Z, Z) - (CAS)	35.02
3	3.557	Propanoic acid, 2-hydroxy- (CAS)	4.15	12.615	Octadecanoic acid	23.82
4	3.655	DIHYDROXYACETICACID	0.93	12.899	Hexadecanoic acid, (3-bromoprop-2-ynyl	2.7
5	3.72	Propanal, 3-ethoxy- (CAS)	1.01	13.018	Hexadecanoic acid, 1-[(2-aminoethoxy)	1.52
6	4.382	Propanoic acid, 2-hydroxy- (CAS)	19.64	13.495	Cis-11-Eicosenoic acid	0.97
7	4.72	trisiloxane, 1,1,1,5,5,5-hexamethyl-3	0.84	13.596	Eicosanoic acid	1.89
8	4.765	Cyclotetrasiloxane, octamethyl- (CAS)	7.61	13.72	SII.1CONE OIL	0.48
9	4.948	1,3-Dioxane (CAS)	2.19	13.809	9,12-0ctadecadienoyl chloride, (Z,Z)-	0.67
10	6.025	0-TRIS-TRIMEfHYLSILYI.rEPIN	0.97	13.94	Cis-9-Hexadecenal	0.98
11	6.098	Cyclopentasiloxane, decamethyl- (CAS)	4.5	14.344	11-Cyclopropyl-4-methyl-5, ll -dihydro-6.	3.76
12	6.87	3,3,5-Triethoxy-1,1,1,7,7,7-hexamethyl-5	0.33	15.003	Silane, dimethyl(dimethyl(3-methylpentyl	0.38
13	7.461	Cyclohexasiloxane, dodecamethyl	2.18	17.538	Docosane (CAS)	0.33
14	8.695	3-Ethoxy-1,1,1,7,7,7-hexamethyl-3,5,5	0.51	18.814	Tetratetracontane (CAS)	0.68
15	8.86	1-Butylimidazole	3.39	20.38	Tetratetracontane (CAS)	0.61
16	8.915	Emylcamate	1.7			
17	8.985	N-(4-ISOPROPYLBENZVL) -N,1-DIME	1.51			
18	9.794	trimethylsilyl [2,3-di(trimethylsiloxy)pher	0.84			
19	10.035	Chloro(dimethyl)phosphine	0.29			
20	10.125	Erythro-dl-0-ethylthreonine	0.28			

21	10.734	Trimethylsilyl) -{bis[methyl(trimethylsilyh	0.36	
22	11.572	3-Butoxy-1,1,1,7,7,7-hexamethyl-3,5,5	0.59	
23	11.65	Histidine, 4-chloro-2-trifluoromethyl	0.46	
24	12.155	1-Methyl-l-n-tetradecyloxy-1-silacyclope	0.27	
25	12.23	Alpha-(N-methoxy-N-(2;1.;l.-trifluoroethoi	0.62	
26	12.338	1,1,1,3,5,7,7,7-0ctamethyl-3,5-bis (trime	0.68	
27	12.83	Acetamide, N-(2-cyano4,5-dimethoxypht	0.56	
28	12.945	Silane, l,l'-[oxybis(methylenesulfonyl-2,1	0.68	
29	12.985	Carbonic acid, isohexyl 2;1.;1.-trichloroeth	0.57	
30	13.025	EICOSAMETHYLCYCLODECASILQ)	0.77	
31	13.185	Succinylacetone diethoxime, trimethylsily	0.29	
32	13.265	Pentanoic acid, butyl ester (CAS)	0.29	
33	13.373	Morpholine, 4-(2,4-dinitrophenylbenzoyl)	0.63	
34	13.585	d-Altronic acid	0.32	
35	13.67	Butyl heptanoate	0.56	
36	13.719	Heptasiloxane, hexadecamethyl	1.07	
37	14.03	N-Acetyl- alpha-aminooxy-propionic acic	0.45	
38	14.392	Benzene, (1-methoxyethenyl)	0.65	
39	14.501	Heptasiloxane, hexadecamethyl-(CAS)	0.62	
40	15.314	5-Chloro-IH-l;1.,4-triazole-3-carboxamid	0.42	
41	15.435	Benzeneacetic acid, alpha.,3,4-tris[(trime	1.55	
42	15.855	(1-methylethyl} -thiirane	0.36	
43	15.92	Ethyl 2-nitropropionatc	0.62	
44	17.548	Nonane, 5-(1-methylpropyl} -	0.93	
45	18.824	Hepladecane, 2,6,10,15-tctramcthyl- (CA	2.94	

46	20.26	D-Glucose, 6-acctamido-6-deoxy-, diethy	0.61	
47	20.398	Sulphurous acid, octadccyl 2-propyl ester	2.2	
48	20.47	1-Phenazinecarboxylic acid, 6-[l-[(l-oxo)]]	0.28	
49	22.255	1,2,4-Triazolo[3,4-a] phthalazine-7-hydrn	0.26	
50	22.318	Octadccane, 5-methyl	1.05	
			100	

Conc: concentration.

Table 5-4.Organic compounds in filtrate from LAM adsorption by HCB.

Initial solution from the Mixture (HCB+ Lamivudine)				Final solution after adsorption (HCB+ Lamivudine)		
Peak	Retention Time (minutes)	Organic compound Name	Conc (%)	Retention Time (minutes)	Organic compound Name	Conc (%)
1	3.34	Cyclotrisiloxane, hexamethyl- (CAS)	1.54	3.35	Cyclotrisilox ane, hexamethyl- (CAS)	0.29
2	3.375	3,4-Dimethylbenzoicacid, TBDMS deri•	0.7	3.518	Cyclotrisiloxane, hexamethyl- (CAS)	0.56
3	3.441	Cyclotetrasiloxane, octamethyl- (CAS)	8.83	4.81	Cyclotetrasiloxane, octamethyl- (CAS)	0.24
4	4.56	Cyclotetrasiloxane, octamethyl- (CAS)	0.54	5.467	1,2,3-Propanetriol (CAS)	98.52
5	4.63	BENZENE, (1,1-DIMETHYLETI YL)	2.55	6.28	Disiloxane, l, l,3,3-tetramethyl-l,3-bis[3]	0.39
6	4.704	Tridecane (CAS)	2.11			
7	4.792	Cyclotetrasiloxane, octamethyl- (CAS)	7.76			
8	5	Butyric acid, 2-phenyl-, hept-2-yl ester	1.06			
9	5.364	Heptane, 5-ethyl-2-methyl-(CAS)	1.3			
10	5.44	Ethyl neopentyl carbonate	0.47			
11	5.612	l-MEfHYL-2-PHENYLCYCLOPROPJ	3.03			
12	5.718	Undecane (CAS)	1.81			
13	6.099	Cyclopentasiloxane, decamethyl- (CAS)	0.66			
14	6.153	Cyclopentasiloxane, decamethyl- (CAS)	0.84			

15	6.757	Dodecane (CAS)	2.9	
16	6.875	Carbonic acid, 2-ethoxyethyl neopentyl {	0.63	
17	7.165	Oxalic acid, hexyl neopentyl ester	0.76	
18	7.19	2-Propyl-5-oxohexanoic acid	0.86	
19	7.234	1-Heptadecanamine (CAS)	2.81	
20	7.465	CYCLOHEXASILOXANE, OODECM	1.1	
21	7.531	Tridecane (CAS)	4.51	
22	8.011	Tetradecane (CAS)	1.59	
23	8.269	Hexadecane (CAS)	2.32	
24	8.33	5-Allyl-6-methyl-2-phenyl-5,6-dihydro-4	0.54	
25	8.695	(E)-2-[(tert-butyl) dimethylsily! J-2- [l'-me	1.93	
26	8.746	Octadecane, l,1'- [1,3-propanediylbis (ox)	0.95	
27	8.941	Pentadecane (CAS)	3.08	
28	9.144	1-Bromo-3,7-dimethyloctane	0.57	
29	9.235	Decanoic acid, nonyl ester	0.59	
30	9.264	PENTASIWXANE, 1, l,3,3,5,5,7,7,9,9-	1.6	
31	9.42	Dodecane, 1,2-dibromo- (CAS)	0.51	
32	9.583	Pentadecane (CAS)	2.12	
33	10.198	Heptadecane (CAS)	2.31	
34	10.435	Tridecane, 6-propyl-	1.92	
35	10.575	3beta,17beta-Diacetoxy-17-isopregn-5-e	0.45	
36	10.772	Octadecane (CAS)	1.29	
37	10.875	9-Oxa-10-thiatricyclo [3.3.I. I (2,7) Jdecar	0.63	
38	11.019	Undecane, 6-ethyl-	0.73	
39	11.105	(-) -Isopulegol	0.51	
40	11.161	DIMETHOXYGLYCEROLDOCOSYL	0.55	
41	11.324	Tricosane (CAS)	1.06	
42	11.843	NONADECANE	1.57	
43	12.346	Tetradecane (CAS)	1.07	
44	12.825	Heptacosane (CAS)	0.69	
45	12.91	Pentasiloxane, 1,1,3,3,5,5,7,7,9,9-decam	0.5	
46	13.01	1-Hcptcnc, 2,6,6-trimethyl-	0.7	

47	14.433	11-Cyclopropyl-4-methyl-5, l l--dihydro-t	21.89	
48	15.435	Benzene, 1-(1, l-dimethylcthyl) -4-(2-ethyl	0.44	
49	18.775	Pentasiloxanc, dodecamethyl-(CAS)	0.55	
50	19.056	3-Thiazolidinccarboxamidine, 2-imino-	0.57	
			100	

Conc: concentration.

5.5.4. Proximate, ultimate, and BET analysis

Table 5-5 provide the proximate and ultimate analysis results of CT, CS, SS, selected hydrochar (HCs) from hydrothermal carbonization (HTC) and Co-hydrothermal carbonization (Co-HTC), and adsorbent residues from the adsorption process under optimal conditions. The HTC and Co-HTC processes proved the ability of enhancing the fixed carbon content of raw materials by releasing mineral matter, oxygen, and sulphur from their molecular structures (Saba *et al*., 2017; Ali Akbari *et al*., 2021). The HTC and Co-HTC processes increased the FC concentration of the raw samples in order to produce hydrochar. The optimum HTC and Co-HTC conditions maintained the liquid state of water and promoted the hydrolysis of aliphatic components, dissolution, and release of mineral materials, resulting in the formation of porous solids (Yoshikawa *et al*., 2014). In addition, the optimum HTC and Co-HTC conditions retained a considerable amount of the atomic carbon content of the feedstock in the solid HC produced, validating the HTC and Co-HTC process's potential for sequestration and repolymerization (Lu *et al*., 2021). The rise in total carbon content in the generated HC may be related to a decrease in hydrogen, oxygen, and total sulphur contents (Table 5-5), while the decrease in sulphur content in the produced hydrochar likely contributes to the enlargement of pores (Channiwala *et al*., 2002). Following the adsorption process, the nitrogen adsorption isotherms of synthesized fresh HCs and spent HCs residues exhibited a decrease in the amount of nitrogen absorbed (Figure 5-5). This confirmed that pores formed during HTC and Co-HTC synthesis of HCs were occluded (Thunshirn

et al., 2022). Figure 5-6 to figure 5-8 demonstrate that the lateral interaction between dissolved drugs molecules and HCs likely contributed to a change in the surface texture of the absorbent. It is also likely that drug molecules repopulate the mesopores created when the initial sulphur and oxygen content is oxidized. As seen in Table 5-5, this decreases the SBET and total pore volume of HCs in the ensuing spent residues.

Table 5-5 illustrates the increase in volatile matter (VM) and total carbon in the spent residues' comparative to the source materials and the synthesized HCs. This provides evidence of NEV and LAM dissolved adsorption on HCs. The NEV and LAM are organic compounds with cyclic carbon structures incorporating nitrogen and sulphur, especially in the case of LAM (Olabode *et al*., 2019). As a result of their adsorption on HCs, the nitrogen and total sulphur content of the solid residues increase.

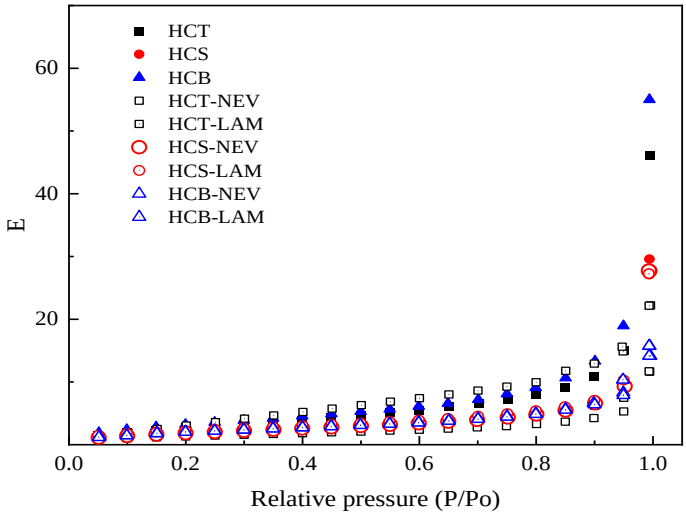

Figure 5-5: Isothermal adsorption plots of raw materials produced hydrochar and spent adsorption residues

Table 5-5.Physicochemical properties of wastes precursors produced hydrochar and spent residues from NEV and LAM adsorption.

Analyses	CT	HCT	HCT-NEV	HCT-LAM	CS	HCS	HCS-NEV	HCS-LAM	SS	CB	HCB	HCB-NEV	HCB-LAM
Proximate Analysis (wt%, adb)													
Inherent Moisture	4.17	1.07	1.81	1.04	3.94	1.73	1.58	1.26	8.12	2.71	1.72	1.76	1.45
Ash content	38.64	37.96	33.12	33.96	23.22	22.78	19.78	16.78	36.07	37.75	19.56	13.56	19.56
Volatile Matter	21.44	21.04	22.86	24.49	21.28	18.38	19.2	23.72	47.07	21.92	20.31	22.16	25.26
Fixed Carbon	35.75	39.94	42.21	40.51	50.98	57.11	59.44	58.24	8.75	37.62	58.41	62.52	60.73
Ultimate Analysis (wt. %, adb)													
Total Carbon	42.82	49.80	55.23	53.98	61.85	66.90	70.90	69.45	29.7	45.64	67.04	73.85	68.44
Hydrogen	3.01	2.87	2.42	2.39	3.56	2.98	2.28	2.41	4.88	3.05	2.78	1.75	1.57
Nitrogen	1.14	1.72	2.74	2.66	1.39	1.99	2.63	2.84	4.15	1.82	2.43	3.05	2.95
Oxygen	8.79	5.83	3.9	4.21	4.78	2.75	1.91	3.99	15.22	8.2	6.08	5.29	4.15
Total Sulphur (wt. %, adb)	1.43	0.75	0.78	1.76	1.26	0.87	0.92	1.27	1.86	0.83	0.39	0.74	1.88
BET analysis													
S_{BET} (m^2/g)	6.066	11.82	0	0	6.37	14.35	0	0	-	6.17	20.35	0	0
Total pore volume (cm^3/g)	0.034	0.071	0	0	0.048	0.094	0	0	-	0.09	0.38	0	0

CT: Coal Tailing. CS: Coal Slurry. SS: Sewage sludge. CB: Blend (CT+CS: SS). HCT: CT's hydrochar. HCS: CS's hydrochar. HCB: CB's hydrochar, HC-NEV: residue from nevirapine's adsorption. HC-NEV: residue from nevirapine's adsorption. HC-LAM: residue from lamivudine's adsorption. adb: air dried basis. $\text{Oxygen}\% = 100 - (\text{Inherent moiture} + \text{Ash} + \text{Total Carbon} + \text{Hydrogen} + \text{Nitrogen} + \text{Total sulphur})$. BET: Brunauer Emmet Teller. SBET: Specific surface area

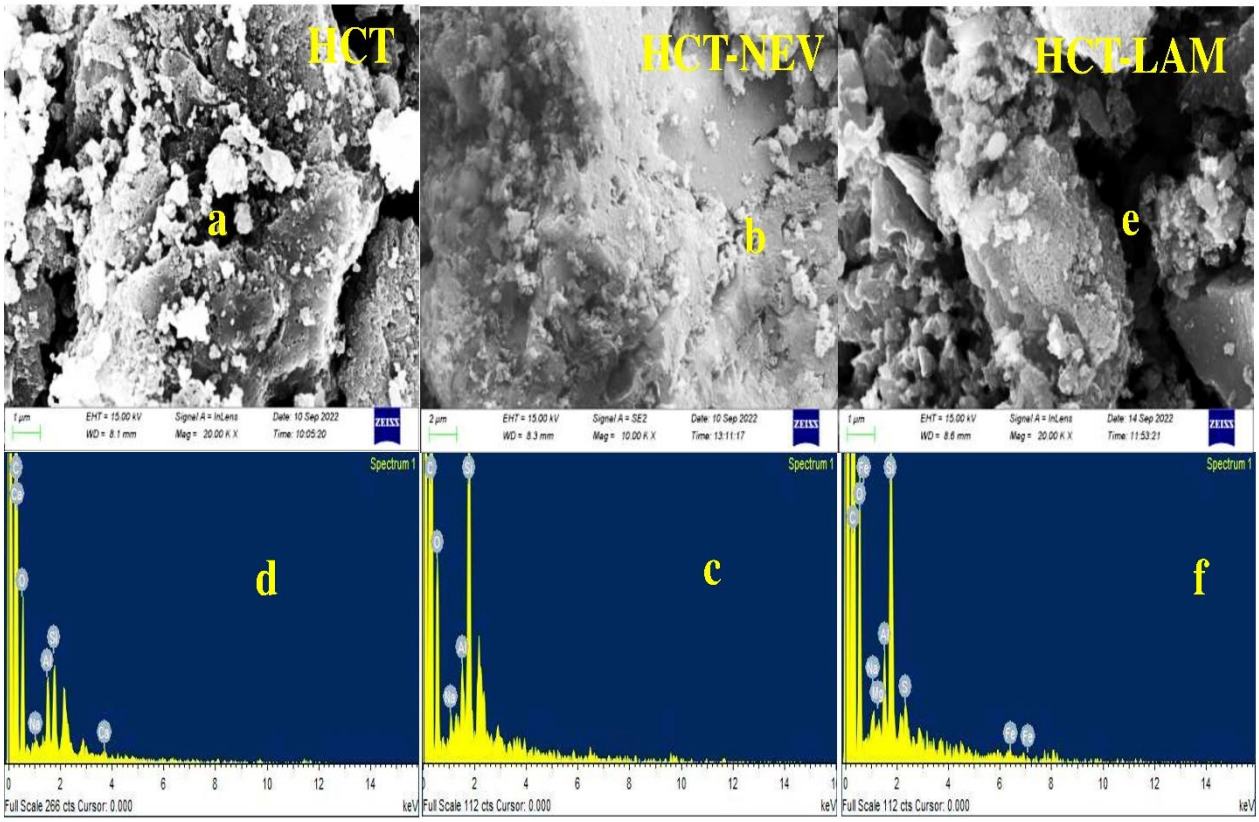

Figure 5-6:SEM images and EDS elemental spectrums of coal tailing's hydrochar (HCT) and spent residues from nevirapine (HCT-NEV) and lamivudine (HCT-LAM) absorption.

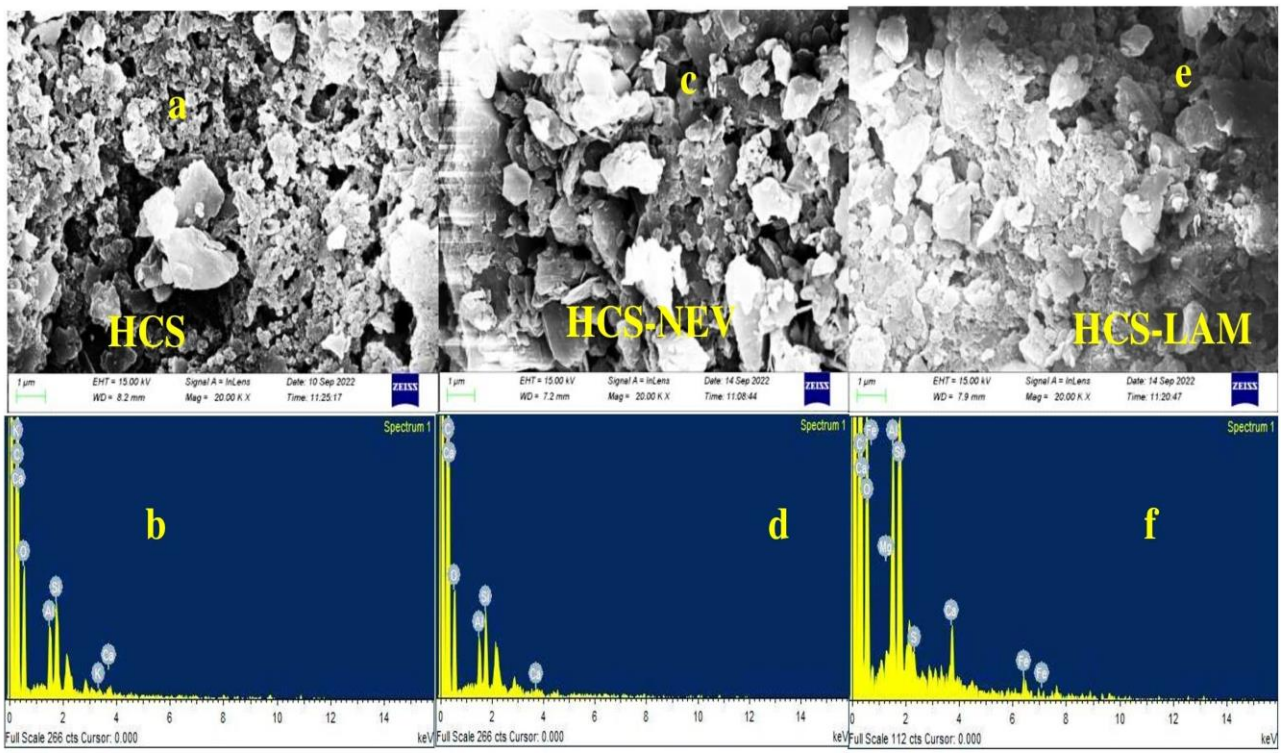

Figure 5-7:SEM images and EDS elemental spectrums of coal slurry's hydrochar (HCS) and spent residues from nevirapine (HCS-NEV) and lamivudine (HCS-LAM) absorption.

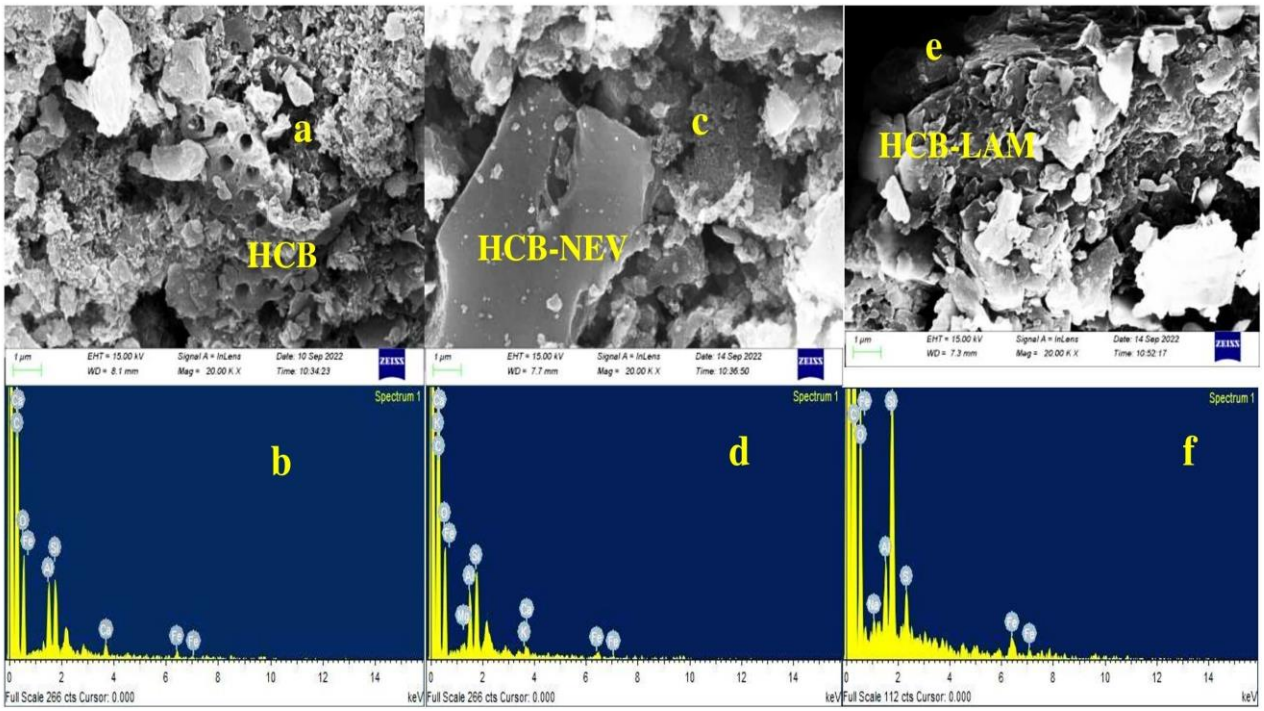

Figure 5-8:SEM images and EDS elemental spectrums of coals and sewage sludge blend's hydrochar (HCB) and spent residues from nevirapine (HCB-NEV) and lamivudine (HCB-LAM) absorption.

The FTIR spectra of NEV and LAM provided by John Wiley &Sons (2022) in Figure 5-9 A and B were used as a reference to illustrate the changes of the chemical structural features of the hydrochar after adsorption of the drug molecules (Figure 5-10, 5-11 and 5-12) (Solomons.2022). Spectra were interpreted using reference tables supplied by Smith Brian (2018). The enhanced peaks at wavelengths between 1700 cm^{-1} and 1350 cm^{-1} observed on Fig 10, 11 and 12 indicated NEV and LAM adsorption. The adsorption peaks identified at the wavelengths 3250 cm^{-1}, 3000 cm^{-1}, and 2250 cm^{-1} were attributed to the absorbed NH_2, aliphatic C-H, and S-H stretch characteristics of the decomposition of NEV and LAM in water. The broad adsorption peaks of S-H stretch vibration validated the better performance of HCB for the adsorption of LAM (Figure 5-12), followed by HCT (Figure 5-10) and then HCS (Figure 5-11). According to Table 5-5, the high porosity of HCB enhanced its absorption capacity. The peaks found at 1650 cm^{-1}wavelength suggested the existence of double-bound carbonyl groups (C=O) associated with aromatic stretch, confirming the presence of cyclic hydrocarbons with carbonyl attached from NEV and LAM (Mishra *et al*., 2018). At 1600 cm^{-1} bands, which correspond to aromatic rings in the NH_2 scissor structure, HCT-LAM has the highest peak intensity, followed by HCB and HCS (Figure 5-10). This demonstrated the ability of HCT to adsorb -NH_2 groups because of its polarity caused by the hydrolysis equilibrium induced by the substitution of higher -OH bending vibrations groups-of $C_{11}H_8O$ (HCT) resulting in a lower probability of hydrogen bond formation (Solomons.2022). The adsorption of -NH rings from NEV was characterized by the peaks seen at 1495 cm^{-1} and 1465 cm^{-1} in wavelength. In the HCB-NEV spectrum (Figure 5-12), the strength of the peaks was found to be greater than in the HCS (Figure 5-10) and HCT (Figure 5-11) spectra, respectively. This was owing to the increased aromatic ring presence in HCB as compared to HCT and HCS, which decreased the basicity of -NH and led to the delocalization of the lone pair of electrons on nitrogen. The displaced pair of electrons could then participate in hydrogen bonding (nitrogen alkyl groups) for the formation of imines or organic compounds containing nitrogen double bonds (Sandler.1983). At a wavelength of 1420 cm^{1}, the OH and aldehyde bend vibrations were detected in the

spectra of all residues, demonstrating the adsorption of NEV. This may be facilitated by the basic light produced by the dissolution of NEV, which promoted the substitution of CH_3 groups by OH- and aldehydes. Peaks at 1385 cm^{-1} were attributable to the symmetric deformation associated with the -CH_3 and –C-CH_3 groups formed by the interaction of hydrophobic hydrochar with the NEV (Madan *et al*., 2016). The -NH group was found at 1350 cm^{-1} in the spectra of NEV spent residues, demonstrating the connection between the aromatic ring and the dissolved amines groups of the non-nucleoside drug medication. Numerous peaks between 900 and 800 cm^{-1} correspond to aromatic species in aromatic rings, trans- and cis-CH_2 in long saturated aromatic -CH-CH chains, C-O stretching vibration of ether groups, and O-H bending vibrations in phenolic, phenoxy, and hydroxybenzene structures. The FTIR results demonstrate the expansion of existing peaks and the emergence of new peaks in spent residues revealing a complex interaction between the HCs and the adsorbates.

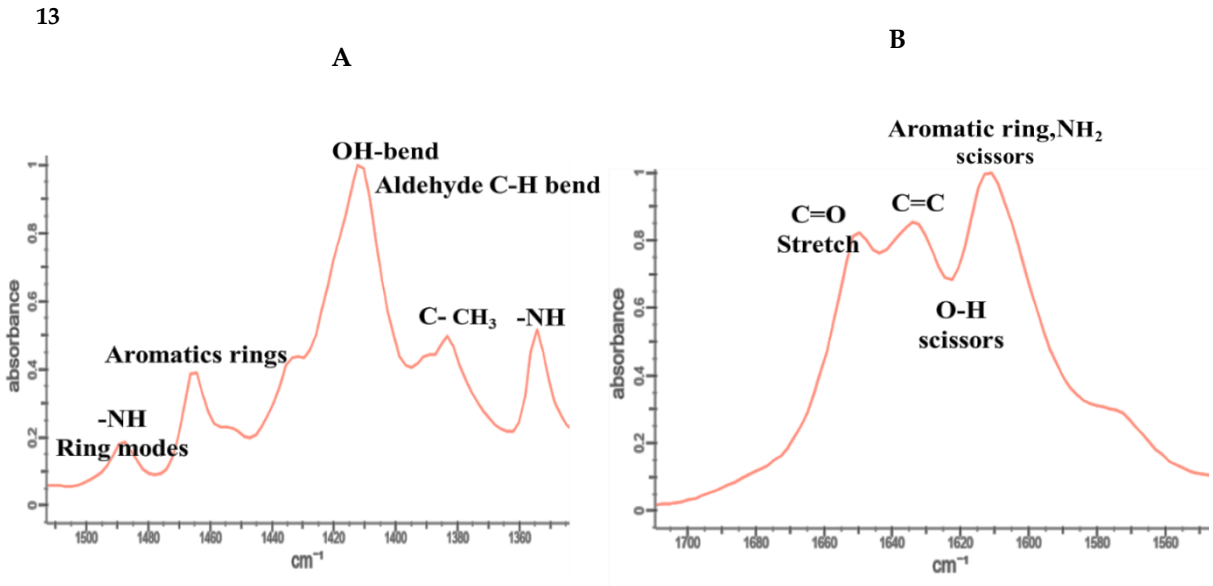

Figure 5-9:Absorbance spectra of nevirapine (A) and lamivudine (B). Source: Forensic Spectral Research John Wiley &Sons, Inc.

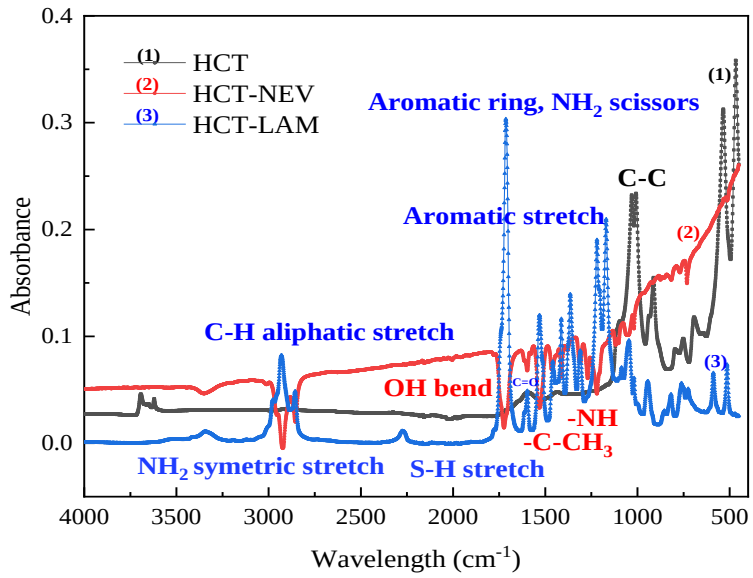

Figure 5-10:Absorbance spectra of nevirapine and lamivudine on the coal tailing's hydrochar (HCT).

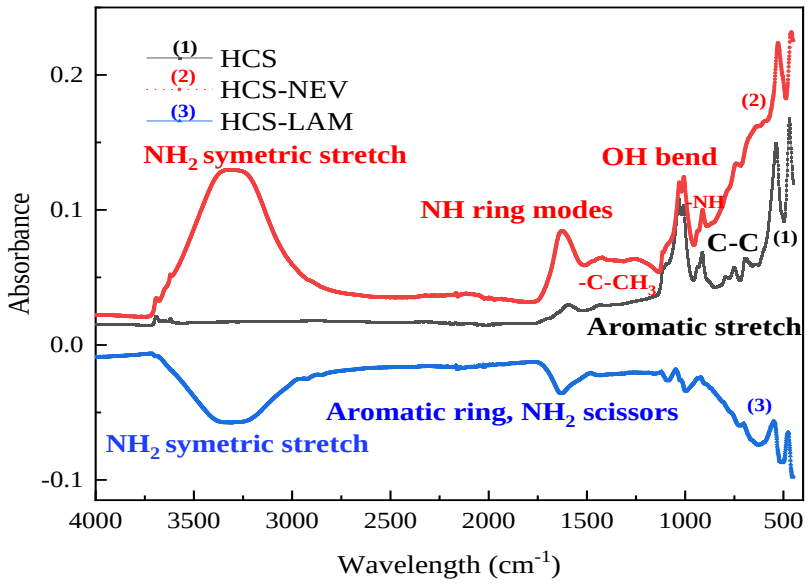

Figure 5-11:Absorbance spectra of nevirapine and lamivudine on the coal slurry's hydrochar (HCS).

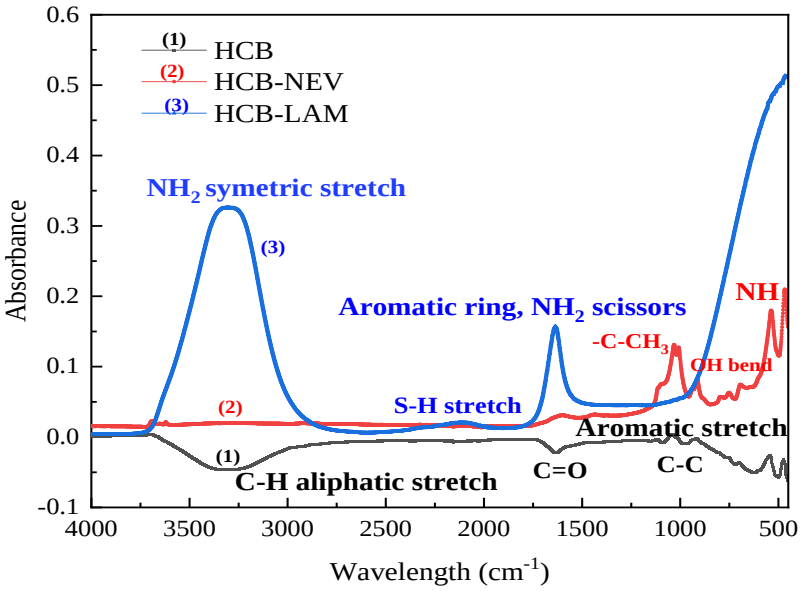

Figure 5-12:. Absorbance spectra of nevirapine and lamivudine on the hydrochar from the blend (HCB) of CD and sewage sludge (SS).

The morphological characteristics of spent adsorbent residues were compared to those of the fresh synthesized HCs. The results show that surface of the HCs (Figure 5-6a, 5-7a and 5-8a) has a more uniform porous structure than the surface of the spent residues (Figure 5-6 (c, e), 5-7 (c, e) and 5-8(c, e)), which lacked a discernible porous structure. The formed pores on the surfaces of HCs generated by HTC and Co-HTC process conditions are covered by absorbates that are roughly aggregated on their surfaces (NEV, LAM)(Figure 5-6 (c, e), 5-7 (c, e) and 5-8(c, e)), During the adsorption process, the surface structural rearrangement of HCs as seen on the surface of spent residues maybe an indication of the ability of HCs to trap drugs molecules in its mesopores (Silva *et al*., 2019). Sousa (2022) demonstrated the ability of carbon compounds (activated carbon) formed from microwave pyrolysis of brewery wastes to adsorb dissolved pharmaceuticals (sulfamethoxazole, trimethoprim, and ciprofloxacin). The study showed that the adsorption performance of the carbon material is dependent on the material's textural (porous) features and the adsorption equilibrium time. Effective contact between the adsorbent and adsorbates had an effect on the

absorbent's well-developed porous structures (0.67 cm^3 g-1). This caused a dispersed distribution of adsorbates within the pores and altered the morphological characteristics of the absorbents (Sousa *et al*., 2022). This study therefore investigated the porous qualities of the generated HCs (total pore volume of 0.071cm^3g^{-1}, 0.048cm^3g^{-1}, and 0.38cm^3g^{-1}) as a potential characteristic for their use in the adsorption of dissolved pharmaceutical contaminants. The SEM pictures of the spent residues (Figure 5-6, 5-7 and 5-8(a, c, e)) reveal the efficiency of pharmaceutical components' capture onto the pores of the absorbents as minute particles that obscure the spots on the surface of HCs. In addition, the elemental composition of the adsorption residues (Figure 5-6, 5-7 and 5-8(b, d, f)) revealed a rise in carbon, sulphur, and the appearance of nitrogen peaks in comparison to the element spectra of HCs. This indicated evidence of components absorbed from the dissolved NEV and LAM onto the pores of the HCs, correlating with the proximate and ultimate analyses.

Table 5-6. Absorbents reported for the removal of ARVDs and other pharmaceutical products in different water matrices.

Adsorbent	Adsorbate (pharmaceutical)	Adsorbent concentration (gL^{-1})	Contact time (min)	Uptake mg g^{-1}	Reference
Commercial carbon	Nalidixic acid	0.08	325	1595	Patiño *et al* (2016)
Carbon nanotube	Nalidixic acid	0.08	150	583	
Graphite	Nalidixic acid	0.08	10	62	
Akaganeite-carbon	Doxycycline	0.027	108	13.4	Zhang *et al* (2016)
Coffee residue/Fe_3O_4	Tetracycline	0.1	85.9	181	Oladipo *et al* (2016)
Bone char	Naproxen	0.01	78	0.11	Reynel *et al* (2015)
Walnut shell carbon	Cephalexin	0.1	117.1	211	Nazari *et al* (2016)
Peach stones carbon	Ibuprofen	0.01	426	55	Álvarez *et al* (2016)
	Tetracycline	0.01	1446	132.6	
Activated biochar	Ranitidine	0.2	63	12	Mondal *et al* (2016)
Akaganeite-carbon	Doxycycline	0.027	-	15	Zhang *et al* (2016)
Date stones carbon	Levofloxacin	0.15	-	2.1	Darweesh *et al* (2017)
Pomegranate carbon	Amoxicillin	0.05	-	5107	Yaghmaeian *et al* (2014)
AC from oak acorn	Paracetamol			45.45	Nourmoradi *et al* (2018)
AC from Babassu coconut				71.39	Ferreira *et al* (2015)

AC from Dende coconut				70.62	
NH_4Cl-induced AC				233	Mashayekh-Salehi and Moussavi (2016)
Acid-treated beverage sludge activated carbon				145.4	Streit *et al* (2021)
AC from vegetable	Ibuprofen			115.1	Frohlich *et al* (2018)
AC from agricultural by-product				12.6	Baccar *et al* (2012)
AC from oak acorn				96.15	Nourmoradi *et al*., (2018)
AC from vegetable	Ketoprofen			79.1	Frohlich *et al* (2018)
Acid-treated beverage sludge activated carbon				57.66	Streit *et al* (2021)
Nanofibers fabricated from Mondia whitei	ARVs	0.04	0-120	75-320	Kebede *et al* (2020)
Graphene-based material	Nevirapine	0.2	1500	48.31	Adeola *et al* (2021)
Graphene-based material	efavirenz	0.2	500	4.41	
AC from Spent brewery grains	sulfamethoxazole	0.025	60	217	Sousa *et al* (2022)
	trimethoprim	0.025	60	229.35	
	ciprofloxacin	0.025	60	205.7	
AC from primary paper mill sludge	sulfamethoxazole	0.8	-	185.14	Silva *et al* (2019)
Functionalized biochar	sulfamethoxazole	0.01		80.79	Ahmed *et al* (2017)
Graphene oxide	lamivudine	0.1	120	10.08	Lan *et al* (2022)
Molecularly imprinted polymers (MIPs)	Abacavir		60	167	Terzopoulou *et al* (2016)
Graphene wool	Efavirenz			4.41	
	Nevirapine			48.31	
Alginate, polyvinylpyrrolidone and activated carbon				44.4	Ndilimeke *et al* (2021)
	Zidovudine			42.2	
Nanofibers (Mondia White roots)	Nevirapine			200.5	Kebede *et al* (2020)
	Didanosine			75.9	
	Ritonavir			86.9	

	Efavirenz			152.1	
	Stavudine			160	
Biochar made from-olive	Abacavir			Optimum value not reported, exhibited poor removal efficiencies	Späth *et al* (2021)
Residues, tomato residues	Atazanavir				
Rice husks, and the African	Darunavir				
Palm tree Raphia farinifera	Lamivudine				
	Nevirapine				
	Raltegravir				
HCT	Nevirapine	100	90	50	**This study**
	Lamivudine			42	
HCS	Nevirapine			52	
	Lamivudine			41.1	
HCB	Nevirapine			53.8	
	Lamivudine			42.8	

HCT:Coal tailing's hydrochar. HCS: Coal slurry's hydrochar. HCB: hydrochar from the blend of coal tailing, coal slurry and sewage sludge.AC: Activated carbon.

Kebede (2020), Ndilimeke Akawa (2021), and Zitha (2022) identified antiviral and other pharmaceutical compounds in bodies of water throughout their studies. According to these findings, the maximum concentrations of nevirapine and lamivudine in South African ambient water were discovered at 1,640ngL-1, posing a substantial environmental danger due to their potential harm to aquatic life and medication resistance in humans (Zitha *et al*., 2022). As a result, pharmaceutical compounds removal strategies for bodies of water are required. Extensive investigations on the removal of these medications from water bodies have not yet been completed, most likely due to the significant cost of prospective remediation technologies (Kebede et al., 2020; Zitha *et al*., 2022). Table 5-6 highlights selected recent adsorption studies for pharmaceutical products removal. Despite the fact that a large amount ($100gL^{-1}$) was required in this study for the efficient removal of nevirapine and lamivudine from water at ambient temperature (rather than the 45°C reported in most research), this investigation shows that HCs give similar performance to other synthetic adsorbents. Furthermore, because coal waste is readily available in South Africa and the HTC process is environmentally friendly, hydrochars formed from HCs could serve as

excellent, cost-effective adsorbents for numerous pharmaceutical compounds discovered in water bodies.

5.5.5. Production and evaluation of AC from spent hydrochar residues from nevirapine and lamivudine adsorption tests

The Fourier transform infrared (FT-IR) spectra of spent hydrochar residues from nevirapine and lamivudine adsorption tests and produced ACs are displayed in Figure 5-13 and Figure 5-14. The observation of these spectra revealed the impact of activation process which leaded to the significant decrease and in some cases disappearance of adsorption peaks. This demonstrates the effectiveness functional groups removal resulting in the transformation of chemical active sites (Genli *et al*., 2022).

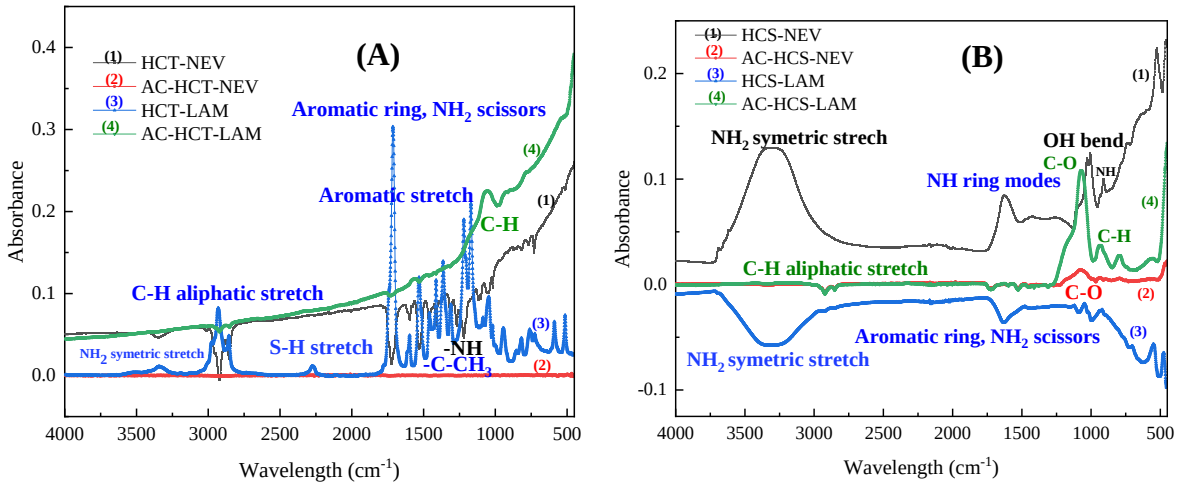

Figure 5-13:FTIR profile of chemically activated spent hydrochar residues from nevirapine and lamivudine adsorption tests using HCT (a) and HCS (b).

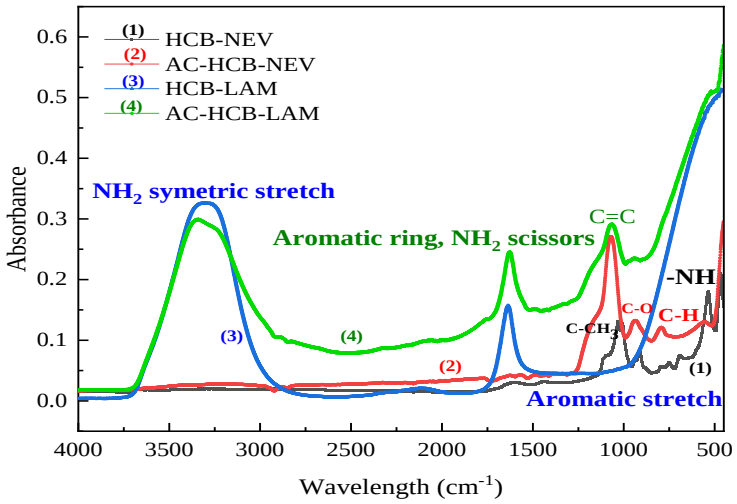

Figure 5-14:FTIR profile of chemically activated spent hydrochar residues from nevirapine and lamivudine adsorption tests using HCB.

The FTIR spectra of the produced ACs presented in Figure5-13 and Figure5-14 depicted few peaks which indicates less functional groups (Smith Brian. 2018). The peak at 3430 cm^{-1} is observed only on the spectra of AC -HCB-LAM (Figure 5-14) and could be assigned to the remaining amines stretch after activation process (Gupta *et al.*, 2022). The peak observed at the adsorption band of 2900 cm^{-1} and 750 cm^{-1} on the spectra of AC-HCT-LAM and AC-HCS-LAM (Figure 5-13) indicate the presence of C–H aliphatic stretching vibrations. arising from C-CH_3 groups of the hydrochar (Elkady *et al.*, 2015). The peaks at 1650 cm^{-1} observed on the spectra of AC-HCB-LAM confirmed the presence of amine group NH_2 (Figure 5-14) (Gupta *et al.*, 2022). The identified peaks at 1050 cm^{-1} indicate the presence of C–O bond and of –C–OH from carboxylic acids, alcohols, and phenols (Osman *et al.*, 2003) whereas the peaks at 1125 cm^{-1} possibly result from C=C vibrations of aromatic rings in the AC-HCB-NEV and AC-HCB-LAM (Figure 5-14) (Das *et al.*, 2010).

The morphologies of the produced ACs from spent hydrochar residues from nevirapine and lamivudine adsorption tests are presented in Figure 5-15. The results show a surface transformation from irregular and rough surfaces (Figure 5-7 and 5-8 (c, e)) to a more porous surface of ACs (Figure 5-15). In addition, the pores distribution of pores on the surface images of ACs seemed heterogenous (Figure 5-15). This is

possibly due to the chemical activation reaction between KOH and the carbon structure of the residues, and most of the organic volatiles evolved, leaving behind the ruptured surface of ACs with many pores (Zhao *et al*., 2014). The diffusion of KOH molecules into the pores of carbonaceous processor during activation process, tend to increase the KOH-carbon interaction and created more pores ultimately increasing the S_{BET} and pore volume of the produced ACs (Zhao *et al*., 2014). The porosity helps in the diffusion of electrolyte ions at the charging-discharging process of supercapacitor cells and thus increases the capacitance performance of the synthesized device (Gupta *et al*., 2022).

The BET results obtained from the analysis of the N_2 adsorption/desorption isotherm at 77K for the produced ACs are represented in Table 5-7. The highest S_{BET} of 2047.5 m^2/g and the lowest SBET of 436.5 m^2/g but higher than the lowest S_{BET} of common activated carbons (290m^2/g) were obtained from the AC-HCT-NEV and AC-HCB-NEV respectively (Sinha *et al*., 2020). This could be due to the relatively high carbon (C-C) bonds identified in the HCT-NEV spectra presented on Fig 10 compared to other spent residues. Under activation conditions, carbon bonds break and create complexes with KOH on the carbon silica matrices (Sethia *et al*., 2016). The average pore diameter and pore volume were in the range of 2.23nm to 3.13nm and 0.373cm^3/g and 1.14cm^3/g respectively which make the produced ACs predominated by mesopores (2-50nm). Though it has Darweesh (2017) demonstrated that mesoporosity is favourable for adsorption-based applications, the synthesized ACs could be beneficial for electrochemical applications. Table 5-7 summarizes the BET results for the produced ACs using spent hydrochar residues from nevirapine and lamivudine adsorption tests. The results indicate that S_{BET} increase is influenced by the generation of pores on the carbon silica matrices (Luo *et al*., 2020). Possibly the KOH-carbon matrix interaction favoured the dilatation of the carbon structure which expends the cross-linked matrix of the CM and generates pores after the acid washing step (Diez *et al*., 2021).

Table 5-7.BET analysis results of the synthesized ACs using spent hydrochar residues from nevirapine and lamivudine adsorption tests.

Material	Surface area (m^2/g)	Total pore volume (cm^3/g)	Micropore volume (cm^3/g)	Average pore diameter (nm)
AC-HCT-NEV	1047.5	1.14	0.986	2.23
AC-HCT-LAM	748.2	0.47	0.353	2.55
AC-HCS-NEV	618.4	0.373	0.289	2.41
AC-HCS-LAM	582.8	0.442	0.255	3.04
AC-HCB-NEV	436.5	0.42	0.16	3.85
AC-HCB-LAM	603.6	0.473	0.262	3.13

BET: Brunauer Emmet Teller. AC-HC-NEV: Activated carbon from nevirapine's adsorption spent residue. AC-HC-LAM: Activated carbon from lamivudine's adsorption spent residue.

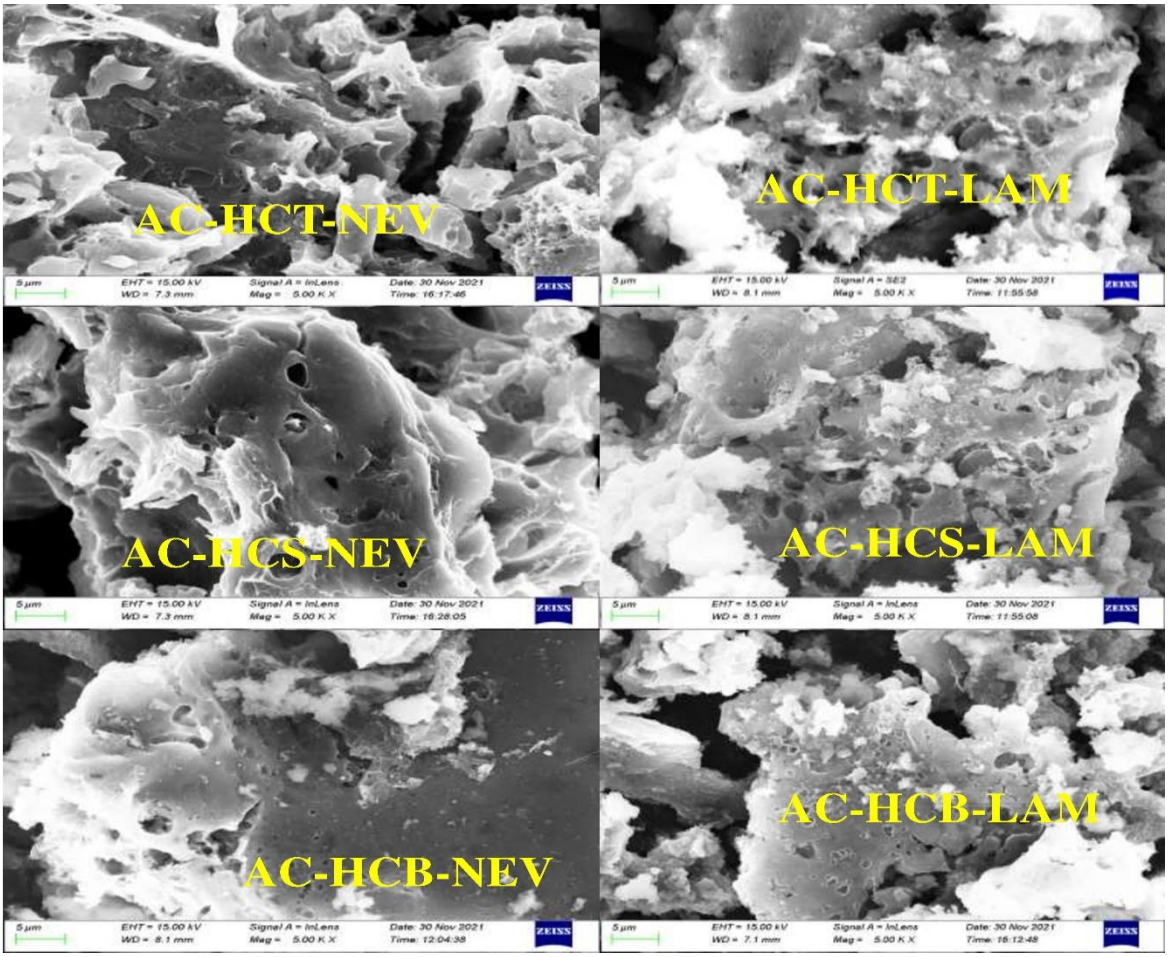

Figure 5-15:SEM images of ACs obtained using spent hydrochar residues from nevirapine and lamivudine adsorption tests.

5.5.6. Electrochemical characterization

The Figure 5-16 (a) depicts the cyclic voltammograms (CV) of the produced ACs at a scan rate of 100mV/s, demonstrating that all sweep curves are symmetric on the positive and negative sweeps, and the current at 0 V for electrodes made of different ACs change. The electrodes built of AC- HCT-NEV (A1) and AC-HCT- LAM (A2) outperform the other four ACs electrodes tested (0.016mA, 1V and 0.015mA, 1V), as indicated by the high current and nearly ideal standard rectangle (Phiri *et al*., 2019). This is consistent with the high S_{BET}, total volume, and micropore volume of the two ACs shown in Table 5-7. This demonstrates that the textural structure of the ACs electrode has a significant impact on the electric conductivity qualities (Veerakumar *et al*., 2020). The roughly rectangular cyclic voltammetry shape implies that the ACs electrodes have a rapid dynamics and good charge propagation. The charge storage mechanism of the ACs was described from the evaluation of scan rates effect. The observation of the results (Figure 5-16 a) revealed that the ACs electrodes exhibited potential independent double-layer capacitance between appreciable voltage ranges of polarization (Tu *et al*., 2017). Figure 5-16 (a) shows an approximately ideal double-layer trend, and the rectangular sharp specific to electrochemical capacitance were seen at tested scan rate.

Equation (5- 6) was used to determine the specific capacitance of ACs electrode from the CV presented in Figure 5-16 (a).

$$C = \left(\frac{I_a - I_c}{2v.m}\right) = \left(\frac{\Delta I}{2v.m}\right) \quad (5\text{-}6)$$

Where, C is the specific capacitance (F/g), DI is the average of anodic and cathodic current, v, the potential scan rate (V/s) and m, the mass of the electrode.

The specific capacitance of the produced ACs electrodes was in the range of 20 to 100 Figure 5-16 (b) at scan rates of 10 to 100 mVs-1. The results obtained is in agreement with prior work which shows that the specific capacitance of electrodes increase is a complex fact not depending only on the specific surface area S_{BET} (Wang *et al*., 2019). Additionally, the results presented on Figure 5-16 b show that the specific capacitance depends on the porous structure of the electrode (Table 5-7). The presence

of macropores in AC-HCT-NEV may favour electrolyte ion displacement into the porous material. As a result, the electrolyte ions can only settle in some of the electrode's pores to form the double-layer (Raj *et al*., 2022). At a current density of 10A/g for ions transportation, the micropores accessibility decreases from AC-HCT-NEV (A1) to other ACs and even becomes inaccessible for AC-HCB-NEV (C1) and thus do not assist in the total double-layer capacitance of the porous electrode, resulting in a null specific capacitance (Uralcan *et al*., 2022). The resonance of narrowed pores (micropores) could increase the ions mobility at high temperature (Uralcan *et al*., 2022). The results of this investigation reveal that when the S_{BET} of the electrode increases, so does the specific capacitance. Furthermore, additional properties of the porous carbonaceous material, such as pore size distribution and surface chemistry, influence its electrochemical capacity (AC-HCB-NEV and AC-HCB-LAM). Furthermore, the ACs produced from NEV and LAM adsorption residues using HCs absorbent exhibited good reversibility and stability, as observed from the ideal double-layer behavior shown in Figure 5-16a (Yang *et al*., 2022), implying that the produced ACs could be used as excellent electrodes for supercapacitors devices with current densities ranging from 1A/g to 5A/g in energy storage applications.

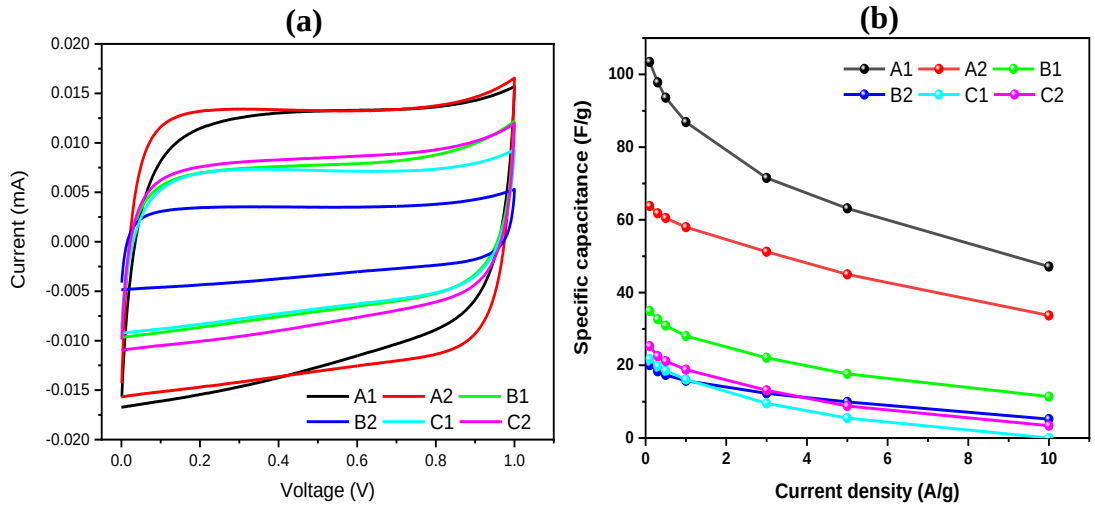

Figure 5-16:(a) Cyclic voltammetry curves @ 100 mV/s (b) and Specific capacitance results from greatest common divisor (GCD) of ACs from spent adsorptions residues (HCT-NEV: A1, HCT-LAM: A2, HCS-NEV: B1, HCS-LAM: B2, HCB-NEV:C1 and HCT-LAM:C2).

Figure 5-17 shows the electrochemical impedance spectroscopy (EIS) results of ACs electrodes, which might be used to test different circuit models for data fitting. Electro-active regions, specific capacitance, and charge transfer resistance of electrodes obtained from CV and EIS studies were evaluated (Ghosh *et al.*, 2019). The spectra depict the contact resistance and material resistance (electrode materials, electrolyte, and separator) values that prevent ions from entering the pores of electrode materials, as well as ion mobility in solution and separator. The real axis is set at 3.5 Ω, suggesting that the AC-HCT-LAM (A2) electrode has a lower contact resistance and higher conductivity than the other five electrodes (Uralcan *et al*., 2022). At lower frequencies, the slope of the ACs curves increases from AC-HCT-LAM (A2), which is roughly vertical, to AC-HCB-NEV (C1), which acquired a considerable slope, indicating that the ions in the electrolyte are difficult to enter the pores of AC-HCB-NEV, as previously described. As a result, the manufactured ACs electrodes have a high potential electrode of an electrochemical double-layer capacitor due to their wide electro-active area (Ghosh *et al.*, 2019). The findings indicate that the structural characteristics of the carbon-silica linkages impact the electrochemical properties of the ACs. The release of volatile matter during the activation process creates pores in the structure of the spent adsorption residues, whereas silica, a component of ash content from the HCs precursors (Table 5-1), remains in the matrix of the produced ACs, reducing its porosity and, as a result, its electrochemical conductivity (Barroso *et al*., 2021). As a result, applying strong compression pressure to the synthesized ACs may shatter the individual particles and condense the materials. This might pull individual particles closer together with other nearby particles, increasing the conductivity of the ACs (Barroso *et al*., 2021; Yang *et al*., 2022). The higher density of the AC produced at high pressure causes potential electron mobility across the material, increasing its electrical conductivity. Nonetheless, the reduced density of AC at low compression pressure leaves large voids between the particles of the carbon matrix, reducing electron mobility dramatically. As a result, the electrical conductivity of the AC used decreases.

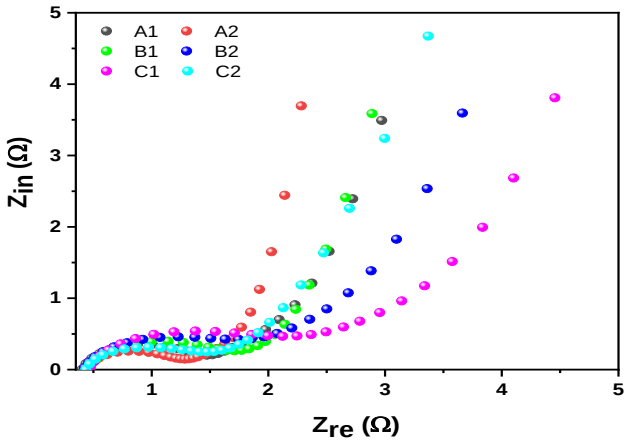

Figure 5-17:Electrochemical impedance spectroscopy (EIS) of the ACs from spent adsorptions residues (HCT-NEV: A1, HCT-LAM: A2, HCS-NEV: B1, HCS-LAM: B2, HCB-NEV:C1 and HCT-LAM:C2).

5.6. Conclusion

This study examined the effects of various parameter interactions on the textural structure of hydrochars produced via hydrothermal (HTC) and co-hydrothermal (Co-HTC) treatments of CD and sewage sludge (wastes), as well as the subsequent utilization of the hydrochar (HCs) synthesized for HIV drugs (nevirapine and lamivudine) removal from wastewater. The HCB synthesized from Co-HTC had a high SBET of 20.35 m^2/g and pore volume of 0.38 cm^3/g, resulting in significant adsorptive removals of NEV and LAM (97.19% and 93.32%), respectively. Despite being less effective than HCB, HCT and HCS displayed good NEV and LAM adsorption capacities. The use of coal waste and sewage sludge for the synthesis of hydrochar for the adsorption of dissolved pharmaceutical resistant substances might be a cost-effective and environmentally friendly option in wastewater treatment. Furthermore, the use of spent adsorption residues for energy storage applications was examined further. The results reveal that spent adsorption residues are an excellent carbonaceous material precursor for the manufacture of EDLCs. This research has shown that using low-cost HTC technologies to generate value-added carbonaceous material (hydrochar) from coal waste and sewage sludge waste could be a long-term recycling strategy that reduces disposal costs while also addressing any environmental contamination caused by the release or solubilization of toxic compounds in these wastes as a result

of landfill disposal. However, additional kinetics study and thermodynamic analyses are necessary to offer a deeper knowledge of HTC and Co-HTC reaction processes, as is the development and testing of a continuous ARVs components adsorption method, as well as its implications for large-scale industrial use. A life cycle evaluation of the hydrothermal treatment and adsorption procedures may also be necessary to determine the long-term sustainability of the options described in this study.

REFERENCES

1. 00/01701 The production of the environment friendly domestic fuel by the coking coal blend briquettes. *Fuel and Energy Abstracts* **2000**, *41*, 196.
2. Mills, E.L.; Ryan, D.G.; Prag, H.A.; Dikovskaya, D.; Menon, D.; Zaslona, Z.; Jedrychowski, M.P.; Costa, A.S.H.; Higgins, M.; Hams, E. Itaconate is an anti-inflammatory metabolite that activates Nrf2 via alkylation of KEAP1. *Nature* **2018**, *556*, 113–117.
3. Onifade, M.; Genc, B.; Bada, S. Spontaneous combustion liability between coal seams: A thermogravimetric study. *International Journal of Mining Science and Technology* **2020**, *30*, 691–698.
4. Water Resources Research Catalog. Volume 10. Water Resources Scientific Information Center, Office of Water Research and Technology, U.S. Department of the Interior, Washington, D.C. 20240. 1975. Various paging. $9.55. *Journal of Travel Research* **1977**, *15*, 34–34.
5. Libhaber, M.; Orozco-Jaramillo, Á. Sustainable Treatment and Reuse of Municipal Wastewater: For Decision Makers and Practicing Engineers. **2012**.
6. Zhou, G.; Gu, Y.; Yuan, H.; Gong, Y.; Wu, Y. Selecting sustainable technologies for disposal of municipal sewage sludge using a multi-criterion decision-making method: A case study from China. *Resources, Conservation and Recycling* **2020**, *161*, 104881.
7. Kacprzak, M.; Neczaj, E.; Fijałkowski, K.; Grobelak, A.; Grosser, A.; Worwag, M.; Rorat, A.; Brattebo, H.; Almås, Å.; Singh, B.R. Sewage sludge disposal strategies for sustainable development. *Environmental Research* **2017**, *156*, 39–46.
8. del Rio, C. The global HIV epidemic: What the pathologist needs to know. *Seminars in Diagnostic Pathology* **2017**, *34*, 314–317.
9. Tompa, D.R.; Immanuel, A.; Srikanth, S.; Kadhirvel, S. Trends and strategies to combat viral infections: A review on FDA approved antiviral drugs. *International Journal of Biological Macromolecules* **2021**, *172*, 524–541.
10. Evans, D.B.; Hsu, J.; Boerma, T. Universal health coverage and universal access. *Bull. World Health Organ.* **2013**, *91*, 546-546A.
11. Reddy, K.; Renuka, N.; Kumari, S.; Bux, F. Algae-mediated processes for the treatment of antiretroviral drugs in wastewater: Prospects and challenges. *Chemosphere* **2021**, *280*, 130674.
12. Kebede, T.G.; Seroto, MB.; Chokwe, R.C.; Dube, S.; Nindi, M.M. Adsorption of antiretroviral (ARVs) and related drugs from environmental wastewaters using nanofibers. *Journal of Environmental Chemical Engineering* **2020**, *8*, 104049.
13. Ndilimeke Akawa, M.; Mogolodi Dimpe, K.; Nosizo Nomngongo, P. An adsorbent composed of alginate, polyvinylpyrrolidone and activated carbon (AC@PVP@alginate) for ultrasound-assisted dispersive micro-solid phase extraction of nevirapine and zidovudine in environmental water samples. *Environmental Nanotechnology, Monitoring & Management* **2021**, *16*, 100559.
14. Zitha, A.B.; Ncube, S.; Mketo, N.; Nyoni, H.; Madikizela, L.M. Antiretroviral Drugs in Water: An African Challenge with Kenya and South Africa as Hotspots and Plausible Remediation Strategies. *Chemistry Africa* **2022**, *5*, 1237–1253.
15. Abafe, O.A.; Späth, J.; Fick, J.; Jansson, S.; Buckley, C.; Stark, A.; Pietruschka, B.; Martincigh, B.S. LC-MS/MS determination of antiretroviral drugs in influents and effluents from wastewater treatment plants in KwaZulu-Natal, South Africa. *Chemosphere* **2018**, *200*, 660–670.
16. Hauser, A.; Sewangi, J.; Mbezi, P.; Dugange, F.; Lau, I.; Ziske, J.; Theuring, S.; Kuecherer, C.; Harms, G.; Kunz, A. Emergence of Minor Drug-Resistant HIV-1 Variants after Triple

Antiretroviral Prophylaxis for Prevention of Vertical HIV-1 Transmission. *PLoS ONE* **2012**, *7*, e32055.
17. Obidike L, Mulopo J. Effect of High Concentration of Nevirapine on the Growth of E. Coli in Wastewater Treatment. InProceedings of the World Congress on Engineering and Computer Science 2018 (Vol. 2).
18. Whiteley, L.; Olsen, E.; Mena, L.; Haubrick, K.; Craker, L.; Hershkowitz, D.; Brown, L.K. A Mobile Gaming Intervention for Persons on Pre-Exposure Prophylaxis: Protocol for Intervention Development and Randomized Controlled Trial. *JMIR Res Protoc* **2020**, *9*, e18640.
19. Deeks, E.D. Bictegravir/Emtricitabine/Tenofovir Alafenamide: A Review in HIV-1 Infection. *Drugs* **2018**, *78*, 1817–1828.
20. Swanepoel, C.R.; Atta, M.G.; D'Agati, V.D.; Estrella, M.M.; Fogo, A.B.; Naicker, S.; Post, Fr.A.; Wearne, N.; Winkler, Ch.A.; Cheung, M. KIDNEY DISEASE IN THE SETTING OF HIV INFECTION: CONCLUSIONS FROM A KIDNEY DISEASE: IMPROVING GLOBAL OUTCOMES (KDIGO) CONTROVERSIES CONFERENCE. *Nefrologiâ (St.-Peterbg.)* **2018**, *22*, 84–100.
21. Yaqoob, A.A.; Parveen, T.; Umar, K.; Mohamad Ibrahim, M.N. Role of Nanomaterials in the Treatment of Wastewater: A Review. *Water* **2020**, *12*, 495.
22. World Health Organization. **2015**, 192e–192e.
23. Prasse, C.; Schlüsener, M.P.; Schulz, R.; Ternes, T.A. Antiviral Drugs in Wastewater and Surface Waters: A New Pharmaceutical Class of Environmental Relevance? *Environ. Sci. Technol.* **2010**, *44*, 1728–1735.
24. Adeola, A.O.; Forbes, P.B.C. Antiretroviral Drugs in African Surface Waters: Prevalence, Analysis, and Potential Remediation. *Enviro Toxic and Chemistry* **2022**, *41*, 247–262.
25. Kovalakova, P.; Cizmas, L.; McDonald, T.J.; Marsalek, B.; Feng, M.; Sharma, V.K. Occurrence and toxicity of antibiotics in the aquatic environment: A review. *Chemosphere* **2020**, *251*, 126351.
26. Silva, A.; Delerue-Matos, C.; Figueiredo, S.; Freitas, O. The Use of Algae and Fungi for Removal of Pharmaceuticals by Bioremediation and Biosorption Processes: A Review. *Water* **2019**, *11*, 1555.
27. Sousa, É.M.L.; Otero, M.; Rocha, L.S.; Gil, M.V.; Ferreira, P.; Esteves, V.I.; Calisto, V. Multivariable optimization of activated carbon production from microwave pyrolysis of brewery wastes - Application in the removal of antibiotics from water. *Journal of Hazardous Materials* **2022**, *431*, 128556.
28. Peng, B.; Chen, L.; Que, C.; Yang, K.; Deng, F.; Deng, X.; Shi, G.; Xu, G.; Wu, M. Adsorption of Antibiotics on Graphene and Biochar in Aqueous Solutions Induced by π-π Interactions. *Sci Rep* **2016**, *6*.
29. Yaqoob, A.A.; Ahmad, H.; Parveen, T.; Ahmad, A.; Oves, M.; Ismail, I.M.I.; Qari, H.A.; Umar, K.; Mohamad Ibrahim, M.N. Recent Advances in Metal Decorated Nanomaterials and Their Various Biological Applications: A Review. *Front. Chem.* **2020**, *8*.
30. Maqhuzu, A.B.; Yoshikawa, K.; Takahashi, F. Stochastic economic analysis of coal-alternative fuel production from municipal solid wastes employing hydrothermal carbonization in Zimbabwe. *Science of The Total Environment* **2020**, *716*, 135337.
31. Wazir, A.H.; Haq, I. ul; Manan, A.; Khan, A. Preparation and characterization of activated carbon from coal by chemical activation with KOH. *International Journal of Coal Preparation and Utilization* **2022**, *42*, 1477–1488.
32. Adinaveen, T.; Kennedy, L.J.; Vijaya, J.J.; Sekaran, G. Studies on structural, morphological, electrical and electrochemical properties of activated carbon prepared from sugarcane bagasse. *Journal of Industrial and Engineering Chemistry* **2013**, *19*, 1470–1476.

33. Kong, L.; Ostadhassan, M.; Hou, X.; Mann, M.; Li, C. Microstructure characteristics and fractal analysis of 3D-printed sandstone using micro-CT and SEM-EDS. *Journal of Petroleum Science and Engineering* **2019**, *175*, 1039–1048.
34. Abdulsalam, J.; Mulopo, J.; Oboirien, B.; Bada, S.; Falcon, R. Experimental evaluation of activated carbon derived from South Africa discard coal for natural gas storage. *Int J Coal Sci Technol* **2019**, *6*, 459–477.
35. Afolabi, O.O.D.; Sohail, M.; Cheng, Y.-L. Optimisation and characterisation of hydrochar production from spent coffee grounds by hydrothermal carbonisation. *Renewable Energy* **2020**, *147*, 1380–1391.
36. Tsai, W.-T.; Liu, S.-C.; Hsieh, C.-H. Preparation and fuel properties of biochars from the pyrolysis of exhausted coffee residue. *Journal of Analytical and Applied Pyrolysis* **2012**, *93*, 63–67.
37. Yang QB. Mechanisms of deicer-frost scaling of concrete (I): Capillary-uptake degree of saturation and ice-formation pressure. J. Build. Mater. 2007;10(5):522-7.
38. AWASTHI, R.; Madan, J.; Kamate, V.; Dua, K. Improving the solubility of nevirapine using a hydrotropyand mixed hydrotropy based solid dispersion approach. *Polim. Med.* **2017**, 83–90.
39. Luan, H.; Wu, J.; Pan, J. Saline water absorption behavior and critical saturation degree of recycled aggregate concrete during freeze-thaw cycles. *Construction and Building Materials* **2020**, *258*, 119640.
40. Abafe, O.A.; Späth, J.; Fick, J.; Jansson, S.; Buckley, C.; Stark, A.; Pietruschka, B.; Martincigh, B.S. LC-MS/MS determination of antiretroviral drugs in influents and effluents from wastewater treatment plants in KwaZulu-Natal, South Africa. *Chemosphere* **2018**, *200*, 660–670.
41. Saba, A.; Saha, P.; Reza, M.T. Co-Hydrothermal Carbonization of coal-biomass blend: Influence of temperature on solid fuel properties. *Fuel Processing Technology* **2017**, *167*, 711–720.
42. AliAkbari, R.; Ghasemi, M.H.; Neekzad, N.; Kowsari, E.; Ramakrishna, S.; Mehrali, M.; Marfavi, Y. High value add bio-based low-carbon materials: Conversion processes and circular economy. *Journal of Cleaner Production* **2021**, *293*, 126101.
43. Yoshikawa, K.; Prawisudha, P. Hydrothermal Treatment of Municipal Solid Waste for Producing Solid Fuel. **2014**, 355–383.
44. Lu, X.; Ma, X.; Chen, X. Co-hydrothermal carbonization of sewage sludge and lignocellulosic biomass: Fuel properties and heavy metal transformation behaviour of hydrochars. *Energy* **2021**, *221*, 119896.
45. Channiwala, S.A.; Parikh, P.P. A unified correlation for estimating HHV of solid, liquid and gaseous fuels. *Fuel* **2002**, *81*, 1051–1063.
46. Thunshirn, P.; Wenzel, W.W.; Pfeifer, C. Pore characteristics of hydrochars and their role as a vector for soil bacteria: A critical review of engineering options. *Critical Reviews in Environmental Science and Technology* **2022**, *52*, 4147–4171.
47. Olabode, G.; Somerset, V. Advances in Chromatographic Determination of Selected Anti-Retrovirals in Wastewater. **2019**, 105–127.
48. *Solomons TG, Fryhle CB. Organic Chemistry, John Wiley&Sons. Inc., 6thed. 2000:646-931.*;
49. *Smith, B., 2018. Infrared spectral interpretation: a systematic approach. CRC press.*;
50. Mishra, R.K.; Mohanty, K. Characterization of non-edible lignocellulosic biomass in terms of their candidacy towards alternative renewable fuels. *Biomass Conv. Bioref.* **2018**, *8*, 799–812.
51. SANDLER, S.R.; KARO, W. PREFACE. **1983**, xi.

52. Madan, H.R.; Sharma, S.C.; Udayabhanu; Suresh, D.; Vidya, Y.S.; Nagabhushana, H.; Rajanaik, H.; Anantharaju, K.S.; Prashantha, S.C.; Sadananda Maiya, P. Facile green fabrication of nanostructure ZnO plates, bullets, flower, prismatic tip, closed pinecone: Their antibacterial, antioxidant, photoluminescent and photocatalytic properties. *Spectrochimica Acta Part A: Molecular and Biomolecular Spectroscopy* **2016**, *152*, 404–416.
53. Patiño, Y.; Díaz, E.; Ordóñez, S.; Gallegos-Suarez, E.; Guerrero-Ruiz, A.; Rodríguez-Ramos, I. Adsorption of emerging pollutants on functionalized multiwall carbon nanotubes. *Chemosphere* **2015**, *136*, 174–180.
54. Zhang, S.; Dong, Y.; Yang, Z.; Yang, W.; Wu, J.; Dong, C. Adsorption of pharmaceuticals on chitosan-based magnetic composite particles with core-brush topology. *Chemical Engineering Journal* **2016**, *304*, 325–334.
55. Oladipo, A.A.; Ifebajo, A.O.; Vaziri, R. Green Adsorbents for Removal of Antibiotics, Pesticides and Endocrine Disruptors. **2018**, 327–351.
56. Reynel-Avila, H.E.; Mendoza-Castillo, D.I.; Bonilla-Petriciolet, A.; Silvestre-Albero, J. Assessment of naproxen adsorption on bone char in aqueous solutions using batch and fixed-bed processes. *Journal of Molecular Liquids* **2015**, *209*, 187–195.
57. Nazari, G.; Abolghasemi, H.; Esmaieli, M.; Sadeghi Pouya, E. Aqueous phase adsorption of cephalexin by walnut shell-based activated carbon: A fixed-bed column study. *Applied Surface Science* **2016**, *375*, 144–153.
58. Álvarez-Torrellas, S.; Ribeiro, R.S.; Gomes, H.T.; Ovejero, G.; García, J. Removal of antibiotic compounds by adsorption using glycerol-based carbon materials. *Chemical Engineering Journal* **2016**, *296*, 277–288.
59. Mondal, S.; Aikat, K.; Halder, G. Ranitidine hydrochloride sorption onto superheated steam activated biochar derived from mung bean husk in fixed bed column. *Journal of Environmental Chemical Engineering* **2016**, *4*, 488–497.
60. Darweesh, T.M.; Ahmed, M.J. Adsorption of ciprofloxacin and norfloxacin from aqueous solution onto granular activated carbon in fixed bed column. *Ecotoxicology and Environmental Safety* **2017**, *138*, 139–145.
61. Yaghmaeian, K.; Moussavi, G.; Alahabadi, A. Removal of amoxicillin from contaminated water using NH 4 Cl-activated carbon: Continuous flow fixed-bed adsorption and catalytic ozonation regeneration. *Chemical Engineering Journal* **2014**, *236*, 538–544.
62. Nourmoradi, H.; Moghadam, K.F.; Jafari, A.; Kamarehie, B. Removal of acetaminophen and ibuprofen from aqueous solutions by activated carbon derived from Quercus Brantii (Oak) acorn as a low-cost biosorbent. *Journal of Environmental Chemical Engineering* **2018**, *6*, 6807–6815.
63. Effect of Solution pH on the Removal of Paracetamol by Activated Carbon of Dende Coconut Mesocarp. *Chem.Biochem.Eng.Q.* **2015**, *29*, 47–53.
64. Mashayekh-Salehi, A.; Moussavi, G. Removal of acetaminophen from the contaminated water using adsorption onto carbon activated with NH4Cl. *Desalination and Water Treatment* **2016**, *57*, 12861–12873.
65. Streit, A.F.M.; Collazzo, G.C.; Druzian, S.P.; Verdi, R.S.; Foletto, E.L.; Oliveira, L.F.S.; Dotto, G.L. Adsorption of ibuprofen, ketoprofen, and paracetamol onto activated carbon prepared from effluent treatment plant sludge of the beverage industry. *Chemosphere* **2021**, *262*, 128322.
66. Fröhlich, A.C.; Ocampo-Pérez, R.; Diaz-Blancas, V.; Salau, N.P.G.; Dotto, G.L. Three-dimensional mass transfer modeling of ibuprofen adsorption on activated carbon prepared by sonication. *Chemical Engineering Journal* **2018**, *341*, 65–74.

67. Baccar, R.; Sarrà, M.; Bouzid, J.; Feki, M.; Blánquez, P. Removal of pharmaceutical compounds by activated carbon prepared from agricultural by-product. *Chemical Engineering Journal* **2012**, *211–212*, 310–317.
68. Adeola, A.O.; de Lange, J.; Forbes, P.B.C. Adsorption of antiretroviral drugs, efavirenz and nevirapine from aqueous solution by graphene wool: Kinetic, equilibrium, thermodynamic and computational studies. *Applied Surface Science Advances* **2021**, *6*, 100157.
69. Ahmed, M.J.; Hameed, B.H. Removal of emerging pharmaceutical contaminants by adsorption in a fixed-bed column: A review. *Ecotoxicology and Environmental Safety* **2018**, *149*, 257–266.
70. Lan, H.; Tao, Q.; Ma, N.; Chen, L.; Wei, L.; Weng, M.; Dai, Q. Electrochemical oxidation of lamivudine using graphene oxide and Yb co-modified PbO2 electrodes: characterization, influencing factors and degradation mechanisms. *Separation and Purification Technology* **2022**, *301*, 121856.
71. Terzopoulou, Z.; Papageorgiou, M.; Kyzas, G.Z.; Bikiaris, D.N.; Lambropoulou, D.A. Preparation of molecularly imprinted solid-phase microextraction fiber for the selective removal and extraction of the antiviral drug abacavir in environmental and biological matrices. *Analytica Chimica Acta* **2016**, *913*, 63–75.
72. Jana Späth; Preyan Arumugam; Richard H Lindberg; Ovokeroye A Abafe; Stina Jansson; Jerker Fick; Chris A Buckley Biochar for the removal of detected micropollutants in South African domestic wastewater: a case study from a demonstration-scale decentralised wastewater treatment system in eThekwini. *WSA* **2021**, *47*.
73. Genli, N.; Kutluay, S.; Baytar, O.; Şahin, Ö. Preparation and characterization of activated carbon from hydrochar by hydrothermal carbonization of chickpea stem: an application in methylene blue removal by RSM optimization. *International Journal of Phytoremediation* **2022**, *24*, 88–100.
74. Gupta, M.; Kumar, A.; Sharma, S.; Bharti; Ghamouss, F.; Singh, P.; Chawla, V.; Kumar, A.; Kumar, Y. Study of electrochemical properties of activated carbon electrode synthesized using bio-waste for supercapacitor applications. *Biomass Conv. Bioref.* **2022**.
75. Elkady, M.F. Synthesis and Characterization of Nano-Activated Carbon from El Maghara Coal, Sinai, Egypt to be Utilized for Wastewater Purification. *AJAC* **2015**, *3*, 1.
76. Osman, Z.; Arof, A.K. FTIR studies of chitosan acetate based polymer electrolytes. *Electrochimica Acta* **2003**, *48*, 993–999.
77. Das, A.; Kothari, V.K.; Makhija, S. Development of a High-Absorbent Sanitary Napkin. **2010**, 148–155.
78. Zhao, X.-Y.; Huang, S.-S.; Cao, J.-P.; Xi, S.-C.; Wei, X.-Y.; Kamamoto, J.; Takarada, T. KOH activation of a HyperCoal to develop activated carbons for electric double-layer capacitors. *Journal of Analytical and Applied Pyrolysis* **2014**, *105*, 116–121.
79. Sinha, P.; Banerjee, S.; Kar, K.K. Characteristics of Activated Carbon. **2020**, 125–154.
80. Sethia, G.; Sayari, A. Activated carbon with optimum pore size distribution for hydrogen storage. *Carbon* **2016**, *99*, 289–294.
81. Luo, Y.; Wang, K.; Fei, L. The effects of activation conditions on physical properties of activated carbon. *BioRes* **2020**, *15*, 7640–7647.
82. Díez, N.; Sevilla, M.; Fuertes, A.B. Synthesis strategies of templated porous carbons beyond the silica nanocasting technique. *Carbon* **2021**, *178*, 451–476.
83. Phiri, J.; Dou, J.; Vuorinen, T.; Gane, P.A.C.; Maloney, T.C. Highly Porous Willow Wood-Derived Activated Carbon for High-Performance Supercapacitor Electrodes. *ACS Omega* **2019**, *4*, 18108–18117.

84. Veerakumar, P.; Sangili, A.; Manavalan, S.; Thanasekaran, P.; Lin, K.-C. Research Progress on Porous Carbon Supported Metal/Metal Oxide Nanomaterials for Supercapacitor Electrode Applications. *Ind. Eng. Chem. Res.* **2020**, *59*, 6347–6374.
85. Tu, J.; Wang, S.; Li, S.; Wang, C.; Sun, D.; Jiao, S. The Effects of Anions Behaviors on Electrochemical Properties of Al/Graphite Rechargeable Aluminum-Ion Battery via Molten AlCl3-NaCl Liquid Electrolyte. *J. Electrochem. Soc.* **2017**, *164*, A3292–A3302.
86. Wang, Y.; Chang, Z.; Qian, M.; Zhang, Z.; Lin, J.; Huang, F. Enhanced specific capacitance by a new dual redox-active electrolyte in activated carbon-based supercapacitors. *Carbon* **2019**, *143*, 300–308.
87. Raj, A.N.P.; Adinaveen, T.; Bennie, R.B.; Joel, C.; Kengaram, S.H.; Sophie, P.L. Nanoarchitectonics and Electrochemical Behavior of Cu Doped h-MoO3 as an Electrode Material for Energy Storage Applications. *J Inorg Organomet Polym* **2022**.
88. Uralcan, B.; Uralcan, I.B. Origin of Enhanced Performance in Nanoporous Electrical Double Layer Capacitors: Insights on Micropore Structure and Electrolyte Composition from Molecular Simulations. *ACS Appl. Mater. Interfaces* **2022**, *14*, 16800–16808.
89. Yang, F.; Huang, H.; Zhu, J.; Dong, W.; Wu, Q.; Li, H. Effects of coal-activated carbon on structure and electrochemical properties of MoS2/C. *J Mater Sci: Mater Electron* **2022**, *33*, 14691–14701.
90. Ghosh, S.; Santhosh, R.; Jeniffer, S.; Raghavan, V.; Jacob, G.; Nanaji, K.; Kollu, P.; Jeong, S.K.; Grace, A.N. Natural biomass derived hard carbon and activated carbons as electrochemical supercapacitor electrodes. *Sci Rep* **2019**, *9*.
91. Barroso Bogeat, A. Understanding and Tuning the Electrical Conductivity of Activated Carbon: A State-of-the-Art Review. *Critical Reviews in Solid State and Materials Sciences* **2021**, *46*, 1–37.

Chapter 6: Systematic physicochemical characterization, carbon balance and cost of production analyses of activated carbons derived from (Co)-HTC of coal discards and sewage sludge for hydrogen storage applications

This chapter has been submitted to the Waste Disposal & Sustainable Energy Journal and is under review.

6.1. Overview

Low-cost HTC technologies for producing value-added carbonaceous material (hydrochar) from coal waste and sewage sludge waste could be a long-term recycling strategy for hydrogen storage applications and lowering disposal costs while also addressing disposal issues of these wastes. In this chapter, a combination of optimal hydrothermal carbonization (HTC and Co-HTC) and chemical activation of coal discards (CD) and sewage sludge (SS) wastes was investigated to produce high carbon content hydrochars (HC). The activated carbons with highest Brunauer Emmet Teller specific surface (S_{BET}) of 2299.25m^2/g and 2243.57m^2/g were obtained at 850°C and 800°C respectively using a residence time of 135 minutes for a KOH/hydrochar ratio of 4:1.Furthemore, the hydrogen adsorption capacity of the produced ACs was evaluated using gas adsorption isotherms at 77K. the results indicate that the values of hydrogen adsorbed onto the ACs were approximatively 6.12wt%, 6.8wt% and 6.57wt% for AC-HCT, AC-HCS and AC-HCB respectively at 35 bar implying that they could be used for hydrogen storage and sustainable carbon emissions management and provide viable pathways for cost-effective energy and material circular economies for both WWTPSs and the mining industry. Furthermore, the production costs of the synthesised Activated Carbons (ACs) for hydrogen storage are comparable to those of commercial carbons. Furthermore, the high proportion of carbon preserved in HTC synthesised ACs (>70%) from coal waste and sewage sludge precursors should restrict their potential carbon emissions.

6.2. Introduction

Carbon technologies have grown rapidly in the last two decades, owing to the introduction of new synthetic techniques such as pyrolysis, high-voltage-arc discharge, chemical vapor deposition, hydrothermal carbonization, and laser ablation, as well as the growing demand for carbon-neutral alternatives due to environmental concerns (Bi *et al*., 2019). South African coal beneficiation process plants generate around 65Mt of coal waste per year, the most of which is disposed of in tailing stockpiles and slurry dams (Van de Venter *et al*., 2021). South Africa, on the other hand, has roughly 824 wastewater treatment plants spread across 152 municipalities, with a total design capacity of 6.5 billion litres of wastewater/day, resulting in vast amounts of Sewage Sludge (Naidoo *et al*., 2016). Numerous recent studies have revealed that due to a lack of feasible practical alternatives, sewage sludge disposal and piling has become the usual management choice for many wastewaters treatment plants across the country (Demirbas *et al*., 2017; Shaddel *et al*., 2019;). Environmental and health concerns related to the accumulation and illegal discharge of sewage sludge and coal waste are very significant (Grobelak *et al*., 2019). Re-using these resources, known as waste, to produce high-quality, advanced materials will reduce the cost of waste disposal. In addition, this will benefit society and mining houses by creating new markets, green jobs and a lower carbon footprint.

It is a known fact that the rapid growth of the world population is straining the sustainability of the earth's natural resources due to modern society's extensive use of these raw materials. With a novel and cost-effective waste repurposing method, activated carbon (AC) can be produced from low quality coal waste from South Africa along with the sewage sludge. Although AC has been widely synthesized from a variety of carbon precursors (petroleum coke, empty fruit bunch, bean husk, wood, palm solid waste, coconut shell, bituminous coals, and coal char), the porous properties of the resulting ACs are dependent on the precursors and the activation techniques used (Saleem *et al*., 2019). Furthermore, AC's physicochemical qualities influence its end application (Ukanwa *et al*., 2019). Several studies have shown that the hydrothermal carbonization (HTC) process has the potential to be environmentally benign and cost-

effective in the synergetic treatment of wet feedstock such as coal ash (CD) and sewage sludge (SS) to produce porous materials with high carbon content (Munir *et al*., 2018; Alatalo *et al*., 2020). HTC combined with chemical activation can improve the textural properties of the resulting AC. Hence, the objective of this study was to use hydrothermal carbonization (HTC) technology in conjunction with chemical activation approach to produce enhanced carbonaceous porous materials from CD and SS. Despite the widespread acceptance of hydrogen and fuel cell technology as possible future energy solutions, demonstrated pathways to the so-called 'hydrogen economy', in which energy is stored and distributed as hydrogen, continue to be limited (Rusman *et al.*, 2016). High-pressure gas, liquid hydrogen, complex hybrids, hydrogen intercalation in metals, and hydrogen adsorption on porous materials are among the technologies being explored for hydrogen storage development (Hirscher *et al.*, 2020). In spite of the fact that none of the aforementioned technologies fully meet all of the hydrogen supply criteria (amount transported and container volume) it is widely acknowledged that adsorptive hydrogen storage on porous materials offers a unique opportunity for future development due to the fact a large quantity of hydrogen can be stored in a small amount of porous solid material (Mohan *et al*., 2019). Numerous analyses of the potential transition from conventional to renewable fuels have demonstrated the high economic potential of hydrogen as a future energy carrier. However, there are still impediments to the widespread adoption of hydrogen, the most significant of which is the absence of effective storage technologies. Several storage technologies have been evaluated, and it has been determined that adsorptive hydrogen storage is one of the most likely solutions in the near future, with porous carbon materials, such as ACs, possessing a higher hydrogen absorption capacity than metal hybrids and complex hydrides (Abdulsalam *et al*., 2019; Anderson *et al*., 2019). However, sufficient research is still lacking on the economics of producing ACs from waste for hydrogen energy and the carbon balance of such systems.

With the transition to a hydrogen economy envisaged by the South African government, this study intends to demonstrate the suitability of different coal wastes and sewage sludge for use in hydrogen storage. The ACs produced by HTC and co-HTC

treatment of coal waste and sewage sludge wastes and their chemical activation were assessed for adsorptive hydrogen storage. In addition, their associated physicochemical properties and the cost of production provided.

6.3. Experimental method

6.3.1. Materials

For this study, coal tailing (CT) and coal slurry (CS) were collected from a coal beneficiation plant in Mpumalanga, South Africa. The obtained samples were dried in an ambient air before being stored and transported in airtight bags to the laboratory, where they were dried once more at room temperature. The dried individual as -received samples were pulverized to -212 µm and – 1 mm fraction in accordance with the ASTM D-2013 (Butt *et al*., 2021), with the physicochemical analyses (proximate, ultimate, total sulphur, SEM and FTIR) conducted on the -212 µm fraction. The sewage sludge (SS) used in this study was collected from a wastewater treatment plant (Ekurhuleni Water Care Company -ERWAT) and split into two portions. The first portion was dried for 24 hours in a laboratory drier at 105 °C and crushed for physiochemical characterization, whereas the second portion was used for HTC experiments as received. The hydrothermal experiment was carried out in a high pressure (110ml) tubular reactor with a -1 mm coal fraction. The hydrothermally treated carbon material obtained was chemically activated using different ratios of analytic grade potassium hydroxide (KOH). The porous material generated from the activation process was neutralized using hydrochloric acid (HCl, 0.5N). Throughout the washing procedure of the neutralized products, deionized water was used. The chemical activation experiments were carried out in a tube furnace at various temperatures and with a flowrate of 150ml/min of nitrogen gas as in Figure 6-1. Hydrogen gas baseline N5.0 from AFROX (African Oxygen Limited company, South Africa) was used to perform the tests of hydrogen adsorption on the synthesized ACs.

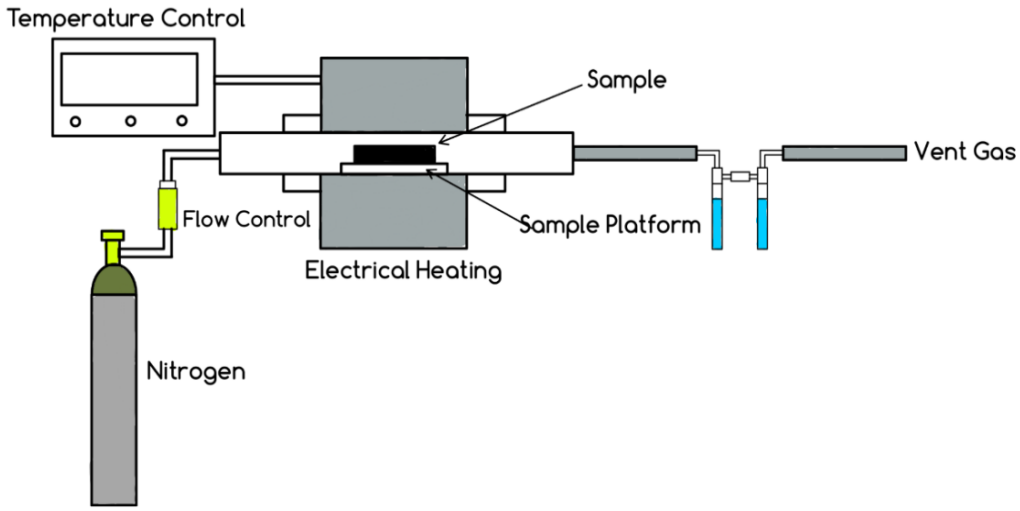

Figure 6-1:Activated Carbon Preparation equipment

6.3.2. Procedure

25g of raw material (coal tailing, coal slurry, mixture of coal tailing, coal slurry and sewage sludge) was mixed with water as input solvent in a solid liquid ratio of 1:4 in the tubular reactor. The HTC and Co-HTC process parameters (temperature and pressure) were varied to obtained to highest fixed carbon content carbonaceous material. The Co-HTC experiments used a feedstock mixture (CB) consisted of 80% (CT+CS) and 20% SS blend, based on previous optimization results obtained in the Co-HTC process study (ref). The coal discards were mixed at a 1:1 ratio for experimental simplicity. In HTC experiment the reactor was heated to desired reaction temperature and held for 95 minutes residence time. However, all Co-HTC experiments were performed in 360 minutes residence time. The solid products obtained from the mix were identified as hydrochar coal tailing, hydrochar coal slurry (HCS) and hydrochar blend coal discard and sewage sludge (HCB). The obtained HCs were dried, characterized, and prepared for chemical activation. Activated carbon synthesis was carried out from the HCs via chemical activation process using potassium hydroxide. The chemical activation tests were performed at temperatures between 800 and 850°C, with a heating rate of 15°C/min. The holding time was varied from 90 minutes to 180minutes before cooling in nitrogen mild. The potassium hydroxide: hydrochar (KOH: HC) ratios of 1:1, 5:2 and 4:1 were utilized to optimize the chemical activation process

in accordance with previous studies (Abdulsalam *et al*., 2019; Musyoka *et al*., 2020). The produced ACs were washed with 0.5N hydrochloric acid (HCl) for residual alkali removal then with distilled water using a centrifuge until the mixture (product/distilled water) reached the neutral pH of ~6. The washed solid product from the mixture was dried at 60°C in an oven for 24 hours then prepared according to the ASTMD5142 standards for characterization and kept in an airtight container for further analysis. The optimized parameters obtained were used for direct chemical activation of coal tailing (CT) and coal slurry (CS) for the evaluation of the Brunauer Emmet Teller specific surface (SBET). The specific surface obtained was then compared to the SBET of activated carbon produced from the combination of HTC and chemical activation. Afterward, the optimized ACs produced were characterized and prepared for hydrogen storage test. The chemical activation process methodology and application of the synthesized products is presented in Figure 6-2.

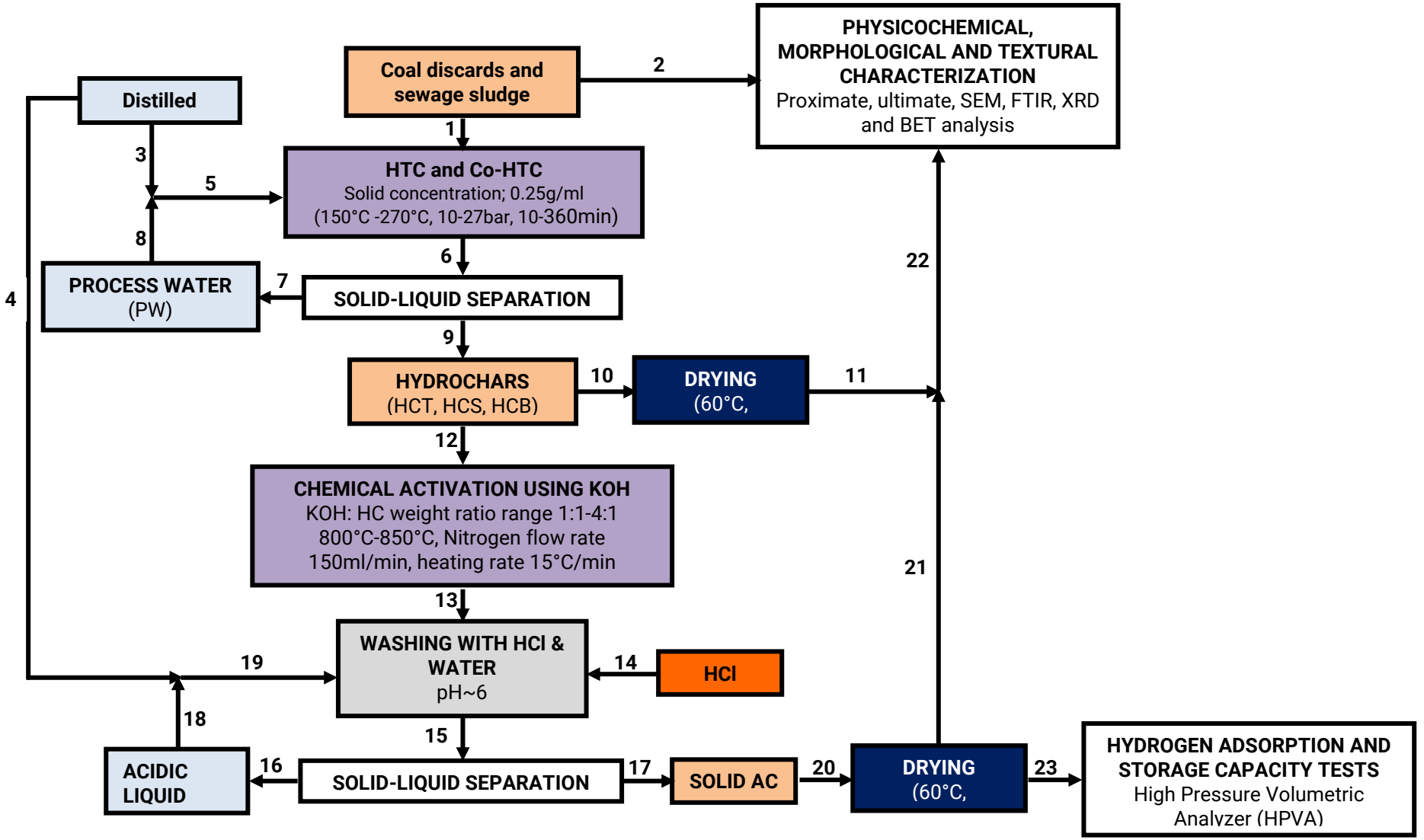

Figure 6-2:Flowsheet of the experimental procedures

6.3.3. Chemical activation

The activation experimental test runs were designed using Design-Expert software (DoE) (Version 13, State–Ease, Inc, Minneapolis, USA). In the design, two parameters of the chemical activation process, namely temperature and residence time, were considered. For the experimental design, the central composite design (CCD) was utilized to know the number of runs that will be required to optimize the process. Chemical activation experiments were conducted using temperatures between 800°C and 850°C and retention times between 90 and 180 minutes. The design matrix obtained for the chemical activation experiment is presented in Table 3-3. Based on the CCD, 13 experimental runs were performed for the optimization of the chemical activation of HCT, HCS and HCB. Five center points, four factorial points and four axial points and was repeated five times to ensure reproducibility of the responses and to determine accurate experimental error. The response surface methodology (RSM) was adopted to understand the interactions of chemical activation factors on the S_{BET} of activated carbon (AC) produced from both HCs samples. The AC with highest S_{BET} by means of the DoE was selected using the RSM as the optimized product. In addition, RSM was used to develop appropriate models to enable the prediction of the optimum operating conditions required to produce high S_{BET}. The analysis of variance (ANOVA) was consulted to evaluate the significancy of the designed models. Using the maximum S_{BET} of the produced ACs as the optimization criteria, the numerical optimum response methodology option was then used to select the best chemical activation process conditions. The characterization of the produced HCs and ACs was done according to the methodology described in chapter 3

6.3.4. Hydrogen adsorption

The measurements were made on a purified hydrogen in an ultra-clean vacuum system with all metal seals with diaphragm and used high-rate vacuum pumps. The density of hydrogen adsorbed was measured by the maximum amount adsorbed obtained from the isotherms compared to the total pore volume of the AC. The hydrogen adsorption capacity was measured according to the ASTM D 4607-94 specifications. Isotherms of hydrogen adsorption on the ACs were measured using

the high-pressure volumetric method at 77K. The automatic high pressure volumetric analyser (HPVA) from Micromeritics Particulate Systems coupled with a single-stage closed-cycle cryogenic refrigerator. was used to performed hydrogen adsorption tests. Before hydrogen adsorption tests, the ACs were degassed in the vacuum system at 373K overnight. Thereafter, the ACs were moved to second degassing system into the HPVA in a $10cm^3$ cell filled with approximatively 1.2g of ACs at 373K under vacuum for another 24 hours. The pressure range of adsorption was fixed from 1bar to 35bar, and the obtained pressures of desorption were from 28bar to 1.6bar. The determination of hydrogen adsorption isotherms was carried out from cold and warm volumes measurement after adsorption-desorption tests to avoid helium capture in narrow pores (Pińkowska *et al*., 2011).

6.4. Results and discussions

6.4.1. Characterization of produced Hydrochars

Tables 6-1 and 6-2 show the proximate and ultimate results of the raw materials and produced HCs. These findings demonstrated that the reaction temperature and pressure had a substantial influence on the HTC and Co-HTC processes. The maximum fixed carbon (FC) and total carbon (C) values were obtained for the HTC and Co-HTC processes, respectively, at 150°C and 210°C. However, raising the temperature above 150°C and 210°C for HTC and Co-HTC, respectively, increases the ash content of the produced HC due to condensation of material dissolved in the solid hydrochars and liquefaction of carbon from the feedstock. The mass yields of Co-HTC decreased more than those of HTC. As a result of the greater degree of thermolytic degradation of cellulose and lignin in the SS under Co-HTC reaction conditions (Pińkowska *et al*., 2011; Smith.2018).

Table 6-1. Proximate and ultimate analysis results of HTC process versus temperature variation

Sample	Temperature (°C)	Proximate analysis			Ultimate analysis					Mass Yield (%)
		A*	FC*	VM*	C (%)	H (%)	N (%)	O*(%)	S (%)	
Coal Tailing (CT)	Raw	40.32	37.31	22.37	42.82	3.01	1.14	11.28	1.43	
	150	38.36	**40.37**	21.27	**49.80**	2.87	1.72	6.50	0.75	97.66
	180	38.16	40.00	21.84	49.25	2.74	1.63	7.37	0.86	92.93
	210	40.16	38.25	21.59	49.14	2.68	1.68	5.56	0.78	96.28
	240	39.29	38.79	21.93	48.74	2.71	1.63	6.88	0.76	92.685
	270	40.41	37.57	22.02	48.42	2.67	1.67	5.99	0.84	92.44
Coal Slurry (CS)	Raw	24.17	53.02	22.69	61.85	3.56	1.39	7.77	1.26	
	150	20.12	**57.69**	22.19	**66.90**	2.98	1.99	7.14	0.87	94.74
	180	23.12	55.72	22.16	63.46	2.80	1.86	8.04	0.72	90.05
	210	21.27	56.27	22.46	62.53	2.75	2.05	10.62	0.78	92.8
	240	20.70	56.00	22.325	62.44	2.71	1.85	11.56	0.74	92.395
	270	26.81	50.83	22.36	60.82	2.67	1.79	7.18	0.72	91.28
Sewage sludge (SS)	Raw	39.25	9.52	51.23	29.70	4.88	4.15	20.16	1.86	
Blend CT+CS+SS	Raw (CB)	38.80	38.67	22.53	45.64	3.05	1.82	9.86	0.83	
	150	27.28	50.86	21.86	63.28	2.70	2.55	3.82	0.37	89.98
	180	28.53	48.32	23.15	65.43	2.78	1.56	1.28	0.42	79.28
	210	19.71	**58.82**	21.46	**67.04**	2.78	2.43	7.65	0.39	88.38
	240	26.51	51.77	21.71	65.26	2.61	2.22	2.92	0.49	80.24
	270	31.65	46.84	21.51	62.98	2.48	1.29	1.11	0.50	71.08

A: Ash content. FC: Fixed carbon. VM: Volatile matter. *: dried basis (moisture free). Solid/ liquid ratio of 1:4. O^{*}= 100-(A*+C+N+H+S).

The results of proximate analysis showed that CS has higher total carbon content compared to CT and CB. From the ultimate analysis results, the hydrothermal carbonization process yield (Cy) was determined using equation 2. Thus, resulted in higher carbonization yields of 113.58%, 102.47% and 129.61% for HCT, HCS and HCB respectively. This agreed with the results obtained by Saba (2017) who evaluated the impact of biomass blend with coal on the increase of carbonization yield during Co-HTC process. The study revealed that the acidic mild increased by the decomposition of biomass (SS) under Co-HTC process conditions, improved the removal of inorganic elements contained in the feedstock. The oxygen content decreased while hydrogen content changed minimally for both coal and SS blend. This can be attributed to the hydrolysis and decarboxylation reaction occurring during HTC and Co-HTC (Afolabi *et al*., 2020). The decrease of sulphur content in the produced hydrochars, contributes to the liberalisation of pores and improve the textural structure as demonstrated in

previous studies (Channiwala *et al*., 2002). This can further increase the porous properties of the AC produced from hydrochars as discussed in the next sections. The slight increase of nitrogen increased in the produced HCs was brought by nitrogen gas used to maintain the inert atmosphere in the HTC reactor.

Table 6-2. Proximate and ultimate analysis results of HTC process versus pressure variation

Sample	Pressure (bar)	Proximate analysis			Ultimate analysis				
		A*	FC*	VM*	C (%)	H (%)	N (%)	O*(%)	S (%)
Coal Tailing (CT) 150C	Raw	40.32	37.31	22.37	42.82	3.01	1.14	11.28	1.43
	10	37.11	39.02	23.86	48.43	2.76	1.71	9.23	0.75
	14.25	38.91	39.84	21.25	48.55	2.63	1.62	7.43	0.86
	18.5	39.89	39.97	20.14	48.88	2.61	1.67	6.18	0.78
	22.75	40.21	40.01	19.78	49.15	2.57	1.66	5.57	0.84
	27	38.36	**40.37**	21.27	**49.80**	2.87	1.72	6.50	0.75
Coal Slurry (CS) 150C	Raw	24.17	53.02	22.69	61.85	3.56	1.39	7.77	1.26
	10	23.82	55.84	20.34	60.99	2.66	1.87	9.94	0.72
	14.25	21.40	56.92	21.67	63.06	2.74	1.92	10.15	0.73
	18.5	20.47	57.40	22.13	64.90	2.79	1.87	9.20	0.78
	22.75	20.28	57.52	22.20	65.24	2.97	1.95	8.70	0.87
	27	20.12	**57.69**	22.19	**66.90**	2.98	1.99	7.14	0.87
Sewage sludge (SS)	Raw	39.25	9.52	51.23	29.70	4.88	4.15	20.16	1.86
Blend CT+CS+SS 210C	Raw (CB)	38.80	38.67	22.53	45.64	3.05	1.82	9.86	0.83
	10	25.04	57.29	17.67	62.17	2.58	2.24	7.35	0.61
	14.25	23.03	57.36	19.61	63.62	2.66	1.73	8.44	0.53
	18.5	20.44	57.57	21.99	63.96	2.50	1.68	10.78	0.64
	22.75	19.71	**58.82**	21.46	**67.04**	2.78	2.43	7.65	0.39
	27	20.85	58.67	20.48	64.12	2.37	1.69	10.58	0.38

A: Ash content. FC: Fixed carbon. VM: Volatile matter. *: dried basis (moisture free). Solid/ liquid ratio of 1:4. O^{*}= 100-(A*+C+N+H+S)

The results presented in Table 6-2 showed that the increase in pressure to 27 and 22.5 bar led to an increased in the FC content of the HTC, HCS and HCB produced. The conditions maintained the water at a liquid state and favoured the hydrolysis of aliphatic components, dissolution of minerals matter and prevent the escaping of the carboxylate's gas. The HCS with the highest FC content were selected for further analysis. Then after characterization, the selected HCs were utilized for the chemical activation experiments according to the design matrix obtained from DoE (Table 3-3). The diffractogram presented in Figure 6-3 (A) illustrates the findings of XRD investigation of coal samples, sewage sludge and produced hydrochars. The mineral

phases identified and labelled accordingly on the diffraction patterns presented on Figure 6-3(A) are; Clays: K(Kaolinite); Silicates: M(Muscovite), A(Anorthite), Q(Quartz), MO (Moganite), O(Orthoclase)); Carbonates: S(Siderite), C(Calcite); Oxide: H(Hematite); Sulphurs: P(Pyrite), and Chlorite: CL(Clinochlore). The mineral phase identification showed that silicates (**$[SiO_{(4-x)}]n$)** and aluminosilicates ($KAl_2(AlSi_3O_{10})(OH)_2$**)** (clay) minerals are present in significant proportion in the CT and CS while the predominant mineral phases in the SS are quartz (SiO_2) and clinochlore ((Mg, $Fe^{(2+)}5Al_2Si_3O_{10}(OH)_8$), showing the trigonal, hexagonal, triclinic and monoclinique, crystal systems of the three materials respectively (Jia *et al*., 2022). The correspondence of XRD profiles of raw materials and produced hydrochars observed on Figure 6-3 A agrees with the reported results in the previous study conducted by Jiang (2019) on characterization of coal/biomass blend. The decrease of peaks intensities of mineral phases observed in the diffraction patterns of the produced hydrochars was proportional to the impact of HTC and Co-HTC operating conditions on the dissolution of mineral content of the feedstock. All in agreement with the proximate analysis presented previously. The observation of the Figure 6-3(A) revealed a significant decrease of mineral phases peak's intensities for Co-HTC process. This was favoured by the strengthen acidic medium produced by the decomposition of SS into organic acid monomers during decarboxylation and dehydration reactions occurring in the HTC and Co-HTC process. The XRD diffractogram shows that the condensation and polymerisation of carboxyl and carbonyl groups produced from decarboxylation during HTC and Co-HTC forms a porous hydrophobic aromatic polymer (Knappe *et al*., 2018). The FTIR spectra (Figure 6-3(B)) were used to describe the chemical structural properties of the raw materials and produced hydrochars. The interpretation of the spectra was performed based on reference tables provided by Smith Brian (2018). Therefore, the peaks at 3620 cm^{-1} band were attributed to O-H stretching vibration linked with kaolinite mineral phase presented on the XRD patterns in the form of silanol (Si-OH). The lower intensity of the O-H observed on the spectrum band of the produced hydrochars compared to untreated coals demonstrated the evidence of dehydration reactions during HTC and Co-HTC process. The intense peak at 2922.63cm^{-1} band was due to higher presence of aliphatic group in the SS characterized by long linear chains $-CH_2$ and $-CH_3$

asymmetric and symmetric vibrations(alkanes) respectively (Mishra *et al*., 2018). The shoulder peaks at 2960 cm^{-1} band observed on the HCT and HCB spectra were assigned to asymmetric aliphatic -CH_3 stretching vibration produced from the interaction of the C-H aliphatic stretch observed at 2850 cm^{-1} and 2920cm^{-1} and C-H alkyl groups from CT and CS spectrums during the process (Doshi *et al*., 2014). The peak observed atb1700cm^{-1} band can be assigned to the aliphatic C=O and -COOH stretching vibrations of carboxyl and carbonyls, mainly ketones, aldehydes, and esters in the SS (Mishra *et al*., 2018). At 1600cm^{-1} bands, corresponding to the aromatic C = C structure, HCS possesses the strongest peak intensity followed by HCB, CS, CB, HCT, CT then SS respectively. This agrees with the distribution of total carbon content (presence of lignin) obtained from ultimate analysis of materials presented in Tables 2 and 3 (Balachandran et al2014). The peaks observed at 1595.25 cm^{-1} wavelength indicated the presence of double bound carbonyl groups (C=O) combined with aromatic stretch confirming the presence of cellulose (Mishra *et al*., 2018). The low intensity of the C=O peaks in the produced HCs confirmed the occurrence of decarboxylation reaction during HTC and Co-HTC. The transmittance peak within the fingerprint region of the spectrum at 1500 and 570 cm^{-1} band in all spectra with downgrading intensity order from CT, SS, CS, CB, HCS, HCT to HCB were assigned to the vibrations associated with –CH_3, C-C, Si-O-Si in quartz and kaolinite, aromatic species in aromatic rings; trans- and cis-CH_2 in long saturated aromatic -CH-CH chains, C-O stretching vibration of ether groups; O-H bending vibrations in phenolic, phenoxy and hydroxybenzene structures. The condensation and polymerisation steps were confirmed by the decrease of peak intensity of the produced HCs compared to the raw materials resulting in the elimination of the oxygen and hydrogen into water in liquid phases and restructuration of the carbon skeleton (Tan *et al*., 2019). The FTIR spectra revealed the complexity of the thermal decomposition and restructuration of HTC and Co-HTC products. The SEM analysis of the feedstocks and produced HCs was conducted to evaluate the structural change on the surface of the materials. The results obtained revealed that the physicochemical properties of the produced HCs were influenced by the HTC process parameters and the nature of the feedstock. The predominance of carbon in the produced HCs was highlighted on the element spectrums obtained from EDS analysis (Figures 6- 4 (d), 6-5 (d), 6-6 (d)) The SEM

images of the feedstocks and produced HCs demonstrated the impact of HTC and Co-HTC process on the surface's structure. The rough and irregular morphologies of the raw materials (Figures 6-4(a), 6-5(a), 6-6(a)) were converted to well distributed porous surface of the produced HCs (Figures 6-4(c). 6-5(c), 6-6(c)). Spotting features were identified on the images of the produced HCs confirming the presence of microstructural pores (Figures 6-4(c), 6-5(c), 6-6(c)). The porous properties of the produced HCs hold a high potential to produce high specific surface activated carbon. The thermolytic effect of HTC and Co-HTC temperature increase on the feedstock generates pores in the material structure through the release of hydrogen, oxygen, sulphur, and the degree of mineral content dissolution (Saba *et al*., 2017). The surface morphology of the produced hydrochar obtained from SEM favoured the evaluation of microstructural changes of the coals and the mixture coal-sewage sludge after HTC (Figure 6- 3A) and Co-HTC (Figure 6-3B) process respectively.

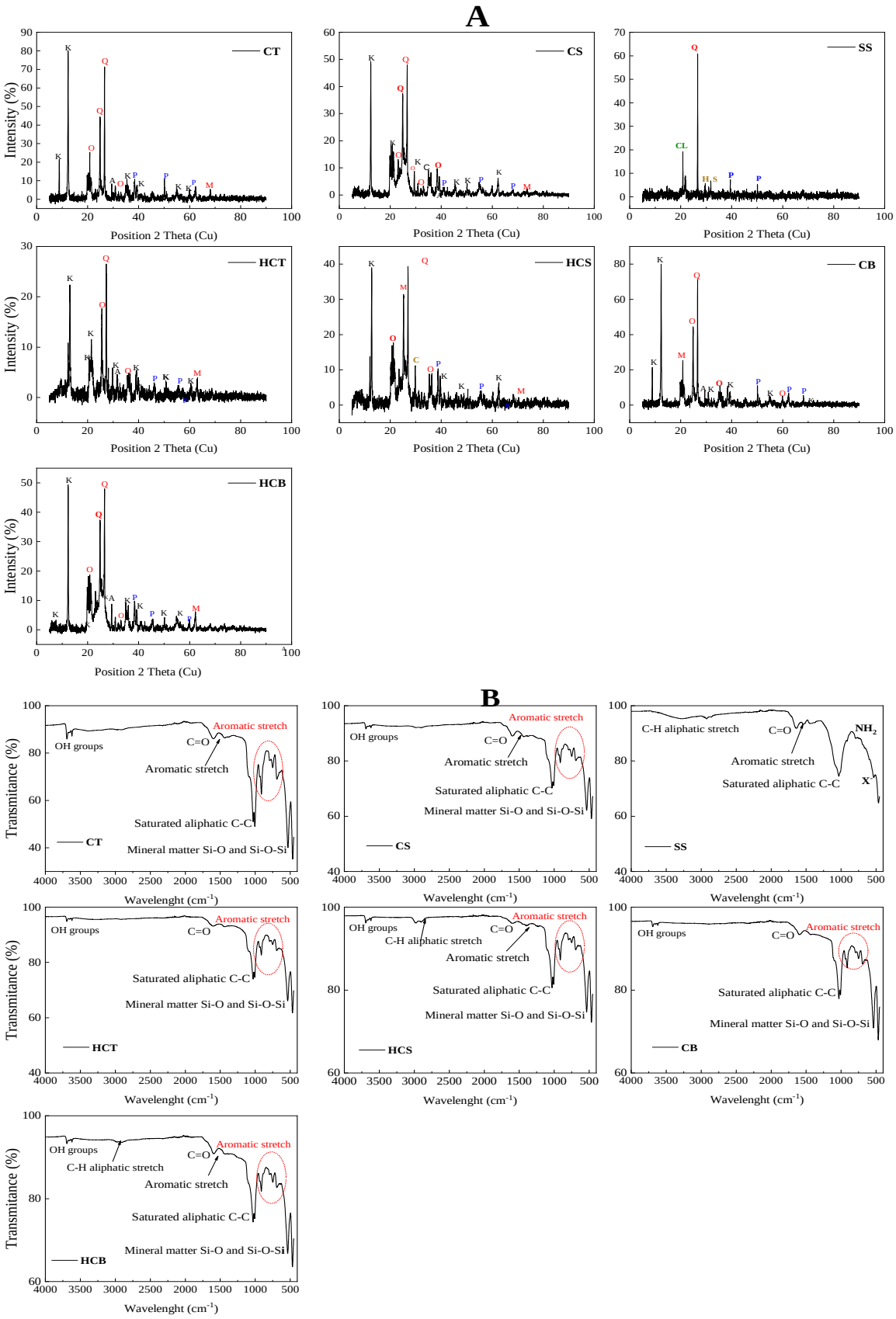

Figure 6-3:XRD patterns of coal, sewage sludge and produced hydrochar (A) and FTIR spectra of coals, sewage sludge and produced hydrochar (B)

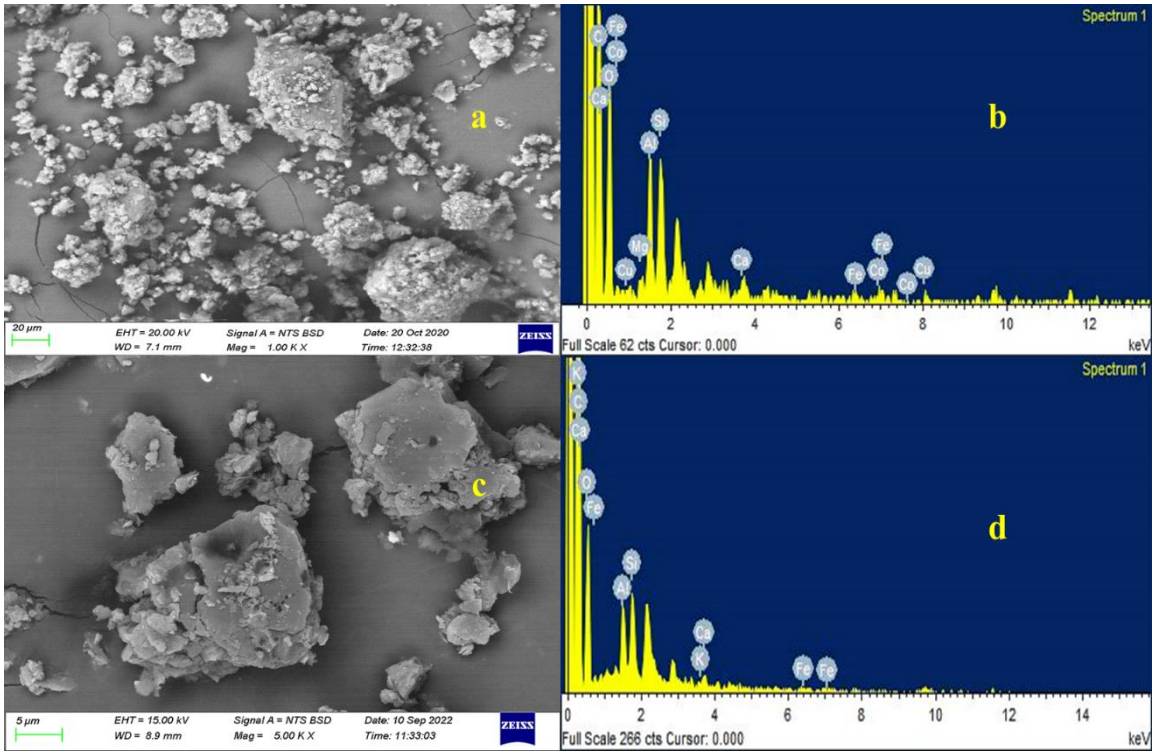

Figure 6-4:SEM images and EDX elemental spectrums respectively of coal tailing (a & c), and coal tailing's hydrochar (b & d)

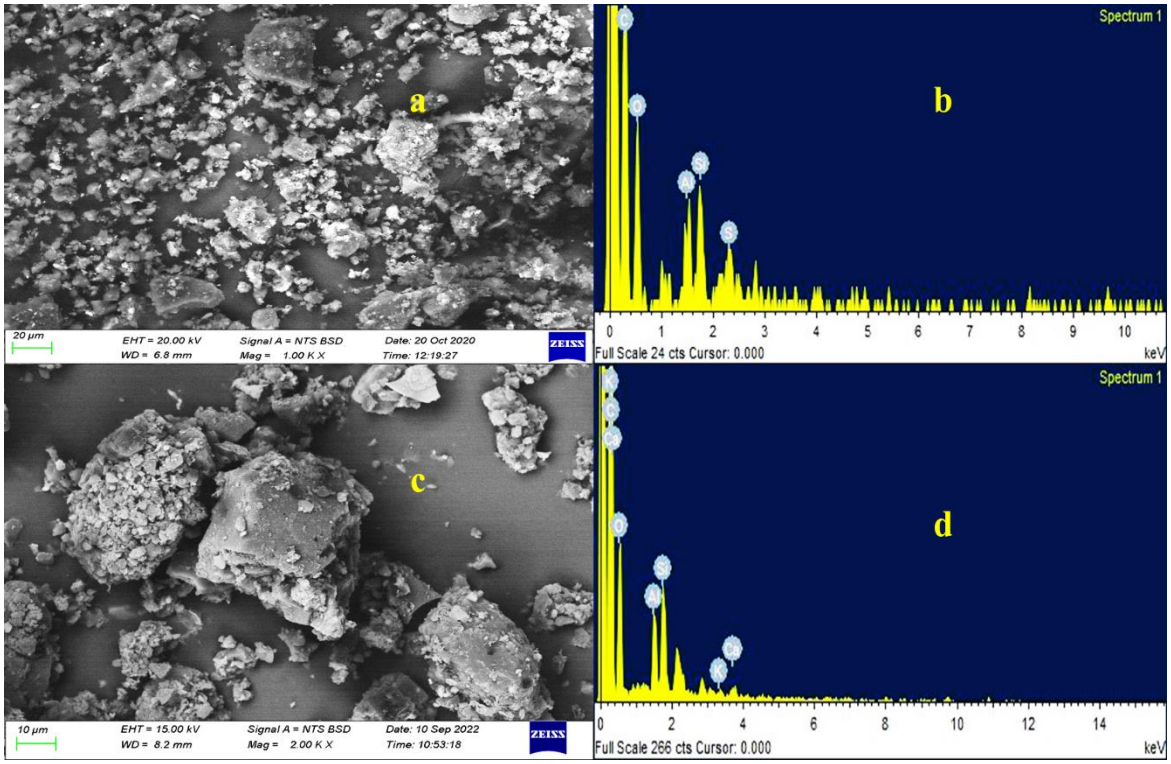

Figure 6-5:SEM images and EDX elemental spectrums respectively of coal slurry (a & c), and coal slurry's hydrochar (b & d)

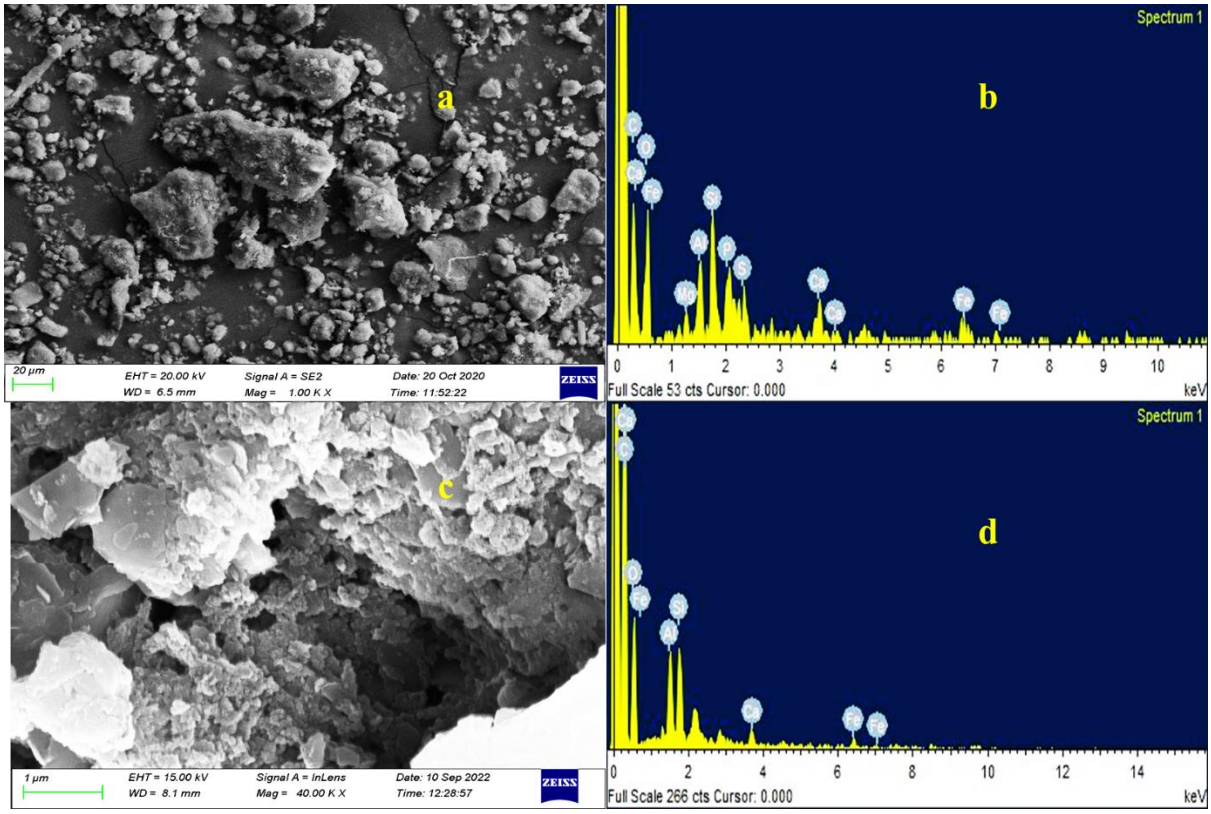

Figure 6-6 :SEM images and EDX elemental spectrums respectively of the mixture of coals and sewage sludge blended in optimized ratio (1CT+1CS:0.4SS) (a & c), and the Co-HTC produced hydrochar (HCB) (b & d).

The characterization of the produced HCs revealed that HTC and Co-HTC process improved the carbon content of the feedstocks. The physicochemical properties of HCs produced in this study were comparable to those of the HCs produced in previous studies (Saba *et al*., 2017; Tasca *et al*., 2019). In addition, the results of this study indicate that the Co-HTC process has a significant carbonization potential to produce hydrochar from the combination of coal discard and sewage sludge (HCB), comparable to HCB produced from other feedstock as reported in previous studies (Saba *et al*., 2017; Wang *et al*., 2019). Furthermore, the optimum HTC and Co-HTC conditions selected in this study have the potential to reduce the energy requirement and cost of the process from a development and economic feasibility standpoint, when compared to the reported operating conditions for other thermal processes, such as pyrolysis and gasification (Afolabi *et al*., 2020). The porous characteristics of the HCs could increase the textural properties of the chemically activated carbon products as discussed in the next section.

6.4.2. Chemical activation results

The statistical parameters were evaluated using the analysis of variance (ANOVA) applied on the results obtained from BET (Brunauer Emmet Teller) analysis presented in Tables 6-3 and 6-4. The ANOVA results are displayed in Appendix L, M and N for AC-HCT, AC-HCS and AC-HCB respectively. The ANOVA results revealed that, the S_{BET} of produced ACs was significantly affected by an interaction effect of process temperature and holding time. The regression models (equations 1-3) were tested using the probability (p-value) and Fischer test values (F-value) for the obtained responses. The F-value and p-value determined the significancy of the independent variables on the surface responses (Afolabi *et al*., 2020). In addition, the obtained regression models (equations 1-3) indicated the influence of the two process factors i.e., temperature and holding time on the S_{BET} of the produced ACs. All models were found statistically significant due to their high F-values and lower p-values (Abdulsalam *et al.*, 2019). The unsignificant lack of fit obtained reveals that the models fitted correctly to the experimental data. The accuracy of the models was evaluated by the coefficient of determination (R^2).

Table 6-3. BET analysis results of the produced activated carbons from HCT and HCS

Run	Factors		AC-HCT			AC-HCS		
	F 1	F 2	Responses			Responses		
			R1	R2	R3	R1	R2	R3
	Temperature (°C)	Activation Time (min)	Carbon Yield (%)	Specific surface (m^2/g)	Pore volume (cm^3/g)	Carbon Yield (%)	Specific surface (m^2/g)	Pore volume (cm^3/g)
HC	-	-	-	11.88	0.071	-	14.35	0.094
1	825	135	66.67	1945.35	1.60	68.65	2246.18	1.95
2	825	135	69.7	1944.39	1.73	66.86	2183.70	1.65
3	825	180	68.67	1675.64	1.90	64.83	1990.84	1.73
4	850	135	66.70	2021.91	1.77	66.28	2299.25	1.96
5	850	180	57.56	1830.66	1.91	67.06	2113.74	1.90
6	825	135	67.03	1943.33	1.86	68.96	2261.78	1.86
7	825	135	65.61	1947.06	1.82	63.89	2176.39	1.93
8	800	135	72.45	1907.28	1.57	65.76	2247.48	1.67
9	850	90	68.38	1971.97	1.55	64.10	2107.31	1.63
10	825	90	71.86	1836.63	1.31	71.67	2042.42	1.70
11	800	90	73.51	1741.81	1.29	64.52	2093.64	1.62
12	800	180	68.12	1686.43	1.44	65.54	2044.57	1.55
13	825	135	69.29	1947.80	1.80	62.01	2267.98	1.88

AC-HCT: Activated Carbon from Coal Tailing's Hydrochar. AC- HCS: Activated carbon from Coal slurry's Hydrochar. BET: Brunauer Emmet Teller

Table 6-4. BET analysis results of the produced activated carbon from HCB

Run	Factor 1	Factor 2	Response 1	Response 2	Response 3
	A: Temperature	B: Activation Time	Carbon yield	Specific surface	Pore volume
	Degree Celsius	Minutes	%	m^2/g	cm^3/g
3	800	135	64.65	2242.69	1.38
6	800	90	66.86	2093.23	1.15
8	800	180	57.83	2064.5	1.1
1	825	135	63.28	1945.82	1.32
2	825	135	61.06	1958.97	1.37
4	825	135	62.96	2021.79	1.33
7	825	180	60.89	1791.95	1.23
9	825	135	63.76	1965.55	1.17
10	825	135	62.10	2021.79	1.38
11	825	90	65.67	1838.38	1.21
5	850	135	58.52	2069.56	1.39
12	850	90	60.54	1896.79	1.16
13	850	180	55.01	1902.57	1.35

AC-HCB: Activated Carbon from coal discard (CT+CS) and sewage sludge blend's hydrochar. BET: Brunauer Emmet Teller Specific area

The significant models to optimise the S_{BET} of produced ACs were observed as a good fit, (R^2 0.9752, R^2 0.9303, R^2 0.9673 at p-value <0.0001) and are represented by Equations (1), (2) and (3) respectively. The adjusted coefficients of determination presented in Appendix L, M and N (Adj R^2) are in reasonable agreement with the predicted coefficients of determination (Pred R^2).

The mathematical equations in term of actual factors obtained from the regression model predicted the responses (S_{BET}) and ensured the reproducibility of the experimentation. The accurate regression models fitted for S_{BET} values of the produced ACs are quadratics.

$$AC - HCT\ S_{BET} = 1941.09 + 81.50A - 59.61B + 21.48AB + 34.74A^2 - 173.73B^2 \quad (6\text{-}1)$$

$$AC - HCS\ S_{BET} = 2223.48 + 22.44A - 15.70B + 13.87AB + 59.21A^2 - 197.53B^2 \quad (6\text{-}2)$$

$$AC - HCB\ S_{BET} = 1982.68 - 88.58A - 13.49B + 5.74AB + 173.71A^2 - 167.52B^2 \quad (6\text{-}3)$$

The negative coefficient of the variables indicates its antagonistic effect on the S_{BET} value of the produced AC. The synergetic effect of the output responses was revealed by the positive coefficients within the equations (Behera *et al*., 2018).

The impact of chemical activation temperature and holding time on the S_{BET} was evaluated and displayed on the 3D surface plots of the responses (Figures 6-7 and 6-8). The evidence of quadratic effect due to reaction temperature and holding time was demonstrated by the curvature observed on the surface plots. The impact of the two process parameters was illustrated by the slopes observed on the surface plots. The increase of temperature and holding time increased the S_{BET} of the produced ACs due to the degradation of cellulose from the precursor into bitumen resulting in the development of the porous structure of ACs (Danish *et al*., 2014). However, a longer residence time (135< t <180min) reduced the S_{BET} of the produced ACs. This could be due to the elimination of internal carbon atoms after the maximum peak of micropores formations which breaks down the internal structure of the produced AC (Yorgun *et al*., 2016). The absence of active sites probably caused by the sintering of the material after the reaction of KOH and carbon leads to the adhesion of surface particles. In this situation, the bonded particles surface flow into the pores which increases the grain size of the material and diminishes its porosity (Zhou *et al*., 2018). As a results, micropores previously developed via the release of gas products were obstructed and decreased the S_{BET} of the produced ACs. Therefore, results obtained showed that the textural characteristics of the produced ACs are influenced by chemical activation process parameters.

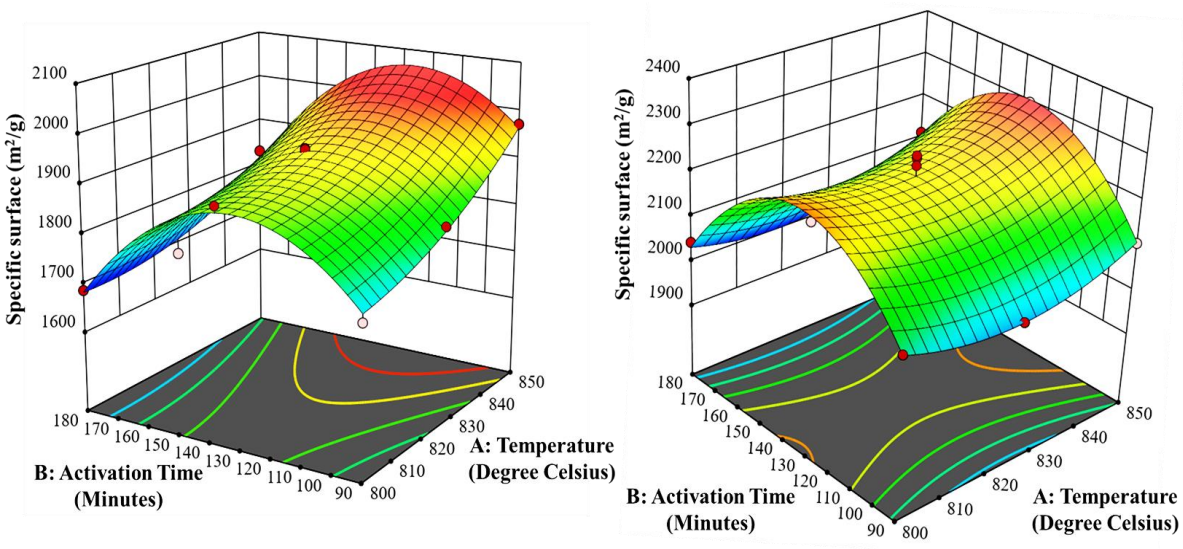

Figure 6-7 :Surface plot showing the influence of temperature and Activation time on surface area of the produced Activated carbon from HCT (left) and HCS (right).

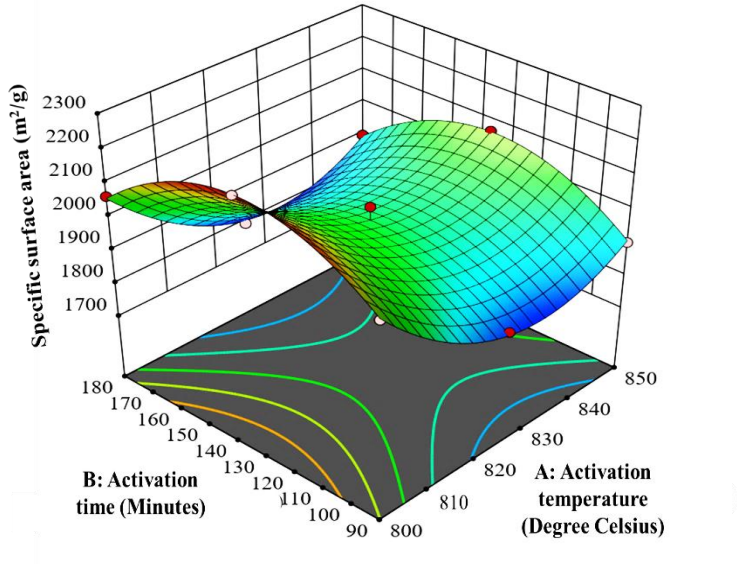

Figure 6-8 :Surface plot showing the influence of activation temperature and residence time on surface area of the produced Activated carbon form HCB

The accuracy of the models was evaluated by the plot of experimental versus predicted values (Figures 6-9 and 6-10). The normal distributions of the residuals are confirmed by the straight lines in the graphs in consistence with the study of Afolabi (2015) on the statistical analysis of the activation process. The figures revealed a good fit confirmed by the clustered data points observed on the regression line showing the correlation between the actual and predicted values for the points of the design matrix. In addition, the figures reveal the accuracy of the designed models and demonstrated the reliability of the models for the determination of S_{BET} of the

produced ACs based on the variation of parameters used within the investigated ranges.

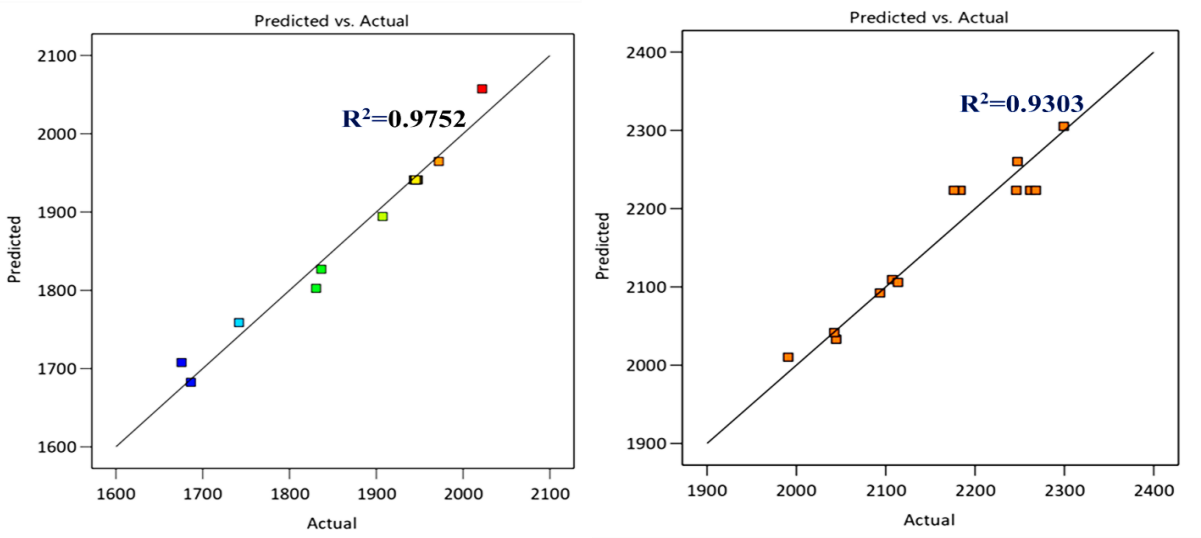

Figure 6-9:Predicted vs Actual plots of the Specific surface area of produced Activated carbons from Coal tailing's HC (left) and Coal slurry's HCs (right).

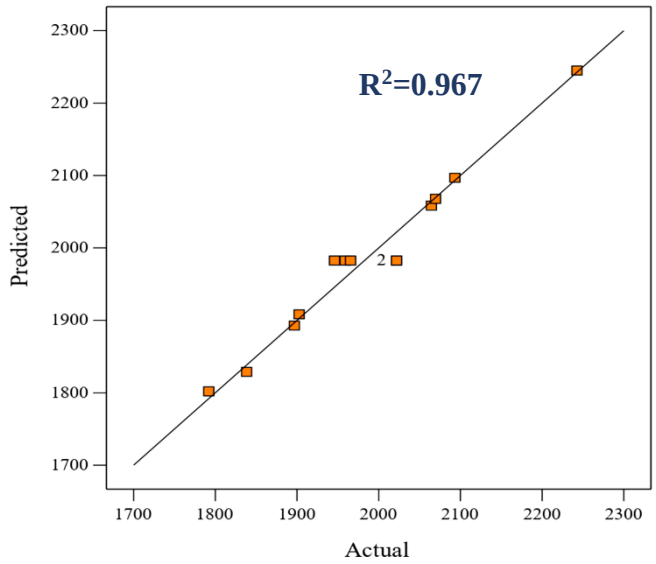

Figure 6-10 :Predicted vs Actual plots of the Specific surface area of produced Activated carbons from Coal discards and sewage sludge blend 's HC (AC-HCB).

6.4.3. Optimum operating conditions

The results obtained from the RSM were evaluated for the optimization of the input factors and constraints (Table.6-5). The goal was to complete the analysis with the determination of maximum possible S_{BET} of the produced ACs. The input factors ranged from 800°C and 90 minutes as lower limits to 850°C and 180 minutes as upper

limits of yielded optimization solutions for activation process. Using the desirability function of the DoE, the conditions that provided the maximum desirability factors were selected as the optimum process parameters (Appendix O, P and Q). The results revealed that 850°C, 147.37 minutes, 849.43°C, 132.31minutes, and 800°C, 133.99 minutes were optimum conditions of activation process of HCT, HCS, and HCB respectively.

Table 6-5. Parameters constraints used for the optimization of the activation process

Name	Goal	AC-HCT		AC-HCS		AC-HCB	
		Lower Limit	Upper Limit	Lower Limit	Upper Limit	Lower Limit	Upper Limit
A: Temperature (°C)	Is in range	800	850	800	850	800	850
B: Residence time (min)	Is in range	90	135	90	135	90	135
S_{BET} (m^2/g)	Minimize	1675.64	2021.91	1990.84	2299.25	1791.95	2249.69
Total pore volume (cm^3/g)	Maximize	1.28	1.91	1.28	1.91	1.1	1.38
Carbon yield (%)	Is in range	57.56	73.51	62.01	71.67	55.01	66.86

AC-HCT: Activated Carbon from Coal Tailing's Hydrochar. AC- HCS: Activated carbon from Coal slurry's Hydrochar. AC-HCB: Activated Carbon from coal discard (CT+CS) and sewage sludge blend's hydrochar. S_{BET}: Brunauer Emmet Teller Specific area

The percentage of absolute error between the predicted and the experimental values was calculated using equation (6-4). The error percentages found are presented in Table 6-6 and revealed that the optimized results were consistent compared to the experimental measurement.

$$Percentage\ of\ absolute\ error\ (POAE) = \frac{Experimental - Predicted}{Experimental} \text{ x } 100\ (\%) \qquad (6\text{-}4)$$

Table 6-6. Chemical activation optimum solutions

Name	AC-HCT	AC-HCS	AC-HCB	POAE
Parameters				
Temperature (°C)	**850**	**849.43**	**800**	0.067-
Time (Min)	**147.37**	**132.31**	**133.99**	0.35-7.4
Results				
Specific surface area (m^2g^{-1})	**2021.91**	**2301.38**	**2243.575**	0.001–0.076
Total pore volume(cm^3g^{-1})	1.89	1.91	1.31	0.005–0.25
Carbon yield	64.38	66.14	63.47	0.21-3.47

AC-HCT: Activated Carbon from Coal Tailing's hydrochar. AC- HCS: Activated carbon from Coal slurry's hydrochar. AC-HCB: Activated Carbon from coal discard (CT+CS) and sewage sludge blend's hydrochar. POE: Percentage of absolute error

The optimum conditions obtained were comparable to the operating conditions widely utilized in previous activation process studies. For example, Abdulsalam (2019) revealed through his study that the optimum conditions of activation process of different coal were 800°C and a KOH: Coal ratio of 1:4 to produce high S_{BET} ACs of 1898.31m^2g^{-1}, 1806.91 m^2g^{-1} and 1486.74 from run of mines, coal discards and coal slurry respectively. Furthermore, in the review study of methods for preparation and activation of activated carbon conducted by Heidarinejad (2020) it was confirmed that the increase of temperature in chemical activation process increases proportionally the S_{BET} of the produced activated carbon. This is due to the acceleration of the thermal degradation of cellulose and elimination of volatiles products resulting in the creation of porous structure. Therefore, an average increase of 13% and 29% was noted for HCT and HCS, as the temperature increases from 800℃ to 850℃ and residence time from 90 mins to 135 mins, respectively. Nevertheless, the highest S_{BET} of AC produced from the HCB (2243.57 m^2/g) was obtained at 800°C. This optimum temperature was slightly lower compared to 850°C needed for the optimization of AC-HCT and AC-HCS. This could be due to the low amount of ash in the HCB which favours the facile interaction and rapid saturation of KOH on the carbon precursor resulting in the faster creation and evaporation of gas products leaving the pores on the surface of the produced AC (Zhou *et al*., 2018). The KOH reacts directly with the carbon atoms from the internal structure of the HCB and releases a considerable amount of gas product which increases the S_{BET} of the produced AC (Huang *et al*.,

2016). However, HCT and HCS contained a considerable amount other metal elements (ash content) susceptible to produce complex hydroxide which assumed to evaporate completely at higher temperature for the increase of the porous structure of the produced ACs (Njoku *et al*., 2014). Furthermore, different chemical impregnation ratios were used to determine the impact of the amount of reagent on the textural characteristics of the produced ACs at obtained optimum parameters. The results revealed that the increase of KOH:HCs ratio from 1:1 to 4:1 increased the S_{BET} of the produced ACs from 780.60, 1170.15, and 1005.24 m^2g^{-1} to 2021.91, 2299.25 and 2243.57 m^2g^{-1} for AC-HCT, AC-HCS and AC-HCB respectively. This agrees with the results obtained by Yorgun (2016) which showed that the increase of the KOH dosage increases the development of microporous structure on the surface of the produced ACs due to the high interaction of KOH with carbon atoms of the precursor. The penetration of activating reagent into the carbon structure of the carbonaceous material leads to the creation of small pores in the produced ACs at higher temperature, thereby increases their surface area (Blankenship *et al*., 2022). The KOH reacts with the carbon matrices and release the gas products to develop porous texture on the surface of the produced ACs. The remaining spent alkali obscuring the pore's cavities of the produced AC is eliminated through a washing step and improves the textural properties of the produced ACs (Wang *et al*., 2019).

Post analyses were performed to confirm the accuracy of the model using optimum parameters as confirmation points (Appendix R). Post experiment results with S_{BET} of 1941.09m^2g^{-1}, 2300 m^2g^{-1} and 2243 m^2g^{-1} for AC-HCT, AC-HCS and AC- HCB respectively were obtained and analysed by the software to validate the regression models. The predicted means obtained compared to the medians using the regression models (equations 3,4 and 5) revealed that the standard deviations and standard errors were in acceptable range. This confirms that; the models can be used to predict the S_{BET} of the produced ACs (Bideskan *et al*., 2020).

6.4.4. Direct Chemical Activation of coal discards

The optimal conditions of 850°C and 135 minutes activation time obtained from the optimization study performed on HCT and HCS were used for the direct chemical activation of CT and CS. The BET results revealed the S_{BET} of 1354.28 m^2/g and 1845.09 m^2/g for the produced ACs from CT and CS, respectively. However, the values of the S_{BET} for the produced AC from direct chemical activation (ACT and ACS) were lower than those of the produced AC from HCT and HCS. The S_{BET} increases obtained using equation 8 were 49.29% from ACT to AC-HCT and 24.61% from ACS to AC-HCS. This suggest that the combination of HCT and chemical activation process led to the production of activated carbons with higher pore volume and larger S_{BET}.

Surface area Increase (SI): $\frac{S_{BET,AC-HCX} - S_{BET,AC-HCX}}{S_{BET,AC-CX}} x100\ (\%)$ (6-5)

Where $S_{BET,\ AC\text{-}HCX}$ represents the specific surface of the activated carbon from produced hydrochars (HCx) and $S_{BET,\ AC\text{-}CX}$ the specific surface of the activated carbon produced from direct activation of coals (CX).

The obtained results corroborate the trends reported in several investigations on the carbonization pre-treatment of different raw materials before activation process with KOH reagent (Zhao *et al*., 2012a; Mistar *et al*., 2020b). Hence, for the sustainability of the HTC technic as a pre-treatment step of activation process the results from direct chemical activation of coal fines were investigated. The results presented in the Table 6-7 demonstrated that the produced activated carbons from HCs presented wider surface area and higher pore volume compared to the activated carbons synthesized from direct activation of coal fines samples used in this study. The textural properties of obtained activated carbon confirmed that the HTC process prior improved the porous properties of the coal samples used then leaded to the production of activated carbons with higher pore volume and specific surface area.

Table 6-7. BET analysis results of the coals, produced HCs and AC

Material	Surface area (m^2g^{-1})	Total pore volume (cm^3g^{-1})	Average pore diameter (nm)
CT	6.066	0.034	2.16
AC-CT	1354.28	1.05	3.02
HCT	11.882	0.071	2.62
AC-HCT	2021.91	1.88	2.75
CS	6.37	0.048	2.65
AC-CS	1845.09	1.21	2.64
HCS	14.35	0.094	3.34
AC-HCS	2299.25	1.96	2.56

CT: Coal tailing. CS: coal slurry. HCT: Hydrochar from coal tailing. AC-CT: Activated carbon from coal tailing. AC-CS: Activated carbon from coal slurry AC-HCT: Activated carbon from coal tailing's Hydrochar. HCS: Hydrochar from coal slurry.AC-HCS: Activated carbon from coal slurry's hydrochar BET: Brunauer Emmet Teller

The produced ACs through HTC process pre-treatment might be categorized as higher surface area ACs compared to a considerable number of ACs produced from other sources of coal used in a wide range of applications such as energy storage (supercapacitor, electrode), natural gas adsorption, wastewater treatment, etc… available in literature presented in Table 6-8. In addition, as from study performed by Thu (2021b) it was found that adsorption capacity of AC depends on its surface area characteristic; the highest adsorption capacity should result from the highest surface area of produced ACs. In fact, during activated carbon activation with alkali substances such as KOH, alkali metals and carbonates are created in the carbon matrix (Heidarinejad *et al*., 2020). The elimination of these substances leads to the stability and expansion of the spaces between the carbon-atom layers which result in the increase of carbonization efficiency and adsorption capacity of the produced AC (Ahmed *et al*., 2014). Therefore, in this project, the capability of country largely available coal wastes and SS to be used for AC production for further probable wastewater treatment and hydrogen gas storage has been investigated.

Table 6-8. Textural properties of the produced AC from other coals sources

Raw material	AC-Surface area (m^2g^{-1})	AC-Pore volume (cm^3/g)	References
Coal tailing from South African coal beneficiation plant in Mpumalanga (CT)	1354.28	1.05	This work
Coal slurry from South African coal beneficiation plant in Mpumalanga CS	1845.09	1.21	
Coal tailing's hydrochar (HCT)	2021.91	1.77	
Coal slurry's hydrochar (HCS)	2299.25	1.96	
Hydrochar from coal-sewage sludge blend (HCB)	2243.57	1.38	
Charcoal (Commercial activated carbon)	900	0.76	Sigma-Aldrich (Granular 4-12 mesh, CAS 7440-44-0
Raw coal indigenously provided by Dara Adam Khel Coal Mines	1598.4		Wazir *et al* (2022)
Malaysian Merit Kapit low rank coal	848.7		Jawad *et al* (2019)
Low rank Rawdon coal	1951	1.049	Gokce *et al* (2021)
Low-quality subbituminous coals from the Changki colliery (Nagaland) and Jadi colliery (Garo Hills, Meghalaya) located in India;	789.910	0.103	Bora *et al* (2021)
Coal from the Shengli lignite at Inner Mongolia.	1489	0.54	Dong *et al* (2020)
Bituminous coal from China	1183	061	Zhang *et al* (2020)
Raw Anthracite from China	836	0.37	
Anthracite from Blaschak Coal Corp. (Mahanoy City, PA, USA) Lattimer mining site	527.43		Song *et al* (2020)
Carbon-rich coal fly ash from power plant in Janikowo, Poland	946.77	0.47	Musyoka *et al* (2020)

Law rank coal from Malaysian Selantik	1094.3	0.076	Jawad *et al* (2022)
Xiaoquan coal, from Ningxia, China	1879	0.93	Wang *et al* (2016)
South African discard coal	1826.41	1.25	Abdulsalam *et al* (2019)
South African coal slurry	1484.96	1.042	
South African coal fines run of mine	1925.34	1.29	
Blackwater coal from Queensland's Bowen Basin in Australia	1401		Gao *et al* (2015)
Commercial AC from Mineral Coal	900	0.73	Carbo-Tech
Commercial AC	1374.00		Srenscek-Nazzal *et al* (2015)
South African bituminous coal	350		Campbell *et al* (2012)
Low-grade Indonesian coal	668		Martin *et al (*2011)
Unburnt coal from China power plant	1520		Wu *et al* (2010)
Amasra bituminous	588		Sutcu *et al (*2006)
Bituminous coal	1150		Himeno *et al* (2005)
Anthracite coal	2085		Lozano-Castello *et al* (2002)
Ning Xia anthracite coal, China	2398.1		Zou *et al* (2002)
Illinois Basin coal	1560		Sun *et al* (1997)
Australia bituminous coal	925		Ahmadpour and Do. (1996)

AC: Activated carbon.

6.4.5. Physicochemical and textural properties

The conversion of physicochemical properties from the raw materials to the optimum activated carbon selected passing by the HCs are depicted in Table 6-9. The results showed the significancy of HTC process for the production of high properties ACs. The HTC and Co-HTC process priory reduced the ash content of the feedstocks. Thereafter, the chemical activation process conditions significantly decreased the volatile matter content of the HCs which resulted in the increase of carbon content in the produced ACs (Table 6-9). The reaction between the activating agent and the precursor of carbon materials at high temperature resulted in the decomposition of

volatile compounds, thus creating a porous structure on the surface of the AC (Thommes *et al*., 2015). As a results, lighter solid materials were produced reflected by the decrease of carbon mass yield (Table 6-9)

Table 6-9.Physicochemical properties of coal, produced hydrochars and activated carbons.

Analysis	CT	HCT	CS	HCS	CB	HCB	AC-HCT	AC-HCS	AC-HCB
Proximate Analysis (wt%, adb)									
Inherent Moisture	4.17	1.07	3.94	1.73	2.71	1.72	1.39	1.19	1.24
Ash content	38.64	37.96	23.22	22.78	37.75	19.56	40.86	23.59	23.17
Volatile Matter	21.44	21.04	21.28	18.38	21.92	20.31	6.81	4.76	6.31
Fixed Carbon	35.75	39.94	50.98	57.11	37.62	58.41	50.94	70.46	69.28
Ultimate Analysis (wt. %, adb)									
Carbon	42.82	49.80	61.85	66.90	45.64	67.04-	51.16	71.30	70.90
Hydrogen	3.01	2.87	3.56	2.98	3.05	2.78	4.13	1.87	2.74
Nitrogen	1.14	1.72	1.39	1.99	1.82	2.43	1.64	1.34	0.94
Oxygen	8.79	5.83	4.78	2.75	8.2	6.08	0.81	0.71	1.01
Total Sulfur (wt. %, adb)	1.43	0.75	1.26	0.87	0.83	0.39	0.01	0	0
Mass yield (%)	-	97.96	-	93.64		88.83	64.38	66.16	64.65

CT: coal Tailing. CS: Coal Slurry. CB: Blend CT+CS+SS. HC: Hydrochar. adb: air dried basis. AC-HCT: Activated Carbon from Coal Tailing's Hydrochar. AC-HCS: Activated Carbon from Coal Slurry's Hydrochar. AC-HCB: Activated Carbon from coal discard (CT+CS) and sewage sludge blend's hydrochar.

Nitrogen adsorption isotherm is the most prevalent and widely utilized method employed to assess the porous natures of ACs. The highest S_{BET} ACs (Tables 6-5) were selected for nitrogen adsorption tests made at 77K. The nitrogen adsorption isotherms depicted in Figure 6-11(A) revealed that all the produced ACs are relatively microporous materials evidenced by the Type I isotherms categorized according to IUPAC with non-obvious hysteresis loop (Zhang.2016; Ansani *et al*., 2020). The isotherms are concave to the relative pressure, P/Po axis and approach a limiting value as P/Po ~ 1. The limiting nitrogen uptake could then be governed by the accessible micropore volume rather than by the internal surface area (Abdulsalam *et al*., 2019). A fold followed by a plateau revealed the development of micropore followed by the constant filling of the wider pore characteristics of mesopores (Sinha *et al*., 2019). At lower pressure a fast nitrogen uptake was assumed by the monolayer adsorbent-adsorptive interaction on the micropores walls (Zhang.2016). The uplift tendency observed after the plateau indicates the presence of pores with width above

the determined critical width which is a function of adsorption temperature (Sinha *et al*., 2019). The nitrogen adsorption isotherms for the produced ACs shown in Figure 6-11(A) reveal the high amount of nitrogen adsorbed on AC-HCS followed by AC-HCB and AC-HCT respectively. Thus, showing that the textural properties of AC-HCS were higher than the AC-HCB and AC-HCT (Heidarinejad *et al*., 2020). This is consistent with the largest $S_{BET,}$ and pore volume obtained for AC-HCS (2299.25m^2g^{-1}, 1.96cm^3g^{-1}) compared to AC-HCB (2242.63m^2g^{-1}, 1.38cm^3g^{-1}) and AC-HCT (2021.91m^2g-1, 1.77cm^3g^{-1}) respectively. The difference in textural properties between the produced ACs could be attributed to the physicochemical properties of the HCs precursors. The development of pores on the ACs is associated with the release of gas formed during the activation reaction with KOH (Heidarinejad *et al*., 2020)]. The reaction between the KOH reagent and the HCs is equivalent to the amount of carbon content of the HCs according to the reaction (1) (Yorgun *et al*., 2016; Heidarinejad *et al*., 2020). Hence, the high textural parameters of AC-HCS compared to AC-HCB and AC-HCT could be assigned to the high carbon content of the HCS precursor (Table 6-10).

$$6KOH + 2C \rightarrow 2K + 3H_2 + 2K_2CO_3 \qquad (6\text{-}6)$$

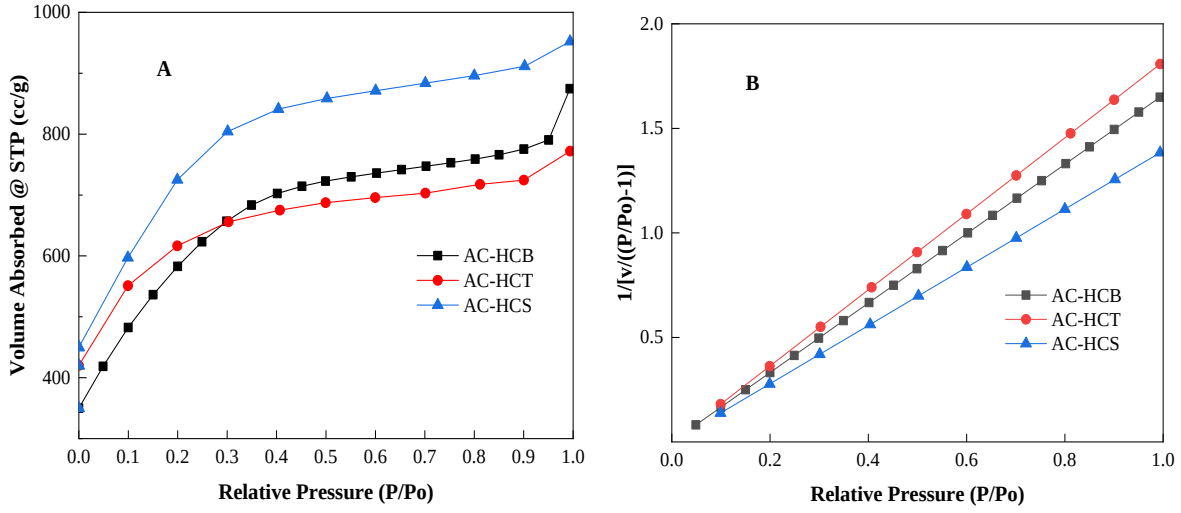

Figure 6-11:Nitrogen adsorption isotherms (A) and surface area plots (B)of produced activated carbons

The observation of the obtained adsorption isotherms (Figure 6-11(A)) showed the difference of adsorption capacity of the three produced ACs. In addition, the Figure 6-11 (B) shows the correlation between the specific surface area and the volume of

nitrogen adsorbed (v) at a relative adsorption pressure of the nitrogen gas adsorbed. The slopes of the lines in the Figure 6-11 (B) showed confirmed that the AC-HCS was characterized by the highest surface area compared to AC-HCB and AC-HCT respectively. The nitrogen adsorption capacity of the ACs is inversely proportional to the slopes of the lines plotted (de Souza *et al*., 2018).

The results obtained for nitrogen adsorption and density measurement are summarized in Table 6-10. The BET and BJH methods were used to determine the surface area, pore volume and average pore sizes of the selected ACs. The results revealed a parallelism between the textural properties of AC-HCS and AC-HCB which were higher compared to those of AC-HCT. This is consistent with the nitrogen adsorption isotherms presented in Figure 6- 11. The pores sizes analysis revealed that the average pore diameter of the produced activated carbon classified them in mesopore range (2 nm < Dp < 50 nm) (Zhang.2016; Ansari *et al*., 2020). The apparent densities of the produced ACs are presented in Table 6-10. The results obtained revealed that the skeleton of the high S_{BET} AC is widely extended which occupies a larger volume compared to other ACs. This agrees with the apparent density measurement of different S_{BET} ACs produced in many studies (Jordá-Beneyto et al., 2007; Delgado et al., 2019). As reported by Jordá-Beneyto (2007), 6.5 wt % of hydrogen could be stored at 77 K and 4 MPa on activated carbon with a minimum S_{BET} and pore diameter of 1000 m^2g^{-1} and 20 Å - 35 Å (10^{-10} m), respectively. Hence, the porous properties of the produced ACs make them suitable for hydrogen storage application.

Table 6-10.Physical and structural properties of the produced activated carbons

Properties	**AC-HCT**	**AC-HCS**	**AC-HCB**
N_2 Adsorption results			
BET surface area (m^2/g)	2021.91	2299.25	2243.57
BET adsorption total pore volume (cm^3/g)	1.77	1.96	1.38
BJH adsorption surface area (m^2/g)	1485.25	1857.42	1797.40
BJH average pore diameter (4V/A) Å	36.6	34.2	32.2
Helium Pycnometer Measurement			
Skeletal (apparent) density (kg/m^3)	2228.35	2346.72	2319.63

BET : Brunauer Emmet Teller. BJH : Barret Joyner Halenda. Å: Angstrom=10^{-1}nm

The cumulative PSDs of the produced activated carbons were determined from the obtained nitrogen isotherms using the Non-Local Density Functional Theory (NLDFT) method and the Barret Joyner Halenda method (for pores diameter above 35 Å) as shown in figure 6-12 (A and B). The NLDFT method normalized the pore volume to pore width interval (differential volume dV/dW, $cm^3Å^{-1}g^{-1}$) to a standard slit-shaped pore model (Sharifigaliuk *et al*., 2022). The results showed different PSDs sharps of the three produced activated carbons. The observation of the figure 6-12 (A) revealed peaks in two zones on the PSDs plots showing a bimodal distribution in the micropore (< 20 Å) and mesopore (20 Å < Pore radius < 500 Å) regions (Raj *et al*., 2022). This is consistent with the isotherm's characteristics described in the previous section. The obtained peaks were identified in the micropore region for AC-HCS at width 16.99 Å, 18,47 Å and 19.22 Å, representing pore volumes of 0.062 $cm^3Å^{-1}g^{-1}$, 0.025 $cm^3Å^{-1}g^{-1}$ and 0.023 $cm^3Å^{-1}g^{-1}$ respectively. Likewise, the PSD plot of the produced AC-HCB presented peaks identified at width 16.79 Å, 18,30 Å and 19.32 Å, corresponding to the pore volumes of 0.062 $cm^3Å^{-1}g^{-1}$, 0.047 $cm^3Å^{-1}g^{-1}$ and 0.042 $cm^3Å^{-1}g^{-1}$ respectively. This confirmed that the produced AC-HCS and AC-HCB were microporous with more micropores in the AC-HCB. Therefore, the observation of the PSD reveals that the textural characteristics of the porous materials (Table 6-10) depend not only on the S_{BET} (Kumar *et al*., 2016). Thus, a large volume of mesopores was identified in the produced AC-HCS on peaks observed at the following width; 24.33 Å, 25.54 Å, 27.85 Å, 34.83 Å, 36.22 Å, 41.61 Å, 43.37 Å, 45.60 Å, 47.55 Å, 52.04 Å and 68.09 Å with corresponding pore volumes of 0.017,0.02, 0.042, 0.023, 0.021, 0.012, 0.013, 0.017, 0.013, 0.006, 0.003 cm^3 $Å^{-1}g^{-1}$ respectively. The mesopores are essential for facilitating many molecules to the inside of the carbon matrix (Bardestani *et al*., 2019). It has been observed that the volume of pores decreased when the width of the pores increased. This shows the limit nitrogen adsorption capacity of the larger pores [69]. In the produced AC-HCT, the peaks were identified only in the mesopore region at width; 20.34 Å, 23.12 Å, 26.37 Å, 27.36 Å, 33.16 Å and 37.89 Å for corresponding pore volumes of 0.037, 0.033, 0.019, 0.019, 0.0058, and 0.001 $cm^3Å^{-1}g^{-1}$ respectively. The total pore volume presented in Table 14 correspond to the sum of different pore sizes described. The observation of the figure 6-12 (B) representing the PSD of the produced ACs obtained by the BJH method with similar trend as the results of NDLFT analysis

method (figure 6-12 (A)). The maximum peak was identified in the AC-HCS which had the most well-developed porous texture. Meanwhile, above 35 Å in the mesopore region, peaks were clearly identified at width 48.91 Å and 78.15 Å for corresponding pore volumes of 0.0121 and 0.0047 cm^3 $Å^{-1}g^{-1}$ only for the AC-HCS. This showed the higher mesopores content of the AC-HCS compared to AC-HCT and AC-HCB respectively (Moliner *et al*., 2021). The observation of PSD profiles of the ACs (figure 6-12) revealed their higher porous properties situated in micropore and mesopore regions. The highest micropore composition was found in the AC-HCS with a higher pore volume peak which conferred a significant adsorption capacity due to potential adsorption forces (Vander Waals) of superposed small pores (Mistar *et al*., 2020a). The pore size distribution of AC-HCS was wider than AC-HCT and AC-HCB. The narrower pore size distribution was found in the AC-HCB. The results obtained from nitrogen adsorption isotherms and PSD analysis presented in figures 6-11 and 6-12 showed that the nitrogen adsorption capacity of the produced ACs is function of porous network in all pore size ranges; the S_{BET} and the pore size distribution.

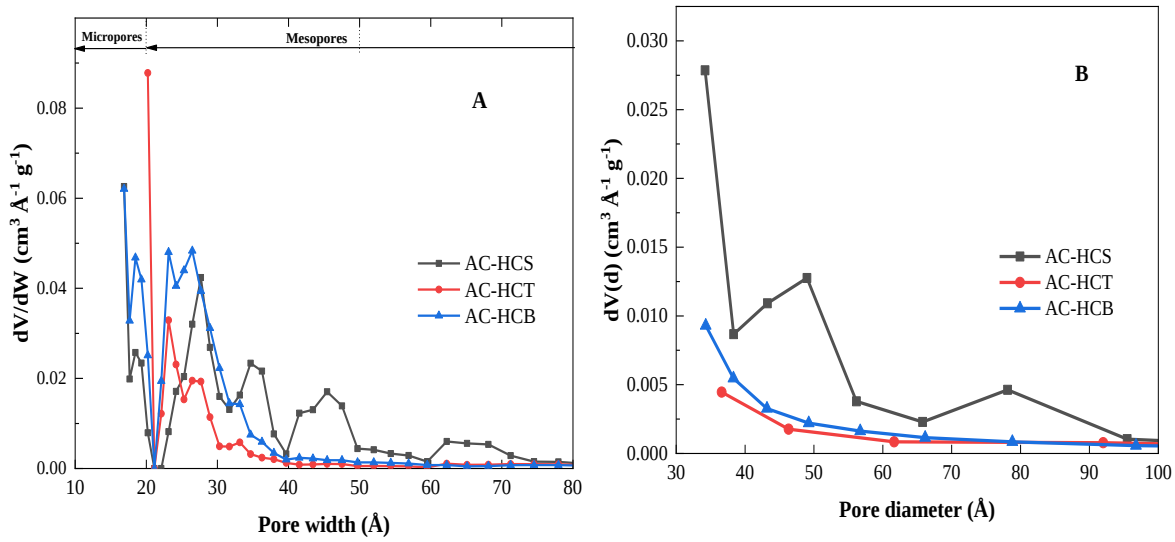

Figure 6-12:Pore size distribution of produced activated carbons obtained from the NLDFT (A) and BJH (B) methods

The SEM images and EDS spectrum of the produced ACs depicted advanced high porosity development formed by KOH-carbon reaction (Figure 6-13). The bodies of the ACs materials are formed by the aggregation of irregular narrowed holes (seen at higher magnitude) characteristics of micropores and mesopores (Omri *et al*., 2012). This agrees with the results of pore structure analysed from N_2 adsorption isotherms and PSDs. The micrographs revealed the progressive creation of cavities or pores on the microstructures wall of the ACs materials due to the reaction of KOH and the carbonaceous precursor (Figure 6-13). The temperature used (800℃ and 850℃) with the amount of activation reagent (KOH) led to the gasification of carbonates created (6-6) and removal of volatiles content of the precursor which subsequently increases the development of pores (Chayid *et al*., 2015). The diffusion of KOH molecules into the pores of HCs during activation process, increased the KOH-Carbon interaction and expends the micro and mesopores in the off-centre walls of created pores. This led to the increase of S_{BET} and pore volume of the ACs (Yang et al., 2010; Chayid *et al*., 2015). The SEM images revealed that the textural properties of the ACs depend on the physicochemical characteristics of the precursors (HCs). The porous properties and diversity of pores sizes in the produced ACs could be observed on the SEM images obtained in agreement with PSD profiles and nitrogen adsorption isotherms. The heterogenous structure with predominance of micropores sizes and randomly

distributed mesopores (larger pores) could be clearly observed on SEM images of AC-HCS (Figure 6-13d) followed by AC-HCB (Figure 6-13g). The relatively homogenous structure of larger and similar pores characteristics of mesopores compared to the AC-HCS and AC-HCB was observed on the SEM image of AC-HCT (Figure 6-13a), which was consistent with the PSD analysis results discussed previously. The SEM images of the produced ACs revealed surfaces plans with well-developed pores structures conferring to the material an amorphous nature. In addition, the corresponding EDS spectrum (Figure 6-13c, f and i) indicate that the produced ACs consist strongly in C, O, Si and Fe characteristics of the HCs precursor (Table 6-11).

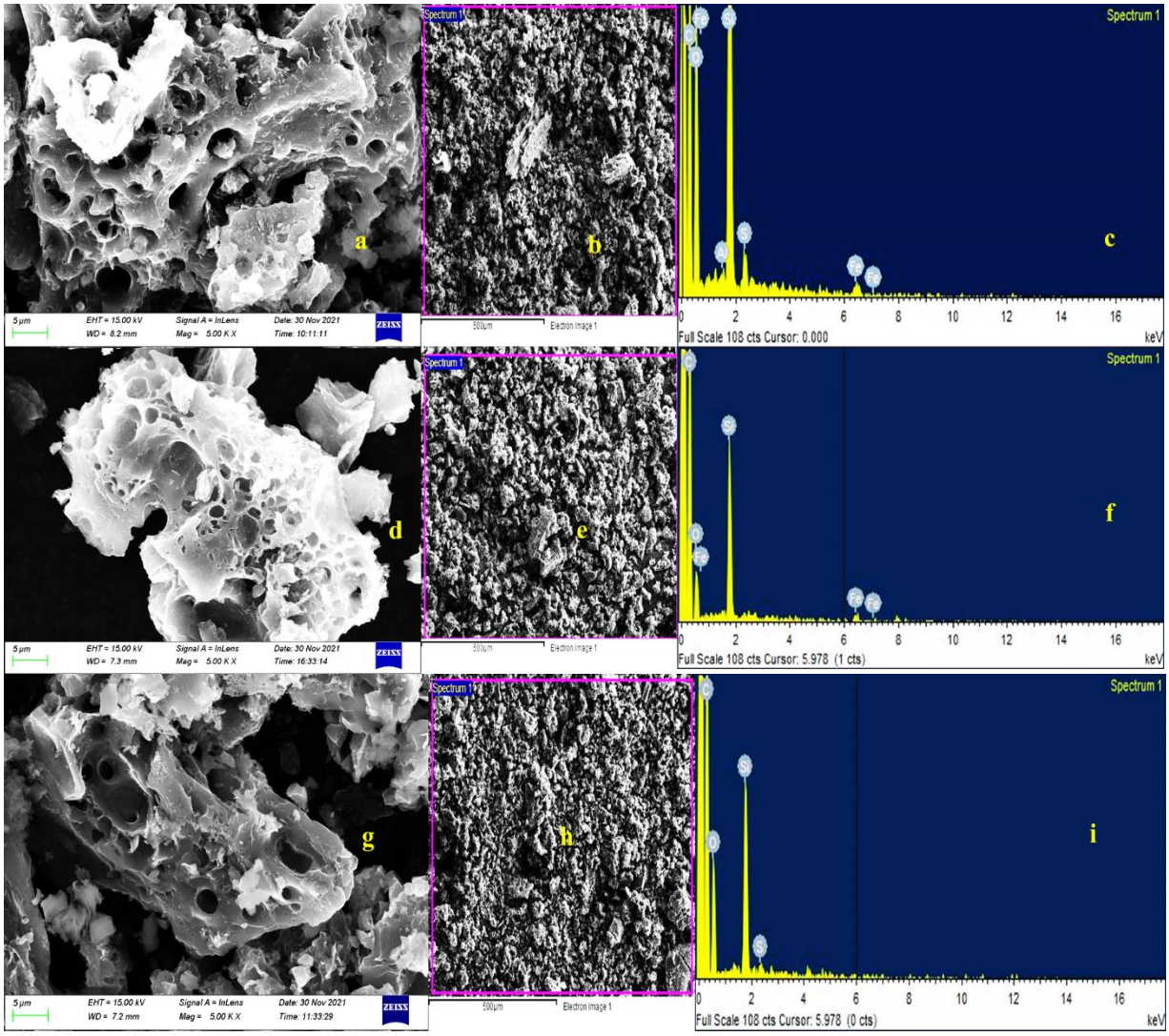

Figure 6-13: SEM images &EDS spectrums and result of AC-HCS (a-c), AC-HCT (d-f) and AC-HCB (g-i)

The FTIR spectrum of the selected ACs produced by chemical activation of HCs using KOH reagent with a KOH to HC ratio of 4:1 at 800°C for HCB and 850°C for HCT and HCS are given in figure 6-14 A. The spectra of ACs show a few numbers of adsorption bands characteristics of chemical functional groups compared to the HCs and raw precursors. This showed that most functional groups identified in the raw materials (CT, CS and CB) and further in the HCs (HCT, HCS and HCB) were removed during the activation process by the breaking of side chains containing considerable number of functional groups separated from the carbon skeleton (Han *et al*., 2015). The peaks identified in the adsorption band region of 3750 cm^{-1} for all the three activated carbons and was assigned to –OH stretching vibrations. Theses peaks in this region have been attributed to the presence of intermolecular H bonds, free OH groups and associated OH groups produced by the oxidation (Bedin *et al*., 2016). The oxygenated functional groups as active sites are capable to interact with other molecules in adsorption applications (Smith.2017). The peaks observed in the adsorption band region between 2920 cm^{-1} and 2840 cm^{-1} could be assigned to the C-H stretching vibrations of the asymmetric aliphatic hydrocarbons. The presence of these peaks revealed that the produced ACs could have some $–CH_2$ and $–CH_3$ groups. The weak peaks at 2100cm^{-1} could be assigned to the stretching vibrations of C=O (Lendzion-Bielun *et al*., 2018). The functional group at that peak could be attributed to different carbonyls (alcohols, phenols and esters). The peaks at 1570 cm^{-1} were assigned to C-C vibration of aromatic nucleus (Martins *et al*., 2015). The peaks at 1100 cm^{-1} showed the presence of C-O stretching vibrations of alcoholic and carboxylic groups (Üner *et al*., 2018; Orguz *et al*., 2019b). The shoulder on AC-HCS and AC-HCB spectra in the adsorption band region between 1650 $cm^{-1}$and 750 cm^{-1} may be ascribed to the C-H stretching vibrations of aromatic rings (Maletić *et al*., 2019). Therefore, vibrations observed on the spectrums were especially due to carbon skeleton of the three produced ACs. The spectrum shows the potential of chemical activation to transform chemical functions through surface reactions and creation of active sites with the formation of a porous structure (Vidal *et al*., 2019). The high temperature used in activation process accelerates the decomposition of KOH interacting with the precursor which increases the number of oxygen groups of on the surface of the produced ACs (Vidal *et al*., 2019).

The chemical activation mechanism was described in previous studies as a 4 main steps reaction starting with the dehydration where KOH is converted into K_2O (step 1), followed by the formation of metallic potassium (step 2) which penetrates the carbon layer and expends its structure. Thereafter, the carbon-potassium compounds formed undergo oxidation (step 3) and hydration (step 4) (Kumar *et al*., 2018). As shown in the FTIR spectrum on figure 6-14 A, the surface chemistry of the produced ACs is basically characterized by carbon layers bonded to different heteroatoms formed during the chemical activation process. These functional groups i.e., phenol, carboxylic anhydride, carboxyl, etc., confer the acidity and basicity characteristic to the surface of the ACs (Lewovehu *et al*., 2021). Hence, the produced ACs could be described as a 2 structures material composed by; oxygen including structure (acid) and oxygen free structure (basic) influenced by the C-H stretching vibrations of aromatic rings (Reddy *et al*., 2020). These properties improve the reactivity of the ACs

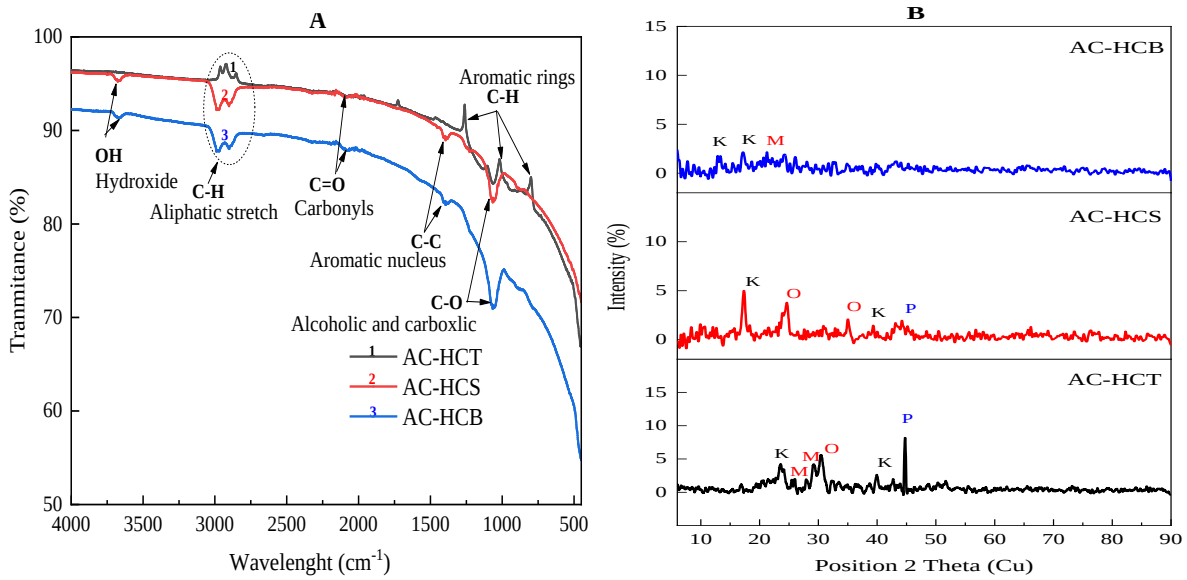

Figure 6-14: FTIR spectra (A) and XRD pattens(B) of produced activated carbons

The XRD patterns of the produced ACs displayed on Figure 6-14 (B) showed that the intensity of inorganic components identified as mineral phases (clay mineral; K (Kaolinite), Silicate mineral; M (Muscovite), O(Orthoclase), Sulphur mineral; P (Pyrite)) at different position 2θ decreased significantly compared to the diffractogram patterns of the precursors presented on Figure 6-3 (B).

This confirmed the decrease of mineral matter of the precursors assumed to end in the ash content of the materials as presented in Table 6-9. The reflection bands (2θ) could be clearly located only at sites comprise between 15° and 45° with weak diffraction peak intensities. As reported by Reddy (2020), this could be assigned to the reflection's characteristic of amorphous carbon structure. Furthermore, the progressive appearance of organic humps and disappearance of broad peaks observed on the XRD patterns from precursors (figure 6-15a-f) to the produced ACs (figure 6-15g-i) show the transformation of crystalline structure into more amorphous structure (Hubbe *et al*., 2019). The remaining weak peaks on the diffractogram of the ACs (fig 15g-i) could be ascribed to the minor crystalline phase's characteristics of the precursors (residual ash) (Köseoğlu *et al*., 2015).

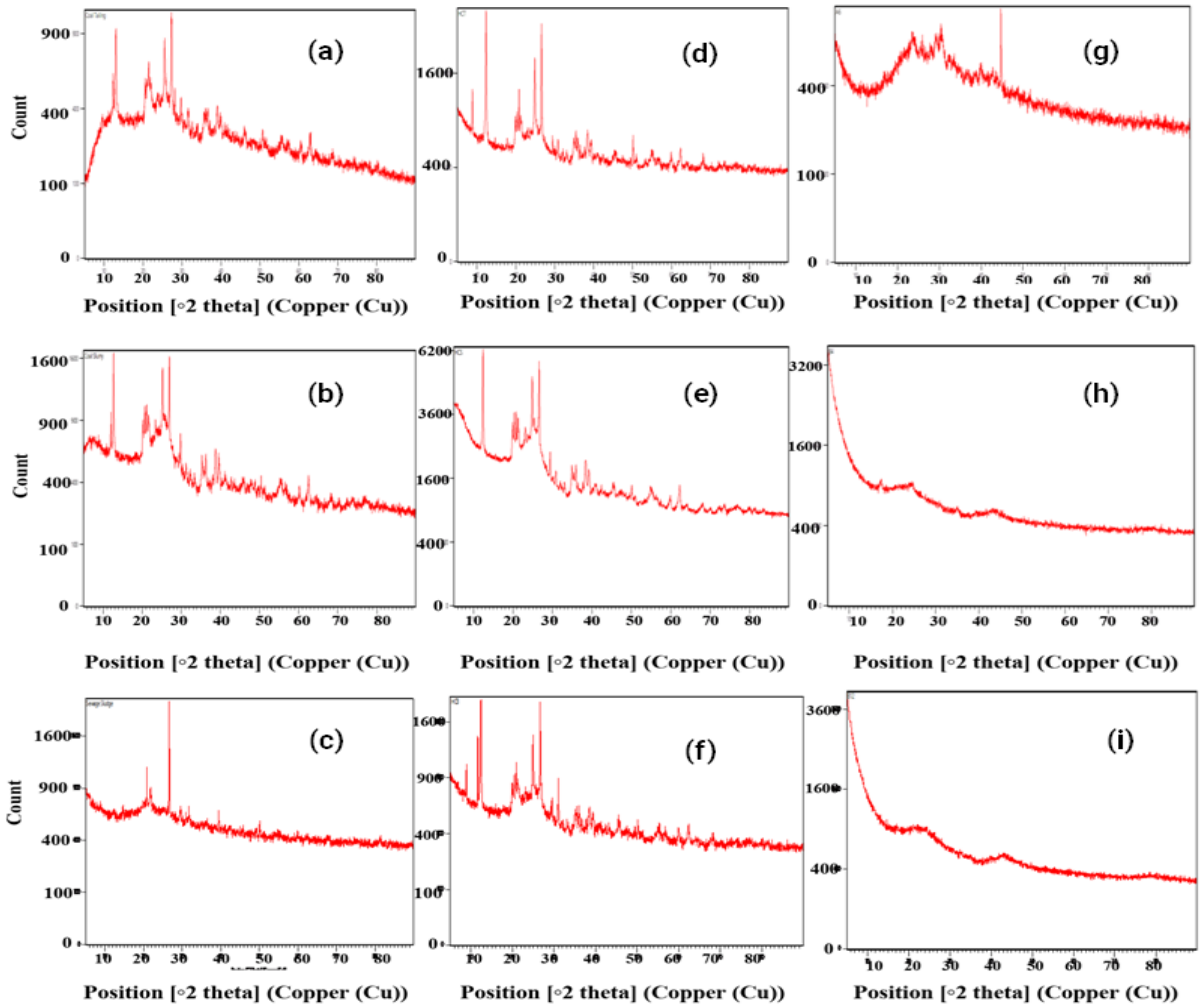

Figure 6-15: Diffractogram profile changes from CT (a), CS (b) and SS (c) through HCT(d), HCS (e) and HCB (f) to AC-HTC(g); AC-HCS (h) and AC-HCB (i)

6.4.6. Hydrogen storage capacity of the produced activated carbons

The hydrogen storage a capacity of the selected ACs with high S_{BET} was evaluated using the adsorption desorption isotherms. The textural properties of the ACs qualified them for hydrogen storage application (Jordá-Beneyto *et al*. 2006). The high-pressure volumetric method was used to measure the isotherms of hydrogen adsorption desorption at different pressure. The experimental results obtained were comparable to some results reported in the literature. The adsorption isotherms models provided by Langmuir, Toth and Dubinin-Astakov could be utilized to validate the experimental results. The results revealed that the minimum amount of hydrogen was adsorbed onto the AC-HCT. However, the amount of hydrogen adsorbed onto the AC-HCS, and AC-HCB was 6.8 wt% and 6.57 wt% respectively. This could be attributed to the textural properties described from BET analysis. The hydrogen adsorption equilibrium and kinetics study were evaluated from the experimental results. In addition, the hydrogen storage capacity of produced ACs was compared to that of some coal-based porous material in the literature. The validation of experimental data on hydrogen adsorption was done with the Langmuir, Toth, and Dubinin-Astakhov models. The Langmuir model describes the monolayer of the gas -solid phase assuming that; the adsorbent surface is homogenous, the adsorption takes place within the definite localized sites, all sites are equal and can contain only one molecule of gas at the time. The kinetic principle used in the Langmuir theory states that the rate of adsorption is equivalent to the rate of desorption on the porous surface and can be described by the equation (6-7) in term of fractional loading (Chiley *et al*., 1895).

$$\theta = \frac{bP}{1+bP} \qquad (6\text{-}7)$$

where θ is the fractional loading, b is the affinity constant (gas attraction strength onto the adsorbent) and P is the pressure of adsorption.

The attraction strength b can be calculated from the equation (6-8);

$$b(T) = b_{\infty} exp\left(\frac{Q}{R_g T}\right) \qquad (6\text{-}8)$$

where b_∞ is the pre-exponential factor to b, Q is the isosteric heat of adsorption, R_g is the gas constant and T the adsorption temperature.

The adsorption isotherms are generally expressed as the amount of adsorbed versus the adsorption pressure. Therefore, the fractional loading equation can be transformed into equation (6-9);

$$C_\mu = C_{\mu s} \frac{b(T)P}{1+b(T)P} \quad (6\text{-}9)$$

where $\theta = \frac{C_\mu}{C_{\mu s}}$, C_μ and $C_{\mu s}$ is the amount of adsorbed and the saturated amount of adsorbate onto the adsorbent respectively and μ is the adsorbed phase.

The inability to fit the adsorption data at high pressure and to describe the heterogenous nature of porous materials limits the use of Langmuir model (Mohan *et al*., 2019). Hence, to address that limitation, the Toth model (Toth.1971) include the heterogenous nature implications of the adsorbent and could be used to describe the adsorption at low and high pressure as presented in equations (6—10 and 6-11);

$$C_\mu = C_{\mu s} \frac{b(T)P}{[1+(bP)^t]^{\frac{1}{t}}} \quad (6\text{-}10)$$

$$t = t_0 + \alpha\left(1 - \frac{T_0}{T}\right) \quad (6\text{-}11)$$

where t represents the parameter that describes the heterogenous nature of the adsorbate/adsorbate system, t_0 is the parameter t at a determined temperature T_0 and α is the adsorption constant.

The simplicity and accuracy of the Toth model in the description of adsorption systems make it more suitable for the evaluation of isotherm data fitting of a couple of adsorbates i.e., carbon dioxide, hydrocarbons, alcohols, hydrogen etc.…onto ACs (Ramirez *et al*., 2021).

However, as reported in previous studies (Hubbe *et al*., 2019; Broom *et al*., 2021) the fitting of physisorption data of different gases onto ACs is usually evaluated by the

Dubinin-Astakhov model (MDA). The MDA model represented by the equation (6-12) can accurately describe the equilibrium data of porous materials with high degree of heterogeneity and extended pore size distribution.

$$W = W_0 exp\left[-\left(\frac{A}{E}\right)^n\right] \quad (6\text{-}12)$$

where; W represents the gas uptake in cm^3/g, W_0 shows the saturated volume uptake of gas in cm^3/g, A is the adsorption potential, E is the energy of adsorption and n is the D-A heterogeneity parameter of the adsorbent. The value of n varies in the range of 2 to 5 depending on the heterogeneity structure of the adsorbent.

As A can be calculated using equation (6-13) ;

$$A = RTln\left(\frac{P_0}{P}\right) \quad (6\text{-}13)$$

the D-A equation becomes;

$$W = W_0 exp\left[-\left\{\frac{RT}{E} ln\left(\frac{P_0}{P}\right)^n\right\}\right] \quad (6\text{-}14)$$

where P_o is the saturation pressure which could be obtained from the equation (15);

$$P_0 = P_c\left(\frac{T}{T_c}\right)^2 \quad (6\text{-}15)$$

where P_c and T_c are the critical points of the gas at temperature T.

The gravimetric measurements of hydrogen adsorption provide the amount of gas confined in a volume that has higher concentration than the bulk free gas defined as absolute hydrogen adsorption (Broom *et al*., 2021). The volume corresponding to the absolute adsorption could be determined by the volume of the adsorbed layer (Sdanghi *et al*., 2020). On the other hand, the volumetric measurements provide the values of excess hydrogen adsorption, n_{exc} expressed as the difference between the hydrogen uptake on the surface of the adsorbent at the defined temperature and pressure and the amount of hydrogen supposed to be present in the same volume under the same conditions in the absence of adsorption forces. The n_{exc} ($molkg^{-1}$) on the produced ACs could be accurately determined by the MDA equation (Lam *et al*., 2018) expressed as;

$$n_{exc} = n_{max} exp\left[-\left(\frac{RT}{\alpha + T\beta}\right)^2 ln^2\left(\frac{P_0}{P}\right)\right] - \rho_g V_a \quad (6\text{-}16)$$

where; n_{max} (molkg^{-1}) is the amount of hydrogen adsorbed at saturated point of the entire available pore volume, R is the gas constant (8.314 J mol^{-1} K^{-1}), α is the enthalpy factor, β (mol J^{-1}K^{-1}) is the entropy factor, P_o (MPa) is the pseudo saturation pressure of Dubinin's model, $\boldsymbol{\rho}_g$ (mol m^{-3}) is the hydrogen bulk phase density and V_a (m^{3}kg^{-1}) is the volume of the adsorbed gas (Lam *et al*., 2018). The calculation was made under the assumptions that; V_a is considered as constant under supercritical, and the adsorbed gas occupies the available pores and the average density increase gradually to an asymptotic value during hydrogen adsorption (Lam *et al*., 2018).

The absolute amount of hydrogen adsorbed n_{abs} (mol kg^{-1}) was determined using the equation (6-17);

$$n_{abs} = n_{exc} + \rho_g V_a \quad (6\text{-}17)$$

The hydrogen adsorption experimental data of the produced ACs were fitted simultaneously for evaluation. The MDA model uses five parameters (n_{max}, α, β, P_o and V_a) to evaluate the experimental data and set the relationship with textural properties of ACs.

The isosteric heat of adsorption Q_{st} (kJ ml ^{1}) could be determined from the MDA equation () by the calculation expressed in equation (6-18);

$$Q_{st}^{MDA} = -\Delta H_{ads} = \alpha \sqrt{-ln\left(\frac{n_{abs}}{n_{max}}\right)} \quad (6\text{-}18)$$

where; n_{abs}/n_{max} represent the fractional filling on the surface of the AC generally noted as **Θ**.

Q_{st} could also be calculated from the equation of Clausius-Clapeyron (6-14) as follows;

$$Q_{st} = -R\left[\frac{\partial lnP}{\partial\left(\frac{1}{T}\right)}\right]_{n_a,V} \quad (6\text{-}19)$$

The Clausius-Clapeyron equation applied to the adsorption isotherms results in the obtention of Q_{st} as a function of temperature and absolute amount of hydrogen adsorbed (Lam *et al*., 2018). The Q_{st} was determined for the 3 ACs using the Sips equation applied to the Clausius-Clapeyron equation for the thermodynamics study of hydrogen adsorption (Rouquerol *et al*., 2014) which will lead to the calculation of the

absolute amount of hydrogen adsorbed (n_{abs}) under the equilibrium pressure. The Sips equation is expressed as follows;

$$n_{abs} = N\frac{bP^k}{1+bP^k} \quad (6\text{-}20)$$

Where N is the maximum adsorption capacity of the AC at a determined temperature, b is the equilibrium constant related to the Langmuir adsorption coefficient, and k is the coefficient related to the Freundlich equation. When P or b approaches 0, the Sips equation is reduced to the equation of Freundlich, whereas if k is equal to 1, the sips equation becomes the Langmuir equation. The absolute hydrogen isotherms were determined from the excess isotherms using equation (6-16). V_a was estimated at the defined temperatures assuming an asymptotic behaviour at high fugacity values (Thomas. 2014).

The specific pressures P used in the Clausius-Clapeyron equation could be calculated using equation (6-21)

$$P = \left[\frac{n_{abs}}{b(N-n_{abs})}\right]^{1/k} \quad (6\text{-}21)$$

The entropy of the adsorbed hydrogen with the respect to the entropy of the perfect gas in normal conditions of pressure and temperature ΔS_{ads}^{MDA} (J kg^{-1} K^{-1}) can be calculated from the MDA equation (Lam *et al*., 2018).

$$\Delta S_{ads}^{MDA} = S_a - n_a {S_g}^0 = \frac{n_{max}\beta\sqrt{\pi}}{2}\left[1 - Erf\left(\sqrt{-ln\left(\frac{n_{abs}}{n_{max}}\right)}\right)\right] + n_{abs}\left[\beta\sqrt{-ln\left(\frac{n_{abs}}{n_{max}}\right)}\right] + n_{abs}Rln\left(\frac{P^0}{P_0}\right) \quad (6\text{-}22)$$

Where S_g^0 is the entropy of the perfect gas in normal conditions of temperature and pressure, Erf is the error function, and P^0 is the pressure reference state which is 0.1Mpa.

Once the adsorption equilibrium is reached and according to the second law of thermodynamic, the variation of entropy due to hydrogen adsorption, ΔS_{ads} (J $mol^{-1}K^{-1}$) could be related to Q_{st} as follows;

$$\Delta S_{ads} = \frac{\Delta H_{ads}}{T} = \frac{-Q_{st}}{T} \quad (6\text{-}23)$$

Hence, ΔS_{ads} could be determined from $-Q_{st}$ and corresponds to a given filling. The ΔS_{ads} is not directly comparable to ΔS_{ads}^{MDA} which corresponds to the total hydrogen adsorbed and refers to the amount of carbon.

Number of studies have been conducted on the potential hydrogen storage capacity of ACs from different precursors because of their low absolute density (Kapelewski *et al*., 2018; Broom *et al*., 2021). The reports reveals that the hydrogen uptake value depend on both the textural properties, chemical stability of ACs and the hydrogen adsorption process parameters. In addition, these studies reported that hydrogen adsorption-desorption isotherms usually display little or no hysteresis and are faster at 77 K than at the temperatures close to ambient temperature (273 K). Therefore, the hydrogen isotherms plots obtained in this study displayed on figures 6-16 to 6-18 are in good agreement with previous findings. The rapid kinetics of adsorption and desorption make the ACs suitable for recharging and discharging of hydrogen (Kapelewski *et al*., 2018). However, the thermodynamics of hydrogen adsorption/desorption process need to be considered for an accurate evaluation. The volumetric and gravimetric measurements results of hydrogen adsorption/desorption onto the produced ACs are represented by the figures 6-16 and 6-18 respectively. Hydrogen adsorption on all produced ACs was found to be completely reversible. The desorption isotherms overlapped with those of adsorption without any hysteresis loop throughout the 0.1 to 3.5 MPa pressure range. The impact of the pressure variation emerges from the significant change of hydrogen volume adsorbed at the same temperature as shown in figure 6-16. The hydrogen adsorption/desorption results show that the hydrogen uptake (wt%) at different temperature increase with the pressure (figure 6-18). This is due to the increase of interaction energy of hydrogen in the pores of the ACs (Kapelewski *et al*., 2018; Lam *et al*., 2018). The comparison of hydrogen isotherms for different temperatures (figures 6-16 and 6-18) revealed the consistence trends of volumetric and gravimetric measures of hydrogen adsorption/desorption onto the produced ACs. The results obtained show that the highest hydrogen uptakes (wt%) at relatively lower pressure were observed onto the AC-HCB (~4 wt%) compared to AC-HCS (~2.5 wt%) and AC-HCT (~2.5 wt%) respectively even though the AC-HCS has the highest S_{BET}. This could be attributed to the presence many wider pores in AC-HCS as shown on the pore sizes distribution

(figure 6-12) and discussed in the previous section which decrease the filling effect capacity of the AC (Kapelewski *et al*., 2018; Lam *et al*., 2018). Therefore, it is apparent that the pore size distribution of the ACs influences the hydrogen adsorption/desorption.

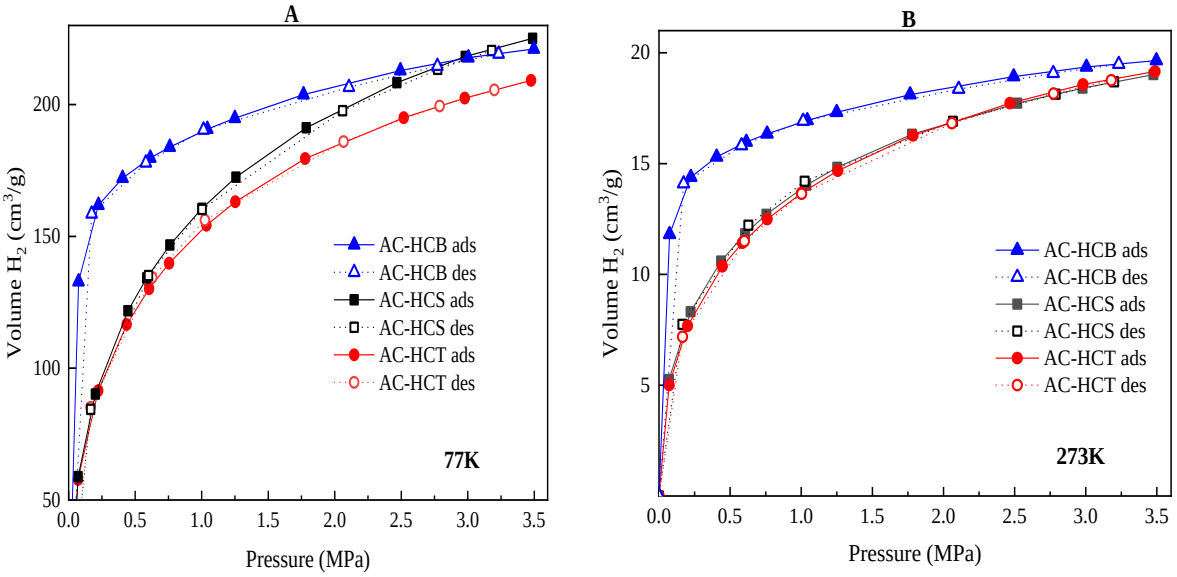

Figure 6-16:Hydrogen isotherms at (A) 77 K and (B) 273 K for the produced ACs. Filled and empty symbols correspond to adsorption and desorption data, respectively.

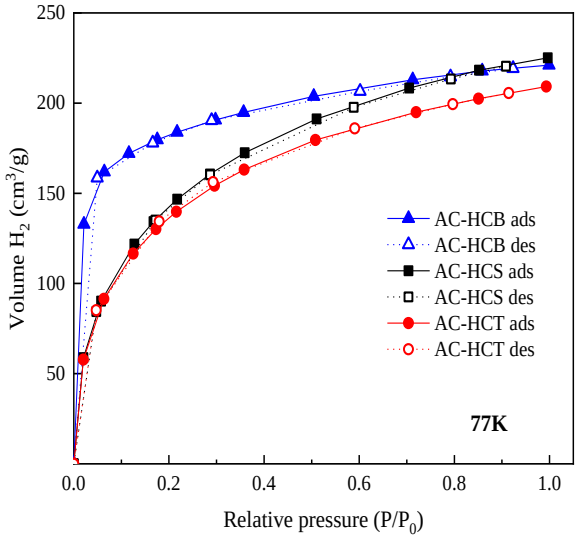

Figure 6-17:Hydrogen isotherms at (A) 77 K versus relative pressure (P/P0) for the produced ACs

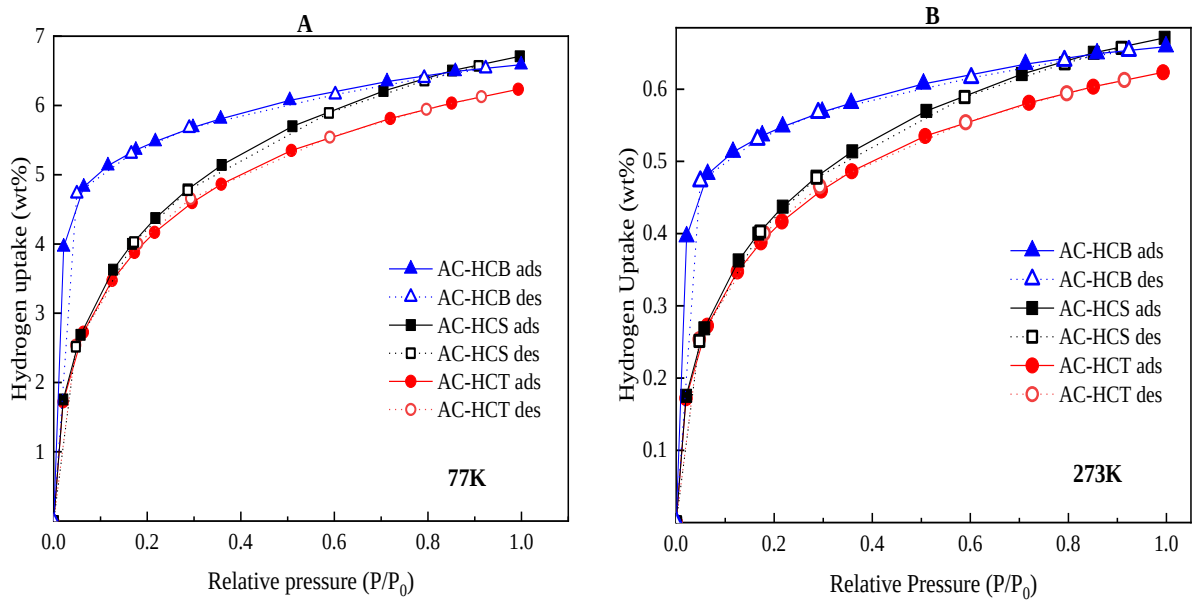

Figure 6-18:Hydrogen isotherms at (A) 77 K and (B) 273 K in wt% versus relative pressure (P/P0) for the produced ACs. Filled and empty symbols correspond to adsorption and desorption data, respectively.

The maximum hydrogen adsorbed onto the ACs could be determined from the isotherms by extrapolation of the adsorption data using different mathematical models fitting experimental data. The isotherms plots presented on figure 6-18 show that maximum adsorption capacity of ACs is directly related to their micropore volume. The results show that AC-HCS has the highest maximum hydrogen uptake of ~6.8 wt% compared to AC-HCB (~6.57 wt%) and AC-HCT (~6.12 wt%) respectively. This is consistent with results of hydrogen adsorption on different ACs with different porous structures presented by Thomas (20214) and Ramirez-Vidal (2021) showing that porous structure is the major factor in determining hydrogen adsorption capacity of ACs. However, Zhao (2012)] revealed that the functionalization of ACs could modify its hydrogen adsorption capacity. The modification of surface chemistry of ACs by the withdrawal or donation of electron could have a significant impact on the functional group effects in hydrogen adsorption. The study reported that the increase in oxygen functional group concentration of the ACs decreases the maximum hydrogen uptake due to the decrease of hydrogen adsorbate density caused by the interaction adsorbate-adsorbate in the presence of oxygen functional groups. The study further demonstrated that even at higher adsorption pressures, considerably low amounts of hydrogen were adsorbed at ambient temperatures. This agrees with the isotherms

results presented in Figures 6-16 and 6-18. The low enthalpy of hydrogen adsorption is responsible of the low amount of hydrogen adsorbed at approximately ambient temperature (273 K) (Nijkamp *et al*., 2001). This demonstrates the temperature dependence of hydrogen adsorption capacity of ACs. The results of maximum hydrogen uptake capacity of ACs from different precursors are presented in Table 6-11. The comparison of hydrogen uptake capacities of different ACs presented in Table 6-11 revealed that the produced ACs from this study are located among the highest hydrogen uptake capacities materials.

Table 6-11. Hydrogen Uptake Capacities of selected ACs

AC Materials	Conditions	Maximum H_2 uptake (wt%)	References
Norit UOK A	0.1MPa, 77K	2.4	Nijkamp *et al* (2001)
Mesoporous		1.75	Pang *et al* (2004)
Takeda 3A (CMS-T3A) coconut shell		1.6	Zhao *et al* (2005)
Mesoporous from silica templates		3	Gadiou *et al* (2005)
Commercially available coconut shell derived	0.1MPa, 77K	1.7	Zhao *et al* (2005)
Pd-doped	8 MPa 298K	5.5	Zhao *et al* (2012b)
KOH-treated	4 MPa, 77K	6.6	Zhao *et al* (2012a)
From bituminous coal	3MPa, 77K	5.7	Xu *et al* (2007)
From Chinese coal	77.4K	4.5	Hirscher *et al* (2005)
Ni-doped	0.1MPa,77K	1.8	Wang *et al* (2011)
Pt-doped	10 MPa, 298K	2.3	Lee *et al* (2011)
Shanghai Dahe (KOH:AC 3:1) K3	2MPa, 77K	5.63	Wang *et al* (2009)
Shanghai Dahe (KOH:AC 5:1) K5		7.08	
AX-21 (10X zeolite template)	1MPa	4.6	Cai *et al* (2014)
KUA -6 (from cellulose hydrochar materials)	4Mpa	5.6	Masika *et al* (2012)
Maxsorb 3000		5.2	
CB 850 h (TC) from metal organic framework	2Mpa	6.9	Ramirez-Vidal *et al* (2021)
TC (alkali metals framework)		5.3	Sharma *et al* (2008)
Maxsorb from Kansai Coke (Japan)	4MPa, 77K	2.31	Ramirez-Vidal *et al* (2021)
MSC30 from Kansai Coke (Japan)		5.78	
MSP20X from Kansai Coke (Japan)		4.74	
SA1500 from Ingevity (USA)		4.04	
SA20 from Ingevity (USA)		3.24	
TH90I from Silcarbon (Germany)		2.90	
Filtrasorb 400 from Chemviron (Belgium)	3MPa, 77K	2.3	
AC-HCT	3.5MPa, 77K	6.12	This study
AC-HCS		6.8	
AC-HCB		6.57	

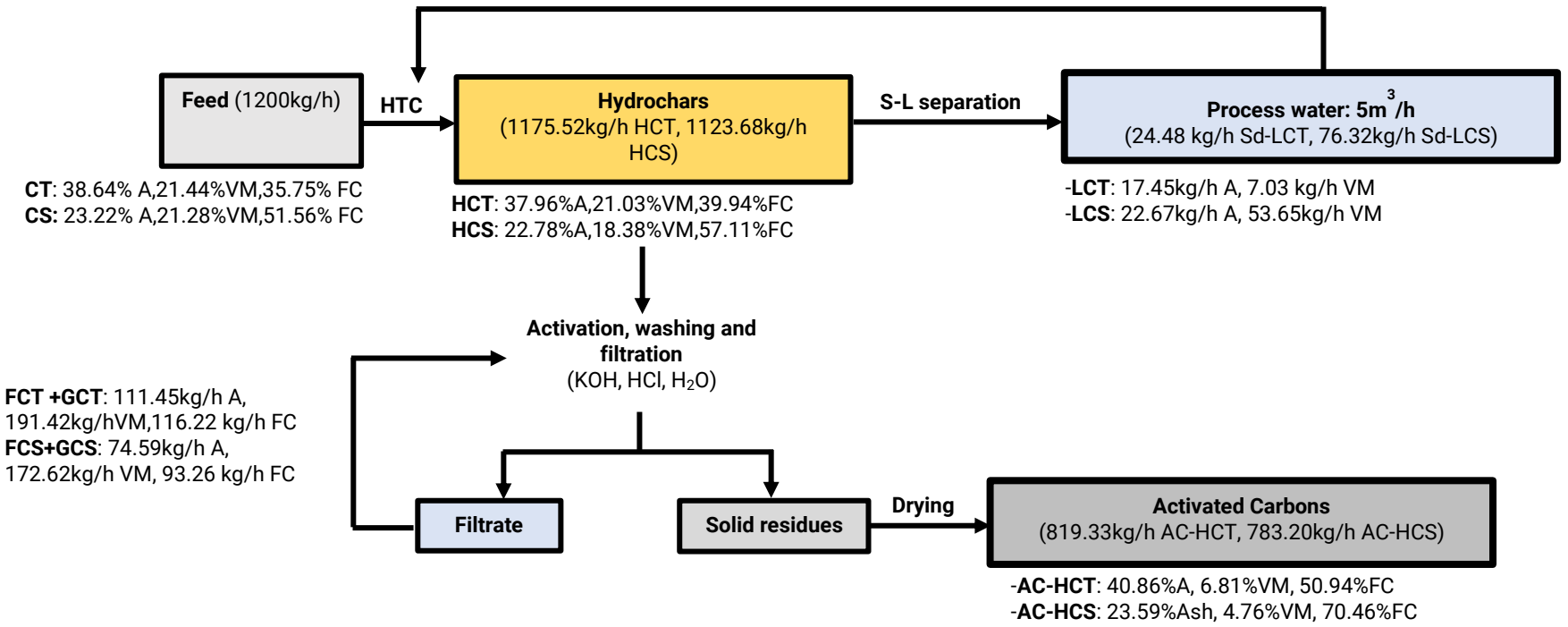

Figure 6-19:Process mass balance

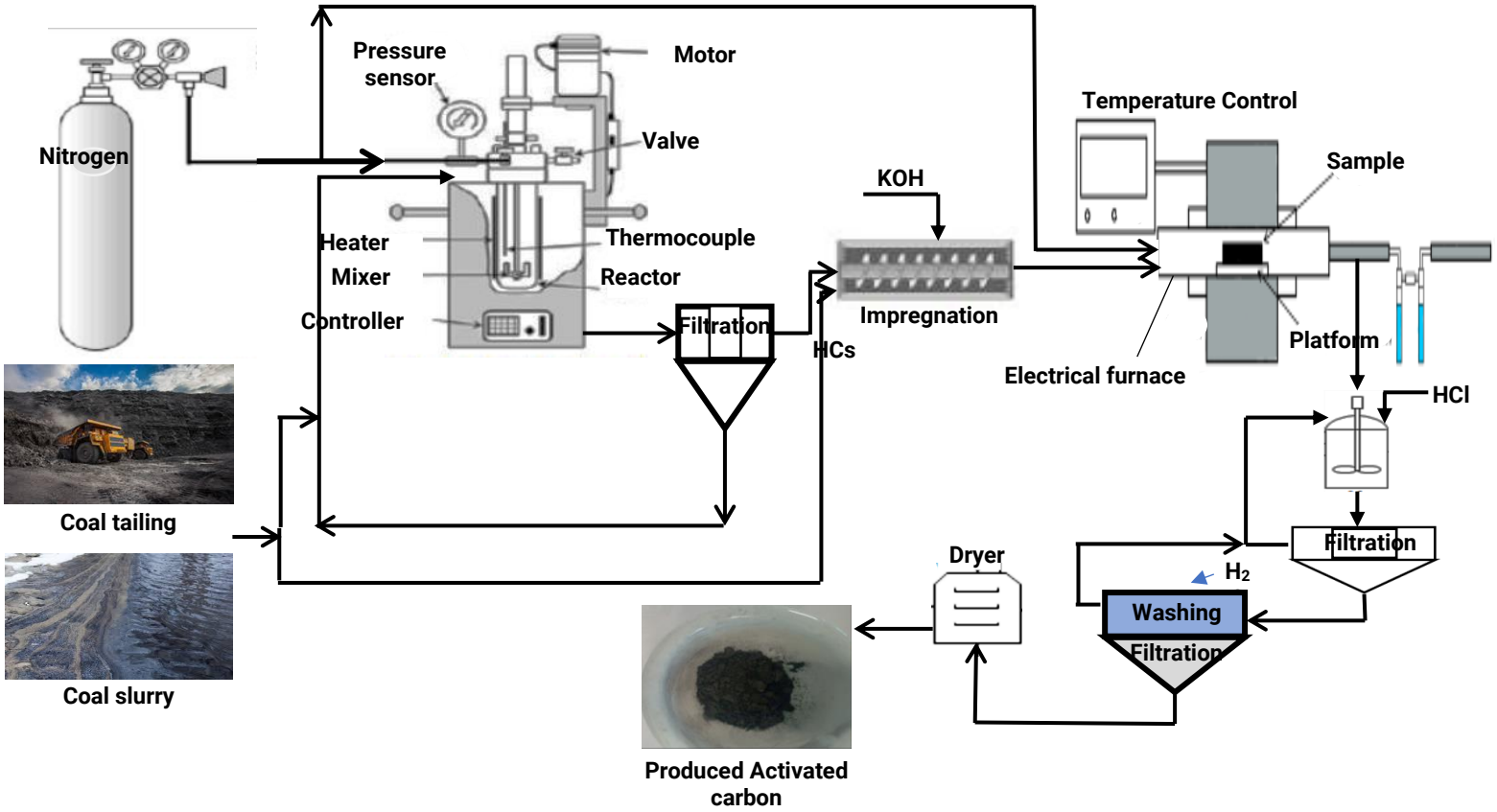

Figure 6-20:Proposed process configuration for the manufacture of AC

6.4.7. Preliminary production cost and carbon emissions estimations

Table 6-12. Production costs estimation of synthesized ACs

Characteristic	Commercial charcoal AC (Sigma-Aldrich CAS 7440-44-0)	AC-HCT	AC-HCS	AC-HCB
Specific surface area (m2/g)	900	2021.91	2299.25	2243.57
Total pore volume (cm3/g)	0.71	1.77	1.96	1.38
Average pore diameter (nm)	3.14	2.75	2.64	2.33
Average price/kg (USD)	0.71	0.77	0.85	0.80
Estimate Annual production (tons/Year) (10 hours/day)	-	2882.25	2680.99	2480.54
Production cost (USD/ton)	-	700	740	790

Exchange rate USD/ZAR = 18.10 (October 2022)

Table 6-13. Preliminary estimation of capitals of investment as shown in Figure 6-20

Type of unit	Quantity	Total cost (USD)
Heat exchanger Steam/water)	1	10031.16
Heat exchanger(water/air)	1	9261.49
HTC Reactor	1	88748.56
Flash tanks	1	24158.99
Pumps	4	13303.87
Mixer	4	21618.78
Air Dryer	1	18803.35
Filter	3	14,.85
Decanter	2	24944.75
Gas cylinder	1	41.57
Regulator	1	569.57
Tube furnace	1	8314.92
Water Tank	1	1330.38
Valves	1	27.43
Total cost for on-site equipment (E)	236121.70	
Fixed Capital of investment (FCI)	1015,32	
Total capital of investment (TCI)	1180,60	
Working Capital (WC)	165285.20	

Exchange rate USD/ZAR = 18.10 (October 2022)

Table 6-14. Components of investment cost

Investment	Description	Cost (USD)
Fixed Capital investment	On site equipment	236121.70
	Utility plants	389600.80
	Contingencies, contractors, and installation's fee	194800.40
	Land	194800.40
Working capital (per month)	Electricity	6886.88
	Chemicals (KOH and HCl) and gas	49723.76
	Labour	35796.44
	Property taxes and insurance	24792.78
	Maintenance	6121.67
	Waste management	11114.15
	Feed Transport	13252.67
	General expenses	12116.31
	Plant commissioning	5480.54
Total investment capital	-	1180,61
Average loan interest rate 5% (10years)	-	59032.88

Exchange rate USD/ZAR = 18.10 (October 2022)

Production costs of synthesized activated carbons shown in Table 6-12 were obtained based on the working capital estimated from result presented in Table 6-13 and 6-14. Considering the production costs of commercial activated carbon, usually in the range 0.5-80 USD/Kg (Table 6-15) and depending on the country considered, the synthesized AC-HCT and AC-HCS seem competitive with commercial coal based activated carbon. Carbon retentions of synthesized ACs are shown in Table 6-16 indicating that the

blending of sewage sludge and coal discards lead to lower carbon emissions than the individual processing of coal discards and sewage sludges. Furthermore, the amount of carbon preserved in the synthesized ACs illustrates the hydrothermal treatment's significant potential to minimize overall carbon emissions from blended coal and sewage wastes. The carbon emissions (11%-21%) reported in Table 6-16 are much lower than those of other thermal processes such as conventional pyrolysis (63%) (Brown *et al*., 2008), microwave (70%) (Sousa *et al*., 2022), and combustion (99%) (Brown *et al*., 2008). As a consequence, HTC might be a viable technique for lowering potential carbon emissions from coal and sewage sludge

Table 6-15. Evaluation of the production costs of coal discard and sewage-based activated carbon (ACs) compared to the production cost of some coal and sewage wastes based ACs together with details on the production methods, surface area and AC production yield.

Precursor	Thermal treatment	Treatment process	Activation conditions	SBET (m2 g-1)	Yield (%)	Estimated production cost (USD kg^{-1})	References
Pet coke	CP	-	Physical activation with steam	1000	63	1.08	Stavropoulos *et al* (2009)
			Chemical activation with KOH	3000	45	1.29	
Carbon black			Physical activation with steam	500	47.5	1.22	
			Chemical activation with KOH	500	60	1.14	
Charcoal			Physical activation with steam	900	45	1.25	
			Chemical activation with KOH	2000	44	1.30	
Lignite			Physical activation with steam	800	15.6	2.18	
			Chemical activation with KOH	2200	25	1.72	
Used tires	CP	-	Physical activation with steam	500	15	2.23	Vanreppelen *et al* (2011)
			Chemical activation with KOH	700	20	1.92	
Sludge of tannery-treatment effluent	MW	4 cycles of carbonization with each cycle (through 20min) consisting of: MW heating at 1200W (150s) during 10 min in a N_2 atmosphere and cooling each cycle in a N_2 atmosphere	Chemical activation with $ZnCl_2$ and lime; ratio tannery sludge: ZnCl2: lime 5:4:1	491	60	32.43	Puchana Rosero *et al*. (2016)

	CP	Carbonization (2.2 kW); 85 min, N2 atmosphere	Chemical activation with $ZnCl_2$ and lime; ratio tannery sludge: ZnCl2: lime 5:4:1	-	-	70.67	
Parthenium hysterophorus derived biochar		1st step: biochar production at 300°C; 1 hour; N_2 atmosphere 2nd step: biochar activation at 500°C; 2 hours; N_2 atmosphere	Chemical activation with NaOH	308	-	2.57	Mondal *et al* (2016)
Raw paper sludge	CP	-	Chemical activation with H_3PO4 85%; ratio 3:2	-	-	2.82	Chowdhury *et al* (2019)
Coal tailing	HTC-CA	1st step: hydrothermal treatment at 150°C, 27 bar, 95 min, solid concentration in water 0.25g/ml, inert atmosphere of N_2 2nd step: chemical activation at 850°C, 135 min	Chemical activation with KOH, KOH:HC ratio 4:1 (w: w)	2021.91	65.33	0.70	This work
Coal slurry				2299.25	62.06	0.74	
Coal discard and sewage sludge blend	Co-HTC & CA	1st step: hydrothermal treatment at 210°C, 18.5bar 95 min, coal discard: sewage sludge ratio; 4:1, solid concentration in water 0.25g/ml, inert atmosphere of N_2 2nd step: chemical activation at 800°C, 135 min		2242.69	57.42	0.79	

HTC-Hydrothermal carbonization. CA-Chemical activation. CP - conventional pyrolysis. MW - microwave heating

According to de Lima (2021), the global demand for ACs will increase in the coming years but this most likely depend of their improved efficiency, and cost-effectiveness. ACs could be used in a variety of applications, including water treatment and energy storage, which are anticipated to be significant growth drivers. AC is produced in various forms (powdered, granular, pelletized, etc.) based on the manufacturing process and the intended application. The powdered type has a larger market size and is anticipated have the fastest growth in the global AC market, up to USD 5,387,6 million by the end of 2026. In 2018, the global AC market was valued at USD 4.72 billion; it is projected to expand at a compound annual growth rate (CAGR) of 9.32%, reaching USD 9.74 billion by 2022 (de Lima *et al*., 2021). Michel Lucian's study revealed that the HTC process is economically competitive, with a biochar (hydrochar) production cost of 0.5 USD per kilogram that is slightly less than the conventional pyrolysis process for producing chars (0.2 USD per kilogram) (Lucian *et al*., 2017). This study provides an economic evaluation of the production of ACs from coal discards and sewage sludge in order to assess the viability of combining the HTC and chemical activation processes. The preliminary results indicate that the combined use of coal discard and sewage sludge provided a lower cost than most conventional processes such as pyrolysis; however, additional data is still needed on the production cost data and environmental impacts of this process before it can be scaled up to become a more sustainable alternative to existing commercial options.

Table 6-16. Calculation of Carbon Emission for synthesized ACs from HCT, HCS and HCB

Parameter	CT (t/a)	CS (t/a)	CB(t/a)
Amount of raw material used	4320	4320	4320
Amount of AC produced	2882.25	2680.99	2480.54
Water content of raw material	180.144	170.20	116.64
Carbon content of dried raw material	1,849.82	2,671.92	1,971.64
Carbon content of produced AC	1,474.55	1,911.54	1,758.70
Percentage of carbon stored in the produced AC	79.71	71.54	89.19

6.5. Conclusion

Low-cost HTC technologies for producing value-added carbonaceous material (hydrochar) from coal and sewage sludge waste could be a long-term recycling strategy for energy storage applications, lowering disposal costs and addressing any environmental contamination caused by the release or solubilization of toxic compounds in these wastes as a result of landfill disposal. To produce high carbon content activated carbon, a combination of optimal hydrothermal carbonization (HTC and Co-HTC) of coal discards (CD) and sewage sludge (SS) wastes and chemical activation was investigated in this chapter. The best parameters for producing high carbon content HCs were 150°C, 27 bar, 95 min and 210°C, 22.5 bar, 360 min for HTC and Co-HTC, respectively. The analysis indicated the effect of various process parameters on the textural properties of the final ACs produced. The activation temperature, holding time, and KOH: HC impregnation ratio of the produced ACs all increase the SBET and total pore volume. The optimum chemical activation conditions chosen were 850°C for HCT and HCS, 800°C for HCB, and a holding time of 135 minutes, with a KOH:HC ratio of 4:1 producing the highest SBET ACs. The SEM micrographs of the produced ACs revealed a highly developed porous surface with a wide range of pore sizes, possibly indicating that they could be used for hydrogen

storage and provide viable pathways for cost-effective energy circular economies for WWTPSs and the mining industry. The hydrogen storage capacity of the produced ACs was further evaluated, and the results showed that the hydrogen adsorption capacity of the produced ACs increased due to an increase in SBET and micropore volumes. The microporous and mesoporous properties of the ACs derived from HCs influenced their high hydrogen adsorption capacity significantly. The decrease in oxygen during HTC and Co-HTC enhanced the chemistry of hydrogen adsorption. The comparison of hydrogen uptake capacities of different ACs tested indicates overall that the produced ACs have a high potential for hydrogen storage capacity.

REFERENCES

1. Bi, Z., Kong, Q., Cao, Y., Sun, G., Su, F., Wei, X., Li, X., Ahmad, A., Xie, L., Chen, C.-M., 2019. Biomass-derived porous carbon materials with different dimensions for supercapacitor electrodes: a review. J. Mater. Chem. A 7, 16028–16045. https://doi.org/10.1039/c9ta04436a
2. Van de Venter, F. F. Producing briquettes for domestic household fuel applications from coal tailings (Doctoral dissertation). (2021)., n.d.
3. Naidoo, N., Pearce, D., Visser, W., Crafford, J.G., Maila, D. and Harris, K.R., 2016. Implementation of Effective Wastewater Charges by Municipalities in South Africa: An Investigation Into the Barriers and Enablers: Report to the Water Research Commission. Water Research Commission., n.d.
4. Demirbas, A., Edris, G., Alalayah, W.M., 2017. Sludge production from municipal wastewater treatment in sewage treatment plant. Energy Sources, Part A: Recovery, Utilization, and Environmental Effects 39, 999–1006. https://doi.org/10.1080/15567036.2017.1283551
5. Shaddel, S., Bakhtiary-Davijany, H., Kabbe, C., Dadgar, F., Østerhus, S., 2019. Sustainable Sewage Sludge Management: From Current Practices to Emerging Nutrient Recovery Technologies. Sustainability 11, 3435. https://doi.org/10.3390/su11123435
6. Flores-Alsina, X., Ramin, E., Ikumi, D., Harding, T., Batstone, D., Brouckaert, C., Sotemann, S., Gernaey, K.V., 2021. Assessment of sludge management strategies in wastewater treatment systems using a plant-wide approach. Water Research 190, 116714. https://doi.org/10.1016/j.watres.2020.116714
7. Grobelak, A., Czerwińska, K., Murtaś, A., 2019. General considerations on sludge disposal, industrial and municipal sludge 135–153. https://doi.org/10.1016/b978-0-12-815907-1.00007-6
8. Saleem, J., Shahid, U.B., Hijab, M., Mackey, H., McKay, G., 2019. Production and applications of activated carbons as adsorbents from olive stones. Biomass Conv. Bioref. 9, 775–802. https://doi.org/10.1007/s13399-019-00473-7
9. Ukanwa, K., Patchigolla, K., Sakrabani, R., Anthony, E., Mandavgane, S., 2019. A Review of Chemicals to Produce Activated Carbon from Agricultural Waste Biomass. Sustainability 11, 6204. https://doi.org/10.3390/su11226204
10. Munir, M.T., Mansouri, S.S., Udugama, I.A., Baroutian, S., Gernaey, K.V., Young, B.R., 2018. Resource recovery from organic solid waste using hydrothermal processing: Opportunities and challenges. Renewable and Sustainable Energy Reviews 96, 64–75. https://doi.org/10.1016/j.rser.2018.07.039
11. Alatalo, S.-M., Sillanpää, M., 2020. Hydrothermal carbonization in the synthesis of sustainable porous carbon materials for water treatment 445–503. https://doi.org/10.1016/b978-0-12-819216-0.00006-0
12. Rusman, N.A.A., Dahari, M., 2016. A review on the current progress of metal hydrides material for solid-state hydrogen storage applications. International Journal of Hydrogen Energy 41, 12108–12126. https://doi.org/10.1016/j.ijhydene.2016.05.244
13. Hirscher, M., Yartys, V.A., Baricco, M., Bellosta von Colbe, J., Blanchard, D., Bowman, R.C., Broom, D.P., Buckley, C.E., Chang, F., Chen, P., 2020. Materials for hydrogen-based energy storage – past, recent progress and future outlook. Journal of Alloys and Compounds 827, 153548. https://doi.org/10.1016/j.jallcom.2019.153548
14. Mohan, M., Sharma, V.K., Kumar, E.A., Gayathri, V., 2019. Hydrogen storage in carbon materials—A review. Energy Storage 1, e35. https://doi.org/10.1002/est2.35
15. Andersson, J., Grönkvist, S., 2019. Large-scale storage of hydrogen. International Journal of Hydrogen Energy 44, 11901–11919. https://doi.org/10.1016/j.ijhydene.2019.03.063
16. Abdulsalam, J., Mulopo, J., Oboirien, B., Bada, S., Falcon, R., 2019. Experimental evaluation of activated carbon derived from South Africa discard coal for natural gas storage. Int J Coal Sci Technol 6, 459–477. https://doi.org/10.1007/s40789-019-0262-5
17. Musyoka, N.M., Wdowin, M., Rambau, K.M., Franus, W., Panek, R., Madej, J., Czarna-Juszkiewicz, D., 2020. Synthesis of activated carbon from high-carbon coal fly ash and its hydrogen storage application. Renewable Energy 155, 1264–1271. https://doi.org/10.1016/j.renene.2020.04.003
18. Smith, B., 2018. Spectral Interpretation Aids 195–205. https://doi.org/10.1201/9780203750841-9
19. Pińkowska, H., Wolak, P., Złocińska, A., 2011. Hydrothermal decomposition of xylan as a model substance for plant biomass waste – Hydrothermolysis in subcritical water. Biomass and Bioenergy 35, 3902–3912. https://doi.org/10.1016/j.biombioe.2011.06.015
20. Saba, A., Saha, P., Reza, M.T., 2017. Co-Hydrothermal Carbonization of coal-biomass blend: Influence of temperature on solid fuel properties. Fuel Processing Technology 167, 711–720. https://doi.org/10.1016/j.fuproc.2017.08.016

21. Afolabi, O.O.D., Sohail, M., Cheng, Y.-L., 2020a. Optimisation and characterisation of hydrochar production from spent coffee grounds by hydrothermal carbonisation. Renewable Energy 147, 1380–1391. https://doi.org/10.1016/j.renene.2019.09.098
22. Channiwala, S.A., Parikh, P.P., 2002. A unified correlation for estimating HHV of solid, liquid and gaseous fuels. Fuel 81, 1051–1063. https://doi.org/10.1016/s0016-2361(01)00131-4
23. Jia, R., Liu, J., Han, Q., Zhao, S., Shang, N., Tang, P., Zhang, Y., 2022. Mineral matter transition in lignite during ashing process: A case study of Early Cretaceous lignite from the Hailar Basin, Inner Mongolia, China. Fuel 328, 125252. https://doi.org/10.1016/j.fuel.2022.125252
24. Jiang, J., Yang, W., Cheng, Y., Liu, Z., Zhang, Q., Zhao, K., 2019. Molecular structure characterization of middle-high rank coal via XRD, Raman and FTIR spectroscopy: Implications for coalification. Fuel 239, 559–572. https://doi.org/10.1016/j.fuel.2018.11.057
25. Knappe, V., Paczkowski, S., Tejada, J., Diaz Robles, L.A., Gonzales, A., Pelz, S., 2018. Low temperature microwave assisted hydrothermal carbonization (MAHC) reduces combustion emission precursors in short rotation coppice willow wood. Journal of Analytical and Applied Pyrolysis 134, 162–166. https://doi.org/10.1016/j.jaap.2018.06.004
26. Mishra, R.K., Mohanty, K., 2018. Characterization of non-edible lignocellulosic biomass in terms of their candidacy towards alternative renewable fuels. Biomass Conv. Bioref. 8, 799–812. https://doi.org/10.1007/s13399-018-0332-8
27. Doshi, P., Srivastava, G., Pathak, G., Dikshit, M., 2014. Physicochemical and thermal characterization of nonedible oilseed residual waste as sustainable solid biofuel. Waste Management 34, 1836–1846. https://doi.org/10.1016/j.wasman.2013.12.018
28. Tan, J., Cheng, H., Wei, L., Wei, C., Xing, Y., Gui, X., 2019. Using low-rank coal slime as an eco-friendly replacement for carbon black filler in styrene butadiene rubber. Journal of Cleaner Production 234, 949–960. https://doi.org/10.1016/j.jclepro.2019.06.221
29. Tasca, A.L., Puccini, M., Gori, R., Corsi, I., Galletti, A.M.R., Vitolo, S., 2019. Hydrothermal carbonization of sewage sludge: A critical analysis of process severity, hydrochar properties and environmental implications. Waste Management 93, 1–13. https://doi.org/10.1016/j.wasman.2019.05.027
30. Zhang, L., Liu, S., Wang, B., Wang, Q., Yang, G., Chen, J., 2015. Effect of Residence Time on Hydrothermal Carbonization of Corn Cob Residual 10. https://doi.org/10.15376/biores.10.3.3979-3986
31. Wang, L., Chang, Y., Li, A., 2019. Hydrothermal carbonization for energy-efficient processing of sewage sludge: A review. Renewable and Sustainable Energy Reviews 108, 423–440. https://doi.org/10.1016/j.rser.2019.04.011
32. Behera, S.K., Meena, H., Chakraborty, S., Meikap, B.C., 2018. Application of response surface methodology (RSM) for optimization of leaching parameters for ash reduction from low-grade coal. International Journal of Mining Science and Technology 28, 621–629. https://doi.org/10.1016/j.ijmst.2018.04.014
33. Danish, M., Hashim, R., Ibrahim, M.N.M., Sulaiman, O., 2014. Optimized preparation for large surface area activated carbon from date (Phoenix dactylifera L.) stone biomass. Biomass and Bioenergy 61, 167–178. https://doi.org/10.1016/j.biombioe.2013.12.008
34. Yorgun, S., Yıldız, D., Şimşek, Y.E., 2016. Activated carbon from paulownia wood: Yields of chemical activation stages. Energy Sources, Part A: Recovery, Utilization, and Environmental Effects 38, 2035–2042. https://doi.org/10.1080/15567036.2015.1030477
35. Zhou, J., Luo, A., Zhao, Y., 2018. Preparation and characterisation of activated carbon from waste tea by physical activation using steam. Journal of the Air & Waste Management Association 68, 1269–1277. https://doi.org/10.1080/10962247.2018.1460282
36. Afolabi, O.O.D., Sohail, M., Thomas, C.P.L., 2015. Microwave Hydrothermal Carbonization of Human Biowastes. Waste Biomass Valor 6, 147–157. https://doi.org/10.1007/s12649-014-9333-4
37. Heidarinejad, Z., Dehghani, M.H., Heidari, M., Javedan, G., Ali, I., Sillanpää, M., 2020. Methods for preparation and activation of activated carbon: a review. Environ Chem Lett 18, 393–415. https://doi.org/10.1007/s10311-019-00955-0
38. Huang, Y., Zhao, G., 2016. Preparation and characterization of activated carbon fibers from liquefied wood by KOH activation 70, 195–202. https://doi.org/10.1515/hf-2015-0051
39. Njoku, V.O., Foo, K.Y., Asif, M., Hameed, B.H., 2014. Preparation of activated carbons from rambutan (Nephelium lappaceum) peel by microwave-induced KOH activation for acid yellow 17 dye adsorption. Chemical Engineering Journal 250, 198–204. https://doi.org/10.1016/j.cej.2014.03.115

40. Blankenship, L.S., Jagiello, J., Mokaya, R., 2022. Confirmation of pore formation mechanisms in biochars and activated carbons by dual isotherm analysis. Mater. Adv. 3, 3961–3971. https://doi.org/10.1039/d2ma00141a
41. Wang, Y., Yang, H., Jin, L., Li, Y., Hu, H., Ding, H., Bai, X., 2019. Effect of mineral in coal on preparation of activated carbon for methane decomposition to hydrogen. Fuel 258, 116138. https://doi.org/10.1016/j.fuel.2019.116138
42. Bideskan, A.S., Ebrahimzadeh, P., Teimouri, R., 2020. Fabrication of bi-layer PMMA and aluminum 6061-T6 laminates by laser transmission welding: Performance prediction and optimization. International Journal of Lightweight Materials and Manufacture 3, 150–159. https://doi.org/10.1016/j.ijlmm.2019.09.008
43. Zhao, W., Fierro, V., Fernández-Huerta, N., Izquierdo, M.T., Celzard, A., 2012a. Impact of synthesis conditions of KOH activated carbons on their hydrogen storage capacities. International Journal of Hydrogen Energy 37, 14278–14284. https://doi.org/10.1016/j.ijhydene.2012.06.110
44. Mistar, E.M., Alfatah, T., Supardan, M.D., 2020b. Synthesis and characterization of activated carbon from Bambusa vulgaris striata using two-step KOH activation. Journal of Materials Research and Technology 9, 6278–6286. https://doi.org/10.1016/j.jmrt.2020.03.041
45. Chairunnisa, Miksik, F., Miyazaki, T., Thu, K., Miyawaki, J., Nakabayashi, K., Wijayanta, A.T., Rahmawati, F., 2021b. Development of biomass based-activated carbon for adsorption dehumidification. Energy Reports 7, 5871–5884. https://doi.org/10.1016/j.egyr.2021.09.003
46. Ahmed, M.J., Theydan, S.K., 2014. Optimization of microwave preparation conditions for activated carbon from Albizia lebbeck seed pods for methylene blue dye adsorption. Journal of Analytical and Applied Pyrolysis 105, 199–208. https://doi.org/10.1016/j.jaap.2013.11.005
47. Wazir, A.H., Haq, I. ul, Manan, A., Khan, A., 2022. Preparation and characterization of activated carbon from coal by chemical activation with KOH. International Journal of Coal Preparation and Utilization 42, 1477–1488. https://doi.org/10.1080/19392699.2020.1727896
48. Jawad, A.H., Ismail, K., Ishak, M.A.M., Wilson, L.D., 2019. Conversion of Malaysian low-rank coal to mesoporous activated carbon: Structure characterization and adsorption properties. Chinese Journal of Chemical Engineering 27, 1716–1727. https://doi.org/10.1016/j.cjche.2018.12.006
49. Gokce, Y., Yaglikci, S., Yagmur, E., Banford, A., Aktas, Z., 2021. Adsorption behaviour of high performance activated carbon from demineralised low rank coal (Rawdon) for methylene blue and phenol. Journal of Environmental Chemical Engineering 9, 104819. https://doi.org/10.1016/j.jece.2020.104819
50. Bora, M., Benoy, S.M., Tamuly, J., Saikia, B.K., 2021. Ultrasonic-assisted chemical synthesis of activated carbon from low-quality subbituminous coal and its preliminary evaluation towards supercapacitor applications. Journal of Environmental Chemical Engineering 9, 104986. https://doi.org/10.1016/j.jece.2020.104986
51. Dong, D., Zhang, Y., Xiao, Y., Wang, T., Wang, J., Romero, C.E., Pan, W., 2020. High performance aqueous supercapacitor based on nitrogen-doped coal-based activated carbon electrode materials. Journal of Colloid and Interface Science 580, 77–87. https://doi.org/10.1016/j.jcis.2020.07.018
52. Zhang, H., Niu, J., Yin, X., Guo, Y., Cheng, F., 2020. Role of inherent pyrite in coal on physicochemical structure of activated carbon and adsorption capacity. Fuel 262, 116527. https://doi.org/10.1016/j.fuel.2019.116527
53. Song, G., Deng, R., Yao, Z., Chen, H., Romero, C., Lowe, T., Driscoll, G., Kreglow, B., Schobert, H., Baltrusaitis, J., 2020. Anthracite coal-based activated carbon for elemental Hg adsorption in simulated flue gas: Preparation and evaluation. Fuel 275, 117921. https://doi.org/10.1016/j.fuel.2020.117921
54. Jawad, A.H., Surip, S.N., 2022. Upgrading low rank coal into mesoporous activated carbon via microwave process for methylene blue dye adsorption: Box Behnken Design and mechanism study. Diamond and Related Materials 127, 109199. https://doi.org/10.1016/j.diamond.2022.109199
55. Wang, D., Fang, G., Xue, T., Ma, J., Geng, G., 2016. A melt route for the synthesis of activated carbon derived from carton box for high performance symmetric supercapacitor applications. Journal of Power Sources 307, 401–409. https://doi.org/10.1016/j.jpowsour.2016.01.009
56. Wang, L., Sun, F., Hao, F., Qu, Z., Gao, J., Liu, M., Wang, K., Zhao, G., Qin, Y., 2020. A green trace K2CO3 induced catalytic activation strategy for developing coal-converted activated carbon as advanced candidate for CO2 adsorption and supercapacitors. Chemical Engineering Journal 383, 123205. https://doi.org/10.1016/j.cej.2019.123205

57. Sreńscek-Nazzal, J., Narkiewicz, U., Morawski, A.W., Wróbel, R.J., Michalkiewicz, B., 2015. Comparison of Optimized Isotherm Models and Error Functions for Carbon Dioxide Adsorption on Activated Carbon. J. Chem. Eng. Data 60, 3148–3158. https://doi.org/10.1021/acs.jced.5b00294
58. Campbell, Q.P., Bunt, J.R., Kasaini, H. and Kruger, D.J., 2012. The preparation of activated carbon from South African coal. Journal of the Southern African Institute of Mining and Metallurgy, 112(1), pp.37-44.
59. Martin, A., Loh, W.S., Rahman, K.A., Thu, K., Surayawan, B., Alhamid, M.I., Nasruddin, Ng, K.C., 2011. Adsorption Isotherms of CH4on Activated Carbon from Indonesian Low Grade Coal. J. Chem. Eng. Data 56, 361–367. https://doi.org/10.1021/je100495w
60. Xu, B., Wu, F., Chen, R., Cao, G., Chen, S., Yang, Y., 2010. Mesoporous activated carbon fiber as electrode material for high-performance electrochemical double layer capacitors with ionic liquid electrolyte. Journal of Power Sources 195, 2118–2124. https://doi.org/10.1016/j.jpowsour.2009.09.077
61. Sutcu, H., Dural, A., 2006. Effect of Hydroxides on Carbonization of Bituminous Coal. Coal Preparation 26, 201–208. https://doi.org/10.1080/07349340601104255
62. Himeno, S., Komatsu, T., Fujita, S., 2005. High-Pressure Adsorption Equilibria of Methane and Carbon Dioxide on Several Activated Carbons. J. Chem. Eng. Data 50, 369–376. https://doi.org/10.1021/je049786x
63. Lozano-Castelló, D., Cazorla-Amorós, D., Linares-Solano, A., 2002. Powdered Activated Carbons and Activated Carbon Fibers for Methane Storage: A Comparative Study. Energy Fuels 16, 1321–1328. https://doi.org/10.1021/ef020084s
64. Li, W., Liang, C., Qiu, J., Zhou, W., Han, H., Wei, Z., Sun, G., Xin, Q., 2002. Carbon nanotubes as support for cathode catalyst of a direct methanol fuel cell. Carbon 40, 791–794. https://doi.org/10.1016/s0008-6223(02)00039-8
65. Sun, J., Hippo, E.J., Marsh, H., O'Brien, W.S., Crelling, J.C., 1997. Activated carbon produced from an Illinois Basin coal. Carbon 35, 341–352. https://doi.org/10.1016/s0008-6223(96)00157-1
66. Ahmadpour, A., Do, D.D., 1996. The preparation of active carbons from coal by chemical and physical activation. Carbon 34, 471–479. https://doi.org/10.1016/0008-6223(95)00204-9
67. Tounsadi, H., Khalidi, A., Machrouhi, A., Farnane, M., Elmoubarki, R., Elhalil, A., Sadiq, M., Barka, N., 2016. Highly efficient activated carbon from Glebionis coronaria L. biomass: Optimization of preparation conditions and heavy metals removal using experimental design approach. Journal of Environmental Chemical Engineering 4, 4549–4564. https://doi.org/10.1016/j.jece.2016.10.020
68. Thommes, M., Kaneko, K., Neimark, A.V., Olivier, J.P., Rodriguez-Reinoso, F., Rouquerol, J., Sing, K.S.W., 2015. Physisorption of gases, with special reference to the evaluation of surface area and pore size distribution (IUPAC Technical Report) 87, 1051–1069. https://doi.org/10.1515/pac-2014-1117
69. Zhang, P., 2016. Adsorption and desorption isotherms. KE Group.
70. Ansari, H., Joss, L., Hwang, J., Trusler, J.P.M., Maitland, G., Pini, R., 2020. Supercritical adsorption in micro- and meso-porous carbons and its utilisation for textural characterisation. Microporous and Mesoporous Materials 308, 110537. https://doi.org/10.1016/j.micromeso.2020.110537
71. Sinha, P., Datar, A., Jeong, C., Deng, X., Chung, Y.G., Lin, L.-C., 2019. Surface Area Determination of Porous Materials Using the Brunauer–Emmett–Teller (BET) Method: Limitations and Improvements. J. Phys. Chem. C 123, 20195–20209. https://doi.org/10.1021/acs.jpcc.9b02116
72. de Souza, T.N.V., de Carvalho, S.M.L., Vieira, M.G.A., da Silva, M.G.C., Brasil, D. do S.B., 2018. Adsorption of basic dyes onto activated carbon: Experimental and theoretical investigation of chemical reactivity of basic dyes using DFT-based descriptors. Applied Surface Science 448, 662–670. https://doi.org/10.1016/j.apsusc.2018.04.087
73. Delgado, N., Capparelli, A., Navarro, A., Marino, D., 2019. Pharmaceutical emerging pollutants removal from water using powdered activated carbon: Study of kinetics and adsorption equilibrium. Journal of Environmental Management 236, 301–308. https://doi.org/10.1016/j.jenvman.2019.01.116
74. Jordá-Beneyto, M., Suárez-García, F., Lozano-Castelló, D., Cazorla-Amorós, D., Linares-Solano, A., 2007. Hydrogen storage on chemically activated carbons and carbon nanomaterials at high pressures. Carbon 45, 293–303. https://doi.org/10.1016/j.carbon.2006.09.022
75. Sermoud, V.M., Barbosa, G.D., Barreto, A.G., Tavares, F.W., 2019. Reconstruction of the pore size distribution of porous materials: The influence of uncertainties in the gaseous adsorption experimental data. Fluid Phase Equilibria 494, 93–102. https://doi.org/10.1016/j.fluid.2019.04.028

76. Sharifigaliuk, H., Mahmood, S.M., Rezaee, R., Ayobami Afolabi, F., Ul Haq, I., 2022. Shale's Pore Structure and Sorption-Diffusion Characteristics: Effect of Analyzing Methods and Particle Size. Energy Fuels 36, 6167–6186. https://doi.org/10.1021/acs.energyfuels.2c00850
77. Raj, F.R.M.S., Boopathi, G., Kalpana, D., Jaya, N.V., Pandurangan, A., 2022. Sustainable development through restoration of Prosopis juliflora species into activated carbon as electrode material for supercapacitors. Diamond and Related Materials 121, 108767. https://doi.org/10.1016/j.diamond.2021.108767
78. Kumar, A., Jena, H.M., 2016. WITHDRAWN: Preparation and characterization of high surface area activated carbon from Fox nut (Euryale ferox) shell by chemical activation with H3PO4. Results in Physics. https://doi.org/10.1016/j.rinp.2016.03.006
79. Bardestani, R., Patience, G.S., Kaliaguine, S., 2019. Experimental methods in chemical engineering: specific surface area and pore size distribution measurements—BET, BJH, and DFT. Can. J. Chem. Eng. 97, 2781–2791. https://doi.org/10.1002/cjce.23632
80. Moliner, C., Antonucci, B., Focacci, S., Heap, J.M., Martel, A.M., Hamzah, F., Martin, C. and Martinez-Felipe, A., 2021. Molecular dynamics simulation of the interactions between carbon dioxide and a natural-based carbonaceous microporous material. Chemical Engineering Transactions, 86, pp.1111-1116.
81. Mistar, E.M., Alfatah, T., Supardan, M.D., 2020a. Synthesis and characterization of activated carbon from Bambusa vulgaris striata using two-step KOH activation. Journal of Materials Research and Technology 9, 6278–6286. https://doi.org/10.1016/j.jmrt.2020.03.041
82. Omri, A. and Benzina, M., 2012. Characterization of activated carbon prepared from a new raw lignocellulosic material: Ziziphus spina-christi seeds. Journal de la Société Chimique de Tunisie, 14, pp.175-183.
83. Chayid, M.A., Ahmed, M.J., 2015. Amoxicillin adsorption on microwave prepared activated carbon from Arundo donax Linn: Isotherms, kinetics, and thermodynamics studies. Journal of Environmental Chemical Engineering 3, 1592–1601. https://doi.org/10.1016/j.jece.2015.05.021
84. Yang, K., Peng, J., Srinivasakannan, C., Zhang, L., Xia, H., Duan, X., 2010. Preparation of high surface area activated carbon from coconut shells using microwave heating. Bioresource Technology 101, 6163–6169. https://doi.org/10.1016/j.biortech.2010.03.001
85. Han, L., Karthikeyan, K.G., Gregory, K.B., 2015. Energy Consumption and Recovery in Capacitive Deionization Using Nanoporous Activated Carbon Electrodes. J. Electrochem. Soc. 162, E282–E288. https://doi.org/10.1149/2.0431512jes
86. Bedin, K.C., Martins, A.C., Cazetta, A.L., Pezoti, O., Almeida, V.C., 2016. KOH-activated carbon prepared from sucrose spherical carbon: Adsorption equilibrium, kinetic and thermodynamic studies for Methylene Blue removal. Chemical Engineering Journal 286, 476–484. https://doi.org/10.1016/j.cej.2015.10.099
87. Smith, B., 2017. The CO bond, Part I: Introduction and the infrared spectroscopy of alcohols.
88. Lendzion-Bieluń, Z., Czekajło, Ł., Sibera, D., Moszyński, D., Sreńscek-Nazzal, J., Morawski, A.W., Wrobel, R.J., Michalkiewicz, B., Arabczyk, W., Narkiewicz, U., 2018. Surface characteristics of KOH-treated commercial carbons applied for CO2 adsorption. Adsorption Science & Technology 36, 478–492. https://doi.org/10.1177/0263617417704527
89. Martins, A.F., Facchi, S.P., Monteiro, J.P., Nocchi, S.R., Silva, C.T.P., Nakamura, C.V., Girotto, E.M., Rubira, A.F., Muniz, E.C., 2015. Preparation and cytotoxicity of N,N,N-trimethyl chitosan/alginate beads containing gold nanoparticles. International Journal of Biological Macromolecules 72, 466–471. https://doi.org/10.1016/j.ijbiomac.2014.08.020
90. Oguz Erdogan, F., Kopac, T., 2019b. Highly Effective Activated Carbons from Turkish–Kozlu Bituminous Coal by Physical and KOH Activation and Sorption Studies with Organic Vapors 17. https://doi.org/10.1515/ijcre-2018-0071
91. Üner, O., Bayrak, Y., 2018. The effect of carbonization temperature, carbonization time and impregnation ratio on the properties of activated carbon produced from Arundo donax. Microporous and Mesoporous Materials 268, 225–234. https://doi.org/10.1016/j.micromeso.2018.04.037
92. Maletić, M., Vukčević, M., Kalijadis, A., Janković-Častvan, I., Dapčević, A., Laušević, Z., Laušević, M., 2019. Hydrothermal synthesis of TiO2/carbon composites and their application for removal of organic pollutants. Arabian Journal of Chemistry 12, 4388–4397. https://doi.org/10.1016/j.arabjc.2016.06.020
93. Vidal, R.V., García, R.V., Martínez, A.F., Santos Estébanez, Fco.J.D. los, 2019. Activated Carbon from Almond Shells for Water Treatment: A Mini Review. AG 40. https://doi.org/10.18805/ag.r-132

94. Kumar, U., Gaikwad, V., Mayyas, M., Sahajwalla, V., Joshi, R.K., 2018. Extraordinary supercapacitance in activated carbon produced via a sustainable approach. Journal of Power Sources 394, 140–147. https://doi.org/10.1016/j.jpowsour.2018.05.054
95. Lewoyehu, M., 2021. Comprehensive review on synthesis and application of activated carbon from agricultural residues for the remediation of venomous pollutants in wastewater. Journal of Analytical and Applied Pyrolysis 159, 105279. https://doi.org/10.1016/j.jaap.2021.105279
96. Reddy, S.S., Sinha, A.K., Amarendra, G., Shekar, N.V.C., Bhalerao, G.M., 2020. Enhancement of graphitic order in carbon black using precursor additive. Diamond and Related Materials 101, 107539. https://doi.org/10.1016/j.diamond.2019.107539
97. Köseoğlu, E., Akmil-Başar, C., 2015. Preparation, structural evaluation and adsorptive properties of activated carbon from agricultural waste biomass. Advanced Powder Technology 26, 811–818. https://doi.org/10.1016/j.apt.2015.02.006
98. Hubbe, M., Azizian, S., Douven, S., 2019. Implications of apparent pseudo-second-order adsorption kinetics onto cellulosic materials: A review. BioRes 14, 7582–7626. https://doi.org/10.15376/biores.14.3.7582-7626
99. Chilev, C., Langlois, P., Lamari, F., 2022. Multi-Compound H_2, CH_4, and N_2 Adsorption Analysis. Metals 12, 1895. https://doi.org/10.3390/met12111895
100. Ramirez-Vidal, P., Canevesi, R.L.S., Sdanghi, G., Schaefer, S., Maranzana, G., Celzard, A., Fierro, V., 2021. A Step Forward in Understanding the Hydrogen Adsorption and Compression on Activated Carbons. ACS Appl. Mater. Interfaces 13, 12562–12574. https://doi.org/10.1021/acsami.0c22192
101. Broom, D.P., Hirscher, M., 2021. Improving Reproducibility in Hydrogen Storage Material Research. ChemPhysChem 22, 2141–2157. https://doi.org/10.1002/cphc.202100508
102. Sdanghi, G., Schaefer, S., Maranzana, G., Celzard, A., Fierro, V., 2020. Application of the modified Dubinin-Astakhov equation for a better understanding of high-pressure hydrogen adsorption on activated carbons. International Journal of Hydrogen Energy 45, 25912–25926. https://doi.org/10.1016/j.ijhydene.2019.09.240
103. Lam, S.T., Ballinger, R., Forsberg, C., 2018. Modeling and predicting total hydrogen adsorption in nanoporous carbon materials for advanced nuclear systems. Journal of Nuclear Materials 511, 328–340. https://doi.org/10.1016/j.jnucmat.2018.09.009
104. Rouquerol, F., Rouquerol, J., Sing, K.S.W., Maurin, G., Llewellyn, P., 2014. Introduction 1–24. https://doi.org/10.1016/b978-0-08-097035-6.00001-2
105. Thomas KM. Hydrogen adsorption and storage on porous materials. InHandbook of Hydrogen Energy 2014 Jul 29 (pp. 726-781). CRC Press.
106. Kapelewski, M.T., Runčevski, T., Tarver, J.D., Jiang, H.Z.H., Hurst, K.E., Parilla, P.A., Ayala, A., Gennett, T., FitzGerald, S.A., Brown, C.M., 2018. Record High Hydrogen Storage Capacity in the Metal–Organic Framework Ni2(m-dobdc) at Near-Ambient Temperatures. Chem. Mater. 30, 8179–8189. https://doi.org/10.1021/acs.chemmater.8b03276
107. Nijkamp, M.G., Raaymakers, J.E.M.J., van Dillen, A.J., de Jong, K.P., 2001. Hydrogen storage using physisorption – materials demands. Appl Phys A 72, 619–623. https://doi.org/10.1007/s003390100847
108. Pang, J., Hampsey, J.E., Wu, Z., Hu, Q., Lu, Y., 2004. Hydrogen adsorption in mesoporous carbons. Appl. Phys. Lett. 85, 4887–4889. https://doi.org/10.1063/1.1827338
109. Zhao, X., Villar-Rodil, S., Fletcher, A.J., Thomas, K.M., 2006. Kinetic Isotope Effect for H2 and D2 Quantum Molecular Sieving in Adsorption/Desorption on Porous Carbon Materials. ChemInform 37. https://doi.org/10.1002/chin.200635021
110. Gadiou, R., Saadallah, S.-E., Piquero, T., David, P., Parmentier, J., Vix-Guterl, C., 2005. The influence of textural properties on the adsorption of hydrogen on ordered nanostructured carbons. Microporous and Mesoporous Materials 79, 121–128. https://doi.org/10.1016/j.micromeso.2004.10.034
111. Zhao, X.B., Xiao, B., Fletcher, A.J., Thomas, K.M., 2005. Hydrogen Adsorption on Functionalized Nanoporous Activated Carbons. J. Phys. Chem. B 109, 8880–8888. https://doi.org/10.1021/jp050080z
112. Zhao, W., Fierro, V., Zlotea, C., Izquierdo, M.T., Chevalier-César, C., Latroche, M., Celzard, A., 2012b. Activated carbons doped with Pd nanoparticles for hydrogen storage. International Journal of Hydrogen Energy 37, 5072–5080. https://doi.org/10.1016/j.ijhydene.2011.12.058
113. XU, W., TAKAHASHI, K., MATSUO, Y., HATTORI, Y., KUMAGAI, M., ISHIYAMA, S., KANEKO, K., IIJIMA, S., 2007. Investigation of hydrogen storage capacity of various carbon materials.

International Journal of Hydrogen Energy 32, 2504–2512 https://doi.org/10.1016/j.ijhydene.2006.11.012
114. Hirscher, M., Panella, B., 2005. Nanostructures with high surface area for hydrogen storage. Journal of Alloys and Compounds 404–406, 399–401. https://doi.org/10.1016/j.jallcom.2004.11.109
115. Wang, Y., Liu, J., Wang, K., Chen, T., Tan, X., Li, C.M., 2011. Hydrogen storage in Ni–B nanoalloy-doped 2D graphene. International Journal of Hydrogen Energy 36, 12950–12954. https://doi.org/10.1016/j.ijhydene.2011.07.034
116. Lee, S.-Y., Park, S.-J., 2011. Effect of platinum doping of activated carbon on hydrogen storage behaviors of metal-organic frameworks-5. International Journal of Hydrogen Energy 36, 8381–8387. https://doi.org/10.1016/j.ijhydene.2011.03.038
117. Wang, H., Gao, Q., Hu, J., 2009. High Hydrogen Storage Capacity of Porous Carbons Prepared by Using Activated Carbon. J. Am. Chem. Soc. 131, 7016–7022. https://doi.org/10.1021/ja8083225
118. Liu, X., Zhang, C., Geng, Z., Cai, M., 2014. High-pressure hydrogen storage and optimizing fabrication of corncob-derived activated carbon. Microporous and Mesoporous Materials 194, 60–65. https://doi.org/10.1016/j.micromeso.2014.04.005
119. Masika, E., Mokaya, R., 2012. Hydrogen Storage in High Surface Area Carbons with Identical Surface Areas but Different Pore Sizes: Direct Demonstration of the Effects of Pore Size. J. Phys. Chem. C 116, 25734–25740. https://doi.org/10.1021/jp3100365
120. Sharma, P., Han, J., Park, J., Kim, D.Y., Lee, J., Oh, D., Kim, N., Seo, D.-H., Kim, Y., Kang, S.J., 2021. Alkali-Metal-Mediated Reversible Chemical Hydrogen Storage Using Seawater. JACS Au 1, 2339–2348. https://doi.org/10.1021/jacsau.1c00444
121. Brown, S., Kruger, C., Subler, S., 2008. Greenhouse Gas Balance for Composting Operations. J. Environ. Qual. 37, 1396–1410. https://doi.org/10.2134/jeq2007.0453
122. Sousa, É.M.L., Otero, M., Rocha, L.S., Gil, M.V., Ferreira, P., Esteves, V.I., Calisto, V., 2022. Multivariable optimization of activated carbon production from microwave pyrolysis of brewery wastes - Application in the removal of antibiotics from water. Journal of Hazardous Materials 431, 128556. https://doi.org/10.1016/j.jhazmat.2022.128556
123. Stavropoulos, G.G., Zabaniotou, A.A., 2009. Minimizing activated carbons production cost. Fuel Processing Technology 90, 952–957. https://doi.org/10.1016/j.fuproc.2009.04.002
124. Vanreppelen, K., Kuppens, T., Thewys, T., Carleer, R., Yperman, J., Schreurs, S., 2011. Activated carbon from co-pyrolysis of particle board and melamine (urea) formaldehyde resin: A techno-economic evaluation. Chemical Engineering Journal 172, 835–846. https://doi.org/10.1016/j.cej.2011.06.071
125. Puchana-Rosero, M.J., Adebayo, M.A., Lima, E.C., Machado, F.M., Thue, P.S., Vaghetti, J.C.P., Umpierres, C.S., Gutterres, M., 2016. Microwave-assisted activated carbon obtained from the sludge of tannery-treatment effluent plant for removal of leather dyes. Colloids and Surfaces A: Physicochemical and Engineering Aspects 504, 105–115. https://doi.org/10.1016/j.colsurfa.2016.05.059
126. Mondal, S., Aikat, K., Halder, G., 2016. Biosorptive uptake of ibuprofen by chemically modified Parthenium hysterophorus derived biochar: Equilibrium, kinetics, thermodynamics and modeling. Ecological Engineering 92, 158–172. https://doi.org/10.1016/j.ecoleng.2016.03.022
127. Chowdhury, S., Sikder, J., Mandal, T., Halder, G., 2019. Comprehensive analysis on sorptive uptake of enrofloxacin by activated carbon derived from industrial paper sludge. Science of The Total Environment 665, 438–452. https://doi.org/10.1016/j.scitotenv.2019.02.081
128. de Lima, N.N., de Souza, J.R.M., Carneiro, A. de C.O., Nunes, Í.L., Viana, A.B.T., da Silva, M.L., 2021. Production, application and market of activated carbon in Brazil: a review. International Wood Products Journal 12, 240–248. https://doi.org/10.1080/20426445.2021.1964311
129. Lucian, M., Fiori, L., 2017. Hydrothermal Carbonization of Waste Biomass: Process Design, Modeling, Energy Efficiency and Cost Analysis. Energies 10, 211. https://doi.org/10.3390/en10020211

Chapter 7: Conclusions

This chapter summarizes the key results of a research on the treatment of coal waste and sewage sludge waste, regarded as environmental hazards in waste management. The first section (7.1) describes the purpose of the research, while the second (7.2) presents the major findings of the research, their potential impacts and provides industrial scale up economic feasibility outlook. Section 7.3 offers a framework for further studies as well as recommendations.

7.1. Background of the study

This study investigated hydrothermal (HTC) and co-hydrothermal carbonization technology (Co-HTC) for enhancing the physicochemical properties of coal discards and sewage sludge in order to produce well-developed adsorbents and potential precursors for high quality and cost-effective activated carbon for hydrogen storage applications and wastewater remediations. This research intends to show the appropriateness of different coal wastes and sewage sludge for use in hydrogen storage in perspective of the South African government's desire to transition to a hydrogen economy. The main results of the research demonstrated that the use of HTC and Co-HTC methods in combination with chemical activation to produce adsorbent and high-quality AC could be ecologically and economically advantageous to the mining and wastewater treatment industries. The study's objective and aims were achieved, and the key findings are presented below.

7.2. Major findings and contribution to the body of knowledge

Findings 1: firstly instance, this research optimized the hydrothermal carbonisation (HTC) of coal discards from coal beneficiation operations and/or sewage sludge by optimizing a number of process parameters such as biomass type, temperature, and residence time to produce hydrochar with improved physicochemical properties.

On a dry basis, the improved HTC conditions (150°C, 27 bar, 95 min) increased the quantity of fixed carbon from 37.31% and 53.02% to 40.31% and 57.69%,

respectively. As a consequence, the total carbon content of the coal discards rose from 42.82 and 61.85% in the HCT and HCS generated, respectively, to 49.80 and 66.90%. Furthermore, the ash content of coal discards reported on a dry basis dropped from 40.32 and 24.17% in the HCT and HCS generated under optimal HTC conditions to 38.3 and 20.17%. While the adjusted Co-HTC conditions of 208°C, 22.5 bars, and 360 minutes for a CT+CS:SS blend ratio of 5:1 raised the fixed carbon reported on a dry basis and total carbon content of CB (a CT+CS+SS blend) from 38.67% to 58.82% and 45.64%, respectively. The concentration of HCB ash dropped from 38.8% to 19.71%. HCT, HCS, and HCB carbonization yields (Cy) were found to be 113.58%, 102.42%, and 129.88%, respectively. The yield (Cy) of co-carbonization HTC was greater than that of HTC alone, probably due to an increase in acidic conditions generated by the breakdown of cellulose, chlorine, and hemicellulose into organic acid monomers during the Co-HTC process's decarboxylation and dehydration processes. As a consequence, the lower pH of the Co-HTC process liquid raises the sulphur removal rate (generation of sulphite and sulphate) from 0.83 to 0.39% and may enable the release of inorganic elements into the liquid phase. This indicates the Co-HTC process's efficacy in decreasing the sulphur content of waste coals and sewage sludge. The physicochemical parameters of HCB synthesized from Co-HTC were equivalent to those of HCS produced from HTC, with the greatest carbon content and the lowest ash content (CS). The feasibility of mixing coal waste with sewage sludge to generate high-quality carbonaceous material for a number of uses was proven.

Findings 2: Secondly instance, this study investigated the effects of various parameter interactions on the textural structure of hydrochars produced by hydrothermal (HTC) and co-hydrothermal (Co-HTC) treatments of CD and sewage sludge (wastes), as well as the subsequent use of the hydrochar (HCs) synthesized for HIV drug (nevirapine and lamivudine) removal from wastewater. The HCB synthesized from Co-HTC has a high S_{BET} of 20.35 m^2/g and pore volume of 0.38 cm^3/g, leading in considerable NEV and LAM adsorptive reductions (97.19% and 93.32%, respectively). HCT and HCS had high NEV and LAM adsorption capabilities while being less effective than HCB. The utilization of coal waste and sewage sludge for the production of hydrochar for the adsorption of dissolved pharmaceutical

resistant compounds in wastewater treatment might be a cost-effective and ecologically beneficial approach. The utilization of wasted adsorption leftovers for energy storage applications was also investigated further. According to the findings, wasted adsorption leftovers are a suitable carbonaceous material precursor for the production of EDLCs. This study found that generating value-added carbonaceous material (hydrochar) from coal waste and sewage sludge waste using low-cost HTC technologies could be a long-term recycling strategy that reduces disposal costs while also addressing any environmental contamination caused by the release or solubilization of toxic compounds in these wastes as a result of landfill disposal. Additional kinetics studies and thermodynamic analyses, as well as the creation and testing of a continuous ARVs components adsorption approach, as well as its implications for large-scale industrial application, are required to provide a better understanding of HTC and Co-HTC reaction processes. To establish the long-term viability of the choices discussed in this work, a life cycle assessment of the hydrothermal treatment and adsorption techniques may be required.

Findings 3: Thirdly, coal waste and sewage sludge waste are thoroughly described and turned into value-added activated carbons for H_2 storage. In order to understand the link between the hydrogen adsorption capacity of synthesized ACs and their physicochemical (carbon, ash, oxygen groups) and textural features, extensive physicochemical characterizations are performed (morphology, specific surface area, pore volume, pore size distribution). Furthermore, the created ACs' physicochemical and textural features are compared to raw materials and realized adsorption capabilities reported in prior literature. The findings demonstrate that activated carbons (AC) with the maximum BET specific surface (S_{BET}) of 2299.25 m^2/g and 2243.57 m^2/g were formed at 850°C and 800°C, respectively, using a 135-minute residence period with a KOH/HC ratio of 4:1. The hydrogen adsorption capacity of the generated ACs was also measured using gas adsorption isotherms at 77 K. At 35 bar, the hydrogen adsorbed onto the ACs was approximately 6.12 weight percent, 6.8 weight percent, and 6.57 weight percent, indicating that they could be used for hydrogen storage and sustainable carbon emissions management, as well as providing viable pathways for cost-effective energy and material circular economies for both WWTPSs and the mining industry.

This demonstrated that HTC can be considered a long-term recycling strategy that reduces disposal costs and addresses environmental contamination caused by the release or solubilization of hazardous compounds in CD and SS wastes as a result of landfill disposal. Results showed that a prior HTC process for the production of activated carbon (AC) from CD and SS increased its adsorption capacity and, consequently, its energy transportation potential (hydrogen storage). In addition, the aim (production of low-cost and high-quality CM) and objectives (characterization of raw materials and products, optimization of HTC treatment, adsorbent properties evaluation of the HCs, production and evaluation of ACs from HCs and HCs adsorption spent residues for electrochemical and hydrogen storage application) of the study were accomplished through these findings

7.3. RECOMMENDATIONS FOR FUTURE RESEARCH

The following are the recommendations for future studies:

- HTC techno-economic analysis (tea) must be carefully evaluated in order to endorse this technology as an alternative strategy for addressing with coal and sewage sludge waste environmental management.

- Future work should include extensive characterization of liquid phases from HTC and Co-HTC experimental runs under optimal conditions. This is critical for achieving a consistent environmentally friendly HTC and Co-HTC process. Furthermore, the footprint of the process could be increased by evaluating the suitability of the optimized hydrochars produced for various industrial wastewater streams and for soil amendment application.

- The kinetics and thermodynamics of the HTC and Co-HTC processes should be discussed in future works for practical validation. The thermodynamic analyses are required to provide a deeper understanding of HTC and Co-HTC reaction processes. Additionally, a life cycle assessment of the hydrothermal treatment and adsorption procedures may be warranted.

- Evaluation of ACs derived from HCs for various electrochemical applications pertinent to renewable energy transition.

Appendices

Appendix A. ANOVA results for Quadratic model of fixed carbon for coal tailing's hydrochar (HCT)

Source	Sum of Squares	df	Mean Square	F-value	p-value	Remark
Model	19.16	9	2.13	21.92	< 0.0001	Significant
A-Temperature	14.30	1	14.30	147.27	< 0.0001	
B-Pressure	0.1188	1	0.1188	1.22	0.2946	
C-Time	0.0002	1	0.0002	0.0016	0.9684	
AB	0.0561	1	0.0561	0.5777	0.4648	
AC	0.0120	1	0.0120	0.1237	0.7324	
BC	0.0091	1	0.0091	0.0938	0.7657	
A^2	2.97	1	2.97	30.54	0.0003	
B^2	0.0355	1	0.0355	0.3656	0.5589	
C^2	0.2025	1	0.2025	2.08	0.1794	
Residual	0.9713	10	0.0971			
Lack of Fit	0.9632	5	0.1926	18.18	< 0.0001	Not significant
Pure Error	0.0082	5	0.0016			
Cor Total	20.13	19				
R^2	0.9517					
Adjusted R^2	0.9083					
Predicted R^2	0.7698					
Adeq Precision	12.5013					

df: - degree of freedom. Adeq. Precision: Adequate Precision.

The **Predicted R^2** of 0.7698 is in reasonable agreement with the **Adjusted R^2** of 0. 9083. **Adeq Precision** measures the signal to noise ratio. A ratio greater than 4 is desirable. The ratio of 12.50 indicates an adequate signal. This model can be used to navigate the design space.

Appendix B. ANOVA for linear model of fixed carbon for coal slurry's hydrochar (HCS)

Source	Sum of Squares	df	Mean Square	F-value	p-value	Remark
Model	112.45	3	37.48	28.64	< 0.0001	significant
A-Temperature	108.24	1	108.24	82.72	< 0.0001	
B-Pressure	3.05	1	3.05	2.33	0.1465	
C-Time	1.16	1	1.16	0.8886	0.3599	
Residual	20.94	16	1.31			
Lack of Fit	20.21	11	1.84	12.70	0.0057	Not significant
Pure Error	0.7233	5	0.1447			
Cor Total	133.39	19				
R^2	0.8430					
Adjusted R^2	0.8136					
Predicted R^2	0.7880					
Adeq Precision	16.3533					

df: degree of freedom. Adeq. Precision: Adequate Precision.

The **Predicted R^2** of 0.7880 is in reasonable agreement with the **Adjusted R^2** of 0.8136. **Adeq Precision** of 16.353 indicates an adequate signal. The observation of the ANOVA results of hydrothermal carbonization experiments revealed that temperature is the most significant model term.

Appendix C ANOVA for Quadratic x Linear model of fixed carbon for the produced carbonaceous material (CM) from the mixture of coals (CT+CS) and sewage sludge (SS)

Source	Sum of Squares	df	Mean Square	F-value	p-value	
Model	6759.13	11	614.47	13.71	< 0.0001	Significant
Linear Mixture	4670.43	1	4670.43	104.20	< 0.0001	
AB	87.55	1	87.55	1.95	0.1732	
AC	628.47	1	628.47	14.02	0.0008	
AD	284.66	1	284.66	6.35	0.0177	
AE	74.15	1	74.15	1.65	0.2089	
BC	3.15	1	3.15	0.0703	0.7929	
BD	0.1104	1	0.1104	0.0025	0.9608	
BE	7.29	1	7.29	0.1626	0.6898	
ABC	87.44	1	87.44	1.95	0.1735	
ABD	35.79	1	35.79	0.7985	0.3791	
ABE	3.79	1	3.79	0.0846	0.7733	
Residual	1254.98	28	44.82			
Lack of Fit	1242.99	23	54.04	12.52	0.0013	Not significant
Pure Error	12.00	5	2.40			
Cor Total	8014.11	39				
R^2	0.8434					
Adjusted R^2	0.7819					
Predicted R^2	0.6434					
Adeq Precision	12.2108					

df: degree of freedom. Adeq. Precision: Adequate Precision.

The **Predicted R^2** of 0.6434 is in reasonable agreement with the **Adjusted R^2** of 0.7819. **Adeq Precision** of 12.211 indicates an adequate signal. The observation of the ANOVA results of Co-hydrothermal carbonization (Co-HTC) experiments revealed that temperature and the (CT+CS): SS blend ratio are the most significant model terms

Appendix D. Process parameters constraints used for the optimization of the HTC

Name	Goal	Coal tailing (CT)		Coal slurry (CS)		Mixture (CB)	
		Lower Limit	Upper Limit	Lower Limit	Upper Limit	Lower Limit	Upper Limit
A: Temperature	Is in range	150	270	150	270	150	270
B: Pressure	Is in range	10	27	10	27	10	27
C: Time	Is in range	10	180	10	180	10	360
E: Coal (CT+CS)	Is in range	-	-	-	-	0	25
D: Sewage sludge (SS)	Is in range	-	-	-	-	0	25
Ash Content	Minimize	38.13	41.39	20.12	28.29	19.71	62.16
Fixed Carbon	Maximize	37.19	**40.37**	48.85	**57.69**	8.59	**58.82**
Volatile matter	Minimize	21.06	24.56	21.39	22.68	17.80	45.28
Mass Yield	Is in range	91.22	98.81	89.85	98.2	44.92	97.24

Appendix E. HCT desirability Solutions

Number	Temperature	Pressure	Time	A*	FC*	VM*	Mass Yield	Desirability	Remark
1	**150.000**	**27.000**	**92.134**	**38.130**	**40.200**	**21.67**	**96.185**	**0.945**	**Selected**
2	150.000	27.000	90.845	38.144	40.198	21.658	96.222	0.944	
3	150.000	26.998	93.217	38.119	40.201	21.68	96.154	0.944	
4	150.000	26.919	93.269	38.130	40.197	21.673	96.165	0.943	
5	150.000	26.999	84.003	38.221	40.188	21.591	96.419	0.942	
6	150.000	27.000	81.296	38.253	40.183	21.564	96.496	0.941	
7	150.417	27.000	94.556	38.124	40.179	21.697	96.126	0.940	
8	150.000	27.000	77.826	38.295	40.176	21.529	96.596	0.939	
9	150.000	27.000	98.838	38.061	40.205	21.734	95.992	0.939	
10	150.000	26.652	97.105	38.130	40.187	21.683	96.100	0.939	
11	150.000	27.000	74.969	38.330	40.169	21.501	96.678	0.938	
12	150.000	26.986	102.907	38.023	40.207	21.77	95.877	0.935	
13	150.971	27.000	96.541	38.130	40.150	21.72	96.084	0.935	
14	150.000	26.297	102.575	38.130	40.173	21.697	96.009	0.932	
15	150.000	27.000	107.863	37.976	40.208	21.816	95.732	0.930	
16	150.000	27.000	63.155	38.488	40.136	21.376	97.016	0.928	
17	150.000	25.978	106.449	38.142	40.159	21.699	95.960	0.926	
18	150.000	27.000	112.885	37.932	40.207	21.861	95.587	0.925	
19	150.000	25.803	111.089	38.130	40.150	21.72	95.868	0.922	
20	150.000	26.507	67.220	38.494	40.125	21.381	96.955	0.922	
21	150.000	25.486	117.400	38.130	40.131	21.739	95.762	0.915	
22	150.000	25.369	119.958	38.130	40.123	21.747	95.719	0.912	
23	150.000	26.997	130.799	37.801	40.186	22.013	95.069	0.905	
24	150.000	27.000	46.341	38.739	40.070	21.191	97.496	0.903	
25	150.000	24.779	136.302	38.130	40.069	21.801	95.431	0.893	
26	150.000	24.718	138.529	38.130	40.061	21.809	95.390	0.891	
27	150.000	24.473	150.828	38.130	40.014	21.856	95.147	0.876	
28	150.000	22.834	84.051	38.679	40.012	21.309	96.969	0.873	
29	150.000	10.000	95.634	38.447	39.817	21.736	98.048	0.866	
30	150.002	10.000	96.385	38.448	39.817	21.735	98.050	0.866	
31	150.000	10.000	98.177	38.452	39.817	21.731	98.055	0.866	
32	150.000	10.000	91.383	38.439	39.816	21.745	98.036	0.866	
33	150.000	10.000	90.016	38.437	39.816	21.747	98.032	0.866	
34	150.000	10.064	95.741	38.454	39.817	21.729	98.044	0.866	
35	150.000	10.000	107.165	38.478	39.813	21.709	98.079	0.865	
36	150.120	10.000	93.997	38.448	39.811	21.741	98.046	0.865	
37	150.000	10.000	81.601	38.429	39.809	21.762	98.008	0.865	
38	150.158	10.000	103.521	38.473	39.807	21.72	98.073	0.864	

39	150.000	10.000	117.858	38.521	39.800	21.679	98.108	0.862	
40	150.000	24.352	163.964	38.130	39.958	21.912	94.859	0.860	
41	150.000	21.782	130.654	38.512	39.963	21.525	96.199	0.858	
42	150.000	10.000	64.560	38.437	39.779	21.784	97.959	0.857	
43	150.723	10.020	113.666	38.534	39.767	21.699	98.115	0.855	
44	150.000	11.416	76.393	38.586	39.798	21.616	97.946	0.849	
45	150.000	11.718	111.100	38.637	39.808	21.555	97.921	0.848	
46	150.000	12.281	93.245	38.655	39.815	21.53	97.888	0.846	
47	150.000	12.363	105.901	38.671	39.814	21.515	97.862	0.844	
48	150.000	10.000	46.581	38.481	39.724	21.795	97.904	0.843	
49	150.000	19.533	118.213	38.710	39.914	21.376	96.822	0.842	
50	150.000	12.712	86.104	38.690	39.813	21.497	97.872	0.842	
51	151.642	10.061	68.319	38.500	39.701	21.799	98.002	0.841	
52	150.000	12.396	117.301	38.697	39.803	21.5	97.838	0.841	
53	150.195	10.000	145.162	38.697	39.717	21.586	98.184	0.840	
54	150.000	13.415	97.942	38.729	39.822	21.449	97.784	0.839	
55	150.000	18.922	90.372	38.836	39.903	21.261	97.306	0.839	
56	150.000	13.344	114.602	38.739	39.812	21.449	97.732	0.837	
57	150.000	18.157	111.716	38.780	39.886	21.334	97.122	0.836	
58	150.000	14.076	102.674	38.760	39.827	21.413	97.701	0.836	
59	150.000	10.000	151.071	38.736	39.705	21.559	98.192	0.835	
60	150.000	14.351	94.116	38.778	39.829	21.393	97.718	0.835	
61	150.000	14.680	104.156	38.782	39.832	21.386	97.629	0.834	
62	150.000	14.869	103.358	38.788	39.835	21.377	97.614	0.833	
63	150.425	26.999	180.000	37.651	39.984	22.365	93.651	0.831	
64	150.000	10.000	22.429	38.598	39.612	21.79	97.828	0.814	
65	270.000	27.000	92.749	40.115	37.643	22.242	91.736	0.344	
66	270.000	27.000	92.028	40.114	37.643	22.243	91.744	0.344	
67	270.000	27.000	82.792	40.109	37.638	22.253	91.843	0.342	
68	270.000	10.000	87.306	39.425	37.597	22.978	93.240	0.342	
69	270.000	10.000	78.343	39.315	37.596	23.089	93.053	0.340	
70	270.000	27.000	76.027	40.112	37.630	22.258	91.915	0.339	
71	269.447	10.000	93.261	39.516	37.585	22.899	93.421	0.338	
72	270.000	10.316	98.022	39.620	37.582	22.798	93.446	0.335	
73	270.000	18.418	81.536	40.278	37.503	22.219	92.711	0.273	
74	270.000	18.514	83.795	40.297	37.504	22.199	92.715	0.273	

A: Ash content. FC: Fixed carbon. VM: Volatile matter. *: dried basis (moisture free).

Appendix F. HCS desirability Solutions

Number	Temperature	Pressure	Time	A*	FC*	VM*	Mass Yield	Desirability	Remark
1	**150.000**	**27.000**	**10.000**	**21.123**	**57.196**	**21.681**	**96.059**	**0.919**	**Selected**
2	150.000	27.000	10.710	21.127	57.193	21.68	96.056	0.918	
3	150.006	26.919	10.000	21.129	57.190	21.681	96.046	0.917	
4	150.000	27.000	11.629	21.132	57.189	21.679	96.052	0.917	
5	150.000	26.821	10.000	21.134	57.184	21.682	96.030	0.916	
6	150.000	27.000	12.320	21.136	57.187	21.677	96.048	0.916	
7	150.000	27.000	12.543	21.137	57.186	21.677	96.047	0.916	
8	150.650	27.000	10.001	21.152	57.160	21.688	96.045	0.915	
9	150.000	27.000	14.001	21.145	57.180	21.675	96.040	0.914	
10	150.000	26.629	10.000	21.146	57.172	21.682	95.998	0.913	
11	150.000	27.000	14.834	21.150	57.177	21.673	96.036	0.913	
12	150.000	26.567	10.002	21.149	57.168	21.683	95.988	0.913	
13	150.000	26.492	10.001	21.154	57.163	21.683	95.976	0.912	
14	150.000	27.000	16.184	21.157	57.171	21.672	96.030	0.911	
15	150.000	27.000	16.393	21.159	57.170	21.671	96.029	0.911	
16	151.436	27.000	10.001	21.187	57.117	21.696	96.027	0.910	
17	150.000	27.000	18.011	21.168	57.164	21.668	96.021	0.909	
18	150.000	27.000	19.712	21.177	57.157	21.666	96.013	0.907	
19	151.937	27.000	10.164	21.210	57.089	21.701	96.015	0.907	
20	150.000	26.144	10.000	21.175	57.140	21.685	95.919	0.907	
21	151.663	27.000	12.016	21.208	57.097	21.695	96.013	0.907	
22	150.000	27.000	20.932	21.184	57.152	21.664	96.007	0.906	
23	152.851	27.000	10.000	21.250	57.040	21.71	95.996	0.902	
24	150.000	26.997	25.551	21.209	57.133	21.658	95.984	0.901	
25	150.000	26.511	20.705	21.211	57.121	21.668	95.928	0.900	
26	153.450	27.000	10.000	21.276	57.007	21.717	95.983	0.899	
27	150.000	25.363	10.000	21.221	57.090	21.689	95.791	0.896	
28	150.000	25.094	10.000	21.237	57.072	21.691	95.746	0.892	
29	150.000	24.972	10.002	21.244	57.064	21.692	95.726	0.890	
30	155.253	27.000	10.000	21.356	56.908	21.736	95.942	0.888	
31	150.000	24.792	10.003	21.255	57.053	21.692	95.697	0.888	
32	150.000	26.977	36.514	21.271	57.088	21.641	95.928	0.887	
33	150.000	24.617	10.000	21.266	57.041	21.693	95.668	0.885	
34	150.000	27.000	43.889	21.310	57.060	21.63	95.896	0.879	
35	150.000	27.000	45.537	21.319	57.053	21.628	95.888	0.877	
36	157.143	27.000	10.002	21.440	56.804	21.756	95.900	0.877	
37	150.000	23.222	10.000	21.349	56.951	21.7	95.439	0.866	
38	150.000	22.770	10.000	21.376	56.921	21.703	95.365	0.859	
39	150.000	22.451	10.000	21.395	56.901	21.704	95.312	0.855	
40	150.000	27.000	74.335	21.477	56.938	21.585	95.749	0.843	
41	150.000	27.000	75.386	21.483	56.934	21.583	95.744	0.841	
42	150.000	27.000	84.614	21.533	56.897	21.57	95.700	0.830	
43	150.000	20.585	10.001	21.506	56.779	21.715	95.006	0.828	

44	150.000	27.000	99.449	21.615	56.837	21.548	95.628	0.812	
45	150.000	19.004	10.005	21.600	56.677	21.723	94.746	0.805	
46	150.000	17.946	10.000	21.664	56.608	21.728	94.573	0.789	
47	150.000	23.704	119.804	21.923	56.541	21.536	94.989	0.747	
48	150.000	13.273	10.000	21.942	56.305	21.753	93.805	0.717	
49	150.000	15.242	78.735	22.202	56.157	21.641	93.797	0.682	
50	150.000	11.606	101.137	22.542	55.831	21.627	93.092	0.610	

A: Ash content. FC: Fixed carbon. VM: Volatile matter. *: dried basis (moisture free).

Appendix G. HCB desirability Solutions

Number	SS	CT+CS	Temperature	Pressure	Time	A*	FC*	VM*	Mass yield	Desirability	Remark
1	**4.984**	**20.016**	**208.708**	**22.551**	**331.02**	**17.425**	**58.882**	**23.697**	**84.670**	**1.000**	**Selected**
2	10.543	14.457	222.387	22.712	320.24	21.673	57.839	20.488	79.667	1.000	
3	10.521	14.479	175.871	23.976	291.15	19.938	57.065	22.997	85.996	1.000	
4	10.182	14.818	167.926	26.799	340.37	15.457	58.868	25.675	87.747	1.000	
5	10.137	14.863	230.628	26.336	313.40	19.556	57.305	23.139	79.501	1.000	
6	9.991	15.009	153.838	25.090	326.49	18.985	58.394	22.621	89.389	1.000	
7	9.527	15.473	189.466	25.054	339.27	18.975	58.194	22.831	85.122	1.000	
8	9.877	15.123	230.270	25.777	319.86	20.151	57.348	22.501	79.742	1.000	
9	10.212	14.788	254.072	26.648	358.98	20.520	58.833	20.647	76.487	1.000	
10	10.549	14.451	245.222	25.832	307.29	21.663	57.238	21.099	77.041	1.000	
11	9.346	15.654	190.083	26.153	304.40	19.236	56.901	23.863	85.312	1.000	
12	10.837	14.163	214.728	24.124	336.82	19.483	58.718	21.799	80.674	1.000	
13	9.739	15.261	208.708	24.551	341.87	19.348	58.232	22.42	82.464	1.000	
14	10.438	14.562	206.083	21.914	336.75	21.112	58.515	20.373	81.845	1.000	
15	11.188	13.812	242.848	24.829	354.13	21.365	59.534	19.101	76.634	1.000	
16	11.482	13.518	217.016	24.392	327.64	20.858	58.654	20.488	79.795	1.000	
17	10.605	14.395	259.864	26.296	359.23	21.461	59.186	19.353	75.206	1.000	
18	10.332	14.668	238.866	24.342	357.89	20.594	59.009	20.397	78.011	1.000	
19	11.912	13.088	163.110	24.836	316.47	20.142	58.317	21.541	87.180	1.000	
20	11.448	13.552	162.591	24.844	283.01	20.102	56.893	23.005	87.368	1.000	
21	10.972	14.028	241.901	26.187	320.99	20.678	58.082	21.24	77.094	1.000	
22	10.193	14.807	209.034	21.821	338.23	21.379	58.405	20.216	81.643	1.000	
23	11.303	13.697	191.322	26.531	291.50	18.012	57.226	24.762	83.715	1.000	
24	10.441	14.559	262.753	26.854	359.09	21.485	59.004	19.511	75.102	1.000	
25	10.532	14.468	238.509	25.372	304.54	21.329	57.161	21.51	77.882	1.000	
26	10.643	14.357	210.314	25.492	359.09	16.833	59.522	23.645	81.686	1.000	
27	9.675	15.325	179.010	26.625	302.06	17.909	57.135	24.956	86.540	1.000	
28	11.369	13.631	198.181	22.255	358.81	21.199	59.882	18.919	82.333	1.000	
29	10.293	14.707	235.869	24.912	300.78	21.586	56.888	21.526	78.418	1.000	
30	11.336	13.664	167.412	23.440	322.21	20.279	58.471	21.25	86.691	1.000	
31	11.127	13.873	227.206	25.728	294.27	20.663	57.134	22.203	78.799	1.000	
32	10.846	14.154	187.370	26.756	304.70	16.649	57.662	25.689	84.667	1.000	
33	12.030	12.970	190.089	26.965	280.45	19.556	56.856	23.588	83.351	1.000	
34	11.624	13.376	161.428	24.272	333.48	19.617	59.022	21.361	87.548	1.000	
35	11.358	13.642	167.733	25.870	284.14	18.745	56.969	24.286	86.848	1.000	
36	9.480	15.520	155.435	25.366	298.65	20.702	57.201	22.097	89.421	1.000	
37	11.647	13.353	154.997	25.790	288.14	19.317	57.147	23.536	88.490	1.000	
38	10.379	14.621	204.960	24.926	293.62	19.434	56.910	23.656	82.391	1.000	

39	10.839	14.161	240.350	26.282	320.23	20.310	57.973	21.717	77.465	1.000	
40	10.489	14.511	219.678	22.817	315.93	21.494	57.666	20.84	80.084	1.000	
41	10.809	14.191	204.965	23.263	301.72	20.845	57.356	21.799	81.803	1.000	
42	11.444	13.556	212.387	26.484	335.77	17.890	59.073	23.037	80.802	1.000	
43	11.640	13.360	235.246	26.919	322.04	20.502	58.568	20.93	77.400	1.000	
44	10.099	14.901	196.433	23.306	335.64	19.671	58.375	21.954	83.569	1.000	
45	11.445	13.555	172.363	25.558	316.85	18.084	58.327	23.589	86.219	1.000	
46	11.350	13.650	209.511	25.736	283.46	20.030	56.822	23.148	81.002	1.000	
47	10.268	14.732	218.794	24.816	309.32	19.884	57.328	22.788	80.686	1.000	
48	10.203	14.797	224.766	25.466	323.87	19.346	57.778	22.876	80.089	1.000	
49	9.846	15.154	236.970	25.552	324.22	20.977	57.408	21.615	78.890	1.000	
50	9.543	15.457	186.902	25.219	340.08	18.719	58.260	23.021	85.458	1.000	
51	10.945	14.055	230.141	26.661	335.45	18.336	58.712	22.952	78.837	1.000	
52	10.492	14.508	263.665	26.758	359.38	21.684	59.059	19.257	74.905	1.000	
53	11.402	13.598	241.149	26.124	323.78	21.283	58.465	20.252	76.721	1.000	
54	10.947	14.053	260.830	26.929	351.65	21.475	59.218	19.307	74.733	1.000	
55	10.164	14.836	230.407	24.983	313.63	20.654	57.325	22.021	79.303	1.000	
56	10.698	14.302	161.788	22.427	356.43	20.098	59.697	20.205	87.716	1.000	
57	11.233	13.767	188.949	25.495	313.67	18.137	58.101	23.762	84.022	1.000	
58	11.623	13.377	207.519	23.504	341.01	21.354	59.258	19.388	80.939	1.000	
59	10.877	14.123	151.044	25.815	286.22	18.825	57.107	24.068	89.395	1.000	
60	9.504	15.496	158.916	25.185	335.78	19.774	58.412	21.814	88.977	1.000	
61	11.027	13.973	248.584	26.787	314.08	21.305	57.825	20.87	76.182	1.000	
62	10.933	14.067	219.017	23.027	327.75	21.259	58.359	20.382	79.823	1.000	
63	10.901	14.099	196.040	23.153	287.65	21.131	56.868	22.001	82.885	1.000	
64	11.651	13.349	214.376	26.457	311.51	19.422	58.121	22.457	80.245	1.000	
65	10.076	14.924	162.360	25.367	285.42	19.399	56.870	23.731	88.224	1.000	
66	9.657	15.343	214.357	24.991	339.14	19.518	58.011	22.471	81.880	1.000	
67	10.266	14.734	197.763	22.965	327.36	20.109	58.150	21.741	83.208	1.000	
68	10.855	14.145	182.376	21.269	333.97	21.703	58.723	19.574	84.630	1.000	
69	12.200	12.800	201.211	26.432	291.43	20.926	57.349	21.725	81.572	1.000	
70	10.360	14.640	159.164	21.955	336.67	21.534	58.837	19.629	88.097	1.000	
71	10.433	14.567	235.907	25.950	335.34	19.461	58.289	22.25	78.484	1.000	
72	9.995	15.005	258.589	26.755	355.62	21.632	58.447	19.921	76.167	1.000	
73	10.021	14.979	175.182	23.530	300.38	20.516	57.265	22.219	86.350	1.000	
74	10.271	14.729	248.538	25.525	359.19	20.680	58.936	20.384	76.980	1.000	
75	11.053	13.947	203.937	26.472	328.42	16.867	58.607	24.526	82.276	1.000	
76	9.513	15.487	213.215	26.059	318.21	19.387	57.199	23.414	82.291	1.000	
77	10.009	14.991	233.896	23.149	351.70	21.706	58.542	19.752	78.800	1.000	
78	12.189	12.811	160.129	26.249	297.94	19.751	57.540	22.709	87.587	1.000	

79	11.253	13.747	188.927	25.079	302.59	18.999	57.634	23.367	83.916	1.000	
80	11.294	13.706	238.441	26.703	300.11	21.004	57.445	21.551	77.221	1.000	
81	10.422	14.578	258.955	26.651	355.66	21.191	58.882	19.927	75.591	1.000	
82	12.206	12.794	217.847	26.282	329.88	21.511	59.123	19.366	79.290	1.000	
83	10.036	14.964	175.247	23.979	323.98	19.374	58.119	22.507	86.435	1.000	
84	10.554	14.446	194.500	23.996	355.72	17.956	59.414	22.63	83.642	1.000	
85	11.496	13.504	172.618	25.990	356.25	16.296	60.022	23.682	86.357	1.000	
86	9.670	15.330	244.380	26.204	333.54	21.476	57.499	21.025	78.248	1.000	
87	10.960	14.040	227.858	26.163	335.18	18.641	58.709	22.65	79.061	1.000	
88	11.222	13.778	261.260	26.954	359.98	21.613	59.806	18.581	74.368	1.000	
89	10.338	14.662	156.640	22.304	324.06	21.619	58.383	19.998	88.465	1.000	
90	10.622	14.378	267.603	27.000	360.00	22.077	59.193	18.73	74.254	0.997	
91	10.716	14.284	269.850	27.000	360.00	22.477	59.276	18.247	73.833	0.994	
92	10.522	14.478	241.362	27.000	268.50	21.714	55.785	22.501	77.669	0.993	
93	11.110	13.890	236.462	27.000	260.93	21.713	55.769	22.518	77.621	0.993	
94	10.998	14.002	269.997	27.000	291.50	25.214	56.803	17.983	73.253	0.970	
95	12.329	12.671	150.001	27.000	196.87	22.363	52.899	24.738	88.628	0.967	
96	10.251	14.749	219.461	27.000	157.22	23.592	51.722	24.686	80.653	0.948	
97	4.658	20.342	191.874	10.000	68.98	24.930	51.002	24.068	87.246	0.932	
98	4.664	20.336	192.740	10.000	69.93	24.922	50.991	24.087	87.158	0.932	
99	4.610	20.390	190.752	10.000	67.81	24.940	51.012	24.048	87.399	0.932	
100	4.745	20.255	194.240	10.000	71.48	24.919	50.980	24.101	86.935	0.932	

A: Ash content. FC: Fixed carbon. VM: Volatile matter. *: dried basis (moisture free).

Appendix H. Organic compounds in filtrate from NEV absorption by HCT

Initial solution from the Mixture (HCT +Nevirapine)				Final solution after absorption (HCT +Nevirapine)		
Peak	Retention time (minutes)	Organic compound -Name	Conc (%)	Retention time (minutes)	Organic compound Name	Conc (%)
1	3.324	Cyclotrisiloxane, hexamethyl- (CAS)	2.7	10.581	l,3 -DIPHENYL-1,3,5,5-TETRAMETHY	2.23
2	3.39	CYCWPROPANECARBOXAIDEHYI	1.56	11.151	2-(l '-Fluoro-2'-oxo-2'-heptyl) -2- (perlluoro	5.15
3	3.687	2-Furanmethanol	5.27	11.564	Glycine, N-methyl-N-(1-oxododecyl)	6.37
4	3.777	2-Furanmethanol	3.75	11.738	Hexadecanoic acid (CAS)	67.25
5	4.329	2-Hexanol, 3-methyl- {CAS)	13.45	14.467	l l -Cyclopropyl-4-methyl-5,11-dihydro-6H	11.89
6	4.665	4-OXOPENTAL	1.53	13.61	Ethyl homovanillate, TMS derivative	1.8
7	4.741	Cyclotetrasiloxane, octamethyl- (CAS)	5.31	13.721	Desmosterol, TMS derivative	2.1
8	5.115	2-FURANOL, TETRAHYDRO	7.87	13.835	1,2-Benzenediol,3,5-bis (l, l -dimethylethy)	3.21
9	5.803	Di-(3-methylbutyl) ether	2.08			
10	5.986	anhydro - sugar	2			
11	6.065	Cyclopentasiloxane, decamethyl- (CAS)	1.31			
12	6.186	5,6-Dihydro-2H-pyran-2-one	2.4			
13	6.443	2,3-Dihydro-3,5-dihydroxy-6-methyl-4H-1	3.33			
14	6.845	2(3H) -Furanone, dihydro-4-hydroxy	1.85			
15	7.205	N-Ethoxyisobuten-3-imine	0.66			
16	7.355	5-Hydroxymethylfurfural	1.03			
17	7.466	Cyclohexasiloxane, dodecamethyl-	1.64			
18	7.816	2,8,4,6-{Epoxyethanediylidenoxy)[l,3] dio	0.79			
19	7.916	1-UNDECENE, 8-METHYL-	1.24			
20	8.445	Butanoic acid, 3-hydroxy-, butyl ester	0.74			
21	8.59	3-Pentanol, 2,3,4-trimethyl-	0.63			
22	8.705	3-Isopropoxy-l, l, l,7,7,7-hexamethyl-3,5	0.24			
23	8.775	Succinic acid, hex-4-yn-3-yl 3,3-dimethyl	0.36			
24	9.097	UNDECANE, 6,6-DIDEUTERO	0.13			
25	9.793	Benzeneacetic acid, alpha.,3,4-tris[(trimet	0.12			
26	9.948	1,2,3,4-Tetrahydro-pyridine-2,5-dicarbonil	0.11			
27	11.576	3-Butoxy-1,1,1,7,7,7-hexamethyl-3,5,5	0.08			

28	11.87	9H-Purin-6-amine, 9-. Beta. -D-psicofurano	0.1	
29	11.945	TRANS-DIDEUTERIOXY-CYCW PENI	0.08	
30	12.077	Methyl 2-(2-(2-butoxyethoxy) ethoxy)acet	0.13	
31	12.215	Benzene, I -methyl-4-(4-morpholyl) etheny	0.16	
32	12.325	Cyclopropanetetradecanoic acid, 2-octyl	0.14	
33	12.375	5-Thiatricyclo [4.I .0.0(2,4)] heptane	0.11	
34	12.575	Methylmalonic acid	0.35	
35	12.688	4-[5-(3,4-Dihydroxyphenyl) -1,2,3,4-tetraz	0.13	
36	13.035	Benzeneacetic acid, alpha.,3,4-tris [(trimethyl)]	1.17	
37	13.67	1,3,4-Thiadiazole-3-carbothioic acid, 2,3	3.28	
38	14.115	Indole, 6-methyl-2-(2-pyridyl) -	4.09	
39	14.366	11-Cyclopropyl-4-methyl-5, l l -dihydro-61	26.17	
40	16.015	N-Tridecanoic acid,methyl(tetramethylene)	0.11	
41	17.36	1,2-Benzenedicarboxylic acid, bis (2-ethyll	0.11	
42	18.311	3-METHYLETHER OF DOPAMINE -T	0.08	
43	19.128	Silane, trimethyl[5-methyl-2-(1 -methyleth)	0.33	
44	20.99	2-Chloro-5-iodobenzarnide	0.21	
45	21.44	Butane, 1,4-bis(methylthio)- (CAS)	0.08	
46	22.008	CIS-1,3-DIDEUTEROMETHOXYCYCL	0.16	
47	22.385	1-(I -Hydroxy- I-methylethyl) -3-methoxyn	0.25	
48	23.215	1,4-Bis(methylsulfinyl)piperazine	0.16	
49	23.68	1-n-Hexadecyloxyl-1-silacyclobutyl	0.34	
50	24.619	5-Bromo-8-(2-hydroxy-1-naphthymethylene	0.08	
			100	

Conc: concentration

Appendix I. Organic compounds in filtrate from NEV absorption by HCS

Initial solution from the Mixture (HCS+ Nevirapine)				Final solution after absorption (HCS +Nevirapine)		
Peak	Retention Time (minutes)	Organic compound Name	Conc (%)	Retention Time (minutes)	Organic compound Name	Conc (%)
1	3.11	Cyclopropanecruboxamide, N-n-heptyl	0.08	3.29	2-Propanone, 1-hydroxy-(CAS)	2.39
2	3.145	3-Ethoxy-1,1,1,5,5,5-hexamethyl-3-(trimethyl)	0.12	3.339	Cyclotrisiloxane, hexamethyl- (CAS)	1.03
3	3.215	Methoxyacetic acid, 6-ethyl-3-octyl ester	0.1	4.181	Propanoic acid, 2-hydroxy- (CAS)	46.66
4	3.325	Cyclotrisiloxane, hexamethyl- (CAS)	1.2	4.245	Methacrylic anhydride	6.44
5	3.398	Cyclotrisiloxane, hexamethyl- (CAS)	3.58	4.373	6-0xa-bicyclo [3.1.0] hexan-3-one·	12.42
6	3.775	2-Furanrnethanol (CAS)	2.45	4.697	Hexane, 3-bromo- (CAS)	2.12
7	3.861	2-Furanrnethanol (CAS)	3.03	4.795	Cyclotetrasiloxane, octamethyl- (CAS)	5.49
8	4.409	2-Hexanol, 3-rnethyl- (CAS)	13.08	4.895	PENTANOIC ACID, 2-HYDROXY-4-Ml	1.17
9	4.771	Cyclotetrasiloxane, octamethyl- (CAS)	5.71	5.115	2-BlITENE-1,4-DIOL	3.14
10	4.98	1,3-Diox ane (CAS)	2.59	5.272	3-Methylcyclopentane-1,2-dione	1.46
11	5.236	Pentane, 2-chloro- (CAS)	4.81	5.809	2-Funmcarboxylic acid, methyl ester (CM	1
12	5.38	Octane, 1-rnethoxy-	1.31	5.899	anhydro - sugar	6.12
13	5.518	1,2,3-Propanetriol (CAS)	3.3	6.341	4H-Pyran-4-one, 2,3-dihydro-3,5-dihydro	7.69
14	5.723	2-Propenoic acid, 2-rnethyl-, 3-rnethylbul:)	2.69	7.325	1,2-Diazabicyclo [2.2.2] octan-3-one,2-hy<	1.38
15	5.995	anhydro - sugar	3.15	7.47	CYCWHEXAS LOXANE, DODECAMJ	1.49
16	6.108	Cyclopentasiloxane, decamethyl- (CAS)	4.79			
17	6.415	4H-Pyran-4-one, 2,3-dihydro-3,5-dihydro	2.44			
18	6.62	1,4-Dioxane-2,5-dione, 3,6-dimethyl- (CA	0.96			
19	6.811	2(3H) -Furanone, dihydro-4-hydroxy-	3.66			
20	7.11	3-(Methylthio)pent-4-yn-1-ol	0.5			
21	7.31	2(3H) -Furanone, 5-butyldihydro- (CAS)	1.75			
22	7.48	Cyclohexasiloxane, dodecamethyl-	1.68			
23	7.779	METHYL 3-METHYL-4-PENTENOATI	1.8			
24	8.017	Propanoic acid, 2-rnethyl-, 2-rnethylpropy	0.89			
25	8.14	Hexanoic acid, 1-rnethyloctyl ester (CAS)	0.46			
26	8.467	Oxirane, [(tetradecyloxy)rnethyl]	1.42			

27	8.6	4-(2-Methyl-2-propenoxy) butanoic acid	0.68	
28	8.71	3-Isopropoxy-l, l, 1,7,7,7-hexamethyl-3,5	0.4	
29	8.82	Octadecane (CAS)	0.12	
30	9.107	3-Pentanol, 2,3,4-trimethyl- (CAS)	1.76	
31	9.47	Nonadecane, 2-rnethyl- (CAS)	0.15	
32	9.59	Ethanediamine, N, N'-bis(2-aminoethyl)	0.41	
33	9.77	Lyxitol, 1-0-decyl-	1.17	
34	10.101	Tridecane, 1-iodo- (CAS)	0.76	
35	10.689	1-Iodo-2-rnethylundecane	0.22	
36	11.027	(+) -Thujan-3-spiro-2'-thiazolidine-4-crubo	0.21	
37	11.25	Ethanol, 2-(dodecyloxy)- (CAS)	0.08	
38	11.48	Dodecanoic acid, 2-butoxyethyl ester	0.25	
39	11.783	Hexadecane (CAS)	0.06	
40	12.034	D-Glucofuranose, pentaacetate (CAS)	0.07	
41	12.67	benzoic acid, 4-[[(trirnethylsilyl)oxy]rneth	0.15	
42	12.86	7,8,17,18-Tetrahydrodibenzo[bj] [1,6,9,1]	0.14	
43	13.033	2'-Deoxyguanosine, tris(trirnethylsilyl)	0.19	
44	13.24	Eicosyl nonyl ether	0.04	
45	13.35	(7R,8R) -cis-anti-cis-Tricyclo[7.3.0.0(2,6)	0.05	
46	14.355	11-Cyclopropyl-4-rnethyl-5,11-dihydro-61	25.12	
47	14.78	dimethyl 4,5-dimethoxybenzene-1,3-dicar	0.05	
48	16.118	(1-Ethylpyrrolidin-3-yl) methanamine	0.06	
49	21.912	2-Chloro-3-rnethyhnaleic anhydride	0.07	
50	22.171	1,3-benzenedisulfonic acid, 4-methyl	0.24	
			100	

Conc: concentration

Appendix J. Organic compounds in filtrate from LAM absorption by HCT

Initial solution from the Mixture (HCT+ Lamivudine)				Final solution after absorption (HCT+Lamivudine)		
Peak	Retention Time (minutes)	Organic compound Name	Conc (%)	Retention Time (minutes)	Organic compound Name	Conc (%)
1	3.425	Cyclotricyloxane, hexamethyl-(CAS)	1.3	3.812	2-Fmanmethanol (CAS)	9.36
2	3.475	1H - 1,4-Diazepine, hexahydro-1,4-dinitros	0.67	3.913	2-Fmanmethanol (CAS)	3.91
3	3.767	2-Heptanol (CAS)	8.76	4.437	2-Heptanol (CAS)	14.79
4	4.665	2-Furanmethanol	5.43	5.07	2-FURANMETHAN OL	3.62
5	4.822	Decane,4-methyl-(CAS)	5.39	5.19	Ethanol, 2-(cyclohexylamino)-(CAS)	4.53
6	5.297	Bezen, (1-methylpropyl) -(CAS)	3.46	5.47	2-Propanamine, N-ethyl-N-nitroso- (CA	2.87
7	5.651	Decane,2-methyl	3.47	6.115	3-Methyl-l ,1-cyclobutanedicarboxylic a	6.58
8	5.822	Undecane(CAS)	1.46	6.481	4H-Pyran-4-one, 2,3-dihydro-3,5-dihydi	1.93
9	6.056	2-Decenoic acid, methyl esther, (E) -(CAS)	1.94	6.799	2(3H) -FW1111one, dihydro-4-hydroxy	4.66
10	6.148	2-Furancarboxylic acid, 2,2-dimethylprop	3.18	7.817	2-Hexenoic acid, methyl ester, (E)- (CA	47.75
11	6.549	Undecane, 5-methyl-(CAS)	2.91			
12	6.748	Dodecane(CAS)	2.37			
13	6.999	2(3H) -Furanone, dihydro-4-hydroxy	3.42			
14	7.381	Tetradecane(CAS)	4.03			
15	7.773	Hexadecane(CAS)	0.64			
16	7.816	Tetradecane(CAS)	6.01			
17	8.821	Tridecane,4-methyl	3.15			
18	9.47	HEPTADECANE	1.52			
19	9.775	Hexadecane(CAS)	1.61			
20	10.095	Pentadecane,2,6,10-trimethyl	1.43			
21	10.373	Nonadecane(CAS)	2.03			
22	10.941	Pentadecane,2,6,10-trimethyl	0.84			
23	11.248	Hexadecane	0.58			
24	11.495	Nonadecane(CAS)	0.25			
25	11.586	Decyl heptyl ether	0.26			
26	11.684	3,3-Dimethyl-1-(5-phenyl-2-tetrahydrofur	0.13			
27	11.788	[3-(2,2-Dichlorovinyl) -2,2-dimethylcyclo]	0.66			
28	12.296	Nonadecane(CAS)	0.52			
29	12.499	Heptacosane (CAS)	0.95			
30	13.079	Oxalic acid, allyl undecyl esther	10.8			
31	13.948	3-Methyl-4-(phenylthio)-2-prop-2-enyl-2	1.03			

32	14.37	Stearic acid,3-(octadecyloxy)propyl esther	19.04	
33	15.82	11-Cyclopropyl-4-methyl-5,11-dihydro-61	0.04	
34	16.093	5-Bromovaleric acid, hex-4-yn-3-yl esther	0.03	
35	16.27	tert-Butyldimethylsilyl 2,3-dimethylbenzo	0	
36	16.345	4,5,6-TRICHLORO-3-PYRIDAZINECA	0.01	
37	16.57	Benzoic acid,2,3,6-trichloro-(CAS)	0.01	
38	17.02	11-BROMO-1,1-DIDEUTERIOUNDEC	0.05	
39	17.52	9,10-secocholesta-5,7,10(19) -triene-3,25	0.05	
40	17.845	2-(Hydroxymethyl)-2,4-diphenyl-4a,10a-c	0.05	
41	17.945	4-(2-Carboxyvinyl) -3-hydroxybenzoic acid	0.01	
42	18.12	Propiolic acid, 3-(1-hydroxy-2-isopropyl)	0.05	
43	18.42	Silane,methylvinyl(hept-3-yloxy)tridecyl	0.06	
44	18.645	3,3-Dietoxy-1,1,1,5,5,5-hexamethyltrisil	0.01	
45	18.925	14-oxabicyclo [10.3.0] pentadecane,2-chl)	0.07	
46	19.195	Chlorthiophos oxygen analog	0.01	
47	19.395	naphth[l ,8-de]-1,3-oxazine-6-sulfonyl chl	0.01	
48	19.47	Cis-1,4-Cyclohexanedicarboxamide	0.01	
49	19.545	N-Octadecyl-3-hydroxypropanamide	0.01	
50	19.697	Benzoic acid, 2-[(2-aminophenyl) [3-(dimethyl)	0.02	
51	19.995	3-(1-Phenyl-2,3-dihydro-l H-isoindol-2-yl	0.03	
52	20.963	N-(4,4-DIDEUTERI0-4 -PHENYL-BUT	0.07	
53	21.27	(+-) -5-(1-Acetoxy-l -methylethyl) -2-methyl	0.03	
54	21.524	2-(6-ETHYL-THIEN0[2,3- D] PYRIMID	0.02	
55	21.721	(4S,5R) -4-Benzyl-2,2-dimethyl-1,3-dioxa	0.01	
56	22.12	Ethanone, 1-[4-[4-(2-hydroxyethyl) - 1-pip	0.06	
57	22.37	4- (N'-NITROMETHYLENE-HYDRAZIL	0.01	
58	23.196	5-Chloroisatin, TMS derivative	0.02	
59	23.345	d-Gluco-d-gulo-heptose, diethyl mercapta	0.02	
60	23.62	1-(2,3-DIHYDRO-lH-INDEN-2-YLCAF	0.04	

	100	

Conc: concentration

Appendix K. Organic compounds in filtrate from LAM absorption by HCS

Initial solution from the Mixture (HCS+ Lamivudine)				Final solution after absorption (HCS+Lamivudine)		
Peak	Retention time (minutes)	Organic compound Name	Conc (%)	Retention Time (minutes)	Organic compound Name	Conc (%)
1	3.175	DECANE	0.19	4.611	DECANE	2.14
2	3.475	Nonane (CAS)	0.18	5.251	Decane, 2-methyl-	3.01
3	3.55	Nonane (CAS)	0.34	5.317	Decane, 3-methyl-	1.73
4	3.665	UNDECANE, 5,6-DIMETHYL	0.52	5.598	Undecane (CAS)	7.67
5	3.863	Carlxmic acid, octyl propyl ester	0.91	6.105	Dodecane	2.17
6	4.205	Decane, 2,5,6-trimethyl	0.94	6.181	Undecane, 2-methyl- (CAS)	2.03
7	4.362	OCTANE, 2,2,6-TRIMETHYL	1.87	6.241	Undecane, 3-methyl-	1.48
8	4.607	DECANE	3.67	6.497	Dodecane	19.51
9	4.774	Benzene, (1-methylpropyl)	3.76	6.946	Tridecane (CAS)	1.78
10	4.905	Decane, 2,2,6-trimethyl	3.07	7.025	Dodecane, 2-methyl- (CAS)	1.35
11	5.229	Hexadecane, 1-cWoro- (CAS)	7	7.083	Dodecane, 3-methyl- (CAS)	1.48
12	5.6	Dodecane (CAS)	8.59	7.317	Tridecane (CAS)	7.27
13	5.753	Butyric acid, 2-phenyl-, dec-2-yl ester	2.87	10.235	Hexanoic acid, heptadecyl ester	37.85
14	5.999	Pentafluoropropionic acid, decyl ester	0.8	7.705	Heptadecane, 2,6-dimethyl-	1.57
15	6.181	Benzene, (2,3-dimethyldecyl)	6.44	8.78	Pentadecane (CAS)	4.16
16	6.502	Dodecane (CAS)	6.58	8.071	Tetradecane (CAS)	4.8
17	6.748	Benzene, (2,3-dimethyldecyl)	0.36			
18	6.948	Undecane, 3,7-dimethyl	3.09			
19	6.992	Dodecane, 4-methyl	1.93			
20	7.085	Dodecane, 3-methyl- (CAS)	1.9			
21	7.325	Tetradecane (CAS)	5.2			
22	7.405	Bicyclo[4.2.0]octa-l,3,5-triene, 7-butyl	1.57			
23	7.616	Benzene, (2,2-dimethylcyclopentyl) - (CM	1.19			
24	7.708	Nonadecane, 1-cWoro	1.54			
25	7.766	2,3-Dimethyldodecane	2.92			
26	8.079	Tetradecane (CAS)	4.16			
27	8.185	I 0-Heneicosene, I I-phenyl- (CAS)	0.67			
28	8.305	Dodecane, 2,6,10-trimethyl- (CAS)	0.64			
29	8.419	5-Ethyldecane	1.41			
30	8.485	Tetradecane, 4-methyl- (CAS)	1.78			
31	8.781	Pentadecane (CAS)	3.56			
32	8.967	2-N-DECYL-2,3-DIHYDROINDENE	0.62			
33	9.085	Pentadecane, 7-methyl	1.15			
34	9.165	1-Heptadecanol (CAS)	0.97			
35	9.328	Undecane, 3-phenethyl-1-phenyl- (CAS)	0.37			

36	9.441	Hexadecane (CAS)	2.4	
37	9.726	Hexadecane, 7-methyl	1.12	
38	9.805	2-Amino-N-(2'-aminobenzoyl) benzamide	0.62	
39	9.965	Benzene, (2,3-dimethyldecyl) - (CAS)	0.21	
40	10.065	Heptadecane (CAS)	1.69	
41	10.204	Behenyl chloride	0.08	
42	10.235	Hexanoic acid, heptadecyl ester	0.05	
43	10.327	Heptadecane, 7-methyl	0.62	
44	10.407	Heptadecane, 4-methyl- (CAS)	0.52	
45	10.657	Nonadecane (CAS)	1.66	
46	10.897	NONADECA.NIl,	0.5	
47	10.985	Heneicosane, 11-(1-ethylpropyl)	0.22	
48	11.065	Octadecane, 3-methyl- (CAS)	0.2	
49	11220	Nonadecane (CAS)	1.08	
50	11.295	N-Nona decane	0.22	
51	11.443	HEXADECANE, 2,6,10,14-TETRAMET	0.3	
52	11.495	Oxalic acid, hexadecyl isohexyl ester	0.06	
53	11.604	Jsopropyl octadecyl ether	0.63	
54	11.756	NONADECANE	0.85	
55	11.855	1-Heneicosanol	0.17	
56	11.964	Eicosane	0.29	
57	12.056	Heneicosane, 11-(1-ethylp ropyl) -(CAS)	0.11	
58	12.125	Eicosane, 3-methyl- (CAS)	0.15	
59	12.265	NONADECANE	0.71	
60	12.365	Dodecane, I -cyclopentyl-4-(3-cyclopentylJ	0.05	
61	12.458	Eicosane	0.13	
62	12.554	Trans-9-0ctadecenoic acid, pentyl ester	0.26	
63	12.622	3-Methylheneicosane	0.16	
64	12.756	Docosane (CAS)	0.53	
65	12.935	Heneicosane (CAS)	0.08	
66	13.233	TETRACOSANE	0.44	
67	13.412	Eicosane	0.14	
68	13.595	HENTRIACONTANE	0.08	
69	13.734	Tetratetracontane (CAS)	0.28	
70	14.065	Dotriacontane (CAS)	0.04	
71	14.284	CELIOONIOL, DEOXY	0.16	
72	14.489	Pentatriacontane (CAS)	0.06	
73	14.911	CELIDONIOL, DEOXY	0.09	
74	15.638	Tetratetracontane	0.05	
75	17.558	Tetratetracontane (CAS)	0.05	
76	18.839	Tetratetracontane (CAS)	0.09	

77	20.42	Tetratetracontane (CAS)	0.09	
			100	

Conc: concentration

Appendix L. ANOVA for quadratic model of S_{BET} for the AC-HCT

Source	Sum of Squares	df	Mean Square	F-value	p-value	
Model	1.496E+05	5	29915.40	54.98	< 0.0001	Significant
A-Temperature	39856.35	1	39856.35	73.25	< 0.0001	
B-Activation Time	21322.85	1	21322.85	39.19	0.0004	
AB	1845.72	1	1845.72	3.39	0.1081	
A^2	3332.44	1	3332.44	6.12	0.0425	
B^2	83357.33	1	83357.33	153.21	< 0.0001	
Residual	3808.62	7	544.09			
Lack of Fit	3794.98	3	264.99	0.81	< 0.0001	Not significant
Pure Error	13.65	4	3.41			
Cor Total	1.534E+05	12				
R^2	0.9752					
Adjusted R^2	0.9574					
Predicted R^2	0.7640					
Adeq Precision	23.656					

df: - degree of freedom. Adeq. Precision: Adequate Precision. AC-HCT: Activated Carbon from Coal Tailing's Hydrochar

The **Predicted R^2** of 0.7640 is in reasonable agreement with the **Adjusted R^2** of 0.9574; i.e., the difference is less than 0.2. **Adeq Precision** measures the signal to noise ratio. A ratio greater than 4 is desirable. The ratio of 23.656 indicates an adequate signal. This model can be used to navigate the design space.

Appendix M. ANOVA for quadratic model of S_{BET} for the AC-HCS

Source	Sum of Squares	df	Mean Square	F-value	p-value	
Model	1.139E+05	5	22773.09	18.67	0.0006	Significant
A-Temperature	3020.09	1	3020.09	2.48	0.1596	
B-Activation Time	1479.65	1	1479.65	1.21	0.3071	
AB	769.80	1	769.80	0.6312	0.4530	
A^2	9681.97	1	9681.97	7.94	0.0259	
B^2	1.078E+05	1	1.078E+05	88.36	< 0.0001	
Residual	8537.51	7	1219.64			
Lack of Fit	844.77	3	281.59	0.1464	0.9268	Not significant
Pure Error	7692.74	4	1923.18			
Cor Total	1.224E+05	12				
R^2	0.9303					
Adjusted R^2	0.88804					
Predicted R^2	0.8518					
Adeq Precision	12.4285					

df: - degree of freedom. Adeq. Precision: Adequate Precision. AC-HCS: Activated Carbon from Coal Slurry's Hydrochar

The **Predicted R^2** of 0.8518 is in reasonable agreement with the **Adjusted R^2** of 0.8804; i.e., the difference is less than 0.2. A ratio greater than 4 is desirable. The ratio of 12.429 indicates an adequate signal. This model can be used to navigate the design space.

Appendix N. ANOVA for quadratic model of S_{BET} for the AC-HCB

Source	Sum of Squares	df	Mean Square	F-value	p-value	
Model	1.647E+05	5	32930.49	41.39	< 0.0001	significant
A-Temperature	47082.04	1	47082.04	59.17	0.0001	
B-Activation Time	1091.88	1	1091.88	1.37	0.2797	
AB	131.68	1	131.68	0.1655	0.6963	
A^2	83341.92	1	83341.92	104.74	< 0.0001	
B^2	77256.60	1	77256.60	97.10	< 0.0001	
Residual	5569.74	7	795.68			
Lack of Fit	296.35	3	98.78	0.0749	0.9703	Not significant
Pure Error	5273.39	4	1318.35			
Cor Total	1.702E+05	12				
R^2	0.9673					
Adjusted R^2	0.9439					
Predicted R^2	0.9370					
Adeq Precision	23.11					

df: - degree of freedom. Adeq. Precision: Adequate Precision. AC-HCB: Activated Carbon from coal discards and sewage sludge blend's hydrochar.

The **Predicted R^2** of 0.9370 is in reasonable agreement with the **Adjusted R^2** of 0.9439. The signal to noise ratio of 23.119 indicates an adequate signal. This model can be used to navigate the design space.

Appendix O. AC-HCT desirability Solutions

Number	Temperature	Activation Time	Carbon Yield	Specific surface	Pore volume	Desirability	
1	850.000	147.370	64.388	2021.910	1.892	0.985	Selected

Appendix P. AC-HCS desirability Solutions

Number	Temperature	Activation Time	Carbon Yield	Specific surface	Pore volume	Desirability	
1	**849.434**	**132.311**	**66.164**	**2301.383**	**1.916**	**1.000**	**Selected**
2	849.466	132.786	66.164	2301.766	1.918	1.000	
3	849.533	139.186	66.164	2300.609	1.934	1.000	
4	850.000	135.000	66.164	2305.121	1.924	1.000	
5	849.297	136.828	66.164	2300.790	1.928	1.000	
6	849.635	135.506	66.164	2303.029	1.925	1.000	
7	849.834	134.655	66.164	2304.190	1.923	1.000	
8	849.202	133.120	66.164	2300.435	1.918	1.000	
9	849.902	139.482	66.164	2302.424	1.935	1.000	
10	849.182	136.017	66.164	2300.425	1.926	1.000	
11	849.317	134.256	66.164	2301.297	1.922	1.000	
12	849.147	137.617	66.164	2299.582	1.930	1.000	
13	849.898	134.040	66.164	2304.501	1.922	1.000	
14	849.061	136.638	66.164	2299.567	1.927	1.000	
15	849.806	133.093	66.164	2303.759	1.919	1.000	
16	849.753	138.041	66.164	2302.699	1.932	1.000	
17	849.723	137.564	66.164	2302.811	1.931	1.000	
18	849.212	135.656	66.164	2300.666	1.925	1.000	
19	849.996	138.907	66.164	2303.449	1.934	1.000	
20	849.523	130.466	66.164	2300.661	1.910	1.000	
21	849.668	133.771	66.164	2303.166	1.921	1.000	
22	849.225	131.780	66.164	2299.962	1.914	1.000	
23	849.644	138.718	66.164	2301.612	1.933	1.000	
24	849.265	135.306	66.164	2301.007	1.924	1.000	
25	849.690	134.094	66.164	2303.343	1.922	1.000	
26	849.182	132.205	66.164	2299.953	1.915	1.000	
27	849.035	134.530	66.164	2299.774	1.922	1.000	
28	849.975	137.085	66.164	2304.473	1.930	1.000	
29	849.341	139.320	66.164	2299.419	1.934	1.000	
30	849.677	136.584	66.164	2302.994	1.928	1.000	
31	849.633	131.696	66.164	2302.150	1.914	1.000	
32	849.176	132.671	66.164	2300.135	1.917	1.000	
33	848.997	135.354	66.164	2299.532	1.924	1.000	
34	849.771	141.439	66.164	2299.514	1.939	1.000	
35	849.551	136.203	66.164	2302.413	1.927	1.000	
36	849.309	134.680	66.164	2301.279	1.923	1.000	
37	849.372	137.927	66.164	2300.645	1.931	1.000	
38	849.158	138.160	66.164	2299.310	1.931	1.000	
39	849.970	140.924	66.164	2301.284	1.938	1.000	
40	848.972	133.611	66.164	2299.318	1.919	1.000	
41	849.382	133.313	66.164	2301.478	1.919	1.000	
42	849.451	135.370	66.164	2302.023	1.925	1.000	
43	849.618	133.389	66.164	2302.802	1.919	1.000	
44	849.965	131.022	66.164	2303.545	1.912	1.000	
45	849.545	140.257	66.164	2299.639	1.936	1.000	
46	849.163	133.918	66.164	2300.411	1.920	1.000	
47	849.702	140.927	66.164	2299.764	1.938	1.000	
48	849.249	136.479	66.164	2300.656	1.927	1.000	
49	849.985	131.455	66.164	2303.953	1.914	1.000	
50	848.978	136.079	66.164	2299.294	1.926	1.000	

51	849.921	132.608	66.164	2304.216	1.917	1.000	
52	849.088	134.862	66.164	2300.067	1.923	1.000	
53	849.744	139.922	66.164	2301.106	1.936	1.000	
54	850.000	144.000	66.164	2296.853	1.944	0.996	

Appendix Q. AC-HCB desirability Solutions

Number	Temperature	Activation Time	Specific surface	Pore volume	Carbon yield	Desirability	
1	**800.100**	**133.996**	**2243.575**	**1.302**	**63.478**	**1.000**	**Selected**
2	800.056	128.206	2243.089	1.299	63.994	1.000	
3	800.000	135.000	2244.973	1.302	63.381	1.000	
4	800.065	131.431	2244.312	1.301	63.707	1.000	
5	800.038	135.337	2244.164	1.302	63.352	1.000	
6	800.125	129.726	2242.749	1.300	63.863	1.000	
7	800.098	131.845	2243.788	1.301	63.672	1.000	
8	800.154	133.076	2242.802	1.301	63.565	1.000	
9	800.037	135.748	2243.966	1.302	63.315	1.000	
10	800.117	133.630	2243.362	1.302	63.513	1.000	
11	800.143	132.621	2243.036	1.301	63.605	1.000	
12	800.045	136.674	2243.234	1.301	63.231	1.000	
13	800.104	134.340	2243.408	1.302	63.447	1.000	
14	800.103	130.623	2243.473	1.301	63.782	1.000	
15	800.078	132.301	2244.173	1.301	63.630	1.000	
16	800.054	136.296	2243.332	1.302	63.266	1.000	
17	800.102	129.150	2242.868	1.300	63.913	1.000	
18	800.029	130.981	2244.842	1.301	63.745	1.000	
19	800.001	137.470	2243.396	1.301	63.155	1.000	
20	800.092	128.573	2242.696	1.299	63.963	1.000	
21	800.000	126.352	2242.490	1.297	64.154	1.000	
22	800.000	141.750	2238.325	1.298	62.757	0.990	
23	800.000	150.750	2217.755	1.284	61.897	0.945	
24	850.000	133.978	2067.896	1.393	58.344	0.612	
25	850.000	134.319	2067.885	1.393	58.326	0.612	
26	850.000	133.456	2067.875	1.394	58.371	0.612	
27	850.000	134.830	2067.833	1.392	58.300	0.612	
28	850.000	135.247	2067.758	1.391	58.278	0.612	
29	850.000	130.499	2066.908	1.398	58.522	0.610	

Appendix R. Chemical activation models' confirmation results

Material	Responses	Predicted Mean	Predicted Median	Std Dev	SE Pred	95% PI low	95% PI high
AC-HCT	Carbon Yield	68.35	68.35	2.63701	2.73655	62.2526	74.4474
	Specific surface	1941.09	1941.09	3.32	5.2566	1881.37	2000.82
	Pore volume	1.75747	1.75747	0.112332	0.121631	1.46986	2.04508
AC-HCS	Carbon Yield	68.35	68.35	2.53864	2.63447	60.4238	71.9039
	Specific surface	1941.09	1941.09	34.9234	42.091	2200.91	2399.96
	Pore volume	1.75747	1.75747	0.0942559	0.113601	1.64958	2.18683
AC-HCB	Carbon Yield	63.9937	63.9937	1.23665	1.50947	60.4243	67.563
	Specific surface	2243.09	2243.09	28.2078	34.4307	2161.67	2324.5
	Pore volume	1.29883	1.29883	0.0790575	0.0964985	1.07065	1.52701

Two-sided Confidence = 95%. Std. Dev: Standard deviation. SE: Standard error. PI: Probability interval